CHEMICAL PHYSICS

R. E. H. Clark
D. H. Reiter (Eds.)

Nuclear Fusion Research

Understanding Plasma-Surface Interactions

Springer

Springer Series in
CHEMICAL PHYSICS 78

Springer Series in

CHEMICAL PHYSICS

Series Editors: A. W. Castleman, Jr. J. P. Toennies W. Zinth

The purpose of this series is to provide comprehensive up-to-date monographs in both well established disciplines and emerging research areas within the broad fields of chemical physics and physical chemistry. The books deal with both fundamental science and applications, and may have either a theoretical or an experimental emphasis. They are aimed primarily at researchers and graduate students in chemical physics and related fields.

65 **Fluorescence Correlation Spectroscopy**
Theory and Applications
Editors: R. Rigler and E.S. Elson

66 **Ultrafast Phenomena XII**
Editors: T. Elsaesser, S. Mukamel, M.M. Murnane, and N.F. Scherer

67 **Single Molecule Spectroscopy**
Nobel Conference Lectures
Editors: R. Rigler, M. Orrit, T. Basché

68 **Nonequilibrium Nondissipative Thermodynamics**
With Application to Low-Pressure Diamond Synthesis
By J.-T. Wang

69 **Selective Spectroscopy of Single Molecules**
By I.S. Osad'ko

70 **Chemistry of Nanomolecular Systems**
Towards the Realization of Molecular Devices
Editors: T. Nakamura, T. Matsumoto, H. Tada, K.-I. Sugiura

71 **Ultrafast Phenomena XIII**
Editors: D. Miller, M.M. Murnane, N.R. Scherer, and A.M. Weiner

72 **Physical Chemistry of Polymer Rheology**
By J. Furukawa

73 **Organometallic Conjugation**
Structures, Reactions and Functions of d–d and d–π Conjugated Systems
Editors: A. Nakamura, N. Ueyama, and K. Yamaguchi

74 **Surface and Interface Analysis**
An Electrochmists Toolbox
By R. Holze

75 **Basic Principles in Applied Catalysis**
By M. Baerns

76 **The Chemical Bond**
A Fundamental Quantum-Mechanical Picture
By T. Shida

77 **Heterogeneous Kinetics**
Theory of Ziegler-Natta-Kaminsky Polymerization
By T. Keii

78 **Nuclear Fusion Research**
Understanding Plasma-Surface Interactions
Editors: R.E.H. Clark and D.H. Reiter

79 **Ultrafast Phenomena XIV**
Editors: T. Kobayashi, T. Okada, T. Kobayashi, K.A. Nelson, S. DeSilvestri

R.E.H. Clark D.H. Reiter (Eds.)

Nuclear Fusion Research

Understanding Plasma-Surface Interactions

With 210 Figures

Springer

Dr. Robert E.H. Clark
IAEA Atomic and Molecular Data Unit, Wagramstraße 5, P.O.Box 100, 1400 Vienna, Austria
E-mail: r.e.h.clark@iaea.org

Professor Dr. Detlev H. Reiter
Institut für Plasmaphysik, Forschungszentrum Jülich GmbH, 52425 Jülich, Germany
E-mail: d.reiter@fz-juelich.de

ISSN 0172-6218

ISBN 3-540-23038-6 Springer Berlin Heidelberg New York

Library of Congress Control Number: 2004115977

Typesetting: Camera-ready copy by the authors
Prodcution: PTP-Berlin, Protago-TEX-Production GmbH, Berlin
Cover concept: eStudio Calamar Steinen
Cover production: *design & production* GmbH, Heidelberg

Printed on acid-free paper SPIN: 11320036 57/3141/YU - 5 4 3 2 1 0

Preface

On October 28–31, 2002, a Technical Meeting of the International Atomic Energy Agency (IAEA) was held at the Institut für Plasmaphysik, Forschungszentrum Jülich, Germany. This was the fourth in a series of such meetings in the past 30 years, having the purpose of reviewing the current status of atomic, molecular, plasma–surface interactions and material data relevant to controlled nuclear fusion energy research and making recommendations on priorities for data generation activities over the next several years.

At all previous meetings in this series, including the last one about 10 years ago in Cadarache, France, there was a clear distinction possible between atomic and surface data needs for (magnetic) fusion research ("high temperature plasma physics") and the corresponding data needs for technical plasma applications ("low temperature plasma physics"). During this last decade the fast progress that has been achieved in plasma conditions (densities, temperatures, thermal insulation and discharge duration), in particular with magnetically confined plasmas, has led to major revisions of concepts for managing the plasma wall contact. This process was stimulated and significantly driven by the design work for the next generation device ITER ("The way" in Latin, formerly interpreted to stand for International Thermonuclear Experimental Reactor). In particular the plasma conditions near exposed parts of the furnace chamber are quite different in present experiments and designs from those of 10 years ago.

According to current knowledge near these target regions a low temperature plasma "cushion", partially recombining in the volume, has to be established, in a way self-sustained by the burning hot plasma core. This necessarily results in a chemical richness of fusion edge plasmas not encountered elsewhere in Nuclear Fusion research. It leads to a merging of the fields of low and high temperature plasma science and, consequently, to an even enlarged relevance for atomic, molecular and surface interaction data for fusion.

This latest meeting in 2002 and also the present volume make these trends very explicit, and are meant to provide a new basis for the nuclear and surface data activities for nuclear fusion research.

Over fifty top researchers were invited to participate in this meeting. Invited and contributed papers summarized the current state of data and suggested areas for which data needs exist or are foreseen. During the course of the meeting all participants were invited to take part in working groups on

the major categories of data and prepare detailed recommendations on the future perceived data needs in those areas. These recommendations have been collected in a Summary Report of the IAEA and will be used in formulating plans for research projects coordinated by the Atomic and Molecular Data Unit over the next several years.

This volume presents the work summarized by the invited speakers from the meeting, supplemented by some selected contributed papers. As such, it represents a thorough picture of the current status of databases and data needs for nuclear fusion research as well as an indication of the directions anticipated for data generation efforts over the next several years. Much of the data from the participants is already available electronically on the Internet. A number of databases have been established and links among databases are being developed with increasing levels of complexity.

This meeting could not have succeeded without the help of a large number of people. The editors thank U. Samm for his willingness to host this meeting at the Institut für Plasmaphysik and A. Pospieszczyk for his efforts on the organization of the meeting. Thanks also go to R.K. Janev for sharing his extensive experience from previous meetings on this series. Special thanks go to all of the invited speakers for the excellent presentations and the work that is represented in the contents of this volume.

Jülich, Wien *D. Reiter*
May 2004 *R.E.H. Clark*

Contents

List of Contributors

G. Bertschinger
Institut für Plasmaphysik
Forschungszentrum Jülich
EURATOM Association
Trilateral Euregio Cluster
52425 Jülich, Germany
g.bertschinger@fz-juelich.de

S. Brezinsek
Institut für Plasmaphysik
Forschungszentrum Jülich
EURATOM Association
Trilateral Euregio Cluster
52425 Jülich, Germany
s.brezinsek@fz-juelich.de

R.E.H. Clark
Atomic and Molecular Data Unit
International Atomic Energy Agency
Vienna, Austria
r.e.h.clark@iaea.org

J.W. Davis
University of Toronto
Institute for Aerospace Studies
4925 Dufferin St.
Toronto, ON M3H 5T6, Canada
jwdavis
@starfire.utias.utoronto.ca

R.P. Doerner
Center for Energy Research
University of California,
San Diego (USCD)
9500 Gilman Dr.
La Jolla, CA 92093-0417, USA
rdoerner@ucsd.edu

U. Fantz
Universität Augsburg
Institut für Physik
Lehrstuhl für Experimentelle
Plasmaphysik
Universitätsstr. 1
86135 Augsburg, Germany
fantz@physik.uni-augsburg.de

G. Federici
ITER JWS Garching Co-center
Boltzmannstrasse 2
85748 Garching, Germany
federig@ipp.mpg.de

S. Feil
Leopold-Franzens-
Universität Innsbruck
Institut für Ionenphysik
Technikerstr. 25
6020 Innsbruck, Austria

L. Feketeova
Leopold-Franzens-
Universität Innsbruck
Institut für Ionenphysik
Technikerstr. 25
6020 Innsbruck, Austria

K.B. Fournier
Lawrence Livermore National
Laboratory
Livermore, CA 94550, USA

K. Gluch
Leopold-Franzens-
Universität Innsbruck
Institut für Ionenphysik
Technikerstr. 25
6020 Innsbruck, Austria

Permanent address:
University Marie Curie Sklodowskiej
Mathematics and Informatics
Department of Physics
Lublin, Poland

A.A. Haasz
University of Toronto
Institute for Aerospace Studies
4925 Dufferin St.
Toronto, ON M3H 5T6, Canada
aahaasz@utias.utoronto.ca

S. Higashijima
Japan Atomic Energy
Research Institute
Naka-machi, Naka-gun
Ibaraki-ken 311-0193, Japan
higashij@naka.jaeri.go.jp

T. Hirai
Institut für Plasmaphysik
Forschungszentrum Jülich
Euratom Association
Trilateral Euregio Cluster
52425 Jülich, Germany

C. Hopf
Max-Planck-Institut
für Plasmaphysik
EURATOM Association
Boltzmannstr. 2
85748 Garching, Germany
Christian.Hopf@ipp.mpg.de

A. Huber
Institut für Plasmaphysik
Forschungszentrum Jülich
EURATOM Association
Trilateral Euregio Cluster
52425 Jülich, Germany

D. Humbert
Atomic and Molecular Data Unit
International Atomic Energy Agency
Vienna, Austria
d.humbert@iaea.org

W. Jacob
Max-Planck-Institut
für Plasmaphysik
EURATOM Association
Boltzmannstr. 2
85748 Garching, Germany
Wolfgang.Jacob@ipp.mpg.de

R.K. Janev
Forschungszentrum Jülich
Institut für Plasmaphysik
EURATOM Association
Trilateral Euregio Cluster
52425 Jülich, Germany
r.janev@fz-juelich.de

Macedonian Academy
of Sciences and Arts
1000 Skopje, Macedonia

T. Kato
Data and Planning Center
National Institute
for Fusion Science
Oroshi-cho, Toki
Gifu, 509-5292, Japan
takako@nifs.ac.jp

A. Kirschner
Institut für Plasmaphysik
Forschungszentrum Jülich
EURATOM Association
Trilateral Euregio Cluster
52425 Jülich, Germany
a.kirschner@fz-juelich.de

S. Kobayashi
Kyoto University
Uji-shi
Kyoto-fu 606-0011, Japan
shinkoba
@center.iae.kyoto-u.ac.jp

H. Kubo
Japan Atomic Energy
Research Institute
Naka-machi, Naka-gun
Ibaraki-ken 311-0193, Japan
kubo@naka.jaeri.go.jp

A. Loarte
European Fusion
Development Agreement
Close Support Unit Garching
Boltzmannstr. 2
85748 Garching, Germany
Alberto.Loarte@efda.org

T.D. Märk
Leopold-Franzens-
Universität Innsbruck
Institut für Ionenphysik
Technikerstr. 25
6020 Innsbruck, Austria
tilmann.maerk@uibk.ac.at

Comenius University
Department of Plasmaphysics
SK-84248 Bratislava
Slovak Republic

C. Mair
Leopold-Franzens-
Universität Innsbruck
Institut für Ionenphysik
Technikerstr. 25
6020 Innsbruck, Austria

O. Marchuk
Institut für Plasmaphysik
Forschungszentrum Jülich
EURATOM Association
Trilateral Euregio Cluster
52425 Jülich, Germany

E.S. Marmar
Plasma Science and Fusion Center
Massachusetts Institute
of Technology (MIT)
Massachusetts Avenue, NW17-174
Cambridge, MA 02139-4307, USA

S. Matt-Leubner
Leopold-Franzens-
Universität Innsbruck
Institut für Ionenphysik
Technikerstr. 25
6020 Innsbruck, Austria

M. Meier
Max-Planck-Institut
für Plasmaphysik
EURATOM Association
Boltzmannstr. 2
85748 Garching, Germany
Matthias.Meier@ipp.mpg.de

Ph. Mertens
Institut für Plasmaphysik
Forschungszentrum Jülich
EURATOM Association
Trilateral Euregio Cluster
52425 Jülich, Germany
ph.mertens@fz-juelich.de

I. Murakami
Data and Planning Center
National Institute
for Fusion Science
Oroshi-cho, Toki
Gifu, 509-5292, Japan

T. Nakano
Japan Atomic Energy
Research Institute
Naka-machi, Naka-gun
Ibaraki-ken 311-0193, Japan
nakanot
@fusion.naka.jaeri.go.jp

M.G. O'Mullane
University of Strathclyde
Department of Physics
and Applied Physics
107 Rottenrow
Glasgow G4 0NG, UK

V. Philipps
Institut für Plasmaphysik
Forschungszentrum Jülich
EURATOM Association
Trilateral Euregio Cluster
52425 Jülich, Germany

A. Pospieszczyk
Institut für Plasmaphysik
Forschungszentrum Jülich
EURATOM Association
Trilateral Euregio Cluster
52425 Jülich, Germany
a.pospieszczyk@fz-juelich.de

D. Reiter
Institut für Plasmaphysik
Forschungszentrum Jülich
EURATOM Association
Trilateral Euregio Cluster
52425 Jülich, Germany
d.reiter@fz-juelich.de

J.E. Rice
Plasma Science and Fusion Center
Massachusetts Institute
of Technology (MIT)
Massachusetts Avenue, NW17-174
Cambridge, MA 02139-4307, USA
rice@psfc.mit.edu

J. Roth
Max-Planck-Institut
für Plasmaphysik
EURATOM-Association
85748 Garching, Germany
roth@ipp.mpg.de

U.I. Safronova
Notre Dame University,
Notre Dame, IN 46556, USA

U. Samm
Institut für Plasmaphysik
Forschungszentrum Jülich
EURATOM Association
Trilateral Euregio Cluster
52425 Jülich, Germany
u.samm@fz-juelich.de

K. Sawada
Shinshu University
Nagano 380-8553, Japan
ksawada@gipwc.shinshu-u.ac.jp

P. Scheier
Leopold-Franzens-
Universität Innsbruck
Institut für Ionenphysik
Technikerstr. 25
6020 Innsbruck, Austria
Paul.Scheier@uibk.ac.at

W. Schustereder
Leopold-Franzens-
Universität Innsbruck
Institut für Ionenphysik
Technikerstr. 25
6020 Innsbruck, Austria

T. Schwarz-Selinger
Max-Planck-Institut
für Plasmaphysik
EURATOM Association
Boltzmannstr. 2
85748 Garching, Germany
Thomas.Schwarz-Selinger
@ipp.mpg.de

G. Sergienko
Institute for High Temperatures
"IVTAN"
Moscow, Russia

K. Shimizu
Japan Atomic Energy
Research Institute
Naka-machi, Naka-gun
Ibaraki-ken 311-0193, Japan
kshimizu@naka.jaeri.go.jp

C.H. Skinner
Princeton Plasma
Physics Laboratory
Princeton NJ, USA

A. Stamatovic
Leopold-Franzens-
Universität Innsbruck
Institut für Ionenphysik
Technikerstr. 25
6020 Innsbruck, Austria

Permanent address:
Faculty of Physics
PO Box 638
Yu-11001 Beograd, Yugoslavia

H.P. Summers
University of Strathclyde
Department of Physics
and Applied Physics
107 Rottenrow
Glasgow G4 0NG, UK
summers@phys.strath.ac.uk

H. Takenaga
Japan Atomic Energy
Research Institute
Naka-machi, Naka-gun
Ibaraki-ken 311-0193, Japan
takenaga@naka.jaeri.go.jp

T. Tepnual
Leopold-Franzens-
Universität Innsbruck
Institut für Ionenphysik
Technikerstr. 25
6020 Innsbruck, Austria

J.L. Terry
Plasma Science and Fusion Center
Massachusetts Institute
of Technology (MIT)
Massachusetts Avenue, NW17-174
Cambridge, MA 02139-4307, USA

E. Vietzke
Institut für Plasmaphysik
Forschungszentrum Jülich
EURATOM Association
Trilateral Euregio Cluster
52425 Jülich, Germany
e.vietzke@fz-juelich.de

W.L. Wiese
National Institute
of Standards and Technology
Gaithersburg, MD 20899 USA
wolfgang.wiese@nist.gov

Part I

Atomic and Surface Data Issues in Nuclear Fusion

1 Plasma–Wall Interaction: Status and Data Needs

U. Samm

1.1 Introduction

A complete design for a machine which will deliver energy from controlled thermo-nuclear reactions under quasi-stationary conditions is now ready for construction – the International Tokamak Experimental Reactor (ITER) [1, 2]. It is based on decades of fusion research resulting in a large data base obtained from many experimental magnetic fusion devices world wide. These data give rise to high confidence about the key objectives of ITER:
a long-pulse (about 8 min) burning fusion plasma at an energy amplification factor Q of at least 10 for the nominal plasma current of 15MA, the capability for investigating steady-state plasma operation, a range of plasma parameters which should allow $Q = 5$ and 'Hybrid' scenarios to extend the pulse length to periods of order 30 min, the integration of all relevant fusion technology and a design with significant flexibility to allow it to exploit progress made in various areas aiming at performance beyond today's expectations.

With ITER we will obtain the proof of principle that the magnetic confinement concept allows to gain energy from controlled thermonuclear fusion processes. It is seen as the last step before a first power plant will be built. On this way some problems have still to be solved, in particular, a power plant has to operate continuously for months, rather than the pulsed operation in present tokamaks or in ITER with 8 minutes burn time. For long time operation two requirements are crucial:

1. a stationary magnetic field configuration for plasma confinement and
2. a sufficient life time of wall components.

The first requirement can be achieved in a tokamak only by external current drive, the efficiency of which has to be proven in ITER. In contrast, this requirement is automatically fulfilled in a stellarator and would not be a problem, provided the larger stellarators still to be built show energy confinement properties at least as good as those in tokamaks.

The second requirement is common to all confinement devices and is related to the erosion and re-deposition processes of wall materials and to high heat loads, both determined by *plasma–wall interaction*. An overview on the key issues in this field is given in Sect. 1.2. The damage to wall components

due to neutron irradiation, in particular to structural materials, is not covered by this article.

In all power plant scenarios it is foreseen to exchange the most heavily loaded wall components several times during the life time of the whole plant. The shut down times required depend on the amount of components to be exchanged. The availability of a power plant will be largely determined by this need for refurbishments and its is just this availability

in addition to the investment cost of the plant which are the main parameters determining the cost of electricity, since the cost of fuel in a fusion reactor does not play any role [3, 4]. Thus, plasma–wall interaction is a key issue for the cost of electricity from a fusion power plant.

Plasma–wall interaction issues are in ITER less critical than for a power plant, moreover, ITER itself is an experiment for studying and optimizing related processes of plasma–wall interaction. However, also in ITER the availability of the experiment must be sufficient. Besides shut downs for enhancements or other progress-depending modifications, the life time of wall components should leave room enough for long term experimental campaigns. To achieve this at least for the first operational phase of ITER, a mix of wall materials has been chosen as is described in Sect. 1.3. It is anticipated that at a later stage another combination of materials is introduced optimized for the phase of full power operation. The optimization of wall materials and the plasma conditions related to it is a major task of ongoing research in the field of plasma–wall interaction.

The design solutions for heat and power exhaust depend on complex processes. For an optimized design it is not sufficient to have empirical data, like it is the case for energy confinement. The major processes have to be understood and only with extensive numerical modeling we may achieve reliable predictions about the life time of wall components and obtain tools for optimization of the wall and divertor design. In Sect. 1.4 the crucial processes in plasma–wall interaction are discussed, addressing the critical issues and the related needs for improved atomic and plasma-material interaction data.

1.2 Key Issues of Plasma–Wall Interaction

In this section the crucial problems of plasma–wall interaction are discussed, which need to be solved in order to achieve a high availability of a fusion power plant.

Most of the fusion power is leaving the plasma in form of neutrons depositing the heat deep in the vessel walls. This will cause after some time a certain damage of structural materials but will not effect directly the surface of plasma facing components. The *average heat load* to the inner wall surface via plasma–wall interaction is given by the plasma heating, i.e., alpha-particle heating and auxiliary heating. E.g., in ITER the total heating of 100 MW alpha particles and 50 MW auxiliary heating distributed onto the whole inner

wall ($680\,m^2$) leads to an average wall load of only $0.15\,MW/m^2$, which would be no problem for steady state operation if the magnetic field were not giving rise to a different distribution of heat: the plasma flow along those magnetic field lines intersecting wall elements inside the scrape-off layer (SOL) leads to a concentration of heat flow onto rather small areas. The thickness of the SOL is only about a centimeter defining, e.g., in ITER an area of heat load by plasma flow (wetted area) of only about $6\,m^2$. This can lead to peak loads of more than $20\,MW/m^2$. Such high heat load densities must be avoided. Today a maximum value of $10\,MW/m^2$ is considered to be acceptable for high heat flux components inside the SOL.

In addition to the average heat load also *transient loads* may be of importance. Such transient loads may occur with an off-normal event, such as a plasma current disruption or with regular short heat pulses typical for high confinement plasmas: the so called Edge Localized Modes (ELM). These ELMs are instabilities at the plasma edge, which appear above a critical high pressure gradient [5]. They partly expel the edge plasma energy content within less than a ms. The frequency at which these ELMs appear (1–30 Hz) and their magnitude (1%–8% of the plasma edge energy content) vary with other plasma parameters. During the heat pulse caused by ELMs the surface temperature should stay below the melt or sublimation threshold of the target material. From this condition one can derive a maximum of energy E being deposited on a certain area.

As important as high heat loads for the damage of the wall is the *erosion of wall materials* due to sputtering by plasma ions and fast neutrals as well as chemical reactions. These erosion processes take place even in case the heat load is rather low. The erosion yields (=eroded particles / impinging plasma particle or neutral) vary strongly between different materials, in particular, the high-Z materials like tungsten show yields which are orders of magnitude below those of low-Z materials like, e.g., graphite with an erosion yield of a few percent [6]. Nevertheless, a material like graphite is attractive for fusion machines, since it has excellent thermal properties and the impact of eroded carbon to the plasma properties is rather weak because of its small number of electrons.

Calculating the gross erosion of graphite leads to rather high values. However, a tokamak is nearly a closed system, i.e., essentially all eroded particles are *re-deposited* on the wall. Most of the eroded particles return even back to those areas from which they came. Therefore, the net-erosion yield is in general much lower than the gross-erosion, but still significant. A major aim of R&D in plasma–wall interaction is to develop scenarios with divertor plates showing an average re-deposition rate as close as possible to 100%.

On those areas with net-deposition the deposited particles form layers which may become a problem because

1. the layer can fall off as flakes after some time disturbing the plasma and
2. tritium can be retained in these layers in amounts which are beyond those allowed according to the license of the device [7].

There are large uncertainties about the *tritium retention* problem. The most pessimistic extrapolations based on data from co-deposition of tritium with carbon [8] conclude that the allowed maximum of 350 g of T retained in the vessel will be reached after only a few ITER discharges. This is seen as a genuine problem with graphite, whereas other candidate wall materials like W do not show such a strong effect of tritium retention. Therefore, already for ITER it is of paramount importance to clarify this problem and to verify that carbon as a wall material is acceptable at all for tritium operation.

The choice of wall materials also influences the plasma properties, since eroded wall materials penetrate as impurities into the main plasma even as far as to the plasma center. There are two aspects which limit the presence of impurities in the confined plasma:

1. fuel dilution in the plasma core leads to a decrease of the fusion power, thus the effective charge Z_{eff} of the core plasma should not exceed certain values,
2. and the radiation from impurities at the plasma edge (mainly line radiation) can change plasma temperatures and plasma pressure gradients such that negative effects on plasma stability, energy confinement (H-mode) or divertor pressure may occur.

Considering the overall impurity content we have also to take into account seeded impurities (see Sect. 1.3) and the fusion product helium (the fusion "ash"). A stationary burning fusion plasma can only be obtained when the helium is exhausted sufficiently fast. The corresponding figure of merit is given by the ratio of the effective He exhaust time over the energy confinement time $\rho_{\mathrm{He}} = \tau_{\mathrm{He}}/\tau_{\mathrm{e}}$ [9].

Requirements for long pulse operation:

acceptable power exhaust peak load for steady state	$< 10\,\mathrm{MW/m^2}$
transient loads (e.g., ELMS, disruptions)	$< 40\,\mathrm{MJ/m^2 s^{0.5}}$ (C)
sufficient target lifetime	3000 pulses for ITER > 1 year for plant
maximum long term tritium retention in wall surface	< 350g T (licensed)
impurity contamination in central plasma sufficient helium exhaust	$Z_{\mathrm{eff}} <\sim 1.8$ $\rho_{\mathrm{He}} = \tau_{\mathrm{He}}/\tau_{\mathrm{e}} <\sim 10$

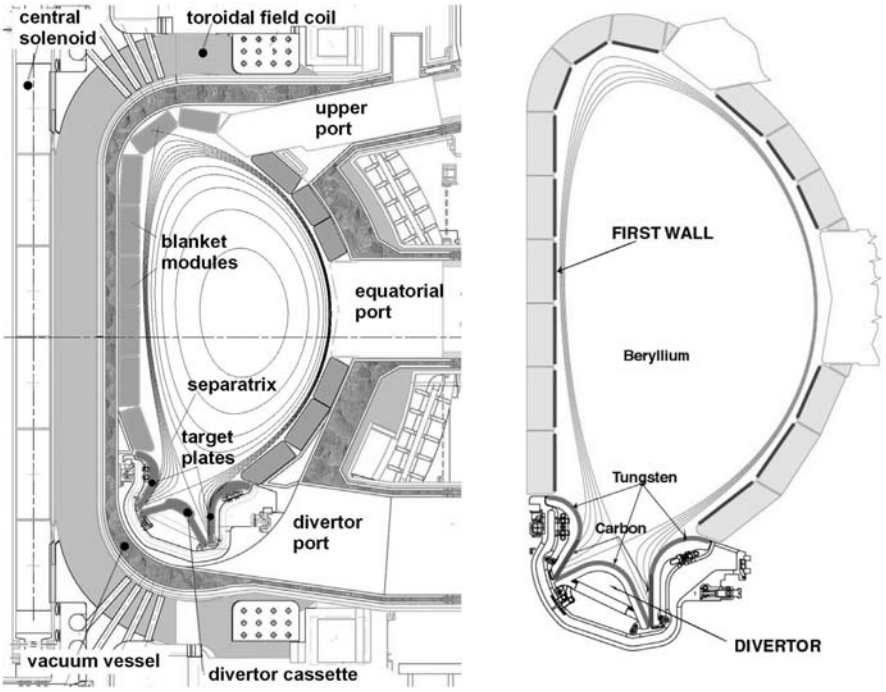

Fig. 1.1. ITER cross-section showing (**a**) main components and (**b**) the choice of materials for plasma facing components

1.3 The ITER-Concept to Control Plasma–Wall Interaction

Plasma–wall interaction in ITER concerns the armor of the first wall in the main chamber and the components of the divertor (Fig. 1.1). The peak heat load of about $10\,\mathrm{MW/m^2}$ occurs at the strike point on the divertor plates (inner and outer divertor) by plasma flow along the magnetic field lines. The baffles, which are introduced to enhance the pressure inside the divertor, are subject mainly to high energetic particles (e.g., charge exchange neutrals). It is expected that the pressure of neutrals is sufficient to allow for a He-exhaust parameter in the range of $\rho_{\mathrm{He}} = 5$. The heat load to the wall of the main chamber is determined by radiation processes (bremsstrahlung from the core and impurity radiation from the plasma boundary). The plasma parameters along the divertor plates as expected from model calculations are displayed in Fig. 1.2.

The main aspects for the selection of plasma facing materials for ITER are the requirements of plasma performance (minimize impurity contamination), engineering integrity, component lifetime and safety (e.g., minimize tritium and radioactive dust inventories) [7]. Currently, the ITER design uses beryl-

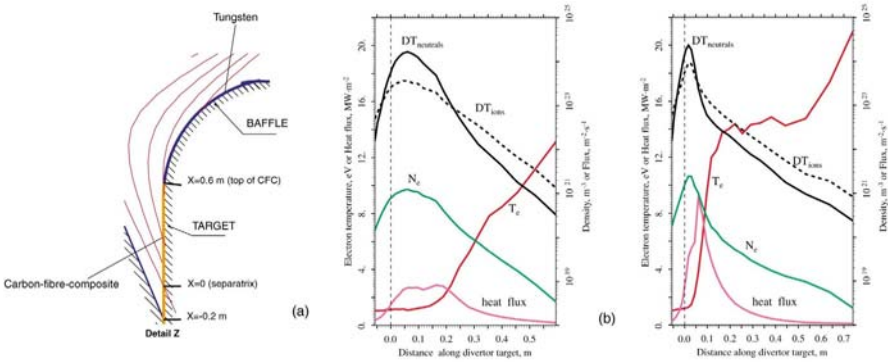

Fig. 1.2. (**a**) detail of the divertor target and (**b**) plasma temperature, density, particle and heat fluxes along the ITER outer divertor target for a reference semi-detached edge plasma (**left**: inboard divertor target; **right**: outboard divertor target) [7]

lium for the first wall in the main chamber, and graphite (CFC) as well as tungsten in the divertor. Each of these three candidate materials has some inherent advantages and disadvantages.

Beryllium is selected because it has the advantages of being a low-Z material with a good thermal conductivity and the ability to getter oxygen from the plasma, which is in particular important for the start-up phase. However, its high sputtering yields and the low melting point limit its power handling capabilities.

Tungsten as a high-Z material with low sputter yield and high melting temperature will be used for the baffle regions of the target and the surface of the divertor dome.

Graphite has been chosen only for those plasma facing components which are subject to the highest heat loads because this material is 'forgiving'; graphite does not melt – its shape is maintained. The graphite components are not destroyed even with transient heat loads much beyond the acceptable steady state heat flow, thus it is an excellent choice for experiments with a natural tendency to explore the operational limits.

Using this armor combination, the erosion lifetime of the plasma facing components is expected to meet the goal of sustaining 3,000 full-power discharges of 400 s duration, with about one in ten discharges ending in a disruption.

The most severe problem with graphite is that the transport of eroded material is very complex and the migration of which over long distances to remote areas may lead to the build-up of thick carbon layers which can trap rather large amounts of tritium (see Sect. 1.4.1). Ongoing R&D is concentrating on an optimized detailed design of the first ITER divertor where the build-up of thick deposition layers is minimized, the formation of layers on

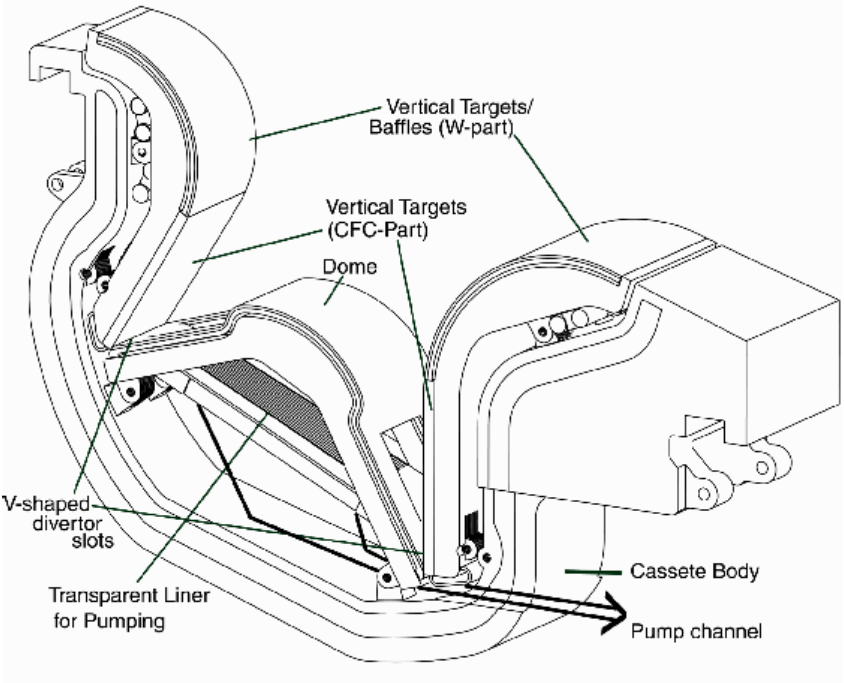

Fig. 1.3. Design of the exchangeable divertor cassette of ITER

remote areas is well controlled and an appropriate access to these areas allows to apply adequate cleaning methods for removing the layers and to recover the tritium (e.g., by heating or chemical reactions).

However, it is not sure that the T-retention limit with graphitic components in ITER will be fulfilled satisfactorily. Therefore a second design avoiding graphite components (all-metal-divertor) has to be developed in parallel. Since the divertor has a modular design the divertor cassettes can be exchanged through a special port by remote handling (Fig. 1.3). It is presently seen as too risky to start ITER with divertor target plates made only from tungsten. During the first years of experiments (mostly without tritium) one will find the optimum plasma scenarios for high power operation and may further optimize the divertor design according to progress in the understanding of the relevant processes. After this stage an exchange of the divertor cassettes may be undertaken.

The peak heat load to the divertor plate is supposed to be limited with the help of impurity radiation and charge exchange processes. Both, photons and charge exchange neutrals, are not affected by the magnetic field, thus allow to distribute the power on the whole vessel surface.

The charge exchange process between cold atoms and hot ions $D_o + ^+ \rightarrow D^+ + D_o$ generates fast neutral atoms. In particular inside the divertor, where we find due to recycling particles a rather high density of neutrals. An energetic photon flux to the whole inner wall can be generated by line radiation emitted from impurities in the plasma boundary. This is the concept of a cold radiating mantle. The radiating impurities can come either from eroded wall material (intrinsic impurities) and/or from injected impurities (seeded impurities) selected according to their radiation properties (e.g., neon, argon, nitrogen). In present tokamak experiments it has been demonstrated that with this method a large fraction of the heating power can be exhausted in a well controlled way and at moderate impurity contamination of the core plasma [10,11]. In ITER it is foreseen that at least 60% of the effective heating power is radiated by a combination of radiation from carbon and argon.

In case graphite would not be used anymore at a later stage in ITER it must be demonstrated that radiation cooling in the absence of carbon as an important radiator can be achieved by seeded impurities only without loosing the good energy confinement properties and the good pumping efficiency of the divertor.

The strategy to cope with transient heat loads, like ELMs and disruptions, is the following. The divertor design with graphite appears to be robust enough to allow to explore in ITER a variety of plasma scenarios, based on R&D in present tokamaks, in order to find an acceptable situation with benign ELMs at acceptable confinement conditions [5] and to implement methods to mitigate the load to the wall during disruptions (e.g., fast gas puffing or pellet injection [12]). Before going to an all-metal divertor it must be demonstrated that transient loads are sufficiently controlled in order to achieve an acceptable lifetime of the tungsten target in view of melt layer erosion.

1.4 The Crucial Processes and Data Needs for Modeling

1.4.1 The Problem of Tritium Retention in Fusion Devices

The retention of tritium in graphite by implantation and the formation of amorphous hydrogen rich carbon layers upon impact of carbon atoms or ions together with hydrogen species is seen as a severe problem for ITER [7,8,13–15]. In the first tritium experiments in TFTR [16] and JET [17] about 3 g and 36 g of T were injected respectively, from which large amounts (30%–40%) were retained on a short time scale (days) in the machine. After applying various cleaning methods (isotope exchange by deuterium plasma discharges, glow discharges, baking and venting), still about 13% and 10% of the T remained in TFTR and JET respectively.

Extrapolating these findings to ITER (fuelling rate 200 Pam^3/s) the T safety limit of 350 g (according to licensing) would be reached in less then 50 plasma discharges. Thereafter, cleaning procedures must be applied to recover the hydrogen isotopes with the possible consequence of shut-down times of unacceptable duration.

It is found that the majority of the long term retained tritium is stored in carbon layers built up by re-deposition of eroded carbon along with the hydrogen isotopes (co-deposits) in various parts of the wall different fusion devices [18–21]. On erosion dominated graphite areas the tritium and deuterium retention is restricted to implantation in a shallow surface layer saturating at a few 10^{17} H/cm^2 [22]. Even when assuming the whole inner wall of ITER made of graphite then we obtain a tolerable amount of only 5 g T retained in the first wall area of ITER. Re-deposited C-layers, however, contain hydrogen fractions up to 1:1 H/C depending on temperature and impact particle energy and with the layer growth continuing for as long as erosion occurs (see also Sect. 1.4.3). Thus, as long as fresh carbon layers are formed no saturation effect is to be expected.

Layers are formed on many locations of the plasma facing wall tiles but also on areas with no direct plasma ion impact ("remote areas"). It turns out that understanding of the tritium-retention requires the understanding of the erosion of carbon, its local and global transport within the device and the details of the deposition mechanisms being responsible for the layer properties.

As seen from the ITER concept, the material choice for plasma facing components does not rely on carbon only. Other materials like tungsten and beryllium are combined with graphite. By erosion and transport of these materials the surface composition of certain plasma facing components may change after some time into a mixture of different species. In such a case the T-retention capability of the layers may change drastically. Pure Be retains only minor amounts of T while incorporation of carbon or oxygen will enhance the retention [23]. Since there is still insufficient knowledge about the retention behaviour of mixed systems, corresponding experiments assessing the various T-retention capabilities is of utmost importance.

In addition, important strategies to cope this problem are

1. the development of carbon-free scenarios (see also Sect. 1.4.2) and
2. to explore techniques for removal of hydrogen isotopes from C-deposits.

On plasma facing surfaces the plasma impact itself can be used to remove the T by isotope exchange or plasma induced surface heating. This puts certain demands on the flexibility of the plasma configuration inside the divertor. On those areas external heating by lamps or lasers might also be possible. These techniques cannot be used on remote areas for which presently mechanical tools or the use of gaseous, chemical treatments by active oxygen or ozone are anticipated [24, 25].

Data needs and issues to be addressed with respect to tritium retention:

understand tritium retention mechanisms, in particular for mixed material systems
understanding of layer formation and material transport
optimization of divertor and main chamber design with respect to, e.g., materials, geometry, temperature and access based on the knowledge on layer formation and tritium retention
exploration of methods to recover the hydrogen isotopes from plasma facing components and from co-deposits (heating, chemical reactions, plasma loads)
development of real-time diagnostics for the determination of the amounts of retained tritium in wall surfaces

1.4.2 Location and Strength of Impurity Sources

Impurity generation by erosion of materials from plasma facing components is an important issue for a fusion device with respect to

1. the life time of wall components and
2. detrimental effects on the plasma performance due to fuel dilution and/or radiation losses at the plasma core.

A major challenge to experiments is the understanding of erosion mechanisms in the complex environment of a fusion device. Predictions about erosion in ITER by numerical modeling are based on related experimental findings in tokamaks, on laboratory measurements (e.g., ion beams or linear plasma devices) and the theoretical understanding of underlying mechanisms. Most experimental data on erosion yields in tokamaks have been obtained from

1. in situ measurements of impurity fluxes based on spectroscopic methods (fluxes, velocities, penetration depth into the plasma) and
2. post mortem analysis of wall tiles (layer thickness, surface composition).

Rather large uncertainties in the spectroscopic measurements are due to uncertainties in the atomic data needed for the calculation of impurity fluxes and the derivation of erosion yields.

Therefore improvements of the atomic data base is of importance and might lead to the necessity of re-evaluation of the measurements of erosion yields obtained under tokamak conditions and the corresponding modification of the numerical modeling of erosion in tokamaks [26, 27]. Impurity fluxes from wall elements entering the plasma can be generated by a combination of different *erosion mechanisms*, the main features and open problems of which are discussed in the following.

Sputtering

Wall material is sputtered due to the bombardment by ions and fast atoms from charge exchange processes. The typical energy of the ions E_i when hitting the wall surface is in the range of 20–1000 eV. The projectile energy is given by the ion temperature T_i, the electron temperature T_e (which determines mainly the electric potential Φ in the Debye sheath in front of the wall; $\Phi \approx 3.5\,T_\mathrm{e}$) and the charge state Z of the ion [28] according to

$$E_\mathrm{i} = T_\mathrm{i} + Z\,\Phi.$$

The principles of the sputtering process are well understood [6]. Sputtering can be calculated by the numerical modeling of collision cascades, e.g., as done in the code TRIM [29]. However, difficulties arise from uncertainties about the actual surface conditions in a tokamak. Deposited layers from different materials, coatings or transient layers only present during the discharge can modify the sputtering properties significantly. Sufficient knowledge about the real surface composition of plasma facing components and the corresponding sputtering yields represents one of the main challenges for the reliable prediction of erosion yields in fusion devices.

Closely related to sputtering are *reflection* processes. Impurity ions contained in the plasma impinge on the wall surface and after neutralization are re-emitted into the plasma with angle and energies according to a collision process between projectile and target. Reflection generates impurity particles which penetrate into the plasma with much higher velocities than from any other erosion mechanism, because of the energy gain $\Delta E = Z\,\Phi$ within the Debye sheath. The particle reflection coefficient R_p and the energy reflection coefficient R_E depend on the combination projectile/target, on the angle of incidence and on the energy of the projectile. In particular light impurities are strongly reflected on heavy targets, with R_p being as high as 80% (e.g., for He on W). The reflection process can be well modeled, but the same uncertainties arise as for sputtering due to the unknown surface composition.

Chemical Erosion

The relevance of chemical erosion became evident when introducing low Z elements, in particular carbon, for plasma facing components in tokamaks. The erosion yields of chemical processes and sputtering can be of the same order of up to a few percent but show significantly different dependencies: physical sputtering has a strong E_i-dependence, whereas the yield Y_ch of chemical erosion varies with surface temperature T_s and flux density, as is shown in the following.

In ion beam experiments [30, 31] a very pronounced T_s-dependence is observed; the yield can vary by nearly two orders of magnitude between room temperature and 900 K. In tokamaks with flux densities several orders of

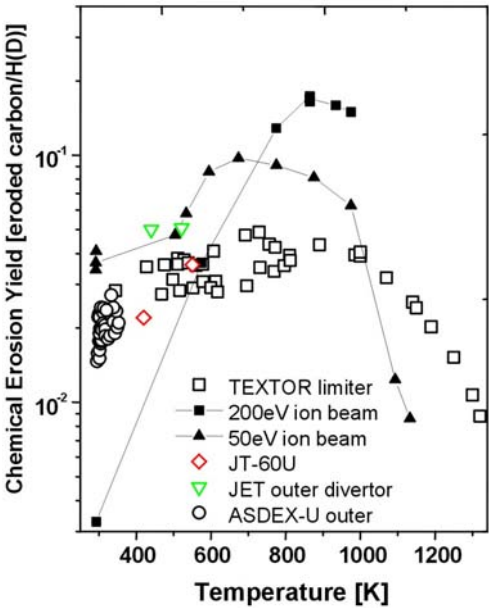

Fig. 1.4. Chemical erosion yield of graphite (methane production) as a function of the surface temperature [26]

magnitude higher and at the same time with lower impact energies, the T_s-dependence turned out to be much weaker and the absolute yields are lower. Figure 1.4 shows the yield of chemical erosion (CD_4) as a function of T_s from various tokamak experiments [26]. For comparison also ion beam experiments are shown. The CD_4 flux in the tokamak is deduced from spectroscopic measurements [32]. The yield in tokamaks shows a rather broad peak around $T_s = 950\,\mathrm{K}$. The absolute yields have quite some uncertainty (50%). The main message of these data is in the relative behaviour. At higher T_s the yield drops significantly and for $T_s > 1300\,\mathrm{K}$ it becomes negligible compared to sputtering for these limiter conditions ($T_e = 20$–$80\,\mathrm{eV}$). Under divertor conditions for high recycling and $T_e < 5\,\mathrm{eV}$ the relative importance of chemical erosion is expected to extend to regions with larger T_s.

The dependence of Y_{ch} on the deuterium flux density has not yet been clarified sufficiently well. A summary of various published data of the CD_4 yield is displayed in Fig. 1.5a as a function of the flux density of the back ground plasma (deuterium) [6, 26]. The flux variations have been obtained either by density scans or for the limiter cases (TEXTOR) by a radial movement of the limiters. These published data suffer from some inconsistencies due to different experimental conditions (electron temperature, surface temperature). The photon efficiency from which particle fluxes are derived [27] depends on the electron temperature. The chemical reactivity [6] depends

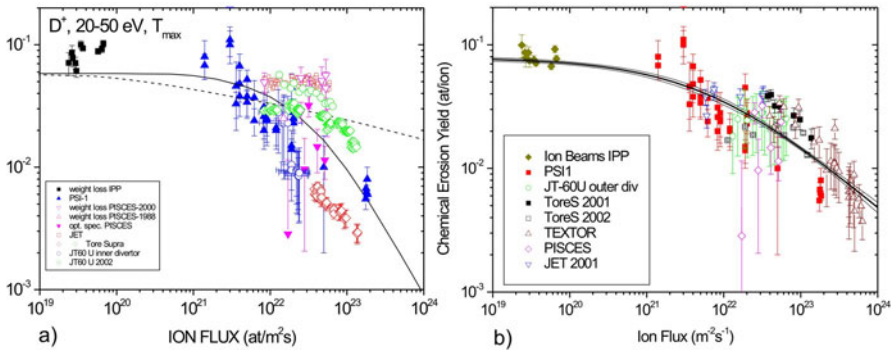

Fig. 1.5. Chemical erosion yield of graphite from spectroscopy as a function of the plasma flux density; (**a**) data collection as published without corrections and (**b**) with normalization to 30 eV plasma temperature. (After Roth, see also [6])

on the energy of the impinging ions influenced strongly by the electron temperature and the surface temperature of the target. Shown in Fig. 1.5b is a first attempt to correct the data for some of the inconsistencies. The dependence of the chemical yield on ion energies as known from laboratory beam experiments has been used to correct the published data obtained on tokamaks [6]. We note that a general decrease of the yield with increasing plasma fluxes is observed. The decrease of Y_{ch} at high flux densities is explained as a saturation effect: when too much deuterium is offered to the surface, the surface layer is overloaded and the average residence time of the impinging deuterium in the surface becomes smaller. As a consequence the reaction rate of hydrocarbon formation decreases [33].

Chemical erosion of graphite can be suppressed by doping graphite with certain elements (Be). Also material transport may lead to a part or even full coverage of the graphite surface with other species suppressing the reactivity of the surface. The chemical properties of such mixed systems need still to be explored thoroughly. The main motivation to introduce beryllium into ITER is to suppress chemistry in the main chamber. For ITER it is predicted that large amounts of Be eroded from the main chamber wall will flow towards the divertor, in particular mainly to the inner divertor, and deposit on the target plates. A challenge is to predict the effect of this Be-deposition on the erosion behaviour of the graphite target tiles in ITER. According to experiments done in the linear plasma device [34] the beryllium deposition can lead to a complete suppression of the chemical erosion of carbon. This confirms the hope that in ITER indeed the carbon erosion and transport in the divertor is much less than what is observed today, e.g., in JET. However it is a matter of concern that transient heat loads, like ELMs, may ablate the protective Be layer. On the other hand the formation of Be-C compounds might also occur. These compounds can withstand much higher power loads than a beryllium layer.

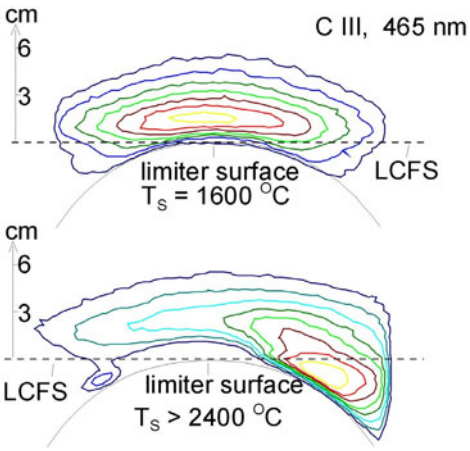

Fig. 1.6. Emission of a carbon CIII line in the vicinity of a limiter in TEXTOR for (**a**) normal conditions with carbon being eroded predominantly by sputtering and (**b**) for a case with a hot spot leading to sublimation of carbon

Melting and Sublimation

The lowest velocity of carbon being released from an erosion process is observed with sublimation. The thermal velocity, well below 0.5 eV, leads to an ionization length of about 1 mm. Figure 1.6 shows a 2d-distribution of CIII radiation obtained from a graphite test limiter. Two cases shown are: a) chemical erosion and sputtering provide the main carbon source and b) the right-hand side of the limiter reaches a surface temperature above 3000 K (hot spot) so that sublimation becomes the main source. As a consequence of the shorter ionization length the main fraction of the C^+ and C^{2+} ions is born inside the scrape-off-layer (SOL). Thus, the probability for local redeposition is high and the fuelling efficiency (probability to enter the main plasma) is low. This may explain why in many cases no dramatic increase of the carbon content in the main plasma is observed with the occurrence of hot spots.

In ion beam experiments, carbon materials show an unexpected additional erosion mechanism which dominates the carbon erosion in the temperature range 1200 K–2200 K, called *radiation enhanced sublimation* (RES) [35, 36]. There are doubts whether this effect also exists with very high particle flux densities as they are typical for tokamaks. Test limiter experiments in TEXTOR have demonstrated that RES is not important under such conditions. However, other devices reported a carbon influx by RES and recent measurements indicate also an enhanced erosion of metals at high temperatures under low energy particle impact [34]. Further R&D is needed to clarify these issues.

With Be or high-Z metal wall melting becomes a matter of concern. The performance of the cooling system should be such that with the average heat load the surface temperature of the plasma facing components is kept well below the melting point. Nevertheless, for a short time elevated temperatures far from the equilibrium values may be caused by transient heat loads (e.g., with ELMs or disruptions). In such a case the resulting surface temperature rise ΔT is proportional to the heat flux density Q and the square root of the duration time t of the heat pulse: $\Delta T \sim Q\,t^{1/2}$. From this relation one can derive for various materials a maximum value for $Q\,t^{1/2}$ below which no melting or sublimation occurs during the heat pulse. The corresponding threshold value for tungsten is about $40\,\mathrm{MJ/m^2 s^{0.5}}$. This is seen as a critical issue, since type I ELMs in ITER are expected to provide heat pulses in the range of (30–200) $\mathrm{MJ/m^2 s^{0.5}}$. Therefore, the development of plasma scenarios with benign ELMs are a necessity when using tungsten for the divertor plates. For the cases of excess heat loads, e.g., with disruptions, the potential material loss due to melting (melt layer loss) has to be calculated. A crucial part in these calculations is the proper treatment of the molten layer (stability) and the effect of vapor shielding, which might lead to a reduction or limitation of the local heat load density [37].

Data needs and issues to be addressed related to impurity sources and erosion processes:

Improvement of the atomic data base needed for the spectroscopic determination of impurity fluxes; critical re-evaluation of erosion yield measurements in tokamaks
Development of methods to determine the real surface composition of plasma facing components and their consequences on sputtering, reflection and chemical reactivity.
Determination and consolidation of the data base about the dependence of chemical erosion on surface temperature and plasma flow density.
Determination of the modification of erosion processes of graphite due to beryllium coverage, doping or the formation of beryllium compounds.
Determination of the threshold conditions for melting and sublimation under realistic tokamak conditions with mixed materials. Development of methods to calculate the melt layer loss in case of transient excess heat loads.

1.4.3 Migration of Eroded Materials and Layer Formation by Deposited Impurities

Since a tokamak or a stellarator represents almost a closed system, the majority of eroded particles must be deposited somewhere in the machine. Therefore, when calculating the life time of plasma facing components it is misleading to consider erosion only. E.g., taking an extreme case on the tip of

a graphite limiter with a hydrogen flux density of $10^{20}\,\mathrm{cm^{-2}s^{-1}}$ and an erosion yield of 1% producing a carbon flux density of about $10^{18}\,\mathrm{cm^{-2}s^{-1}}$ leads to an erosion rate of 150 nm/s or, for continuous operation, 4.5 m/year. But experiments show that most of the eroded particles are transported as ions via the plasma flow along field lines back close to those wall areas where they came from. Integrated over the whole wall area there must be a balance between erosion and deposition. However, locally we find areas of net-erosion and net-deposition. Only at the boundary line between such zones there is an exact balance between erosion and deposition.

On a given area we have to consider a simultaneous flow of eroded (Γ_{ero}) and deposited (Γ_{dep}) particles and the effective erosion rate Γ_{eff} is then $\Gamma_{\mathrm{eff}} = \Gamma_{\mathrm{ero}} - \Gamma_{\mathrm{dep}}$. The erosion rate is given by the hydrogen ion flow Γ_{H} and the impurity ion flow Γ_{i} out of the plasma and the respective erosion yields Y_{H} and Y_{i} according to

$$\Gamma_{\mathrm{ero}} = \Gamma_{\mathrm{H}}\, Y_{\mathrm{H}} + \Gamma_{\mathrm{i}}\, Y_{\mathrm{i}}.$$

Deposition depends on the sticking coefficient S for the impinging impurity ion flow Γ_{i}

$$\Gamma_{\mathrm{dep}} = \Gamma_{\mathrm{i}}\, S.$$

The ratio $R_{\mathrm{ero}} = \Gamma_{\mathrm{ero}}/\Gamma_{\mathrm{dep}}$ determines whether we have a net-erosion or a net-deposition zone

$$R_{\mathrm{ero}} = \frac{1}{S}\left(\frac{Y_{\mathrm{H}}}{c_{\mathrm{i}}} + Y_{\mathrm{i}}\right)$$

where c_{i} is the impurity concentration in the SOL assuming equal flow velocity of hydrogen and the impurity ions. $R_{\mathrm{ero}} > 1$ corresponds to net-erosion. The effective erosion rate Γ_{eff} can be expressed now as $\Gamma_{\mathrm{eff}} = \Gamma_{\mathrm{ero}}(1-1/R_{\mathrm{ero}})$.

In experiments the distinction between areas of net-erosion and net-deposition can be rather easy. Figure 1.7 shows an example of a test limiter (twin-limiter) in TEXTOR, which was made out of two different materials: tungsten and graphite [38]. In a carbon dominated environment (main limiter graphite) the tungsten side is subject to carbon deposition. The boundary $R_{\mathrm{ero}} = 1$ between the zones of net-erosion (metallic) and net-deposition (black) is clearly seen in Fig. 1.7. In the net-deposition zone a carbon layer is growing, such that after only eight ohmic discharges a layer of about 90 nm thickness is produced.

The calculation of R_{ero} , and therefore also of Γ_{eff}, contains quite some uncertainties. Knowledge about the local plasma parameters, erosion yields and sticking coefficients is required [39]. A possible mix of different erosion mechanisms and a surface layer composition with different materials adds some complexity to the problem. However, the extreme case of erosion mentioned above with a layer of 4.5 m eroded per year is unrealistic, since it is only valid for $\Gamma_{\mathrm{dep}} = 0$ or $\mathrm{R_{ero}} = \infty$. Instead, experiments indicate that R_{ero} does not deviate very much from unity. Indeed, with values typical for carbon, namely $S = 0.75$, $Y_{\mathrm{H}} = 0.015$, $Y_{\mathrm{i}} = 0.02$–0.5, $c_{\mathrm{i}} = 0.01$–0.03, we obtain R_{ero} in the range of $R_{\mathrm{ero}} = 0.7$–2.7.

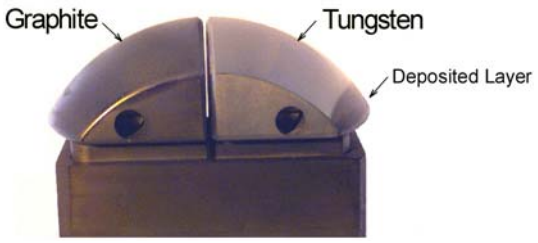

Fig. 1.7. Twin-limiter made of graphite und tungsten showing net-erosion and net-deposition of C on W after exposure to TEXTOR

Spectroscopy shows that already with the first exposure of the twin-limiter to the plasma a carbon atom flux is being emitted on the tungsten-side at a rate about equal to that on the graphite-side. But, a post-mortem analysis showed that no significant carbon layer is found on the tungsten surface (< 1 monolayer) except on those parts with net-deposition. This observation exhibits that a flow of carbon ions hitting the limiter is partially reflected from the surface leading to the release of carbon atoms observed. The particle reflection coefficient for C on W is about 65% (angle 60°, $Z = 4$, $T_e = T_i = 50\,\mathrm{eV}$). The remaining carbon particles build up a transient layer (< 1 monolayer) which is subject to erosion.

The complex environment of a tokamak does not only contain carbon and tungsten. In devices which apply boronization we find also boron. JET evaporates routinely beryllium in the main chamber leading to a flow of beryllium into the divertor. A similar behaviour we also expect from ITER. Moreover, as in all vacuum devices, there is always some residual oxygen in the machine. For a reliable prediction of erosion and deposition it is necessary to obtain knowledge about sources, transport and deposition of all those species in a fusion device.

The present understanding of impurity migration in JET is that there is a strong flux of C and Be from the main chamber into to the divertor at a ratio of 12:1 [40]. But the layers formed on the plasma facing side of the divertor tiles are Be-rich with a typical ratio of C:Be = 0.3–1 [41]. This shows that carbon does not remain in these primary layers and undergoes further erosion induced transport whilst Be adheres to the surface. The majority ($> 90\%$) of the carbon flowing into the divertor is found on shadowed areas of the divertor tiles and on the water cooled louvers at the entrance of the pump duct. In experiments it has been found that the carbon ions hitting the graphite surface have a rather high sticking probability [18, 42]. Thus, carbon can only migrate to remote areas via multi-step processes when the re-erosion yield of deposited carbon due to plasma impact or neutral particles is sufficiently high – at least much higher than the erosion yield of the base graphite material. There is experimental evidence from laboratory

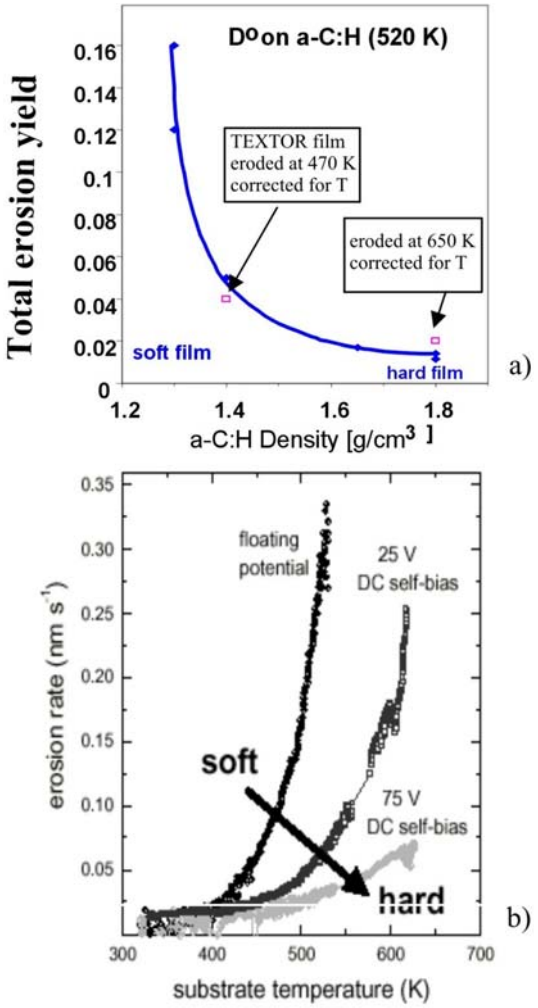

Fig. 1.8. (**a**) Chemical erosion yield for different carbon films by thermal atomic deuterium as a function of film density and (**b**) erosion rate for different carbon films as a function of temperature by thermal hydrogen impact [43–45]

experiments about "soft" carbon layers being formed under conditions with "cold" plasmas which show indeed very high erosion yields. In Fig. 1.8 the erosion yields of such "soft" and "hard" films are displayed for layers being formed inside the tokamak TEXTOR and under well defined laboratory conditions [43–45]. There is the need for a much better understanding of these processes and for the generation of a reliable data base with erosion yields for different types of deposited materials as a crucial input to the modeling codes with which the erosion and deposition behaviour of ITER is predicted.

Data needs and issues to be addressed related to erosion and deposition processes:

Investigation of the layer formation with different species and under various edge plasma conditions
Determination of the re-erosion yields of the various types of deposited layers and the determination of sticking coefficients for ions and radicals under various conditions

1.4.4 Modeling of Erosion and Deposition

Numerical codes are used to predict fuel retention and the lifetime of target plates of ITER. Such a code is the three dimensional Monte-Carlo ERO [46,47] which was developed originally to model the impurity transport in TEXTOR (ERO-TEXTOR). Meanwhile, various divertor configurations such as ASDEX, JET and ITER (program versions ERO-ASDEX, ERO-JET and ERO-ITER) as well as the linear plasma device PISCES have been implemented.

ERO is a three dimensional Monte Carlo code calculating the erosion and deposition and the transport of impurities in the vicinity of wall elements in the boundary-layer of magnetically confined fusion plasmas. The modeling takes into account the following processes: Impinging background plasma ions (fuel and impurities) erode particles from the limiter surface by physical sputtering and chemical erosion. The released particles (atoms in the case of physical and radical molecules C_xD_y in the case of chemical erosion) leave the limiter as neutrals. These particles are ionized or dissociated at some distance from the wall. The charged particles underlie forces from the magnetic and electric fields and they interact with the background plasma through Coulomb collisions resulting in frictional and thermal forces. Eroded particles return to the limiter surface with certain probability. For the returning atomic species the reflection coefficient is calculated using the TRIM database [48]. In case of radical molecules the reflection probability is determined by input parameters. If the particle is not re-deposited it moves once more into the plasma as a neutral and the procedure described above starts again until the particle is re-deposited or finally leaves the observation volume. Eroded particles returning to the surface erode further material which then is transported through the edge plasma. The codes allows also to model the transport of externally injected hydrocarbons (C_xH_y) or silane (SiH_4) molecules.

Such a code needs benchmarks with experimental data. Furthermore, improvements in the underlying data bases on atomic and molecular data and surface processes have to be implemented. The most recent developments are:

1. Implementation of new rate coefficients for the methane reaction chain. In the past the rate coefficients for the methane family were taken from

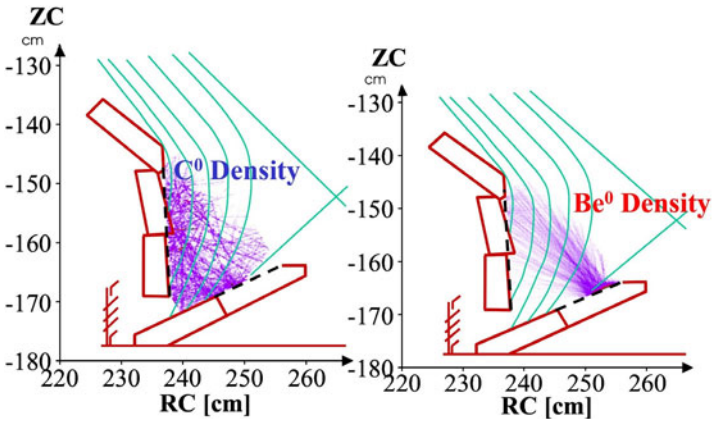

Fig. 1.9. ERO code simulation of carbon and beryllium erosion and transport inside the divertor of JET showing the multi-step transport of C in contrast to the one step erosion-deposition of Be

the Ehrhardt-Langer database from 1986 [49]. Meanwhile these data have been improved by adding new atomic processes and reactions [50–53].

2. The consideration of higher hydrocarbons was introduced. The former version of the ERO code considered only the methane family CH_y whereas higher hydrocarbons C_xH_y were not included. Especially at low electron temperatures as they can develop in the divertor higher hydrocarbons become more and more important [54]. Thus, the higher hydrocarbons C_2H_y and C_3H_y are now included in the code.
3. The reflection of carbon atoms and ions at the limiter or divertor surfaces in the ERO modeling is determined by TRIM [29]. However, the binary collision approximation used in the TRIM code is no longer valid at small energies of the incoming particles where chemical effects start to influence the interaction of the particles with the solid. To take this into account reflection coefficients calculated with a molecular dynamic code MolDyn [55] were implemented.
4. The recombination of carbon ions has been included since this process can become important at the low temperatures in certain divertor conditions. Indeed, at very low temperatures ($<\sim 2\,\mathrm{eV}$) recombination is more probable than ionization.

Modeling of impurity migration in JET revealed that our knowledge about carbon sticking end re-erosion needs to be improved. The distribution of beryllium on the target plates is well reproduced (see Fig. 1.9). But with standard assumptions about carbon erosion the code could not reproduce the migration of carbon to remote areas. Only by introducing much higher re-erosion rates or equivalently very low effective sticking probabilities the code reproduces the experimental findings about carbon layers in JET [56].

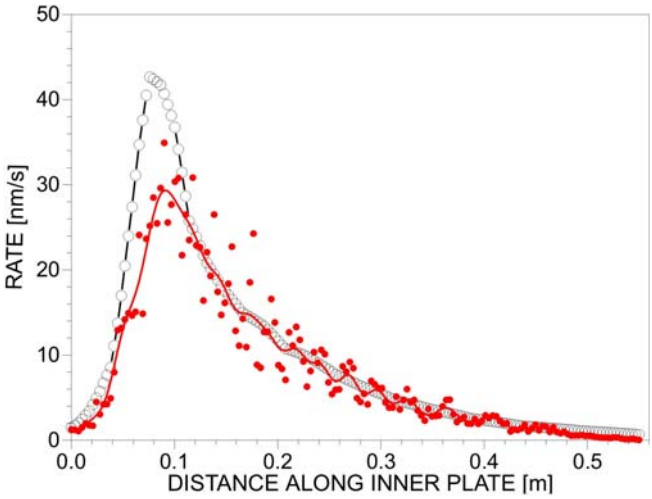

Fig. 1.10. Erosion (*open circles*) and deposition (*closed circles*) rates of C predicted by the ERO code for the ITER-divertor

Similar conclusions have to be drawn from simulations of $^{13}CH_4$ puffing experiments in TEXTOR. Again only the assumption of an enhanced re-erosion of redeposited carbon results in an extremely low local ^{13}C deposition efficiency ($\sim 0.5\%$) in agreement with the measurement [57].

For predictive calculations for ITER the two-dimensional plasma parameters are taken from B2–EIRENE. For comparison the sticking probability of hydrocarbons is assumed to be either zero or one. The chemical erosion yield is assumed to be 2%. Figure 1.10 summarizes the profiles of erosion and re-deposition along the outer divertor plate. The net deposition profiles result from the difference of re-deposition and erosion. Zero sticking of hydrocarbons leads to an overall deposition of about 86% and a net erosion peak of 15 nm/s near the strike point. Assuming a sticking probability of one leads to an increased deposition of about 95% and a decreased erosion peak of 8 nm/s. Particles not re-deposited at the divertor plate are lost into the private flux region – mainly as neutrals. To make an estimation of the long-term tritium retention it is assumed that only these "lost" particles lead to a build-up of net deposition layers at remote layers. The safety limit of 350 g tritium would then be reached after already 60 discharges of 1000 s duration. This shows that the tritium retention is a much more crucial than the lifetime of the target plates. However, these calculations have to be improved by taking into account a beryllium background flux and Be-C mixing effects of the deposited layers on the targets.

Data needs and issues to be addressed related to modeling of erosion and deposition:

Assessment of the need to implement further atomic and molecular reactions into the modeling.
Improvements in the modeling of the re-erosion yields, sticking coefficients for ions and radicals under various conditions
Further improvement of molecular dynamics calculations for higher impact energies
Calculation of reflection coefficients for hydrocarbon molecules and radicals
Benchmarks of the model with dedicated experiments
Calculations for ITER taking into account a beryllium background flux and Be-C mixing effects on the targets

1.4.5 Release of Hydrogen Atoms and Molecules from Recycling Processes

Only a small fraction of the particles needed to fuel the plasma will be injected from external sources, like gas puff, neutral beams or pellets. The majority enters the plasma via recycling from divertor plates, baffles, limiters and wall. This motivates investigations about the actual recycling mechanisms. In particular, the velocities of the hydrogen particles are of interest in view of the penetration depth, and they are closely connected to the recycling mechanisms.

A similar measurement, based on molecular spectroscopy, has been made with a pre-heated test limiter in TEXTOR [59, 60]. This case, with high flux densities, also shows a transition from molecules to atoms with increasing surface temperature as indicated also in Fig. 1.11. Compared to the beam experiments, the transition temperature is shifted by some 100 K.

From beam experiments, we know that, at room temperature, hydrogen is re-emitted from a graphite surface completely in form of H_2 molecules and this changes gradually to the emission of H^o atoms at higher surface temperatures. The transition temperature is around $T_s = 1200$ K [58], as displayed in Fig. 1.11. In order to derive fluxes from the measurement of H_α light, it is important to know the ratio of molecules/atoms because the overall photon yield varies quite strongly with this parameter. The photon rates for atoms are in general larger than for the atoms coming from the dissociation of H_2. This has been investigated carefully by spectroscopic measurements with different limiter temperatures and in experiments where gas has been puffed through a small hole in the limiter. It turns out that the photon yields used in earlier investigations underestimated the particle fluxes significantly. In the case of H_α this results in a factor of two; for higher Balmer lines this factor is even larger [61].

The velocity of the recycling hydrogen atoms is determined by reflection, desorption and ion-induced desorption. The atoms originating from H_2 gain their energy from the dissociation process. The velocity distribution contains

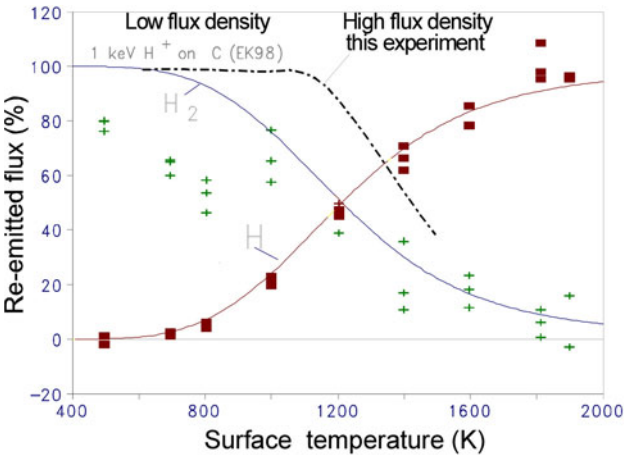

Fig. 1.11. Emission of hydrogen as molecules and atoms depending on the surface temperature from laboratory beam experiments and from the TEXTOR tokamak with higher flux densities

various parts. An asymmetric part comes from particles released from the limiter, that are moving inwards, towards the plasma. We observe a slow fraction around 1 eV and a fast fraction of 10–100 eV from directly reflected hydrogen.

The more symmetric distributions are due to charge exchange and radiative dissociation of H_2. From both processes the atoms are emitted isotropically. The fast part of the velocity distributions is well understood based on our knowledge about reflection and charge exchange processes. The slow part of the velocity distribution is more difficult. It can be modeled by assuming desorbed atoms having an average energy of about 1 eV or even less. But we can distinguish between these desorbed atoms or atoms from molecular dissociation, which are both so slow, only – if ever – with high resolving powers ($\lambda/\Delta\lambda \geq 60.000$) [62,63]. These low energies, below 1 eV, were not expected, since the Franck–Condon values for the products of dissociation from the molecular ground state are about 2.2 eV. Significantly lower energies have been found [44,64,65]. This has been verified, e.g., by laser-induced fluorescence (L_α) measurements of the radial velocities of recycling H showing an average energy of 0.3 eV. It can be explained by the fact that the molecules are highly vibrationally excited, which may lead to much lower dissociation energies.

The population of these vibrational states can be described by a collisional–radiative model [66,67], where the population density is mainly a function of T_e. It can explain why at low T_e (high-density case) the energies of the dissociated atoms can be higher than at higher T_e: at low T_e more molecules are dissociating from the ground state delivering atoms with 2.2 eV, whereas

the probability for highly excited molecules, thus low energies (0.3 eV) of the dissociation products, increases with higher T_e. Excitation due to electron impact, as is described in the collisional–radiative model, may not be the only mechanism to generate excited molecules. The analysis of molecular spectra obtained from the limiter in TEXTOR-94 [44] show evidence for rotational energies which follow the surface temperature over a rather wide range ($T_s = 500\,\mathrm{K}$–$1500\,\mathrm{K}$). Usually, most molecules are already vibrationally excited when they leave the surface. Usually, most molecules are already vibrationally excited when they leave the surface. An important result of this analysis is a new, effective value D/XB of the so-called inverse photon efficiency, for the conversion of photon fluxes into particle fluxes [60, 61, 68]. These latest findings on recycling and molecular physics are presently being implemented in the neutral particle transport code EIRENE [69, 70].

1.5 Summary and Conclusions

The requirements for long pulse operation in the next step fusion device ITER and beyond, like acceptable power exhaust, peak load for steady state, transient loads, sufficient target lifetime, limited long term tritium retention in wall surfaces, acceptable impurity contamination in central plasma and efficient helium exhaust, depend on complex processes. The input to the numerical codes, which are used for the optimization of divertor and wall components, relies to a large extend on our understanding of the major processes related to erosion and deposition, tritium retention, impurity sources and erosion processes. The reliability of predictions made with these codes depends crucially on the accuracy of the atomic and plasma-material interaction data available.

It is important to assess the need to implement further atomic and molecular reactions into the modeling. Our knowledge about the re-erosion yields of deposited layers has to improved urgently. A better understanding of hydrocarbon molecules and radicals is needed, in particular with respect to layer formation and material transport. The atomic data bases needed for the spectroscopic determination of impurity fluxes has to be improved for a critical re-evaluation of erosion yield measurements in tokamaks. The behaviour of mixed material systems (C, Be, W, etc.) deserves special attention. The data base about the dependence of chemical erosion on surface temperature, plasma flow density and ion energies needs to be consolidated. Finally the benchmarks of the numerical models with dedicated experiments must be one of the prime tasks of ongoing experiments.

References

1. Campbell D.J., Physics goals of RTO/RC ITER, Plasma Phys. Control. Fusion **41** (1999) B381
2. Shimomura Y. et al., Plasma Phys. Control. Fusion **43** (2001) A385
3. Ward D.J., Cook I., Knight P.J., Proceedings of the 18th Fusion Energy Conference, 2000, IAEA-CN-77/FTP2/20 and Ward D.J., Cook I., Taylor N.P., Power Plant Conceptual Study (PPCS) Stage II
4. Borrelli G. et al., Socio-Economic Research on Fusion, summary of EU Research 1997–2000, EFDA-RE-RE-1, Brussels 2001
5. Loarte A., In: this volume
6. Roth J., In: this volume
7. Federici G. and Skinner C.H., In: this volume
8. Philipps V. et al., Proc. of the 30th EPS Conference on Controlled Fusion and Plasma Physics, St. Petersburg 2003, PPCF in print
9. Reiter D., Wolf G. H. and Kever H. Nucl. Fusion **30** 10 (1990) 2141
10. Samm U. et al., Plasma Phys. Control. Fusion **35** (1993) B167
11. Kallenbach A. et al., Nucl. Fusion **35** 10 (1995) 1231
12. Finken K.H. et al., J. Nucl. Mater. **313-316** (2003) 1247
13. Federici G., Skinner C.H., Brooks J.N. et al., Nucl. Fusion **41**, No 12R (2001) 1967
14. Rubel M., Philipps V., Tanabe T. et al., Physica Scripta **T103** (2003) 20–24
15. Loarer T. et al., Proc. of the 30th EPS Conference on Controlled Fusion and Plasma Physics, St. Petersburg 2003, ECA Vol. 27A, P-1.161
16. Skinner C.H. et al., J. Nucl. Mater. **241-243** (1997) 214
17. Andrew P., Brennan P.D., Coad J.P., Fusion Engineering and Design **47** (1999) 233–245
18. Wienhold P. et al., J. Nucl. Mater. **313-316** (2003) 311
19. Roth J., Janeschitz G., Nuclear Fusion **29** (1989) 915
20. Coad P. et al., J. Nucl. Mater. **313-316** (2003) 419
21. Rohde V. et al., J. Nucl. Mater. **313-316** (2003) 337–341
22. Maier M. et al., J. Nucl. Mater. **266-269** (1999) 1003
23. Anderl R.A., Causey R.A., Davis J.W. et al., J. Nucl. Mater. **273** (1999) 1–26
24. Moormann R., Alberici S. et al., Fusion Engineering and Design **49-50** (2000) 295–301
25. Philipps V. et al., J. Nucl. Mater. **266-269** (1999) 386
26. Philipps V. et al., J. Nucl. Mater. **313-316** (2003) 354
27. Pospieszczyk A., In: this volume
28. Stangeby P.C., *The Plasma Boundary of Magnetic Fusion Devices*, Plasma Physics Series (IOP Publishing Ltd, Bristol, UK 2000)
29. Eckstein W., *Computer Simulation of Ion-Solid Interactions*, Vol. **10**, Springers Series in Material Sciences (Springer, Berlin 1991)
30. Roth J., In: *Atomic and PMI Processes in Control. Thermonucl. Fusion*, ed. by R.K. Janev and H.W. Drawin (Elsevier 1993) p. 381
31. Vietzke E., Haasz A.A., In: *Physical Processes of the Interaction of Fusion Plasmas with Solids*, ed. by W.O. Hofer and J. Roth (Academic Press 1996)
32. Pospieszczyk A. et al., J. Nucl. Mater. **241-243** (1997) 833
33. Roth J., J. Nucl. Mater. **266-269** (1999) 51
34. Doerner R. et al., submitted to Physica Scripta

35. Philipps V. et al., J. Nucl. Mater. **220-222** (1995) 467
36. Roth J., Bohdanski J., Wilson K.L., J. Nucl. Mater. **111-112** (1982) 775
37. Doerner R. et al., private communication
38. Huber A. et al., Proc. of 26th EPS Conf. on Controlled Fusion and Plasma Physics, Maastricht 1999, ECA Vol. 23J (1999) 685
39. Naujocks D., Eckstein W., J. Nucl. Mater. **230** (1996) 93
40. Matthews G. et al., Proc. of the 30th EPS Conference on Controlled Fusion and Plasma Physics, St. Petersburg 2003, ECA Vol. 27A, P-3.198
41. Rubel M. et al., J. Nucl. Mater. **313-316** (2003) 321
42. Mayer M. et al., Proc. of the 30th EPS Conference on Controlled Fusion and Plasma Physics, St. Petersburg 2003, ECA Vol. 27A, O-2.6A
43. Vietzke E. et al., J. Nucl. Mater. **145-147** (1987) 443
44. Schwarz-Seliger T. et al., J. Vac. Sci. Techn. **A18** (2000) 995
45. Keudell von A.W., Jakob W., J. Appl. Phys. **79** (1996) 1092
46. Kögler U., Winter J., *ERO-TEXTOR: 3D-Monte-Carlo Code for Local Impurity Modeling in the Scrape-Off-Layer of TEXTOR*, Report Jül-3361, Jülich, 1997
47. Kirschner A. et al., Nucl. Fus. **40**, No. 5 (2000) 989
48. Eckstein W., *Computer Simulation of Ion Solid Interaction* (Springer, Berlin 1991)
49. Ehrhardt A.B., Langer W.D., *Collisional Processes of Hydrocarbons in Hydrogen Plasmas*, PPPL Report (Princeton 1986)
50. Brooks J.N., Wang Z., Ruzic D.N., Alman D.A, ANL/FPP/TM-297, May 1999
51. Alman D.A. et al., Phys. Plasmas **7** (2000) 1421
52. Janev R.K., Wang J.G., Kato T., NIFS-DATA-64, May 2001
53. Janev R.K., Reiter D., *Collision Processes of Hydrocarbons Species in Hydrogen Plasmas: I. The Methane Family,* Jül-3966, Jülich, 2002
54. Mech B.V., Haasz A.A., Davis J.W., J. Nucl. Mater. **241-243** (1997) 1147
55. Alman D.A., Ruzic D.N., J. Nucl. Mater. **313-316** (2003) 182
56. Kirschner A., Brooks J.N., Philipps V., Coad J.P., Plasma Phys. Control. Fusion **45** (2003) 309
57. Kirschner A., Brezinsek S., Esser H.G. et al., contribution to the 30^{th} EPS Conference on Controlled Fusion and Plasma Physics, St. Petersburg 2003, ECA Vol. 27A, P-3.196
58. Franzen P., Vietzke E., J. Vac. Sci. Technol. **A12** (1994) 820
59. Haasz A.A., Davies J.W., In: this volume
60. Brezinsek S. et al., Contrib. Plasma Phys. **42** (2002) 668
61. Mertens Ph. et al., Plasma Phys. Control. Fusion **43** (2001) A349
62. Hey J.D. et al., Contrib. Plasma Phys. **36** (1996) 583
63. Brezinsek S. et al., Contrib Plasma Phys. **42** (2002) 657
64. Mertens Ph., Silz M., J. Nucl. Mater. **241-243** (1996) 842
65. Mertens Ph., Pospieszczyk A., J. Nucl. Mater. **266-269** (1999) 884
66. Fantz U., Heger B., Plasma Phys. Control. Fusion **40** (1998) 2023
67. Fantz U., In: this volume
68. Brezinsek S. et al., Plasma Phys. Control. Fusion (2003) submitted
69. Reiter D., http://www.eirene.de (2002)
70. Greenland P.T., Proc. R. Soc. London **457** (2001) 1821

2 Modeling of Fusion Edge Plasmas: Atomic and Molecular Data Issues

D. Reiter

The physics of the boundary region of magnetically confined fusion plasmas remains a major scientific challenge. Transport processes in special divertor chambers, where the plasma is only partially ionized, determine the plasma surface interaction (PSI), on which the success of nuclear fusion depends to a large extent. Detailed numerical modeling of these edge plasmas is currently the only tool to separate, computationally, the principally unknown turbulent plasma transport from the chemistry and surface effects, so that the former can, ultimately, be determined experimentally. This procedure relies heavily upon the quality and completeness of atomic, molecular and surface interaction data. The current status of this data, as used in edge plasma modeling, is discussed.

2.1 Introduction

Fusion edge plasma physics (plasma temperatures in the 1 to 100 eV range) has become a key issue in controlled nuclear fusion research [1]. Just as any other kind of steady burning process a thermonuclear burning fusion flame depends upon both sufficient thermal insulation (in this case provided by the confining magnetic field) to keep the temperature in the flame above a critical value and, at the same time, sufficient particle throughput, i.e., refuelling and ash removal. In the flame of a usual fire, this temperature is of the order of 1000 Kelvin, and the buoyancy driven flow of hot (used) air out of the flame provides the particle throughput. For example a simple candle flame is choked within seconds by its own ash, if gravity is absent, as has for example been shown in demonstration experiments carried out during space flights.

For a D-T fusion plasma flame, these considerations can be translated into the terse statement, that the quality of thermal insulation (quantified by an energy confinement time τ_{E}) must exceed one tenth of the particle lifetime in the flame $\tau_{\mathrm{P}} : \rho = \tau_{\mathrm{P}}/\tau_{\mathrm{E}} \leq 10$, see Fig. 2.1, [2].

Reducing the particle lifetime can be achieved through pumping, via the neutral gas component produced by surface recombination of the plasma at target surfaces. It hence requires at least a minimum level of plasma wall contact, and therefore of plasma surface interaction and edge plasma control. Magnetic confinement has to be sufficiently good for the burning central

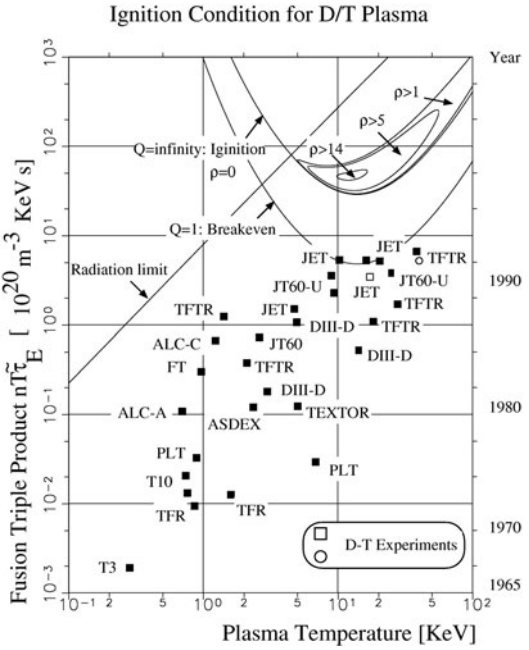

Fig. 2.1. Fusion triple product $nT\tau_{\mathrm{E}}$, vs. temperature (KeV), and contours of constant plasma surfaces interaction intensity ρ (definition: see text). Q is the ratio of output fusion power to input heating power. The upper left part (beyond the "radiation limit" line) is not accessible, due to unavoidable radiation losses (Bremsstrahlung) already exceeding fusion power production

plasma ("plasma core region") and sufficiently poor for the plasma edge region.

As for the physics of the fully ionized hot plasma core, appropriate dimensionless parameters have been identified: present fusion research acts like wind-channel experiments on down-scaled models, with respect to future fusion power reactors.

This is no longer possible for the plasma edge region due to dominant effects on the plasma flow from atomic and surface processes (chemical reactions) on the plasma flow. The divertor plasma dynamics, and more generally the entire edge plasma physics in a fusion device is strongly influenced, and partially even controlled, by the strong mutual interaction and exchanges of 3, sometimes of all 4 states of matter.

2.1.1 Computational Edge Plasma Models

Integrated computational models comprising the physics of the plasma flow near boundaries, the atomic and molecular processes and the particle-surface

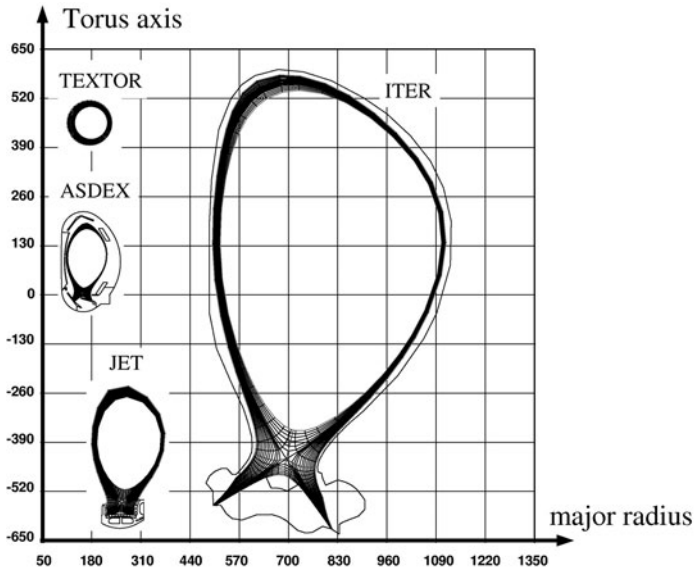

Fig. 2.2. 2D "poloidal" cross-sections of existing tokamaks (TEXTOR, ASDEX Upgrade, JET and a future large fusion machine (here labelled ITER, from an early ITER-design). Also indicated is the large torus radius ("major radius"). 2D plasma edge flow simulations are carried out on the *shaded* (grid) areas

interactions are the only tool to evaluate present experimental results (TEXTOR, ASDEX Upgrade, Tore Supra, JET, ...) with respect to their possible quantitative relevance for future fusion power experiments (ITER) or a future reactor.

These models are limited, because at least one important ingredient, the (turbulent) plasma transport across the B-field, is not understood and this is likely to remain so in the future.

The goal of present numerical code development is, therefore, to treat all the other, predictable, physical components of the model accurately. This applies, in particular, for the atomic, molecular and surface processes, which largely control the plasma flow and plasma energy content in the important near target region. If that can be achieved, then the unknown "anomalous" cross field transport can be separated and isolated computationally, and can then perhaps be determined experimentally even in the edge region.

The peculiarities of plasma flow in the edge region of magnetic confinement fusion machines result from the strong stiffness of the equations (very different timescales within one problem), the inherently (at least) two-dimensional nature of the flow (on multiple connected domains), the extreme anisotropy (by a factor 10^6) in the flow, the strongly nonlinear dependence of the transport coefficients on the flow parameters, the large number of species (equations) to be considered simultaneously, and the nonlocal nature

of the often dominant sources and sinks resulting from atomic, molecular and surfaces processes in the fluid equations. In addition, these sources usually have to be computed on a kinetic level, turning edge plasma flow modeling into a combined "complex micro-macro simulation problem". As in other fields of science where such problems are encountered (e.g., simulation of viscoelastic flows with flow-induced evolution of molecular configurations of polymers) this is also likely to remain a major challenge for future computational edge plasma physics. It has become a common approach to employ two-dimensional (projecting into a poloidal cross-section of the torus) numerical laminar fluid models for the main plasma components (electrons, hydrogenic ions) of the axisymmetric edge plasma (tokamaks). 3D fluid models, e.g., for stellarator edges, which are similar in the physics they contain have only become available more recently. To facilitate the presentation of results we will restrict examples in this chapter to 2D edge plasmas, because the basic atomic and surface processes discussed in this volume are independent of this extra configurational complication.

Currently only Monte Carlo approaches can handle the wide range of surface geometries, reflection models and support complex atomic and molecular processes that occur in real fusion edge plasmas. Therefore the neutral particle transport (ionization, dissociation, etc.) as well as impurity ion transport in the edge region of fusion plasmas is often treated by Monte Carlo simulation on a kinetic level.

The above listed complications, together with rather poor experimental access to the various important places in the edge plasma of magnetic confinement machines have limited the predictive quality of plasma edge models in the past. Plasma edge models can presently be regarded as describing and bookkeeping of, rather than explaining or even predicting, the relevant processes in this outer region of fusion plasmas.

Despite these limitations computer simulations have become a key method in dealing with the various critical issues related to plasma edge phenomena on the path towards economical fusion power reactors, by quantifying at least the known parts of edge science, in a most detailed and complete way possible today.

New operational regimes, such as the chemically rich "detached plasma" conditions and so called "gas target" divertor concepts, are characterized by the particularly strong mutual impact of these neutral particles and the plasma flow. It seems clear that such conditions have to be accessible in the ITER divertor. This increased degree of non-linearity in the model requires special attention to be paid for the numerical procedure, but also requires a far more detailed treatment of the atomic and molecular processes, in particular in the low temperature region near surfaces (0.5–5 eV). This is because the gas-plasma friction, associated energy loss rates, volume recombination, etc. all seem to act together in a most complicated way, also depending on geometrical details, under such favorable divertor operating scenarios.

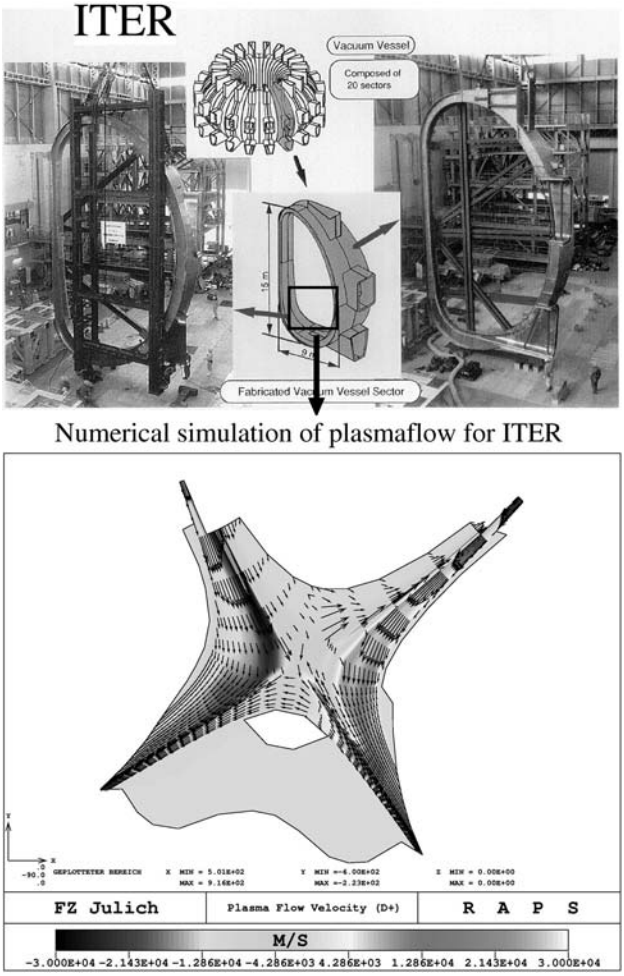

Fig. 2.3. Principle of 2D projection in edge modeling of axisymmetric devices, such as ideal tokamaks (pictures from an ITER coil construction site). Atomic and surface processes are most relevant in the lower section ("divertor") of this cross-section (marked in middle part of **upper figure**). Also shown: typical plasma flow field from 2D edge modelling in this divertor region (**bottom**). See also figures in Sect. 2.3.2

This remainder of this section is organized as follows: in the next section we will briefly describe physical basis of current edge models, focussing on the relevant data and data-format for atomic and molecular processes embedded in such models. In Sect. 2.3 we will show typical results from such model calculations, one for a hot, ionizing limiter edge plasma and one other for a cold, partially recombining divertor edge plasma. Finally some concluding remarks will close this section.

2.2 The Fusion Edge Plasma Models

There exists a large literature concerning the derivation and application of the fluid models for fusion edge plasmas, covering a wide spectrum from rather crude (so called 2-point models) to the most detailed models presently implemented in large 2D edge codes. For an overview see [1] and references therein. For a comprehensive discussion of the plasma equations, with particular emphasis on the special ordering of terms for fusion edge plasmas, self consistent electrical drifts and currents etc., we refer to [3, 4]. Furthermore a good overview of all relevant developments in edge plasma modeling from 1988 until now is provided by the proceedings of the bi-annual international Plasma Edge Theory (PET) conference, published as special issues in the journal "Contributions to Plasma Physics". In this present section we focus on the particular issue of detailed and consistent incorporation of atomic, molecular and surface effects into such models. These are often conflicting requirements: Consistency with plasma transport is easily achieved with highly simplified, either semi-analytical kinetic or numerical diffusion models. These models, however, are disadvantageously lacking in detail. The alternative approach giving a virtually exact description via Monte Carlo synthesis of the relevant processes, has the complementary problem now occurring of achieving a similar level of consistency [5]. In this section we focus on this particular aspect and the consequences for data format and less so on data needs (but see [6, 7] for this latter aspect). As for surface processes this format is established, and has been detailed for example, in [8, 9]. We therefore restrict the discussion here to atomic and molecular processes.

The plasma fluid equations, in their classical form, for magnetized plasmas as in fusion devices, are given, for example, in the fundamental work by Braginskii [10].

In order to obtain reduced sets that can be solved numerically, parameter ordering and symmetry assumptions are made such that the essential physics is still contained. An important ingredient is a set of boundary conditions consistent with these choices. Such boundary conditions have recently been reviewed, [11].

As also in technical plasma applications, the strong mutual interaction between solid surfaces, gas dynamics and plasma flow makes is necessary to take account of a coupling of plasma transport (electron and hydrogenic ion) with the chemical kinetics. In typical low temperature technical plasma applications (lighting, plasma processing, etc.) usually the electron energy distribution function (EEDF) is solved for on a kinetic level, often by "particle in cell" (PIC) methods. The neutral particle densities are found from solving reaction-diffusion equations with a strongly simplified treatment of the transport part (diffusion approximation, or even 0-dimensional confinement time formulations). Here emphasis is on the balance of chemical (atomic and molecular) processes ("reaction kinetics"). The situation is reversed in fusion plasma edge models. Here, due to the larger electron density the en-

tropy production rate for the charged particles is sufficiently large to allow a (electrical conducting)-fluid formulation for electrons and main ion components, but, instead, the neutral particles and the chemistry now have to be dealt with on a detailed kinetic transport level.

We start with a kinetic equation for each particle species. The number of different species is large, even for a pure hydrogen plasma. Already in this ideal case we have to deal, at least, with electrons, hydrogen ions, hydrogen atoms in the ground state and in their various excited states n. Hydrogenic molecules, and hydrogen molecular ions may, in addition, even have to be resolved with respect to their vibrational and rotational degrees of freedom. The excited levels of the neutral particles have to be considered because the ionization and dissociation processes are often step-wise processes, leading from the usually predominantly populated ground states through various excited levels (by a balance of sub- and super-elastic electron impact collisions and radiative decay) to the ionized or dissociated state [12, 13]. The system of kinetic equations for the various atomic and molecular species involved in the divertor chemistry, despite the assumption of 2D toroidal symmetry and near Maxwellian electron and hydrogenic atomic ion distributions, is still far too complex for a full computer simulation. The origin of this complexity is the left-hand side (the transport part) of (2.2) given below, which describes motion between two atomic/molecular collision events. Without this transport part, or with a strong simplification possible here, a large but still easily tractable system of linear algebraic rate equations would result, or, at least, a system of ordinary differential equations for the local temporal evolution.

In practise, the upper principal quantum number n is limited by Lorentz ionization. For hydrogen it is given roughly by

$$n_{\mathrm{c}} = 39/\left(B[T]\sin\Theta\sqrt{E[\mathrm{eV}]/A}\right)^{1/4} .$$

Θ is the angle between the particle trajectory and the field B, E is the kinetic energy and A is the atomic number. Typical conditions in present fusion experiments are

$$B \approx 2\,T\,, \quad \sin\Theta = 0.5\,, \quad E \approx 10\,\mathrm{eV}\,, \quad A = 1\,, \quad \text{hence:} \quad n_{\mathrm{c}} \approx 29\,.$$

Thus, usually a large number of species (10–100) is involved. Fortunately, the non-diagonal, e.g., the radiative, transitions leading from one species to another, which contribute to the coupling term in the set of equations, are often very fast compared to the convective transport time scale of these particles. This leads to a significant simplification of the problem, since for such states the (convective part) left-hand side of (2.2) given below can be neglected compared to the right-hand side. One can consider these "fast species" to be in a local quasi steady state (QSS) with the longer living states. These latter ("slow species") are, usually, the ground states, meta-stable states, and the vibrationally excited states of the electronic ground state. One may

view this approximation as if each of the slow species, described by transport equations, has a train of fast species travelling with it in collisional (and radiative) equilibrium. The relative population of the fast species is then only an algebraic function of the local parameters (densities, temperatures) of the flow fields of the slow species.

A linear algebraic system of rate equations for the "fast species" results, which can be solved a priori. Hence a strongly reduced (in the number of species to be treated) system is obtained. This concept originates from astrophysical applications and from Laser physics. It is in some instances also referred to as "collisional–radiative approximation", for the fast species, "lumped species concept", "bundle-n method" or: "intrinsic low dimensional manifold" (ILDM) method in the literature. We refer to [9,12,13] for further references on this.

The Kinetic Equations for Neutral and Charged Species

We will use Greek letters to label charged species (α, β, ...) and Roman letters (n, m, ...) to label neutral particle species.

From collisionality considerations in fusion edge plasmas one can conclude that a collisional transport model for the charged plasma components is adequate at least for transport along the field lines. By contrast, core plasma transport in the only relevant transport directions there, across the magnetic field, is often studied on the basis of the Vlasov-equation (see below), e.g., in the drift-wave theory of plasma transport.

As an appropriate kinetic equation for the charged particles we take

$$\frac{\partial f_\alpha}{\partial t} + \boldsymbol{v}_\alpha \nabla_{\boldsymbol{r}} (f_\alpha) + \frac{q_\alpha}{m_\alpha} \left\{ \boldsymbol{E} + \frac{1}{c} [\boldsymbol{v} \times \boldsymbol{B}] \right\} \nabla_{\boldsymbol{v}} (f_\alpha) = \sum_\beta C_{\alpha\beta}[f_\alpha, f_\beta] + \sum_m C_{\alpha m}[f_\alpha, f_m] \tag{2.1}$$

and, analogously for the neutral particle component:

$$\frac{\partial f_n}{\partial t} + \boldsymbol{v}_n \nabla_{\boldsymbol{r}} (f_n) = \sum_m C_{nm}[f_n, f_m] + \sum_\beta C_{n\beta}[f_n, f_\beta] \,. \tag{2.2}$$

The collision operators C are bi-linear in the distribution functions, and the summation indices run over all charged species β and neutral species m in the plasma, respectively.

It is an experimental fact that cross field transport in fusion edge plasmas cannot be realistically described by the classical Coulomb collision effects. Strictly then a term $-q_\alpha/m_\alpha \nabla_{\boldsymbol{v}} \langle\langle \delta E \delta f_\alpha \rangle\rangle$ resulting from turbulent fluctuations in the electric field δE and in the phase space density δf_α must be included on the right-hand side of (2.1), see [3].

On the left-hand side of these equations one may replace

$$\boldsymbol{v} \nabla_{\boldsymbol{r}} (f) \quad \text{with} \quad \nabla_{\boldsymbol{r}} (\boldsymbol{v} f) \,,$$

because of the independence of $\boldsymbol{r}$ and $\boldsymbol{v}$. Likewise one may use

$$\frac{q_\alpha}{m_\alpha}\left\{\boldsymbol{E}+\frac{1}{c}[\boldsymbol{v}\times\boldsymbol{B}]\right\}\nabla_{\boldsymbol{v}}\left(f_\alpha\right)=\nabla_{\boldsymbol{v}}\left(\frac{q_\alpha}{m_\alpha}\left\{\boldsymbol{E}+\frac{1}{c}[\boldsymbol{v}\times\boldsymbol{B}]\right\}f_\alpha\right)\,,$$

because of the fact that the Lorentz acceleration force is divergence-less in velocity space. This provides equations in a more conservative form.

Even without the fluctuation term the plasma equations differ from the neutral particle equations in two important aspects:

- one: the Lorentz force term (including electromagnetic fields generated by the plasma particles themselves in addition to externally applied fields). No force terms are included in the neutral particle equations, since gravity and inertial forces are irrelevant for the cases considered here.
- two: the collision integral. For neutral particles, and because of the Monte Carlo method of solution envisaged, it is most convenient to take Boltzmann collision integral expressions in the form based on the Waldmann transition probability formulation [14], and with particular emphasis on the often inelastic nature of the neutral plasma interaction.

For the neutral particle plasma interaction the collision operator then reads:

$$C_{n\beta}[f_n,f_\beta]=\iint(f_n'f_\beta'-f_nf_\beta)\frac{d\sigma_{n\beta}}{d\Omega}|\boldsymbol{v}_n-\boldsymbol{v}_\beta|d^3\boldsymbol{v}_\beta d\Omega\,. \tag{2.3}$$

As usual, f' denotes the distribution function f evaluated at the post collision velocity $\boldsymbol{v}'$ of the collision process $\boldsymbol{v}\rightarrow\boldsymbol{v}'$.

Collision operators of this form keep the neutral particle equations linear, if they are considered separate (decoupled) from the charged particle equations.

The bi-linear collision term resulting from neutral neutral interaction C_{nm} is simplified in present edge models to non-linear BGK-like model collision expressions [15].

$$C_{nm}[f_nf_m]=-\frac{1}{\tau_{nm}}(f_n-f_{nm}^M)\,.$$

In this case no detailed collision kinetics are involved. The collision parameters τ_{nm} and the parameters in the Maxwellian post-collision velocity distribution f_{nm}^M are derived from experimentally determined gas viscosity or diffusivity, and the collisional invariants, respectively. Usually this term is negligible in present experiments, but exceptions exist [16]. In particular for ITER, and the high collisionality there, these terms are expected to become more relevant. However, due to the BGK-approximations made, their implementation into the models does not require further discussion here.

The interactions between charged particles described by $C_{\alpha\beta}$ result from elastic Coulomb interactions and are extensively studied in the classical plasma literature, e.g., [10, 17]. Expressions to account for these Coulomb

interactions with varying degree of complexity are utilized in plasma kinetic theory. Starting with the BBGKY hierarchy equations for the one, two, three, ... particle distribution functions f^1, f^2, f^3, ..., (loc. cit.) one obtains as the simplest form the Vlasov equation. This results from excluding from consideration all multi-particle correlation contributions g^s to f^s, $s > 1$. Interaction between charged particles is accounted for exclusively by an averaged force, in our case by the self consistent electric field. This description is often used for the plasma transport in the core region of tokamaks and stellarators, well inside of the boundary plasma described here. In the next approximation only $g^s = 0$, $s > 2$ is assumed, but with additional assumptions on g^2, namely basically excluding all contributions to g^2 from third particles. One obtains an equation for g^2 in terms of the product $f^1\ f'^1$ alone ("Stosszahlansatz"). By this procedure a closed equation for f^1 can be derived, resulting, e.g., in the famous "Landau Collision Integral" $C^L_{\alpha\beta} f_\alpha(\boldsymbol{v}_\alpha)$ (see again, for example [10]).

Still employing the assumption $g^3 = 0$, but allowing for some of the contributions of third particles to g^2, ("dynamical screening"), results in the even more complicated Lenard-Balescu collision integral $C^B_{\alpha\beta}$.

Also for the neutral particle component a strict derivation of the Boltzmann collision integral from the BBGKY hierarchy is not obvious. However, the approximations leading the Landau and to the Boltzmann integral in terms of neglected multi-particle correlations (Stosszahlansatz) are at a similar level. These two integrals provide the basis for the system of equations for neutral and charged particles used in plasma edge modeling. In this respect this system is consistent with regard to the level of rarefication of the two types of gases.

The Braginskii Moment Equations

As pointed out above the typical fusion edge plasmas are sufficiently collisional ($C_{\alpha\beta}$ is large enough compared to competing terms in (2.1)) so that a plasma fluid prescription is adequate. For a pure plasma (electrons and hydrogen ions) there are 11 unknown 2D profiles: the ion- and electron density, the ion- and electron temperatures, the ion- and electric flow velocity vector and the electrostatic potential. Ion- and electron densities are identical to a very large degree, due to the smallness of the plasma Debye-length λ_D relative to the system size $L : \lambda_D/L \leq 10^{-5}$, which eliminates the Poisson equation from the system. One proceeds by taking 5 moments $\int d^3\boldsymbol{v}$, $\int d^3\boldsymbol{v}\ m\boldsymbol{v}$ and $\int d^3\boldsymbol{v}\ \frac{m}{2}v^2$ of the two equations (2.1) for $\alpha = e$ (electrons) and $\alpha = i$ (protons), and defines, in standard notation:

$$\int d^3\boldsymbol{v} f = n\,, \quad \text{the particle density}\,,$$

$$\int d^3\boldsymbol{v}\boldsymbol{v} f = n\boldsymbol{V}\,, \quad \boldsymbol{V} \quad \text{the fluid velocity}\,,$$

and with the random velocity $\boldsymbol{v}' = \boldsymbol{v} - \boldsymbol{V}$:

$$\int d^3\boldsymbol{v}'\boldsymbol{v}'\boldsymbol{v}' f = \mathsf{P}\,, \quad \text{the total pressure tensor}\,.$$

The (scalar) pressure $p = \int d^3\boldsymbol{v}' \frac{m}{3} v'^2 f = nT$ is the trace $Tr\mathsf{P}$ of the pressure tensor and the off-diagonal elements of the pressure tensor are defined as the (viscous) stress tensor Π:

$$\Pi = \mathsf{P} - p\,\mathsf{I}$$

Finally:

$$\int d^3\boldsymbol{v}' \ \frac{m}{2} v'^2 \boldsymbol{v}' f = \boldsymbol{q}\ , \quad \text{the heat flux vector.}$$

Using these standard notations one obtains the ten equations listed now. The terms $S_n[f_\alpha]$ in these equations due to atomic and molecular interactions with neutral particle species n will be detailed below. For simplicity here the fluctuation term will not be considered. It is common (bad) practise in plasma edge modeling to account for its effect only in an ad-hoc manner (see below) after the fluid equations have first been derived without it. A comprehensive discussion, and proper derivation with this term included from the beginning, for plasma edge models, is given in [4].

– Particle density conservation equation for ions:

$$\frac{\partial}{\partial t} n_\mathrm{i} + \nabla \cdot (n_\mathrm{i} \boldsymbol{V}_\mathrm{i}) = \sum_m S_m[f_\mathrm{i}] \tag{2.4}$$

– and for electrons:

$$\frac{\partial}{\partial t} n_\mathrm{e} + \nabla \cdot (n_\mathrm{e} \boldsymbol{V}_\mathrm{e}) = \sum_m S_m[f_\mathrm{e}] \tag{2.5}$$

– The momentum (or: force-) balance equation for ions is

$$\begin{aligned} \frac{\partial}{\partial t} (m_\mathrm{i} n_\mathrm{i} \boldsymbol{V}_\mathrm{i}) + \nabla \cdot (m_\mathrm{i} n_\mathrm{i} \boldsymbol{V}_\mathrm{i} \boldsymbol{V}_\mathrm{i}) = &-\nabla p_\mathrm{i} - \nabla \cdot \Pi_\mathrm{i} \\ &+ e Z_\mathrm{i} n_\mathrm{i} \left\{ \boldsymbol{E} + \frac{1}{c} [\boldsymbol{V}_\mathrm{i} \times \boldsymbol{B}] \right\} \\ &+ \boldsymbol{R}_\mathrm{ie} + \sum_m \boldsymbol{S}_m[m_\mathrm{i} \boldsymbol{v} f_\mathrm{i}] \end{aligned} \tag{2.6}$$

Utilizing the particle conservation equation, the left-hand side terms can be expressed as the time rate of momentum change plus the particle source contribution (if any)

$$mn\frac{d\boldsymbol{V}_\mathrm{i}}{dt} + m\boldsymbol{V}_\mathrm{i}\sum_m S_m[f_\mathrm{i}].$$

The right-hand side terms are the forces due to pressure, viscous stress, the electric and magnetic forces, respectively, and the friction force due to collisions with electrons

$$\boldsymbol{R}_\mathrm{ie} = \int d^3\boldsymbol{v}\; m\boldsymbol{v}C_\mathrm{ie}[f_\mathrm{i}, f_\mathrm{e}].$$

– For electrons, neglecting inertia and viscous stress terms due to $m_\mathrm{e} \ll m_\mathrm{i}$, the momentum conservation equation reduces to

$$0 = -\nabla p_\mathrm{e} - en_\mathrm{e}\left\{\boldsymbol{E} + \frac{1}{c}[\boldsymbol{V}_\mathrm{e}\times\boldsymbol{B}]\right\} + \boldsymbol{R}_\mathrm{ei} + \sum_m \boldsymbol{S}_m[m_\mathrm{e}\boldsymbol{v}f_\mathrm{e}] \quad (2.7)$$

Of course, due to momentum conservation in the elastic Coulomb collisions, one has:

$$\boldsymbol{R} = \boldsymbol{R}_\mathrm{ei} = -\boldsymbol{R}_\mathrm{ie}.$$

The Chapman–Enskog procedure to approximate the distribution functions f_i, f_e by a linear perturbation ansatz, the Landau form of the Coulomb collision integral together with the small mass ratio $m_\mathrm{e}/m_\mathrm{i}$ expansions in the classical work of Braginskii results in the friction term $\boldsymbol{R}$ given as

$$\boldsymbol{R} = en_\mathrm{e}\left(\frac{\boldsymbol{j}_\parallel}{\sigma_\parallel} + \frac{\boldsymbol{j}_\perp}{\sigma_\perp}\right) - 0.71n_\mathrm{e}\nabla_\parallel T_\mathrm{e} - \frac{3}{2}\frac{en_\mathrm{e}^2}{\sigma_\perp B^2}[\boldsymbol{B}\times\nabla T_\mathrm{e}]$$

with the electrical current density $\boldsymbol{j}$

$$\boldsymbol{j} = Z_\mathrm{i}en_\mathrm{i}\boldsymbol{V}_\mathrm{i} - en_\mathrm{e}\boldsymbol{V}_\mathrm{e}.$$

The subscripts $\parallel$ and $\perp$ denote vector components parallel and normal to $\boldsymbol{B}$, respectively.

– Energy conservation equation for ions (of charge eZ_i)

$$\frac{\partial}{\partial t}\left(\frac{3}{2}n_\mathrm{i}T_\mathrm{i} + \frac{m_\mathrm{i}n_\mathrm{i}}{2}\boldsymbol{V}_\mathrm{i}^2\right) + \nabla\cdot\left[\left(\frac{5}{2}n_\mathrm{i}T_\mathrm{i} + \frac{m_\mathrm{i}n_\mathrm{i}}{2}\boldsymbol{V}_\mathrm{i}^2\right)\boldsymbol{V}_\mathrm{i} + \Pi_\mathrm{i}\cdot\boldsymbol{V}_\mathrm{i} + \boldsymbol{q}_\mathrm{i}\right]$$
$$= (eZ_\mathrm{i}n_\mathrm{i}\boldsymbol{E} + \boldsymbol{R}_\mathrm{ie})\cdot\boldsymbol{V}_\mathrm{i} + Q_\mathrm{ie} + \sum_m S_m[\frac{m_\mathrm{i}}{2}v_\mathrm{i}^2 f_\mathrm{i}]\,. \quad (2.8)$$

The second term on the left is the heat transport $\nabla\boldsymbol{Q}$ with $\boldsymbol{Q} = \int d^3\boldsymbol{v}\;\frac{m}{2}v^2\boldsymbol{v}f$, due to convection, viscous heat transport and conduction, respectively. On the right-hand side one has the heating due to the work done by the electric field, the collisional frictional force due to the flow relative to the other species (here: electrons) and from the collisional heating due to collisions with other species (electrons):

$$Q_\mathrm{ie} = \int d^3\boldsymbol{v}'\;\frac{m}{2}v'^2C_\mathrm{ie}[f_\mathrm{i}f_\mathrm{e}]$$

– For the electron energy conservation equation, again utilizing $m_\mathrm{e} \ll m_\mathrm{i}$, one finds:

$$\frac{\partial}{\partial t}\left(\frac{3}{2}n_\mathrm{e}T_\mathrm{e}\right) + \nabla\cdot\left(\frac{5}{2}n_\mathrm{e}T_\mathrm{e}\boldsymbol{V}_\mathrm{e} + \boldsymbol{q}_\mathrm{e}\right) = -en_\mathrm{e}\boldsymbol{E}\cdot\boldsymbol{V}_\mathrm{e} + \boldsymbol{R}_\mathrm{ei}\cdot\boldsymbol{V}_\mathrm{e} + Q_\mathrm{ei} + \sum_m S_m[\frac{m_\mathrm{e}}{2}v_\mathrm{e}^2 f_\mathrm{e}] \tag{2.9}$$

As before, due to conservation of energy in the elastic Coulomb collisions, the total collisional transfer of energy between electrons and ions Q^T must fulfill:

$$Q^T = Q^T_\mathrm{ie} = -Q^T_\mathrm{ei}\,,$$

i.e.,

$$\int d^3\boldsymbol{v}\ \frac{m}{2}v^2 C_\mathrm{ie}[f_\mathrm{i}f_\mathrm{e}] = Q_\mathrm{ie} + \boldsymbol{V}_\mathrm{i}\cdot\boldsymbol{R}_\mathrm{ie} = -(Q_\mathrm{ei} + \boldsymbol{V}_\mathrm{e}\cdot\boldsymbol{R}_\mathrm{ei}),$$

and hence:

$$Q_\mathrm{ei} = -Q_\mathrm{ie} + \boldsymbol{R}\cdot(\boldsymbol{V}_\mathrm{e} - \boldsymbol{V}_\mathrm{i})$$

Within the above mentioned "Braginskii approximation" one finds:

$$Q_\mathrm{ie} = \frac{3m_\mathrm{e}}{m_\mathrm{i}}\frac{n_\mathrm{e}}{\tau_\mathrm{e}}\,(T_\mathrm{i} - T_\mathrm{e})$$

The transport relations, providing the closure of the system by expressing the viscous tensor and the heat flux vector in terms of the moments n, $\boldsymbol{V}$ and T and gradients thereof, are obtained as a result of the above mentioned "Braginskii approximation" for the distribution function as

$$\boldsymbol{q}_\mathrm{i} = -\kappa^\mathrm{i}_\parallel\nabla_\parallel T_\mathrm{i} - \kappa^\mathrm{i}_\perp\nabla_\perp T_\mathrm{i} + \kappa^\mathrm{i}_\wedge\left[\frac{\boldsymbol{B}}{B}\times\nabla_\perp T_\mathrm{i}\right] \tag{2.10}$$

and

$$\boldsymbol{q}_\mathrm{e} = -\kappa^\mathrm{e}_\parallel\nabla_\parallel T_\mathrm{e} - \kappa^\mathrm{e}_\perp\nabla_\perp T_\mathrm{e} - \kappa^\mathrm{e}_\wedge\left[\frac{\boldsymbol{B}}{B}\times\nabla_\perp T_\mathrm{e}\right] - 0.71\frac{T_\mathrm{e}}{e}\boldsymbol{j}_\parallel - \frac{3}{2}\frac{T_\mathrm{e}}{e\omega_\mathrm{e}\tau_\mathrm{e}B}\left[\boldsymbol{B}\times\boldsymbol{j}_\perp\right] \tag{2.11}$$

This set of equations is completed by the classical transport relations

– $\sigma_\parallel, \sigma_\perp$ = classical electrical conductivities
– $\kappa^\alpha_\parallel, \kappa^\alpha_\perp, \kappa^\alpha_\wedge$ = classical thermal conductivities
– ω_e = electron gyro-frequency
– τ_e = collision-time for electrons.

The transport coefficients are given in Braginskii's original work (loc.cit), in many textbooks on plasma physics and in a particularly compact form in the plasma formulary [18].

The resulting set of 10 equations, assuming toroidal symmetry and replacing the radial component of the ion momentum balance equation by an ad hoc diffusions ansatz (likewise: the other radial transport coefficients are replaced by ad hoc anomalous expressions) is the basis for most current edge plasma simulation models. These "anomalous" ad-hoc coefficients are free model parameters. They, and their empirical scalings, can be determined by comparison with experimental plasma profile data, if one can be sure that all other terms in the equations, and in particular the source terms S_m resulting from atomic and molecular processes, are accurately known and implemented.

Most 2-dimensional edge plasma transport codes employ more or less standard numerical techniques to solve the plasma fluid equations.

2.2.1 Collisional Contributions to Braginskii Equations

Collisional contributions in the above set of equations due to the elastic Coulomb interactions are the terms $\boldsymbol{R}_{\alpha\beta}$ and $Q_{\alpha\beta}$. We now proceed to express more explicitly the source terms $S_n[f_\alpha]$ due to atomic and molecular interactions with neutral particles. These result from the collision integrals $C_{\alpha n}$ in (2.1). These integrals may be considered separately for each individual collision process, and then summed up. We omit the index labelling a particular type of process in the following discussion.

The dominant processes to be considered here are inelastic, reactive and even chemical processes, such as formation and breakup of molecules at the surfaces and by volume processes respectively. For large, cold divertor plasmas as currently envisaged for, e.g., ITER, also elastic neutral-ion collisions gain relevance, due to their frictional effects on the plasma flow.

According to the definitions in (2.1) and (2.2), and with $A = 1$, $m\boldsymbol{v}$, $m/2v^2$, respectively, we have:

$$S_n[Af_\alpha] = \int d^3\boldsymbol{v}_\alpha \; A \cdot C_{\alpha n}[f_\alpha, f_n] \,. \tag{2.12}$$

As pointed out above, we adopt the Boltzmann gas approximation

$$N \to \infty, \quad N\sigma^2 \to b = \text{const.}, \quad \text{hence} \quad N\sigma^3 \to 0,$$

(N: number of particles, σ: range of inter-particle forces). If the collision process is binary and non-reactive (post-collision species i', j' remain the same as pre-collision species i and j), these indices do not appear in the collision integral, and we can adopt the standard notations of a binary collision turning the two velocities $\boldsymbol{v}, \boldsymbol{v}_1$ into $\boldsymbol{v}', \boldsymbol{v}_1'$, with the corresponding abbreviations for the distribution functions f, f_1 and f', f_1', respectively. Let $W(\boldsymbol{v}, \boldsymbol{v}_1 \to \boldsymbol{v}', \boldsymbol{v}_1')$ denote the probability for such a transition, then

$$C[f, f_\alpha] = \iiint d^3\boldsymbol{v}_\alpha d^3\boldsymbol{v}' d^3\boldsymbol{v}'_\alpha \; [W(\boldsymbol{v}', \boldsymbol{v}'_\alpha \to \boldsymbol{v}, \boldsymbol{v}_\alpha) \; f' f'_\alpha - W(\boldsymbol{v}, \boldsymbol{v}_\alpha \to \boldsymbol{v}', \boldsymbol{v}'_\alpha) \; f f_\alpha] \tag{2.13}$$

For all collision processes of interest in the present context a splitting of the collision integral (2.13) into a gain (first term) and a loss (second term) is possible.

$$C[.,.] = C^+[.,.] - C^-[.,.]$$

The nine-fold integration for the gain term is over both pre-collision velocities and over the second (all but the first) post-collision velocity. Both pre-collision states are folded with their corresponding distribution function.

In the loss term the integration is over both (all) post-collision velocities and over the second of the two pre-collision velocities. Again both pre-collision states are folded with their corresponding distribution functions.

A generalization to reactive and chemical processes is straight forward and indicated by the brackets in the previous two statements. The collision integrals remain bi-linear in the two distribution functions of the two particles entering the collision. We must introduce appropriate Kronecker-Delta's and allow for more than two post-collision particles. We obtain, e.g., for three post-collision particles (in processes such as $e + H_2 \to e + H + H$, dissociation, or: $e + H \to e + H^+ + e$, ionization) for the gain term in the equation for species j:

$$C^+_{n,\alpha\to j_1,j_2,j_3}[f, f_\alpha] = \delta_{j,j_1} \iiiint d^3\boldsymbol{v}' d^3\boldsymbol{v}'_\alpha d^3\boldsymbol{v}_{j_2} d^3\boldsymbol{v}_{j_3} \times [W(\boldsymbol{v}', \boldsymbol{v}'_\alpha \to \boldsymbol{v}_{j_1}, \boldsymbol{v}_{j_2}, \boldsymbol{v}_{j_3}) \; f' f'_\alpha] \tag{2.14}$$

and for the loss term in the equation for species n:

$$C^-_{n,\alpha\to j_1,j_2,j_3}[f, f_\alpha] = \iiiint d^3\boldsymbol{v}_\alpha d^3\boldsymbol{v}'_{j_1} d^3\boldsymbol{v}'_{j_2} d^3\boldsymbol{v}'_{j_3} \times \left[W(\boldsymbol{v}, \boldsymbol{v}_\alpha \to \boldsymbol{v}'_{j_1}, \boldsymbol{v}'_{j_2}, \boldsymbol{v}'_{j_3}) f f_\alpha\right] , \tag{2.15}$$

i.e.,

$$C^-_{n,\alpha\to j_1,j_2,j_3}[f, f_\alpha] = f \cdot \iiiint d^3\boldsymbol{v}_\alpha d^3\boldsymbol{v}'_{j_1} d^3\boldsymbol{v}'_{j_2} d^3\boldsymbol{v}'_{j_3} \; [W \; f_\alpha] . \tag{2.16}$$

This loss term is linear in f.

With these specifications, and with the appropriate neutral particle–plasma collision terms put into the combined set of neutral and plasma equations, internal consistency within the system of equations is achieved. Overall particle, momentum and energy conservation properties in the combined model result from the symmetry properties of the transition probabilities W: indices of pre-collision states may be permuted, as well as indices of post-collision states. For elastic collisions even pre- and post collision states may be exchanged in W.

2.2.2 Standard Form of Source Terms

The remaining problem is to evaluate the terms (2.12) for all collision processes to be considered. Due to the special notation chosen here, however, these terms are already exactly in the format to which Monte Carlo kinetic particle transport codes can be applied directly. The probabilistic formulation is particularly suitable for these procedures. We refer to standard literature on Monte Carlo methods for linear transport, such as [19]. Here it is only important to note that one may write equation (2.12) as linear functional of the neutral particle distribution function f_n

$$S_n[Af_\alpha] = \langle g_A, f_n \rangle_{\boldsymbol{v}_n} \tag{2.17}$$

where f_n is the solution of the Boltzmann equation (2.2) and the scalar product is induced by the conventional L_2 norm. Hence: $\langle ., . \rangle_{\boldsymbol{v}_n}$ means integration over the neutral particle velocities $\boldsymbol{v}_n$ as it is readily carried out by Monte Carlo procedures when averaging over a large number of simulated neutral particle trajectories.

From the above consideration one can furthermore infer that the "detector functions" g_A are always of the form

$$g_A = \int d^3\boldsymbol{v}_\alpha \; f_\alpha \cdot A \; \cdots = \langle A \cdot \ldots, f_\alpha \rangle_{\boldsymbol{v}_\alpha} \tag{2.18}$$

Here ... depends on the W-kernels introduced above, but in general stands for terms of the form $\sigma^l(v_{\rm rel}) \cdot v_{\rm rel}$. σ^l is a cross-section, appropriately weighted by factors $[1 - \cos^l(\theta)]$, $l = 1, 2, \ldots$, if the efficiency of exchange of quantity A in a collision depends on the scattering angle θ in this way (as, e.g., in case of elastic neutral particle – ion collisions, see Sect. 2.2.4). In case of inelastic collision processes σ is simply the total cross-section, denoted σ^0 (if no confusion with the weighting exponent $l = 1, 2, \ldots$ is possible) or σ^t. In principle the detector functions g_A must be obtained by numerical integration and tabulated for the parameters of the relevant distribution functions f_α.

However, a much more tractable form can be derived, strongly reducing the number of parameters in these data tables. The first step follows from the fact, that consistent with the fluid approximation for the charged particles α we can make the assumption of a near Maxwellian distribution

$$f_\alpha \approx f_\alpha^M(1 + \Phi) = n_\alpha \left(\frac{m_\alpha}{2\pi T_\alpha} \right) \exp \left[-\frac{m_\alpha}{2T_\alpha} (\boldsymbol{v}_\alpha - \boldsymbol{V}_\alpha)^2 \right] \; (1 + \Phi) \tag{2.19}$$

and $\Phi \ll 1$. Regardless of the precise form of the expansion of f_α or Φ , e.g., in the Hermite Tensor polynomials as in Grad's procedure, or in Sonine polynomials for $\Phi(v)$ (plus an expansion in spherical harmonics for the dependence on ϕ and ψ, with $\boldsymbol{v} = (v, \phi, \psi)$), as in the Braginskii (Enskog–) formulation, the detector functions g_A in (2.18) can be evaluated as linear expressions

$$g_A = \sum_T a_T \; g_A^T$$

of detector functions g_A^T with

$$g_A^T = \langle A \ldots, f_\alpha^T \rangle \quad \text{with} \quad f_\alpha^T = f_\alpha^M \cdot (v_\alpha^T - V_\alpha^T),$$

hence

$$g_A^T = \langle A \ldots, f^M \cdot v^T \rangle - V^T \cdot \langle A \ldots, f^M \rangle$$

f^M is the Maxwellian distribution of (2.19) with spatially varying n, T, and $\boldsymbol{V}$ and v^T stands for any element of tensors $\boldsymbol{v}\ \boldsymbol{v} \ldots\ \boldsymbol{v}$ (any rank, i.e., any number of factors in this outer product). We may even omit the shift vector $\boldsymbol{V}$ in the Maxwellian and in the arguments of the expansion polynomials, due to the fact that $|\boldsymbol{V}| \ll v_T = \sqrt{2T/m}$ in many fusion plasma applications usually. Hence f_α can equally well be expanded in polynomials in either $\boldsymbol{v}$ or in the random velocity $\boldsymbol{v}'$.

The problem can further be reduced by noting that the weighting functions A themselves are tensor elements of the type v_α^T. The product will henceforth be denoted $v_{\alpha,A}^T$, or simply v_A^T.

2.2.3 The I-Integral Representation

With the specifications from above and with the choices $\boldsymbol{v_\alpha} = (v_\alpha, \psi, \phi)$, $\boldsymbol{v_n} = (v_n, 0, 0)$ we can write for the Maxwellian average g_A^T

$$g_A^T = \left(\frac{1}{u^2\pi}\right)^{\frac{3}{2}} \int_0^\infty dv_\alpha \int_0^{2\pi} d\phi \int_0^\pi d\psi \; \sigma^l(v_{\text{rel}}) \; v_{\text{rel}} \; v_\alpha^2 \; v_{\alpha,A}^T \; \sin(\psi) \; e^{-\frac{v_\alpha^2}{u^2}} \tag{2.20}$$

Here $u = \sqrt{2T_\alpha/m_\alpha}$, the thermal velocity, $\boldsymbol{v_{\text{rel}}} = \boldsymbol{v_\alpha} - \boldsymbol{v_n}$ is the relative velocity, ψ was chosen as the angle between the velocity of the charged particle α and the neutral particle labelled $'n'$.

We are considering collision processes with azimuthal symmetry only: hence $\int_0^{2\pi} d\phi \cdots = 2\pi \ldots$.

After substitution $\boldsymbol{v_\alpha} = \boldsymbol{v_{\text{rel}}} + \boldsymbol{v_n}$, and with $v_\alpha^2 \sin\psi \, dv_\alpha \, d\psi = v_{\text{rel}}^2 \sin\psi^* dv_{\text{rel}} d\psi^*$ the integration over the resulting angular co-ordinate ψ^* can be carried out, and one obtains:

$$\begin{aligned} g_{\alpha,A}^T = \left(\frac{1}{u^2\pi}\right)^{\frac{1}{2}} \frac{1}{v_n} \; e^{-\frac{v_n^2}{u^2}} \int_0^\infty dv_{\text{rel}} \; \sigma^l(v_{\text{rel}}) \; v_{\text{rel}}^2 \; v_{\alpha,A}^T \; e^{-\frac{v_{\text{rel}}}{u^2}} \\ \times \left[e^{2\frac{v_{\text{rel}} v_n}{u^2}} - e^{-2\frac{v_{\text{rel}} v_n}{u^2}} \right] \end{aligned} \tag{2.21}$$

For $v_{\alpha,A}^T = 1$ this is the ordinary rate coefficient for an interaction of a mono-energetic beam with a Maxwellian host medium (e.g., [20]). Since any

$v_{\alpha,A}^T$ can be expressed as polynomial in $v_{\rm rel}$. Hence, depending on details of the plasma fluid model, a number of such integrals, with $v_{\rm rel}^2\ v_{\alpha,A}^T$ replaced by $v_{\rm rel}^{2+k}$, need to be provided. However, an only slightly modified definition allows one to reduce this set of data to only one single basic rate-coefficient: We define

$$I_{k,l} = \left(\frac{1}{\pi}\right)^{\frac{1}{2}} \frac{1}{v_n}\ \frac{1}{u^{k+1}}\ e^{-\frac{v_n^2}{u^2}} \int_0^\infty dv_{\rm rel}\ \sigma^l(v_{\rm rel})\ v_{\rm rel}^{2+k}\ e^{-\frac{v_{\rm rel}}{u^2}} \times \left[e^{2\frac{v_{\rm rel}v_n}{u^2}} - (-1)^k\ e^{-2\frac{v_{\rm rel}v_n}{u^2}}\right] \tag{2.22}$$

Note that all these integrals have dimensions of a rate coefficient: volume/time.

In summarizing, we note that any source term in the fluid equations due to neutral particle plasma interaction, retaining the full kinetic level for the neutrals, is a linear expression of linear functionals

$$S_n[Af_\alpha] = \sum a_k \langle I_k, f_n\rangle_{\boldsymbol{v}_n} \tag{2.23}$$

with appropriate values of l and with these "I-Integrals" as weighting functions.

In particular, for sources and sinks due to inelastic processes in the Braginskii equations, and with $f_\alpha = f_\alpha^M$, we see that integrals $I_{0,0}, I_{0,1}$ and $I_{0,2}$ are involved, whereas the integrals $I_{1,0}, I_{1,1}$ and $I_{1,2}$ (i.e., with the diffusion- or transport cross-sections) appear in the expressions from elastic neutral particle plasma interactions.

Furthermore, the representation (2.23) is possible regardless of the level of approximation involved in deriving the fluid equations, and regardless of whether the Braginskii (Enskog) method or Grad's expansion ansatz (e.g., 13 or 21 moments) is used. Clearly this role of the I-Integrals this corresponds to the similar role played by the Ω-integrals (see below) in the kinetic theory of gases, when transport coefficients for fluid approximations are expressed in terms such elementary functions.

It is worth mentioning the following relation to similar integrals commonly used in gas dynamics, the so called Ω integrals. For a detailed discussion of hydrodynamic models in terms of the Ω-integrals we refer to standard textbooks on the kinetic theory of gases, e.g., to the monograph by Hirschfelder, Curtiss and Bird [21], or to the monograph by Chapman and Cowling [22].

Inspecting formula (2.22), two consequences are immediate (we omit the cross-section label index l, when it is not relevant): I_{k+2} can be expressed linearly in terms of I_k, the derivative $dI_k/d\ \ln(T_\alpha)$ and I_{k+1}:

$$\frac{dI_k}{d\ \ln(T_\alpha)} + \left(\frac{k+1}{2} - \beta^2\right) I_k + 2\beta I_{k+1} = I_{k+2}, \quad \beta = v_n/u_\alpha \tag{2.24}$$

Furthermore, I_{k+1} is given by a linear expression in terms of I_k and the derivative $dI_k/d\ \ln(v_n)$:

$$\frac{dI_k}{d\ \ln(v_n)} + \left(1 + 2\beta^2\right) I_k = 2\beta I_{k+1}\,. \tag{2.25}$$

Thus:

$$\frac{dI_k}{d\ \ln(T_\alpha)} + \left(\frac{k+3}{2} + \beta^2\right) I_k + \frac{dI_k}{d\ \ln(v_k)} = I_{k+2}. \tag{2.26}$$

Considering the $I_{k,l}$ rates for even values of k, say $k = s \cdot 2$, and averaging these rates with a Maxwellian distribution for the neutral particle velocity, then, up to normalizing factors, the above mentioned $\Omega^{s,l}$ integrals result:

$$\Omega^{s,l} = \frac{1}{\sqrt{4\pi} w^{3+2s}} \int_0^\infty dv_{\rm rel}\ v_{\rm rel}^{3+2s} \cdot \sigma^l(v_{\rm rel}) \cdot e^{-(\frac{v_{\rm rel}}{w})^2}\,. \tag{2.27}$$

This can readily be seen by using the formula:

$$\int_0^\infty dx\ x \cdot \exp(-\beta \cdot x^2) \cdot sh(\gamma \cdot x) = \frac{\gamma}{4\beta} \cdot \sqrt{\frac{\pi}{\beta}} \cdot \exp\left(\frac{\gamma^2}{4\beta}\right) \quad \text{for } Re(\beta) > 0. \tag{2.28}$$

The general relation reads:

$$\langle I_{k,l} \rangle = 8 \left(\frac{w}{u_\alpha}\right)^{2s} \Omega^{s,l}, \quad s = k/2, \quad \frac{1}{w^2} = \frac{1}{u_n^2} + \frac{1}{u_\alpha^2} \tag{2.29}$$

i.e., w denotes the thermal speed corresponding to the effective temperature $T_{\rm eff}$ in the Maxwellian distribution of relative velocities. For example, up to the numerical factor 8, which results from transforming the velocities v_1 and v_2 into $v_{\rm rel}$ and $v_{\rm com}$, the $\Omega^{0,0}$ integrals are the single parameter collision rates (depending on electron temperature only, assuming stationary neutral particles) usually employed to model inelastic electron-neutral interactions (e.g., ionization, dissociation, etc.). A large collection of such rates relevant for fusion plasmas is again given in [20] and, more recently, in [7].

Furthermore, the Ω-integrals are the basic quantities entering the formulas for the transport coefficients in a hydrodynamic approximation (diffusion, viscosity, conductivity, etc.). Also well known is the recursive relation for the higher Ω-integrals:

$$\frac{d\Omega^{s,l}}{d\ \ln(T)} + (s + \frac{3}{2})\Omega^{s,l} = \Omega^{s+1,l} \tag{2.30}$$

which directly relates to the above mentioned recursions for the I-integrals.

Advanced Monte Carlo algorithms, developed in other fields (e.g., for electron transport studies in solids), automatically switch from a kinetic Boltzmann-like to a diffusive ("Brownian motion-like") description, depending on the local background medium conditions, in order to improve statistical performance at high collisionality.

Hence not only for numerical "neutral gas diffusion models", but also for such hybrid Monte Carlo techniques internally consistent expressions for the $\Omega^{0,1}$ integrals, for $(l = 0, 1, 2)$ must be computed. These fits should then, again, preferentially be given in terms of $\ln(T_{\text{eff}})$.

All aforementioned integrals can in principle be obtained by numerical integration from the cross-sections and then fitted or tabulated.

Internal consistency in the data for σ^l, $I_{k,l}$ and $\Omega^{s,l}$ is a crucial prerequisite for particle, momentum and energy conservation in such models. The consistency amongst the rates is ensured by employing the above mentioned recursive relations. This can be achieved either by fitting expressions which can be differentiated with respect to T_α and v_n, or e.g., by employing data tables only for the lowest rate I_0 and B-splines with sufficient smoothness to permit evaluation of the derivatives.

2.2.4 Application to Elastic Neutral Ion Collisions

An application of the procedures outlined above, to the special case of elastic neutral-ion collisions, has been made in [23]. The relevance of this particular type of neutral-plasma interaction, in particular for helium pumping, has been pointed out already since the early nineties [9,24,25]. The hydrogenic proton-molecule collision system provides a relevant frictional force on the parallel (to the B-field) plasma flow to target surfaces, and hence it may be an important ingredient in the transition to the detached divertor regime. Elastic proton-hydrogen atom collisions have also been discussed in [9], but, due to the indistinguishability of this process from resonant charge exchange, at least at low collision energies, in edge models typically only the combined effect (elastic plus charge exchange) is treated. Note: The classical elastic reaction should only be used, if the resonant charge exchange differential cross-section (and hence: diffusion cross-section) is reduced accordingly. The sum: elastic plus charge exchange transport ("diffusion"-) cross-section should be twice the charge exchange total cross-section, to a very good approximation. The assumption of an exchange of identity (scattering angle π in the center of mass system, i.e., backward scattering) at charge exchange, common to most fusion edge plasma neutral gas models, produces already that factor 2. Hence there is the need for either a revised charge exchange scattering angle distribution, if an elastic collision contribution (forward scattering) is explicitly added in, or the "true" elastic component must be ignored in order to avoid double counting.

For the other elastic processes the procedure outlined above leads to the following results [23]:

– *Momentum exchange:* The momentum exchange in a single collision between a neutral particle n and an ion α is given as

$$\triangle \boldsymbol{P}_\alpha = m_{\alpha,n}(1 - \cos\theta)(\boldsymbol{v}_n - \boldsymbol{v}_\alpha) \tag{2.31}$$

$m_{\alpha,n}$ is the reduced mass. For the $\triangle \boldsymbol{P}_\alpha$ weighted rate coefficient $\langle \sigma v_{rel} \triangle \boldsymbol{P}_\alpha \rangle$ one finds, after carrying out the integrations over a Maxwellian distribution (temperature T_α) of the ions (with $a = v^2_{\alpha,\mathrm{therm}} = 2kT_\alpha/m_\alpha$), and using the definitions of the I-integrals ((2.22) given above):

$$\langle \sigma v_{\mathrm{rel}} \triangle \boldsymbol{P}_\alpha \rangle = -m_{\alpha,n} \frac{\boldsymbol{v_n}}{v_n} \left[\frac{a}{2v_n} I_{0,1} - a^{1/2} I_{1,1} \right] \tag{2.32}$$

The I-Integrals are functions of temperature T_α and individual neutral particle velocity v_n. It is these expressions that have to be integrated along Monte Carlo test trajectories in order to include the friction between neutrals and ions, due to these elastic processes, consistently into edge plasma models. In terms of required data and data format this means that in addition to the differential scattering cross-section (only needed as prescription to sample the scattering angles while computing the trajectories) only the rate coefficient $I_{0,1}$ (as a function of plasma temperature T_α and individual neutral particle velocity v_n) is required. The $I_{1,1}$ rate can be expressed in terms of the $I_{0,1}$ and its derivatives, according to the recursive relations given above. The same remains true, of course, if a drifting Maxwellian is assumed, by transforming into a coordinate system drifting with this mean ion velocity.

– *Energy exchange:* The energy exchange in a single collision between a neutral particle n and an ion α is given as

$$\triangle E_\alpha = \kappa_{\alpha,n} \left((1 - \cos\theta) \left[\frac{m_\alpha}{2} v_\alpha^2 - \frac{m_n}{2} v_n^2 + \frac{m_n - m_\alpha}{2} \boldsymbol{v_\alpha} \boldsymbol{v_n} \right] \right) \tag{2.33}$$

with $\kappa_{\alpha,n} = 2m_\alpha m_n/(m_\alpha + m_n)^2$, the energy exchange coefficient. Again, integrating the product $\sigma v_{\mathrm{rel}} \triangle E_\alpha$ over a Maxwellian distribution, yields:

$$\langle \sigma v_{\mathrm{rel}} \triangle E_\alpha \rangle = \kappa_{\alpha,n} \left[\frac{m_\alpha + m_n}{4} a I_{0,1} - \frac{m_\alpha + m_n}{2} v_n a^{1/2} I_{1,1} + \frac{m_n}{2} a I_{2,1} \right] \tag{2.34}$$

(This expression corrects the related formula equ. 61 in [23], which contains an algebraic error.) Again, strictly speaking, only the rate coefficient $I_{0,1}$ is needed, due to the recursive relations. Because $I_{0,1}$ only depends upon the relative velocity of particles, these rates can also be given for stationary neutral particles and drifting Maxwellian averages, as function then of T_α and V_α, the drift velocity. Using the same argument they can also be scaled to rates for cases in which both particles have a Maxwellian distribution and, in addition, these may be drifting relative to each other. This is because the distribution of relative velocities of two drifting Maxwellian distributions is again a drifting Maxwellian. Care is needed in databases to specify precisely which masses (of the charged and of the neutral particle) have been used in setting up the rate-coefficients $I_{0,0}$ or $I_{0,1}$, for otherwise these rescalings to other masses cannot be carried out.

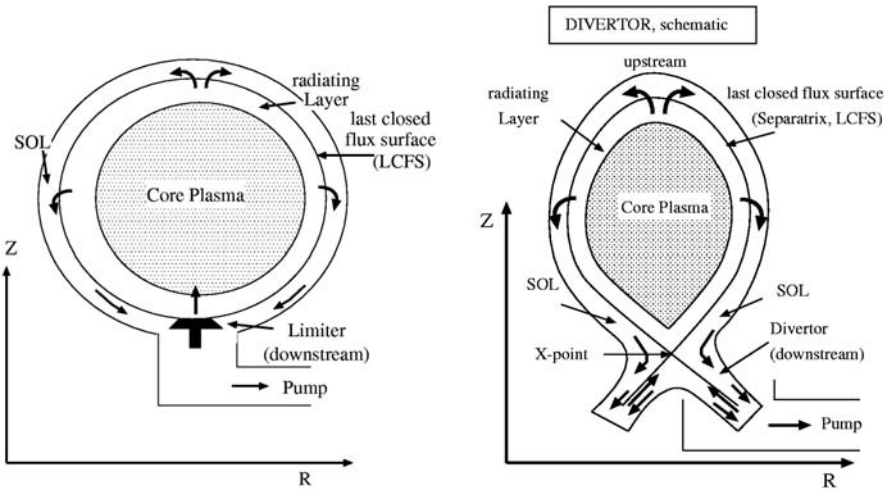

Fig. 2.4. Schematic of the toroidally symmetric limiter (**left**) and divertor (**right**) configurations. Indicated are also major plasma flow directions. Note the typical flow reversal on top of the limiter, radially inward across the B-field, and in the divertor flow channel, parallel to the B-field. Both are, in part, driven by atomic and molecular processes (ionization sources)

2.3 Applications

In this section we will discuss typical results obtained with the coupled plasma fluid-neutral kinetic ("micro-macro-") simulation procedure often employed to fusion edge plasmas. We will exemplarily show results from 2 cases here, one corresponding to an ionizing edge plasma (see also [26] in this volume for experimental and plasma diagnostics details), as typical for limiter configurations. It is a low recycling limiter scrape-off layer (SOL) with model parameters chosen to be typical for TEXTOR discharges. The second sample case corresponds to an at least partially recombining and friction dominated condition now typical of divertor plasmas, here taken from ASDEX Upgrade (for experimental and diagnostics details see [27] in this volume). These so called "detached divertor" conditions are expected to be of direct relevance for ITER. Edge modeling of atomic, molecular and surface processes has to provide the extrapolation from the basic processes identified in current experiments to the much higher collisionality regime (characteristic system size to collision mean free path) in ITER. However, during the initial phase of a discharge ITER will operate as a limiter machine (of the order of a minute discharge time) and only then switch into the divertor mode for the long steady state phase. Figure 2.4 shows, schematically, the difference between these two concepts. In both cases the core plasma feeds by radial (cross field) flows and conduction (particles and heat) the edge region. These flows are

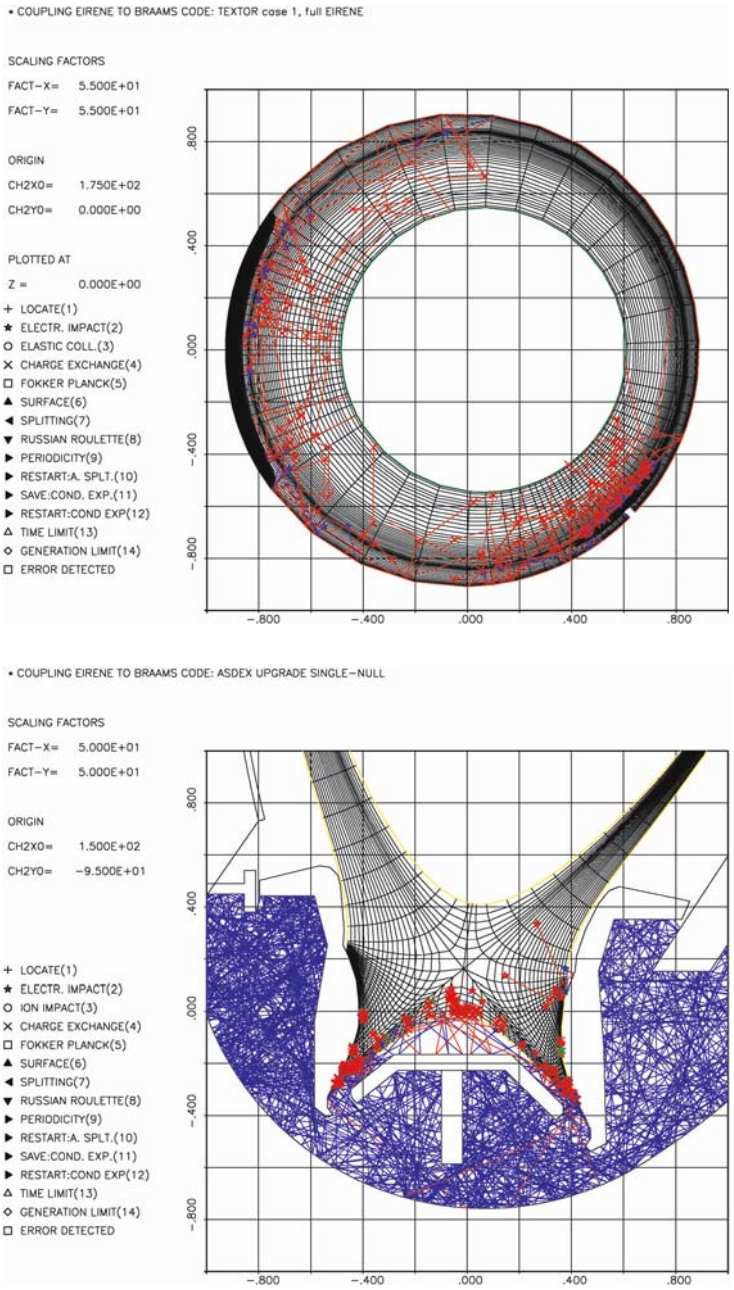

Fig. 2.5. Trajectories of neutral atoms (*red*) and molecules (*blue*) near a limiter (**top**) and in a partially detached divertor (**bottom**), in tokamaks of similar size and core plasma conditions

then turned into strong parallel flows due to the sink action of the limiter or divertor targets.

Figure 2.5 shows typical neutral hydrogen atom and molecule (Monte Carlo) trajectories in both configurations (TEXTOR and ASDEX Upgrade). In the limiter case the gas is largely dissociated, due to the direct contact of these recycling particles with a rather hot (20–50 eV) plasma. A significant fraction (10–30%) of the atoms penetrates back into the core region and are ionized there. By contrast in the divertor chamber and in the outer layers of the divertor plasma a large volume of molecular gas is established. The dissociation takes place in a narrow layer in the divertor plasma, roughly at the 10–15 eV contour of the electron temperature profile. Even further inside into the divertor plasma is a layer of atomic gas, but even this is well shielded from the core plasma region. Almost 100% or the recycling particles are either pumped in the divertor or re-ionized already in this outer scrape of layer.

2.3.1 Applications to TEXTOR

Applications of the plasma edge codes to limiter tokamaks have, until now, always confirmed a linear, so called sheath limited plasma flow regime with very little variation of plasma parameters along the magnetic field. For the medium size (R=1.75, a=0.50) limiter tokamak TEXTOR (FZ-Jülich) this has been documented by a series of papers (see, e.g., [28, 29]). The computational grid and a typical computed Balmer alpha radiation pattern near recycling surfaces is shown in Fig. 2.6. It is taken from a series of runs [29] covering a wide range of ohmically and NBI heated discharges at medium density ($\overline{n} = 1.75 \cdot 10^{19}\,\mathrm{m}^{-3}$, power into SOL: $\approx 260\,\mathrm{kW}$, particle flux to limiter: $\approx 9 \cdot 10^{21}\,\mathrm{s}^{-1}$.

It is chosen here to illustrate the following characteristic features of limiter tokamak recycling models:

- Although there is significant local recycling near the limiter blade, it is still too weak to cause substantial poloidal variations in the plasma density and temperature profiles. The plasma flow is in a simple isothermal regime, with weak influence of atomic processes, and with the power flow to the limiter being determined by the electrostatic sheath in front of the limiter [1] (and not by atomic and molecular processes).
- Various processes contribute to emission of the visible H_α light. Excitation of ground state atoms, dissociation of H_2 into an excited state of one of the Franck Condon atoms, likewise for H_2^+, and recombination (radiative or three-body) of H^+ into an excited state of the atom. In this example, but more generally for all current limiter tokamak experiments one finds that the first contribution is dominant globally, the second and third are important in a narrow layer near the limiter and, usually, the last one is irrelevant. In order to extract the various contributions from the simulation model, collision radiative models [9, 12, 13] are been employed.

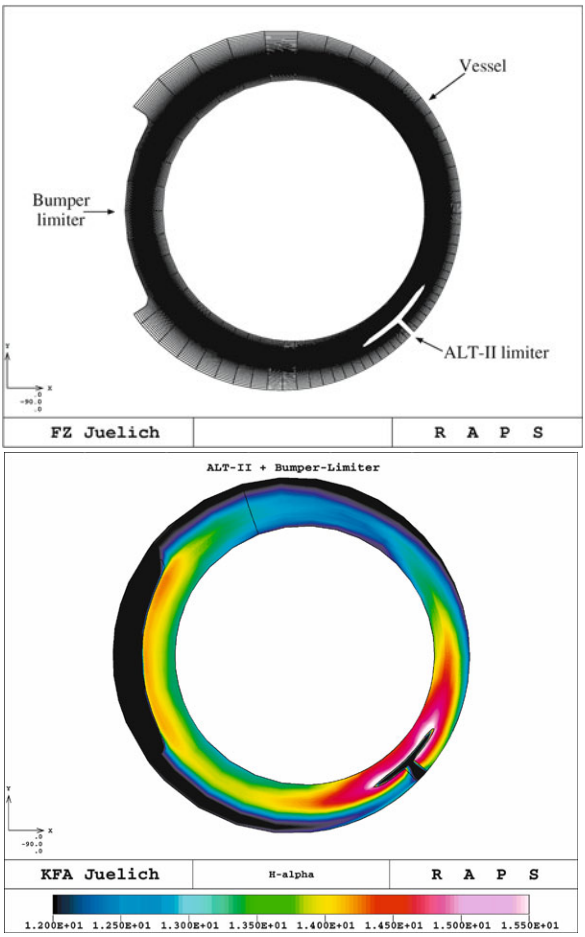

Fig. 2.6. Top: section of computational domain for TEXTOR model, showing also the cross-section of the toroidal ALT-II limiter 45 degrees underneath the outer mid-plane. **Bottom**: computed Balmer-alpha emission profile (photons/s/cm^3, logarithmic colour scale) in the TEXTOR edge plasma, as used for interpretation of visible spectroscopy [26] and determination of plasma particle confinement

– Although the atomic and molecular processes are too weak to influence the plasma dynamics significantly in limiter scrape-off layers, they are essential for interpretation of edge diagnostics. In particular the molecular contribution in the recycling flux, and it's correct identification is essential for a quantification of plasma flows, due to large difference in the Balmer emissivity from the four channels mentioned above (see [26, 30] for more details). They are also essential to study the main chamber recycling by high energy charge exchange neutrals (and resulting erosion there), an important issue also raised in recent ITER design work.

2.3.2 Applications to ASDEX Upgrade

Probably the most systematic predictive and scaling studies with emphasis on an as complete as possible implementation of atomic, molecular and surface effects for a divertor configuration have been carried out for the ASDEX Upgrade tokamak. Making connection here in particular to the chapter by U. Fantz in this volume (and references therein) we discuss here the initially unexpected role played by the molecular chemistry in dense cold divertor plasmas.

Detached divertor plasmas are characterized by a spatial pattern of recombining and ionizing layers. H_2 molecules (and their isotopomeres) have recently been identified as important species which may influence the energy balance and the ionization degree. Indeed, Molecular Assisted Recombination (MAR) had been suggested in this context, relying on significant vibrational excitation of the electronic ground state molecules. It was speculated (loc. cit. and references therein), that, e.g., for an ITER size machine, detachment of the divertor plasma might be achievable under somewhat relaxed upstream conditions (lower densities at the separatrix, higher heat fluxes into the SOL) as compared to what was predicted by the usual divertor models.

The chain of reactions, which played the key role in these arguments, was, firstly, a vibrational excitation of molecules by electron impact (through resonant H_2^- levels), then, secondly, an ion conversion: $p + H_2(v) \rightarrow H + H_2^+$, followed by, thirdly, an immediate dissociative recombination: $e + H_2^+ \rightarrow H + H^*$. The excited atom decays by spontaneous emission. At the end of this chain, one electron-ion pair has recombined into an H-atom, and the H_2 molecule has dissociated into $H + H$.

The second step in this reaction chain is resonant (comparable to resonant charge exchange between H-atoms and protons), if the molecules are vibrationally excited in the $v = 4$ level.

Under typical high recycling divertor conditions, when molecules travel in a bath of 7–8 eV (or hotter) electrons, the molecules are destroyed before they reach such vibrational levels. Hence this chain of reactions is irrelevant there. For detached divertor plasma conditions this is not necessarily so.

From inspecting the atomic database of the EIRENE code [31], which is used in many applications to a large number of different tokamaks, including for the ITER design, in particular its collisional–radiative models for molecules, it was clear that matters can be more complicated. The relaxation time for establishing a vibrational distribution of the ground state molecule is comparable to the transport time of the molecule, hence the applicability of local collisional–radiative approximations is questionable. Furthermore, one of the two atoms created in dissociative recombination is electronically excited, and, hence, can be ionized very effectively even at low divertor plasma temperatures (instead of radiative decay). In this case, the whole chain of reactions would be just an enhanced ("molecular activated") dissociation (MAD, i.e., dissociative excitation of those H_2^+, which have been produced

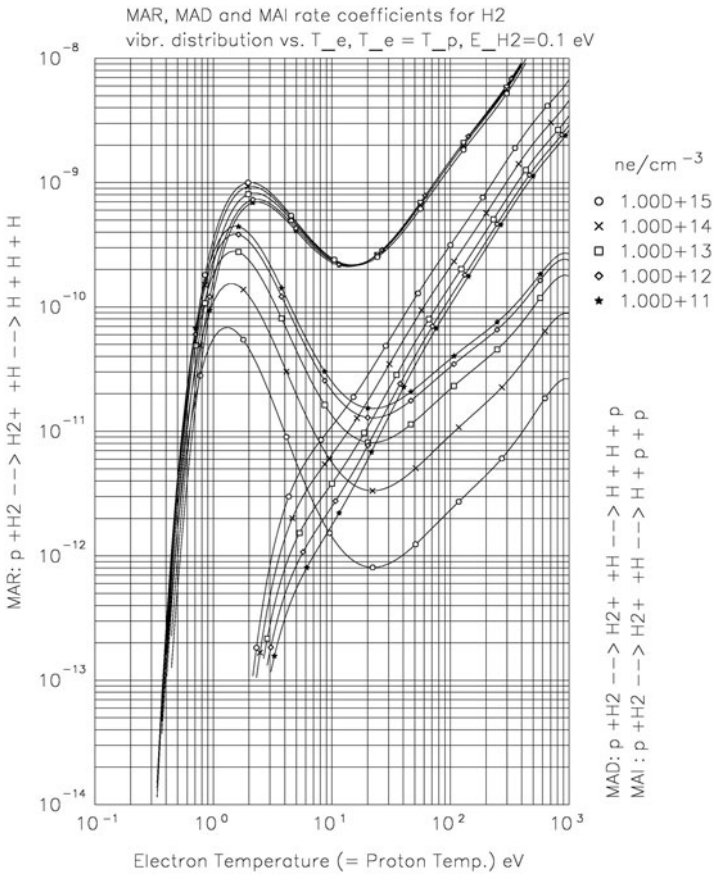

Fig. 2.7. Rate coefficients for so called MAR, MAD and MAI processes, vs. electron temperature (assumed to be the same as the proton temperature), and electron (=proton) density. For neutral hydrogen molecule energies of 0.1 eV, and for the H_2^+ density assumed to be given by a local equilibrium between production (by proton impact) and destruction by electron impact (ignoring H_2^+ transport effects)

by ion-conversion), rather than a recombination (MAR), see Fig. 2.7. (The third possible channel also included in Fig. 2.7, in which there are, at the end of the chain, two protons and only one atom, is irrelevant under all conditions).

In order to eliminate this uncertainty from current edge plasma models an experimental campaign was carried out at ASDEX Upgrade by using, amongst others, the divertor spectrometer [27]. It has been adjusted to measure lines of the molecular Fulcher band (an $n = 3$ to $n = 2$ transition in the molecular triplet system, in the visible range, hence corresponding closely to the H_α line for atomic hydrogen). By this means, and in combination

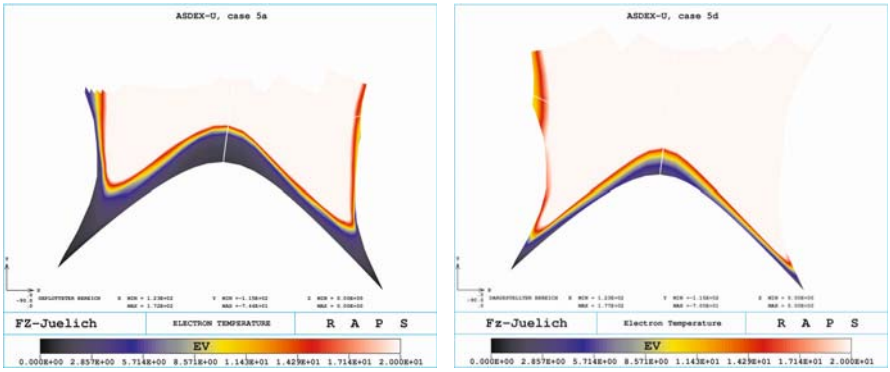

Fig. 2.8. Divertor electron temperature profiles, **left**: case 1, **right**: case 2. Temperatures above 20 eV are not resolved and fall into the bright color region. Near target temperatures in case 1 are below 5 eV (left target, *blue colors*) and below 10 eV (right target, *yellow colors*). Both temperatures are increased significantly in case 2, to values above 20 eV at the outer target

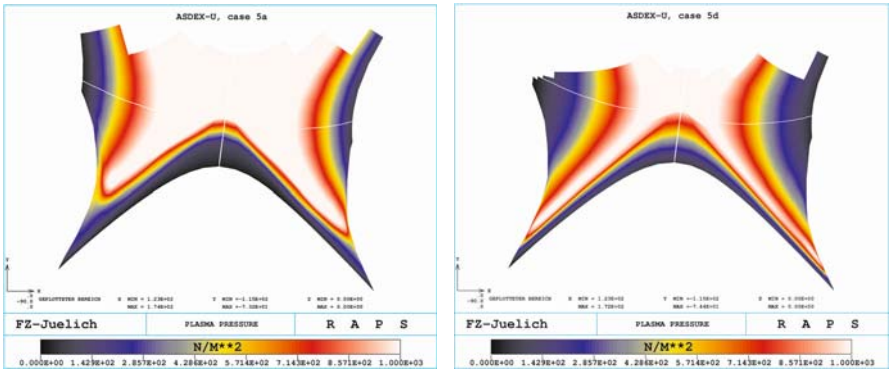

Fig. 2.9. Divertor plasma pressure profiles. Clearly visible: strong pressure drop in front of inner target in the **left** (case 1) figure, indicative of a detached plasma state there. This has disappeared in the **right** (case 2) figure, showing re-attachment of the inner leg

with a proper model for the electronic excitation of hydrogen molecules (as, e.g., available in EIRENE), it has become possible to measure molecules directly. Below we compare results from two such simulations, regarding them es "mathematical experiments" on the relevance of these processes for divertor dynamics. The verification of the simulations by experimental data and further details are again given in the chapter by U. Fantz in this present volume [27].

The two simulations, basically solutions to the edge plasma model described in the previous section, for a typical set of ASDEX Upgrade model parameters, are identical in all aspects but one: in case 1 (labelled 5a on

the figures below) the conventional collisional–radiative model [13] as used in most applications, also for ITER-predictions, was chosen. This model does not include vibrational excitation, hence it includes only ground state and electronically excited molecules. In case 2 (labelled 5d on the figures below) vibrational excitation and de-excitation by electron impact was added. Therefore, in case 2 the chain of reactions (MAR, MAD) described above have become possible. In both cases the plasma solutions are evolved consistently with these modifications in the molecular model. As can be seen in Fig. 2.8, quite opposite from the expected effects of an enhanced recombination due to the MAR channel the electron temperatures near the divertor target have increased significantly, in particular at the outer target.

The behaviour of the divertor pressure is a clear indication of the divertor regime. In Fig. 2.9 one can see a significant pressure drop in front of the inner target (caused by a number of effects, but amongst them also (elastic and charge exchange) neutral ion friction, and volume recombination (radiative and threebody) processes. This pressure drop has disappeared in case 2, although, one would have hoped, an additional recombination such as MAR might have increased it. The (inner leg) of the divertor has re-attached in case 2. The reason for this is the dominance, under the studied conditions, of dissociative excitation (MAD) over dissociative recombination (MAR), at high plasma densities. Also the plasma flow field (Fig. 2.10) has changed significantly from case 1 to case 2, in which the spatial redistribution of neutral particle recycling source terms towards higher temperatures have even led, locally in some flow channels, to the flow reversal already indicated in the schematic Fig. 2.4. Apparently, as also clearly seen in Fig. 2.11, the self-sustained molecular cushion protecting the inner divertor target is greatly reduced by the additional molecular brake up channels. As a consequence also neutral ion friction is strongly reduced.

This complicated situation is fundamentally different from small linear plasma devices, in which the MAR chain has been seen to lead to enhanced plasma recombination: In a tokamak divertor, distinct from these divertor-simulation experiments, the molecular pressure is not an externally controlled parameter but must be established by the recycling plasma itself. Detailed and consistent modeling, verified by dedicated spectroscopy, shows that processes that lead to a reduction of the molecular density (such as MAR and MAD), therefore, can have entirely different effects on plasma dynamics in real divertors and in divertor simulators.

In summary: The ASDEX Upgrade modeling results could be grouped into two cases: one with explicit treatment of the vibrationally excited molecules (and the consequences thereof), and one without. Agreement with experimental (spectroscopic) data could only be achieved in the first case.

The models within each group differed by assumptions of surface processes involving vibrational excited molecules (Eley-Rideal processes, etc.). These effects have so far not been identified as significant. The relevance of vibrationally excited molecules on the divertor dynamics seems to be pre-

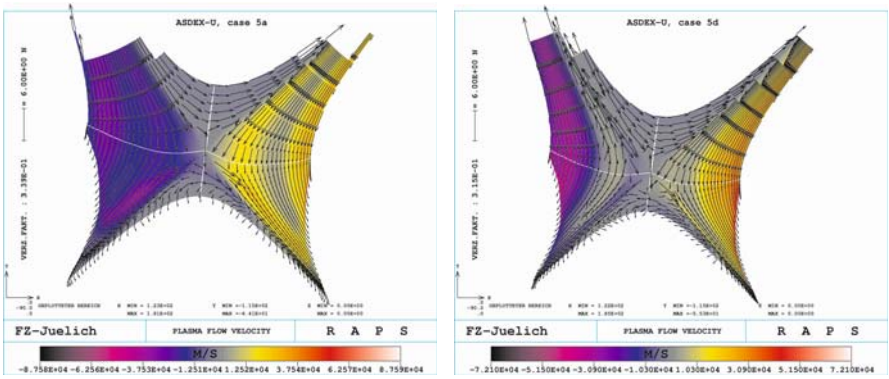

Fig. 2.10. Plasma flow profiles for case 1 (**left**) and case 2 (**right**). The plasma flows to the divertor targets, but in case 2 there are also some inverted flow channels, away from the target. Modification of the molecular model (here vibrational kinetics) can be powerful enough to change the sign of the dominant force (friction) in the parallel plasma momentum balance

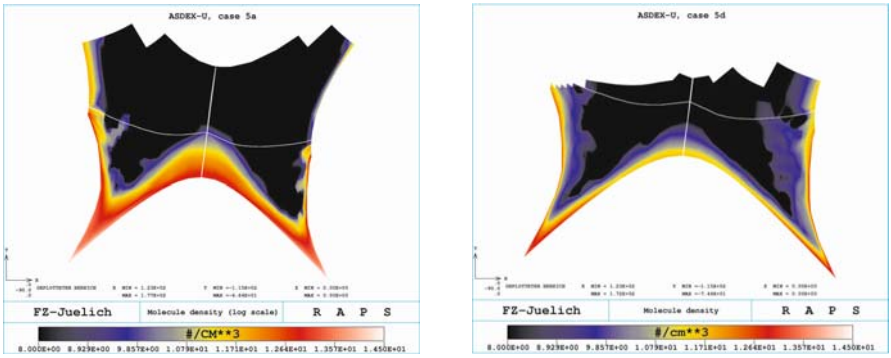

Fig. 2.11. Neutral molecule densities in divertor chamber (logarithmic color code). Strongly reduced self sustained neutral density after including vibrational kinetics of molecules in the model

dominantly due to volume processes, at least in these examples, and likely too under even higher collisionalities (e.g., in ITER).

For ASDEX Upgrade, detachment is harder to achieve with the presence of vibrationally excited molecules than without. This result is exactly the opposite of what one would have expected without such a detailed bookkeeping of the various competing processes and forces, as it is currently only provided by the edge plasma simulation codes employed here.

2.4 Conclusions, Outlook

The purpose of this section was to describe the standard computational tools currently employed in fusion research to study (describe, interpret and extrapolate) the important plasma edge region. Leaving aside computational issues, intrinsic plasma-physical topics (edge flows, drifts, sheath boundary conditions, turbulent transport across the confining B-field), we have focused on the level and format of atomic and molecular data that can be used in integrated edge plasma code. The most demanding, in this respect, are Monte Carlo codes, because they can treat these processes on the most detailed level. Still, for example for neutral-neutral (viscous gas) effects, strong simplifications are made and only crude collisionality-expressions are used here.

With the re-orientation of fusion edge plasma science, towards a chemically rich, partially recombining low temperature plasma the relevance of precise atomic, molecular and surface interaction data has become even larger, because it is this very strong exchange between the gas and the plasma phases which determines the divertor dynamics and therewith also the operational window of a fusion reactor. It has been shown with examples from current divertor modeling that predictions for ITER may depend, critically, on a number of typical low temperature plasma processes, such as the entire hydrogen chemistry including electronically and vibrationally excited states.

Despite many successes in explaining spectroscopic and vacuum system data in many divertors and near limiters, and even predicting the existence of the high recycling regime prior to its experimental verification, the predictive quality of neutral particle models is far less certain at low temperature, high-density divertor regimes. Future studies of neutral-plasma interaction physics, theoretically and experimentally, will have to focus on a combination of typical low temperature hydrogen chemistry within a sufficiently detailed kinetic gas transport model.

Due to availability of 2D and 3D Monte Carlo procedures the quantification of neutral particle (atomic, molecular and surface-) effects on the divertor performance in fusion devices is presently limited by the availability of atomic and molecular data as well as of surface interaction data, not by the configurational complexities nor by computational restrictions.

References

1. P.C. Stangeby: *The Plasma Boundary of Magnetic Fusion Devices* (Institute of Physics Publishing, Bristol 2000)
2. D. Reiter, G.H. Wolf, H. Kever: Nucl. Fusion **30** (1990) 2141
3. F.L. Hinton, Y.B. Kim: Nucl. Fusion **34** (1994) 899
4. T.D. Rognlien, D.D. Ryutov: Contrib. Plasma Physics **38** (1998) 1/2, 152
5. G.P. Maddison, D. Reiter: Recycling source terms for edge plasma fluid models and impact on convergence behavior of the BRAAMS "B2" code, KFA Jülich report **JUEL-2872** (Mar. 1994)

6. D.E. Post: J. Nucl. Mater. **220-222** (1995) 143
7. R.K. Janev, D. Reiter, U. Samm: Collision Processes in Low-Temperature Hydrogen Plasmas, Report **JUEL-4105** (2003)
8. D. Reiter, W. Eckstein, G. Giesen, H.J. Belitz: Database for recycling an penetration of neutral helium atoms in the boundary of a fusion plasma, Report **JUEL-2605** (1991)
9. D. Reiter: Neutral gas transport in fusion devices. In: *Atomic and Plasma Material Interaction Processes in Controlled Thermonuclear Fusion*, R.K. Janev, H.W. Drawin (Eds.), (Elsevier Science Publishers, 1993)
10. S.I. Braginsikii: Transport Processes in a Plasma. In: *Reviews of Plasma Physics*, Vol. 1, M. Leontovich (Ed.), (Consultants Bureau, New York 1965)
11. R.H. Cohen, D.D. Ryutov: Contrib. Plasma Physics **44**, Issue 1-3, 111
12. D. Wünderlich, U. Fantz: Report **IPP 10/18** (2001)
13. K. Sawada, T. Fujimoto: J. Appl. Phys. **78** (1995) 2913
14. L. Waldmann. In: *Handbuch der Physik*, 12, (Springer-Verlag 1958)
15. D. Reiter, C. May et al.: J. Nucl. Mater. **220** (1994) 987
16. S. Lisgo: OSM-EIRENE Modeling of Neutral Pressures in the Alcator C-Mod Divertor, J. Nucl. Mater. (2004), to appear
17. B.A. Trubnikov: Particle Interactions in a fully ionized Plasma. In: *Reviews of Plasma Physics*, Vol. 1, M. Leontovich (Ed.), (Consultants Bureau, New York 1965)
18. *NRL Plasma Formulary, revised 2002*, NRL Publication 6790-02-450 (Naval Research Laboratory, Washington D.C., USA 2002)
19. J. Spanier, E.M. Gelbard: *Monte Carlo Principles and Neutron Transport Problems* (Addison Wesley Publication Company 1969)
20. R.K. Janev, W.D. Langer et al.: *Elementary Processes in Hydrogen-Helium Plasmas* (Springer-Verlag 1987)
21. O. Hirschfelder, C.F. Curtiss, R.B. Bird: *Molecular Theory of Gases and Liquids* (Wiley, New York 1954)
22. S. Chapman, T.G. Cowling: *The Mathematical Theory of Non-uniform Gases*, 3rd edn (Cambridge University Press 1970)
23. P. Bachmann, D. Reiter: Contrib. Plasma Phys. **35** (1995) 1, 45–100
24. H.H. Abou-Gabal, G.A. Emmert: Nucl. Fusion **31** (1991) 407
25. P. Bachmann, D. Reiter, A.K. Prinja: J. Nucl. Mater. **196-198** (1992) 865
26. A. Pospieszczyk: High Temperature Plasma Edge Diagnostic. In: this volume
27. U. Fantz: Molecular Diagnostics of Cold Edge Plasmas. In: this volume
28. M. Baelmans, D. Reiter, H. Kever et al.: J. Nucl. Mater. **196-198** (1992)
29. D.S. Gray, M. Baelmans, J.A. Boedo, D. Reiter, R.W. Conn: Physics of Plasmas **6**, No 7 (1999) 2816–2825
30. S. Brezinsek, P.T. Greenland, Ph. Mertens, A. Pospieszczyk, D. Reiter, U. Samm, B. Schweer, G. Sergienko: J. Nucl. Mater. **313-316** (2003) 967
31. D. Reiter: The EIRENE code, Version Jan. 92, User manual, KFA Jülich report **JUEL-2599** (Mar. 1992), and: www.eirene.de

3 Energy Deposition from ELMs in Fusion Devices

A. Loarte

3.1 Introduction

An outstanding problem for the operation of the next generation of fusion devices, in which large energy gain ($Q_{\mathrm{DT}} \sim 10$) from the fusion process should be demonstrated [1], is the control of the interaction between the plasma and the plasma facing components (PFCs) installed in the vacuum vessel of the device. These PFCs are made of specific materials (Carbon Fibre Composites, Tungsten, Beryllium, etc.) and specially designed (precise alignment to the magnetic field, etc.) to withstand the large energy and particle fluxes deposited on them by the thermonuclear plasma without loosing thermomechanical integrity and to protect the vacuum vessel of the fusion device from such fluxes.

Within this field, a major research area is that of the deposition of plasma energy onto the PFCs, particularly during transient events such as ELMs and disruptions. During ELMs, 1–10% of the plasma thermal energy is lost to the PFCs in time scales of $\sim$ 100–1000 µs [2], leading to very large energy fluxes being deposited on the PFCs [1]. These large fluxes of high energy electrons and ions can cause significant material damage and limit the PFC lifetime, if its surface temperature reaches its evaporation or melting threshold [3]. This effect is of more concern in the next generation of burning plasma experiments such as ITER, because for ITER-like devices the plasma thermal energy scales with its major radius (R) as $\sim R^{4-5}$, while the area of the PFCs on which the energy is deposited increases only as $\sim R$. Hence, the magnitude of the energy fluxes on the PFCs scales as $\sim R^{3-4}$, that is, the energy fluxes expected in ITER will be more than an order of magnitude larger than those measured in JET and close to two orders of magnitude larger than those in DIII-D and ASDEX Upgrade [4].

This chapter describes, the present understanding of the ELM energy fluxes in existing fusion devices and their extrapolation to burning plasma experiments, taking ITER as the reference for such extrapolation. The chapter is divided into four sections: Section 3.1 provides the necessary background to the theme of the chapter, such as a description of the regime of enhanced energy confinement (H-mode), the classification of ELMs into three types, the relation between ELM type and plasma energy confinement and a description of the basic features of the plasma pressure collapse during Type I

ELMs and of the associated energy fluxes to PFCs. Section 3.2 describes in more detail the losses of energy and particles from the confined plasma during Type I ELMs, their time scale and their extrapolation to burning plasma experiments. Section 3.3 describes the spatial and temporal characteristics of the energy fluxes to PFCs during Type I ELMs in existing experiments, their extrapolation to burning plasma experiments and discusses the implications of such extrapolation for the operation of ITER. Finally, Sect. 3.4 summarizes the chapter and the conclusions are drawn.

3.1.1 Features of the Regime of Enhanced Energy Confinement (H-Mode)

A common observation in most magnetic confinement devices is that the energy confinement time (τ_{E}) decreases with the level of additional heating (typically provided by fast neutral atoms and/or microwaves) injected in the plasma. The energy confinement time is defined as the ratio between the plasma thermal energy (W_{th}) and the power input into the plasma (P_{INP}) in steady state conditions, $\tau_{\mathrm{E}} = W_{\mathrm{th}}/P_{\mathrm{INP}}$. As a result of this confinement deterioration, the plasma thermal energy increases with input power more weakly than linear, typically $W_{\mathrm{th}} \sim P_{\mathrm{INP}}^{0.3-0.5}$. If the level of input power exceeds a threshold, which depends on the discharge characteristics, the plasma discharge experiences a bifurcation and the energy confinement time increases sharply. This energy confinement mode is called H-mode , in contrast to the "normal" energy confinement mode called L-mode. The H-mode was observed first in tokamaks operating with a poloidal divertor [5] in which, by achieving a poloidal field null inside the vacuum vessel, the plasma–wall interaction zone is separated from the confined plasma [6], in contrast to the limiter configuration in which the confined plasma is in direct contact with a material limiter. Since this first observation, the H-mode has been obtained in a large number of tokamak devices and has been observed in stellarators as well [7]. Figure 3.1 shows the measured energy confinement time τ_{E} for a series of JET discharges in the L-mode (limiter) and the H-mode (divertor) energy confinement regimes for a range of input powers into the plasma discharge. As can be seen from the figure, the typical increase of τ_{E} for a discharge in H-mode with respect to L-mode is a factor ~ 2, and τ_{E} decreases is a similar fashion with the level of input power both in L-mode and H-mode. Thus, for similar plasma conditions and levels of input power, the thermal plasma energy (W_{th}) in H-mode is typically more than a factor of 2 larger than in L-mode. In burning plasma experiments, such as ITER, the fusion power output of the device scales approximately with $\sim W_{\mathrm{th}}^2$ [1]. Hence, for similar discharge conditions, a plasma discharge in the H-mode energy confinement regime will have a fusion power output larger than four times than in L-mode and, therefore, the H-mode has been chosen as the reference regime for high fusion energy gain ($Q_{\mathrm{DT}} = P_{\mathrm{fusion}}/P_{\mathrm{input}}$), for which $Q_{\mathrm{DT}} \sim 10$, in the next generation of tokamak burning plasma devices such as ITER [1].

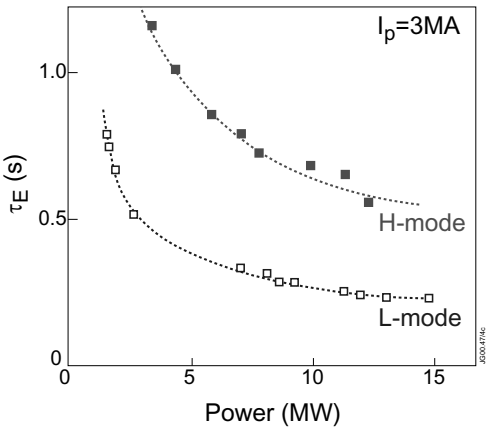

Fig. 3.1. Energy confinement time for JET L-modes and H-modes with 3 MA of plasma current versus the level input power into the discharge [8]

Since the discovery of the H-mode, this energy confinement mode has been a major focus of research in most fusion devices and the plasma properties as well as the conditions required to access this confinement mode have been thoroughly characterized. As mentioned before, in order to access the H-mode, the input power into the discharge must be above a certain threshold. For tokamaks, this threshold increases with the toroidal field of the discharge, the density of the plasma and the size of the device. Using observations from a large number of tokamak experiments, the following experimental scaling for the access power to H-mode has been derived : $P_{\mathrm{th\_L-H}}\,(\mathrm{MW}) = 2.84\,M(\mathrm{amu})^{-1}\,n(10^{20}\,m^{-3})^{0.58}\,B_{\mathrm{t}}(\mathrm{T})^{0.82}\,R(\mathrm{m})^{1.00}\,a(\mathrm{m})^{0.81}$ [9], where M is the average hydrogen isotope mass, n is the plasma density, B_{t} the toroidal field, and R and a the major and minor radius of the toroidal discharge, respectively.

The increase of plasma thermal energy and energy confinement time observed in H-mode is mostly due to a reduction of the effective plasma energy transport coefficients at the plasma edge region. This leads to the creation of a so-called Edge Transport Barrier and to an overall decrease of the plasma energy losses, which leads to an increase of the plasma energy density (i.e., plasma pressure) throughout the plasma. Due to the reduced energy transport at the edge transport barrier, the radial plasma gradients in this region are very large and there appears a narrow region in which the gradients change sharply from values typical of the edge transport barrier to much smaller values typical of the core plasma. This transition point is called the pedestal top. The reason for such a name is clear from the profiles in Fig. 3.2. The core plasma pressure profiles in H-mode are similar (somewhat steeper) to those in L-mode but with a constant (across the plasma radius) positive offset equal to the plasma pressure at the pedestal top. The contribution of the edge

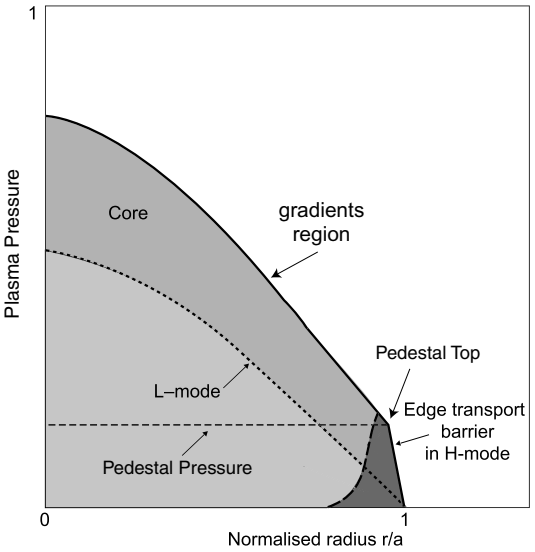

Fig. 3.2. Pressure radial profile structure in the H-mode regime compared to L-mode, showing the characteristic features of the H-mode: Edge transport barrier and plasma pedestal

transport barrier to the total plasma thermal energy is characterized by the pedestal energy, which is defined as $W_{\rm ped} = 3/2\, n_{\rm ped}\, (T_{\rm e,ped} + T_{\rm i,ped})\, V_{\rm plasma}$, where $n_{\rm ped}$, $T_{\rm e,ped}$ and $T_{\rm i,ped}$ are the values of the plasma density, electron and ion temperature at the pedestal top, respectively, and $V_{\rm plasma}$ is the total plasma volume. The typical ratio between the pedestal energy and the total thermal energy for JET ELMy H-modes with good energy confinement is in the range $W_{\rm ped}/W_{\rm th} = 20$–$50\%$ [10] and similar ratios are found in other experiments such as ASDEX Upgrade and DIII-D.

Discharges in the H-mode regime are routinely obtained in all divertor tokamaks in, essentially, steady-state conditions ($\Delta t_{\rm H-mode}/\tau_{\rm E} \gg 5$). In these discharges the average core plasma parameters remain in steady state over many seconds as shown in Fig. 3.3 for a JET discharge. However, the pedestal plasma parameters experience quasi-periodic relaxations as shown in Fig. 3.3 by the pedestal electron temperature. These relaxations are due to the appearance of ELMs (edge localized modes) [2], which are observed when the pedestal pressure (or its pressure gradient) exceeds given stability thresholds [11–13]. ELMs lead to a sudden decrease of the pedestal plasma density and temperature and to significant energy and particle fluxes to be expelled from the confined plasma onto PFCs protecting the vacuum vessel of the device. These fluxes can be measured by the incoming neutral atoms following the neutralization of the expelled ion fluxes on the PFCs, as shown in Fig. 3.3 by the large spikes in the divertor D_α emission coincident with the collapse of the electron pedestal temperature caused by the ELMs.

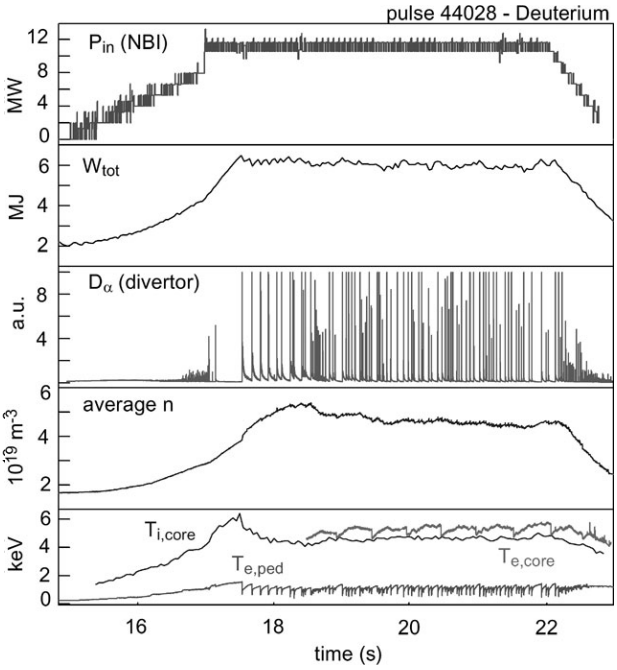

Fig. 3.3. Time traces for a JET discharge evolving from L-mode to Type I ELMy H-mode [15]. $P_{\rm in}$ (NBI) is the input power into the plasma by fast neutral beams, $W_{\rm tot}$ is the total plasma energy (thermal + non-thermal component), $\rm D_\alpha$ (divertor) is the deuterium emission in the Balmer α line from neutrals coming into the plasma in the divertor area, average n is the average density of the discharge, $T_{\rm i,core}$ and $T_{\rm e,core}$ are the ion and electron temperatures in the centre of the discharge and $T_{\rm e,ped}$ is the electron temperature at the top of the pedestal

ELMs are commonly associated with the H-mode regime and, as such, they are observed both in tokamaks [2] and stellarators [14]. The understanding of ELMs in tokamaks is more advanced than in stellarators, in part because of the much larger experimental database available for ELMs in tokamaks. Because of this, the rest of the chapter focuses on ELMs in tokamak discharges, but many of the qualitative features described for tokamaks are common to ELMs in stellarator as well. The majority of the experimental results in this chapter will be taken from the Joint European Torus (JET) tokamak because, being the largest experiment of its type, it can achieve plasma parameters closer to those expected in next step devices. However, the results shown here are of a general nature and have been obtained in other tokamak experiments such as ASDEX Upgrade, DIII-D and JT-60U, apart from the obvious quantitative differences associated by the different range of plasma parameters achievable in each device because of their different size, available input power, etc.

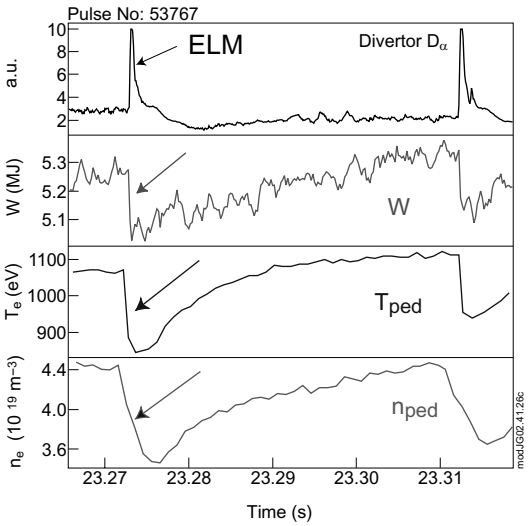

Fig. 3.4. Evolution of the plasma energy (W), pedestal temperature ($T_{\rm ped}$) and density ($n_{\rm ped}$) and the divertor D_α emission in a JET H-mode discharge showing the collapse of W, $n_{\rm ped}$ and $T_{\rm ped}$ and the increase of the D_α emission caused by the Type I ELMs [16]

3.1.2 Characteristics of ELMs and Their Effects on the Pedestal Plasma

ELMs can be classified into three types (I, II and III) depending on their frequency dependence on input power and pedestal plasma pressure [2], as will be described in detail below. For all ELM types, the qualitative behaviour of the pedestal plasma parameters (at and in-between ELMs) is similar, although there are large quantitative differences among different ELM types. At the ELM, the pedestal plasma temperature and density experience sudden drops in timescales of few hundred microseconds, as shown in Fig. 3.4 for a JET discharge with Type I ELMs [16]. Between ELMs, both density and temperature increase until the plasma pressure reaches again a threshold value and a new ELM is triggered. Typical density and temperature drops at the pedestal top during Type I ELMs are in the range of 5–50%, which lead to a decrease of the total thermal plasma energy by 1–10%, as shown in Fig. 3.4. The reason for this relatively small influence of the ELMs in the overall plasma energy confinement is that the collapse of the plasma parameters following the ELMs remains limited to the outer regions of the plasma, typically 10–25% of the plasma radius, as shown in Fig. 3.5 for a JET discharge with Type I ELMs [16].

The short time scales over which this collapse takes places ($\sim 200\,\mu$s for the case in Fig. 3.4) leads to very large power ($\sim$ GW/m^2 in JET) and particle fluxes reaching the material elements in contact with the plasma. These large

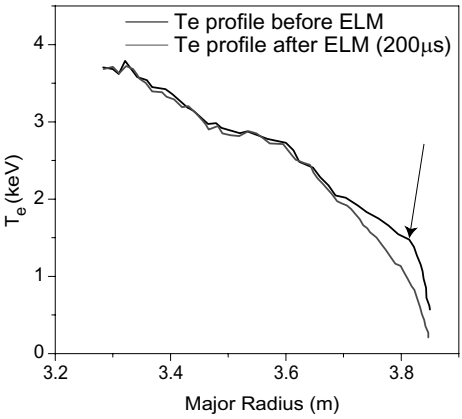

Fig. 3.5. Plasma electron temperature before and after a Type I ELM in JET versus the major radius of the torus, showing the collapse of the plasma temperature in the peripheral plasma region caused by the ELMs [16]

power fluxes cause a very fast increase of the PFCs surface temperature, as shown in Fig. 3.6 for a JET discharge. If the surface temperature approaches the sublimation or melting temperature of the material during the ELM energy pulse, the PFCs can suffer sizeable erosion by the ELMs and a fraction the material eroded can reach the confined plasma and increase the impurity concentration of the core plasma significantly. Increases of the core plasma average charge $Z_{\rm eff}$ by 0.5–1.0 have been measured following large ELMs in JET with the MkIIA CFC divertor, for which $\Delta W_{\rm ELM} \sim 1\,{\rm MJ}$, where $\Delta W_{\rm ELM}$ is the decrease of plasma thermal energy caused by the ELM.

The quantitative characteristics of the collapse of pedestal parameters and of the energy and particle fluxes onto PFCs caused by the ELMs depend on the ELM type. Three types of ELMs have been identified and characterized according to their frequency dependence with input power and pedestal plasma pressure:

a) Type I ELMs. These ELMs are observed when the level of input power ($P_{\rm INP}$) is significantly larger than the power threshold for H-mode access ($P_{\rm th\_L-H}$), typically $P_{\rm INP} > 2\,P_{\rm th\_L-H}$. The Type I ELM frequency increases with the level of input power and plasmas in the Type I ELMy H-mode have large values of the pedestal pressure and energy confinement time. The Type I ELMy H-mode regime shows the largest ELM energy losses ($\Delta W_{\rm ELM}$), which are typically in the range $\Delta W_{\rm ELM} = 2$–10% of the total thermal plasma energy, $W_{\rm th}$, and/or 3–20% of the pedestal energy, $W_{\rm ped}$. Discharges in H-mode with Type I ELMs have been obtained in many tokamak experiments and over a large range of plasma configurations, currents and fields (i.e., for all the plasma shapes and all the safety factor (q_{95}) range for which tokamak discharges are MHD stable).

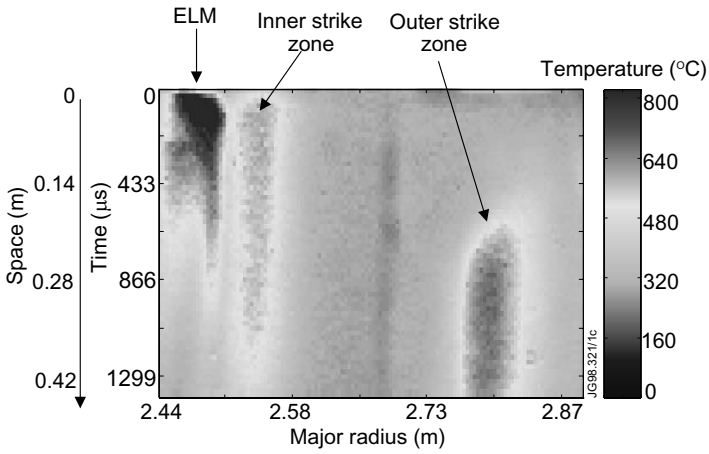

Fig. 3.6. Divertor surface temperature in the JET tokamak during a discharge with Type I ELMs [17]. The origin for the time axis is taken as the beginning of the ELM power flux (seen at the inner divertor for this ELM). The surface temperature of the inner divertor rises by more than 500°C in less than 200 μs following the ELM event

b) Type II ELMs. These ELMs are also observed when the level of input power is larger than the power threshold for H-mode access, but only for discharges within a restricted set of plasma magnetic configurations with $q_{95} > 3.5$–4.0 and large plasma triangularity [18, 19] and/or with a second poloidal field null close to the field line that forms the poloidal divertor configuration (dominant poloidal field null) and high plasma density [20]. Discharges in the Type II ELMy H-mode have also large values of the pedestal pressure and energy confinement time, although somewhat smaller than the Type I ELMy H-mode (by $\sim$ 10%). The Type II ELMy H-mode regime shows small ELM energy losses, which are typically $\sim 1\%$ of the total thermal plasma energy $W_{\rm th}$ or smaller.

c) Type III ELMs. These ELMs are observed when the level of input power ($P_{\rm INP}$) is close to the power threshold for H-mode access ($P_{\rm th\_L-H}$), typically $P_{\rm INP} < 1.5\,P_{\rm th\_L-H}$. The Type III ELM frequency decreases with the level of input power and plasmas in the Type III ELMy H-mode have much lower values of the pedestal pressure and energy confinement time than the Type I ELMy H-mode (typically by 30–50%). The Type III ELMy H-mode regime shows very small ELM energy losses, which are typically smaller than 1% of the total thermal plasma energy $W_{\rm th}$. Discharges in H-mode with Type III ELMs have been obtained in many tokamak experiments and over a large range of plasma configurations, currents and fields (i.e., for all the plasma shapes and all the safety factor (q_{95}) range for which tokamak discharges are MHD stable).

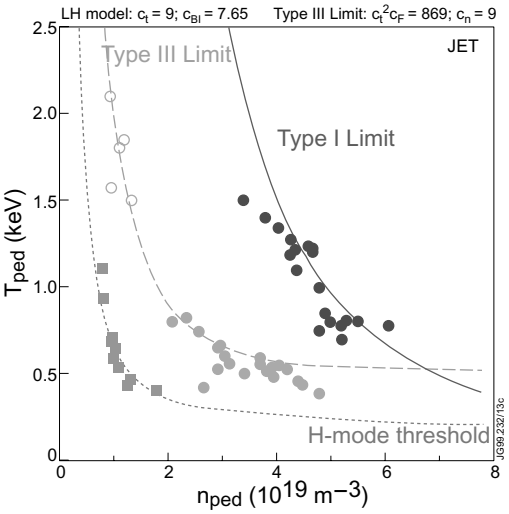

Fig. 3.7. Values of the pedestal temperature and density at the transition to H-mode, before Type III and Type I ELMs for a large range of JET discharges. The curves indicate the predictions for the corresponding boundaries from various models, as explained in detail in [21]

The Type II ELMy H-mode regime is very attractive for the operation of the next generation of burning plasma experiments, but its restricted dominion of existence and the present difficulties to reproduce it in many divertor tokamak experiments does not allow to consider it, at this stage, as the reference regime for high fusion power gain ($Q_{\mathrm{DT}} \sim 10$) experiments in the next generation of tokamak burning plasma devices, such as ITER. Because of this, the reference operating scenarios of most burning plasma experiments are based on achieving the Type I and Type III ELMy H-mode regimes in the plasma discharges in those devices.

Besides global conditions for the access to the H-mode regime and the characterization of the type of ELMs via their frequency behaviour, the access to the H-mode regime and ELM type can be discriminated by the values of the pedestal plasma parameters for the various confinement/ELM Types, as shown in Fig. 3.7 for a set of JET discharges. Both Type I and III ELMs occur when the value of the pedestal pressure exceeds a given limit, as shown in this figure. The Type I ELM limit is believed to be determined by the MHD instability of peeling and ballooning modes in the pedestal region as proposed in [11, 12]. The Type III pressure boundary is lower than that of the Type I ELMs (particularly at lower densities) and it is well described by the destabilization of resistive interchange modes, where the driver is the magnetic flutter [13]. The discussion of these models and the agreement of their predictions with the experiment is outside of the scope of this chapter

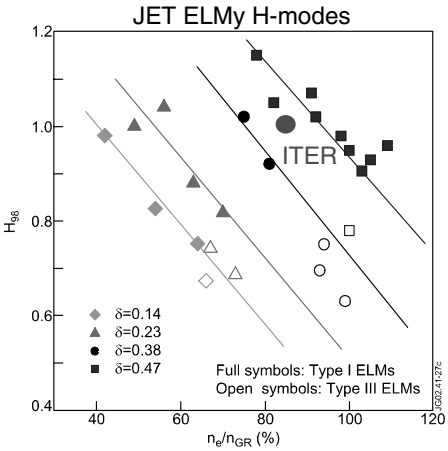

Fig. 3.8. Normalized energy confinement in JET Type I and Type III ELMy H-modes versus plasma density normalized to the Greenwald value for various plasma shapes [10]

and the reader is referred to reference [21] and references therein for a further insight into this topic.

As explained in Sect. 3.1.1 the overall energy confinement in H-modes is deeply influenced by the pedestal plasma behaviour. In general, H-modes with lower pedestal pressure have lower overall energy confinement and, hence, discharges in the Type III ELMy H-mode have lower energy confinement times than similar discharges in the Type I ELMy H-mode. Figure 3.8 shows the normalized energy confinement time for a set of density scans with constant input power in JET, for various plasma triangularities (δ) in the Type I and Type III ELMy H-mode. In this figure, the energy confinement time has been normalized to the ITER-98(y,2) scaling law [1] with the energy confinement enhancement factor, H_{98}, defined as $H_{98} = \tau_{\mathrm{E}}^{\mathrm{experiment}}/\tau_{\mathrm{E}}^{\mathrm{scaling-98(y,2)}}$. With increasing density the normalized energy confinement time decreases and, when the input power approaches the threshold for H-mode access ($P_{\mathrm{th\_L-H}} \sim n(10^{20}\ m^{-3})^{0.58}$), the discharge changes confinement mode from Type I to Type III ELMy H-mode. Together with this confinement mode change there is a sizeable decrease of the normalized energy confinement time, clearer at higher plasma triangularities, which is consistent with the smaller pedestal pressure in Type III ELMy H-modes. Next step burning plasma experiments are designed to operate at high densities, typically close to the Greenwald limit value [22] and with good energy confinement ($H_{98} \sim 1$). The fusion energy gain, Q_{DT}, scales as $Q_{\mathrm{DT}}/(Q_{\mathrm{DT}} + 5) \sim H_{98}^3$ for these conditions [9]. Hence, only the Type I ELMy H-mode regime provides a reasonably wide range for operation of next step fusion devices with high fusion power gain ($Q_{\mathrm{DT}} \sim 10$ and larger).

Because of this, the Type I ELMy H-mode regime has been chosen as the reference operating regime for high fusion gain experiments in next step devices, such as ITER and FIRE [23], despite the drawbacks associated with the large energy and particle fluxes on the PFCs inherent to the Type I ELMs themselves.

3.2 Characteristics of Type I ELM Energy and Particle Losses from the Core Plasma

Type I ELMs lead to energy losses which are typically in the range of 2–10% of the total plasma energy. The timescale for this loss as well as the mechanisms for the transport of energy from the core plasma to the material elements play a very important role on the magnitude and spatial distribution of the power fluxes onto the PFCs caused by ELMs. Hence, in order to understand and characterize the ELM energy fluxes on PFCs it is necessary to consider their source, i.e., the energy and particle losses from the core plasma during Type I ELMs. We will first describe the global characteristics of such losses and then we will consider in detail the timescale for the ELM energy losses as well as the mechanisms for energy transport out of the core plasma during the ELM.

The frequency of Type I ELMs increases with increasing fuelling rate and, simultaneously, the ELM energy losses decrease [2]. Increasing the fuelling rate increases the pedestal density and decreases the pedestal temperature, with the pedestal pressure following the Type I pressure limit boundary illustrated in Fig. 3.7. At high fuelling rates, the ELM type can change from Type I to Type III, with a large frequency increase, or to mixed periods of Type I and II ELMs or pure Type II ELMs, depending on details of the magnetic configuration of the discharge. In the first case, the ELM energy losses decrease further at the Type I to Type III transition together with the increase of frequency. During the mixed Type I/Type II periods, the ELM energy losses at the Type I ELMs remain approximately constant while the Type I ELM frequency decreases [16]. Figure 3.9 shows the normalized ELM energy losses (to the total plasma energy determined with diamagnetic measurements, W_{dia}) for a series of JET H-mode discharges displaying the typical behaviour described above.

Contrary to ELM energy losses, the ELM particle losses seem to remain relatively independent of the Type of ELM and of the frequency of the Type I ELMs, as shown in Fig. 3.10 for the same set of discharges in Fig. 3.9. This behaviour of ELM energy and particle losses illustrates that the mechanisms behind both ELM losses are different and depend on a different way on pedestal plasma parameters. As a consequence, the convective ELM energy losses (associated with the ELM particle losses) and the conductive ELM energy losses (associated with the loss of temperature caused by the ELM) display a contrasting behaviour, as will be shown in detail in Sect. 3.2.2.

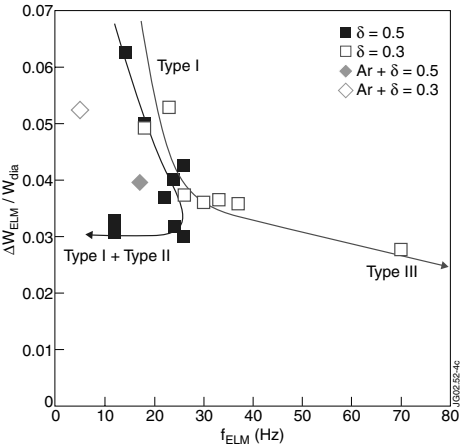

Fig. 3.9. Normalized ELM energy loss ($\Delta W_{\mathrm{ELM}}/W_{\mathrm{dia}}$, where W_{dia} is the plasma total energy) versus ELM frequency (f_{ELM}) for JET discharges with plasma current $I_{\mathrm{p}} = 2.5\,\mathrm{MA}$, toroidal field $B_{\mathrm{t}} = 2.4$–$2.7\,\mathrm{T}$, input power $P_{\mathrm{input}} = 14$–$17\,\mathrm{MW}$ and medium ($\delta = 0.3$) and high ($\delta = 0.5$) triangularity. The unusual decrease of f_{ELM} with constant $\Delta W_{\mathrm{ELM}}/W_{\mathrm{dia}}$ for discharges with $\delta = 0.5$ is typical of ELMy H-mode discharges with a mix of Type I and Type II ELMs. Two discharges (at medium and high δ) in which Argon has been injected to increase the level of plasma radiation are shown for comparison. Lines are to guide the eye [16]

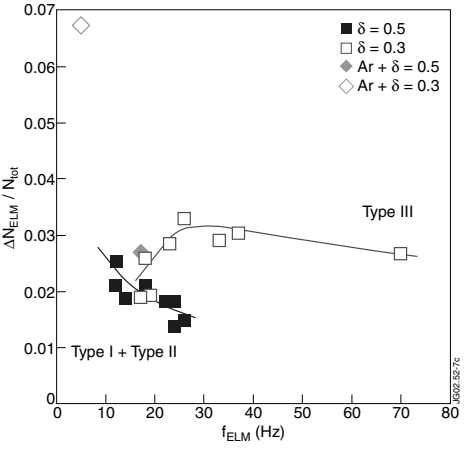

Fig. 3.10. Normalized ELM particle loss ($\Delta N_{\mathrm{ELM}}/N_{\mathrm{tot}}$, where N_{tot} is the total particle content) versus ELM frequency (f_{ELM}) for JET discharges with plasma current $I_{\mathrm{p}} = 2.5\,\mathrm{MA}$, toroidal field $B_{\mathrm{t}} = 2.4$–$2.7\,\mathrm{T}$, input power $P_{\mathrm{input}} = 14$–$17\,\mathrm{MW}$ and medium ($\delta = 0.3$) and high ($\delta = 0.5$) triangularity. Two discharges (at medium and high δ) in which Argon has been injected to increase the level of plasma radiation are shown for comparison. Lines are to guide the eye [16]

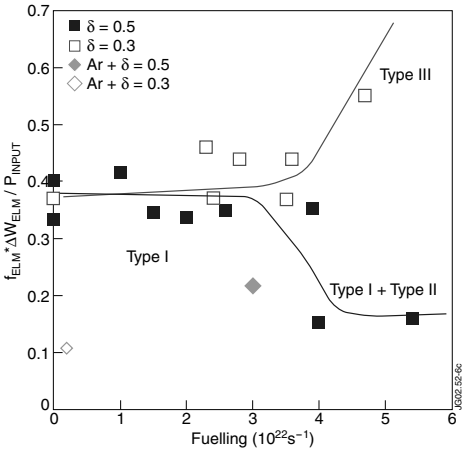

Fig. 3.11. Normalized ELM power loss ($f_{\mathrm{ELM}} \times \Delta W_{\mathrm{ELM}}/P_{\mathrm{input}}$) versus gas fuelling rate for JET discharges with plasma current $I_{\mathrm{p}} = 2.5\,\mathrm{MA}$, toroidal field $B_{\mathrm{t}} = 2.4$–$2.7\,\mathrm{T}$, input power $P_{\mathrm{input}} = 14$–$17\,\mathrm{MW}$ and medium ($\delta = 0.3$) and high ($\delta = 0.5$) triangularity. The unusual decrease of the normalized ELM power loss for discharges with $\delta = 0.5$ at high fuelling rates is typical of ELMy H-mode discharges with a mix of Type I and Type II ELMs. Two discharges (at medium and high δ) in which Argon has been injected to increase the level of plasma radiation are shown for comparison. Lines are to guide the eye [16]

Because of the different behaviour of ELM energy and particle losses with increasing pedestal density (or fuelling rate), the total particle out-flux from the core plasma driven by the Type I ELMs ($f_{\mathrm{ELM}} \times \Delta N_{\mathrm{ELM}}$), where ΔN_{ELM} is the drop in plasma particle content caused by the ELM, basically follows the increase or decrease of the ELM frequency as the fuelling rate is varied. On the contrary, the Type I ELM power loss ($f_{\mathrm{ELM}} \times \Delta W_{\mathrm{ELM}}$) remains approximately independent of the fuelling rate (or pedestal density), as shown in Fig. 3.11 for the same set of discharges as in Figs. 3.9 and 3.10. In the transition from Type I to Type III the ELM power loss increases, indicating that part of the energy confinement degradation observed at this transition (see Fig. 3.8) may be caused by enhanced ELM losses in the Type III regime. For regimes with Type I/Type II mixed ELMs, the ELM power loss caused by Type I ELMs experiences a clear reduction, as compared to H-modes with only Type I ELMs (by more than a factor of 2 in the discharges shown in Fig. 3.11). Despite this Type I ELM power loss reduction, the total plasma energy does not increase at this transition, which is consistent with the Type II ELMs (that occur in the periods between Type I ELMs) compensating for the decrease of the Type I ELM energy loss [10].

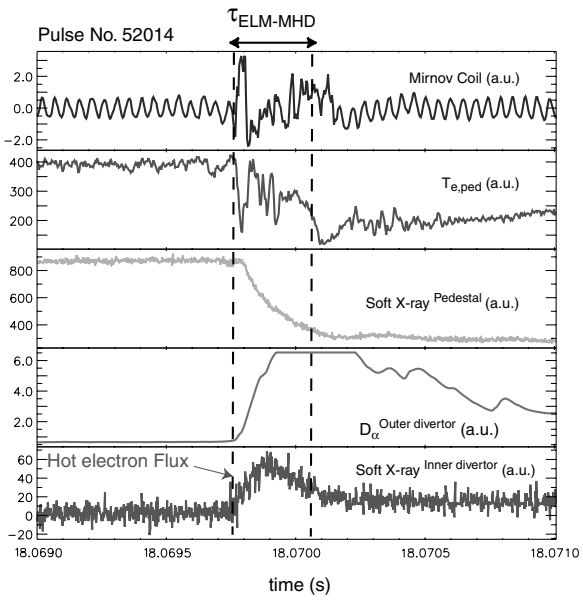

Fig. 3.12. Measurements with high time resolution ($\sim 4\,\mu$s) of the MHD activity (measured with Mirnov coils), pedestal temperature ($T_{\mathrm{e,ped}}$) and soft X-ray emission collapse, and outer divertor D_α emission and inner divertor X-ray bremsstrahlung (from hot electron impact) during a Type I ELM in JET. The collapse of $T_{\mathrm{e,ped}}$, pedestal soft X-ray emission and the increase of the inner divertor bremsstrahlung emission occur over a time interval of 200–300 μs, similar to the period of large MHD activity [27]

3.2.1 Dynamics and Timescales for the Type I ELM Energy and Particle Losses from the Core Plasma

The collapse of the pedestal plasma parameters during ELMs is associated with a phase of enhanced broadband activity (as measured by Mirnov coils) up to frequencies ~ 100 kHz lasting several hundred microseconds [2]. During this phase both the pedestal plasma density [24] and the pedestal temperature [16] experience a sudden drop and, consequently, the plasma thermal energy decreases as well. An example of the pedestal plasma parameters collapse during Type I ELMs in JET is shown in Fig. 3.12. For this case, the collapse phase lasts $\sim 300\,\mu$s. The pedestal parameters are characterized in this figure by measurements with high time resolution of the pedestal temperature and soft X-ray emissivity of the pedestal plasma, which depends on the electron temperature and density in this region ($n_{\mathrm{e,ped}}$ and $T_{\mathrm{e,ped}}$). During the phase of enhanced broadband MHD activity, the poloidal field structure of closed flux surfaces is distorted considerably and field lines inside the confined plasma connect directly to the plasma facing components in the vacuum vessel. As a consequence, high energy electrons and ions, with energies typical

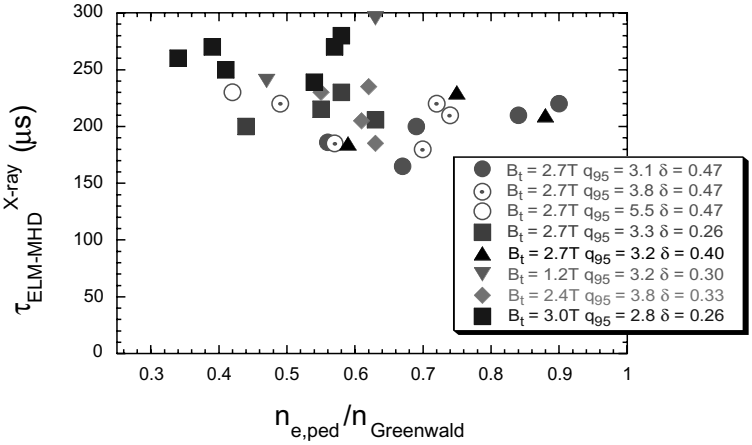

Fig. 3.13. Time duration of the edge plasma collapse phase determined from the edge soft X-ray emission for a large range of JET Type I ELMy H-mode plasmas [27]

of the pedestal plasma ($\sim$ keV for JET Type I ELMy H-modes), flow towards these PFCs, leading to the large energy fluxes and sudden temperature rise of the PFC surface, as shown in Fig. 3.6. Between ELMs, due the thermal insulation provided by the poloidal magnetic field closed flux surfaces, the typical energies of the electrons and ions reaching the PFCs are in the range of 1–100 eV. The high energy electrons flowing to the PFCs during ELMs emit strong bremsstrahlung radiation as they slow down in the material element. Because of their high energy and the large fluxes, this bremsstrahlung emission can be comparable to the local emissivity of the core plasma in the soft X-ray wavelength range and, hence, can be measured by the usual soft X-ray diagnostics installed in all fusion devices [25,26]. The last row in Fig. 3.12 shows the increase of soft X-ray emission from the inner divertor in a JET Type I ELM caused by the impact of high energy electrons (the pedestal temperature is $\sim$ 1 keV for this experiment). The duration of the enhanced broadband MHD activity phase ($\tau_{\mathrm{ELM-MHD}}$), the duration of the pedestal plasma collapse and the duration of the hot electron pulse on the PFCs are all very similar, indicating that it is only for this enhanced broadband MHD activity phase during which there is a direct connection, along magnetic field lines, between the regions located in the confined plasma in-between ELMs (closed flux surfaces) and the PFCs.

The duration of the enhanced broadband MHD activity phase and of the pedestal parameter collapse determines the shortest timescale for the energy to flow to the PFCs during Type I ELMs. The transport of energy from the pedestal plasma to the PFCs along the magnetic field lines can only contribute to lengthen the timescale for the energy fluxes to the PFCs beyond this minimum value. Hence, it is important to characterize, experimentally

and theoretically, the duration of this phase. From the practical point of view, the best way to characterize the ELM pedestal collapse phase is with the time behaviour of soft X-ray pedestal emissivity. As mentioned before, this characterization provides a very similar answer to that with the duration of the broadband MHD activity phase ($\tau_{\mathrm{ELM-MHD}}$) [28]. Figure 3.13 shows the results of such $\tau_{\mathrm{ELM-MHD}}$ characterization for a set of JET discharges expanding a very large range of experimental conditions in the Type I ELMy H-mode regime. No obvious trend for the duration of the collapse phase with the magnetic characteristics of the discharge (B_{t} and q_{95}), plasma shape (described by the triangularity, δ) or input power has been identified so far in JET nor in other experiments [4]. In particular, this collapse phase duration does not seem not scale with pedestal plasma parameters as expected from a Kadomtsev-like reconnection phenomenon [29]. Models for the growth of the ELM MHD activity based on an explosive ballooning-like instability, similar to that occurring in solar flares, have been proposed recently [30], but the detailed comparison between the predictions of these models with respect to ELM duration and the experimental results remains to be carried out.

3.2.2 Magnitude of the Type I ELM Energy and Particle Losses from the Core Plasma and Their Extrapolation to Next Step Burning Plasma Experiments

The contrasting behaviour of ELM energy and particle losses with increasing plasma density indicates that the mechanisms that leads to the ELM energy loss (conduction and convection) depend on different ways on the parameters of the plasma at the pedestal. This is indeed the case, as illustrated in Figs. 3.14 and 3.15 for a series of experiments in JET and DIII-D. With increasing pedestal plasma density, the normalized ELM energy loss (to the pedestal energy) decreases. This is mostly due to the decrease of the normalized pedestal plasma temperature drop (to the pedestal temperature before the ELM) caused by the Type I ELMs. The normalized pedestal plasma density drop (to the pedestal density before the ELM), however, remains approximately constant independent of the pedestal plasma density. Hence, the reduction of the ELM energy loss with increasing plasma density is due to the decrease of the ELM conductive losses (associated with the $T_{\mathrm{e,ped}}$ drop), while the ELM convective losses remain approximately constant.

Although the qualitative behaviour of the ELM energy convective and conductive losses is common to most experimental devices [16, 31–33], the detailed physics processes that determine such behaviour remain to be precisely identified. Depending on the process that controls the ELM energy loss, the expected magnitude of the ELM energy loss in next step devices can vary significantly [34] and, together with it, the expected damage to the material elements inside the vacuum vessel of these devices, which will be exposed to the high energy fluxes caused by the ELMs.

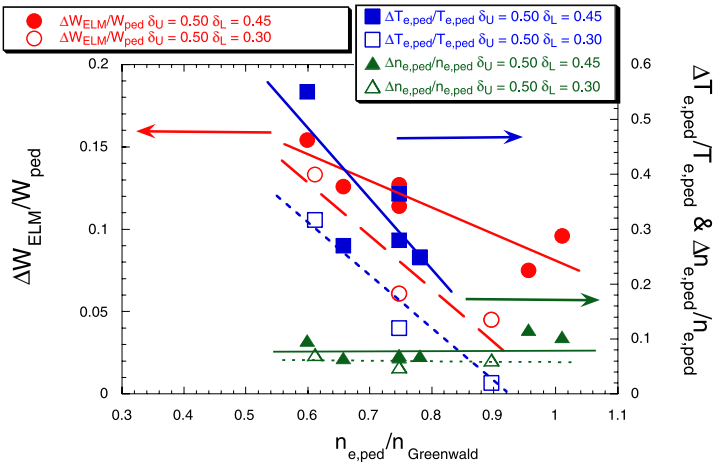

Fig. 3.14. Normalized ELM energy loss ($\Delta W_{\mathrm{ELM}}/W_{\mathrm{ped}}$) and pedestal temperature ($\Delta T_{\mathrm{e,ped}}/T_{\mathrm{e,ped}}$) and density ($\Delta n_{\mathrm{e,ped}}/n_{\mathrm{e,ped}}$) drop versus pedestal density normalized to the Greenwald limit ($n_{\mathrm{e,ped}}/n_{\mathrm{Greenwald}}$) for JET discharges with high upper and high/medium lower triangularities. The decrease of $\Delta W_{\mathrm{ELM}}/W_{\mathrm{ped}}$ with $n_{\mathrm{e,ped}}$ is associated with the decrease of $\Delta T_{\mathrm{e,ped}}/T_{\mathrm{e,ped}}$, as $\Delta n_{\mathrm{e,ped}}/n_{\mathrm{e,ped}}$ seems independent of $n_{\mathrm{e,ped}}$. At the highest $n_{\mathrm{e,ped}}$, the ELM energy loss is due almost entirely to the ELM particle loss, for discharges with medium lower triangularities. Lines are to guide the eye [16]

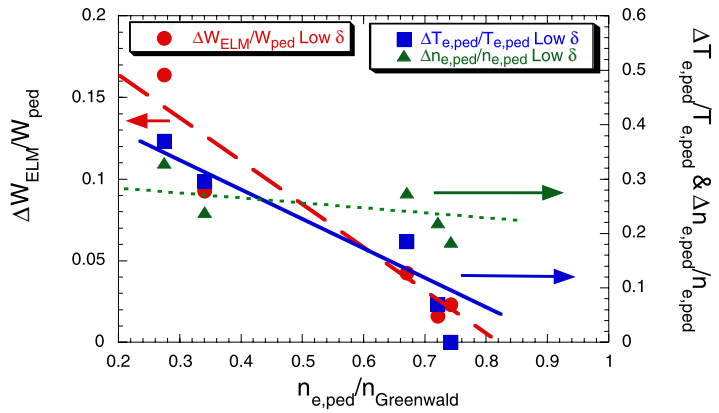

Fig. 3.15. Normalized ELM energy loss ($\Delta W_{\mathrm{ELM}}/W_{\mathrm{ped}}$) and pedestal temperature ($\Delta T_{\mathrm{e,ped}}/T_{\mathrm{e,ped}}$) and density ($\Delta n_{\mathrm{e,ped}}/n_{\mathrm{e,ped}}$) drop versus pedestal density normalized to the Greenwald limit ($n_{\mathrm{e,ped}}/n_{\mathrm{Greenwald}}$) for low triangularity DIII-D discharges. The decrease of $\Delta W_{\mathrm{ELM}}/W_{\mathrm{ped}}$ with $n_{\mathrm{e,ped}}$ is associated with the decrease of $\Delta T_{\mathrm{e,ped}}/T_{\mathrm{e,ped}}$, as $\Delta n_{\mathrm{e,ped}}/n_{\mathrm{e,ped}}$ seems independent of $n_{\mathrm{e,ped}}$. At the highest $n_{\mathrm{e,ped}}$, the ELM energy loss is due almost entirely to the ELM particle loss. Lines are to guide the eye [31]

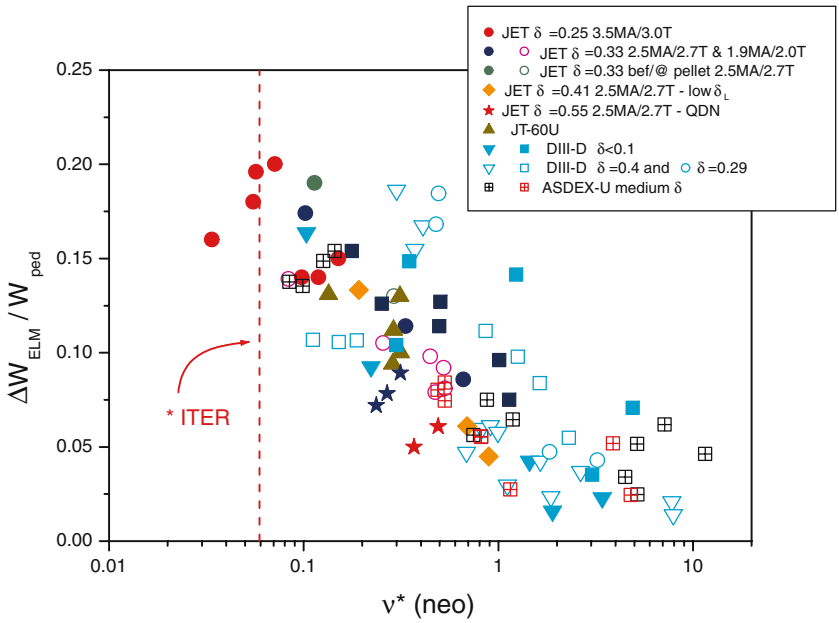

Fig. 3.16. Normalized ELM energy loss ($\Delta W_{\mathrm{ELM}}/W_{\mathrm{ped}}$) versus pedestal plasma collisionality for a large range of Type I ELMy H-mode plasmas in ASDEX Upgrade, DIII-D, JT-60U and JET including various plasma triangularities, ratios of $P_{\mathrm{INPUT}}/P_{\mathrm{L-H}}$ and pellet triggered ELMs and $q_{95} = 3$–4 [33]

In the absence of a firm theoretical basis to describe the dependence of the ELM energy loss on pedestal plasma parameters and on other discharge characteristics, several empirical scalings with a physics basis, have been derived in order to extrapolate the ELM energy losses in present experiments to next step devices, such as ITER.

One such scaling is based on the observed empirical correlation between the normalized ELM energy loss and the pedestal plasma collisionality $\nu *_{\mathrm{ped}}\ (\mathrm{neo}) = R\, q_{95} \varepsilon^{g3/2} (\lambda_{\mathrm{e,e}})^{-1}$, where $\lambda_{\mathrm{e,e}}$ is the electron-electron coulomb collision mean free path, q_{95} is the safety factor, R is the major radius of the discharge and ε is its inverse aspect ratio ($\varepsilon g R/a$) [34]. The physics processes that may lead to such dependence are connected to the trigger mechanism of the ELM, which is affected by the edge bootstrap current in the peeling-ballooning ELM model [12], and to the transport of energy in the reconnected layer during the phase of enhanced broadband MHD activity [27]. However, no detailed physics model based on these ideas has been quantitatively compared with the experiment so far. This empirical correlation between ELM energy loss and pedestal plasma collisionality holds for measurements in many experimental devices, as shown in Fig. 3.16 [33]. The expected ELM energy losses in the ITER reference $Q_{\mathrm{DT}} = 10$ regime from

this empirical scaling are in the range $\Delta W_{\mathrm{ELM}}/W_{\mathrm{ped}} = 0.17$–$0.20$ which, for the expected pedestal energy in ITER of $W_{\mathrm{ped}} \sim 100\,\mathrm{MJ}$, leads to ELM energy losses $\Delta W_{\mathrm{ELM}}^{\mathrm{ITER}} \sim 20\,\mathrm{MJ}$. As it will be shown in Sect. 3.3.2, if such energy fluxes would repeatedly reach the divertor in ITER discharges, the divertor target lifetime would be severely restricted by the ELM-caused erosion [3].

The remaining scatter in Fig. 3.16 indicates that other parameters besides plasma collisionality play a role in determining the ELM energy loss. One such parameter, recently identified, is the safety factor of the discharge, q_{95} [28]. Type I ELMs in discharges with higher q_{95} cause smaller energy losses than in similar discharges with the same values of pedestal collisionalities but lower q_{95}. The identification of the additional parameters to the pedestal collisionality that influence the ELM energy loss is an active field of research and a common picture from all available experiments remains to emerge.

The other empirical scaling which describes satisfactorily the observations from a large set of experiments in all major divertor tokamaks is based on the limitation to the ELM energy transport associated with the formation of a sheath at the PFC surface in equilibrium with the pedestal plasma during the phase of enhanced MHD broadband activity [35]. Following this hypothesis, the characteristic time for ELM energy loss is determined by the ion transit time along the field line from the pedestal plasma to the divertor target $\tau_{||}^{\mathrm{Front}}$, defined as $\tau_{||}^{\mathrm{Front}} = \frac{2\pi R q_{95}}{c_{\mathrm{s,ped}}}$, where R is the major radius of the tokamak and $c_{\mathrm{s,ped}}$ is the ion sound speed calculated with the values of the pedestal plasma temperature. The ELM energy loss according to this physics picture should decrease with increasing $\tau_{||}^{\mathrm{Front}}/\tau_{\mathrm{ELM-MHD}}$, i.e., as the characteristic time for energy loss along the field increases with respect to the time during which magnetic field lines connect the pedestal plasma to the PFCs. Because the duration of the enhanced broadband MHD phase ($\tau_{\mathrm{ELM-MHD}}$) is empirically found to be independent of pedestal plasma parameters (see Fig. 3.13), an inverse correlation between $\Delta W_{\mathrm{ELM}}/W_{\mathrm{ped}}$ and $\tau_{||}^{\mathrm{Front}}$ is expected from this physics model. This correlation is indeed found experimentally and describes satisfactorily the observations in most divertor tokamak experiments, as shown in Fig. 3.17 [4]. The expected ELM energy losses in the reference $Q_{\mathrm{DT}} = 10$ regime in ITER from this empirical scaling are in the range $\Delta W_{\mathrm{ELM}}/W_{\mathrm{ped}} = 0.05$–$0.10$, which for the expected pedestal energy in ITER of $W_{\mathrm{ped}} \sim 100\,\mathrm{MJ}$ leads to ELM energy losses $\Delta W_{\mathrm{ELM}}^{\mathrm{ITER}} \sim 5$–$10\,\mathrm{MJ}$. As will be shown in Sect. 3.3.2, if such energy fluxes would occur during Type I ELMs in ITER, the divertor target lifetime time would be marginally acceptable for ITER operation, once realistic assumptions for the ELM divertor target energy flux calculations are taken into account [3].

The reason behind the widely different extrapolations to ITER by the $\nu *_{\mathrm{ped}}$ (neo) and $\tau_{||}^{\mathrm{Front}}$ scalings is that with increasing device size, and for discharges at similar normalized densities to the Greenwald limit, the pedestal temperature increases approximately as $T_{\mathrm{ped}} \sim R^2$ [16]. As a consequence, the pedestal collisionality decreases as $\nu *_{\mathrm{ped}}$ (neo) $\sim \mathrm{R}^{-3}$, while the ion

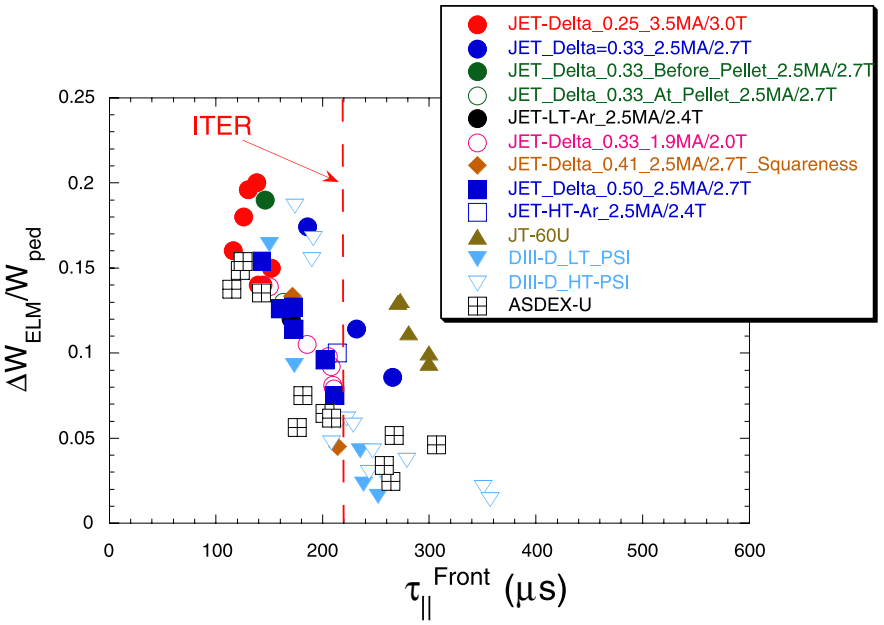

Fig. 3.17. Normalized ELM energy loss ($\Delta W_{\mathrm{ELM}}/W_{\mathrm{ped}}$) versus SOL ion flow parallel time calculated with the pedestal plasma parameters ($\tau_{||}^{\mathrm{Front}}$), for a large range of Type I ELMy H-mode plasmas in ASDEX Upgrade, DIII-D, JT-60U and JET including various plasma triangularities, ratios of $P_{\mathrm{INPUT}}/P_{\mathrm{L-H}}$, impurity seeding (Ar) and pellet triggered ELMs [4]

transit time $\tau_{||}^{\mathrm{Front}}$ does not depend on device size, for these assumptions on pedestal plasma conditions. This is clearly seen by comparing Fig. 3.16 with Fig. 3.17; in Fig. 3.16 the data from the largest experiments, such as JET, is concentrated in the low collisionality range compared to that of smaller experiments, such as ASDEX Upgrade and DIII-D. On the contrary, the range of $\tau_{||}^{\mathrm{Front}}$ covered by the JET data overlaps well with the range achieved in ASDEX Upgrade and DIII-D, as shown in Fig. 3.17. In this context, the expected values of $\tau_{||}^{\mathrm{Front}}$ in ITER fall in the upper range of those seen in existing experiments, despite the very small collisionality of the pedestal plasma in ITER. In existing experiments, large values of $\tau_{||}^{\mathrm{Front}}$ in Fig. 3.17 correspond to Type I ELMy H-modes at high densities and low pedestal temperatures, for which the ELM conductive losses are smaller and, consequently, the total ELM energy losses are small as well.

3.3 Energy Fluxes to PFCs During Type I ELMs in Existing Experiments and Implications for Burning Plasma Experiments

3.3.1 Spatial and Temporal Characteristics of the Type I ELM Energy Fluxes to PFCs

The magnitude of the energy fluxes deposited by the ELMs on PFCs is determined not only by the core plasma ELM energy loss and the time scale of such loss but also by their spatial distribution on the material elements in contact with the plasma during ELMs and by the timescale of the energy fluxes onto the PFCs, which, as we will show in this section, is different from that of the core plasma ELM energy loss described in Sect. 3.2.1.

During Type I ELMs the poloidal flux magnetic surfaces are distorted and field lines originating in the confined plasma can reach the PFCs. As a consequence, a high temperature and high-density plasma comes in contact with the material elements inside the vacuum vessel of the device and large energy fluxes reach these elements. Despite this distortion of the flux surfaces, most of the ELM energy arrives to the same PFCs and over a similar area to that of the inter-ELM energy fluxes, i.e., the divertor targets. This indicates that, at least, the magnetic field structure associated with the poloidal magnetic field null, characteristic of poloidal divertor discharges, survives the ELM. The balance of energy deposition to the inner and outer divertors during ELMs changes in asymmetry with respect the energy flux between ELMs. For discharges with the "usual" ion grad-B drift direction towards the divertor, the energy flux is typically 2–4 times larger at the outer divertor than at the inner divertor. During Type I ELMs, this balance changes and the energy flux to the inner divertor is typically 2–4 times larger than at the outer one [36]. This indicates that the mechanism controlling the transport of energy from the confined plasma to the divertor target changes substantially at the ELMs (distorted magnetic flux surfaces) with respect to between ELMs (nested magnetic flux surfaces).

Figure 3.18 shows the ratio between the poloidal width for energy flux during ELMs measured at the outer divertor and this same width between ELMs, for a large range of experiments in the ASDEX Upgrade tokamak [36]. As shown in the figure, both areas are approximately similar, indicating that the ratio between energy transport along and across the magnetic field, which determines the width of the energy flux on the divertor, is similar during ELMs and in-between ELMs. Thus, the increase of parallel transport during ELMs is compensated by a simultaneous large increase of transport across the field. At present, it is not known if there is any correlation between the poloidal extent of the divertor ELM energy fluxes and other global ELM characteristics, such as the size of ΔW_{ELM} or the pedestal plasma parameters, or if the scatter shown in Fig. 3.18 is just due to the "natural" ELM variability.

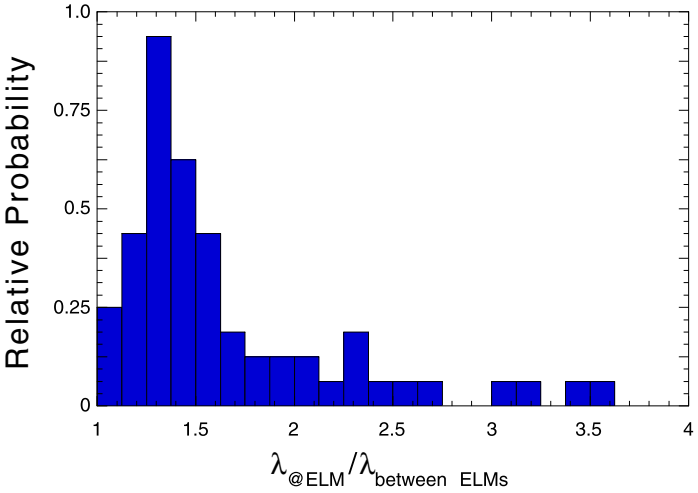

Fig. 3.18. Histogram of the probability distribution function of the poloidal width for divertor energy flux during ELMs ($\lambda_{@\mathrm{ELM}}$) compared to that in-between ELMs ($\lambda_{\mathrm{between\ ELMs}}$) for ASDEX Upgrade discharges [4, 36]

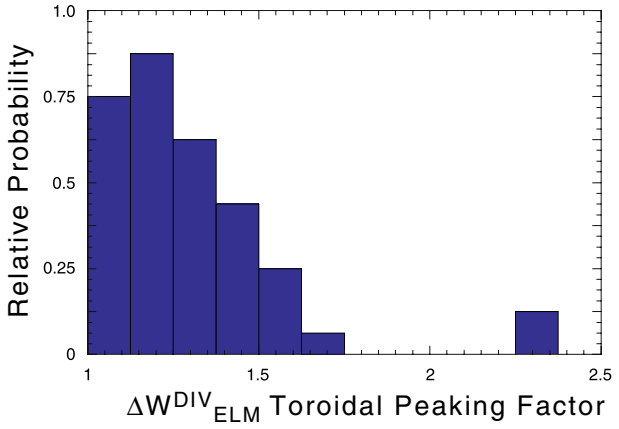

Fig. 3.19. Histogram of the probability distribution function of the toroidal peaking factor (toroidal asymmetry from measurements at two toroidal locations) for ELM energy deposition at the divertor target in DIII-D discharges [33, 37]

Measurements of the poloidal distribution of the ELM energy deposition at the divertor target, such as those in Fig. 3.18, are usually taken at only at one toroidal location. Few experiments have been carried out with measurements of the divertor ELM energy and particle fluxes (with infra-red cameras and Langmuir probes) at various toroidal positions. These experiments show that the divertor ELM energy flux is, approximately, toroidally

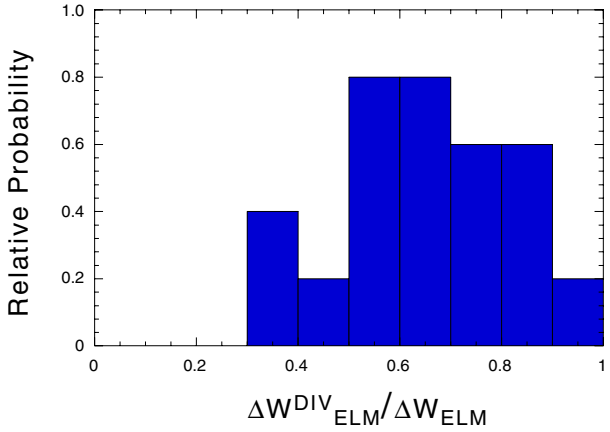

Fig. 3.20. Histogram of the probability distribution function for the proportion of main plasma ELM energy loss (ΔW_{ELM}) that reaches the divertor target ($\Delta W_{\mathrm{ELM}}^{\mathrm{DIV}}$) for ASDEX Upgrade discharges [33, 44]

symmetric [36–38]. An example of such measurements is shown in Fig. 3.19 for the probability distribution function of this asymmetry obtained in DIII-D experiments [33, 37]. At present, it is not known if there is any correlation between the toroidal symmetry of the divertor ELM energy fluxes and other global ELM characteristics, such as the size of ΔW_{ELM} or the pedestal plasma parameters, or if the scatter shown in Fig. 3.19 is due to the "natural" ELM variability and/or to issues related to the relative calibration of the two IR-camera diagnostics used in this study.

Assuming that the divertor ELM energy flux is toroidally symmetric for all conditions, it is possible to determine the global energy balance during ELMs, i.e., how much of the energy lost from the main plasma reaches the divertor target. Both in JET and ASDEX Upgrade, it is found that more than 50% of ΔW_{ELM} reaches the divertor target [39, 40]. Interaction of the plasma expelled during an ELM with the main chamber PFCs is usually observed in most divertor experiments such as ASDEX Upgrade, DIII-D and JET [41–43], but the magnitude of this interaction is difficult to quantify. An example of the probability distribution function for the energy arriving at the divertor ($\Delta W_{\mathrm{ELM}}^{\mathrm{div}}$) versus main plasma energy loss (ΔW_{ELM}) from ASDEX Upgrade experiments [33, 44] is shown in Fig. 3.20. As in the case of toroidal symmetry described above, it is not know if the scatter in this figure is associated with the "natural" ELM variability or if there is any dependence on other ELM characteristics.

The data in Fig. 3.20 and similar observations in JET [39, 40] imply that a non-negligible amount of the main plasma ELM energy loss may reach plasma facing components (PFCs) in the main chamber of the device and not the divertor target. While this can enlarge the range for ITER oper-

ation with acceptable divertor target lifetime, it may restrict severely the lifetime of main chamber PFCs. Contrary to the divertor target, PFCs is the main chamber are usually not toroidally symmetric and the interaction of ELMs with these elements is concentrated in relatively small areas [43]. Direct measurements of the ELM energy flux onto the main chamber PFC elements in ASDEX Upgrade have indeed demonstrated that this flux is concentrated in the protruding elements of the vacuum vessel which are closer to the confined plasma, such as poloidal limiters and protection elements of radio-frequency antennas [41]. The estimated amount of energy reaching these elements ($\Delta W_{\mathrm{ELM}}^{\mathrm{main\ chamber}}$) from the available measurements is in the range of 10–20% of the main plasma ELM energy loss (ΔW_{ELM}), which is in reasonable agreement with the previous measurements of the divertor target ELM energy flux shown in Fig. 3.20.

Once we have characterized the area of the PFCs onto which the ELM energy flux lands, we turn now to the timescale of the ELM energy flux on the PFCs. This is the second parameter that determines the surface temperature rise and, together with it, the possible ELM enhanced erosion of these material elements. As described in Sect. 3.2.1, the pedestal collapse duration is similar to the phase of enhanced MHD broadband activity and does not depend on pedestal plasma parameters. Despite this constant timescale for the "source" of the ELM energy flux, it has been found that the time scale for the ELM energy flux reaching the divertor target is well correlated with pedestal plasma parameters [16, 39, 40], in particular with the pedestal plasma temperature before the ELM pedestal collapse. In order to facilitate the comparison of experimental results among several fusion devices, the duration of the divertor ELM energy flux pulse is characterized by the rise time of the divertor surface temperature, as measured with IR diagnostics ($\tau_{\mathrm{IR}}^{\mathrm{ELM}}$). Figures 3.21 and 3.22 show measurements of the divertor target surface temperature evolution and of the calculated ELM power fluxes for two discharges in JET with Type I ELMs [40] at low density (high pedestal temperature in Fig. 3.21) and medium density (lower pedestal temperature in Fig. 3.22). The definition of $\tau_{\mathrm{IR}}^{\mathrm{ELM}}$ is illustrated in both cases. The ELM power flux for the lower density discharge (Fig. 3.21) is much larger (by a factor ~ 4) than the one for the medium density discharge (Fig. 3.22). This is due to two factors: a) ELMs of discharges at higher densities cause smaller energy losses from the core plasma, as described in Sect. 3.2.2 and b) the duration of the ELM power flux pulse is much longer for the higher density case (by more than a factor of ~ 2). The first factor leads to a straightforward reduction of the energy flux by $\sim 50\%$, when comparing the measurements at low and medium densities. The second factor, together with the independence of $\tau_{\mathrm{ELM-MHD}}$ (and of the duration of the hot electron pulse on the divertor target described in Sect. 3.2.1) on pedestal plasma parameters, proves that the transport of ELM energy from the core plasma to the divertor (and not the source of the ELM energy flux) plays a major role in determining the timescale of the ELM energy flux to the divertor target. Furthermore, because the flux of hot electrons

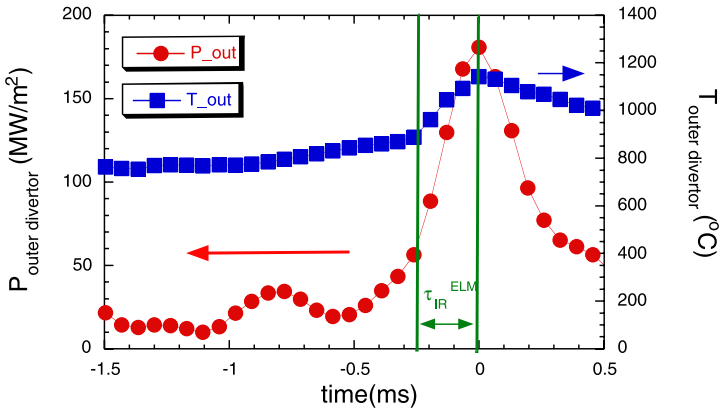

Fig. 3.21. Time evolution of the surface temperature of the outer divertor target and the deduced power flux, for typical low density ELMy H-mode conditions in JET ($n_{\mathrm{e,ped}} = 5.2\ 10^{19}\mathrm{m}^{-3}$, $T_{\mathrm{e,ped}} = 1650\,\mathrm{eV}$). For inter-machine comparisons, the duration of the ELM power pulse is characterized by the rise time of the surface temperature during the ELM ($\tau_{\mathrm{IR}}^{\mathrm{ELM}}$), as illustrated in the figure [16, 40]

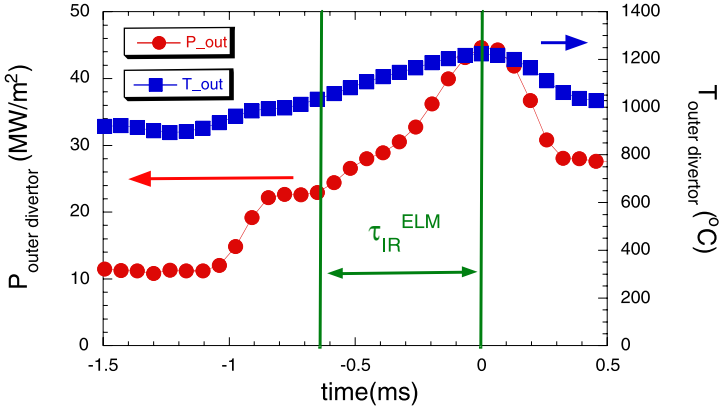

Fig. 3.22. Time evolution of the surface temperature of the outer divertor target and the deduced power flux, for typical medium density ELMy H-mode conditions in JET ($n_{\mathrm{e,ped}} = 6.4\ 10^{19}\mathrm{m}^{-3}$, $T_{\mathrm{e,ped}} = 850\,\mathrm{eV}$). For inter-machine comparisons, the duration of the ELM power pulse is characterized by the rise time of the surface temperature during the ELM ($\tau_{\mathrm{IR}}^{\mathrm{ELM}}$), as illustrated in the figure [16, 40]

(with energies typical of the pedestal plasma) is limited in time to the phase of enhanced MHD broadband activity (with duration $\tau_{\mathrm{ELM-MHD}} \sim 200$–$300\,\mu\mathrm{s}$ in JET), the measurements in Fig. 3.22 indicate that part of the ELM energy flux reaches the divertor when this MHD phase is over and the hot electron flux to the divertor target has stopped. This is consistent, with the change in the nature of the core plasma ELM energy loss from conductive

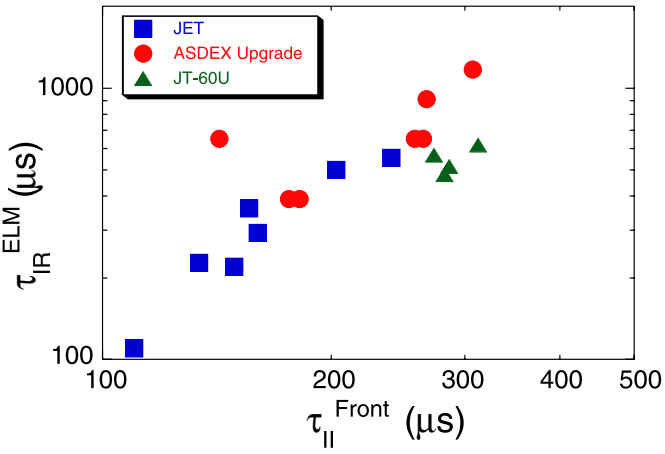

Fig. 3.23. Duration of the ELM power pulse from infrared measurements for Type I ELMs ($\tau_{\mathrm{IR}}^{\mathrm{ELM}}$) in ASDEX Upgrade, JET and JT-60U versus the SOL ion flow parallel time calculated for the pedestal plasma parameters ($\tau_{||}^{\mathrm{Front}}$). $\tau_{||}^{\mathrm{Front}}$ increases with decreasing pedestal plasma temperature [4]

dominated to convective dominated with increasing pedestal plasma density (and decreasing pedestal plasma temperature) described in Sect. 3.2.2.

The observations for JET shown in Figs. 3.21 and 3.22 have been confirmed in other divertor experiments and have allowed the identification of the processes that control the energy flux to the divertor target during Type I ELMs. Measurements of $\tau_{\mathrm{IR}}^{\mathrm{ELM}}$ over a large set of experiments covering a wide range of pedestal plasma parameters in ASDEX Upgrade, JET and JT-60U have shown that the duration of the ELM energy pulse on the divertor target is well correlated with the transit time for pedestal ions to reach the divertor target ($\tau_{||}^{\mathrm{Front}} = \frac{2\pi R q_{95}}{c_{\mathrm{s,ped}}}$) and not with the duration of the ELM MHD event and/or the duration of the flux of hot electrons onto the divertor target [4]. Figure 3.23 shows the measured $\tau_{\mathrm{IR}}^{\mathrm{ELM}}$ versus the calculated $\tau_{||}^{\mathrm{Front}}$ for the available multi-machine data set. For the calculation of $\tau_{||}^{\mathrm{Front}}$, the values of the pedestal electron and ion temperatures before the ELM are used ($T_{\mathrm{e,ped}} = T_{\mathrm{i,ped}}$ is assumed when no pedestal ion temperature measurements are available). The experimental scaling derived from these measurements is $\tau_{\mathrm{IR}}^{\mathrm{ELM}}(\mu\mathrm{s}) = 0.29[\tau_{||}^{\mathrm{Front}}(\mu\mathrm{s})]^{1.38}$. The correlation of the divertor ELM energy flux time ($\tau_{\mathrm{IR}}^{\mathrm{ELM}}$) with $\tau_{||}^{\mathrm{Front}}$ reveals that the duration of the ELM power flux pulse is controlled by the parallel ion dynamics during the ELM event. Such finding is in agreement with kinetic simulations of the divertor power flux during ELMs carried out under the assumption that a high energy sheath is established at the divertor target during the ELM and that secondary electron emission remains moderately low during this phase [45]. Simultaneous measurements of the ion flux entering the divertor with Langmuir probes

and of the divertor ELM power flux deposition with an IR camera in JT-60U are also in agreement with the hypothesis of the dynamics of the ion flow controlling the energy flux to the divertor during ELMs [46]. This set of observations indicates that the ionization of neutrals in the divertor plasma and/or of those created by the desorption of neutrals trapped in the target by the high energy electron flux does not play a major role on the ELM energy flux duration, but further research is needed to confirm this hypothesis.

As shown in Figs. 3.21 and 3.22, the temporal evolution of the power flux during Type I ELMs is much more complicated than what is described in a simple way by $\tau_{\mathrm{IR}}^{\mathrm{ELM}}$. In particular, the power flux during an ELM is substantially different from a square waveform in time with duration $\tau_{\mathrm{IR}}^{\mathrm{ELM}}$, as it was assumed in the initial calculations carried out to estimate the threshold for material damage by ELMs in ITER [1,34,35]. The actual temporal waveform of the divertor ELM power flux is closer to a triangle, with a substantial amount of the ELM energy arriving to the divertor target after the maximum temperature has been reached [40]. This has sizeable and positive implications for the expected power fluxes during Type I ELMs and the subsequent divertor target damage in next step burning plasma experiments, such as ITER [3]. The most recent estimates of the expected ELM energy fluxes and subsequent PFC material damage in next step burning plasma experiments, with ITER as the most relevant example, are described in the next section.

3.3.2 Implications of the Type I ELM Energy Fluxes to PFCs in Burning Plasma Experiments: Application to the ITER Reference $Q_{\mathrm{DT}} = 10$ Scenario

When the surface temperature of the material elements in the PFCs reaches high values ($\sim$ 3000–4000 K for Carbon and Tungsten based materials), the sublimation rate of these components is in the range of several μm/s. This leads to erosion rates which are several orders of magnitude larger than the "usual" gross erosion of the PFCs, associated with physical and chemical sputtering during "normal" plasma operation, i.e., when the PFC surface temperature is much lower than the sublimation temperature. Figure 3.24 shows the sublimation rates for carbon and tungsten as a function of the material temperature illustrating this point. Two conditions are considered for the calculations of carbon sublimation: one in which the evaporation of single atoms is the dominant sublimation mechanism and the other (more realistic) in which the release of tri-atomic carbon cluster dominates the composition of the sublimated material.

For metals, such as W, an additional erosion mechanism exists due to the formation of a melt layer on the PFC surface, once the surface temperature exceeds the melting temperature of the metal. This layer can reach a width of several tens of microns for W under energy fluxes of $\sim 1\,\mathrm{MJ/m^2}$ sustained during several hundreds of microseconds. The stability of this layer in realistic tokamak geometries and in contact with the plasma is difficult to describe by

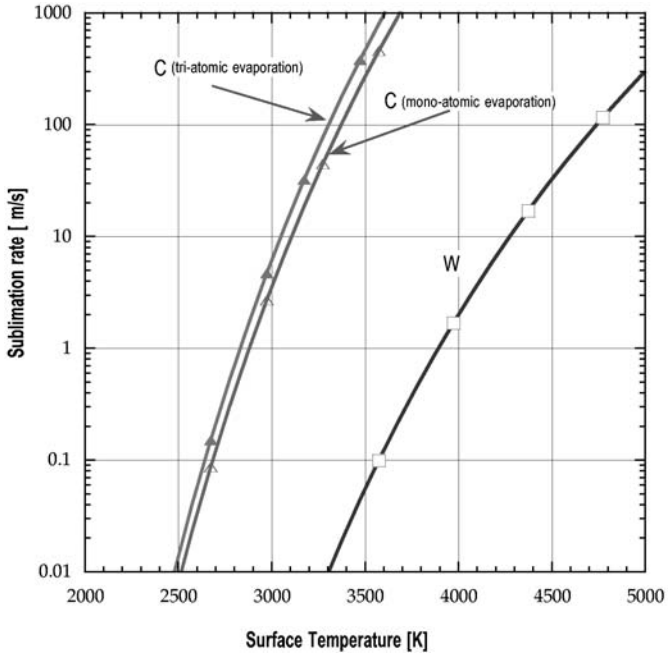

Fig. 3.24. Sublimation rate (in μm/s) as a function of surface temperature for C and W. For C, two cases are shown: (1) mono-atomic evaporation predominates, (2) C_3 cluster evaporation dominates [3]

models validated by the experiment. However, even the loss by splashing of a small proportion of this melt layer can be the dominant erosion mechanism for metal PCFs at high surface temperatures [3].

ELM energy fluxes that lead to the PFC surface temperature reaching these values repeatedly are rare in the present generation of fusion devices and have only been reached occasionally in high current/low density JET ELMy H-modes, as mentioned in Sect. 3.1.2. However, the unfavorable energy to area scaling in toroidal fusion devices makes the ELM energy fluxes to be much larger in the next generation of fusion experiments, aimed at the demonstration of high fusion energy gain such as ITER and FIRE. As described in Sect. 3.2.2, the expected energy loss from the main plasma for the ITER reference $Q_{\mathrm{DT}} = 10$ scenario is in the range $\Delta W_{\mathrm{ELM}} = 5$–$20\,\mathrm{MJ}$. Of this energy, 60 to 80% will reach the divertor target, that is $\Delta W_{\mathrm{ELM}}^{\mathrm{DIV}} = 3$–$16\,\mathrm{MJ}$ according to the experimental data described in Sect. 3.3.1. This ELM energy flux is expected to fall on an area which is 1–1.5 times larger than the one for the energy flux between ELMs, as discussed in the previous section. The power flux width between ELMs at the ITER outer midplane from present scalings is $\lambda = 5\,\mathrm{mm}$, which corresponds to an area of $3\,\mathrm{m}^2$ for the ITER divertor target reference design [47]. As a consequence, the energy flux

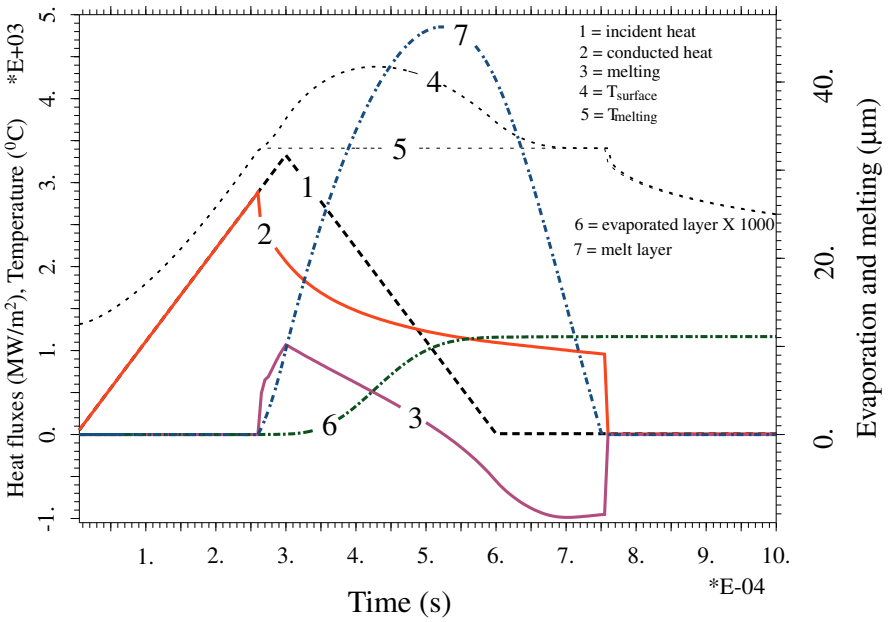

Fig. 3.25. Heat flux histories following an ELM of $1\,\mathrm{MJ/m^2}$ with a power flux triangular waveform (curve 1) with ramp-up and ramp-down phases lasting $300\,\mu\mathrm{s}$ each on a 10 mm thick W target under an inter-ELM power flux of $10\,\mathrm{MWm^{-2}}$. *Curves*: (1) incident heat flux load; (2) conducted heat flux into the material; (3) heat flux spent in melting of the material (the evaporation and black-body radiation heat fluxes are comparatively small and not shown). Curve (4) shows the surface target temperature and (5) shows the temperature of the melt layer. Curve (6) shows the vaporized thickness (amplified of a factor of 1000) and (7) the melt layer assuming that no losses of molten material occur during the ELM [3]

reaching the divertor target during Type I ELMs in ITER will be in the range $\Delta W_{\mathrm{ELM}}^{\mathrm{DIV}}/A_{\mathrm{ELM}} = 0.6\text{–}5.3\,\mathrm{MJ/m^2}$. The predicted pedestal plasma parameters for the ITER reference $Q_{\mathrm{DT}} = 10$ scenario are $n_{\mathrm{ped}} = 8.0\,10^{19}\,\mathrm{m^{-3}}$, $T_{\mathrm{ped}} = 3.5\,\mathrm{keV}$ [34]. Hence, $\tau_{||}^{\mathrm{Front}}$ in ITER will be $\sim 220\,\mu\mathrm{s}$, as already discussed in Sect. 3.2.2. Applying the scaling in Sect. 3.3.1 for the timescale of the ELM energy flux to PFCs with this $\tau_{||}^{\mathrm{Front}}$, the expected timescale for the ELM energy flux on the ITER divertor target is $\tau_{\mathrm{ELM}}^{\mathrm{IR}} \sim 500\mu\mathrm{s}$. Hence, in order to predict the lifetime of PFCs in next step devices, it is necessary to model accurately the surface temperature evolution (and the associated sublimation/melting) of such elements exposed to power fluxes in the range $1\text{–}10\,\mathrm{GW/m^2}$ for several hundreds of microseconds. This range has been deduced here taken ITER as an example, but it is common to all burning plasma experiments whose operating regime is based on the Type I ELMy H-mode such as FIRE.

Figure 3.25 shows the results of the calculated temperature evolution and of the development of the melt layer in a 10 mm thick W divertor target under an energy flux of 1 MJ/m^2 reaching the target surface with a triangular waveform with 300 μs ramp-up/ramp-down times (i.e., 3.3 GW/m^2 peak power flux) [3]. Around 250 μs after the beginning of the ELM energy pulse, the surface temperature reaches the solid to liquid transition threshold and a melt layer starts to form at the target surface. This melt layer grows reaching its maximum width of $\sim 50\,\mu$m around 550 μs, i.e., well after the time of maximum incident heat flux. As a consequence of the heat spent in melting the material, the heat flux that is conducted to the bulk material is smaller than the incident flux during the phase of increasing melt layer growth but is larger than this flux when the melt layer re-solidifies. The amount of evaporated tungsten during this transient energy pulse is relatively small and leads to a 10^{-2}gμm erosion of the target. From this value and that of the width of the melt layer, it is clear that any significant fraction of melt layer loss due to splashing in the time interval [250, 750] μs would dominate the material erosion during the ELM transient energy pulse.

Comparing the values of the divertor ELM power fluxes expected in next step devices with those for which significant melting (for W) or ablation (for C) causes large erosion of the material target (such as in those shown in Fig. 3.25), it is clear that detailed calculations are necessary to estimate the effect of ELM power fluxes on the divertor target and on its expected lifetime. An extensive study on this topic, which is beyond the scope of this chapter, has been carried out for ITER [3] from which we will highlight a couple of examples that summarize its major findings. For details of the calculations themselves and of the range of conditions explored, the reader is referred to [3].

Figure 3.26 shows the decrease of the ITER W ($\sim$ 10 mm thick) and CFC ($\sim$ 20 mm thick) divertor targets for a steep divertor design (i.e., with a poloidal angle for plasma impact a factor 2 smaller than the reference design) for various values of the ELM energy loss from the main plasma. The expected ELM frequency in ITER is in the range of 1–5 Hz, hence, in every reference full performance $Q_{\rm DT} = 10$ discharge, which lasts about 300 s, around 300–1500 ELMs will occur. The results in Fig. 3.26 show that ELMs which lead core plasma energy losses larger than 15% in ITER would lead to unacceptable erosion rates of the divertor target, according to our present knowledge. These large erosion rates would require the replacement of the divertor target every several tens of discharges. The expected ELM energy loss in ITER, on the basis of the scalings in Sect. 3.2.2, covers the range from $\Delta W_{\rm ELM} = 5$–20%. This indicates that the operation of ITER (and/or FIRE) in the Type I ELMy H-mode regime may indeed be marginal with respect to the divertor target lifetime and that the target may need to be replaced more frequently than so far anticipated. However, the existing uncertainties in many of the extrapolations and in the modeling of the material damage do not allow us to extract a firmer conclusion on this issue at this stage.

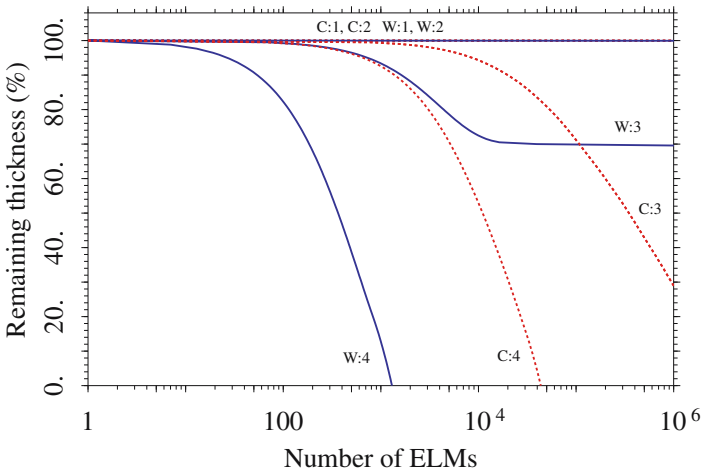

Fig. 3.26. Remaining thickness vs. number of ELMs for a CFC target (*dotted lines*) and W target (*solid lines*). The different curves refer to different assumed fraction of the ITER pedestal energy ($W_{\mathrm{ped}} \sim 105\,\mathrm{MJ}$) loss during Type I ELMs (i.e., $\Delta W_{\mathrm{ELM}}/W_{\mathrm{ped}}$: (1) 5%, (2) 10%, (3) 15%, and (4) 20%). The cases shown in this figure refer to an option of the ITER divertor geometry with a more inclined target than the reference case, with inter-ELM e-folding length of λg 5 mm at the plasma outer midplane, for an inter-ELM heat flux of $5\,\mathrm{MWm}^{-2}$, and assuming ELMs with a triangular power flux waveform with ramp-up and ramp-down phases lasting 500 µs each [3]. For details on the modeling assumptions the reader is referred to [3] and references therein

One of the issues that remains to be addressed properly, which also prevents us from extracting firm conclusions on the issue of the expected divertor target lifetime in ITER, is that of the influence of the "natural" Type I ELM variability on these lifetime estimates. This is mostly due to the lack of a proper experimental characterization of this variability. So far, most experimental studies have concentrated on the study of average ELM characteristics [16, 34, 42] and only recently the characterization of the individual ELM properties has been carried out [27, 28]. For discharges with stationary fuelling and power input, the ELM core plasma energy and particle losses and other core plasma ELM characteristics are reproducible, although not identical, as expected for a phenomenon triggered by a MHD instability. For instance, the typical scatter of ΔW_{ELM} around its average value in the JET stationary Type I ELMy H-modes is $\sim 20\%$. Similarly, there is a significant scatter in the value of the area for ELM energy deposition at the divertor target and in the proportion of ELM energy that reaches the divertor target for stationary Type I ELMy H-modes, as discussed in Sect. 3.3.1. This has a deep influence on the estimate of the erosion of the divertor target by ELMs, because this is mostly driven by the material surface temperature reaching

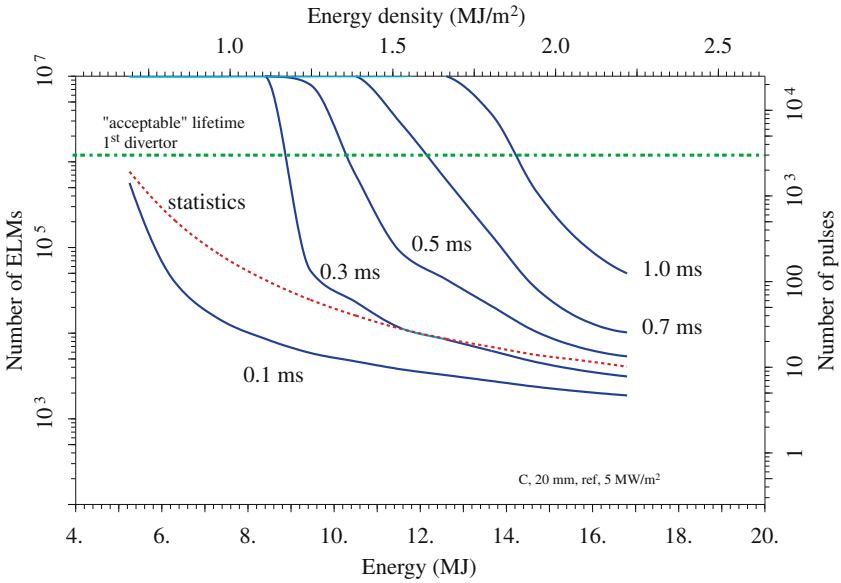

Fig. 3.27. Erosion lifetime (in number of ELMs or corresponding ITER full power pulses) of a CFC target (20 mm thick) as a function of the ELM energy loss for various assumptions on the value of $\tau_{\mathrm{IR}}^{\mathrm{ELM}}$. *Continuous curves* refer to analysis done assuming that all ELMs are characterized by the same parameters. The *dotted curve* refers to an analysis done by means of a statistical approach using experimentally determined probability distribution functions for the characteristics of the ELM energy pulse [3]

a threshold value during the ELM energy pulse or not. A comparison of the estimated ITER divertor target lifetime assuming that all ELMs are identical (using the expected average values for the proportion of energy reaching the divertor, area for ELM energy deposition, etc.) and taking into account the experimental variability of these ELM characteristics is shown in Fig. 3.27.

The calculated lifetime is much smaller when using the statistical approach because the erosion of the CFC target is dominated by the ELMs that cause very large energy fluxes on the divertor (much larger than the average), which bring the target surface temperature to a range in which significant sublimation occurs. These ELMs can be a very small proportion of those occurring in the discharge ($< 1\%$) and, despite this, dominate the erosion of the divertor target. As mentioned before, we are at a very early stage for the quantitative evaluation of the effect of the natural ELM variability on the divertor target lifetime in next step devices, mostly because of our very primitive knowledge of the characteristics of this variability and its dependence on plasma parameters. Furthermore, the calculations carried out so far assume that all measured variability is of a statistical nature and there is no cross-correlation among the various ELM parameters (ΔW_{ELM},

$\Delta W_{\mathrm{ELM}}^{\mathrm{DIV}}$, $\tau_{\mathrm{ELM}}^{\mathrm{IR}}$, A_{ELM}, etc.). Existing experimental evidence, albeit anecdotal, indicates that this is not the case and, for instance, measurements for JET show that $\Delta W_{\mathrm{ELM}}^{\mathrm{DIV}}/\Delta W_{\mathrm{ELM}}$ is smaller for ELMs with larger ΔW_{ELM} and, hence, the ELM energy loss and the proportion of energy reaching the divertor may be inversely correlated, which would increase the expected divertor lifetime with respect to the results in Fig. 3.27. Only when these possible cross-correlations are identified, it will be possible to determine quantitatively if the "natural" ELM variability will lead to a longer or shorter divertor lifetime in next step devices than presently expected. However, first estimates indicate that the "natural" ELM variability is likely to restrict the range of core plasma ELM energy losses which are compatible with an acceptable divertor target lifetime in burning plasma experiments with respect to those calculated for "average" ELMs.

3.4 Summary and Conclusions

The control of plasma–wall interactions in present and, more importantly, in the next generation of fusion devices poses major physical and technological challenges for the plasma facing components. Within this area, the issues related to transient energy fluxes on PFCs caused by ELMs and their influence on the PFCs lifetime remain to be resolved. The understanding of the factors determining the size of the core plasma ELM energy losses, the associated energy fluxes on the PFCs and their scaling to next step devices is presently emerging. Analysis of Type I ELMs from existing experiments shows that ELM energy losses are correlated with the density and temperature of the pedestal plasma before the ELM crash. The Type I ELM plasma energy loss (normalized to the pedestal energy) is found to correlate across experiments with the collisionality of the pedestal plasma ($\nu*_{\mathrm{ped}}$), decreasing with increasing $\nu*_{\mathrm{ped}}$ and/or with the typical ion transport time from the pedestal to the divertor target ($\tau_{||}^{\mathrm{Front}} = \frac{2\pi R q_{95}}{c_{\mathrm{s,ped}}}$). With increasing values of $\nu*_{\mathrm{ped}}$ and $\tau_{||}^{\mathrm{Front}}$ the ELM energy loss is dominated by convection (i.e., driven by the ELM particle loss). The duration of the divertor ELM power pulse is correlated with $\tau_{||}^{\mathrm{Front}}$, i.e., with the transport of particles during the ELM event, and not with the duration of the MHD activity and the loss of high energy electrons from the pedestal plasma, as previously thought. The extrapolation of the expected ELM energy fluxes from existing experimental results to the next generation of burning plasma experiments remains uncertain because of the lack of a validated physics model for the ELM collapse and for the transport of energy from the pedestal plasma to the divertor target during the ELM itself. However, present estimates of the erosion under Type I ELMs in ITER and FIRE indicate that ELM-caused erosion may limit the divertor target lifetime requiring a more frequent replacement of the divertor target than presently planned. Because of this, the development of H-mode

regimes which combine the good confinement features of the Type I ELMy H-mode with small or no ELMs remains a high priority for the experimental programme of the existing fusion experiments.

The quantitative analysis of the experimental measurements during ELMs and the modeling of ELM-caused erosion in present and next step fusion devices require an extension of the material and atomic physics database towards parameters and processes which are relevant for these conditions, such as:

a) Measurement of material properties under high energy ($> 1\,\mathrm{keV}$) electron/ion fluxes, such as thermal conductivity, secondary electron emission, rates for material ejection and state (C-clusters, W-droplets, ...), etc.

b) Characterization of plasma facing materials after sublimation, melting. Determination of long term effects, such as material thermo-mechanical properties, due to repetitive energy fluxes leading to $> 1000\,\mathrm{K}$ temperature excursions.

c) The requirements on atomic data concentrate on those related to the impact of the hot plasma ($T \sim$ keV) coming from the pedestal region of the core plasma, which are released by the ELM, on the cold ($T < 5\,\mathrm{eV}$) and dense divertor plasma ($n > 10^{20}\,\mathrm{m}^{-3}$) with significant electromagnetic radiation emissivity (by neutral hydrogen and partially ionized impurities) and the transient ionization and electromagnetic radiation emission processes associated with such impact.

References

1. Nucl. Fusion **39** (1999) 2137
2. Zohm, H., Plasma Phys. Control. Fusion **38** (1996) 1213
3. Federici, G. et al., Plasma Phys. Control. Fusion **45** (2003) 1523
4. Loarte, A. et al., Jour. Nucl. Mat. **313-316** (2003) 962
5. Wagner, F. et al., Phys. Rev. Lett. **49** (1982) 1408
6. Feneberg, W., Phys. Lett. A **36** (1971) 125
7. Erckmann, V. et al., Phys. Rev. Lett. **70** (1993) 2086
8. Tanga, A. et al., Nucl. Fusion **27** (1987) 1877
9. Technical Basis for the ITER Final Design, ITER EDA Documentation Series, No. 22, IAEA, Vienna 2001
10. Saibene, G. et al., Plasma Phys. Control. Fusion **44** (2002) 1769
11. Gohill, P. et al., Phys. Rev. Lett. **61** (1988) 1603
12. Connor, J.W., Plasma Phys. Control. Fusion **40** (1998) 191
13. Igitkhanov, Y. et al., Contrib. Plasma Phys. **40** (2000) 368
14. Wagner, F. et al., Plasma Phys. Control. Fusion **36** (1994) A61
15. Saibene, G. et al., Nucl. Fusion **39** (1999) 1133
16. Loarte, A. et al., Plasma Phys. Control. Fusion **44** (2002) 1815
17. Clement, S. et al., Jour. Nucl. Mat. **266-269** (1999) 285
18. Ozeki, T. et al., Nucl. Fusion **30** (1990) 1425
19. Kamada, Y. et al., Plasma Phys. Control. Fusion **42** (2000) A247
20. Stober, J. et al., Nucl. Fusion **41** (2001) 1123

21. Sartori, R. et al., to be published in Plasma Phys. Control. Fusion **45** (2003)
22. Greenwald, M. et al., Nucl. Fusion **28** (1988) 2199
23. Meade, D.M. et al., Fusion Energy 2000, FTP2/16, Proc. 18th IAEA Fusion Energy Conference (Sorrento, Italy, 2000), IAEA, Vienna 2001 (ISSN 1562-4153)
24. Oyama, N. et al., Plasma Phys. Control. Fusion **43** (2001) 717
25. Lingertat, J. et al., Jour. Nucl. Mat. **241-243** (1997) 402
26. Gill, R. et al., Nucl. Fusion **38** (1998) 1461
27. Loarte, A. et al., Fusion Energy 2002, Proc. 19th IAEA Fusion Energy Conference (Lyon, France, 2002)
28. Loarte, A. et al., Proc. 30th EPS Conf. on Controlled Fusion and Plasma Physics, St. Petersburg, Russia, 2003, Vol. 27A, p-1.96
29. Igitkhanov, Y., et al., Proc. 28th EPS Conf. on Controlled Fusion and Plasma Physics, Funchal, Portugal, 2001, Vol. 25A, p. 1693.
30. Cowley, S. et al., Proc. 30th EPS Conf. on Controlled Fusion and Plasma Physics, St. Petersburg, Russia, 2003. to be published in Plasma Phys. Control. Fusion **45** (2003)
31. Leonard, A. et al., Jour. Nucl. Mat. **266-269** (2001) 1097
32. Leonard, A. et al., Plasma Phys. Control. Fusion **44** (2002) 945
33. Loarte, A. et al., Plasma Phys. Control. Fusion **45** (2003) 1549
34. Loarte, A. et al., Fusion Energy 2000, ITERP/11(R), Proc. 18th IAEA Fusion Energy Conference (Sorrento, Italy, 2000), IAEA, Vienna 2001 (ISSN 1562-4153)
35. Janeschitz, G. et al., Jour. Nucl. Mat. **290-293** (2001) 1
36. Herrmann, A., Plasma Phys. Control. Fusion **44** (2002) 883
37. Leonard, A. et al., Jour. Nucl. Mat. **241-243** (1997) 628
38. Monk, R.D., Ph. D. Thesis, Royal Holloway College, University of London, 1996
39. Herrmann, A. et al., Jour. Nucl. Mat. **313-316** (2003) 759
40. Eich, T. et al., Jour. Nucl. Mat. **313-316** (2003) 919
41. Herrmann, A. et al., Proc. 30th EPS Conf. on Controlled Fusion and Plasma Physics, St. Petersburg, Russia, 2003, Vol. 27A, p. 1.155
42. Leonard, A., et al., Phys. Plasmas **10** (2003) 1765
43. Ghendrih, Ph. et al., Jour. Nucl. Mat. **313-316** (2003) 914
44. Herrmann, A. et al., Proc. 24th EPS Conf. on Controlled Fusion and Plasma Physics, Berchtesgaden, Germany, 1997, Vol. IV, p. 1417
45. Bergmann, A., Nucl. Fusion **42** (2002) 1162
46. Asakura, N. et al., Plasma Phys. Control. Fusion **44** (2002) A313
47. Kukushkin, A. et al., Jour. Nucl. Mat. **290-293** (2001) 887

Part II

Plasma Diagnostics

4 Molecular Diagnostics of Cold Edge Plasmas

U. Fantz

The presence of molecules in cold edge plasmas requires detailed investigations on the basis of simple diagnostic methods. For this purposes, the powerful tool of molecular emission spectroscopy in the visible spectral range is introduced. Applications to divertor plasmas of fusion experiments (ASDEX Upgrade) are shown. Special emphasis is given to the role of molecular hydrogen in these low temperature plasmas. The combination of emission spectroscopy with a collisional–radiative model and a plasma edge code 2D edge modeling offers the possibility to investigate the interplay of hydrogen molecules and detached plasma regimes, i.e., plasma volume recombination. In particular, the importance of vibrational population is discussed. Hydrocarbons, which are formed by chemical erosion processes of carbon tiles in the divertor, are also accessible by optical emission spectroscopy. The method to determine fluxes of hydrocarbons is introduced and applications to higher hydrocarbons (C_2H_y) are shown. Furthermore, systematic measurements of erosion yields in low pressure plasmas are discussed which can improve the understanding of chemical enhanced erosion mechanisms in cold edge plasmas.

4.1 Molecules in Low Temperature Plasmas

The plasma of magnetically confined fusion experiments can be described by a hot plasma core and a cold plasma edge. These two types are commonly separated by the last closed flux surface, the so–called separatrix . In the plasma edge the plasma particles are in contact with the surfaces of the vessel, which means in this region plasma wall interaction occurs. In order to control and to reduce the energy and particle flow onto the surfaces, the particles are forced to flow along the separatrix into a special designed chamber, the divertor. This concept is often used in tokamaks, e.g., ASDEX Upgrade (Germany), DIII-D (USA) or JT-60 (Japan), to mention some of them. An overview of physics of divertor plasmas is given in Stangeby's book [1]. Other machines such as TEXTOR (Germany) run with limiters. One of the main differences between these two concepts is the plasma parameter range of the edge plasma. For example, lower plasma temperatures are achieved in divertor plasmas (typically below 10 eV) than in limiter plasmas (some 10 eV). Additionally, divertor machines can operate in different plasma recycling regimes [1], where

in extreme cases recombination of plasma particle occurs either completely at the surfaces or in the plasma volume, the attached or completely detached divertor plasma, respectively. Therefore, the plasma parameters can vary in a wide parameter range. In particular, detached plasmas are characterized by very low temperatures combined with high densities (T_e below 1 eV, n_e up to $10^{21}\,m^{-3}$). This regime is preferred since the heat load to the divertor tiles is reduced.

Recombination of plasma particles in the edge plasma leads to the formation of neutral particles which will be re-ionized in the plasma volume or carry out further processes. The colder the temperature the longer the molecules survive, i.e., the penetration depth of the neutrals increases. In this edge plasma the atomic physics part takes place, as described by Reiter [2]. Besides atoms hydrogen molecules are formed by recombination of hydrogen particles (atoms and ions). Molecules can undergo a variety of additional reactions (e.g., dissociation processes) which have to be considered, for example, in plasma edge codes. Due to the manifold of energetic levels of a molecule, further low energy reaction channels are opened, such as dissociative attachment and ion conversion which are very sensitive on the vibrational population of the molecule. In order to characterize the influence of molecules on the plasma behaviour, the quantity of molecules, i.e., molecular fluxes are to be determined in a first step. Here, simple and easy handling diagnostic tools are required and, furthermore, basic investigations with respect to isotope effects are needed. H and D atoms can be treated as one species, however this will not hold for molecules, since the energy levels of vibrational and rotational states differ. Section 4.2 addresses this subject. In Sect. 4.3 reaction chains which are of relevance in cold divertor plasmas are analyzed by a combination of measurements and modeling. The special role of vibrational population of hydrogen molecules is discussed separately in Sect. 4.4.

The plasma wall interaction of plasma particles with plasma facing materials, which are typically carbon, beryllium or tungsten surfaces, is characterized by physical sputtering and/or chemical erosion [3–5]. As a consequence material is removed. The processes have to be quantified and investigated in detail, in particular to allow predictions and extrapolations to future fusion experiments. For chemically active materials such as carbon (graphite) the chemical erosion mechanism by hydrogen ions and atoms leads to the formation of molecules. In this case, hydrocarbons are released from the surface and penetrate into the plasma. The process is characterized by the erosion yield, i.e., the ratio of carbon flux to hydrogen flux. The erosion yield and, therefore, the quantity of molecules depends on a manifold of parameters: material composition, surface temperature and plasma parameters such as ion energy, ion species (isotope) and particle fluxes. The hydrocarbons are molecules originating from the methane family and also from higher hydrocarbons such as C_xH_y. The diagnostic tool for methane is already well-established: the methane flux is determined by the measurement of the photon flux of the

CH radical and by the quantity of the (inverse) photon efficiency (D/XB ratio). This quantity describes the destruction events per emitted photon and is usually calculated with dissociation models. It will be convenient to quantify the formation of the C_2H_y family in a similar manner. Section 4.5 discusses a correlation of the radiation of the carbon molecule (C_2) with particle fluxes of C_2H_y molecules. Results of measurements in a tokamak machine are presented as well as results from chemical erosion experiments in low pressure laboratory plasmas, which offer the opportunity to carry out systematic investigations at well defined parameters.

4.2 Molecular Emission Spectroscopy

Spectroscopic diagnostic of plasmas in the visible spectral range offers the possibility to obtain a manifold of plasma parameters without affecting the plasma. Additionally, the simple and easy to handle equipment needs only fibre optics to have access to the plasma. One of the features of optical emission spectroscopy is the simplicity to measure radiation of atoms, ions or molecules and to obtain variations with changes in the plasma or to detect impurities, i.e., the application as plasma monitor. However, the interpretation of radiation in detail can be quite complex which is compensated by the variety of results for plasma parameters: electron temperature T_e, electron density n_e, neutral particle temperature T_n or particle densities of neutrals or ions, to name some of them. If the plasma is inhomogeneous along a line of sight, one has to kept in mind that integral quantities are obtained. Principles of spectroscopy applied to plasmas are explained in [6]. The maximum of information can be received if the spectral system is absolutely calibrated in wavelength and in intensity. In the following, the interpretation of molecular radiation is discussed, provided that the spectral system is absolutely calibrated. Nevertheless, some basic principles can be applied also if just relatively calibrated systems are available.

The radiation of diatomic molecules such as H_2, C_2 (homonuclear) or CH, SiH, BeH, BH (heteronuclear) and their isotopes is mostly accessible in the visible spectral range. Due to the additional degrees of freedom of a molecule in comparison to an atom, vibrational and rotational energy levels exist in the ground state and in each electronically excited state of the molecule. The molecular spectrum in the visible range corresponds usually to an electronic transition coupled with a vibrational transition. These vibrational bands consist of individual rotational lines originating from different rotational branches ($P-$, $Q-$, $R-$branch). Examples of spectra from H_2 and D_2 ($d\,^3\Pi_u - a\,^3\Sigma_g^+$ transition) are shown in the left part of Fig. 4.1. Some rotational lines (quantum number J') from the $Q-$branch of the first diagonal vibrational transitions ($v' = v''$) are indicated. A comparison of these spectra clarify the influence of the molecular mass on the wavelength position

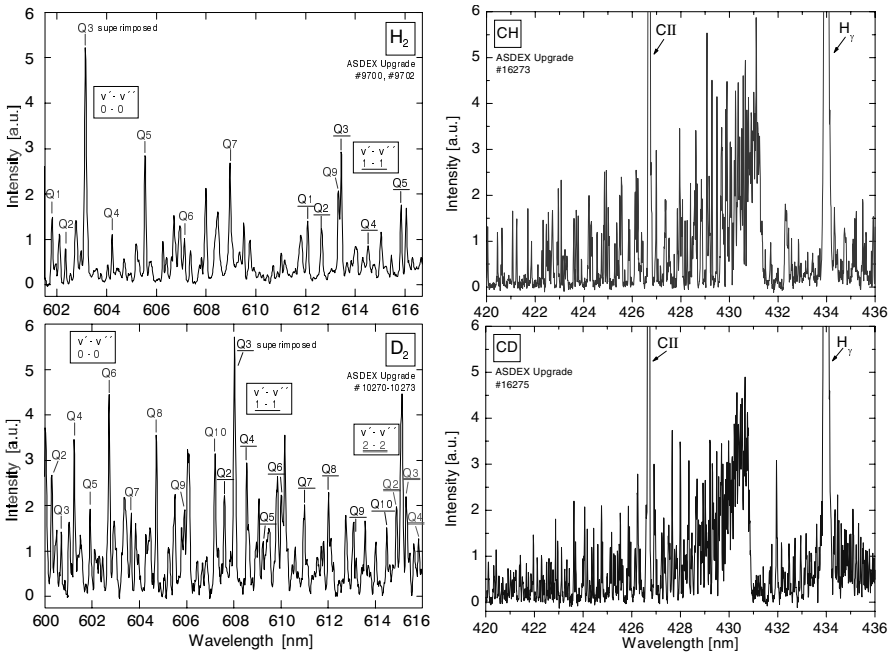

Fig. 4.1. Emission spectra of H_2 and D_2 (**left column**) and of CH and CD (**right column**) obtained in the divertor of ASDEX Upgrade during gas puff experiments

of rotational lines. The intensity alternation of lines with even and odd rotational quantum numbers is caused by the influence of the nuclear spin. The right part of Fig. 4.1 shows the corresponding isotope effect for a transition in CH and CD. Due to the heavier mass of these molecules with respect to hydrogen molecules, the rotational lines and the vibrational bands overlap. In case of the $A\,^2\Delta - X\,^2\Pi$ transition all three rotational branches and the first three diagonal vibrational bands overlap. It is obvious that such a molecular band is extended to a wide wavelength range which must be considered for an integral intensity of the whole transition.

4.2.1 Interpretation of Molecular Spectra

The rotational intensity structure of a vibrational band provides information about the rotational population in the electronically excited state and the vibrational bands originating from an electronically excited state provide information about the corresponding vibrational population. Finally, the sum of the vibrational and rotational populations yields the population in the electronically excited state.

Rotational Structure

The small energy distance between rotational levels in a vibrational state justify the assumption of a Boltzmann population. This means, that the rotational population is characterized by a rotational temperature T_{rot}. In a Boltzmann plot, where the intensities of rotational lines of one branch divided by the line strength (Hönl–London factors) and the statistical weight are plotted against the relative energy, the slope of the straight line represents T_{rot}. In some cases two slopes are observed, i.e., a two temperature distribution exists. For radicals, such as CH or SiH, this distribution is caused by the dissociative excitation process of the parent molecule, CH_4 or SiH_4, respectively. This process populates preferentially higher rotational levels (e.g., $J > 8$ for CH). The identification of individual rotational lines in the spectrum is very difficult for these heavy molecules due to the overlap of rotational branches and vibrational transitions. In such cases, a computer simulation of spectra, which is based on molecular constants, is fitted to the measured spectrum by using T_{rot} as fit parameter. The fit yields the integral intensity of the band without disturbing lines, which is a great advantage of this method. This procedure is commonly applied to CH, SiH and N_2 [7,8]. Under the assumption that electronic excitation from the ground state of the molecule preserves the rotational quantum number, the rotational distribution of the excited state can be projected to the ground state: $T_{\mathrm{rot}}^{\mathrm{ground}} = T_{\mathrm{rot}}^{\mathrm{excited}} \times B_v/B_{v'}$. The rotational constants B_v of the corresponding vibrational levels (v' denotes the vibrational quantum number in the excited state and v that of the ground state) take into account changes in the energy distance of rotational levels. Since the electronic ground state of the molecule is labelled with the letter X, $T_{\mathrm{rot}}^{\mathrm{ground}}$ can be expressed as $T_{\mathrm{rot}}(X)$. For stable and heavy molecules, such as N_2, $T_{\mathrm{rot}}(X)$ can be identified with the heavy particle temperature, i.e., the gas temperature T_{gas} in technical plasmas [7].

The rotational temperatures which are obtained from the $Q-$branch of the $v' = 0 - v'' = 0$ transition in the hydrogen spectra of Fig. 4.1 are $T_{\mathrm{rot}}(X) = 6000\,\mathrm{K}$ and $4500\,\mathrm{K}$ for H_2 and D_2, respectively. Evaluation of the $v' = 1 - v'' = 1$ transition yields lower temperatures: $T_{\mathrm{rot}}(X) = 2000\,\mathrm{K}$ (H_2) and $T_{\mathrm{rot}}(X) = 1500\,\mathrm{K}$ (D_2) typically decreasing with increasing vibrational quantum number. Detailed experimental investigations of laboratory plasmas have shown that the $v' = 2 - v'' = 2$ transition should be used preferentially for gas temperature determination. For CH and CD molecules, the dissociative excitation mechanism contributes to the rotational population and therefore, T_{rot} represents the temperature of the excited state only. Calculated spectra of CH and CD bands fit best to the measurements shown in Fig. 4.1 for $T_{\mathrm{rot}} = 3000\,\mathrm{K}$.

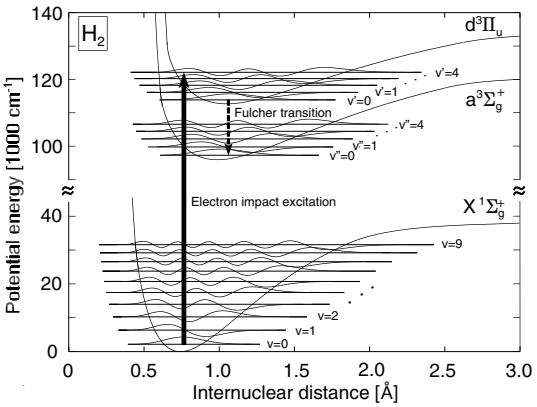

Fig. 4.2. Potential curves, vibrational energy levels and wave functions for some states of H_2

Vibrational Distribution

In order to obtain a vibrational distribution, several vibrational bands must be observable in a well separated wavelength region. This is, for example, fulfilled for the Fulcher system of the hydrogen molecules. The Fulcher transition ($d\,^3\Pi_u - a\,^3\Sigma_g^+$) is a very intense transition and the first four diagonal vibrational bands are readily observed in the wavelength region $\lambda = 600$–$650\,\mathrm{nm}$ (Fig. 4.1). Line identification is based on the tables provided by Dieke [9,10]. Once the rotational temperature is obtained from the first lines of the $Q-$branch a scaling factor to extrapolate to the radiation of the whole vibrational band can be calculated. This scaling factor takes into account radiation of remaining lines of the $Q-$branch as well as intensities of the $P-$ and $R-$branch (deduced from the corresponding Hönl–London factors).

The radiation of a vibrational band is directly correlated to the vibrational population in the excited state: $I(v' - v'') = n(v') \times A_{v'v''}$. $A_{v'v''}$ is the transition probability. Thus, several vibrational bands which originate from different vibrational levels yield the corresponding vibrational population. In case of hydrogen or deuterium molecules the population of the first four or five vibrational levels, respectively, is accessible. Higher vibrational levels are disturbed by pre-dissociation processes. For further analysis, it is very convenient to use the relative vibrational population $n(v')/n(v' = 0)$.

The vibrational population in the excited state $n(v')$ is determined by the vibrational population in the ground state $n(v)$, if the electron impact excitation from the ground state is the most dominant excitation mechanism. The application of the Franck–Condon principle for electron impact excitation allows a calculation of $n(v')$ from $n(v)$ based on the Franck–Condon factors between ground and excited state. Figure 4.2 illustrates this scheme for the three states involved in the Fulcher transition: upper and lower state, $d\,^3\Pi_u$ and $a\,^3\Sigma_g^+$ respectively, in the triplet system and the ground state

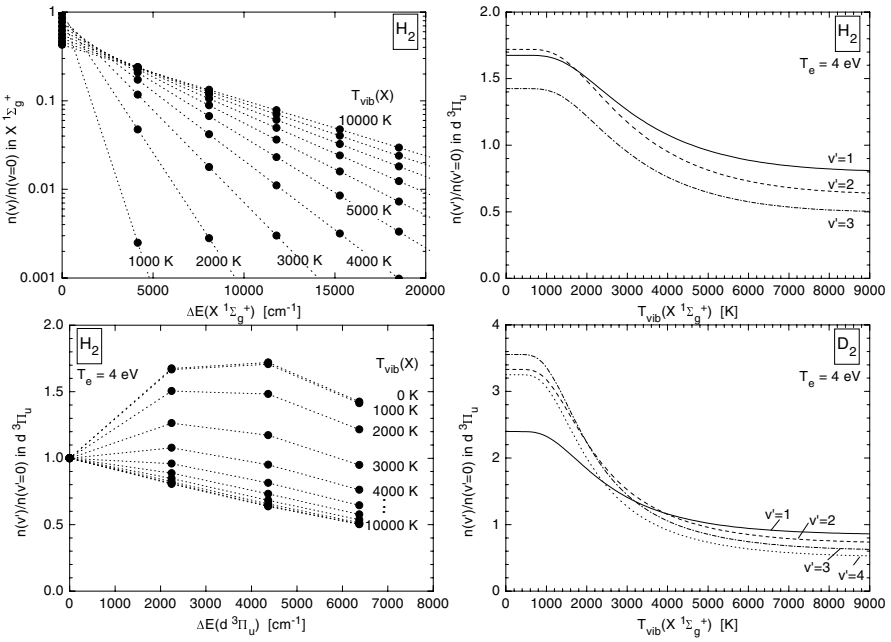

Fig. 4.3. Left column: relative vibrational population in ground and excited state of H_2 with $T_{vib}(X)$ as parameter. **Right column**: relative vibrational population in the excited state for H_2 and D_2 as a function of $T_{vib}(X)$

$X\,^1\Sigma_g^+$ in the singlet system of the molecule. The Franck–Condon factors $q_{v'v''}$ can be obtained usually from quantum mechanics, i.e., calculations of wave functions based on potential curves. The overlap integral of the vibrational wave functions yields the Franck–Condon factors and, together with the electronic dipole transition moment, transition probabilities $A_{v'v''}$can be calculated. Examples for hydrogen and deuterium are presented in [11, 12].

In a first step, the vibrational population in the ground state is characterized by a Boltzmann distribution, i.e., $n(v')/(n(v'=0)$ depends on $T_{vib}(X)$. The left column of Fig. 4.3 shows relative vibrational populations in the ground state $(X\,^1\Sigma_g^+)$ and in the upper state of the Fulcher transition $(d\,^3\Pi_u)$ with $T_{vib}(X)$ as parameter, assigned to the 15 vibrational levels of H_2, i.e., $v = 0$–14. The right column shows the relative vibrational population in the excited state as a function of $T_{vib}(X)$ for H_2 and D_2. Due to the usage of vibrationally resolved excitation rate coefficients a dependence on electron temperature is obtained. $T_e = 4\,\mathrm{eV}$ is chosen in Fig. 4.3.

In the final step, the comparison of measured with calculated vibrational populations yields $T_{vib}(X)$. Small corrections are obtained due to the dependence of lifetimes on vibrational quantum number. Details of the method are described in [8]. Due to the strength of the Franck–Condon factors between ground and excited state the sensitivity of the method is limited to relative

populations $n(v)/(n(v=0)$ above $\approx 1\%$. Nevertheless, this method is very convenient (visible spectral range, simple equipment) to obtain vibrational populations in the ground state although it is based on the assignment of a vibrational temperature. Otherwise, expensive laser methods such as CARS or VUV–LIF [13,14] can be applied. In principle, they give access to populations in higher vibrational quantum numbers.

Population in Electronically Excited States

The sum of the vibrational populations in the electronically excited state represents the population of the corresponding electronic level $n(p)$ with number p. Usually measurements of several vibrational bands give access to populations of various vibrational levels. The populations in the other remaining vibrational quantum numbers (up to the dissociation limit) can be extrapolated by using the projection of a vibrational temperature in the ground state into the excited level, the procedure which was explained in the previous paragraph. The error bar of this extrapolation can be estimated directly from the strength of the Franck–Condon factors, i.e., the importance of contributions to higher vibrational quantum numbers can be foreseen.

4.2.2 Molecular Hydrogen and Collisional–Radiative Modeling

In order to correlate radiation of molecules with plasma parameters such as T_e, n_e or molecular densities population models are necessary. In the simplest cases, either a Boltzmann equilibrium holds (collision dominated plasma) or the corona model can be applied. The latter is valid for low electron densities and balances (in its simplest case) excitation by electron impact collisions from the ground state with de-excitation by spontaneous emission: $n_{mol} \times n_e \times X_{exc}(T_e) = n(p) \times \sum_{k<p} A_{pk}$. n_{mol} is the molecular density in the ground state. $X_{exc}(T_e)$ denotes the excitation rate coefficient which is obtained from a convolution of the corresponding cross-section with the electron energy distribution function, i.e., mostly a Maxwell distribution. Since excited levels are underpopulated in comparison to a Boltzmann distribution the ground state density represents the molecular density. However, if the energy gap is small or if the first excited levels are meta-stable states, their contribution to the molecule density has to be taken into account as it is the case for the carbon molecule. If other mechanisms than electron impact excitation from the ground state and radiative decay are important so-called collisional–radiative models (CR–model) must be applied. Such models take into account the manifold of excitation and de-excitation processes and exist commonly for atoms or ions (for example the ADAS code package [15]). For molecules the situation is more complex due to the presence of additional energy levels, i.e., vibrational and also rotational levels in each electronic state.

For hydrogen, a CR–model for H_2 and H is provided by Sawada [16] and was extended by Greenland and Reiter [17]. The model is described

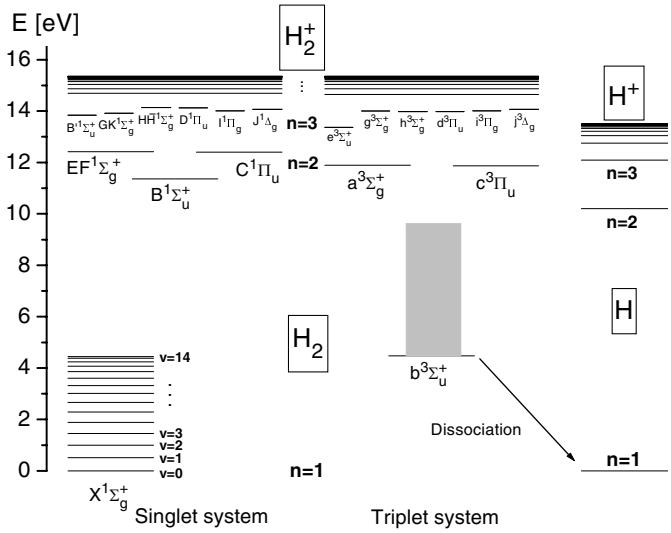

Fig. 4.4. Schematic energy level diagram for H_2 and H

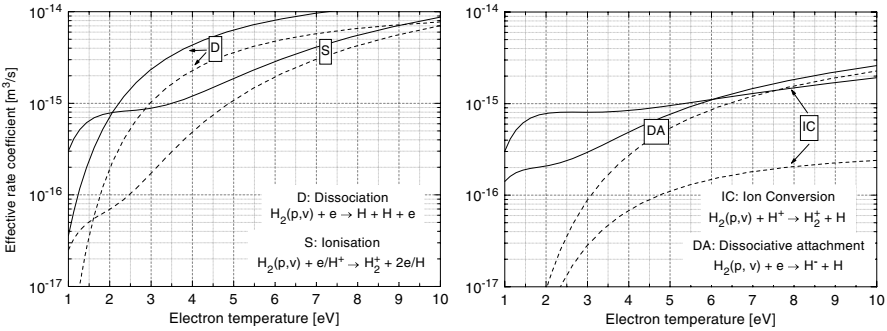

Fig. 4.5. Effective rate coefficients calculated with the present CR–model with (*full curve*) and without (*dashed curve*) taking into account the vibrational population

in detail in [18] where also further improvements are described and some applications are shown. Validation of such a model is typically carried out in laboratory plasmas at well defined plasma parameters which are known from other diagnostic techniques [19]. In this CR–model each multiplet system (singlet and triplet) consists of 40 electronic levels. Additionally, the ground state is vibrationally resolved (15 levels). Features of the hydrogen molecules are the repulsive $b\,^3\Sigma_u^+$ state and the meta-stable $c\,^3\Pi_u$ ($v = 0$) level in the triplet system. The $n = 2$ states (united atom approximation) are split up in their electronic levels. Figure 4.4 shows a schematic energy level diagram of H_2 as well as the connection to the model for H.

Typical results of such models are effective rate coefficients which depend not only on T_e but also on n_e and the vibrational population in the ground state. The importance of the vibrational population on some effective rate coefficients can be seen in Fig. 4.5. Especially for low T_e, the enhancement can exceed one order of magnitude. Details of the calculation of vibrational populations are described in Sect. 4.4.1. For the analysis of radiation it is very convenient to apply the aforementioned corona model formula in which the pure excitation rate coefficient is replaced by the effective rate coefficient.

4.2.3 Flux Measurements

A first step in the investigation of hydrogen molecules in cold edge plasmas is the quantification of the amount of molecules penetrating from the surface into the plasma. The particle fluxes (or to be more precise the influxes) $\Gamma_{\mathrm{particle}}$ can be deduced from measured photon fluxes Γ_{photon}. This method is well-established for the determination of atomic hydrogen fluxes from H–Balmer lines or methane fluxes from the radiation of CH radicals [20]. The underlaying principle requires a line of sight which is perpendicular to the surface and is based on the assumption that the particles which are released from the surface will be fully ionized or dissociated in the plasma. The quantity which relates these two fluxes is the (inverse) photon efficiency, i.e., the destruction events per emitted photon. In case of atomic hydrogen ionization is important, for methane the dissociation has to be taken into account which requires a dissociation model. In case of molecular hydrogen the effective ionization and dissociation processes are important which means the CR–model is needed.

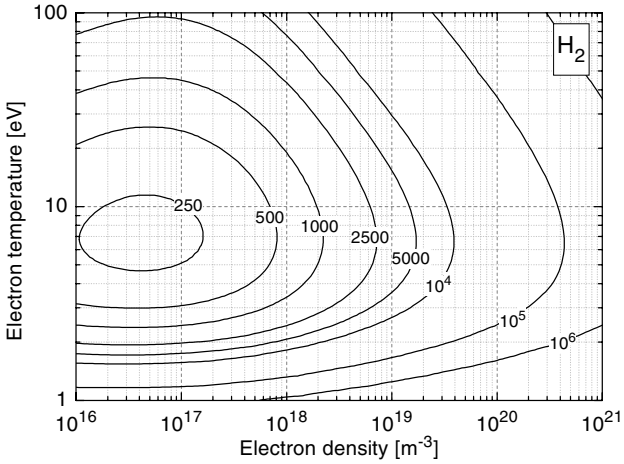

Fig. 4.6. (Inverse) photon efficiency for the Fulcher radiation of hydrogen molecules as calculated by the present CR-model for H_2. The *curves* represent lines of constant values for $(S_{\mathrm{eff}} + D_{\mathrm{eff}})/XB_{\mathrm{Ful}}$

Molecular hydrogen fluxes are obtained from measured Fulcher photon fluxes. The corresponding (inverse) photon efficiency $(S_{\text{eff}} + D_{\text{eff}})/XB_{\text{Ful}}$ is shown in Fig. 4.6 as a function of T_{e} and n_{e}. XB_{Ful} denotes the effective Fulcher emission rate coefficient. The lowest value for $(S_{\text{eff}} + D_{\text{eff}})/XB_{\text{Ful}}$ is obtained in a small parameter range: $n_{\text{e}} = 10^{16} - 10^{17}\text{m}^{-3}$ and $T_{\text{e}} = 5$–$10\,\text{eV}$. This means that the radiation of the molecules is intense in this parameter range. For higher electron densities which are typical for divertor plasmas, the radiation decreases. In other words, a weak intensity of molecular radiation does not correspond automatically to a low particle flux, the molecules are rather destroyed than they radiate. Roughly speaking, the destruction is approximately ten times higher in a cold divertor plasma ($T_{\text{e}} \leq 5\,\text{eV}$, $n_{\text{e}} \simeq 10^{19}\,\text{m}^{-3}$) than in a limiter plasma ($T_{\text{e}} \simeq 20\,\text{eV}$, $n_{\text{e}} \simeq 10^{17}\,\text{m}^{-3}$) which can be mostly attributed to the vibrational population of the molecules. Since the (inverse) photon efficiency is a very critical value, experimental campaigns were carried out to validate the calculations. This was done by calibrated gas puff experiments in the divertor of ASDEX Upgrade [21] as well as in the limiter machine TEXTOR [22]. Both experimental results confirm the calculations within the error bars. Thus, measurements of molecular hydrogen fluxes should be now reliable in a wide parameter range.

4.3 Role of Molecular Hydrogen in Recombination (MAR)

Since divertor plasmas of fusion experiments can operate in different recycling regimes, the plasma parameters T_{e} and n_{e} vary in a wide range. In particular, in the detached regime low temperatures are achieved and volume recombination occurs. Detached divertor plasmas are characterized by a spatial pattern of recombining and ionizing layers. H_2 molecules (and their isotopes) have recently been identified as important species which may influence the energy balance and the ionization degree. Indeed, Molecular Assisted Recombination (MAR) was suggested in this context [23], relying on significant vibrational excitation of the electronic ground state molecules. It was speculated, that, e.g., for an ITER size machine [24] detachment of the divertor plasma might be achievable under somewhat relaxed upstream conditions as compared to what was predicted by the usual divertor models.

The chain of reactions which plays a key role in MAR is the vibrational excitation of molecules by electron impact, then an ion conversion: $H_2(v) + H^+ \rightarrow H_2^+ + H$, followed by dissociative recombination: $H_2^+ + e \rightarrow H + H^*$ [25]. The excited atom decays by spontaneous emission or electron collisions into the ground state. Other possibilities are re-ionization of the excited atom or both atoms are ionized, these processes are the Molecular Assisted Dissociation (MAD) and Molecular Assisted Ionization (MAI), respectively. At the end of the MAR chain, one electron–ion pair is recombined

into an H-atom, and the H_2 molecule is dissociated into $H + H$. The ion conversion part is resonant (comparable to resonant charge exchange between H-atoms and protons), if the molecules are vibrationally excited in the $v = 4$ level. A second chain is less dominant but is mentioned here for completeness: the dissociative attachment: $H_2(v) + e \rightarrow H^- + H$ followed by mutual neutralization: $H^- + H \rightarrow H + H^*$. This chain is also triggered by the vibrational population because dissociative attachment is again a resonant process for $v = 7$. A remarkable vibrational population is achieved only in low temperature plasmas otherwise the molecules are destroyed and these reaction chain become irrelevant, which is, for example, the case in limiter machines. The role of molecules in such edge plasmas is discussed in [28–30].

Experimental and theoretical evidence for Molecular Assisted Recombination (MAR) was achieved by a combination of emission spectroscopy, CR–modeling and B2–EIRENE (plasma edge code [26, 27]) calculations [31, 32]. Starting point was the measurement of rotational and vibrational population of the molecules in attached and detached divertor plasmas of ASDEX Upgrade as well as the molecular hydrogen flux [33]. In particular, in the detached regime high rotational temperatures ($T_{\mathrm{rot}} \simeq 6000\,\mathrm{K}$), high vibrational temperatures ($T_{\mathrm{vib}} \simeq 9000\,\mathrm{K}$) and high molecular particle fluxes ($\Gamma_{\mathrm{H_2}} \simeq 10^{22}\,\mathrm{m^{-2}s^{-1}}$) were observed. In this case, the molecular particle flux is comparable to the atomic hydrogen flux. In a next step, measured Fulcher photon fluxes were compared with predictions of the B2–EIRENE code. Good agreement was achieved only by implementing the vibrational states as metastable particles (distinct particles) in the plasma edge code and applying the CR–model. Then, particle densities and electron temperatures were calculated spatially resolved along the line of sight of emission spectroscopy. These parameters were applied for calculating rates, i.e., processes per unit volume and time. At this point, the usual three–body and radiative recombination (EIR) rate could be compared with the MAR rate. The effective rate coefficients which are needed for this evaluation are calculated with the CR–model. A compilation of data is presented in Fig. 4.7 where part (a) gives a comparison of rate coefficients for the competing processes MAR, MAD and MAI. MAD and MAR are in the same order of magnitude whereas MAI is negligible at low T_e. Part (b) and (c) of Fig. 4.7 show the dependence on electron density for MAR and EIR, respectively. While MAR decreases with increasing n_e, EIR increases, in particular at low electron temperatures. Finally, part (d) of Fig. 4.7 shows the ratio of these effective rate coefficients. The comparison of spatially resolved rates leads to the statement that molecules contribute to the plasma recombination near the surfaces. This effect is due to the strong dependence of MAR along the line of sight decreasing more than three orders of magnitude from the surface to the center, whereas the usual plasma recombination (EIR) is more or less spatially independent.

On the basis of these investigations, it is concluded that the overall contribution of molecules to recombination is in the order of some percent. However, it has to be kept in mind that the vibrational population plays a key

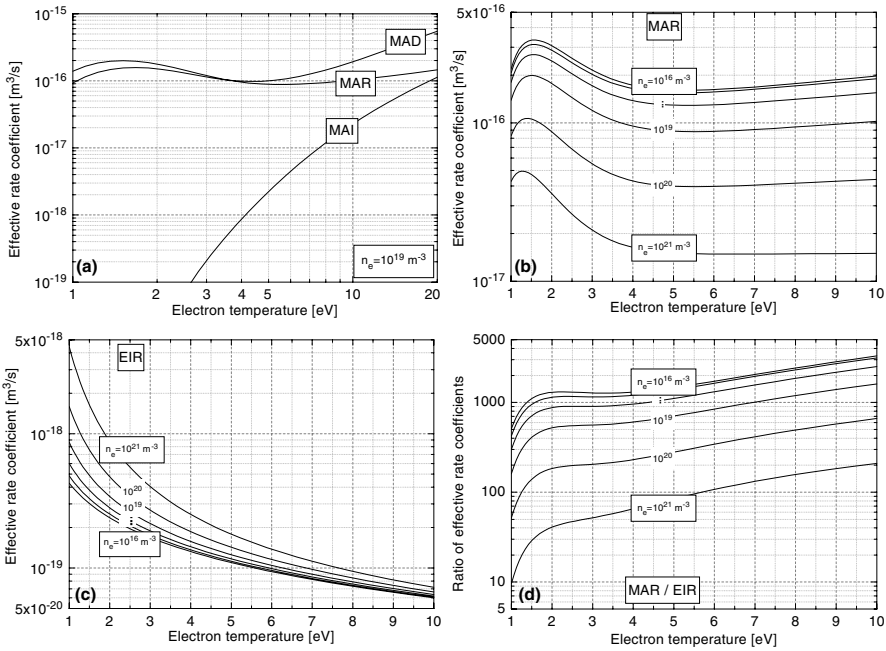

Fig. 4.7. Compilation of effective rate coefficients which are of importance for MAR and EIR processes. Calculations are based on the present CR-model for H_2

role in the whole reaction chain. Further conclusions are derived from comparing B2–EIRENE runs with and without full (vibrational) treatment of the molecules [32]: the reaction chains for the molecules lead to an increase of dissociation and ionization, in particular reducing the ionization length of the particles. As a consequence, the potential energy stored in the divertor plasma increases, the plasma re-attaches. This means that in the code a divertor detachment is harder to achieve.

While these investigations succeeded in a better qualitative understanding of the role of molecules in a divertor, it has to be kept in mind that quantitative predictions may be different for hydrogen and deuterium. Concerning deuterium, the vibrational levels and some selected rate coefficients have to be replaced in the codes and in addition the application of isotopic relations has to be critically reviewed. Another aspect is the influence of surfaces (particularly carbon material) on the vibrational population of the molecule (see Sect. 4.4.2).

4.4 Vibrational Population of Hydrogen

The vibrational population of hydrogen molecules in the ground state opens a manifold of low energy channels so that the knowledge of this parameter

is of importance. A possibility to measure the population in low vibrational quantum numbers is mentioned in Sect. 4.2.1. This can be completed by calculations of vibrational populations as provided by the CR–model. Besides volume processes the vibrational population can be modified by plasma wall interaction processes. Therefore, the formation mechanisms of vibrational population are quite complex and the underlaying data base is far from being complete. Overviews for kinetics of hydrogen plasmas can be found in [34,35]. However, for edge plasmas the situation can be simplified, for example in a first approach, heavy particle collisions in the plasma volume are negligible, except the charge exchange which is, on the other hand, of minor importance in plasma processing.

4.4.1 Measurements and Calculations

The spectroscopic method to determine vibrational populations in the ground state (Sect. 4.2.1) relies on the assumption of a population which corresponds to a vibrational temperature. Furthermore, the method gives access only to relative populations higher than one percent. Therefore, additional information is required. Since the population processes are dominated by electron and proton impact reactions as well as radiation, CR–modeling can be applied. The results can prove whether the population follows a vibrational temperature. In addition, such calculations support investigations on isotope effects. The basis is the availability of vibrationally resolved rate coefficients and transition probabilities. The aforementioned CR–model contains a routine to calculate vibrational populations on the basis of five (volume) processes. Rotational populations are neglected. In order to compare the results for isotopes the input data was critically selected [36]. The first four processes are: electron excitation and de-excitation ($H_2(v) + e \leftrightarrow H_2(w \neq v) + e$), electron impact dissociation ($H_2(v) + e \rightarrow H_2(b\,^3\Sigma_u^+) + e \rightarrow H + H + e$), ion conversion ($H_2(v) + H^+ \rightarrow H_2^+ + H$) and dissociative attachment ($H_2(v) + e \rightarrow H_2^- \rightarrow H^- + H$). Besides the electron impact excitation all these processes are depopulation processes. The fifth process is a two step process: electron impact excitation into the singlet states $B\,^1\Sigma_u^+$ and $C\,^1\Pi_u$, followed immediately by radiative decay ($H_2(v) + e \rightarrow H_2(B, C) + e \rightarrow H_2(w) + e + h\nu$). Due to the corresponding Franck–Condon factors this chain leads to a strong repopulation, i.e., higher vibrational levels are populated preferentially.

For the isotopes similar populations in the vibrational quantum numbers are obtained. This is confirmed by spectroscopic measurements [11]. Furthermore, the vibrational population correlates with the electron temperature for $1\,\mathrm{eV} \leq T_e \leq 10\,\mathrm{eV}$ and offers a diagnostic tool for T_e [36]. Figure 4.8 shows examples for hydrogen. Obviously, the higher vibrational levels are overpopulated with respect to a population according to a vibrational temperature, e.g., $T_{vib} = 7300\,\mathrm{K}$ (filled small circles). The levels which are accessible by emission spectroscopy are indicated (filled symbols). A comparison with calculations for $T_e = 2\,\mathrm{eV}$ show that the assignment of a vibrational temperature

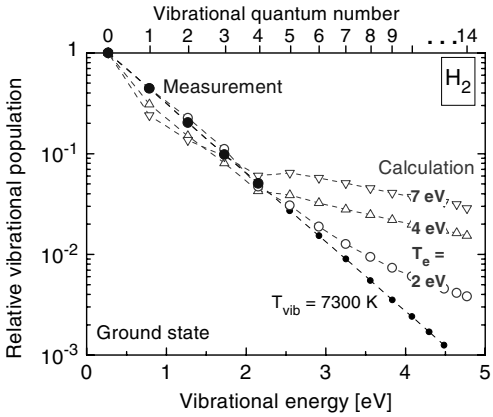

Fig. 4.8. Calculated vibrational populations in the ground state of hydrogen (*open symbols*). Filled symbols represent populations which are accessible by the spectroscopical method and correspond to a vibrational temperature (*small filled symbols*)

is justified for the first four to five levels, exactly those which can be measured. This means the two methods, measurements and calculations complete each other.

The consequences of such high populations in higher vibrational quantum numbers are enormous: rate coefficients for dissociative attachment or ion conversion increase several orders of magnitude (e.g., five orders of magnitude for dissociative attachment). Therefore, a relative population of less than one percent in higher quantum numbers has a large effect on the effective rates for these processes.

4.4.2 Surface Effects

Besides volume processes wall collisions of hydrogen particles can contribute to the vibrational population. A direct process is the interaction of already vibrationally excited molecules with the surface: $H_2(v) + \text{wall} \rightarrow H_2(w)$ mostly depopulating the vibrational levels. Further fundamental mechanisms are the Langmuir–Hinshelwood and the Eley–Rideal mechanism. They are based on recombining hydrogen atoms or ions: $H_{ads/gas} + H_{ads} \rightarrow H_2(v)$. In the first case an adsorbed particle at the surface recombines with another adsorbed particle (Langmuir–Hinshelwood mechanism). In the second case one particle from the gas phase recombines with an adsorbed particle (Eley–Rideal mechanism). For these processes the data base is scarce and often not determined from plasma material interaction experiments. A dependence on particle densities, surface material and surface treatment as well as surface temperature can be expected.

Investigations are carried out in low pressure laboratory plasmas with well defined and uniform plasma parameters above an additional surface in

the plasma chamber [19, 37]. Since the spectroscopic diagnostics cannot distinguish between populations formed in the plasma and those formed at the surface an overlap of both effects is observed. However, this is exactly the situation in cold edge (divertor) plasmas. For reference purposes results were obtained without additional surface. It has to be kept in mind that each plasma experiment is surrounded by stainless–steel or quartz walls. Several materials (steel, quartz, aluminium, copper, tungsten and graphite, all of them plasma treated) were tested. To obtain a possible correlation with surface temperature, the substrate holder can be cooled actively. The atomic hydrogen density is determined as well as T_e and n_e. Thus, a correlation of measured vibrational populations with plasma parameters can be discussed also. Additional information is obtained by spatially resolved measurements, a variation of the line of sights with respect to the distance from the surface.

For metallic surfaces, such as steel, copper, aluminium and tungsten, which are exposed additionally to hydrogen and deuterium plasmas, no change of $T_{vib}(X)$ was detected at low pressures, within the error bars of the method. Of course, the surfaces themselves were plasma treated and it was assumed that the substrate temperature is close to the gas temperature ($T_s \simeq 600\,\mathrm{K}$). For tungsten, a decrease of substrate temperature from 600 K to 300 K enhances $T_{vib}(X)$ (from 5000 K to 6000 K). A large effect of substrate temperature variation on $T_{vib}(X)$ was obtained for quartz. Again cooling of the surface increases $T_{vib}(X)$. However, additional investigations have shown that the absolute value depends on the plasma exposure time of quartz. A correlation of $T_{vib}(X)$ with the atomic hydrogen density could be noticed. Furthermore, graphite surfaces, which are chemically active due to the chemical erosion process, were investigated. Graphite has the highest influence on $T_{vib}(X)$ depending also on substrate temperature. Spatially resolved measurements showed the strongest influence near the target. This might be explained by the formation of hydrocarbons which penetrate into the plasma and dissociate in already vibrationally excited hydrogen molecules. In addition, interaction of hydrocarbons with hydrogen molecules may occur, being also of interest for chemical erosion processes in cold divertor plasmas.

These investigations on plasma wall interaction show clearly that the vibrational population of hydrogen molecules can be influenced by surfaces. As a consequence it is not sufficient to consider just plasma volume processes for plasma modeling in edge codes. Detailed investigations on a dependence on material and substrate temperature have to follow to provide a data base for these kind of processes.

4.5 Hydrocarbons and Chemical Erosion

Hydrocarbon particles are formed by chemical erosion of carbon surfaces in hydrogen plasmas [3, 4]. The molecules such as methane or higher hydrocarbons are released from the surface and penetrate into the edge plasma. A

common diagnostic method to quantify the amount of carbon, i.e., the carbon particle flux, is the analysis of radiation from molecular radicals [20]. This requires dissociation modeling and knowledge of the excitation mechanisms. Detailed investigations are carried out for the correlation of CH (CD) radiation with methane particle fluxes. First investigations were started to obtain a correlation of higher hydrocarbon particle fluxes with radiation of hydrocarbon radicals such as C_2 [38–40]. Therefore, the following discussion is focussed on a possible correlation of C_2 radiation with particles of the C_2H_y group. Comparisons with the analysis of CH radiation are presented. Applications to laboratory plasmas show the relevance of higher hydrocarbons in chemical erosion processes.

4.5.1 Dissociation, Radiation and Carbon Fluxes

From all the hydrocarbons only the radiation of CH radicals and carbon molecules is accessible in the visible spectral range with sufficient intensity. In case of CH (CD) radiation the most prominent molecular band originates from the $A\,^2\Delta - X\,^2\Pi$ transition with a band head at 431.42 (430.82) nm (vibrational transition: $v' = 0 - v'' = 0$). Rotational lines of the first three diagonal vibrational transitions form this molecular band. The spectrum can extend over 10 nm to the lower and higher wavelength region depending on the rotational population, i.e., T_{rot}. Typical rotational temperatures are $T_{\mathrm{rot}} \approx 3000\,\mathrm{K}$. The Swan band system ($d\,^3\Pi_{\mathrm{g}} - a\,^3\Pi_{\mathrm{u}}$ transition) of the C_2 molecule has several intense vibrational bands in the visible spectral range. The most prominent vibrational transition is the $v' = 0 - v'' = 0$ transition with a clear band head at 516.52 nm, degrading approximately 5 nm to the blue. At 512.93 nm the band head of the next diagonal transition ($v' = 1 - v'' = 1$) appears. Usually, the spectra of these molecules are superimposed by lines of carbon ions. For both molecules CH and C_2 a wavelength region of 1.5 nm and 1.2 nm, respectively, from the band head towards lower wavelengths is undisturbed. To extrapolate from the integral intensity of this part to the intensity of the whole band scaling factors are needed. They come either from measurements of undisturbed spectra (laboratory plasmas) or from computer simulations of molecular bands [7]. For $T_{\mathrm{rot}} = 3000\,\mathrm{K}$ the factor is 2.5 (CH, CD band), whereas for C_2 a factor of four is obtained. C_2 radiation shows a stronger dependence of the scaling factor on T_{rot} than CH (CD) radiation.

The upper states of both emission bands can be populated by either direct excitation from the ground state of the corresponding molecule or by dissociative excitation from methane or higher hydrocarbons. Figure 4.9 shows a compilation of emission rate coefficients for the $A\,^2\Delta - X\,^2\Pi$ CH band ($v' = 0, 1, 2, 3 - v'' = 0, 1, 2, 3$) and the C_2 Swan band ($v' = 0 - v'' = 0$) [41]. There is experimental evidence that for CD the same rate coefficients than for CH can be applied [42]. The emission rate coefficient for direct excitation is several orders of magnitude higher than the emission rate coefficient for dissociative excitation. The dominant excitation mechanism depends on the

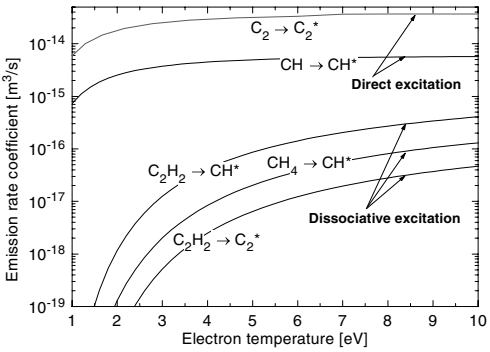

Fig. 4.9. Emission rate coefficients for direct and dissociative excitation of CH and C_2

values of the corresponding particle densities (CH_4 and C_2H_2). They are usually higher than the densities of the radicals. For conditions of edge plasmas, the direct excitation channel contributes most to the measured radiation. However, for CH dissociative excitation contributes most to the radiation in methane laboratory plasmas [42], whereas for C_2 direct excitation is always dominant. In summary, this means that the radiation of CH or C_2 in edge plasmas is related to the ground state density of the particles CH or C_2, respectively, by applying the corona model.

The correlation of CH or C_2 particle densities with methane or higher hydrocarbons is obtained from dissociation models. The dissociation chain of methane contributes most to the formation of CH particles. The contribution of higher hydrocarbons is negligible due to the higher number of processes which are needed to form CH and due to the lower density of C_2H_y particles in comparison to the CH_4 density. In case of C_2 particles it is expected that dissociation of C_2H_y particles is the dominant formation channel. Subsequently substraction of hydrogen particles from methane leads to carbon atoms which then have to recombine in the volume to contribute to C_2 formation. However, rate coefficients for these heavy particle collisions are very low. First investigations are started to obtain dissociation models for the higher hydrocarbons, i.e., the C_2H_y group wit respect to C_2 formation [41]. Calculated densities are then verified by well defined laboratory plasmas in hydrocarbons, where densities are known from mass spectrometry.

As described in Sect. 4.2.3 the (inverse) photon efficiency is the basis for the determination of particle fluxes from measured photon fluxes. For hydrocarbons, the destruction events are dissociation processes of the parent molecule. Following the discussion in the previous paragraphs two relations can be now defined: (1) $\Gamma_{CH_4} = (D_{eff}/XB)_{CH}^{CH_4} \times \Gamma_{CH}^{ph}$ and (2) $\Gamma_{C_2H_y} = (D_{eff}/XB)_{C_2}^{C_2H_y} \times \Gamma_{C_2}^{ph}$. These correlations offer a method to quantify the methane flux as well as the flux of the higher hydrocarbons which are re-

leased from the graphite targets by bombardment of atoms and ions. Finally, measurements of erosion yields $Y = \Gamma_C/\Gamma_H$ can be extended by the contribution of higher hydrocarbons to the carbon flux: $\Gamma_C = \Gamma_{CH_4} + 2 \times \Gamma_{C_2H_y}$.

4.5.2 Gas Puff Experiments

Measurements of carbon fluxes rely on the precise knowledge of (inverse) photon efficiencies. Since the underlying models have uncertainties, e.g., due to the input data base, validation by experiments is needed. The wide parameter range of plasmas in present and future fusion machines requires a manifold of parameter investigations. Once the particle flux is known and once the corresponding photon flux is measured, the (inverse) photon efficiencies are determined. Well–defined particle fluxes are obtained by puffing gas through calibrated valves into the edge plasma. In order to compare measured values to calculations, the corresponding T_e and n_e have to be assigned. Our further discussion is focussed to the investigations on gas puff experiments with C_2H_6 and the correlation with C_2 radiation.

The gas puff experiments described here are carried out in the divertor of ASDEX Upgrade. CH_4, CD_4, C_2H_6 with the same particle flux were used as puffing gas through a calibrated valve above the strike–point in L–mode (low confinement) discharges. The plasma parameters were in the range of $T_e \approx 5$–$15\,\mathrm{eV}$ and $n_e \approx 10^{18}$–$10^{19}\,\mathrm{m}^{-3}$ obtained from Langmuir probes. The radiation of CH and C_2 was measured simultaneously using the same line of sight. This can be achieved by using a wide range spectrometer with sufficient spectral resolution (FWHM $\approx 30\,\mathrm{pm}$). Starting the discussion with the radiation of CH (CD), it turned out that measured (inverse) photon efficiencies from CH_4, CD_4 and C_2H_6 are comparable. This confirms that, within the error bars of the method, the isotopes show no differences in terms of dissociation and radiation, which is an important issue for future applications in tritium discharges. The same amount of CH radiation is produced if CH_4 or C_2H_6 dissociates. As a consequence, the CH radiation does not only refer to methane fluxes but also to C_2H_6 fluxes, or in other words, to obtain a methane flux, the amount of radiation which originates from the higher hydrocarbons has to be subtracted first. However, since it is expected that less higher hydrocarbons than methane are released from a graphite surfaces, the error bar should be less than 10%. The C_2 radiation which is observed by gas puffs of CH_4 is one order of magnitude below the C_2 radiation obtained from C_2H_6 particle fluxes. This means the C_2 radiation can be related to C_2H_6 particles and gives a upper limit for the higher hydrocarbons. However, a definite correlation needs further detailed experiments.

4.5.3 Erosion Yields in Laboratory Plasmas

Low pressure laboratory plasmas offer a possibility to measure erosion yields in hydrogen as well as in deuterium plasmas under well–defined experimen-

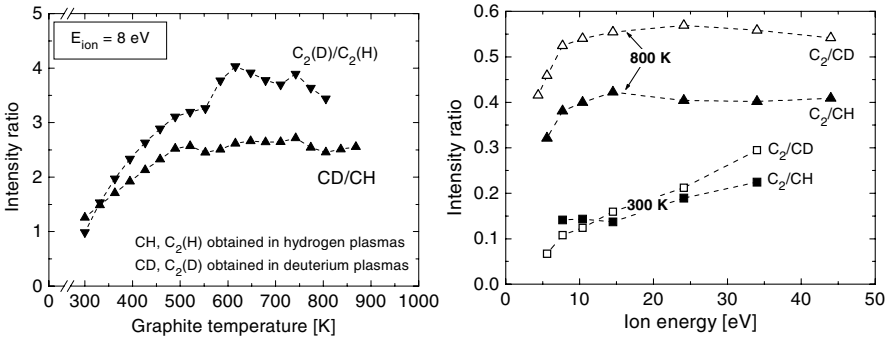

Fig. 4.10. Intensity ratio of molecular bands in hydrogen and deuterium plasmas as a function of graphite temperature (**left**) and ion energy (**right**)

tal conditions. Additionally, the spectroscopic methods can be proved and are supported by other diagnostic techniques such as mass spectrometry or Langmuir probes. Spectroscopic measurements of carbon fluxes can be verified by weight loss measurements of the graphite substrate. Due to the typical plasma parameters of such low pressure discharges the atomic hydrogen flux exceeds more than one order of magnitude the ion flux which consists of mainly molecular ions (H_3^+ or H_2^+). As a consequence, the so–called chemical enhanced erosion is investigated in such plasmas. Typical plasma parameters are $T_e \approx 2$–$4\,eV$, $n_e \approx 10^{17}$–$10^{18}\,m^{-3}$ and $T_{gas} \approx 400$–$1000\,K$ (heavy particle temperature). They depend on the individual type of discharge and discharge pressure. Additionally, the experimental set-up can be designed to heat or cool actively the substrate and to vary the ion energy by applying a bias voltage. Such investigations are used to verify and complete present erosion models (see, for example, [43]). Furthermore, comparisons of graphite surfaces with doped graphite under same conditions are carried out. The spectroscopic techniques offer time–resolved measurements, i.e., erosion yields as a function of the fluence are readily observed.

The formation of higher hydrocarbons can be investigated in detail. It is assumed that the CH radiation represents the methane formation, whereas the C_2 radiation correlates with the formation of C_2H_y. Figure 4.10 shows intensity ratios of the emission bands CD and CH obtained in hydrogen and deuterium plasmas, respectively, as well as the intensity ratio of the corresponding molecular carbon bands as a function of graphite temperature. At room temperature the same amount of methane is released in hydrogen and deuterium plasmas. This is also observed for the higher hydrocarbons. With increasing substrate temperature at fixed ion energy ($E_{ion} = 8\,eV$) an isotope effect appears in the methane formation as well as in the formation of higher hydrocarbons. The intensity ratio of C_2/CH in hydrogen or deuterium plasmas is also shown in Fig. 4.10 as a function of ion energy. The data show that more higher hydrocarbons are formed if the ion energy increases.

Even at room temperature the isotope effect appears, i.e., deuterium plasmas produce more higher hydrocarbons than hydrogen plasmas. The dependencies are confirmed by weight loss measurements.

The analysis of erosion yields from spectroscopic investigations showed that the absolute values of carbon fluxes are matched only if besides the radiation of CH the radiation of C_2 is considered, i.e., the amount of higher hydrocarbons is taken into account [43].

4.6 Conclusions

Spectroscopic diagnostics offers a tool to quantify the formation of hydrogen molecules as well as hydrocarbon molecules in edge plasmas of fusion devices. Besides the particles fluxes, the rotational temperature as well as the vibrational population is diagnosed. The vibrational population in the ground state of hydrogen molecules provides a manifold of low energy processes. Therefore, the population plays a dominant role in cold edge plasmas, where molecules have a long penetration depth and can undergo a variety of processes. For hydrogen molecules, the interpretation of data is supported by collisional–radiative modeling, which is essential in these non-equilibrium plasmas. For hydrocarbons, dissociation models are needed. They provide the correlation between particle fluxes and photon fluxes. The formation of hydrocarbons by bombardment of graphite surfaces with hydrogen particles, i.e., the chemical erosion, is quantified by spectroscopic techniques. In principle, the CH radiation is correlated with methane formation and first investigations indicate that the C_2 radiation refers to particle fluxes of the C_2H_y group.

Acknowledgments

The author would like to mention the contributions of D. Wünderlich for the calculations with the collisional–radiative model, D. Reiter and D. Coster for running the B2–EIRENE code and the ASDEX Upgrade Team as well as the plasma spectroscopic team at Augsburg University for their assistance.

References

1. P.C.Stangeby: *The Plasma Boundary of Magnetic Fusion Devices* (Institute of Physics Publishing, Bristol 2000)
2. D. Reiter: Modeling of Fusion Edge Plasmas. In: this volume
3. U. Samm: Plasma Wall Interaction: Status and Data Needs. In: this volume
4. J. Roth: Review and Status of Physical Sputtering and Chemical Erosion of Plasma Facing Materials. In: this volume
5. R. Behrisch, D.E. Post: *Physics of Plasma–Wall Interactions in Controlled Fusion* (Plenum Press, New York 1986)

6. A. Thorne, Litzén, S. Johansson: *Spectrophysics: Principles and Applications* (Springer, Berlin Heidelberg New York 1999)
7. K. Behringer: Plasma Phys. Contr. Fusion **33** 997 (1991)
8. U Fantz: Plasma Phys. Contr. Fusion **40** 1035 (1998)
9. G.H. Dieke: *The Hydrogen Molecule Wavelength Tables* (Wiley-Interscience, New York 1972)
10. R.S. Freund, A. Schaivone, H.M. Crosswhite: J. Phys. Ref. Data **14** 235 (1985)
11. U. Fantz, B. Heger: Plasma Phys. Contr. Fusion **40** 2023 (1998)
12. U. Fantz, B. Schalk, K. Behringer: New J. Phys. **2** 7.1 (2000)
13. H. Kempkens, J. Uhlenbusch: Plasma Sources Sci. Technol. **9** 492 (2000)
14. Th. Mosbach, V. Schulz-van der Gathen, H.F. Döbele: Contrib. Plasma Phys. **42** 650 (2002)
15. H.P. Summers: *ADAS User Manual Version 2.5.6* (University of Strathclyde, Glasgow 2002), http://adas.phys.strath.ac.uk
16. K. Sawada, T. Fujimoto: J. Appl. Phys. **78** 2913 (1995)
17. P.T. Greenland, D. Reiter: Report **JUEL-3258** (1996)
18. U. Fantz, D. Wünderlich: Report **IPP 10/18** (2001)
19. B. Heger: PhD Thesis, University of Augsburg (2002)
20. K. Behringer: J. Nucl. Mater. **176&177** 606 (1990)
21. U. Fantz, B. Heger, D. Wünderlich: J. Nucl. Mater. **313-316** 743 (2003)
22. S. Brezinsek: Report **JUEL-3962** (2002)
23. S.J. Krasheninnikov, A. Yu Pigarov, T.K. Soboleva et al.: J. Nucl. Mater. **241-243** 283 (1997)
24. ITER Physics Basis: Nucl. Fus. **39** (1999)
25. D. Reiter, C. May, M. Baelmans et al.: J. Nucl. Mater. **241-243** 342 (1997)
26. R. Schneider et al.: J. Nucl. Mater. **196-198** 810 (1992)
27. D. Reiter: J. Nucl. Mater. **196-198** 80 (1992)
28. A. Pospieszczyk, S. Brezinsek, Ph. Mertens et al.: Contrib. Plasma Phys. **42** 663 (2002)
29. S. Brezinsek, Ph. Mertens, A. Pospieszczyk et al.: Contrib. Plasma Phys. **42** 668 (2002)
30. A. Pospieszczyk: High Temperature Plasma Edge Diagnostics. In: this volume
31. U. Fantz, K. Behringer, R. Schneider et al.: Europhysics Conference Abstracts (ECA) **23J** 1549 (1999)
32. U. Fantz, D. Reiter, B. Heger et al.: J. Nucl. Mater. **290–293** 367 (2001)
33. U. Fantz, K. Behringer, J. Gafert et al.: J. Nucl. Mater. **266–269** 490 (1999)
34. M. Capitelli, R. Celiberto, E. Esposito et al.: Plasma Sources Sci. Technol. **11**, A7 (2002)
35. W.G. Graham: Plasma Sources Sci. Technol. **4** 281 (1995)
36. U. Fantz, B. Heger, D. Wünderlich: Plasma Phys. Control. Fusion **43** 907 (2001)
37. B. Heger, U. Fantz: Europhysics Conference Abstracts (ECA) **25A** P1.064 (2002)
38. R.C. Isler, J. Colchin, N.H. Brooks et al.: Phys. Plasmas **8** 4470 (2001)
39. T. Nakano, H. Kubo, S. Higashijima et al.: Nucl. Fusion **42** 689 (2002)
40. U. Fantz: Report **IPP 10/21** (2002)
41. S. Meir, U. Fantz: Paper contribution to the 16th ISPC conference, accepted
42. T. Schütte: PhD Thesis, University of Stuttgart (1995)
43. U. Fantz, H. Paulin: Physica Scripta **T91** 43 (2001)

5 Divertor Spectroscopy with Molecular Transport

H. Kubo, H. Takenaga, T. Nakano, S. Higashijima, K. Shimizu, K. Sawada, S. Kobayashi, and the JT-60 Team

5.1 Introduction

In the tokamak fusion reactor, heat and particle (hydrogen isotopes, helium and impurity) control are essential for obtaining high fusion performance and preventing damage of the plasma facing components. The poloidal divertor is the most promising method for the heat and particle control [1]. Heat and particles from the main plasma flow to the divertor plates along magnetic field lines. Most of the hydrogen ions arriving at the divertor plates are absorbed and eventually desorbed as hydrogen molecules. The hydrogen molecules can play an important role as a hydrogen ion source and sink. Since excited hydrogen atoms can be produced by dissociation of the hydrogen molecules, the hydrogen molecules can affect emission from the hydrogen atoms. For high-heat-load divertor plates, carbon materials are used in present- and next-generation tokamaks because of their high thermal-shock resistance, high thermal conductivity and low atomic number [2]. At the carbon divertor plates, hydrocarbon molecules are produced by chemical sputtering. The hydrocarbon molecules can play important roles in impurity contamination and radiative losses. In the International Thermonuclear Experimental Reactor (ITER) [3], the lifetime of the divertor plates can be determined by chemical erosion, and tritium retention due to hydrocarbon molecule codeposition can be a significant problem for safety. Therefore, understanding the behavior of hydrogen and hydrocarbon molecules in divertor plasmas is important in tokamak fusion research.

In this chapter, some topics of divertor spectroscopy with molecular transport are presented, mainly based on recent studies in JT-60U, which is a large tokamak (the major radius is around 3.4 m, and the minor radius is around 1.0 m) with a W-shaped poloidal divertor in the bottom [4]. (General molecular diagnostics without transport analysis are described in [5].) The plasma parameters in the divertor plasma change as two-dimensional spatial functions, and analysis with consideration of the divertor structure is necessary for understanding the particle behavior. On the other hand, molecular reactions are very complex. Thus, transport codes using Monte Carlo techniques become useful for analysis of the molecular behavior. Applications of molecular data and the data requirements for the analysis are also discussed. In the attached divertor plasma, where the electron temperature is high (> 5 eV)

and the molecules are ionizing, spectroscopy has successfully been applied to studying the behavior of hydrogen and hydrocarbon molecules. In Sect. 5.2, spectroscopic observations of hydrogen molecules in attached divertor plasmas are analyzed with a neutral particle transport and a collisional–radiative model code. The effect of the dissociative excitation of hydrogen molecules and molecular ions on the emission from hydrogen atoms is also described. In Sect. 5.3, the study of hydrocarbon molecule transport in attached divertor plasmas is described. In Sect. 5.4, problems with molecular spectroscopy in detached divertor plasmas, where the electron temperature is low and the ion flux to the divertor plates is reduced by plasma volume recombination, are discussed. The detached divertor plasma regime is attractive for mitigating the severe problem of concentrated power loading of the divertor plates. In Sect. 5.5, a summary of divertor spectroscopy with molecular transport and molecular data needs for the divertor spectroscopy is given.

5.2 Hydrogen Molecules in Attached Divertor Plasmas

The behavior of hydrogen particles in attached divertor plasmas is schematically shown in Fig. 5.1 [6]. While some of the hydrogen ions arriving at the divertor plates are reflected in the form of hydrogen atoms, most of them are absorbed in the divertor plates and desorbed in the form of hydrogen molecules from the divertor plates. For example, in the case where the divertor plates are made of carbon materials and the electron temperature of the divertor plasma is 20 eV, only $\sim 20\%$ of the hydrogen ions are reflected and the others are absorbed. The reflected atoms have rather high kinetic energy almost corresponding to the electron temperature of the divertor plasma, and the desorbed molecules have very low kinetic energy corresponding to the surface temperature of the divertor plates. The hydrogen molecules are dissociated or ionized near the divertor plates. The hydrogen atoms produced by dissociation of the hydrogen molecules or molecular ions have the Franck–Condon energy ($\sim$ several eV) determined by the dissociation processes. Some of the hydrogen atoms experience charge exchange with the hydrogen ions, and the hydrogen atoms produced by the charge exchange have rather high kinetic energy corresponding to the plasma ion temperature. In the attached divertor plasma, the molecules and the atoms are ionizing, and they are important hydrogen ion sources.

In order to directly study hydrogen molecule behavior in divertor plasmas, hydrogen molecular line emission has recently been observed [5]. Figure 5.2 shows Fulcher ($d^3\Pi_u \rightarrow a^3\Sigma_g^+$) lines observed near the divertor plates in an attached divertor plasma. The Q branches for the $v = 0-0$, $1-1$ and $2-2$ transitions are identified. The vertical lines indicate the line intensities calculated on the assumption that $T_{\rm rot}(0) = 0.040\,{\rm eV}$, $T_{\rm rot}(1) = 0.057\,{\rm eV}$, $T_{\rm rot}(2) = 0.046\,{\rm eV}$, $n(1)/n(0) = 0.76$, and $n(2)/n(0) = 0.60$. Here, $T_{\rm rot}(v)$ and $n(v)$ are the rotational temperature and the population of the vibrational

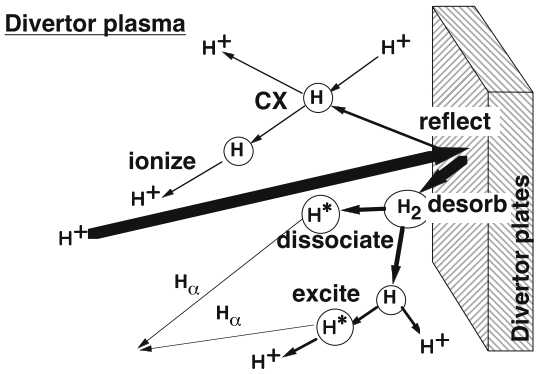

Fig. 5.1. Behavior of hydrogen particles in attached divertor plasmas

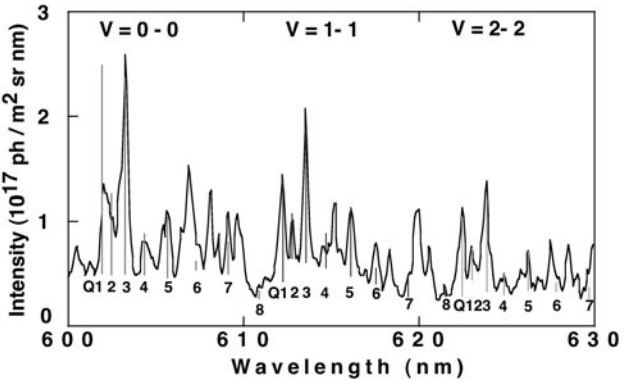

Fig. 5.2. Fulcher lines observed near the divertor plates in an attached divertor plasma in JT-60U [7]. Calculated Q-branch line intensities for the $v = 0 - 0, 1 - 1, 2 - 2$ transitions are also shown as *vertical lines*. The electron temperature and density measured with a Langmuir probe near the separatrix strike point were 20 eV and $0.7 \times 10^{19}\,\mathrm{m}^{-3}$, respectively

level v of the $d^3\Pi_\mathrm{u}$ state, respectively. The $T_\mathrm{rot}(v)$ and $n(v)$ were determined to fit the calculation to the measured values. The vibrational population ratios correspond to a vibrational temperature of ~ 1 eV. Figure 5.3a shows the intensity of the Fulcher $v = 1 - 1\,\mathrm{Q3}$ line as a function of the distance from the outer divertor plates. In the attached divertor plasma, the decay length of the line intensity is ~ 1 cm, and it suggests that the H_2 molecules are localized near the divertor plates. The line intensity has been calculated using a three-dimensional neutral transport code [9] and a collisional–radiative model code [10]. Then, the background plasma parameters were determined using a simple divertor code from the electron temperature and density measured with the Langmuir probes at the divertor plates [11]. It was assumed that all the H^+ ions arriving at the divertor plates were reflected as hydrogen

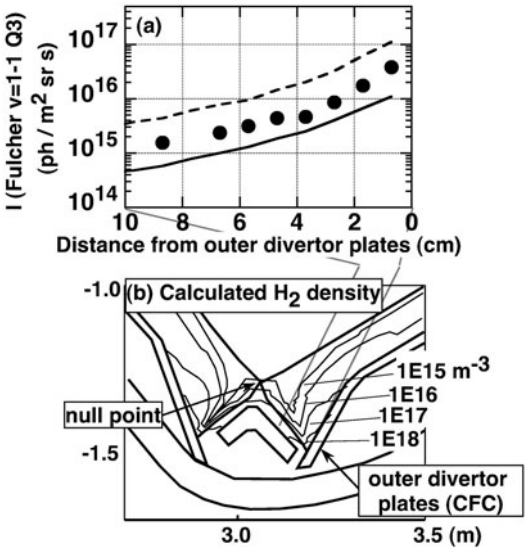

Fig. 5.3. (**a**) Measured and calculated intensity of the Fulcher $v = 1 - 1\,\mathrm{Q3}$ line as functions of the distance from the outer divertor plates in an attached divertor plasma [8]. The *circles* indicate the measurement, and the continuous and broken lines indicate the calculations with and without inclusion of the dissociative attachment from the H_2 $n = 3$ state. (**b**) Calculated H_2 molecule density in the attached divertor plasma [7]. The viewing chords are also shown in (**b**)

atoms or desorbed as hydrogen molecules. In the collisional–radiative model, the vibrational levels were separately considered for the $n = 1$ state, the electronic states for the $n = 2$ state, and the singlet and triplet states for the $n = 3$ state. The total intensity of Fulcher lines was calculated by assuming the statistical weight for the populations of the $n = 3$ triplet levels. The calculated intensity is compared with the measured one in Fig. 5.3a. Here, two calculations are shown; the continuous line is a calculation with inclusion of dissociative attachment from the $n = 3$ state ($H_2(n = 3) + e \rightarrow H + H^-$), and the broken line is a calculation without. The observed intensity was between the intensities calculated with and without considering dissociative attachment. Although more accurate rate coefficients are required, the agreement of the fall in the intensity profile between calculation and observation suggests that the H_2 molecule density distribution was fairly well reproduced by the neutral particle transport calculation. The calculated H_2 molecule density is shown in Fig.5.3b. The H_2 molecules are locally distributed near the separatrix strike points.

As shown in Fig. 5.1, since excited hydrogen atoms can be produced by dissociation of hydrogen molecules and molecular ions, the hydrogen molecules can affect emission from the hydrogen atoms. Therefore, by investigating emission from the hydrogen atoms, we can study hydrogen molecule behav-

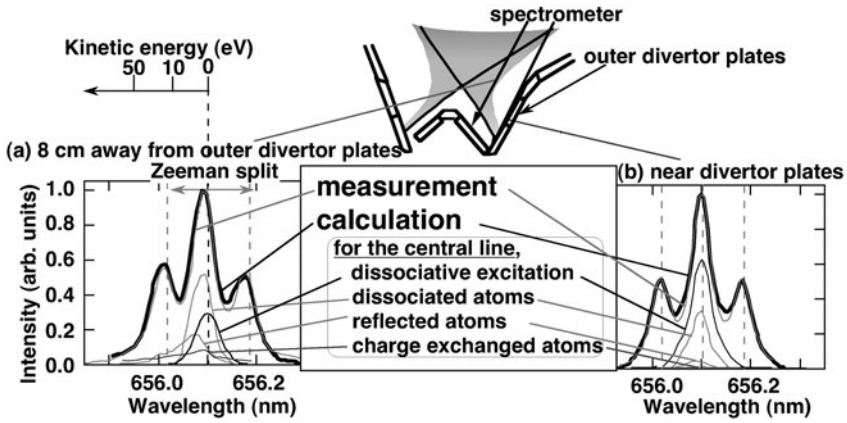

Fig. 5.4. Spectral profiles of Dα line [12]. (**a**) 8 cm and (**b**) 0.5 cm away from the outer divertor plates. The viewing chords are shown in the upper figure. The *thick* and *thin lines* indicate the observed and simulated profiles, respectively. Compositions for the simulated π-component line are also shown. The kinetic energy of the D atoms corresponding to the wavelength shift is indicated above figure (**a**). The electron temperature and density were, respectively, 90 eV and $0.5 \times 10^{19} \mathrm{m}^{-3}$ at the outer separatrix strike point. The toroidal magnetic field at the outer separatrix strike point was 4.15 T

ior. On the other hand, understanding the processes of emission from the hydrogen atom is necessary in order to utilize the emission for diagnosis. Understanding the processes of the Balmer-α line (Hα line) is especially important, since this line emission is generally used for a measure of the hydrogen ion source rate. The spectral profile of the Balmer-α line gives information on the velocity distribution of the hydrogen atoms and their basic recycling processes.

Spectral profiles of Dα lines observed in an attached divertor plasma are shown in Fig. 5.4. A high-resolution spectrometer with an echelle grating was used for the observation [13]. The spectra split into three components due to the Zeeman effect. The spectral profile observed near the divertor plates is narrower than that observed in the upstream of the divertor plasma. The spectral profiles simulated with a three-dimensional neutral particle transport code are also shown in the figure. The simulated profiles agree reasonably with the observed ones. Compositions for the simulated π-component line are also shown. The Dα emission is attributed to collisional excitation of D atoms produced by dissociation, reflection, and charge exchange and dissociative excitation of D_2 molecules. The atoms produced by reflection and charge exchange have rather high kinetic energy almost corresponding to the temperature of the divertor plasma. The D atoms produced by dissociation have the Franck–Condon energy. Molecular processes considered in the simulation are shown in Table 5.1. The average kinetic energy of the atoms

Table 5.1. Molecular processes considered in the simulation [14]. E_{H} is the average kinetic energy of the atoms produced by the reaction, and T_{e} is the electron temperature of the plasma

Process	E_{H} (eV)
$H_2 + e \rightarrow H_2^+ + 2e$	–
$H_2 + e \rightarrow 2H(1s) + e$	3.0
$H_2 + e \rightarrow H(2s) + H(1s) + e$	0.3
$H_2 + e \rightarrow H(2s) + H(2p) + e$	4.85
$H_2 + e \rightarrow H(n = 3) + H(1s) + e$	7.0, 0.3
$H_2 + e \rightarrow H(1s) + H^+ + 2e$	7.8, 0.25
$H_2^+ + e \rightarrow 2H^+ + 2e$	–
$H_2^+ + e \rightarrow H(n = 2) + H(1s)$	$0.37\,T_{\mathrm{e}}^{0.91}$
$H_2^+ + e \rightarrow H(1s) + H^+ + e$	4.3
$H_2^+ + e \rightarrow H(n = 2, 3) + H^+ + e$	1.5

produced by the reaction is also shown in the table. In the simulation, the data for hydrogen molecules were used, because enough data were not available for deuterium. As seen in Fig. 5.4, near the divertor plates, dissociative excitation plays an important role in the line emission. In the upstream, the contribution of the dissociative excitation decreases and that of the electron collisional excitation of atoms produced by reflection and charge exchange increases. Because the kinetic energy of the atoms produced by reflection and charge exchange is higher than that of the atoms produced by dissociation, the spectral profile in the upstream region is broader than that near the divertor plates.

As a result, molecular spectroscopy has successfully been applied to understanding the behavior of hydrogen molecules in attached divertor plasmas. The agreement of the fall in the intensity profile between calculation and observation suggests that the distribution of the H_2 molecule density can be calculated fairly well for attached divertor plasmas. Simulated Dα spectral profiles agree reasonably with the observed ones, suggesting that effect of D_2 molecules and D_2^+ molecular ions on the Dα emission can be described by the simulation. However, the codes used for the analysis should still be improved, since the excitation rate coefficients for hydrogen molecules are not known satisfactorily at present. For the study of hydrogen particle transport, the kinetic energy of hydrogen atoms produced by dissociation is also necessary. Hydrogen molecular data have been used for deuterium molecules, because sufficient data are not available for deuterium.

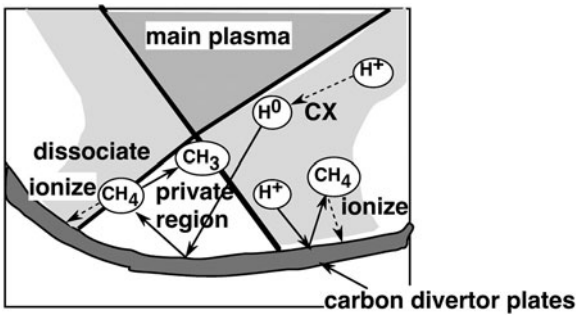

Fig. 5.5. Behavior of hydrocarbon molecules in a divertor region

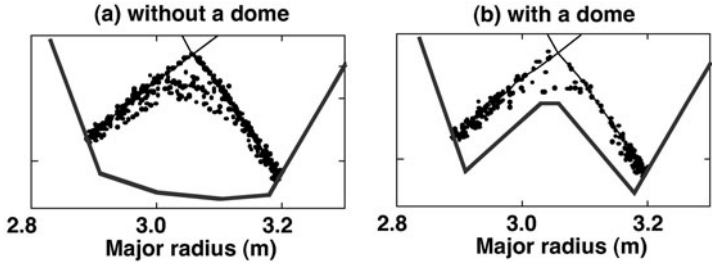

Fig. 5.6. Simulated result for birth positions of C^+ ions originated from CH_4 molecules released from the private flux region by charge exchange neutrals (**a**) without and (**b**) with a dome in the private flux region [15]

5.3 Hydrocarbon Molecules in Attached Divertor Plasmas

The behavior of hydrocarbon molecules in a divertor region is shown in Fig. 5.5 [15]. At the carbon divertor plates, hydrocarbon molecules such as methane molecules are produced due to chemical sputtering by hydrogen ions. These hydrocarbon molecules are ionized near the divertor plates, and they readily return to the divertor plates along the magnetic field lines. At the wall in the private region, hydrocarbon molecules are also produced due to chemical sputtering by hydrogen atoms produced by charge exchange. The resulting neutral hydrocarbon molecules can go across the private flux region. The hydrocarbon molecules are ionized or dissociated by interaction with the divertor plasma. While the produced ions readily return to the divertor plates along the magnetic field lines, some of the dissociated neutral hydrocarbon molecules can again go across the private flux region. Transport of hydrocarbon molecules to the upstream of the divertor plasma causes carbon impurity contamination of the main plasma. It is important to control transport of the hydrocarbon molecules by optimization of the divertor structure.

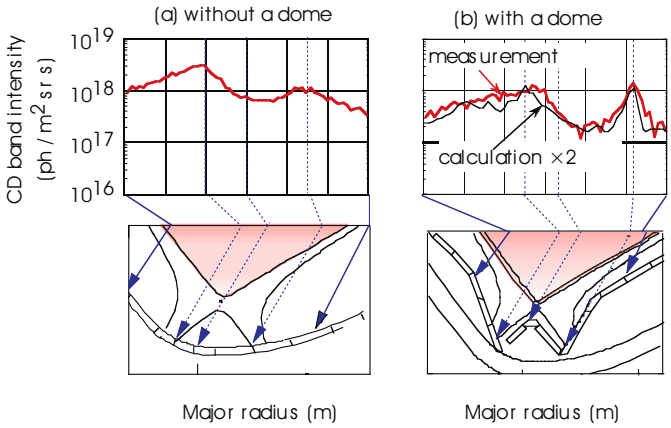

Fig. 5.7. Spatial distribution of the CD band ($A\ ^2\Delta - X\ ^2\Pi$, $v = 0 - 0$) intensity (**a**) without and (**b**) with a dome in the private flux region. The *thick lines* indicate the measured intensity. The *thin line* shows the simulated intensity multiplied by two [16]

Figure 5.6 shows a simulated result for the birth positions of the C^+ ions originated from the CH_4 molecules released from the private flux region by charge exchange neutrals. Without a dome in the private flux region, the neutral hydrocarbon molecules can go across the private flux region, and the birth positions of the C^+ ions are broadly scattered up to the vicinity of the null point. On the other hand, with a dome, the birth positions of the C^+ ions are dominantly distributed near the separatrix strike points. Therefore, it is predicted that carbon impurity transport to the upstream region of the divertor plasma can be suppressed with a dome in the private flux region. Figure 5.7 shows the spatial distribution of the CD-band intensity observed in divertors without a dome (open divertor) and with a dome (W-shaped divertor). The intensity around the null point in the W-shaped divertor is obviously lower than that in the open divertor. The simulated intensity distribution is also shown for the W-shaped divertor. The observed intensity distribution is reproduced by the simulation within a factor of two. The results suggest that the dome works to prevent the hydrocarbon impurity from invading the upstream as predicted.

In the above simulation, only production of CD_4 molecules at the divertor plates is considered, although higher hydrocarbon molecules such as C_2D_n are also produced by chemical sputtering at the actual divertor plates, and they can also contribute to the CD band emission [17]. The reason for the discrepancy between the observed CD band intensity and the simulated one might be that only CD_4 production is considered in the simulation. Reliable data for all relevant hydrocarbon molecules are required for more accurate simulations.

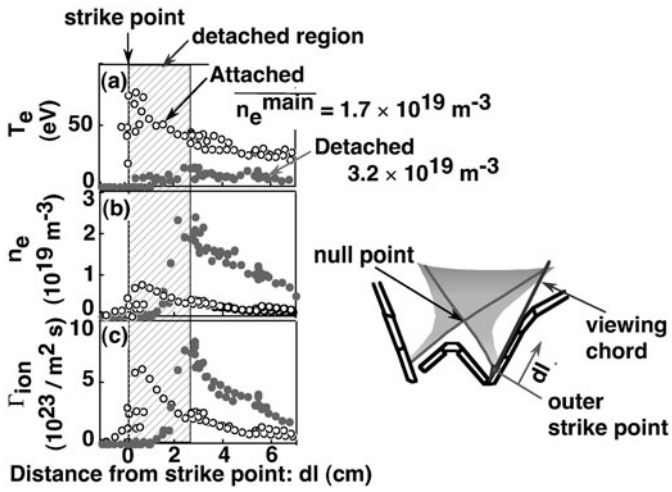

Fig. 5.8. Profiles of (**a**) electron temperature, (**b**) density, and (**c**) ion flux measured with Langmuir probes at the divertor plates in an attached and a detached divertor plasma. The distance from the strike point (dl) is measured along the outer divertor plates as shown in the **right**-hand figure

5.4 Molecules in Detached Divertor Plasmas

As the electron density increases in the main plasma, the divertor plasma becomes dense and cold and then detached from the divertor plates: the momentum and the ion flux to the divertor plates decrease [18]. The detached divertor regime is attractive for mitigating the severe problem of concentrated power loading of the divertor plates [19]. Figure 5.8 shows profiles of electron temperature, density, and influx measured with Langmuir probes at the divertor plates in an attached and a detached divertor plasma. In the low-density case (the attached divertor plasma), the profiles have peaks at the separatrix strike point. On the other hand, in the high-density case, the electron temperature, density, and ion flux decrease near the strike point: the divertor plasma is partially detached. The width of the detached region is ~ 2.5 cm. Just outside of the detached region, the plasma is still attached and the electron temperature and density are ~ 10 eV and $\sim 2 \times 10^{19}$ m^{-3}, respectively. Figure 5.9 shows a spectrum of hydrogen Balmer series lines observed in a detached divertor plasma. The Balmer series lines with upper levels of $n = 7$–10 are identified, where n is the principal quantum number. The observed spectrum can be fitted on the assumption of a Boltzmann distribution with an electron temperature of 0.4 eV for the upper level populations and Stark broadening with an electron density of 1×10^{20} m^{-3}. The spectroscopic measurement is not consistent with the Langmuir probe measurement. It is considered that the Langmuir probe measurement overestimates the electron temperature due to the influence of plasma resistance and fluctuations in the detached

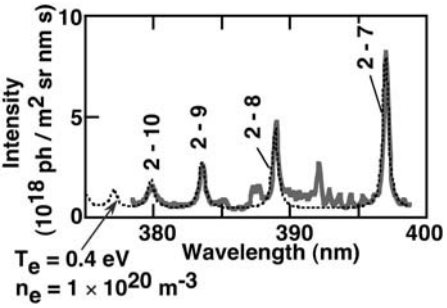

Fig. 5.9. Spectrum of hydrogen Balmer series lines observed in a detached divertor plasma [20]. The spectrum was observed with the viewing chord shown in Fig. 5.8. The fitted spectrum is also shown as a *broken curve*

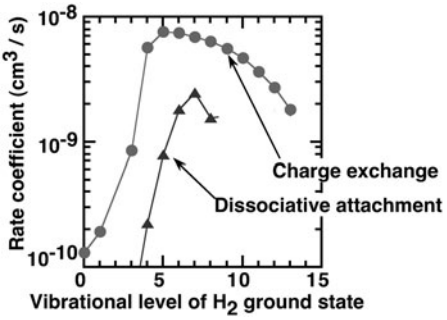

Fig. 5.10. Rate coefficients of the charge exchange ($H_2(v)+H^+ \rightarrow H_2^+ + H$) [23] and dissociative attachment ($H_2(v) + e \rightarrow H^- + H$) [24] for the vibrational levels v of the ground state $X\ ^1\Sigma_g^+$

divertor plasma [21]. For understanding the detached divertor plasmas, more exact measurement of the plasma parameter distribution is required.

In the detached divertor plasma, reduction in the ion flux is considered to be due to plasma volume recombination. By observation of spectra near the hydrogen Balmer series limit, it has been found that recombination of hydrogen ions and electrons is dominant in the detached divertor plasma [22]. It is also expected that hydrogen and hydrocarbon molecules can play some roles as an ion sink (Molecular Assisted Recombination: MAR) [5,8]. For hydrogen molecules, two MAR processes are considered: the first is charge exchange with subsequent dissociative recombination ($H_2(v) + H^+ \rightarrow H_2^+ + H$ and $H_2^+ + e \rightarrow 2H$, here $H_2(v)$ indicates the vibrational level v in the ground state $X^1\Sigma_g^+$ of the H_2 molecule), and the second is dissociative attachment with subsequent mutual neutralization ($H_2(v) + e \rightarrow H^- + H$ and $H^- + H^+ \rightarrow 2H$). Figure 5.10 shows the rate coefficients of the charge exchange and the dissociative attachment for the vibrational levels. The reaction rate coefficients depend strongly on the vibrational excitation. Therefore, the vibrational pop-

ulation should be considered for understanding the roles of MAR. Collisional–radiative models considering the vibrational levels have been developed [10]. In the collisional–radiative model, the following rate equations are solved:

$$\mathrm{d}n_k/\mathrm{d}t = \Sigma R_{k,j}(n_\mathrm{e}, T_\mathrm{e}, \dots)n_j(t) + \Gamma_k\,. \tag{5.1}$$

Here, n_k is the population of the level k, $R_{k,j}$ is the rate at which population is transferred from the level j to the level k by collisional transitions with plasma particles (electrons, hydrogen ions, etc.) and radiative transitions, and Γ_k is the external flux of the level-k population. To solve the equations, the quasi-steady-state approximation (for all the excited levels, $\mathrm{d}n_k/\mathrm{d}t = 0$ and $\Gamma_k = 0$) is usually assumed in order to make the differential equations simple linear equations except the equation for the ground level. This assumption is applicable when the relaxation times of the excited levels are much shorter than that of the ground state (in other words, the populations of the excited levels are much smaller than that of the ground level) and much shorter than the plasma transport time (in other words, the relaxation path length for the excited levels is much shorter than the length for change of the plasma). However, these two conditions are necessarily not satisfied for the vibrational levels of the H_2 molecules in detached divertor plasmas. In Fig. 5.11, the time evolution of the vibrational populations of the H_2 molecular ground state calculated with and without the quasi-steady-state approximation is shown. The decay time of the ground level population is $\sim 8\mu$s. The ratios of the excited level populations to the ground level populations changes for $\sim \mu$s, which indicates the relaxation times for the excited levels. Since the relaxation times of the excited levels are not much shorter than that of the ground level, the populations of the excited levels are not much smaller than that of the ground level. As a result, the populations calculated with the quasi-steady-state approximation are different from the population calculated without the approximation. The kinetic energy of the hydrogen molecules desorbed from the divertor plates corresponds to the surface temperature of the divertor plates. When the kinetic energy of the H_2 molecules corresponds to a temperature of 300°C, the distance corresponding to the time is also shown in the figure. The length for the relaxation time of the excited levels is ~ 1 cm. Since the plasma parameters can change rapidly in a short distance in the detached divertor plasma (as seen in Fig. 5.8), the relaxation path length for the excited levels is not much shorter than the length for change of the plasma. Therefore, the change of the plasma should be considered in solving the rate equations: the particle transport should simultaneously be considered in solving the populations. Monte Carlo transport codes treating the vibrationally excited molecules as distinct particles can be a useful method in such a case. In ASDEX, it was estimated from observation of the Fulcher lines that in detached divertor plasmas the vibrational population was significant and only 45% of the molecules were in the $v = 0$ level. The observation was also compared with B2–EIRENE calculations where the vibrationally excited molecules were treated as distinct particles [25]. In JT-60U, it has been

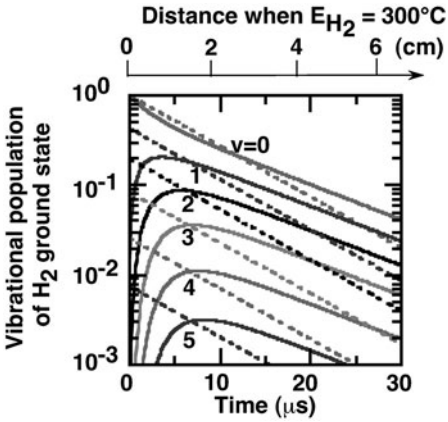

Fig. 5.11. Time evolution of the vibrational ($v = 0 - 5$) populations of the H_2 molecule ground state ($X^1\Sigma_g^+$). Here, it is assumed that all the molecules are initially populated in the $v = 0$ level. The initial $v = 0$ level population is normalized to be unity. The *broken* and *continuous lines* indicate the populations calculated with and without the quasi-steady-state approximation, respectively. Here, the electron temperature is 2 eV, and the electron density is $1 \times 10^{20}\,\mathrm{m}^{-3}$. The *upper scale* indicates the distance corresponding to the time when the kinetic energy of the H_2 molecules corresponds to a temperature of 300°C

suggested from observation of the Fulcher line emission that H_2 molecules penetrate more deeply in detached divertor plasmas with a MARFE than in attached divertor plasmas [8]. Since the excitation energy of the upper state for the Fulcher transition is much higher (14 eV) than the electron temperature in the detached divertor plasma, the Fulcher line emission may not be necessarily the best measure in the detached divertor plasma.

In summary, for study of the detached divertor plasma, more exact measurements of the plasma parameter distributions are required. A Monte Carlo transport code treating the vibrationally excited molecules as distinct particles has been developed for analysis of molecular behavior in the detached divertor plasma, since vibrational excitation becomes important in such low-temperature plasmas. Requirements for molecular data are increasing to facilitate such analysis. Since the rates for the vibrational excitation are different between the hydrogen isotope molecules, data for molecules including deuterium and tritium are especially required.

5.5 Conclusions

The investigation of molecular behavior in the divertor plasmas is important for establishment of heat and particle control in the tokamak. For attached divertor plasmas, where the electron temperature is high and the molecules

are ionizing, spectroscopy with molecular transport has successfully been applied to studying the behavior of hydrogen and hydrocarbon molecules. However, for the detached divertor plasma, which is attractive for mitigating the severe problem of concentrated power loading of the divertor plates, spectroscopic data have been hardly analyzed quantitatively at present. The detached plasma region, where the temperature is low and plasma volume recombination occurs, is located near an attached divertor plasma region, and the plasma parameter distribution is desired to be measured exactly. Sophisticated models considering more complex molecular reactions such as vibrational excitation are necessary for understanding molecular behavior in the detached divertor plasma. Requirements for molecular data are increasing to facilitate such measurement and analysis.

Acknowledgments

The authors would like to express their thanks to Dr. K.W. Hill of Princeton Plasma Physics Laboratory for reading the manuscript and for useful comments. Distinguished contributions of Dr. T. Shirai of Japan Atomic Energy Research Institute to atomic and molecular data compilation for fusion research are acknowledged.

References

1. P.C. Stangeby: *The Plasma Boundary of Magnetic Fusion Devices* (Institute of Physics Publishing, Bristol Philadelphia 2000)
2. G. Federici, C.H. Skinner, J.N. Brooks, J.P. Coad, C. Grisolia, A.A. Haasz, A. Hassanein, V. Philipps, C.S. Pitcher, J. Roth, W.R. Wampler, D.G. Whyte: Nucl. Fusion **41** 1967 (2001)
3. *ITER Technical Basis*, ITER EDA Documentation Series No. 24 (International Atomic Energy Agency, Vienna 2002)
4. A. Kitsunezaki, M. Shimizu, H. Ninomiya, M. Kuriyama and the JT-60 Team: Fusion Science and Technology **42** 179 (2002)
5. U. Fantz: in this volume
6. D.B. Heifetz: Neutral Particle Transport. In: *Physics of Plasma–Wall Interactions in Controlled Fusion*, ed. by D.E. Post, R. Behrisch (Plenum Press, New York London 1986) pp. 695–772
7. H. Kubo, K. Sawada, H. Takenaga, T. Nakano, S. Kobayashi: H_2 Molecule Spectroscopy in Divertor Plasmas. In: *Review of JT-60U Experimental Results in 2001 and 2002*, JAERI-Review (Japan Atomic Energy Research Institute 2003)
8. H. Kubo, H. Takenaga, K. Sawada, T. Nakano, S. Kobayashi, S. Higashijima, N. Asakura, K. Shimizu: J. Nucl. Mater. (2005) in press
9. D.P. Stotler, C.F.F. Karney: Contrib. Plasma Phys. **34** 392 (1994)
10. K. Sawada, T. Fujimoto: J. Appl. Phys. **78** 2913 (1995)
11. K. Shimizu, K. Itami, H. Kubo, N. Asakura, M. Shimada: J. Nucl. Mater. **196-198** 476 (1992)

12. A. Kumagai, H. Kubo, H. Takenaga, S. Suzuki, K. Shimizu, N. Asakura, M. Shimada: Plasma Phys. Control. Fusion **42** 529 (2000)
13. H. Kubo, T. Sugie, H. Takenaga, S. Higashijima, A. Sakasai: Fusion Engineering and Design **34-35** 277 (1997)
14. H. Kubo, H. Takenaga, T. Sugie, S. Higashijima, S. Suzuki, A. Sakasai, N. Hosogane: Plasma Phys. Control. Fusion **40** 1115 (1998)
15. K. Shimizu, T. Takizuka, A. Sakasai: J. Nucl. Mater. **241-243** 167 (1997)
16. S. Higashijima, H. Kubo, T. Sugie, K. Shimizu, A. Kumagai, A. Sakasai, N. Asakura, S. Sakurai, N. Hosogane, S. Konoshima, H. Tamai, T. Ishijima, H. Takenaga, K. Itami, M. Shimada: J. Nucl. Mater. **266-269** 1078 (1999)
17. T. Nakano, H. Kubo, S. Higashijima, N. Asakura, H. Takenaga, T. Sugie, K. Itami: Nucl. Fusion **42** 689 (2002)
18. G. F. Mathews: J. Nucl. Mater. **220-222** 104 (1995)
19. G. Janeschitz, H.D. Pacher, G. Federici, Yu. Igitkhanov, A. Kukushkin, E. Martin, D. Post, M. Sugihara, R. Tivey, T. Ando, A. Antipenkov, S. Chiocchio, S. Hiroki, P. Ladd, H. Nakamura, R. Parker, K. Schaubel, Divertor Expert Groups for ITER Joint Central Team and Home Teams: ITER Divertor, and Pumping and Fueling System Designs. In: *Fusion Energy 1996*, Vol. 2 (International Atomic Energy Agency, Vienna 1997) pp. 755–767
20. H. Kubo, T. Nakano: Volume Recombination in Divertor Plasmas. In: *Review of JT-60U Experimental Results in 2000*, JAERI-Review 2002-022, (Japan Atomic Energy Research Institute 2002) pp. 118–201
21. N. Ohno, N. Tanaka, N. Ezumi, D. Nishijima, S. Takamura: Contrib. Plasma Phys. **41** 473 (2001)
22. D. Lumma, J.L. Terry, B. Lipschultz: Phys. Plasmas **4** 2555 (1997)
23. A. Ichihara, O. Iwamoto, R.K. Janev: J. Phys. B **33** 4747 (2000)
24. J. M. Wadehro, J.N. Bardsley: Phys. Rev. Lett. **41** 1797 (1978)
25. U. Fantz, D. Reiter, B. Heger, D. Coster: J. Nucl. Mater. **290-293** 367 (2001)
26. R. K. Janev, T. Kato, J. G. Wang: Phys. Plasmas **7**, 4364 (2000)

6 High-Temperature Plasma Edge Diagnostics

A. Pospieszczyk

With contributions by
S. Brezinsek, D. Borodin, M. Brix, A. Huber, A. Kirschner, Ph. Mertens,
V. Philipps, G. Sergienko, B. Schweer, C.C. Chu, J.D. Hey, I.L. Beigman,
L.A. Vainshtein, P.T. Greenland

6.1 Introduction

The plasma edge of a fusion plasma is characterized by both a wide range of variations in the plasma parameters and their steep gradients within a couple of centimeters. For an estimation one may regard the ionization length of hydrogen as a guide for its width in plasmas characterized by $10^{17}\,\mathrm{m}^{-3} < n_\mathrm{e} < 10^{20}\,\mathrm{m}^{-3}$, $1\,\mathrm{eV} < T_\mathrm{e} < 100\,\mathrm{eV}$, $10^{-3}\,n_\mathrm{e} < n_\mathrm{I} < 10^{-1} n_\mathrm{e}$, $n_\mathrm{Ho} \approx 10^{-3} n_\mathrm{e}$. In the last decade of fusion plasma edge research it turned out that this definition had to be refined. The intensive use of divertors in present day tokamaks [1] and the operation in high-density [2] and high-confinement [3] regimes have led to the existence of high-density ($> 10^{20}\,\mathrm{m}^{-3}$) and low temperature ($< 5\,\mathrm{eV}$) plasmas as one can find them in the detached divertor cases [4–6] and MARFEs [7,8]. In addition the neutral particle density (atoms and molecules) can well be in the same order as the electron density and the interaction of those particles can in particular influence the particle balance via specific recombination processes [9]. The resulting processes under these plasma conditions will not be covered in this paper but treated from a broader view point by another chapter in this volume (see U. Fantz). Here we will concentrate on the description of such processes, which take place under ionizing conditions.

These conditions are characterized by a predominant influence of the (energetic) electrons on the recycling/production and transport of both the working gas and the impurities (atoms and molecules). Although many of these processes are known and have been studied intensively in the last decades the growing influence of molecules and high-Z impurities in a carbon surrounding and in high-density plasma regimes, where ultimately the fusion plasmas will operate, has attracted interest and demands further activities in this field of plasma boundary research. Moreover, the introduction of seed impurities either for diagnostic purposes [10] or influencing the radiation properties of the boundary plasma [11] causes additional effort in the study of their behavior with respect to production and transport. High plasma temperatures will result in high sputtering yields, changes in the dissociation chain for molecules from recombination to ionization, changes in the re-deposition, which might increase, and a strong influence on the higher atomic/molecular levels (mixing).

For the measurement of these atomic and molecular properties, as well as the profiles of the electron density $n_e(r)$, temperature $T_e(r)$, and the ion temperature $T_i(r)$, optical detection techniques can be used. These have been considerably improved in the last decade so that a simultaneous detection of a wide wavelength and spatial range by fast and sensitive 2D arrays in combination with highly resolving spectrometers is now possible [12]. This is predominantly important when identical plasma discharges cannot routinely be performed, as is the case in large plasma machines, e.g., JET. Photon fluxes from wall and limiters have now routinely been detected by passive emission spectroscopy for a long time. The properties of an ionizing plasma allow in this case the determination of the respective fluxes via the (density and temperature dependent) ionization rate, which is representative for their influx and total photon emission (see below). However, there is still a big demand for a more accurate interpretation of the measured photon fluxes in terms of particle fluxes – even in the case of radiation from hydrogen. Also, the fluxes of hydrogen and hydrocarbon molecules have turned out to be important quantities for the interpretation of recycling and carbon transport, erosion and deposition. Collisional–radiative models have been developed in recent years for a variety of atoms and even for hydrogen molecules so that the hydrogen, carbon and other impurity fluxes can now be determined with higher accuracy.

The same holds for the determination of $T_e(r)$ and even $n_e(r)$, where the spectroscopy of the radially measured line intensities of injected impurities is

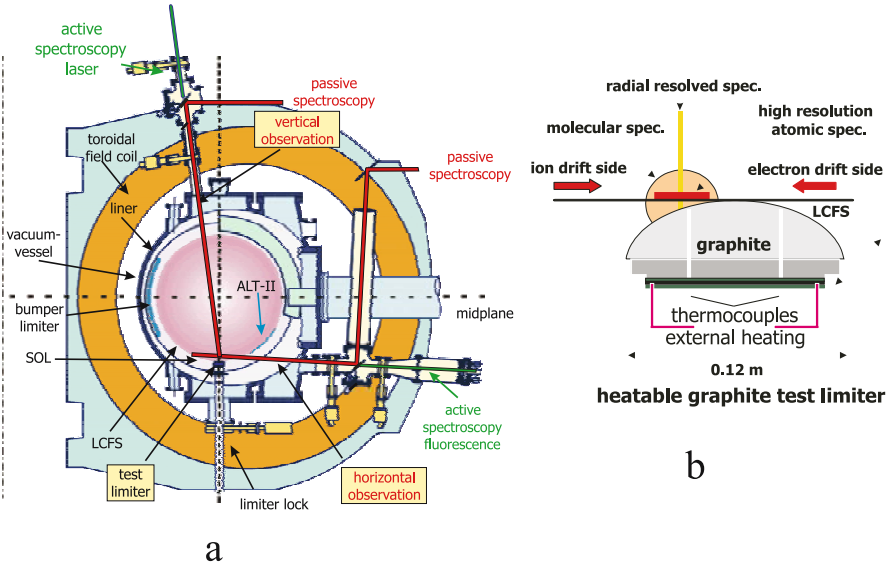

Fig. 6.1. Observation geometry at a limiter lock of TEXTOR (global: **a**), which shows the detailed observation volumes for the different spectroscopic systems (**b**)

accomplished by means of atomic beam methods. Here the use of collisional–radiative models has led to considerable improvements in the interpretation of these kinds of measurements. For the interpretation of the impurity line radiation, collisional–radiative models may also with the help of T_e- and n_e-profiles lead to a more accurate determination of the corresponding fluxes and hence the release mechanisms.

6.2 Techniques and Methods

The following list contains quantities, which can be derived – as a function of time – from spatially resolved spectral line intensity measurements, and the corresponding plasma parameters which can be deduced [16]:

(a) intrinsic impurities

(a1) $I_{\mathrm{tot}}(\lambda) = \int_{t_1,r_1}^{t_2,r_2} I(\lambda,r,t)\mathrm{d}t\mathrm{d}r$ → identification of species (discrimination of different charge states by different penetration depths)

(a2) $I_{\mathrm{tot}}(t) = \int_{\lambda_1,r_1}^{\lambda_2,r_2} I(\lambda,r,t)\mathrm{d}\lambda\mathrm{d}r$ → particle fluxes $\Phi = \Phi(\mathrm{r})$

(a3) $I(\lambda,t) = \int_{r_1}^{r_2} I(\lambda,r,t)\mathrm{d}r$ → velocity distribution (along line-of-sight)

=> particle release mechanisms; B-field; E-field; plasma rotation

(a4) $I(r,t) = \int_{\lambda_1}^{\lambda_2} I(\lambda,r,t)\mathrm{d}\lambda$ → penetration depth

=> velocity distribution (perpendicular to line-of-sight); particle release mechanisms

(b) injected impurities

(b1) $I(\lambda,r,t)$ → B-field; ion temperatures

(b2) $I(r,t) = \int_{\lambda_1}^{\lambda_2} I(\lambda,r,t)\mathrm{d}\lambda$ → penetration depths (perpendicular to line-of-sight);
=> profiles $n_e(r)$, $T_e(r)$ [fluctuations]; transport (confinement times), intrinsic impurity concentrations

6.2.1 Observation Geometries

In order to fulfil the requirements for the measurement of radially ($f(r)$) and spectrally ($g(\lambda)$) resolved measurements in the ionizing part of the boundary plasma good viewing access to wall and limiter components, which define the last close flux surface, is absolutely necessary. An example of such an observation geometry can be seen in Fig. 6.1, where the capabilities of such diagnostics are demonstrated. It shows the arrangement in the sector of one

of the vacuum locks in TEXTOR [13], which is used to bring test limiters and other plasma-facing components (PFCs) from the bottom into the torus. Two ports are directed towards the observation volume in front of the inserted components. One line-of-sight looks at the limiter head from the top, the other one tangentially from the side, in the poloidal direction. Both directions of observation can be equipped according to the needs for atomic spectroscopy with spectrometers of high resolving powers ($\lambda/\Delta\lambda \approx 10^5$) or, alternatively, to record velocity distributions of the flux perpendicular to the limiter surface [14, 15]. To cover the ranges of the molecular emissions, a dedicated spectrometer with medium resolution ($\lambda/\Delta\lambda \approx 10^4$) is used for molecular flux determination and with the goal of assigning rotational and vibrational temperatures to the observed isotopomers. Additional devices include a camera with 2 nm-wide interference filters for the determination of the full 2D-emission pattern at the same location and an additional spectrometer (with $\lambda/\Delta\lambda \approx 8 \times 10^3$) at the tangential port to record spectra *and* penetration depths with a resolution of 0.2 mm. The vacuum lock is quite flexible and allows the insertion of various limiter heads and other PFCs, with active heating and bulk temperature stabilization up to an homogeneous $T = 1500\,\mathrm{K}$ or with holes for gas injection, or even, for calibration purposes, heated gas inlet nozzles at pre-set radial positions.

6.2.2 Evaluation Methods

Figure 6.2 displays the capabilities of such a 3D recording of spectra in the wavelength range $420\,\mathrm{nm} < \lambda < 440\,\mathrm{nm}$ in front of a limiter with the intensity as the third coordinate. One can clearly see the different penetration depth of molecules ($< 15\,\mathrm{mm}$), atoms ($\approx 15\,\mathrm{mm}$) and ions ($> 15\,\mathrm{mm}$). These differences can also serve as identification attributes for charge states or unknown spectral lines. An evaluation according to (a1)–(a4) with one or two coordinates fixed will then yield the corresponding parameters.

One of the most important parameters for the study of the plasma–wall interaction is the determination of the respective fluxes of molecules and atoms from wall and limiter components. The principle has already been outlined in detail in [16], therefore, only a brief summary will be given here.

The line intensity $h\nu$ emitted at a position r from particles $n_\mathrm{A}(r)$ excited by electrons $n_\mathrm{e}(r)$ from the ground state with an excitation rate $< \sigma_\mathrm{Exg} v_\mathrm{e} >$ integrated over the whole emitting volume is given by

$$I_\mathrm{tot} = \Gamma \frac{h\nu}{4\pi} \int_{r_1}^{r_2} n_\mathrm{A}(r)\, n_\mathrm{e}(r)\, \langle \sigma_\mathrm{Exg} v_\mathrm{e} \rangle \, \mathrm{d}r \,. \tag{6.1}$$

The flux $\Phi(r)$ of atoms with a velocity v_A into a plasma integrated over the whole attenuation length, which is assumed to be equivalent to the numbers of ionization events with an ionization rate $\langle \sigma_\mathrm{I} v_\mathrm{e} \rangle$, is governed by the relation:

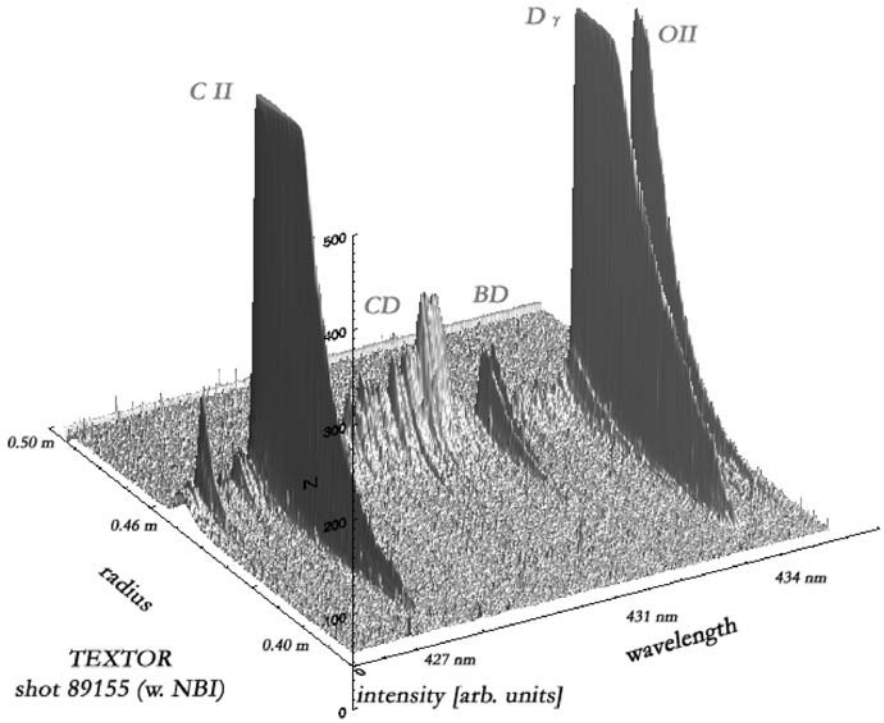

Fig. 6.2. 3D recording of spectra in the wavelength range 420 nm $< \lambda <$ 440 nm in front of a TEXTOR limiter with the intensity as the third coordinate

$$\Phi_{\mathrm{A}} = \int_{r_1}^{r_2} n_{\mathrm{A}}(r)\, n_{\mathrm{e}}(r)\, \langle \sigma_{\mathrm{I}} v_{\mathrm{e}} \rangle \, \mathrm{d}r \,. \tag{6.2}$$

By taking the ratio of both expressions, one obtains a formula, which in the case of an ionizing plasma couples the particle flux to the spatially integrated line emission from that element, provided that the ratio $\langle \sigma_{\mathrm{I}} v_{\mathrm{e}} \rangle / \langle \sigma_{\mathrm{Exg}} v_{\mathrm{e}} \rangle$ is not strongly temperature or density dependent:

$$\Phi_{\mathrm{A}} = \frac{4\pi}{\Gamma} \frac{I_{\mathrm{tot}}}{h\nu} \frac{\langle \sigma_{\mathrm{I}} v_{\mathrm{e}} \rangle}{\langle \sigma_{\mathrm{Exg}} v_{\mathrm{e}} \rangle} = 4\pi \frac{I_{\mathrm{tot}}}{h\nu} \frac{S}{XB} \,. \tag{6.3}$$

Thus, with knowledge of the factor S/XB, which $S \equiv \langle \sigma_{\mathrm{I}} v_{\mathrm{e}} \rangle$, $X \equiv \langle \sigma_{\mathrm{Exg}} v_{\mathrm{e}} \rangle$, and $B \equiv \Gamma$, the photon fluxes can be converted into particle fluxes. In general terms the excitation rate X can be replaced by a population rate provided by a collisional–radiative model, which treats the excitation and de-excitation from all possible levels into the emitting one. The same holds for all possible ionization processes. In the case of molecules not only ionization but also dissociation will play a significant role, and, therefore, the ionization rate S

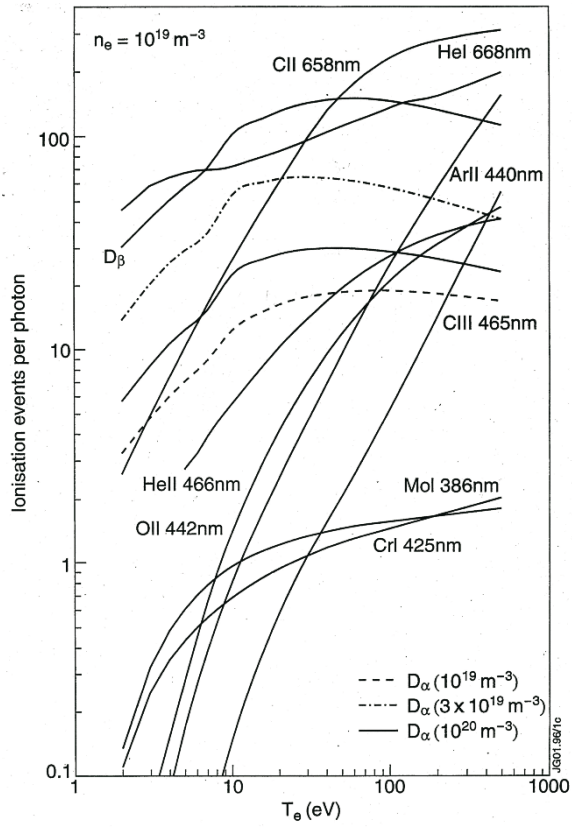

Fig. 6.3. Ionization events per photon for several fusion relevant atoms and ions (from [24])

is replaced by a decay rate D, and the conversion factor is named D/XB accordingly. Collisional–radiative models for hydrogen molecules have also recently become available (see below), which makes the determination of molecular hydrogen fluxes possible and will lead to a more perfect description of the recycling processes.

In the data bank ADAS (**A**tomic **D**ata **A**nalysis **S**tructure) [23, 24] one can find S/XB-values for some important elements and lines, e.g., hydrogen, helium, beryllium, carbon, nitrogen, oxygen, neon, chromium, and molybdenum. However, there is still a lack of values for significant impurities with a number of their ionization states, e.g., neutral neon, silicon, tungsten, etc. (see below). A more elaborate version of the graph shown in [16] is provided in Fig. 6.3, which already contains improved numbers for CrI, MoI and D_α for different densities.

In the case where neither rates and/or models are available for the conversion factor *S(D)/XB* it can, in favorable cases, be determined experimentally by injecting a known number of particles into a well-diagnosed plasma via, for example, laser-blow-off [17] or gases. The respective *S(D)/XB* can then be evaluated by reversing (6.3):

$$\frac{\langle \sigma_{\mathrm{I}} v_{\mathrm{e}} \rangle}{\Gamma \langle \sigma_{\mathrm{Exg}} v_{\mathrm{e}} \rangle} = \frac{\Phi_{\mathrm{A}}}{4\pi \left(I_{\mathrm{tot}} / h\nu \right)} \,. \tag{6.4}$$

Another important quantity, which can serve for the determination of flows and (ion)-temperatures, for example, is the line shape of the emission lines from the working gas and impurities. Plasma movements and rotations can be derived from

$$\Delta\lambda = \lambda - \lambda_0 = \frac{v}{c}\lambda_0 \,, \tag{6.5}$$

where c is the speed of light. For $v = 10^4\,\mathrm{m/s}$ a resolution of $\lambda/\Delta\lambda > 10^4$ is needed, which can only be accomplished at large wavelengths, i.e., in the visible wavelength region. The line width itself is used for the determination of impurity and ion temperatures via

$$\Delta\lambda = \frac{(2k \ln 2)^{1/2}}{c} \sqrt{\frac{T}{M}} \lambda_0 = 7.16 \times 10^{-7} \sqrt{\frac{T}{M}} \lambda_0 \,. \tag{6.6}$$

6.3 Results

6.3.1 Relevant Elements

Table 6.1 displays the most important elements which play a role in present fusion research:

Table 6.1.

Working gas	**H, D, H_2, D_2,** T_2, TD**,** (He)
Wall constituents	**B**, Be, **C**, **Si**, Cr, Fe, Ni, **Mo**, Ta, (V), **W**
Reaction Products	**O**, CO, $\mathbf{C}_x\mathbf{H}_y$, HD, $\mathrm{Si}_x\mathrm{H}_y$, carbides, oxides
Diagnostics	$\mathbf{H_2/D_2}$, **He**, Li, F, Na, Mg, Al, Ar, Xe
Radiation cooling	N, **Ne**, Ar, **Si**, Kr

It is out of the scope of this paper to address all the elements noticed. Therefore, only those marked in bold letters in Table 6.1 will be discussed in more detail in the following paragraphs.

6.3.2 Carbon

Besides the working gas hydrogen, carbon is presently the most interesting element in fusion plasma research. Nearly all present day larger fusion experiments contain carbon both as wall and divertor/limiter material, as it reduces the oxygen level and shows favorable properties against high heat loads. Therefore, it is vital to study its erosion, deposition, flow and migration within the vessel. This is the more important as redeposited carbon layers are very hydrogen rich (H/C ≈ 0.4 [18]), which could be a major problem for a fusion reactor with an undesired high tritium wall inventory.

In order to identify the location of the carbon sources, Zeeman spectroscopy has turned out to be a valuable tool. The principles of the influence of the magnetic field on carbon and oxygen ions in the fusion edge plasma ($B \cong 1$ to 10 T) have been outlined in [19,20]. The method works well when the Zeeman (Paschen–Back) effect plays an important, or dominant, role in relation to other broadening mechanisms. In general the line splitting is given by:

$$\Delta\lambda = \frac{eB}{4\pi m_e c}\lambda^2 \left(M_1 g_1 - M_2 g_2\right), \quad \text{with} \quad g = 1 + \frac{J\left(J+1\right) + S\left(S+1\right) - L\left(L+1\right)}{2J\left(J+1\right)}$$

as the Landé factor in LS coupling.

In Fig. 6.4 a relatively simple Zeeman spectrum from a CIII multiplet in TEXTOR is shown [21]. Because the observation is roughly tangential to the magnetic flux surfaces, only the σ components contribute considerably. The very characteristic shape of this multiplet (note that the contribution of oxygen ions can additionally be detected in this range) also allows the discrimination of carbon sources from locations with strongly different magnetic fields as it has been worked out in JET [22]. In Fig. 6.5 the effect of two CIII-emissions from different fields on the resulting spectrum is demonstrated (note that an additional π component appears because of the observation perpendicular to the magnetic field). While in the left-hand part of Fig. 6.5 the contributions from low and high field were assumed to be equal, in the right-hand part the relative amount of the low field component was varied from 0.2 to 5.0. These differences in the line shape served for the determination of the CIII–distribution between inner and outer scrape-off layer from the experimental spectra.

In the ADAS data bank [23, 24] one can find further spectral transitions. The so-called "*X-Paschen*" program, which was brought in as module 603, allows us to display the Zeeman pattern for a variety of elements like BII, BeI-III, CI-V, HeI, OI, KrI, MgII, NaI, CaI-II, NeI-II, SiI-IV, and 60 lines from 115 nm to 910 nm. The variation of the pattern can be studied for different T_i, B, field direction, observation angle, and apparatus function.

High-resolution spectroscopy on carbon (and its hydrocarbon radical derivatives) has been performed in the divertor of DIII-D [25, 26]. In [25] ion temperatures for CII, and CIII have been measured under various conditions and found to be usually in the range of 4–20 eV. Velocities determined from

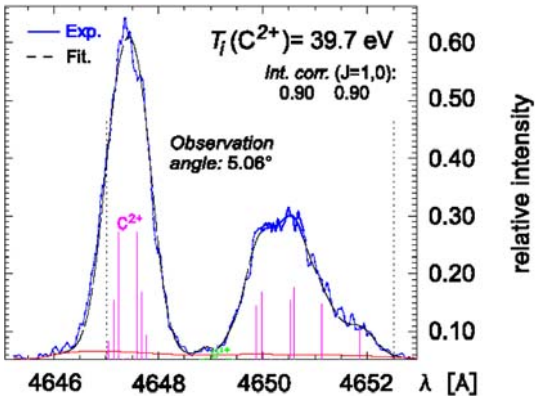

Fig. 6.4. Zeeman spectrum of a CIII multiplet in TEXTOR for $B = 1.79\,\mathrm{T}$ under longitudinal observation (from [21])

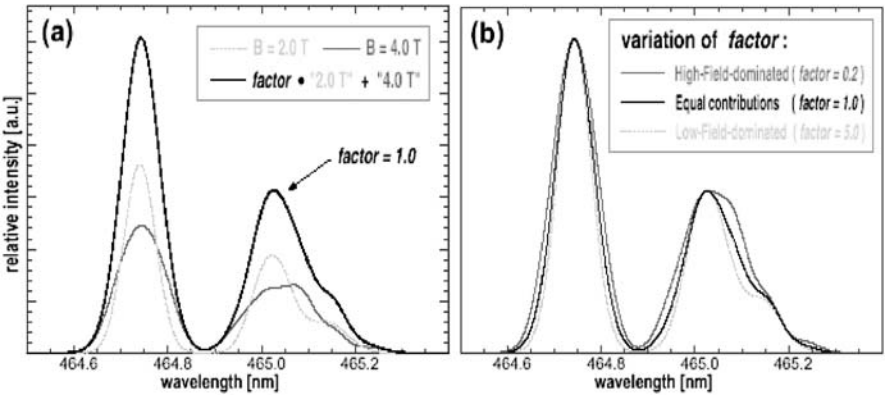

Fig. 6.5. (**a**) Spectral Line Shapes for $B = 2.0\,\mathrm{T}$ (*dotted grey line*) and $B = 4.0\,\mathrm{T}$ (*thin dark grey line*) and resulting spectrum for equal contributions (factor = 1.0, *thick black line*). (**b**) Resulting spectra for varying contributions (factor = 0.2, 1.0, 5.0) from low field ($B = 2.0\,\mathrm{T}$); normalized to maximum of each spectrum (assumption: $T = 5\,\mathrm{eV}$)

Doppler shifts indicate flows from $3 \times 10^3\,\mathrm{m/s}$ to $1.5 \times 10^4\,\mathrm{m/s}$ in the outer and $1 \times 10^4\mathrm{m/s}$ to $3.5 \times 10^4\,\mathrm{m/s}$ in the inner leg, indicating a flow reversal in the outer leg. Such measurements can strongly help to elucidate the transport of wall materials into the divertor chamber. The atomic temperatures found in [26] are typically 1.1 eV, as expected from molecular dissociation, which is one of the main channels for carbon sources in the divertor.

Because carbon can practically be found everywhere in graphite-containing fusion devices, the presence of highly charged ions (C^{6+}) in the boundary layer offers an interesting diagnostic tool for ion temperature measurements in front of neutral-hydrogen-emitting PFCs [21]. Excited hydrogen atoms un-

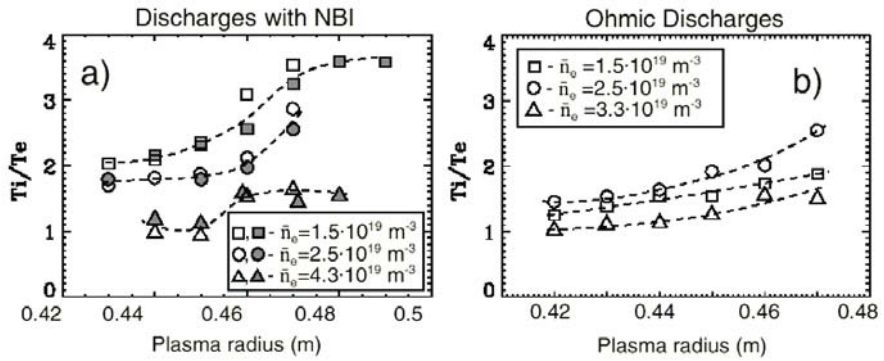

Fig. 6.6. The $T_\mathrm{i}/T_\mathrm{e}$ ratio as a function of the plasma radius for beam heated (**a**) and ohmically heated (**b**) discharges at different line-averaged electron densities. The *open* and *full symbols* show the $T_\mathrm{i}/T_\mathrm{e}$ ratio measured by means of different spectrometers

dergo very effective charge exchange with the ions mentioned, which results in easily observable radiation from CVI at 520 nm, which stems from highly excited levels ($n = 8 \rightarrow 7$). As the highly charged ions are very representative for the ion temperature at the radial position of emission, ion temperature profiles can well be determined in front of hydrogen atom sources. Figure 6.6 displays the ratio of $T_\mathrm{i}(r)/T_\mathrm{e}(r)$ determined by this procedure in front of a TEXTOR limiter [27]; the expected result shows a growing ratio with larger radii and increased heating power, which should be taken into account for plasma boundary modeling purposes.

6.3.3 Hydrocarbons

A reliable determination of hydrocarbon fluxes is a vital task since the introduction of carbon as a PFC in fusion plasma devices. However, what looked promising after the work of [16, 28] has turned out to be a real nightmare in plasma–wall interaction research. A taste of that is seen in Fig. 6.7 where the dependence of chemical erosion yields evaluated in different devices on ion flux density is plotted using the published D/XB-values for CD. Even stronger discrepancies from the general trend have been reported in [29, 30].

The reasons for these discrepancies are still unclear – there might be stronger varying rates with density and temperature than published, problems in the molecular physics, and last but not least, influences from the emitting surfaces themselves on the measured molecular bands. Therefore, a clarification of the quantities used is urgently necessary as follows:

(a) The molecular emission within one electronic transition is in general distributed over several 10 nm. Thus a confinement to a specific band is necessary or else a model which allows the extrapolation of the measured into

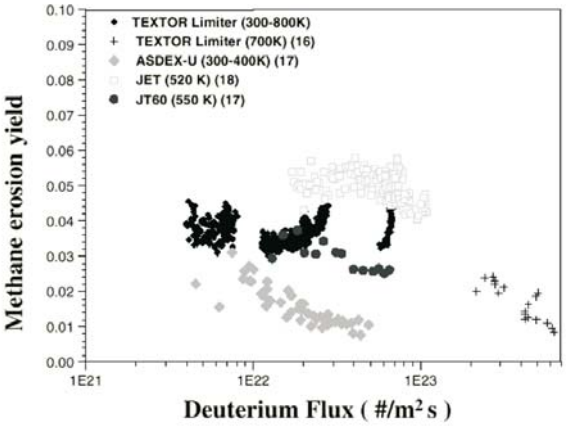

Fig. 6.7. Chemical erosion yields evaluated in different devices depending on ion flux density

the non-measured lines (see also Sect.6.3.4 on hydrogen). This requires a knowledge of the some molecular temperatures (T_{rot} and T_{vib}). In [16] it was assumed from former measurements that in the case of CD/H these do not change considerably within a band of 1.5 nm ($T_{rot} \approx 3500$ K). For extreme density and temperature cases this might not be longer valid and result in different intensities for the same fluxes.

(b) The dissociation chain from CD_4 to CD [31] might be influenced by both the plasma electrons (high temperatures will favor the path via molecular ions, low temperatures via neutrals) and the condition of the starting molecule from the surface. The latter may already be in an excited state, which leads into different dissociation channels.

(c) Carbon surfaces can release re-deposited carbon very effectively so that a high CD photon flux is not necessarily connected to a high net carbon flux. Also higher hydrocarbons than CD as C_xD_y (with $x \geq 2$) will contribute to the chemical erosion. This, however, can be checked by simultaneous observation of the Swan bands of C_2 in the 500 nm range [28].

All the arguments listed and the fact that CD is the last molecular radical in the chain will probably lead to such variations as those shown in Fig. 6.7. An example for the variation of D/XB for growing ion fluxes (i.e., higher densities and smaller temperatures) is given in Fig. 6.8 [32]. This is in some contradiction to that published in [16, 33], where an opposite behavior was found in pure gas blow experiments. A plausible explanation for these findings might lie in the influence of the graphite surface, which acts as an additional moderator on the CD-emission. This is to our knowledge the first time that atomic and/or molecular rates have been coupled to a third party, which is

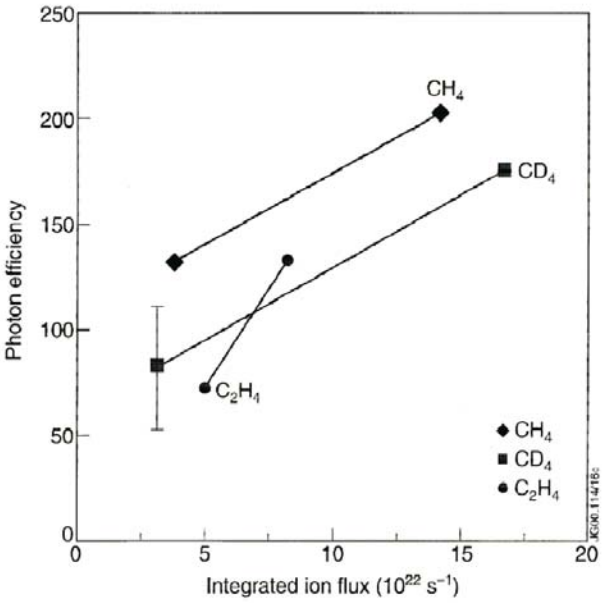

Fig. 6.8. Hydrocarbon photon efficiencies as a function of integrated ion flux to the JET outer divertor

not pure atomic or electronic and is not the usual way it has been treated in the past and needs special attention and caution in interpretation.

This is also true for comparisons of such rates calculated via erosion and deposition codes (e.g., ERO-TEXTOR [34,35]) with those measured. Not only should the conditions under which both values are derived be compatible, but also the spectroscopic ranges for observation should be identical, which they are not in most cases. For practical reasons the measurements only cover a limited spectral range, which would lead to a strong underestimation of the chemically released flux, if the numbers from the ERO-model are used. This is illustrated in Fig. 6.9, where D/XB-values for CD from CD_4 have been calculated under the assumption of no friction, no diffusion, no electrical field and no re-deposition (no surface !). Therefore, only the influence of rate coefficients such as in a pure gas blow can be seen [36]. A comparison with Fig. 6.9 in [16] yields a factor of about 3 by which the chemical fluxes from spectroscopy will be underestimated. However, a full treatment with the latest values for the reaction chain [37,38] for a graphite surface and recycling with non-zero sticking values would lead to values a factor of 10 larger than those in Fig. 6.9. All these arguments will be treated in more detail in [39].

Presently there seems to be only one way out of the dilemma. As emission spectroscopy is mainly restricted to the visible wavelength region where only a few molecules (like CD or C_2) are detectable, one has to find a possibility

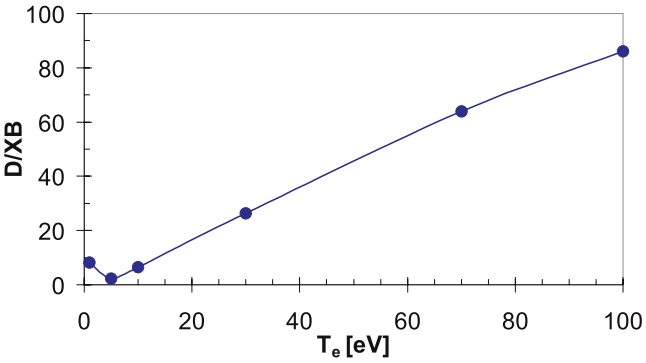

Fig. 6.9. *D/XB*-values for CD from CD_4 under the simplifying assumptions for the simulation of a pure gas blow

to detect more members of the dissociation chain independently. This can be achieved by absorption spectroscopy, where both a wide wavelength region is accessible (up to 20 µm) and the expected source molecules and break-up products are detectable (CD_4, CD_3, etc.). The principles of this method are outlined in [40]. A diode laser for this specific wavelength region is required, which provides a high sensitivity due to the low expected densities ($n_{CH_4} \sim 10^{18}\,m^{-3}$, $n_{CH_3} \sim 10^{17}\,m^{-3}$ for an absorption path of about 1.0 m). This can easily be achieved with a multipass observation system in laboratory experiments, but needs some sophisticated observation geometry in toroidal geometry.

6.3.4 Hydrogen/Deuterium

Although the diagnostics of hydrogen seems to be a relatively simple task, it is complicated by the fact that it is partly both fuelled and released from plasma-facing components as molecules. These molecules will be dissociated and the resulting atoms can heavily influence the boundary plasma, especially through their penetration depth, and, indirectly, the plasma and its confinement properties as a whole. Recent experiments on different tokamaks have brought to light the deep interdependence between atomic and molecular species in this respect, e.g., [41]. One of the most striking results was the detection of hydrogen and deuterium atoms with extremely low energies, definitely below 1 eV [20], which gave information on release processes where molecules are involved. Chapter 4 in this volume is completely devoted to the diagnostics and processes of hydrogen in low-temperature plasmas, which can be found, for example, in divertors and detached plasma regimes [9], this chapter will only deal with the interaction of hydrogen in front of limiters and hot surfaces.

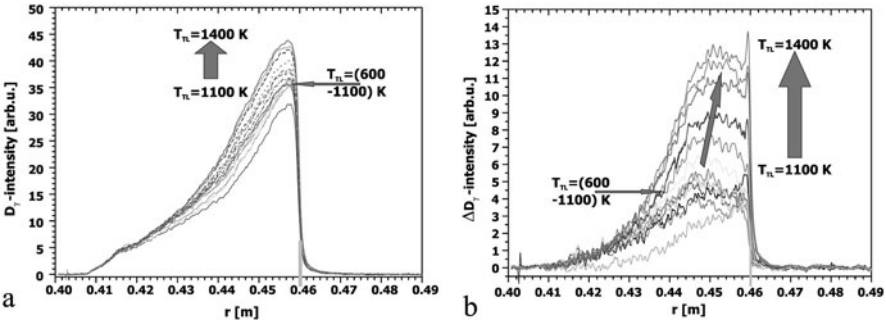

Fig. 6.10. (**a**) Variation of the penetration depth of atomic deuterium in the light of D_γ as a function of the limiter temperature. (**b**) Differences of the D_γ–light between cold and heated limiters

Figure 6.10 shows the decreasing (!) penetration depth of atoms in front of a heated graphite surface. In [41, 42] it was shown by monitoring the molecular emission from the Fulcher-α band ($3p\,^3\Pi_u - > 2s\,^3\Sigma_g^+$) that the reason for this change is the reduction of formation of hydrogen/deuterium molecules for temperatures higher than 1100 K as already seen in laboratory experiments [43]. Above that temperature the composition of the release mechanisms obviously changes. From the reduced penetration depth and line width measurements of D_γ [44, 45] one can deduce a reduction of the energy of the atoms down to 0.18 eV at $T = 1400$ K. More atoms are released from the surface, and these are colder on average. It is reasonable to assume that at temperatures where the hydrogen is only released via atoms – these could not be reached by external heating in this experiment – this happens with thermal energies of the emitting surface.

Simultaneously the intensity of the atomic Balmer lines (in this case D_γ) increases by nearly a factor of two. Thus, in the presence of molecules it obviously turns out that corrections to the estimated hydrogen flux may be required in such a form that the atomic S/XB (which is about 15 for densities 10^{18}–$10^{19}\,\mathrm{m}^{-3}$ and temperatures above 15 eV) is replaced by an effective one, which is determined by the molecular deuterium flux Γ_{D_2}:

$$(S/XB)_{\mathrm{eff}} = S/XB\left(1 + \frac{2\eta\Gamma_{D_2}}{\Gamma^{\mathrm{tot}}}\right). \tag{6.7}$$

The factor η accounts for the number of emitted Balmer-α photons per molecule, which involves the type of dissociation process. $\eta = 1$ holds for dissociative excitation with the products $D^0(n = 3) + D^0(1s)$, i.e., only one atom will directly emit Balmer-α radiation whereas the other is set free already as a proton. In the worst case of a pure molecular flux the total deuterium flux would be underestimated by a factor of 2 by determining it from the Balmer-line emissions solely. More details concerning the energies of the dissociated atoms and accompanying heating mechanisms can be found in [46] and below.

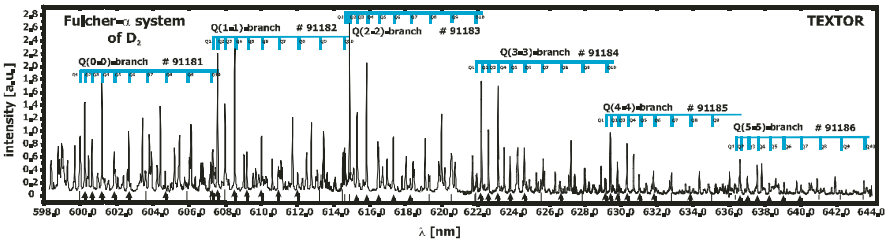

Fig. 6.11. The Fulcher-band system of D_2 observed in front of a gas inlet. The *first lines* of each Q-branch of the visible diagonal transitions are marked (#91181-86)

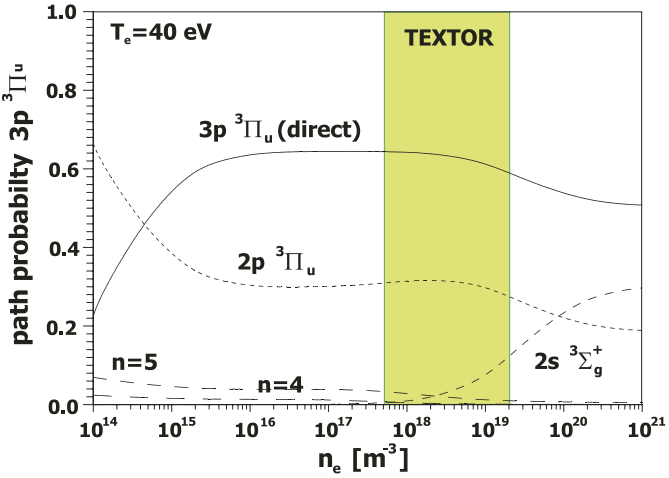

Fig. 6.12. Path population of the $3p\ ^3\Pi_u$ state (direct means: population of that level directly from the ground state)

An important task is of course a quantitative determination of the contributing molecular to the atomic flux. This requires the knowledge of the full population of the upper Fulcher-α state ($3p\ ^3\Pi_u$). In practice it will in most cases not be possible to measure all rotational and vibrational bands with a high resolution spectrometer. Figure 6.11 displays such a spectrum from which a rotational temperature of $T_{rot} = 500\,K$ and a vibrational temperature of $T_{vib} = 5000\,K$ for the molecular ground-state $1s\ ^1\Sigma_g^+$ was deduced. The procedure to obtain the latter is described in more detail in [47]. With these temperatures it is then possible to add lines, which could not be directly measured.

In order to convert the photons into molecular fluxes the D/XB-value for the Fulcher-α band is needed. For this purpose a collisional–radiative model (CRM) has been set up which includes all levels that could contribute to the population of the $3p\ ^3\Pi_u$ state. Figure 6.12 shows that under the conditions of the TEXTOR scrape-off layer the levels $2p\ ^3\Pi_u$ and $2s\ ^3\Sigma_g^+$ also contribute to

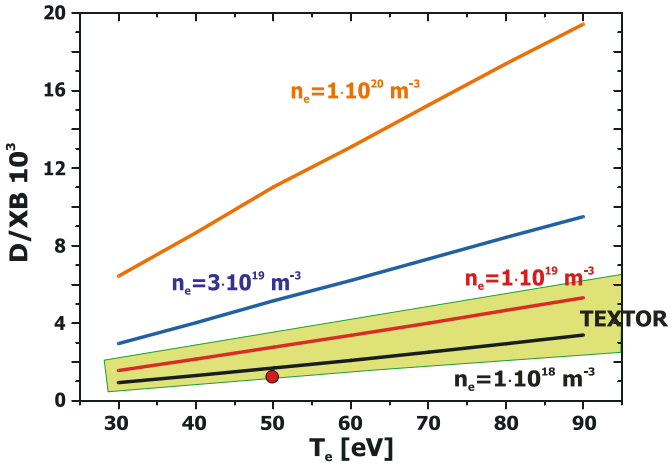

Fig. 6.13. Calculations of D/XB for the Fulcher-band from the collisional–radiative model CRMOL. The *solid dot* is an experimentally obtained value via a calibrated gas blow

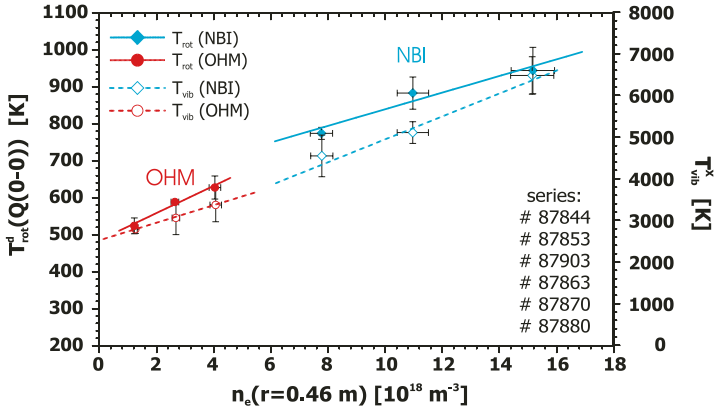

Fig. 6.14. Variation of T_{rot} and T_{vib} as a function of n_e

the direct excitation path from the ground state. The result of the CRM can be seen in Fig. 6.13 with both the operation regime for TEXTOR indicated (shadowed area) and an experimental value obtained by a calibrated D_2-gas blow, which fits well onto the respective curve. In all experiments carried out on TEXTOR so far, a high fraction of molecular deuterium has been detected in the case of high-density discharges. More experimental results and a detailed description of the procedure can be found in [48].

Actually under the conditions of a hot boundary plasma the two temperatures T_{rot} and T_{vib} are not independent of each other. Figure 6.14 shows that both temperatures are proportional to each other for a variety of different

boundary electron densities. This coupling considerably reduces the effort to model the full Fulcher emission spectrum. In the case of a restricted wavelength range it is in principle sufficient to use only the vibrational population of the $3p\,{}^3\Pi_u$ state and the intensity of one Q-branch. Another interesting diagnostic capability is offered by the density dependence of the temperatures. At locations which are not accessible for electron density measurements by, for example, probes or diagnostic beams but are a source of molecular deuterium it is now possible to determine n_e by measuring the rotational temperature of the molecules with sufficient spatial resolution because the molecules are normally very localized sources.

6.3.5 Low-Z Impurities: Oxygen

The most direct way to determine the total flux of oxygen into the plasma is to use the diagnostics based on OI spectral lines. However, all OI lines in the visible range are very weak or blended with OII or other impurity lines. The strongest lines in the IR range ($2s^2\,2p^3[^4S]3s$–$2s^2\,2p^3[^4S]3p$) can be strongly influenced by continuum radiation, because limiters and even the liner can become hot. A way out of this dilemma is to use the OII lines instead. A conventional choice are the $2p^2\,[^3P]3s\,{}^4P$–$2p^2\,[^3P]3p^4D$ lines of OII around 441 nm in the blue visible wavelength range (which is less influenced by the black-body radiation). For these lines *S/XB*-values have already been reported in [16]. These and some other lines in this wavelength range have recently been measured in the boundary plasma of TEXTOR after the injection of oxygen-containing molecules near the last closed flux surface (LCFS). Several OII multiplets were identified and found to be suitable for evaluation. An appropriate CRM was developed on the base of the 'GKU' code. The atomic data (rate coefficients, radiative probabilities, etc.) were calculated by the code 'ATOM' using the K-matrix (KM) method [49].

Figure 6.15 displays the *S/XB*-values measured and modeled for a number of lines, experimental conditions and injected gases (O_2, CO, CO_2). The lines applicable for an interference filter diagnostic should be rather strong and isolated (a convenient filter transmission 'window' is about 3.0 nm). The a4P–b4S lines 371.2 and 372.7 nm between quartet states satisfy these conditions; however, they lie in the near-UV spectral region. The a2P–b2D lines 441.5 nm and 441.7 nm of the doublet system, which are often used in plasma boundary diagnostics, also satisfy the conditions, but they have a dependence on the populations of the meta-stable 2D and 2P levels of the ground configuration! In principle it is possible to use the a4P–b4P lines 431.7 nm and 431.9 nm; however, they are rather weak. Thus, a combination of the a4P–b4S and a2P–b2D lines seems to be the preferred choice.

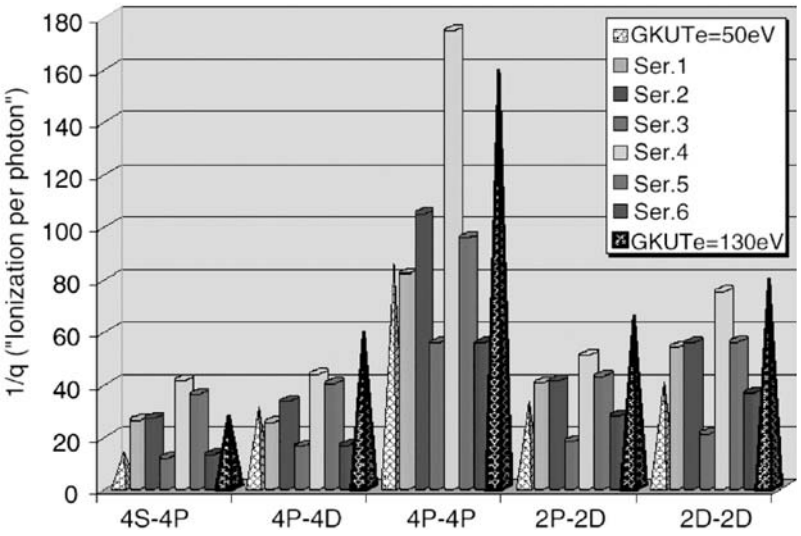

Fig. 6.15. S/XB values measured and modeled for a number of lines, experimental conditions and injected gases (O_2 (Ser. 1), CO (Ser. 2,3), CO_2(Ser. 4,5,6)). The experimental values are framed by GKU-code calculations respectively

6.3.6 Medium-Z Impurities: Neon and Silicon

The two elements neon and silicon have been used in the past for radiation cooling of the plasma boundary in order to remove energy from the particles impinging on the vessel walls by converting it into radiation. Thus, the erosion of the PFCs is minimized and the influx of material into the core plasma reduced. Neon is very easy to apply as it is a noble gas and not stored in the walls so that its recycling can easily be controlled. However, the present spectroscopic situation for neon is by no means satisfactory; this is especially true for the atoms. Neither gas injection experiments nor modeling have so far lead to relevant data. There are several reasons for this. The ionization potential of neutral neon is still high (19 eV) so that it is difficult to detect the injected gas over the whole attenuation range both in plasma simulators and under constant fusion boundary conditions. Secondly, the modeling can no longer be treated in LS-coupling, but an JL intermediate coupling case has to be applied. This makes it difficult to attribute the correct contributions from all possible levels. Therefore, even the most simple cases like line ratios from the singlet to the triplet states show opposite trends in experiments and modelling. ADAS provides *S/XB* data for lines in the triplet system, but they all lie above 600 nm and have weak intensities so that they cannot be used routinely for standard flux measurements.

Silicon is normally applied via glow discharges or the injection of silane (SiH_4). As silicon is non recycling and sticks on the PFCs, a more or less continuous getter effect for oxygen will result. However, this is not so easily

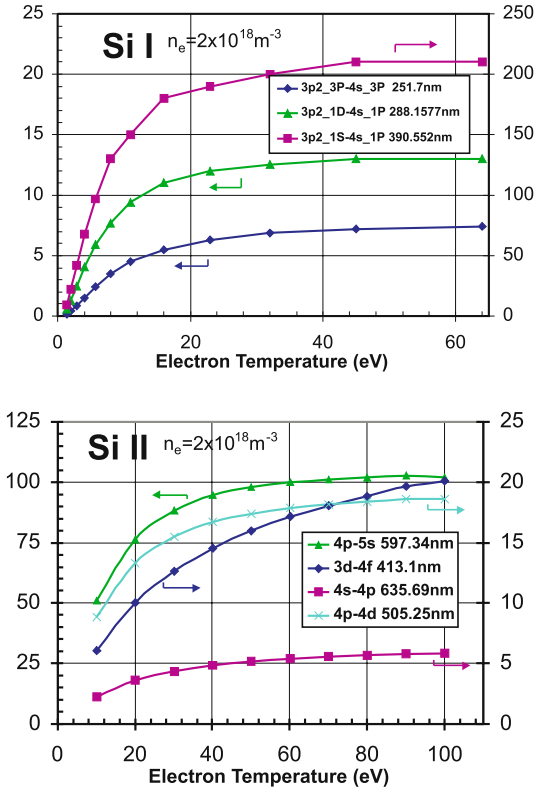

Fig. 6.16. Ionization events per photon (S/XB) for several SiII- and SiIII-emissions lines for an electron density of $2.0 \times 10^{18}\,\mathrm{m}^{-3}$

manageable as in the case of neon and, therefore, a knowledge about the silicon fluxes is vital. Concerning the atomic data the situation is a bit better than for neon. On TEXTOR lines from both neutrals and singly charged ions have been quantitatively measured and modeled by the GKU-code. In Fig. 6.16 the temperature dependence of the calculated S/XB-values are plotted for SiII and SiIII and a fixed density. The values for SiII do not show a strong temperature dependence but lie unfortunately mostly outside the visible part of the spectrum. Therefore, a determination of the Si-flux via SiIII seems to be the more attractive choice. The experimental values agree very well with the calculated ones so that silicon fluxes should now reliably be obtained by spectroscopic methods. A detailed description of these calibration measurements and the related models can be found in [50].

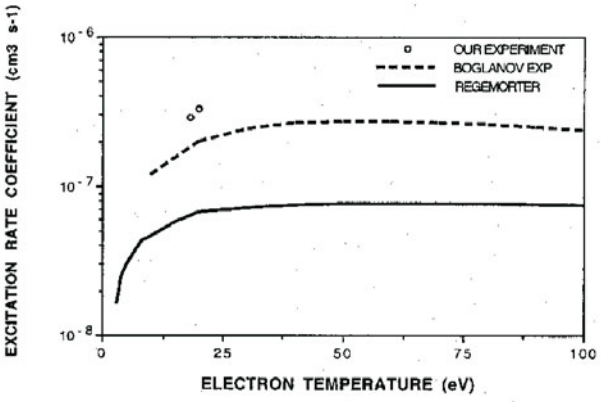

Fig. 6.17. Excitation rate coefficient for the MoI (379.8 nm) transition as a function of electron temperature

6.3.7 High-Z Impurities: Molybdenum and Tungsten

The use of high-Z impurities as PFCs has not been favored for a long time as the radiation from only a small number of these elements in the plasma center will inevitably lead to a disruption of the discharge. Since very effective plasma heating in the MW-range can be applied, the transport of these impurities into the center is successfully suppressed [51, 52] and their use is already foreseen again as baffle and liner material for ITER. The main advantage of molybdenum and tungsten is their high melting point and low erosion yield for the working gas, which results in a reduced particle flow. Full metal tokamaks – preferably with molybdenum – have already been in operation for nearly a decade and work without major impurity problems [53, 54].

Initially the molybdenum fluxes in [55] measured via atomic Mo-lines (379.8 nm, 386.4 nm and 390.3 nm) led to unreasonably high flux values. This was the case because for the calculation of the respective excitation rates the formula of van Regemorter was used [56], as these lines are optically coupled to the ground state (resonance lines). Therefore, experiments were performed to measure the excitation and ionization rates directly both in a linear plasma machine [57] and in a crossed beam experiment with a thermal molybdenum emitter [58]. The results can be seen in Fig. 6.17 and show that the experimental values for excitation are about a factor of 5 larger than those from the van Regemorter formula, which leads to a reduction of the flux by the same order according to the smaller S/XB. More refined R-Matrix calculations have later confirmed the same factor and are included in Fig. 6.3.

Tungsten is presently one of the favorite metals for a PFC in a fusion reactor as it even exceeds the properties of molybdenum concerning melting and sputtering. In [59] the inner wall and divertor were covered with tungsten-coated carbon tiles without a serious confinement in plasma opera-

tion. Although neutral tungsten reveals some very remarked emission lines in the visible spectral range (400.8 nm, 429.0 nm, 429.7 nm) no calculations for excitation rates have been performed so far because of the complexity of the atomic level structure. The only *S/XB*-values for the lines above have been obtained experimentally, both in a linear plasma machine with a metal W-target and a thermal tungsten emitter from an organic compound ($W(CO)_6$) in ASDEX Upgrade [60].

6.3.8 Atomic Helium Beams

Since about 10 years ago (thermal) helium beams have been used for the diagnostics of fusion boundary plasmas as they can penetrate relatively far because of the high ionization potential of the atoms (nearly 25 eV) [61, 62]. From the line ratios of the triplet and singlet lines one can derive local electron temperatures and densities (Fig. 6.18) provided the population rates and their equipartition times are known and allow the application of a steady state model [63]. The corresponding rates have been improved during the last few years, and although it is now a well-established technique, there are still open questions and scope for future developments.

The influence of high–n shells, electron loss processes and level mixing should be further investigated. Also, the line emission from the $n = 5$ (4, 3) levels should additionally be measured and compared with the model. In ADAS there should be an update of the He adf04 data set with respect to ionization, excitation, charge exchange, and $n = 5$ contributions. As the

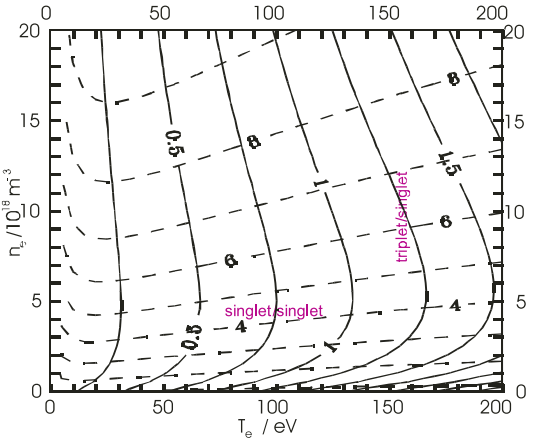

Fig. 6.18. Calculated line intensity ratios of He for the determination of electron density and temperature. The *dashed line* represents the ratio of the transitions at 668 nm (2^1P–3^1D) and 728 nm (2^1P–3^1S), which is n_e-sensitive. The *solid line* stands for the ratio of the transitions at 728 nm and 706 nm (2^3P–3^3S), which is used for the determination of T_e

Table 6.2. Availability of rates, CRMs and recommendations for atoms

Species	ionizat. rates	excitat. rates	coll.rad. models	remarks
H, D	+	+	+	ionizations/photon for H_α, H_β, H_γ for edge plasmas available; more data needed for CEX (Ne,Si,B,...)
He	+	+	+	reliable profile measurements for T_e and n_e with thermal He-beams possible; ionizations/photon for HeII and CRM available; more data needed for CEX (Ne,Si,B,...) and proton collisions; high $n(>3)$?
Li	+	+	+	reliable profile measurements for n_e with thermal, suprathermal, and high energy Li-beams possible; data for n_e-dependence of the ionization rate for LiI OK
B	+	+	+	check of the excitation rates needed (discrepancies); n_e-dependence?
Be	+	+	+	extensive data set (JET)
C	+	+	+	no bright atomic lines in the visible; rates and n_e-dependence OK
O	+	+	+	no bright atomic lines in the visible; rates and n_e-dependence OK
Ne	(−)	(o)	(+)	candidate for radiation cooling with recycling; excitation rates needed
Mg	(+)	(−)	−	candidate for radiation cooling with no recycling; excitation rates needed
Al	(+)	o	−	candidate for radiation cooling with no recycling;
Si	(+)	+	−	candidate for radiation cooling with no recycling;
Ar	(+)	+	+	candidate for radiation cooling with recycling;
Mo	+	+	+	candidate for wall material;
Ta	+	−o	−	candidate for wall material with strong recycling;
W	(+)	(+)	−	candidate for wall and divertor

beams penetrate into relatively high-density plasmas, the influence of high optical depth, step processes, and heavy particle collisions [e.g., from protons] should be studied. The latter effect has already partly been treated by [64]. This should enlarge the range of applications considerably beyond the pure influence of electron collisions. Concerning further developments with fast diagnostic He-beams (1 keV), which would provide an even larger spatial diagnostic capability, one has to solve the problem of the population of meta-

Table 6.3. Availability of rates, CRM and recommendations for molecules

Species	ionizat. rates	excitat. rates	coll.rad. models	remarks
H_2, D_2, HD	+	+	+	Bands near carbon walls, limiters & divertors identified; excitation rates for bands in the visible available, CRM for the Fulcher-band exists; other bands may be useful
(CH_4, CD_4)	+	(o)	−	Bands of radicals (CH, CH_2,...) near carbon walls, limiters and divertors; excitation rates for the visible exist and have been measured in plasma simulators and tokamaks
$CH/D_{4,3}$	+	(o)	−	possible by absorption spectroscopy; lack of information on the line strength of deuterium compounds
CH,CD	+	+	−	Bands been measured in plasma simulators at limiters & divertors; further check of break-up chain advisable; include new data; origin molecule of CH?; n_e-dependence?
OH, OD	+	−	−	Bands not yet well defined in the tokamak edge; bands seen in plasma simulators
CO	+	o	-	Bands near carbon wall and limiters identified; ionization of the molecule is very likely; excitation rates needed; candidate for E-field measurements ?
$C_{2,3}$	+	−	−	Bands near carbon wall and limiters identified; good indicator for evaporation; excitation rates still needed
O_2	+	o	−	Bands not yet well identified in the tokamak edge; seen in plasma simulators
N_2	+	o	−	Bands not yet well identified in the tokamak edge; seen in plasma simulator

stable states, which will be predominantly influenced by charge exchange processes. However, because the population mechanisms will be dominated by proton collisions, the triplet population is not affected and, therefore, a T_e-determination via these states – as in the case of electron collisions – will no longer be possible.

6.4 Conclusions and Recommendations

Tables 6.2 and 6.3 are an attempt to extend the tables which have already been shown in [16]. Changes since then are marked in bold, and again complete information is marked by [+], and incomplete or missing information by (o) and (–) respectively. The latter case is still predominantly true for molecules, for which the transitions, where rates are known at all, are in the vacuum UV and difficult to access. Two exceptions are the CH/CD radical and H_2/D_2, where – especially for the latter – in the past few years considerable progress has been achieved both experimentally and in the modeling. Concerning the atoms the needs for medium and high-Z impurities have increased. Although some experiments and calculations have partly filled the gaps there is still some work to be done – predominantly for tungsten.

Acknowledgement

I would like to thank numerous colleagues of my institute who contributed with their work to this article.

References

1. F.C. Bennett, Poloidal Divertor Experiment, Phys. Today **29** (1976) 17
2. L.D. Horton, Plasma Phys. Control. Fusion **38** (1996) A269
3. G.F. Counsell, J.W. Ahn, R. Akers, E. Arends, R. Buttery, A.R. Field, M. Gryaznevich, P. Helander, A. Kirk, H. Meyer, M. Valovic, H.R. Wilson, Y. Yang, Plasma Phys. Control. Fusion **44** (2002) B23–B37
4. S.I. Krasheninnikov, A.Y. Pigarov, T.K. Soboleva, D.J. Sigmar, J. Nucl. Mater. **241** (1997) 283
5. J.L. Terry, B. Lipschultz, A.Y. Pigarov, S.I. Krasheninnikov, B. LaBombard, D. Lumma, H. Ohkawa, D. Pappas, M. Umansky, Phys. Plasmas **5** (1998) 1759
6. G.M. McCracken, M.F. Stamp, R.D. Monk, A.G. Meigs, J. Lingertat, R. Prentice, A. Starling, R.J. Smith, A. Tabasso, Nucl. Fusion **38** (1998) 619
7. U. Samm, M. Brix, F. Durodié, M. Lehnen, A. Pospieszczyk, J. Rapp, G. Sergienko, B. Schweer, M.Z. Tokar' and B. Unterberg, J. Nucl. Mater. **266-269** (1999) 666
8. G. Sergienko, A. Pospieszczyk, M. Lehnen, M. Brix, J. Rapp, B. Schweer and P.T. Greenland, J. Nucl. Mater. **290-293** (2001) 720
9. U. Fantz, D. Reiter, B. Heger and D. Coster, J. Nucl. Mater. **290-293** (2001) 367
10. G.M. McCracken, U. Samm, S.J. Fielding, G.F. Matthews, R.A. Pitts, C.S. Pitcher, D. Gray, Y.T. Lie, R.A. Moyer, G. Bertschinger, A. Pospieszczyk, D. Rusbüldt, P.C. Stangeby, B. Schweer, D. Elder, J. Nucl. Mater. **176** (1990) 191
11. P. Monier-Garbet, J. Nucl. Mater. **241** (1997) 92
12. S. Brezinsek, P.T. Greenland, Ph. Mertens, A. Pospieszczyk, U. Samm, B. Schweer, G. Sergienko, Physica Scripta **T103** (2003) 63

13. S. Brezinsek, to be published in Plasma Phys. Control. Fusion
14. P. Bogen, D. Rusbüldt, J. Nucl. Mater. **196** (1992) 179
15. P. Bogen, Physica Scripta **T47** (1993) 102
16. A. Pospieszczyk, *Diagnostics of Edge Plasmas by Optical Methods*. In: Atomic and Plasma-Material Interaction Processes in Controlled Thermonuclear Fusion, R.K. Janev and H.W. Drawin (eds.) (Elsevier 1993) pp. 213–242
17. A. Pospieszczyk, G.G. Ross, Rev. Sci. Instrum. **59** (1988) 1491
18. J.C. Angus, P. Koidl, S. Domitz, *Carbon Thin Films*. In: J. Mort and F. Jansen (eds.) (CRC Press, Boca Raton 1986)
19. J.D. Hey, Y.T. Lie, D. Rusbüldt, E. Hintz, Contrib. Plasma Phys. **34** (1944) 25
20. J.D. Hey, M. Korten, Y.T. Lie, A. Pospieszczyk, D. Rusbüldt, B. Schweer, B. Unterberg, J. Wienbeck, E. Hintz, Contrib. Plasma Phys. **36** (1996) 583
21. J.D. Hey, C.C. Chu, Ph. Mertens, 16th Conf. on Spectral Line Shapes, Vol. 12, p. 35, AIP Conf. Proceedings, Vol. 645, Melville, NY, 2002
22. J. Gafert, W. Fundamenski, M. Stamp, J.D. Strachan, 28th EPS Conference on Control. Fusion and Plasma Phys., Funchal, ECA **25A** (2001) 1637
23. H.P. Summers, M. von Hellermann. In: *Atomic and Plasma-Material Interaction Processes in Controlled Thermonuclear Fusion*, R.K. Janev and H.W. Drawin (eds.) (Elsevier 1993) pp. 87–117
24. The Atomic Data Analysis Structure; Chap. 18 in this volume; see also http://www.patiala.phys.strath.ac.uk
25. R.C. Isler, N.H. Brooks, W.P. West, A.W. Leonard, G.R. McKee, G.D. Porter, J. Nucl. Mater. **266-269** (1999) 376
26. R.C. Isler, R.J. Colchin, N.H. Brooks, T.E. Evans, W.P. West, D.G. Whyte, Phys. Plasmas **8** (2001) 4470
27. A. Huber, A. Pospieszczyk, B. Unterberg, M. Brix, Ph. Mertens, V. Philipps, B. Schweer, Plasma Phys. Control. Fusion **42** (2000) 569
28. A. Pospieszczyk, Y. Ra, Y. Hirooka, R.W. Conn, D.M. Goebel, B. LaBombard, and R.E. Nygren, Spectroscopic studies of carbon containing molecules and their breakup in PISCES-A, University of California at Los Angeles Report No. UCLA-PPG-1251, 1989. See National Technical Information Service Document No. DE91004936INZ. Copies may be ordered from The National Technical Information Service, Springfield, VA.
29. D.G. Whyte, R. Bastasz, J.N. Brooks, W.R. Wampler, W.P. West, C.P.C. Wong, O.I. Buzhinskij, I.V. Opimach, J. Nucl. Mater. **269** (1999) 67
30. D.G. Whyte, G.R. Tynan, R.P. Doerner, J.N. Brooks, Nucl. Fusion **41** (2001) 47
31. A.B. Erhardt and W.D. Langer, Collisional processes of hydrocarbons in hydrogen plasmas, Princeton Plasma Physics Laboratory Report No. PPPL-2477, 1987. See National Technical Information Service Document No. DE88003462. Copies may be ordered from The National Technical Information Service, Springfield, VA.
32. M. Stamp, S.K. Erents, W. Fundamanski, G.F. Matthews, R.D. Monk, Physica Scripta **T91** (2001) 13
33. A. Pospieszczyk, V. Philipps, E. Casarotto, U. Kögler, B. Schweer, B. Unterberg, F. Weschenfelder, J. Nucl. Mater. **241-243** (1997) 833
34. U. Kögler, F. Weschenfelder, J. Winter, H.G. Esser, V. Philipps, A. Pospieszczyk, B. Schweer, J. von Seggern, M.Z. Tokar' and P. Wienhold, J. Nucl. Mater. **241-243** (1997) 816

35. A. Kirschner, V. Philipps, J. Winter, U. Kögler, Nucl. Fusion **40** (2000) 989
36. A. Kirschner, J.N. Brooks, V. Philipps, P. Wienhold, A. Pospieszczyk, R.K. Janev, U. Samm, J. Nucl. Mater. **313-316** (2003) 444
37. R.K. Janev, D. Reiter, Phys. Plasmas **9** (2002) 4071
38. R.K. Janev, D. Reiter, J. Nucl. Mater. **313-316** (2003) 1202
39. S. Brezinsek et al., to be published in Plasma Phys. and Control. Fusion
40. C. Busch, I. Möller, H. Soltwisch, Proc. of 9th Int. Symp. on Laser-Aided Plasma Diagnostics (LAPD), (1999) 92, Lake Tahoe, CA, USA
41. A. Pospieszczyk, Ph. Mertens, G. Sergienko, A. Huber, V. Philipps, D. Reiter, D. Rusbüldt, B. Schweer, E. Vietzke, P.T. Greenland, J. Nucl. Mater. **266-269** (1999) 138
42. S. Brezinsek, Ph. Mertens, A. Pospieszczyk, G. Sergienko, P.T. Greenland, Contrib. Plasma Phys. **42** (2002) 668
43. P. Franzen, E. Vietzke, J. Vac. Sci. Technol. A **12** (1994) 820-825
44. S. Brezinsek, P.T. Greenland, J.D. Hey, M. Lehnen, Ph. Mertens, A. Pospieszczyk, U. Samm, B. Schweer, G. Sergienko, E. Vietzke, 28th EPS Conference on Control. Fusion and Plasma Phys., ECA **25A** (2001) 2077
45. R. Guirlet, A. Escarguel, S. Brezinsek, J. Hogan, A. Pospieszczyk, C. De Michelis, 28th EPS Conference on Control. Fusion and Plasma Phys., ECA **25A** (2001) 201
46. Ph. Mertens, S. Brezinsek, P.T. Greenland, J.D. Hey, A. Pospieszczyk, D. Reiter, U. Samm, B. Schweer, G. Sergienko, E. Vietzke, Plasma Phys. Control. Fusion **43** (2001) 349–373
47. U. Fantz, K. Behringer, J. Gafert, D. Coster, and ASDEX Upgrade Team, J. Nucl. Mater. **266-269** (1999) 490
48. S. Brezinsek, P.T. Greenland, Ph. Mertens, A. Pospieszczyk, D. Reiter, U. Samm, B. Schweer, G. Sergienko, J. Nucl. Mater. **313-316** (2003) 967
49. D. Borodin, I.L. Beigman, L.A. Vainshtein, A. Pospieszczyk, S. Brezinsek, A. Huber, Plasma Phys. Control. Fusion **44** (2002) 2251
50. A. Huber, I.L. Beigman , D. Borodin, Ph. Mertens, V. Philipps, A. Pospieszczyk, U. Samm, B. Schweer, G. Sergienko, L.A. Vainshtein, Plasma Phys. Control. Fusion **45** (2003) 89–103
51. V. Philipps, T. Tanabe, Y. Ueda, A. Pospieszczyk, M.Z. Tokar', B. Unterberg, L. Konnen, B. Schweer, U. Samm, P. Wienhold, J. Winter, M. Rubel, B. Emmoth, N.C. Hawkes, and the TEXTOR TEAM, Nucl. Fusion **34** (1994) 1417–29
52. A. Pospieszczyk, T. Tanabe, V. Philipps, G. Sergienko, T. Ohgo, K. Kondo, M. Wada, M. Rubel, W. Biel, A. Huber, A. Kirschner, J. Rapp, N. Noda, J. Nucl. Mater. **290-293** (2001) 947–952
53. B. Lipschultz, H. Becker. P. Bonoli, J. Coleman, C. Fiore, S. Golovato, R. Granetz, M. Greenwald, D.G.D. Humphries, I. Hutchinson, J. Irby, E. Marmar, D.B. Montgomery, F. Najmbadi, R. Parker, M. Porkolab, J. Rice, E. Sevillano, Y. Takase, J.L. Terry, R. Watterson, S. Wolfe, J. Nucl. Mater. **162** (1989) 793
54. R. Andreani, L. Bettinali, A. Cecchini, M. Gasparotto, L. Lovisetto, A. Pizzut, G.B. Righetti, J. de Physique **45** (1984) 153
55. B. Lipschultz, D.A. Pappas, B. LaBombard, J.E. Rice, D. Smith, S. Wukitch, J. Nucl. Mater. **290** (2001) 286
56. H. van Regemorter, Astrophys. J. **136** (1962) 906
57. R. Boivin, Y. Hirooka, J. Won, J.N. Brooks, M.J. Khandagle, J. Nucl. Mater. **230** (1996) 101

58. S.N. Bogdanov, A.Y. Bodylev, A.N. Kuchenev, Y.M. Smirnov, J. Appl. Spectrosc. **37** (1982) 365
59. H. Maier, J. Luthin, M. Balden, S. Lindig, J. Linke, V. Rohde, H. Bolt, J. Nucl. Mater. **307** (2002) 116
60. A. Thoma, K. Asmussen, R. Dux, K. Krieger, A. Herrmann, B. Napiontek, R. Neu, J. Steinbrink, M. Weinlich, U. Wenzel, and the ASDEX Upgrade Team, Plasma Phys. Control. Fusion **39** (1997) 1487
61. A. Pospieszczyk, G. Chevalier, Y. Hirooka, R.W. Conn, R. Doerner, L. Schmitz, Nucl. Instrum. Methods **B72** (1992) 207 and report UCLA-PPG-1402, University of California at Los Angeles (Dezember 1991)
62. B. Schweer, G. Mank, A. Pospieszczyk, B. Brosda, B. Pohlmeyer, J. Nucl. Mater. **196-198** (1992) 174
63. M. Brix, Messung von Elektronentemperatur und -dichte mittels Heliumstrahldiagnostik im Randschichtplasma eines Tokamaks, PhD Thesis Jülich (1999), Report Jül-3638, FZ-Jülich, Central Library, D-52425 Jülich, Germany
64. I.L. Beigman, D.V. Borodin, L.A. Vainshtein, Optics and Spectroscopy **95** (2003) 493

7 X-ray Spectroscopy of High n Transitions of He- and Ne-Like Ions in Alcator C-Mod Plasmas

J.E. Rice, K.B. Fournier, E.S. Marmar, J.L. Terry, and U.I. Safronova

The Rydberg series ($1s^2$–1snp) up to n = 14 of helium-like argon (Z=18) has been observed from Alcator C-Mod plasmas using a high resolution X-ray spectrometer array. High n satellites to these lines of the form $1s^2$2s–1s2snp and $1s^2$2p–1s2pnp with $3 \leq n \leq 12$ have been recorded. X-ray spectra of $2l$–nl' transitions with $3 \leq n \leq 18$ in molybdenum (Z=42) and $3 \leq n \leq 12$ in krypton (Z=36) and niobium (Z=41) from charge states around neon-like have also been measured. Numerous examples of the configuration interaction, which alters the line intensities in some transitions of neon-like ions with nearly degenerate upper levels, have been observed. Accurate wavelengths of all of these transitions ($\pm.5$ mÅ) have been determined by comparison to neighboring reference lines from H- and He-like charge states. Line identifications have been made by comparison to ab initio atomic structure calculations, using a fully relativistic, parametric potential code. Measured line intensities have been compared with collisional–radiative modeling that includes the contributions from dielectronic recombination and inner-shell excitation rates, with good agreement.

7.1 Introduction

A wide variety of plasma diagnostic applications is available from the measurement of the relatively simple X-ray spectra of He-like ions [1] and references therein. The n = 2 and n = 3 X-ray spectra from many mid- and high-Z He-like ions have been studied in tokamak plasmas [2–4] and in solar flares [5,6]. The high n Rydberg series of medium Z helium-like ions have been observed from Z-pinches [7,8], laser-produced plasmas [9], exploding wires [8], the solar corona [10], tokamaks [11–13] and ion traps [14]. Always associated with X-ray emission from these two electron systems are satellite lines from lithium-like ions. Comparison of observed X-ray spectra with calculated transitions can provide tests of atomic kinetics models and structure calculations for helium- and lithium-like ions. From wavelength measurements, a systematic study of the n and Z dependence of atomic potentials may be undertaken. From the satellite line intensities, the dynamics of level population by dielectronic recombination and inner-shell excitation may be addressed.

Satellites to the Ar^{16+} Rydberg series for n = 2 [11, 15], n = 3 [8, 13] and n = 4, 5 [11, 12, 16] have been examined extensively. Theoretical calculations

of $n \geq 3$ satellites for argon (and other elements) are plentiful [12, 16–20]. The diagnostic potential of He-like spectra for $n = 3$ and higher n transitions has been exhaustively developed [21, 22] as well as the use of inner-shell excited satellites as a measure of Li-like to He-like ion abundance [23]. For $n \geq 6$ satellites, some wavelengths have been reported [8, 11, 12, 16], and wavelengths and oscillator strengths have been calculated up to $n = 7$ [7,8,16], but various wavelength calculations differ from the measured values by 3 mÅ. A comprehensive study of satellites up to $n = 12$ in argon and chlorine may be found in [16]. Observations for Cl^{15+} $n = 2$ transitions have been made in Alcator A [24], Alcator C [25], JET [26] and COMPASS-D [26] plasmas, and $n = 3$ transitions have been seen in laser-produced plasmas [9].

There has also been considerable interest in X-ray transitions from high Z atoms with charge states around the neon-like isosequence, attained in pulsed power [8, 27–29], tokamak [30–36] and laser-produced [37–39] plasmas. X-ray lasing [40, 41] has been demonstrated in neon-like ions, and a need to understand the kinetics of this system has motivated development of very precise collisional–radiative modeling tools [42]. The identifications of many X-ray lines from neon-like ions allow high resolution experimental data to be used for benchmarking multi-electron atomic structure calculations [32–34,36,43–47]. Collisional–radiative modeling of line intensities from neon-, fluorine-, sodium- and magnesium-like ionization states has demonstrated the importance of excitation-autoionization in overall charge state balance in tokamak plasmas [48]. Rates for this process, in conjunction with the latest dielectronic recombination rates [49], have led to a reassessment of the importance of molybdenum radiation in energy balance [50] in tokamak plasmas. Most of the work that has been done previously has been limited to 3–3, 2–3 and 2–4 transitions in the Ne-I iso-electronic sequence and adjacent charge states. Recently, high n lines in neon-like iron have been observed from astrophysical plasmas [51]. High temperature, optically thin tokamak plasmas enable the measurement of many lines originating in transitions from levels having $n \geq 5$; in fact, all of the transitions in the 2p–nd series in Mo^{32+} lying under the ionization potential have been measured [33]. The availability of a large number of transitions in several adjacent elements provides the opportunity to study the systematics of configuration interaction (CI) effects [34,36]. Numerous instances of different transitions that are enhanced or suppressed by CI are presented in [36].

The organization of this paper is as follows. The experimental setup and code description are reviewed in Sects. 7.2 and 7.3. Observations and code comparisons for the Rydberg series of helium-like Ar^{16+} between $n = 3$ and 14, and the high n satellites of Ar^{15+} with $3 \leq n \leq 12$ are presented in Sect. 7.4. In Sect. 7.5, experimental results for high n ground state transitions in Mo ($n \leq 18$) and Kr ($n \leq 12$) are compared with theory, with numerous examples of configuration interaction effects being demonstrated. A summary is given in Sect. 7.6.

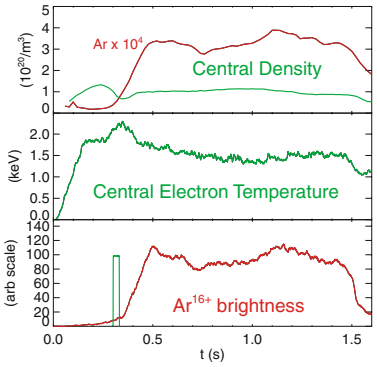

Fig. 7.1. Argon injection via a piezo-electric valve, with the opening voltage waveform shown in the **bottom** frame along with the Ar^{16+} X-ray brightness time history. The electron density and temperature, along with the argon density are shown in the **top** two frames

7.2 Experiment Description

Most of the X-ray observations described here were obtained from the Alcator C-Mod [52] tokamak. Alcator C-Mod is a compact high field device (minor radius of 21 cm) with all molybdenum plasma facing components, strong shaping capabilities and auxiliary heating by ICRF waves. For the measurements presented here, plasma parameters were in the range of $0.9 \times 10^{20}/\mathrm{m}^3 \leq \mathrm{n_{e0}} \leq 3.4 \times 10^{20}/\mathrm{m}^3$ and $900\,\mathrm{eV} \leq T_{\mathrm{e0}} \leq 3000\,\mathrm{eV}$. Molybdenum is an intrinsic impurity and argon and krypton were introduced through a piezo-electric valve. An example of argon injection is shown in Fig. 7.1. The 30 ms wide voltage waveform for the piezo valve is shown in the bottom frame, along with the Ar^{16+} X-ray brightness, which peaks after about 200 ms, and stays relatively constant thereafter because of the recycling properties of argon. Also shown in the figure are the electron density and temperature, and the deduced argon density, which is about about 3×10^{-4} of the electron density, not enough to perturb the plasma. A laser blow-off impurity injection system [53], which has been used to study impurity transport, was employed to inject palladium, niobium and zirconium. Shown in Fig. 7.2 is the time history of neon-like Nb^{31+} X-ray emission following a niobium injection at 0.5 seconds into an L-mode discharge, when the central electron temperature was 2200 eV and the central electron density was $1.3 \times 10^{20}/\mathrm{m}^3$. The niobium stayed in the plasma for about 100 ms, as shown by the bottom frame of the figure, indicative of anomalously fast impurity transport [54]. This fast L-mode transport, which is comparable to some recombination times, creates a 'recombining plasma' at the edge [11].

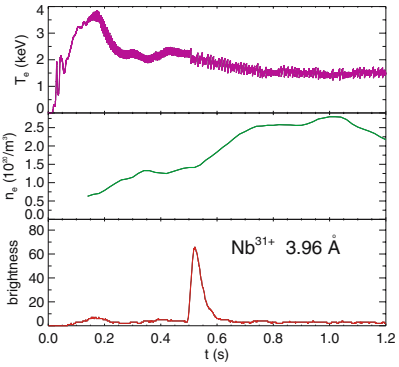

Fig. 7.2. Electron temperature, density and Nb^{31+} X-ray brightness time histories for an L-mode discharge with niobium injection at 0.5 s

The X-ray spectra from Alcator C-Mod were recorded by a five chord, independently spatially scannable, high resolution X-ray spectrometer array [55]. Four of these von Hamos type spectrometers had quartz crystals with 2d spacings of 6.687 Å, and wavelength coverage from 2.7 to 4.1 Å, 120 mÅ at a time. The remaining spectrometer had an ammonium dihydrogen phosphate (ADP) crystal with a 2d spacing of 10.640 Å, and a wavelength range from 4.3 to 6.5 Å. Each spectrometer has a resolving power, $\lambda/\Delta\lambda$, of 4000, a 2 cm spatial resolution and a luminosity function of 7×10^{-9} cm^2sr. Wavelength calibration [30–34, 36] has been achieved by determining the instrumental dispersions in reference to H- and He-like argon, chlorine and sulphur lines. The $2l$–$3l'$ spectra of krypton (from Alcator C) were obtained with a von Hamos type spectrometer equipped with a pentaerythritol (PET) crystal (2d = 8.742 Å), and with wavelength coverage between 6 and 8 Å. The active area of the position sensitive proportional counter detector was large (12 cm), which allowed for up to 400 mÅ coverage in one wavelength setting, but non-uniformities along the length of the Be entrance window led to sensitivity variations, so some line ratios from opposite ends of the detector may be up to 25% off.

7.3 Code Descriptions

Ab initio atomic structure calculations for the lithium-, helium- and hydrogenlike isosequences of S, Cl and Ar (Z=16, 17 and 18) with $2 \leq n \leq 14$, and the aluminum- through oxygen-like isosequences (ground states $2p^6 3s^2 3p$ to $2s^2 2p^4$, respectively) of Kr (Z=36), Mo (Z=42), Nb (Z=41), Zr (Z=40) and Pd (Z=46) have been generated using the HULLAC package. HUL-

LAC includes ANGLAR, which uses the graphical angular recoupling program NJGRAF [56] to generate fine structure levels in a JJ-coupling scheme for a set of user-specified electron configurations. HULLAC then generates atomic wavefunctions using the fully relativistic, parametric potential code RELAC [57, 58], which calculates the full multi-configuration, intermediate coupled level energies and radiative transition rates. RELAC also computes semi-relativistic autoionization transition rates [59] to the ground and excited levels of an adjacent ion. The CROSS [60] suite of codes in the HULLAC package uses a factorization theorem to compute the distorted wave approximation electron-impact excitation rates between all levels of each charge state mentioned above. This includes levels formed by exciting valence shell electrons as well as deeply bound inner-shell electrons. Energy levels and transition probabilities for helium- and lithium-like ions have also been calculated by using the Z-expansion method (MZ code). The energy matrix is constructed in an LSJ coupling scheme and relativistic corrections are included within the framework of the Breit-Pauli operator using a perturbation approach. The MZ method uses hydrogenic wave-functions. However, the calculation energies and other characteristics by this method are greatly improved by using many-body perturbation theory to include the Coulomb interaction between electrons as well as relativistic corrections . The Z-expansion method has been described in detail in [61, 62].

7.4 He-Like and Neighboring Ions

Shown in Fig. 7.3 are X-ray spectra in the vicinity of the first three resonance lines, w_2 ($1s^2\ ^1S_0$–$1s2p\ ^1P_1$), w_3 ($1s^2\ ^1S_0$–$1s3p\ ^1P_1$) and w_4 ($1s^2\ ^1S_0$–$1s4p\ ^1P_1$) in Ar^{16+}. In the n = 2 spectrum, the forbidden line, z ($1s^2\ ^1S_0$–$1s2p\ ^3S_1$), and the inter-combination lines, x ($1s^2\ ^1S_0$–$1s2p\ ^3P_2$) and y_2 ($1s^2\ ^1S_0$–$1s2p^3P_1$) are prominent. Also apparent are the n = 2 dielectronic satellites k and j, the n = 2 inner-shell satellites q, r, s and t, and the satellites with n = 3 and n = 4 spectators, all from lithium-like argon. (See [11] for the wavelengths and line designations.) For the n = 3 spectrum, w_3 is dominant, the inter-combination line, y_3 ($1s^2\ ^1S_0$–$1s3p\ ^3P_1$), is greatly reduced in relative magnitude and wavelength (the excitation rates for x_3 and z_3 are minuscule so they are not seen) and the satellites have formed four unresolved features. (See [11, 13, 16] for the wavelengths and line designations.) The upper levels of these satellites are the same as for the unresolved satellites marked 3 in the n = 2 spectrum; in this case the n = 3 electron makes the transition with the n = 2 electron as the spectator, whereas for the satellites marked 3 in the n = 2 spectrum, the n = 2 electron makes the transition while the n = 3 electron is the spectator. For the n = 4 spectrum, w_4 dominates and the satellites have blended to form three unresolved groups: A_4 is related to k and j in the n = 2 spectrum, B_4 to q and r, and C_4 to s and t. (See Table 6 of [16] for the wavelengths and line designations of these satellite groups.) The upper levels of these transitions

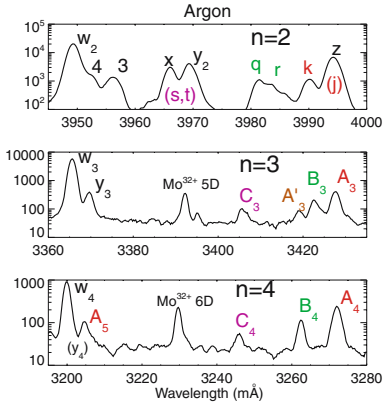

Fig. 7.3. X-ray spectra in the vicinity of the n = 2, 3 and 4 resonance lines, w_2 (**top**), w_3 (**middle**) and w_4 (**bottom**), showing the n = 2 dielectronic satellites k and j, and n = 2 inner-shell satellites q, r, s, and t, along with the related higher n satellite groups A_n, B_n and C_n. The A_5 dielectronic satellite group associated with w_5 is also visible, along with two high n neon-like Mo^{32+} lines (see next section)

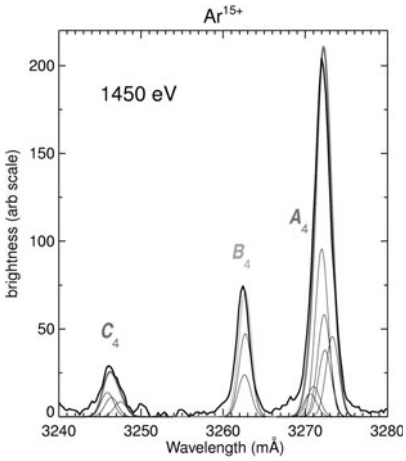

Fig. 7.4. Expanded view of the n = 4 satellite groups of Ar^{15+}. The calculated individual constituents of the three groups A_4, B_4 and C_4 are shown by the *thin lines* with each composite depicted by the *thick lines*, for comparison with the observed spectrum

are the same as for the shoulder marked 4 in the n = 2 spectrum. Presented in Fig. 7.4 is an expanded view of the n = 4 satellite groups, showing the individual constituents (see Table 6 of [16]). The relative intensities of these lines are in good agreement with the calculations.

Spectra of w_4 and satellites for plasmas with different central electron temperatures [16] are shown in Fig. 7.5. As the temperature decreases, the

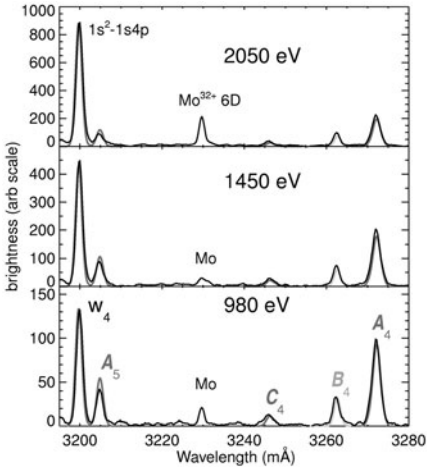

Fig. 7.5. The observed X-ray spectra of Ar^{16+} w_4 with satellites, for three different central electron temperatures, are shown for comparison with the calculated spectra for w_4, A_4, B_4, C_4, and A_5

intensities of the satellite groups (relative to w_4) increase; in the bottom frame with an electron temperature of less than 1000 eV (from an off-axis view), the satellite group A_4 is nearly as bright as the resonance line. Similar observations were made from Alcator C [11], from radial profile measurements; in fact near the recombining plasma periphery, the satellite group A_5 was actually brighter than w_5. Also shown in Fig. 7.5 are the corresponding synthetic spectra, generated as described in [16], which have been normalized to w_4. The relative intensities of the satellites A_4, B_4 and C_4 (and A_5) are well reproduced for these three different electron temperature plasmas, supporting the dielectronic recombination and inner-shell excitation rates. (A strong Mo^{32+} 6d-2p line [33] at 3230.1 mÅ is visible in these spectra, see next section.) Shown in Fig. 7.6 is a spectrum from argon including w_4, w_5 and w_6 from Ar^{16+}, Ly_β from Ar^{17+} and the satellite groups A_5–A_{12}, B_5–B_8 and C_5–C_7, in an overlapping 'triplet' pattern. Plasma parameters for the discharge from which this spectrum was obtained were $n_{e0} = 1.3 \times 10^{20}/m^3$ and $T_{e0} = 1550$ eV. A synthetic spectrum is shown in the bottom frame, and the agreement is quite good.

The transition designations, calculated wavelengths, satellite capture energies, oscillator strengths/satellite intensity factors and inner-shell excitation rates (evaluated at 2000 eV) for Ar^{15+} satellites between n = 4 and n = 12 may be found in Tables 6–10 of [16]. The measured wavelength differences between the resonance lines, w_n, and the satellite groups A_n, B_n and C_n, as a function of n for argon are shown in Fig. 7.7. Also shown are the theoretical values (curves), from the calculated wavelengths of Tables 6–10 of [16]; the solid lines are from the MZ wavelengths and the dotted lines represent the

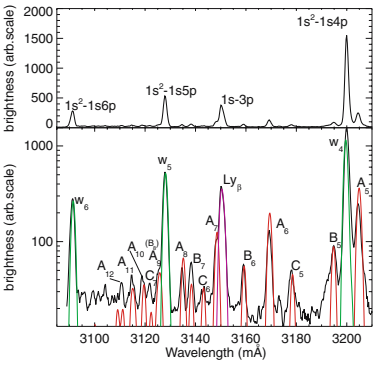

Fig. 7.6. The linear scale X-ray spectrum of helium-like Ar^{16+} w_4, w_5 and w_6, with satellites, and hydrogen-like Ar^{17+} Ly_β, is shown in the **top** frame. In the *bottom* frame is the log scale observed spectrum and the computed spectrum for Ar^{16+}, Ar^{17+}, and Ar^{15+}

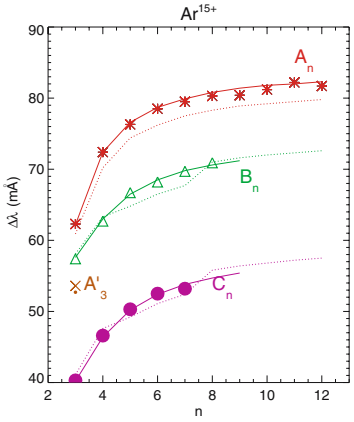

Fig. 7.7. The difference between the satellite wavelengths and the resonance line wavelengths in Ar^{16+} as a function of n, for the three satellite groups, along with the theoretical wavelengths. The measured values for A_n, B_n and C_n are depicted as *asterisks*, *triangles* and *dots*, respectively. The satellite group A_3' is shown as the $\times$. The theoretical wavelength differences are shown by the *curves*, with the calculated value for A_3' (from RELAC) given by the *dot*. The *solid lines* are from MZ, while the *dotted lines* are from RELAC

wavelengths from RELAC. The agreement between the observed wavelengths and those calculated from MZ is excellent. This figure may be compared to Fig. 3 in [12].

Spectra near the Ar^{16+} Rydberg series limit [11] are shown in Fig. 7.8. The top spectrum was taken along the central chord of a plasma with $n_{e0} = 0.9 \times 10^{20}/m^3$ and $T_{e0} = 2600\,eV$. The resonance lines from w_6 to

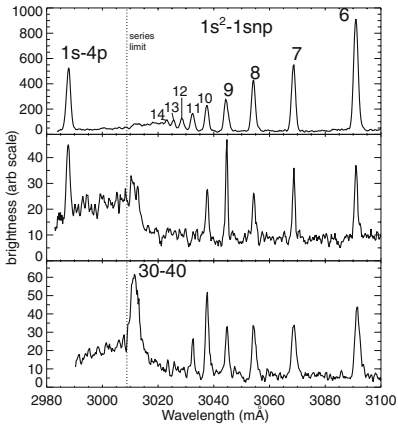

Fig. 7.8. Spectra near the Ar^{16+} series limit. In the **top** frame is the spectrum from a central chord view, in the **middle** frame is a spectrum from an identical plasma with a view 18.5 cm above the midplane (r/a=.67) and in the **bottom** frame is a spectrum from a similar plasma with a view 19.7 cm below the midplane (r/a=.62). The ionization limit is shown as the *vertical line*. The lower spectrum was cut off below 2990 mÅ

w_{14} are clearly resolved, and there is a region of enhanced brightness from w_{15} up to the series limit at 3008.8 mÅ, presumably due to unresolved lines. Along this chord, most of the line emission is from the plasma center where electron impact excitation is the dominant mechanism for populating the upper levels. Ar^{17+} Ly_γ near 2987.4 mÅ is also prominent. The corresponding spectrum from an identical plasma, but taken along a chord viewing through r/a = 0.67 (away from the X-point), where the electron temperature was 1100 eV and the electron density was $0.8 \times 10^{20}/m^3$, is shown in the middle frame of Fig. 7.8. The lines are greatly reduced in intensity and the widths are very narrow due to the lower ion temperature. The intensities of w_9 and w_{10} are enhanced relative to the trend of decreasing intensity with increasing n number, which is due to population by charge exchange recombination with intrinsic neutral deuterium in the ground state, near the plasma edge [11,63]. Emission from the very high n levels (n > 25) is also visible just on the long wavelength side of series limit. Along this chord, however, the lines w_{11} through w_{14} are not visible. The viewing chord of the middle spectrum was 18.5 cm above the mid-plane in a discharge with a lower X-point. The continuum at wavelengths shorter than the limit is greater than the continuum level between the resonance lines, and is due to radiative recombination [11]. The spectrum shown in the bottom frame is from a somewhat similar plasma, from a chord viewing through r/a = 0.62, but 19.7 cm below the mid-plane, for a lower X-point discharge. In this case w_{10} is enhanced relative to the

other w_n lines (due to population by charge exchange with intrinsic neutral deuterium in the ground state) and the feature on the long wavelength side of the limit is now dominant. This feature is from n numbers between 30 and 40, and is due to charge exchange between hydrogen-like argon and intrinsic neutral deuterium in the n = 3 and n = 4 excited states [11, 63].

7.5 Ne-Like and Neighboring Ions

Shown in Fig. 7.9 is the 2–3 spectrum of neon-like krypton (Kr^{26+}), with satellites [36]; previous observations can be found in [8, 28, 37, 38]. This is a composite spectrum obtained by scanning in wavelength during a sequence of reproducible Alcator C discharges [36], with a peak electron density of $2.6 \times 10^{20}/m^3$ and a peak electron temperature of 1450 eV. The spectrum is dominated by the neon-like electric-dipole transitions 3C ($2p_-$–$3d_-$ or $2p^6$–$(2p^5)_{\frac{1}{2}}3d_{\frac{3}{2}}$) and 3D ($2p_+$–$3d_+$ or $2p^6$–$(2p^5)_{\frac{3}{2}}3d_{\frac{5}{2}}$). (The standard notation for Ne-like transitions [64] is used.) The 3F and 3G ($2p_{\mp}$–$3s_+$) transitions, including the magnetic quadrupole line (M2, $2p_+$–$3s_+$, $\Delta J = 2$) at 7519.2 mÅ, are also intense. Transitions with a 2s hole (3A, 2s–$3p_+$ and 3B, 2s–$3p_-$) are bright, including the electric quadrupole 2s–$2d_+$ line at 6103.8 mÅ. Also apparent are F-, Na- and Mg-like satellites. This composite spectrum is comprised of 6 individual spectra from different discharges, and considering non-uniformities along the detector (as mentioned above), the relative intensities of lines separated by more than 150 mÅ have a 25% uncertainty. Shown in the bottom of Fig. 7.9 is a synthetic spectrum, which is in good qualitative agreement. Transition designations, experimental and theoretical wavelengths and calculated oscillator strengths for all of these lines are presented

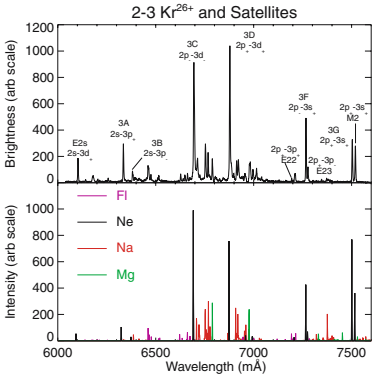

Fig. 7.9. The Kr^{26+} 2–3 spectrum with satellites (composite over several similar discharges) is shown in the **top** frame, including the neon-like transition designations. In the **bottom** frame is a synthetic spectrum

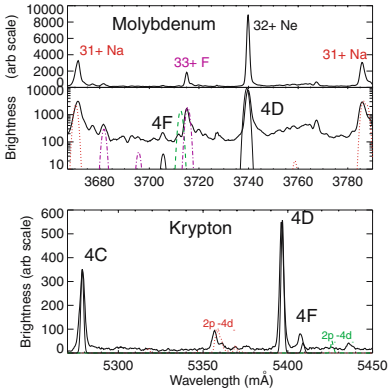

Fig. 7.10. Linear and log spectra in the vicinity of 4D in Mo^{32+} are shown in the **top** frame. Also shown is the synthetic collisional–radiative synthetic spectrum, with Ne-like lines shown in *solid*, Na-like transitions depicted by the *dotted lines*, the Mg-like transition shown as the *dashed line* and F-like transitions shown by *dash-dot lines*. The spectrum of the Kr^{26+} 4C, 4D and 4F transitions, with Na- and Mg-like $2p_-$–$4d_-$ satellites is shown in the **bottom** frame. Also shown is the synthetic spectrum, with Ne-like lines shown in *solid*, Na-like transitions depicted by the *dotted lines* and the Mg-like $2p_-$–$4d_-$ transition shown as the *dashed line*

in Tables I–IV of [36]. Most observed transitions are within 3 mÅ of the calculated wavelengths, or about 0.04%. The synthetic spectrum was computed for $T_e = 1600\,\text{eV}$ and $n_e = 1.0\times10^{20}/\text{m}^3$.

Moving to higher n transitions, shown in Fig. 7.10 are $\Delta n = 2$ spectra, with the upper levels in $n = 4$, for the neon-like ions Mo^{32+} and Kr^{26+}. The 4D line [33,48] dominates the molybdenum spectrum, and similar transitions from the Na- and F-like charge states are prominent. (See Tables in [33] for wavelengths and transition designations.) Radial brightness profiles [48] of the five intense $n = 4$ molybdenum lines (F-like 3.6149, Ne-like 4C 3.6261, Na-like 3.6710, Ne-like 4D 3.7398 and Na-like 3.7857 Å), obtained during a series of several similar shots, are shown in Fig. 7.11. The Mo^{32+} profiles (Xs, 4D and plus signs, 4C) dominate over the inner half of the plasma. The Mo^{31+} profile shapes (squares and diamonds) are broader, and the Mo^{33+} profile (asterisks) is narrower than the Mo^{32+} profiles. Also shown in the top frame of the figure are the calculated brightness profiles (curves) for the five lines, using the charge state density profiles of Fig. 4a of [48] which includes the effects of excitation-autoionization. All of the profile shapes and the relative intensities are well matched by the calculations. This agreement indicates that the combination of the electron temperature and density profiles, the transport coefficients and the excitation, ionization and recombination rates is well characterized for these ionization states over the inner 10 cm. In this re-

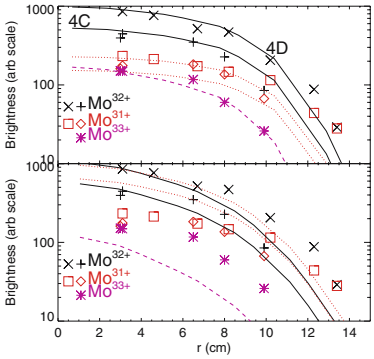

Fig. 7.11. Measured (*symbols*) and calculated (*lines*) X-ray brightness profiles using the charge state density profiles of Fig. 4a of [48] are shown in the **top** frame. The *solid lines* are from Ne-like molybdenum, *dotted lines* from Na-like and *dashed lines* from F-like. Calculated brightness profiles for the ionization balance of Fig. 4b in [48] are shown in the **bottom**

gion the electron temperature and density profiles and transport coefficients are independently measured and well known. The match in the top frame of Fig. 7.11 is taken as evidence in support of the charge profiles shown in Fig. 4a of [48]. The brightness profiles calculated from the charge state profiles of Fig. 4b of [48] (i.e., those without inclusion of excitation-autoionization) are shown in the bottom frame of Fig. 7.11, along with the measured profiles. Both the profile shapes and the relative intensities do not represent the data, demonstrating the importance of excitation-autoionization in the overall ionization rate and the sensitivity of this comparison.

Shown in the bottom of Fig. 7.10 are the 4D ($2p_+$–$4d_+$) and 4C ($2p_-$–$4d_-$) lines of Kr^{26+} at 5396.4 and 5278.7 mÅ, respectively, along with neighboring satellites and the neon-like 4F ($2p_-$–$4s_+$) line at 5407.3 mÅ. Central parameters for the plasma from which this spectrum was obtained were $T_e = 1150\,\text{eV}$ and $n_e = 1.6\times10^{20}/\text{m}^3$. These transitions have been studied extensively in molybdenum [33, 48]. Also shown is a synthetic spectrum, which is in good agreement with the observations, although there is a ~ -10 mÅ shift of the calculated wavelength for the magnesium-like $2p_-$–$4d_-$ transition at 5436.6 mÅ. The 4F transition at 5407.3 mÅ is readily noticeable, having about 10% of the intensity of the 4D transition; the 4F line in Mo^{32+} at 3705.6 mÅ was too weak to be reported in [33], but can be seen in the top of Fig. 7.10, with about 1% of the intensity of 4D. The reason the 4F line is so intense in Kr^{26+} is because of its close proximity to the 4D line; the upper levels are separated by only 4.6 eV, and significant configuration interaction results that transfers strength from 4D to 4F [36]. The energy level diagrams

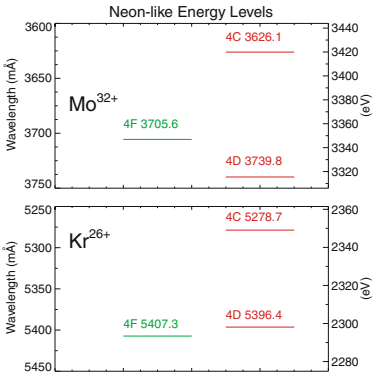

Fig. 7.12. The n = 4 energy level diagrams for Mo^{32+} (**top**) and Kr^{26+} (**bottom**) with the left ordinates expressed in the transition (to the ground state) wavelengths and the right ordinates in eV. Upper levels for s are on the left and d on the right. Measured transition wavelengths (to the ground state) are given for each of the upper levels

for n = 4 transitions in neon-like molybdenum and krypton are shown in Fig. 7.12. As can be seen, the upper levels for the 4D and 4F transitions in Kr^{26+} are very close, within 4.6 eV, while in Mo^{32+} these levels are 31 eV apart, too far away for any significant configuration interaction.

This phenomenon has been seen between the 7D and 6C levels in Mo^{32+} [33, 34, 36, 65], but in contrast here, the *shorter* wavelength line is the beneficiary of the enhanced intensity. This effect is summarized in Fig. 7.13, top frame, where the calculated oscillator strengths of the 6D $(2p^6–(2p^5)_{\frac{3}{2}}6d_{\frac{5}{2}})$, the 6C $(2p^6–(2p^5)_{\frac{1}{2}}6d_{\frac{3}{2}})$, the 7D $(2p^6–(2p^5)_{\frac{3}{2}}7d_{\frac{5}{2}})$ and the 7C $(2p^6–(2p^5)_{\frac{1}{2}}7d_{\frac{3}{2}})$ lines are plotted as a function of atomic number. The oscillator strengths of the 6D and 7C lines are relatively insensitive to atomic number. The magnitude of the configuration interaction between the 6C and 7D levels is quite apparent; as the atomic number increases from Y to Mo, the g*f value of the 7D line increases while the value of the 6C line decreases. At technetium (Z=43), this effect dramatically switches; for Tc and higher Z elements, the 6C line is at shorter wavelength and the 7D line is the *weaker* of the two. The wavelength differences between the two levels is shown in Fig. 7.13 in the bottom frame. The brightness ratios for these lines as a function of level separation are shown in Fig. 7.14, which is similar to Fig. 5 of [65], but with the inclusion of the krypton points [36]. The agreement between experiment and theory is quite good; it would certainly be gratifying to verify that this effect changes sign in Tc or in Ru. It is noteworthy that in the case of the 2p–nd configuration interaction, as in Figs. 7.13 and 7.14, the 'beneficiary' of the enhanced intensity is on the short wavelength side (higher energy side)

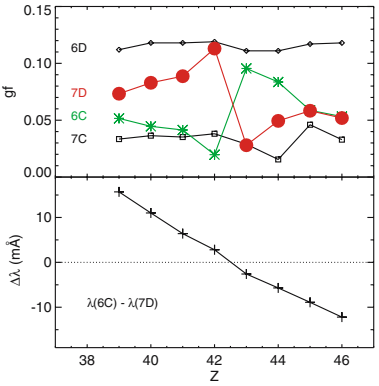

Fig. 7.13. Calculated oscillator strengths (**top**) of 2p–6d and 2p–7d transitions and calculated wavelength differences (**bottom**) between 6C transitions and 7D transitions as a function of atomic number Z

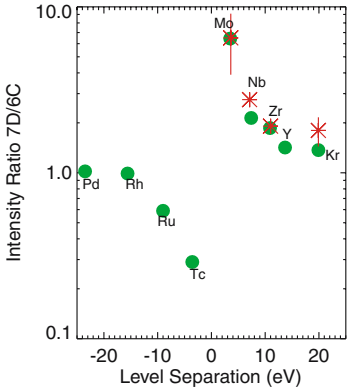

Fig. 7.14. The intensity ratios of Ne-like 7D to 6C transitions as a function of energy level separation. Calculations are shown as *dots*, measurements are represented as *asterisks*

whereas in the case of 2p–ns level enhancement, Fig. 7.10, the 'beneficiaries' are on the long wavelength side (lower energy side) of the 'donor' transition.

Moving to even higher n transitions, shown in Fig. 7.15 is a spectrum [33] from 2.9 to 3.0 Å, obtained from a series of identical discharges with $n_{e0} = 1.7 \times 10^{20}/\mathrm{m}^3$ and $T_{e0} = 2300\,\mathrm{eV}$. The nD $(2p_{\frac{3}{2}}\text{–}nd_{\frac{5}{2}})$ series up to $n = 18$ and the nC $(2p_{\frac{1}{2}}\text{–}nd_{\frac{3}{2}})$ series with $8 \leq n \leq 12$ are clearly resolvable. Above $n = 18$, the lines of the nD series blend together, up to the series limit at 2914.78 mÅ. Also shown are two Ar^{17+} lines used for the wavelength calibration, and

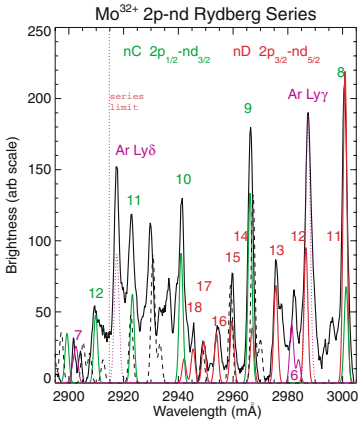

Fig. 7.15. Transitions in Mo^{32+} near the$2p_{3/2}$–$nd_{5/2}$ series limit, including the $2p_{1/2}$–$nd_{3/2}$ series with $8 \leq n \leq 13$ and the $2p_{3/2}$–$nd_{5/2}$ series with $11 \leq n \leq 18$. Theoretical lines for Mo^{32+} (*solid*), Mo^{33+} (*dashed*), and Ar^{17+} (*dotted*) are shown at the **bottom**

a strong F-like Mo^{33+} line at 2929.9 mÅ. At the bottom of the figure are calculated lines from Mo^{32+} (solid), Mo^{33+} (dashed) and Ar^{17+} (dotted). Also visible are the Mo^{32+} 2s-6p and 2s-7p doublets at 2983 and 2903 mÅ, respectively.

Spectra [34] including the nD series limit at 2914.78 mÅ, and the nC series limit at 2841.44 mÅ in Mo^{32+} are shown in Fig. 7.16. The wavelength calibration for these spectra was obtained from the high n series of hydrogen-like Ar^{17+}, transitions from 1s-5p to 1s-10p, with wavelengths of 2917.50, 2881.04, 2859.38, 2845.51, 2836.07 and 2829.36 mÅ [66]. The calculated nC series in Mo^{32+} [33] with n between 10 and 19 is shown by the thick solid lines, and the 2s-7p and 2s-8p transitions are shown as the thin solid lines. This region of the spectrum is complicated by the presence of many Mo^{33+} transitions, shown as dashed lines. Clearly identified in the top spectrum are the Mo^{32+} 10C line at 2941.0 mÅ, the Mo^{32+} 2s-7p and 2s-8p lines at 2902.1 and 2853.0 mÅ, respectively (see Table II, [34]), the Mo^{33+} 2p-7d lines at 2935.8 mÅ, and the Mo^{33+} 2p-9d lines at 2930.2 mÅ and 2849.1 mÅ. Clearly missing from this spectrum are the transitions from the Mo^{32+} nC series with $n = 13$, 14, 17, 18 and 19, which were seen in the nD series. The $n = 11$, 12, 15 and 16 lines have nearby transitions from Mo^{33+}, so the line identifications are ambiguous. The top spectrum of Fig. 7.16 was from a plasma with an electron temperature of 3.4 keV and an electron density of $7.7 \times 10^{19}/m^3$. At this temperature, Mo^{33+} is the dominant ionization state [67], so the presence of strong fluorine-like lines is expected. In contrast, shown in the bottom of Fig. 7.16 is a spectrum taken from a plasma with $T_e = 2.1$ keV and $n_e = 8.8 \times 10^{19}/m^3$, where Mo^{32+} is the dominant charge state. In this

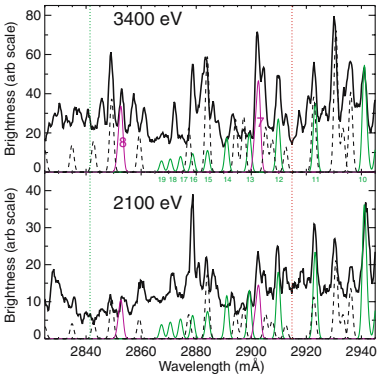

Fig. 7.16. Transitions in Mo^{32+} near the $2p_{1/2}$–$nd_{3/2}$ series limit for (**top**) T_e = 3400 eV and (**bottom**) T_e = 2100 eV. Theoretical lines for Mo^{32+} (*solid*) and Mo^{33+} (*dashed*) are shown at the **bottom**, and the *vertical dashed lines* indicate the series limits

spectrum, all of the Mo^{33+} lines have dropped in intensity, which suggests that the line at 2883.7 mÅ might be due to 2p-8d Mo^{33+} transitions, and the lines at 2922.8, 2910.2 and 2878.6 mÅ, respectively, are the 11C, 12C and 16C transitions. The nC transitions with n $\geq$ 13 (with the possible exception of 16C) are missing from the spectra of Fig. 7.16 because the upper states of these transitions lie above the ionization limit of the nD at 2914.78 mÅ, and the branching ratios towards autoionization is greater than 0.9 in every case [34].

7.6 Conclusions

The high n Rydberg series of helium-like Ar^{16+} has been resolved up to n = 14 in Alcator C-Mod plasmas, and the associated lithium-like satellites up to n = 12 have also been seen. Comparison of observed satellite wavelengths has been made with calculations from two different atomic structure codes, RELAC and MZ, and there is good agreement in general. The calculated intensities of the satellite groups relative to the resonance lines are also in good agreement with the observed line brightness, verifying the dielectronic recombination and inner-shell excitation rates.

2–3 transitions in neon-like Kr has been observed from Alcator C plasmas, in addition to associated fluorine-, sodium- and magnesium-like satellites. Accurate wavelengths have been determined in reference to nearby calibration lines from hydrogen- and helium-like ions. Measured wavelengths and line intensities have been compared with atomic structure calculations and

collisional–radiative modeling from the RELAC code, with very good overall agreement. High n transitions (up to n = 18) in neon-like molybdenum and (up to n = 12) in neon-like krypton have also been recorded. Radial profiles of 2p-4d transitions of Na-, Ne- and F-like molybdenum demonstrate the importance of excitation-autoionization in overall charge state balance. Configuration interaction effects in certain neon-like line intensities have been observed, for transitions with nearly degenerate upper levels; comparison of observed line intensities with theory is excellent.

Acknowledgements

The authors would like to thank J. Irby for electron density measurements, A. Hubbard for electron temperature measurements and the Alcator C-Mod operations groups for expert running of the tokamak. Work supported at MIT by DoE Co-operative Agreement No. DE-FC02-99ER54512. This work was performed under the auspices of the U.S. Department of Energy by the University of California Lawrence Livermore National Laboratory under contract No. W-7405-Eng-48.

References

1. J.E. Rice, F. Bombarda, M.A. Graf, E.S. Marmar, J.L. Terry, Y. Wang: Fusion Eng. Des. **34**, 159 (1997)
2. TFR Group, J. Dubau, M.L. Loulergue: J. Phys. B **15**, 1007 (1981)
3. M.L. Apicella, R. Bartiromo, F. Bombarda, R. Giannella: Phys. Lett. **98**, 174 (1983)
4. M. Bitter, K.W. Hill, M. Zarnstorff, S. von Goeler, R. Hulse, K.M. Young, L.C. Johnson, N.R. Sauthoff, S. Sesnic, M. Tavernier, F. Bely-Dubau, P. Faucher, M. Cornille, J. Dubau: Phys. Rev. A **32**, 3011 (1985)
5. C.P. Bhalla, A.N. Gabriel, L.P. Presnyakov: Mon. Not. R. Astron. Soc. **172**, 359 (1975)
6. P. Beiersdorfer, R. Philips, V.I. Jacobs, K.W. Hill, M. Bitter, S. von Goeler, S.M. Kahn: Astrophys. J. **409**, 846 (1993)
7. N.J. Peacock, R.J. Speer, M.G. Hobby: J. Phys. B **2**, 798 (1969)
8. P.G. Burkhalter, J. Shiloh, A. Fisher, R.D. Cowan: J. Appl. Phys. **50**, 4532 (1979)
9. V.A. Boiko, A.Ya. Faenov, S.A. Pikuz, I.Yu. Skobelev, A.V. Vinogradov, E.A. Yukov: J. Phys. B **10**, 3387 (1977)
10. J.F. Seely, U. Feldman: Phys. Rev. Lett. **54**, 1016 (1985)
11. J.E. Rice, E.S. Marmar, E. Kallne, J. Kallne: Phys. Rev. A **35**, 3033 (1987)
12. E. Kallne, J. Kallne, J. Dubau, E.S. Marmar, J.E. Rice: Phys. Rev. A **38**, 2056 (1988)
13. P. Beiersdorfer, A. Osterheld, S.R. Elliott, M.H. Chen, D. Knapp, K. Reed: Phys. Rev. A **52**, 1980 (1995)
14. A.J. Smith, P. Beiersdorfer, V. Decaux, K. Widmann, K.J. Reed, M.H. Chen: Phys. Rev. A **54**, 462 (1996)

15. E. Kallne, J. Kallne, J.E. Rice: Phys. Rev. Lett. **49**, 330 (1982)
16. J.E. Rice, K.B. Fournier, U.I. Safronova, J.A. Goetz, S. Gutmann, A.E. Hubbard, J. Irby, B. LaBombard, E.S. Marmar, J.L. Terry: New J. Phys. **1**, 19 (1999)
17. L.A. Vainshtein, U.I. Safronova: At. Data Nucl. Data Tables **25**, 311 (1980)
18. C.P. Bhalla, T.W. Tunnell: J. Quant. Spectrosc. Radiat. Transfer **32**, 141 (1984)
19. M.H. Chen: At. Data Nucl. Data Tables **34**, 301 (1986)
20. J. Nilsen: At. Data Nucl. Data Tables **38**, 339 (1988)
21. F. Bely-Dubau, A.H. Gabriel, S. Volonte: Mon. Not. R. Astr. Soc. **186**, 405 (1979)
22. F. Bely-Dubau, A.H. Gabriel, S. Volonte: Mon. Not. R. Astr. Soc. **189**, 801 (1979)
23. F. Bely-Dubau, J. Dubau, P. Faucher, A.H. Gabriel: Mon. Not. R. Astr. Soc. **198**, 239 (1982)
24. J.E. Rice, E.S. Marmar, T. Coan, S.L. Allen, R.D. Cowan: Phys. Rev. A **22**, 310 (1980)
25. E. Kallne, J. Kallne, E.S. Marmar, J.E. Rice: Phys. Scr. **31**, 1985 (1985)
26. I.H. Coffey, R. Barnsley, F.P. Keenan, P. McGinnity, M.G. O'Mullane, N J. Peacock: Cl XV and Cl XVI in the JET and COMPASS-D Tokamaks. In: *UV and X-ray Spectroscopy of Astrophysical and Laboratory Plasmas*, ed. by K. Yamashita and T. Watanabe (Universal Academy Press, Tokyo, Japan 1996)
27. P. Burkhalter, R. Schneider, C.M. Dozier, R.D. Cowan: Phys. Rev. A **18**, 718 (1978)
28. H. Gordon, M.G. Hobby, N.J. Peacock, R.D. Cowan: J. Phys. B **12**, 881 (1979)
29. E.V. Aglitski, V.V. Vikhrev, A.V. Gulov: Phys. Scr. **40**, 601 (1989)
30. E. Kallne, J. Kallne, R.D. Cowan: Phys. Rev. A **27**, 2682 (1983)
31. P. Beiersdorfer, M. Bitter, S. von Goeler, S. Cohen, K.W. Hill, J. Timberlake, R.S. Walling, M.H. Chen, P.L. Hagelstein, J.H. Scofield: Phys. Rev. A **34**, 1297 (1986)
32. P. Beiersdorfer, S. von Goeler, M. Bitter, E. Hinnov, R. Bell, S. Bernabei, J. Felt, K.W. Hill, R. Hulse, J. Stevens, S. Suckewer, J. Timberlake, A. Wouters, M.H. Chen, J.H. Scofield, D.D. Dietrich, M. Gerassimenko, E. Silver, R.S. Walling, P.L. Hagelstein: Phys. Rev. A **37**, 4153 (1988)
33. J.E. Rice, K.B. Fournier, M.A. Graf, J.L. Terry, M. Finkenthal, F. Bombarda, E.S. Marmar, W.H. Goldstein: Phys. Rev. A **51**, 3551 (1995)
34. J.E. Rice, K.B. Fournier, J.L. Terry, M.A. Graf, M. Finkenthal, E.S. Marmar, W.H. Goldstein: Phys. Rev. A **53**, 3953 (1996)
35. D. Pacella, K.B. Fournier, M. Zerbini, M. Finkenthal, M. Mattioli, M.J. May, W.H. Goldstein: Phys. Rev. E **61**, 5701 (2000)
36. J.E. Rice, K.B. Fournier, J.A. Goetz, E.S. Marmar, J.L. Terry: J. Phys. B **33**, 5435 (2000)
37. S.Ya. Khakhalin, A.Ya. Faenov, I.Yu. Skobolev, S.A. Pikuz, J. Nilsen, A. Osterheld: Phys. Scr. **50**, 106 (1994)
38. S.Ya. Khakhalin, B.A. Bryunetkin, I.Yu. Skobelev, A.Ya. Faenov, J. Nilsen, A.L. Osterheld, S.A. Pikuz: JETP **78**, 633 (1994)
39. S.Ya. Khakhalin, V.M. Dyakin, A.Ya. Faenov, H. Fiedorowicz, A. Bartnik, P. Parys, A.L. Osterheld, J. Nilsen: J. Opt. Soc. Am. B **12**, 1203 (1995)

40. M.D. Rosen, P.L. Hagelstein, D.L. Matthews, E.M. Campbell, A.U. Hazi, B.L. Whitten, B. MacGowan, R.E. Turner, R.W. Lee, G. Charatis, G.E. Busch, C.L. Shepard, P.D. Rockett: Phys. Rev. Lett. **54**, 106 (1985)
41. D.L. Matthews, P.L. Hagelstein, M.D. Rosen, M.J. Eckart, N.M. Ceglio, A.U. Hazi, H. Medecki, B.J. MacGowan, J.E. Trebes, B.L. Whitten, E.M. Campbell, C.W. Hatcher, A.M. Hawryluk, R.L. Kauffman, L.D. Pleasance, G. Rambach, J.H. Scofield, G. Stone, T.A. Weaver: Phys. Rev. Lett. **54**, 110 (1985)
42. A.L. Osterheld, R.S. Walling, B.K.F. Young, W.H. Goldstein, G. Shimkaveg, B.J. MacGowan, L. Da Silva, R. London, D. Matthews, R.E. Stewart: J. Quant. Spectrosc. Radiat. Transfer **51**, 263 (1994)
43. P. Beiersdorfer, M.H. Chen, R.E. Marrs, M. Levine: Phys. Rev. A **41**, 3453 (1990)
44. G.A. Chandler, M.H. Chen, D.D. Dietrich, P.O. Egan, K.P. Ziock, P.H. Mokler, S. Reusch, D.H.H. Hoffmann: Phys. Rev. A **39**, 565 (1989)
45. D.D. Dietrich, G.A. Chandler, P.O. Egan, K.P. Ziock, P.H. Mokler, S. Reusch, D.H.H. Hoffmann: Nucl. Instrum. Methods B **24**, 301 (1987)
46. E. Avgoustoglou, W.R. Johnson, Z.W. Liu, J. Sapirstein: Phys. Rev. A **51**, 1196 (1995)
47. W.R. Johnson, J. Sapirstein, K.T. Cheng: Phys. Rev. A **51**, 297 (1995)
48. J.E. Rice, J.L. Terry, K.B. Fournier, M.A. Graf, M. Finkenthal, M.J. May, E.S. Marmar, W.H. Goldstein, A.E. Hubbard: J. Phys. B: At. Mol. Phys. **29**, 2191 (1996)
49. K.B. Fournier, M. Cohen, W.H. Goldstein, A.L. Osterheld, M. Finkenthal, M.J. May, J.L. Terry, M.A. Graf, J. Rice: Phys. Rev. A **54**, 3870 (1996)
50. K.B. Fournier, D. Pacella, M.J. May, M. Finkenthal, W.H. Goldstein: Nucl. Fusion **37**, 825 (1997)
51. G.V. Brown, P. Beiersdorfer, D.A. Liedahl, K. Widmann, S.M. Kahn: Ap. J. **502**, 1015 (1998)
52. I.H. Hutchinson, R. Boivin, F. Bombarda, P. Bonoli, S. Fairfax, C. Fiore, J. Goetz, S. Golovato, R. Granetz, M. Greenwald, S. Horne, A. Hubbard, J. Irby, B. LaBombard, B. Lipschultz, E. Marmar, G. McCracken, M. Porkolab, J. Rice, J. Snipes, Y. Takase, J. Terry, S. Wolfe, C. Christensen, D. Garnier, M. Graf, T. Hsu, T. Luke, M. May, A. Niemczewski, G. Tinios, J. Schachter, J. Urbahn: Phys. Plasmas **1**, 1511 (1994)
53. M.A. Graf, J.E. Rice, J.L. Terry, E.S. Marmar, J.A. Goetz, G.M. McCracken, F. Bombarda, M.J. May: Rev. Sci. Instrum. **66**, 636 (1995)
54. J.E. Rice, J.L. Terry, J.A. Goetz, Y. Wang, E.S. Marmar, M. Greenwald, I. Hutchinson, Y. Takase, S. Wolfe, H. Ohkawa, A. Hubbard: Phys. Plasmas **4**, 1605 (1997)
55. J.E. Rice, E.S. Marmar: Rev. Sci. Instrum. **61**, 2753 (1990)
56. A. Bar-Shalom, M. Klapisch: Comput. Phys. Comm. **50**, 375 (1988)
57. M. Klapisch: Comput. Phys. Comm. **2**, 239 (1971)
58. M. Klapisch, J.L. Schwob, B.S. Fraenkel, J. Oreg: J. Opt. Soc. Am. **67**, 148 (1977)
59. J. Oreg, W.H. Goldstein, M. Klapisch, A. Bar-Shalom: Phys. Rev. A **44**, 1750 (1991)
60. A. Bar-Shalom, M. Klapisch, J. Oreg: Phys. Rev. A **38**, 1773 (1988)
61. L.A. Vainshtein, U.I. Safronova: Phys. Scr. **31**, 519 (1985)
62. U.I. Safronova, J. Nilsen: J. Quant. Spectrosc. Radiat. Transfer **51**, 853 (1994)

63. J.E. Rice, E.S. Marmar, J.L. Terry, E. Kallne, J. Kallne: Phys. Rev. Lett. **56**, 1986 (1986)
64. J.H. Parkinson: Astron. Astrophys. **24**, 215 (1973)
65. J.E. Rice, K.B. Fournier, J.L. Terry, M. Finkenthal, E.S. Marmar, W.H. Goldstein, U.I. Safronova: 2l – nl′ X-ray Transitions from Neonlike Charge States of the Row 5 Metals with $39 \leq Z \leq 46$. In: Proceedings of the 10th Topical Conference on Atomic Processes in Plasmas (1996)
66. P.J. Mohr: Phys. Rev. A **26**, 2338 (1982)
67. K.B. Fournier, W.H. Goldstein, D. Pacella, R. Bartiromo, M. Finkenthal, M. May: Phys. Rev. E **53**, 1084 (1996)

8 High-Temperature Plasmas Diagnostics by X-ray Spectroscopy in the Low Density Limit

G. Bertschinger and O. Marchuk

X-ray spectroscopy is an important tool for the diagnostic of space and fusion plasmas. The X-ray spectra of He-like ions of intermediate-z elements provide information on the ion temperature and plasma motion via Doppler broadening and shift, as well as on the electron temperature via intensity ratios between the resonance lines and associated satellites. The theoretical description of the spectra has been developed to high precision with deviations between the experiment and the theoretical model below 10%. It is shown, that the accuracy of the plasma parameters as obtained from the spectra is compatible with the needs for plasma diagnostics. The same technique can be used for astrophysical objects and solar flares, where the spectra provide the only information. In addition, the ratio between the concentrations of different ionization stages can be obtained. The densities of the ionization stages provide insight into particle transport and the recombination processes in the center of a thermonuclear plasma. X-ray spectroscopy will be applied to the next generation of thermonuclear experiments. To this end, imaging spectrometers with high wavelength and moderate spatial resolution are being developed.

8.1 Introduction

During the last 25 years X-ray spectroscopy has been intensively developed for plasma diagnostics. Since the first application of X-ray spectrometers on the early fusion devices such as PLT and TFR, it has been used to determine basic plasma parameters such as the temperature of ions and electrons. It is now frequently being applied not only to low density plasmas in tokamaks and astrophysical objects [1], but also to laser-produced plasma [2]. It has been shown, that the precision of plasma parameters as obtained from X-ray spectroscopy is competitive to the standard methods for plasma diagnostics, such as Thomson scattering and charge exchange spectroscopy for electron and ion temperature, respectively [3].

Most of the experiments have been performed on He-like ions. This is due to the large range of plasma temperatures, where the fractional abundance is dominated by He-like ions, and in addition they are ideal for the diagnostics of hot plasmas. On the one hand, the spectra of He-like ions are rather simple to be calculated accurately, on the other hand, they are complicated

enough to provide reliable information on the plasma parameters even with some redundancy.

Most frequently X-ray spectroscopy is applied to the diagnostics of magnetically confined high temperature plasmas for thermonuclear fusion. The range of electron temperature is between $0.5 \ldots 15\,\mathrm{keV}$ and the electron density 10^{19}–$10^{20}\,\mathrm{m}^{-3}$, the operational conditions are ideal to observe the spectra of impurities with intermediate Z such as silicon, argon, chromium, iron, nickel, copper and krypton. In the hot plasma center, the density is low enough to be dealt in the low density limit, where most of the ions are in the ground state and only a negligible fraction is found in excited states. The ions are excited by collisions with electrons and are de-excited by photon emission. For ions with intermediate and high charge, the de-excitation rate by photons is high enough, even for the meta-stable states. These conditions were first found in the low density plasmas of the solar corona and they are frequently present in plasmas for magnetic fusion experiments such as tokamaks and stellarators. In the low density limit, not only the relative abundances between the excited states and the ground state of an ionization stage are independent of the electron density, but also the ratio between different ionization stages. The ionization is caused by electron collisions, the recombination consists of a radiative and a dielectronic part. The distribution between the ground state and the excited states, as well as relative abundances between different ionization stages are independent of the electron density and depend only on the electron temperature. Small deviations from coronal equilibrium can occur due to the finite size of the devices and hence finite confinement of the ions, as well as by additional recombination processes, e.g., charge exchange recombination. For laser produced plasmas, the electron density is higher and more sophisticated collisional–radiative models are required to take into account the collisional excitation and de-excitation of excited states.

The instruments provide information not only on the electron and ion temperatures, but also on plasma velocity, charge state distribution and line polarization. Whereas the first experiments on X-ray spectroscopy at the Princeton Large torus (PLT) [4] and the Tokamak Fonteney-aux-Roses (TFR) measured ion temperatures via Doppler broadening [5], Doppler shift measurements of the resonance lines were used to determine toroidal plasma rotation on Alcator C-Mod, Tore Supra and TEXTOR [3,6,7]. Measurement of the Doppler shift of spectral lines requires either precise reference lines in the X-ray spectral range [6] or a difference measurement by reversing the external magnetic fields to reverse the plasma rotation in plasmas with ohmic heating [3,7]. Another approach for the measurement of the toroidal plasma velocity, based on the analysis of different lines in the same spectra with different observation angles was suggested at the tokamak TEXTOR [8].

The information on the relative abundances of ionization stages is found by detailed modeling of the spectra. The density of Li-like ions is obtained from the intensity of doubly excited satellites, which are predominately populated by collisional inner-shell excitation with small contributions of dielec-

tronic recombination. The density of H-like ions can be estimated from the increase of the intensity of He-like lines due to recombination. Even though most of the investigations have been performed on the lowest lying Kα transitions, additional information on the electron temperature has been obtained by the Kβ lines of He-like argon on TEXTOR [9].

For accurate modeling, the wavelengths of the components must be known with precision well below the Doppler widths. The most accurate experimental values for the wavelengths are obtained from measurements on EBIT sources. There, the ion temperature and hence the Doppler broadening can be minimized by special cooling techniques of the ions [10]. In addition, the excitation energy can be controlled accurately and therefore the different processes which contribute to the spectra can be discriminated according to the excitation energy. However, due to the excitation of the ions by an electron beam, the line radiation may be polarized and the intensity of the lines depends on the direction of observation and the polarization properties of the detection system. Therefore the measurements on plasmas with isotropic electron distribution functions are required to determine relative intensities between lines.

X-ray spectroscopy has also been applied to the interpretation of solar spectra, which are emitted by solar flares. Now stellar objects are under investigation by X-ray satellites such as Chandra and XMM. Whereas the present X-ray telescopes are medium resolution devices, the next generation (Constellation-X, XEUS) will provide sufficient spectral resolution for detailed analysis. The spectra from distant object usually suffer from low statistics: solar flares have low emission time and the observation time of stellar objects is limited. In addition, the electron distribution is not Maxwellian, in general, and some of the spectral lines may be polarized. Therefore, verified theoretical data are of great importance to interpret solar and stellar spectra, where they provide the only source of information on the plasma state.

In this contribution, we will show that the spectra of He-like ions can be modeled with high accuracy, using physically relevant parameters only, such as ion and electron temperatures, plasma motion and relative ion abundances. It is organized as follows: in Sect. 8.2 there is a brief discussion on X-ray spectrometers used on fusion experiments, Sect. 8.3 contains the detailed theoretical description of the He-like system, in Sect. 8.4 some results are shown as obtained by a self-consistent procedure based on the detailed modeling of the spectra.

8.2 X-ray Spectrometers

High resolution spectrometers on fusion devices are based on Bragg reflection. The photon energy extends from about 2 keV up to about 15 keV. In this spectral range, crystal spectrometers in the reflective mode have the highest throughput and high spectral resolution. Three types of spectrometers have

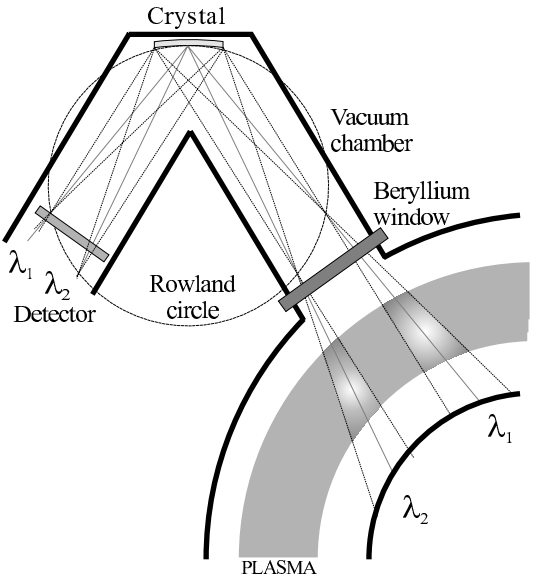

Fig. 8.1. Overview of X-ray spectrometer (Johann type) installed at a tokamak

been used on fusion devices: the traditional Bragg spectrometer with a flat crystal as a diffractive element and van Hamos and Johann spectrometers, which have cylindrically bent crystals.

Bragg spectrometers have been applied for X-ray overview instruments on JET and ASDEX Upgrade, a van Hamos type instrument has been used on Alcator C-Mod. Both the Bragg spectrometer and the van Hamos spectrometer need an entrance slit, the dimensions of the instrument and the size of the crystal determine the spectral range. In both spectrometers, the spectral resolution depends on the width of the entrance slit and the resolving power ("rocking curve") of the crystal. The van Hamos mount is more efficient due to focusing of the X-ray radiation.

Most of the high-resolution spectrometers on tokamaks and stellarators are based on the Johann mount. In this instrument, the crystal is bent cylindrically in the dispersion plane. The combination of Bragg reflection and the imaging properties of the bent crystal focuses the X-ray radiation on the Rowland circle. Each position on the Rowland circle corresponds then to a certain wavelength. The radiation is detected by position sensitive detectors, either gas detectors such as Multi-Wire-Proportional-Counters (MWPC) or one of its variants, Microstrip or Gas-Electron-Multipliers (GEM), which provide simultaneous wavelength and time information by detecting single photons, or by solid state detectors such as CCD or photo-diode arrays. The Johann spectrometer is more efficient than Bragg- or van Hamos spectrometers, as no entrance slit is required and the X-ray radiation is reflected by the full

crystal surface. The resolution is determined by the intrinsic resolution of the crystal, ("rocking curve") the geometrical errors of the Johann configuration and the resolving power of the detector.

A schematic of a typical Johann spectrometer on a tokamak is shown in Fig. 8.1. Typically, the detectors limit the resolution, as long as gas detectors are used.

Future designs of X-ray spectrometers will be equipped with spherical crystals, which provide simultaneously spatial and wavelength resolution and provide higher throughput by combining the favorable imaging properties of the Johann and the van Hamos configuration. The properties of imaging instruments are discussed in more detail in [11].

8.3 Atomic Physics of He-Like Spectra

The spectra are dominated by triplet and singlet transitions in He-like ions and associated satellite transitions in the Li- and Be-like system. The spectrum of He-like argon and iron ions is shown in Fig. 8.2.

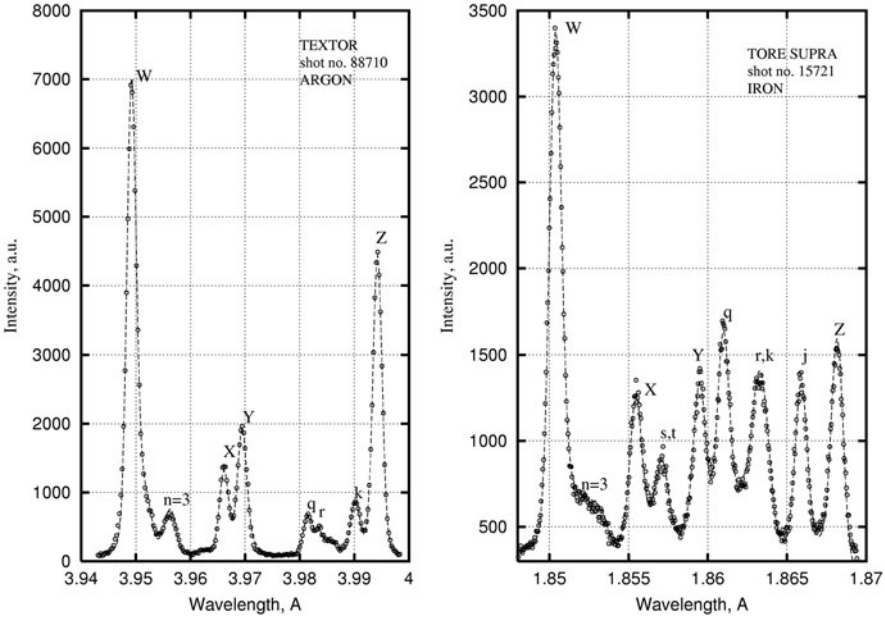

Fig. 8.2. (**a**) Spectrum of He-like argon obtained on tokamak TEXTOR: *open points* – experimental spectrum, *dashed line* – theoretical fit. Spectrum was recorded at 3.7–4.7 s, $T_e = 1.1$–1.2 keV. (**b**) Spectrum of He-like iron from the tokamak Tore Supra: *open points* – experimental spectrum, *dashed line* – theoretical fit. Spectrum was recorded at time 4.0–6.0 s, $T_e = 2.0$–2.2 keV

The He-like lines, determining the spectrum, are following Gabriel's notation [12], the resonance line **w** : $1s^2(^1S^0)$–1s2p ($^1P_1$), the inter-combination line **y**: $1s^2(^1S^0)$–1s2p($^3P_1$), and the forbidden lines **x**: $1s^2(^1S^0)$–1s2p($^3P_2$) and **z**: $1s^2(^1S^0)$–1s2s($^3S_1$). These lines are produced mainly by direct collisional excitation of the He-like ground state with contributions of cascades from higher levels in the He-like system. The satellites present in the spectra arise due to transitions $1s^2$nl–1s2lnl' with $n \geq 2$ in the doubly excited Li-like system. These doubly excited levels in the Li-like system are either populated by dielectronic recombination or by collisional inner-shell excitation. The most intense satellites are: **k**: $1s^22p(^2P_{1/2})$–$1s2p^2(^2D_{3/2})$, **j**: $1s^22p(^2P_{3/2})$–$1s2p^2(^2D_{5/2})$, **q**: $1s^22s(^2S_{1/2})$–$1s2s2p(^2P_{3/2})$, **r**: $1s^22s(^2S_{1/2})$–$1s2s2p(^2P_{1/2})$, **s**: $1s^22s(^2S_{1/2})$–$1s2s2p(^2P_{3/2})$, **t**: $1s^22s(^2S_{1/2})$–$1s2s2p(^2P_{1/2})$.

The **k** and **j** satellites are the strongest dielectronic satellites to the He-like lines, the **q**, **r**, **s** and **t** satellites have strong contributions due to inner-shell excitation from the Li-like ground state. Besides the dominant collisional excitation of He-like ions in the ground state, recombination processes (radiative, dielectronic and charge exchange) of H- and He-like ions, inner-shell excitation of the Li-like ions and, in the case of the **z** line, also inner-shell ionization process contribute to the intensity of the He-like lines. We will discuss these processes in detail.

8.3.1 Excitation

The excitation processes occur in the He-like system by collisions with free electrons, having kinetic energies above the excitation threshold. Due to a collision, one of the target electrons can be excited either directly to the observed excited state or indirectly to a higher lying state $1s^2$-1snl with $n \geq 2$, and consecutive radiative decay. The calculation of excitation cross-sections of two- and three- electron systems is subject to theoretical works using different approaches [13–15]. The new radiation-damped R-matrix method for He-like systems was shown to be in very good agreement with experiments for a number of elements in corresponding temperature intervals [14, 16]. Another approach based on the Coulomb-Born approximation as used in the ATOM program [17] is in agreement with the R-matrix method in the temperature range interval of 0.4 ... 5 keV, with maximum deviations of about 8%.

The role of cascades is different for the singlet and the triplet system and most noticeable for the forbidden transition $1s^2(^1S_0)$–1s2s($^3S_1$) (**z** line). The upper level of the resonance line **w** is weakly affected by cascades; this suggests to use the **w** line as the reference line in the interpretation of the spectra. Another reason is the high line intensity with respect to all other transitions. Among the transitions in the $n = 2$ levels one has to take into account $\Delta n = 0$ dipole transitions, as well as the 1s2s($^1S_0$) to the ground state for the description of the spectra. The line emission due to excitation is expressed as

$$e^{\mathrm{exc}}_{\mathrm{line}}(r) = n_{\mathrm{e}}(r) \cdot n_{\mathrm{He}}(r) \cdot \langle v\sigma \rangle^{\mathrm{exc}}_{\mathrm{line}}(r), \tag{8.1}$$

where $n_e(r)$, $n_{He}(r)$ are the electron density and the density of He-like ions, $\langle v\sigma \rangle$-the excitation rates coefficient for the corresponding level followed by radiative decay. The direct excitation rates and the cascades are combined to effective rates, which also depend on the electron temperature only. The cascades depend on the transition probabilities in the He-like system and require precise structure calculation for $n \geq 3$.

8.3.2 Dielectronic Recombination

The process of dielectronic recombination appears on the spectrum directly as dielectronic satellites of the transitions $1s^2nl$–$1s2l'nl$ in the Li-like system originating from recombination of He-like ions, and indirectly by recombination of H-like ions, which contribute by cascades to the He-like lines. In the case of Li-like dielectronic satellites, the levels are shifted due to the shielding by the 'spectator electron', the lines of the doubly excited Li-like ions are therefore separated from the He-like lines. The separation is largest for the $n = 2$ group. The presence of dielectronic satellites of Li- and Be-like ions is a significant feature of the He-like spectra. Most of these satellites are produced by dielectronic capture of a free electron to the target ion with simultaneous excitation of one of the bound electron. The produced doubly-excited level is energetically unstable and two competitive processes take place, either radiative stabilization to the ground (excited) state of Li-like ion or auto-ionization of one of the excited electrons. The first process is present on the spectra as the line intensity of the satellite with corresponding wavelength. The second channel contributes to the excitation of He-like ions as a resonance process [16]. The intensity of Li-like dielectronic satellites is described by the following expression:

$$e_s(r) = n_e(r) \cdot n_{He}(r) \cdot \frac{4\pi^{3/2} a_0^3}{T_e^{3/2}} \frac{g_s}{g_0} \frac{A_r \cdot A_a}{\sum_j A_r + \sum_i A_a} \exp(-E_s/T_e), \qquad (8.2)$$

where A_r, A_a are the radiative and auto-ionization rates of doubly excited levels in the Li-like system, g_s, g_0 the statistical weights of the upper level and the ground state of the He-like ion. E_s is the excitation energy of the electron over the He-like ground state and corrected by the ionization energy of the Li-like system, T_e the electron temperature, in fractions of the Rydberg constant, respectively. The first summation includes all levels of the Li-like system lying below the upper level of the transition. The second sum includes the auto-ionization channels of the upper level. The satellites belonging to the group of $n = 2$ are well separated on the spectra and their intensity with respect to the He-like lines is used as a diagnostic tool. The distinct separation of the group $n = 2$ dielectronic satellites decreases with higher n, the satellites with higher n approach the **w** and **y** lines. The group of satellites with $n \geq 4$ is not resolved on the He-like spectra due to Doppler broadening of the He-like lines and their small intensity relative to $n = 2$. The total intensity of the

satellites belonging to different groups is proportional to $1/n^3$, this is why the satellites with $n = 2, 3, 4$ have the largest contribution to the experimental spectra. Some of the $n = 2$ satellites, seen on the spectra, have except of the dielectronic part strong contributions due to inner-shell excitation. At plasma conditions with lower temperature the Be-like dielectronic satellites contribute to the He-like spectra as well. These satellites are due to transitions $1s^2 2l' nl$–$1s2l'2l'' nl$. Their emission is proportional to the charge state of Li-like ions and is seen on the low energy side of the spectra.

Recently, it has been found, that some of the doubly excited levels, are influenced by radiative cascades within the Li-like system. This is especially important for levels with small auto-ionization rates A_a and hence low population due to dielectronic recombination. The temperature dependence is taken into account by corrections to (8.2) [18].

The dielectronic satellite calculations for different He-like ions were carried out by Dubau and Safronova for different ions [19, 20]. The first method involves the program SUPERSTRUCTURE and the associated DISTORTED-WAVE collision program and follows the procedure described in [21]. The MZ program uses 1/Z–perturbation theory expansion for the structure calculation. The satellite intensity based on the first approach is roughly consistent with the experiment [22]. In contrast, deviations of about 10–15% between different groups of $n = 2$ and $n = 3$ dielectronic satellites as calculated by the MZ program and experimental values have been reported on some experiments [23–25]. Recent calculations, based on the AUTOSTRUCTURE code [26], which is part of the ADAS package, provided the best agreement between the experiment and the theory, especially for the consistency between the $n = 2$ satellites and the $n > 3$ satellites with the measurement. Within this paper, these data have been used for the modeling of the spectra. However, the wavelength calculations made by the MZ program describe best the position of the satellites on the spectrum within the experimental errors which are now about 0.1 mA.

8.3.3 Radiative Recombination

The excited levels of the He-like ions are also populated via recombination processes of H-like ions. The line emission due to radiative recombination is expressed as:

$$e_{\text{line}}(r) = n_e(r) \cdot n_H(r) \langle v\sigma \rangle_{\text{line}}^{\text{rec}} , \tag{8.3}$$

where $n_e(r)$, $n_H(r)$ are the electron density and the density of H-like ions, $\langle v\sigma \rangle$ is the rate coefficient for radiative recombination, respectively. The contribution of radiative recombination to singlet and triplet He-like lines increases at higher temperatures due to the increase of the H-like ions abundance. The different character of dielectronic and radiative recombination (resonant and non-resonant) for H-like ions requires different methods for the calculation of the two processes; nevertheless, both processes must be taken into account to identify the H-like ion charge states.

8.3.4 Charge Exchange Recombination

The process of charge exchange occurs by capture of a bound electron from neutral hydrogen by H-like ions followed by radiative decay. As in the case of radiative recombination or cascades in He-like ions, the contribution of charge transfer is stronger to the triplet lines than to the resonance line **w**. The emission via charge-transfer is determined by:

$$e_{\mathrm{line}}(r) = n_0(r) \cdot n_{\mathrm{H}}(r) \langle v\sigma \rangle_{\mathrm{line}}^{\mathrm{CX}} , \tag{8.4}$$

where $n_0(r)$ is the density of neutral hydrogen atoms in the plasma volume and $\langle v\sigma \rangle$ is the charge exchange rate coefficient. The contribution of this process depends on the operating conditions. It can influence considerably the charge state equilibrium in the plasmas [27, 28]. The strongest influence on the spectra by charge exchange recombination arises during neutral beam injection. The different collision energies for the neutral background and atoms in the neutral beam require different approaches in the cross-section calculations [29, 30].

8.3.5 Inner-Shell Excitation

Inner-shell excitation of the Li-like ion core is the second mechanism to populate the doubly excited levels. For the three electron system, the cascade effect between doubly excited levels is negligible compared to dielectronic recombination. This is justified by the fact that for highly charged ions the states with higher n, n > 3, have large initial populations, so therefore the contribution due to the cascade is negligible. The emission of the satellite line is then:

$$e_{\mathrm{line}}^{\mathrm{is}}(r) = n_{\mathrm{e}}(r) \cdot n_{\mathrm{Li}}(r) \cdot \langle v\sigma \rangle_{\mathrm{line}}^{\mathrm{is}} , \tag{8.5}$$

where $n_{\mathrm{Li}}(r)$ is the concentration of the Li-like ion in the plasma. The Coulomb-Born calculations of inner-shell excitation coincide with the R-matrix calculations for this process to within 10% percent.

8.3.6 Inner-Shell Ionization

In addition, inner-shell ionization contributes to the intensity of the **z** line. The removal of an inner-shell electron leads directly to the 1s2s excited level of the He-like system. The contribution of this process is proportional to the concentration of the Li-like ions and should be taken into account at low electron temperatures or if the charge state distribution differs from ionization equilibrium.

$$e_{\mathrm{z}}(r) = n_{\mathrm{e}}(r) \cdot n_{\mathrm{Li}}(r) \cdot \langle v\sigma \rangle_{\mathrm{Z}}^{\mathrm{ion}} \tag{8.6}$$

The assumption of the low density limit substantially simplifies the calculation of the corresponding cross-sections and decreases the number of atomic processes involving in line emission. At higher plasma densities, a full collisional–radiative model must be used including all the process mentioned. Additional processes such as three-body recombination [17] start to play a role for the level population and change the equilibrium correspondingly. In existing magnetic fusion experiments, the density range of 10^{13}–$10^{14}\,\mathrm{cm}^{-3}$ is low enough, so that the low density limit is valid for the description of the experimental spectra. However, the ion-ion collisions are considered on the basis of an unperturbed model [31].

Wavelength calculations for high Z ions include relativistic corrections that are performed to a certain level of accuracy. In these calculations the wavelengths are obtained by perturbation theory methods using 1/Z expansion. These values are cross checked via relativistic all order calculations of the He-like ions [32]. If available, measurements on EBIT sources are used for the verification of theoretical calculations based on different approaches [33, 34]. For a given spectrometer setting, a reference lines is needed for an *ab initio* wavelength calibration. To calculate the dispersion, either the geometry of the Bragg spectrometer or a second spectral line is needed.

The ratio between the **w**-line, which is predominantly excited by electron collisions (8.1), and the **k**-satellite, which is populated by dielectronic recombination (8.2), depends on the electron temperature only. The ratio between the **w** line and the intensity of the collisional excited Li-like satellites (8.5), depends on the density ratio between the Li-like and He-like ions, as the collisional excitation rates for the allowed transitions in the He-like system and in the doubly excited Li-like system are similar.

8.4 Determination of Plasma Parameters

The determination of plasma parameters using He-like spectra is based on a self-consistent modeling of the theoretical spectra. The following variables take part in the variation procedure based on least-squares fitting: electron and ion temperatures, toroidal plasma velocity, concentrations of H-, He- and Li-like ions. In addition, a background function was used to subtract the plasma background from the experimental spectra. The background consists of continuum radiation from the plasma and detector noise.

The line shapes are described by Voigt functions, which reflect the Lorentzian line profiles due to natural line width and Gaussian profiles due to Doppler broadening. The instrumental broadening by the rocking curve of the crystal, de-focusing and the finite resolution of the detector is described well by a Voigt profile shape too [3].

The analysis of the spectra and the fitting procedure is straight forward due to the properties of the He-like systems. The information on the different plasma parameters is obtained from well separated portions on the

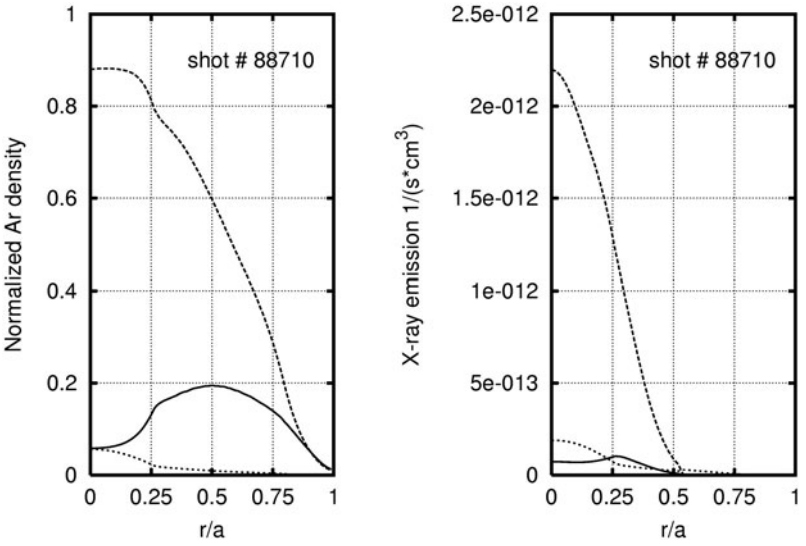

Fig. 8.3. (**a**) Radial profiles of argon density in TEXTOR: *point* line H-like, *dashed* line He-like; *solid* line Li-like ions. Emissivity profiles of the different argon stages presented in (**b**): *point* line H-like, *dashed* line He-like, *solid* line Li-like ions

spectrum, which considerably reduces the correlations between the variables and increases the stability of the fitting procedure. The ion temperature and the plasma motion contribute to the line widths and the line shifts only, the electron temperature is obtained mainly from the ratio between the n = 2 satellites and the resonance line **w**, with smaller dependence on satellites n > 2 and the differences between the excitation rates for the singlet and the triplet lines. The density of Li-like and Be-like ions is proportional to the intensity of the lines excited by inner-shell excitation. Finally, the density of H-like ions is obtained from the contribution to the triplet lines.

Although the X-rays are emitted mainly from the plasma center, small corrections are necessary, since the spectrometer integrates over the line of sight through the plasma. In TEXTOR the shapes of the radial profiles of the electron temperature and density are taken from ECE measurements [35] and HCN interferometer data [36] respectively. These radial profiles are normalized to the spectroscopic values as obtained from the fit. The radial distribution of highly ionized ions is taken from independent transport code calculations, reflecting the atomic physics of charge state distribution, transport properties of the plasma and fluxes of neutral hydrogen [37]. We present the charge state distribution and emission profiles for He-like argon ions in Fig. 8.3. The emission profiles of highly ionized ions are steep functions of temperature, this reflects the local character of this diagnostic with respect to other passive spectroscopic methods.

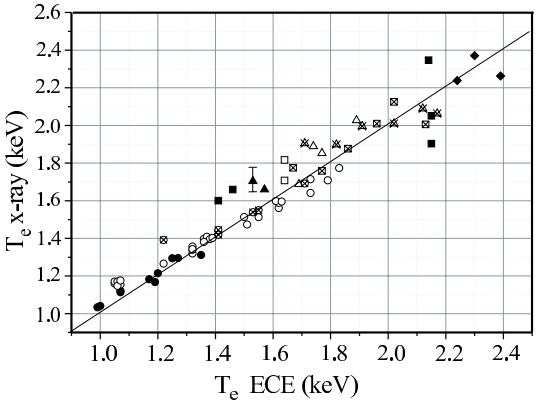

Fig. 8.4. Comparison of the electron temperature measured in the plasma center by the X-ray spectrometer and the ECE diagnostics with hydrogen (*solid points*) and deuterium (*open points*) as working gas. The *squares* and *triangles* correspond to discharges with neutral beam injection [3]

8.4.1 Electron and Ion Temperature, Toroidal Plasma Velocity

As for all collision processes the electron temperature is the most important parameter for the formation of the spectra, and inversely, this parameter is determined with the highest accuracy. The comparison of the electron temperature to measurements by electron cyclotron emission is shown in Fig. 8.4. The ECE measurements have been cross-calibrated to Thomson scattering data, which for TEXTOR are available for one time per discharge only. The ion temperature, as well as the plasma rotation, is shown in Fig. 8.5 and Fig. 8.6. In these experiments, the ion temperature was measured independently by charge exchange spectroscopy. A tangential neutral beam has been used for the charge exchange diagnostics.

Unfortunately, the beam heats up the plasma considerably and increases the momentum of the plasma column, influencing the rotational speed of the plasma as well. Therefore, charge exchange spectroscopy can be used only in discharges with additional heating. In ohmic plasmas and plasmas heated by electromagnetic waves X-ray spectroscopy is the only diagnostic to determine the ion temperature, as well as the plasma rotation.

8.4.2 Relative Abundance of Charged States

To determine the relative abundance of ionization stages, there are no alternatives to spectroscopic measurements. In fusion devices, the distribution of the ionization stages deviates from coronal equilibrium, due to transport and finite confinement of the ions as well as charge exchange recombination with neutral hydrogen. Both the particle transport and the diffusion reduce the

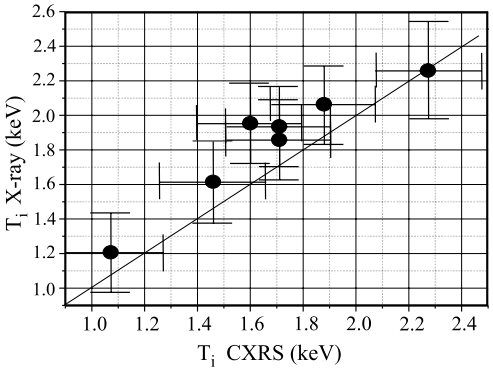

Fig. 8.5. Comparison between the central ion temperature measured by the X-ray spectrometer and the ion temperature by charge exchange recombination spectroscopy (CXRS) [3]

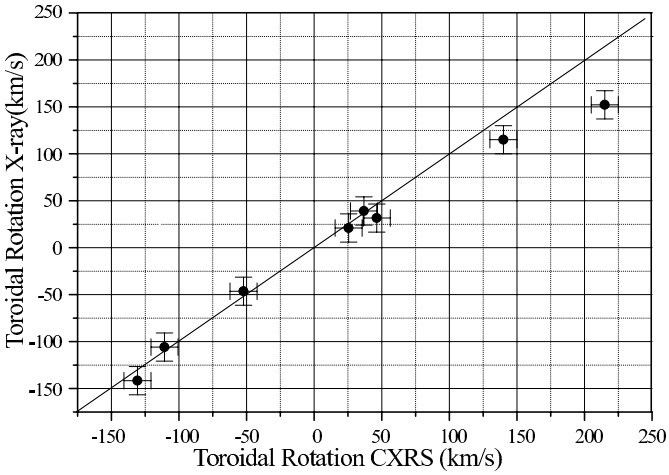

Fig. 8.6. Comparison between the measurements of toroidal plasma velocity by X-ray spectrometer and charge exchange recombination spectroscopy (CXRS) in the plasma center [3]

charge state by reducing the ionization or increasing the recombination, respectively and shift the ionization equilibrium to lower ionization states. The transport of neutral hydrogen deviates strongly from the transport of the ions, as the neutrals are not confined by the magnetic fields. In present devices for magnetic fusion, neutral hydrogen is produced at the plasma facing components by recombination of the out flowing hydrogen ions. The neutrals rapidly gain energy by charge exchange, and have rather high mean free paths before being ionized. Therefore, the concentration of neutral hydrogen is much larger than the equilibrium value. Up to now, the diagnostic for the

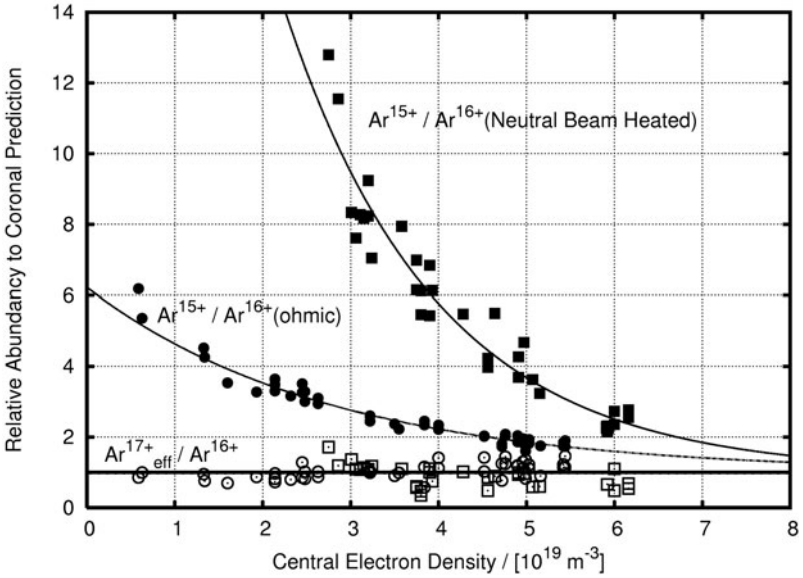

Fig. 8.7. Comparison of the ratio Ar^{15+}/Ar^{16+} (*solid symbols*) and Ar^{17+}/Ar^{16+} (*open symbols*) in discharges in TEXTOR, normalized to the coronal ionization equilibrium. The *circles* are for plasmas with ohmic heating, squares for plasmas with additional heating by injection of neutral hydrogen beams

measurement of neutral density in the plasma is not well-established. Detailed analysis of the highly ionized X-ray spectra is a candidate for this measurement. In Fig. 8.7, the charge state distribution of Li-like argon normalized to the ionization balance is shown, as well as the effective concentration of H-like argon. This effective concentration is determined from the contribution of the H-like ions to the He-like lines due to recombination. It is larger than the real concentration, as it contains both the radiative and dielectronic recombination with electrons, as well as charge exchange recombination with neutral hydrogen atoms. The concentration of Li-like ions has been obtained from the satellites **q** and **r**, which are mainly populated by inner-shell excitation of Li-like ions in the ground state. The dielectronic part of these satellites represents no more than 20% of their total intensities and has been taken into account. The precision of the determination of Li-like ions has been improved by taking into account the cascades within the doubly excited Li-like levels. The **q** and **r** satellites are only weekly populated by direct dielectronic capture and cascade effects increase their intensity up to a factor 2. Some Be-like dielectronic satellites contribute to the intensities of **q** and **r** satellites too. These satellites significantly contribute only at smaller temperatures and hence high Li-like density.

In contrast to the density measurements of Li-like ions by means of inner-shell excitation , the spectra provide information not directly on the density

of H-like ions, but on their total recombination. As both radiative and dielectronic recombination with electrons, as well as charge exchange recombination with neutral hydrogen atoms contribute to the spectra, the fraction of charge exchange recombination and hence the density of neutral hydrogen can be estimated using a transport model. In low density TEXTOR discharges, the dominant process for the recombination of H-like ions is charge exchange with neutral hydrogen. The diffusion coefficient in the plasma core, which is derived from the density of Li-like ions and the recombination rate of H-like ions, coincides with the measurement by gas injection experiments [37].

In neutral beam heated plasmas, the density of the neutrals is still increased due to the injected particles, therefore the recombination is enhanced and the charge state distribution is shifted to lower values. For higher plasma densities, the role of charge exchange is reduced, as the penetration of the neutral particles to the center and hence the deviation from the equilibrium distribution is smaller. At these plasma parameters, the charge state distribution approaches the coronal distribution, both for plasmas heated by the plasma current (ohmic) or by Neutral Beam Injection (NBI). The recombination rate of H-like ions should not exceed the coronal value. In steady state, the recombination cannot be larger than the ionization. The slight increase above the coronal value is explained by the spatial distribution of the neutral hydrogen atoms in the plasma. The ionization, as well as radiative and dielectronic recombination, is uniform in the hot plasma column whereas the charge exchange recombination is restricted to the locations of high neutral density, e.g., the crossing of the neutral beam with the plasma.

8.5 Conclusions

Within the last 25 years of X-ray spectroscopy on fusion devices, the theory of He-like ions has been developed to an impressive precision. The spectra can be modeled with deviations not more than 10% on all lines. For the modeling, only parameters with physical meaning and no additional approximation factors are required. Even the small effects due to recombination of H-like atoms, which contribute only a few percent to the line intensity, can be used to explain consistently the recombination processes and hence the charge state distribution in a hot plasma. The measurements on fusion devices such as tokamaks or stellarators allow the comparison to the standard diagnostics for the same parameters. As these diagnostics are based on different physical processes, they provide sensitive tests for the atomic physics used for the synthetic spectra. They also allow distinguishing between different theoretical approaches to predict the spectra of other elements within the iso-electronic series. The modeling of the X-ray spectra of astronomical objects or solar flares, which are now frequently explored by X-ray satellite missions, is now more reliable. In these experiments, the statistical quality of the spectra is limited due to the finite observation time or the lifetime of

the events and no redundancy is available in the spectra. The more precise evaluation of the plasma parameters is the basis for the evaluation and the understanding of the processes on stars and the sun.

The X-ray spectrometers on fusion devices are now being upgraded to imaging instruments, which allow the measurements of plasma parameters not only in the plasma center but along different cords within the plasma. These instruments will improve the understanding of transport processes and confinement properties in hot plasmas. In addition, they will extend the high precision measurements and modeling to elements with higher charge and will help to further improve the quality of the atomic physics data.

Acknowledgments

The authors are glad to thank many scientists, who have contributed to the results. The TEXTOR team, where the measurements were performed and highly reproducible plasmas were provided, especially to Dr. W. Biel, who did the experiments on the transport properties of TEXTOR, Prof. L. Vainshtein, Dr. A. Urnov and F. Goryaev provided us with the results of atomic data calculation. Dr. N. Badnell trained one of us (O. M.) to get the results on dielectronic recombination using atomic codes. Dr. S. Fritzsche put our attention to the cascades within the Li-like ions and Prof. R. Janev discussed the charge exchange recombination processes. Princeton Plasma Physics Laboratory supported the measurements on TEXTOR, both by cooperation with Dr. M. Bitter, and loan of X-ray detectors.

References

1. Phillips K.J.H. et al., Astron. Journal **419**, 426 (1993)
2. Faenov A.Ya. et al., Physica Scripta **T80**, 536–538 (1999)
3. Weinheimer J. et al., Rev. Sci. Instrum. **72**, 2566–2574 (2001)
4. Bitter M. et al., Phys. Rev. Lett. **43**, 129 (1979)
5. TFR Group, M. Cornille, J. Dubau, M. Loulergue, Phys. Rev. A **32**, 3000 (1985)
6. Rice, J.E., Marmar E.S., Bombarda F., Qu L., Nuclear Fusion **37**, 421–426 (1997)
7. Platz P., Cornille M., Dubau J., J. Phys. B : At. Mol Opt. Phys. **29**, 3787–3797 (1996)
8. Bertschinger G. et al., Proc. 27th EPS Conference on Controlled Fusion and Plasma Phys., Budapest, **24B**, 840–843 (2000)
9. Bertschinger G., Goryaev F., Kunze H.-J., Marchuk O., Urnov A., 7th Int. Colloquium on At. Spectra for Astr. Plasmas, Belfast (2001)
10. Beiersdorfer P. et al., Physica Scripta **80**, 312 (1999)
11. Bertschinger G., Bitter M., Workshop on Adv. Diagnostics for Magnetic and Inertial Fusion, Varenna, Italy (2001)
12. Gabriel A.H., Paget T. M., J. Phys. B **5**, 673 (1972)

13. Keenan F.P., McCann S. M., Kingston A.E., Physica Scripta **35**, 432 (1987)
14. Kimura E., Nakazaki S., Berrington K.A., Norrington P.H., J. Phys. B: At. Mol. Opt. Phys. **33**, 3449–3466 (2000)
15. Bely-Dubau F., Dubau J., Faucher P., Gabriel A., Mon. Not. R. astr. Soc. **198**, 239 (1982)
16. Whiteford A. et al., J. Phys. B: At. Mol. Opt. Phys. **34**, 3179–3191 (2001)
17. Sobelman I., Vainshtein A., Yukov E., *Excitation of Atoms and Broadening of Spectral Lines* (Springer, Heidelberg 1998)
18. Marchuk O., Bertschinger. G., Badnell N.R., Fritzsche S., J. Phys. B: At. Mol. Opt. Phys. **37**, 1951–1960 (2004)
19. Bely-Dubau F. et al., Phys Rev. A **26**, 3459–3468 (1982)
20. Safronova U.I., Lisina T.G., At. Data Nucl. Data Tables **24**, 49 (1979)
21. Bely-Dubau F., Gabriel A. H., Volonte S., Mon. Not. R. astr. Soc. **186**, 405 (1979)
22. Bely-Dubau F. et al., Mon. Not. R. astr. Soc. **201**, 1155–1169 (1982)
23. Bitter M. et al., submitted to Phys. Rev. Lett.
24. Bertschinger G. et al., Physica Scripta **T83**, 132–141 (1999)
25. Marchuk O. et al., Proc. 23rd International Conference on Photonic Electronic and Atomic Collisions, Stockholm (2003)
26. Badnell N., J. Phys B: At. Mol. Phys. **19**, 1541–1552 (1986)
27. Marchuk O., Bertschinger G., Kunze H.-J., Goryaev F., Urnov A., Proc. DPG Spring Conference, Aachen (2003)
28. Marchuk O., Bertschinger G., Kunze H.-J., Goryaev F., Urnov A., Proc. German-Polish Conference on Plasma Diagnostics for Fusion and Applications, Greifswald (2002)
29. Whyte D.G et al., Phys. Plasmas **5**(10), 3694 (1998)
30. Janev R., private communication (2003)
31. Walling R.S., Weisheit J.C., Physics Reports **162**, 1–43 (1988)
32. Johnson W.R., Plante D.R., Sapirstein J., Adv. in At., Mol. and Opt. Physics **35**, 255–329 (1995)
33. Beiersdorfer P., private communication
34. Tarbutt M.R., Barnsley R., Peacock N.J., Silver J.D., J. Phys. B: At. Mol. Opt. Phys. **34**, 3979–3991 (2001)
35. Waidmann G., P.C. de Vries, Krämer-Flecken A., Rev. Sci. Instrum. **68**, 492 (1997)
36. Soltwisch H., Stodiek W., Manickam J., Schlueter J., Proc. 11th Int. Conf. Plasma Physics Controlled Nuclear Fusion Research, Kyoto, Vol. 1, 263 (1986)
37. Biel W. et al., Proc. 28th EPS Conference on Controlled Fusion and Plasma Physics, Madeira, Protugal (2001)

Part III

Surface Processes and Material Issues

9 Review and Status of Physical Sputtering and Chemical Erosion of Plasma Facing Materials

J. Roth

The present knowledge of ion induced erosion processes for plasma facing components, such as physical sputtering and chemical erosion, is presented and extrapolated to fusion reactor conditions. While physical sputtering of elemental materials is reasonably well understood, thermal effects and effects due to material mixing need further investigation. In chemical erosion the basic underlying processes were elucidated within the last decade. More data are needed for the composition of hydrocarbon and radicals in the eroded flux and their transport and deposition properties. The investigation of doped graphites has progressed and promises the development of low chemical erosion materials.

9.1 Introduction

The erosion of plasma facing materials in magnetically confined fusion devices, such as ITER, is a key issue in several aspects: Component lifetime in the interaction with the edge plasma and plasma contamination by eroded surface atoms are longstanding issues for the material choice in ITER. Safe management and accounting of tritium in ITER and future fusion power reactors will be crucial for the acceptance of fusion as an environmentally benign power source. Tritium retention in plasma-facing components (PFCs) with CFC has emerged as a primary concern for next-step fusion devices fuelled with mixtures of D and T, with strong implications for in-vessel component design, material selection, operational schedule and safety. The issue of tritium retention is dominated by the inventory retained in deposited layers of eroded material, such that again erosion as the starting point of processes leading to build-up of tritium inventory is of prime importance.

A key decision for ITER is, therefore, the choice of plasma facing materials. Despite the prevalence and strong historic trend of operating tokamaks to rely on carbon-based PFCs (mainly to optimize plasma performance – in combination with oxygen gettering techniques such as boronization or siliconization – and to enable access to large plasma operational space), its application to a D-T next-step must be restricted due to its strong chemical affinity to hydrogen-isotopes, which affects erosion lifetime and tritium inventory.

During the last few years there have been considerable advances in experiments and theory (for a comprehensive review see [1]) with respect to the mechanisms leading to the erosion of plasma facing materials. Physical sputtering appears to be well understood for elemental materials, while sputtering by non-recycling ions leads to material modifications which need to be investigated and modeled in more detail. Chemical erosion has seen a remarkable degree of clarification of the fundamental reaction steps since the last IAEA Workshop in 1992. However, there are still several issues, identified in this review that require further work and whose resolution requires a co-ordinated effort by all parts of the fusion community. The progress since 1992 and remaining open questions are summarized below.

Erosion due to energetic particle bombardment depends on a number of parameters such as mass ratio of incident particles to surface atoms, particle energy and flux, as well as surface temperature. In the following, the physical understanding of different erosion mechanisms occurring at different wall components in fusion devices will be presented together with supporting data from laboratory experiments.

9.2 Physical Sputtering

9.2.1 Sputtering of Pure Elements

Kinetic Effects

Physical sputtering is a well investigated erosion mechanism and a sound physical theory exists for the dominant processes under fusion plasma–wall interaction conditions [2,3]. For the considered plasma facing materials, such as Be, C, and W, erosion data exist for H, D and He in the energy range of 10 eV up to 10 keV [4,5]. The data are extended to higher energies and to T using computer simulation [5,6].

Physical sputtering results from elastic energy transfer from incident particles to target atoms. Surface atoms can be ejected if they receive enough energy to overcome the surface binding energy E_s, be it directly from bombarding ions or through a collision cascade involving other target atoms. In the limit of energies high enough to develop an isotropic collision cascade the sputtering yield is proportional to the energy deposited in elastic collisions within a near-surface layer which is mostly described by the nuclear stopping power, $S_n(E)$. At low ion energies, where the transferred energy to surface atoms is comparable with the surface binding energy, the sputtering yield decreases strongly and becomes zero below a threshold energy.

For light ions incident on heavy materials, the threshold energy, E_{th}, is determined by the energy which can be transferred to target atoms and can be analytically approximated by [6]

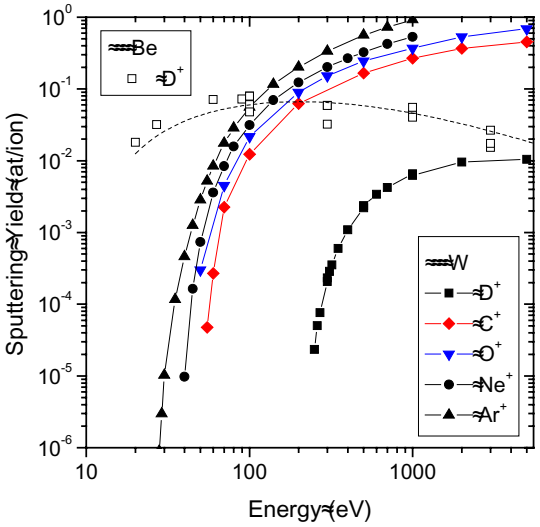

Fig. 9.1. Energy dependence of the sputtering yields of Be and W bombarded by D, C, O, Ne and Ar ions. Experimental data are fitted using an empirical equation for the sputtering yields [5]

$$E_{\mathrm{th}} = \frac{(M_1 + M_2)^4}{4M_1M_2\,(M_1 - M_2)^2} E_{\mathrm{s}}, \tag{9.1}$$

where M_1 and M_2 are the incident particle mass and target mass respectively, and E_s is the surface binding energy. The energy dependence of the yield, Y, at normal incidence can empirically be described by the following expression:

$$Y = QS_{\mathrm{n}}(E)\left(1 - \frac{E_{\mathrm{th}}}{E}\right)^2 \left(1 - \left(\frac{E_{\mathrm{th}}}{E}\right)^{2/3}\right), \tag{9.2}$$

where $S_{\mathrm{n}}(E)$ is the function for the energy dependence of the energy deposited in elastic collisions. Values for the fitting parameters Q and E_{th} are tabulated for many ion-target combinations [5].

At grazing incidence the erosion yield is enhanced relative to the yield at normal incidence, as more energy is deposited within the near-surface layer. The dependence on angle of incidence is well described theoretically for light ions [7], and parameter fits exist for light and heavy ions [5]. Surface roughness tends to reduce the pronounced dependence of the sputtering yield on angle of incidence. This has been demonstrated and interpreted in Monte Carlo simulations for different kinds of graphite materials [8] and beryllium [9].

For Be and W, experimental data and the fit for the sputtering yield at normal incidence are shown in Fig. 9.1 for D ions as a function of incident particle energy. Physical sputtering data are available for both materials from energies close to the threshold energy (9 eV for D on Be and 200 eV for D on

W) up to the high keV range and have been collected in data summaries [5, 10, 11]. The data shown in Fig. 9.1 are taken from [5]; very similar data exist for H and He ion bombardment. All experimental data shown were obtained from the weight loss of polished samples after ion bombardment. In the case of Be, clean surfaces could only be obtained at temperatures above 900 K where Be diffuses through the surface oxide layer [12], while at lower temperatures, oxidation from the residual gas reduced the erosion yield [5].

The high threshold energy for hydrogen isotope sputtering of W reduces the yields drastically at energies below 1000 eV. Ion energies in the divertor are expected to be in the 20 to 100 eV range, and charge exchange (CX) neutrals have their maximum below 20 eV. For the low-Z element Be, the threshold energy is not high enough to strongly reduce physical sputtering.

However, the situation is different for heavier ions, such as C, O, Ne or Ar. Heavier ions can transfer almost all their energy onto target atoms. In this case, the threshold energy is determined by the energy loss in inelastic stopping of atoms in the process of the reversal of momentum that requires several collisions inside the target [3, 13]. The resulting threshold energy is of the order of 4 to 8 times the surface binding energy E_s, i.e., about 30 eV for W (Fig. 9.1).

Additionally, the incident impurity ions in a fusion device will be multiply charged, e.g., a charge state of 4 can be assumed for Be, C, O, and even higher values for W ions. This will result in increased acceleration of the ions in the sheath potential such that the most probable energies for multiply charged ions in a divertor plasma with $T_e = 10$ eV will be around 200 eV, i.e., well above the threshold energy.

Data for the sputtering yield of impurity ions, such as C, O, Be, and W ions, are shown in Fig. 9.2 for C-based materials. The erosion processes for C^+, Be^+ and W^+ are predominantly due to physical sputtering. Chemical effects may contribute through the reaction with oxygen [14]. In the case of carbon, volatile CO and CO_2 formation enhances the erosion yield. Oxygen will lead to the formation of oxide layers in Be and W (see Sect. 9.2.2) and, in general, decrease the erosion yield. For Be, an increase of surface binding energy results, leading both to a decrease of the sputtering yield and to a shift of the threshold energy for sputtering to higher energies according to (9.1). The data for deuterium sputtering of a fully oxidized BeO surface are given in [15, 16]. For W, the dilution of W atoms in a surface oxide layer also decreases the erosion yield [17]. In addition. the oxidation of the surface may lead to the formation of oxides with much lower surface binding energies, such as WO_3. The enhanced erosion due to WO_3 appears, however, to be a small effect that could not be observed during oxygen ion sputtering even at temperatures up to 1900 K [18]. However, sputtering by hydrogen isotopes, near the threshold energy for sputtering, results in such small yield values that the additional release of oxide molecules during simultaneous impact by oxygen can be observed [19]. This effect results in small, but measurable erosion yields even below the threshold energy for sputtering of clean tungsten.

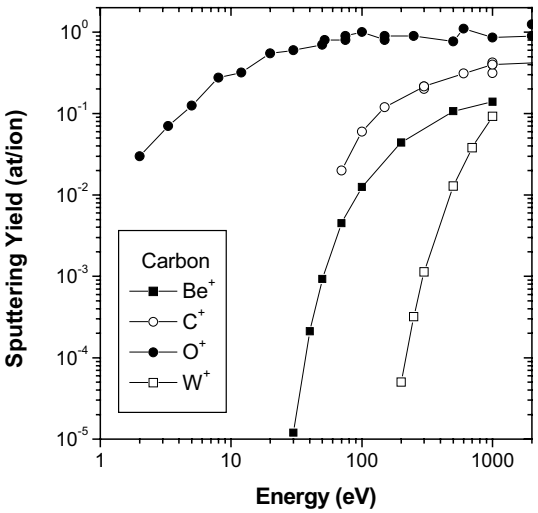

Fig. 9.2. Calculated energy dependence of the sputtering yield of carbon by plasma impurity ions Be, C and W. Experimental data for O sputtering are shown for comparison [14]

With the exception of sputtering by C^+ ions, the physical sputtering of Be and W appears to be well documented. Carbon bombardment, in general, leads to the deposition of protective surface layers (see Sect. 9.2.2). Only in conditions where carbon self-sputtering exceeds unity, i.e., at grazing incidence or at temperatures above $\sim 1800\,\mathrm{K}$, could a few yield data points be obtained for clean W surfaces.

No experimental data are available for Be^+ and W^+ bombardment. Corresponding data shown in Fig. 9.2 are from TRIM.SP calculations [20].

Thermal Effects

The kinetic theory of physical sputtering does not predict effects of surface temperature. This was verified in [21] for sputtering of Ag and Cu up to temperatures of about 0.7 melting temperature. However, recently erosion yields were published showing an enhancement of the sputtering yield with increasing surface temperature starting at about 0.8 melting temperature for Be [22,23], Li [24] and Ga [25]. Figure 9.3 shows results for Be sputtered by D in the plasma simulator PISCES-B (Fig. 9.3a [23]) and for D^+ and B^+ sputtering in ion beam experiments (Fig. 9.3b, [4,22]). A theory, developed for the case of W in 1981 [26], assumed the formation of hot spots with temperatures causing local sublimation of the material, while recent modeling [23] assumes a two step erosion process: the formation of adatoms due to ion impact followed by thermal sublimation. Surface adatoms are less strongly bound to the surface than atoms embedded within the lattice structure and are, there-

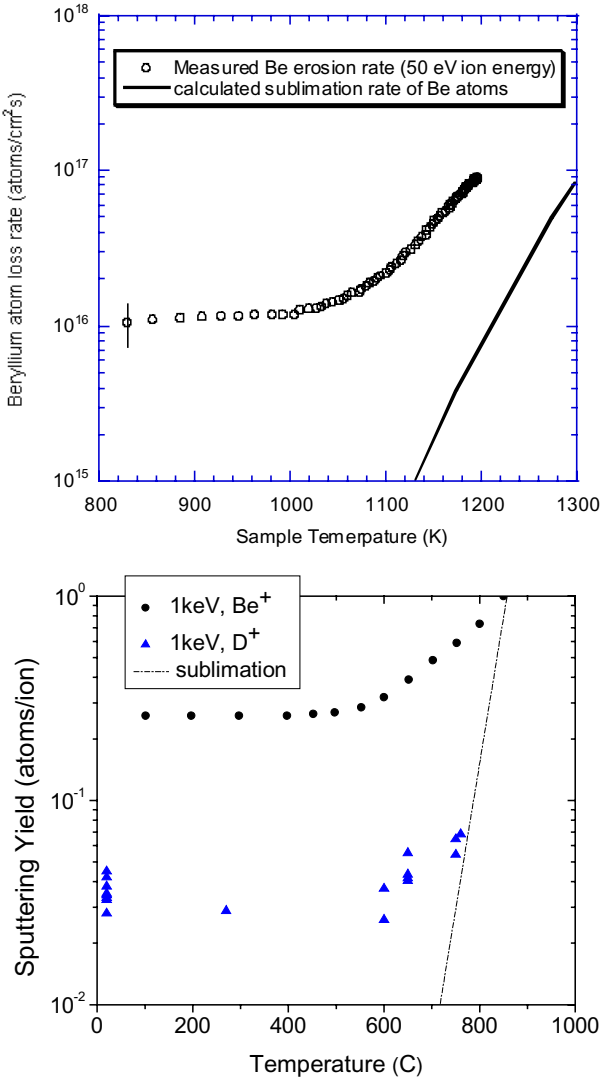

Fig. 9.3. (**a**) Erosion yield of Be as function of surface temperature as measured in the plasma simulator PISCES-B [23]. (**b**) Sputtering yield of Be for Be and D ions as function of surface temperature measured by ion beams [4, 22]

fore, more likely to sublimate/evaporate at a lower surface temperature. The calculated adatom lifetime and the experimentally determined adatom activation energy can be used to predict the observed temperature dependent material loss rate and are in excellent agreement throughout the temperature range of the experiments [23]. More experimental and modeling efforts are necessary to elucidate the temperature effects near the melting point.

This effect is similar to the effect found in graphite [27, 28] and named radiation enhanced sublimation (RES). In case of graphite not only displaced surface atoms have a certain lifetime on the surface, but displaced bulk atoms throughout the ion range can diffuse between the graphitic lattice plains and either recombine with vacancies or reach the surface and sublimate. At temperatures above 1200°C vacancies get mobile and cluster to dislocation loops and excess interstitial atoms will increasingly reach the surface for sublimation, leading to an monotonically increasing yield with increasing temperature.

9.2.2 Sputtering by Non-recycling Ions (Mixed Materials)

Kinetic Effects

During bombardment of solid surfaces with non-recycling ions the composition within the surface layer will get modified. At high fluences, metal and carbon impurity ions can form a solid layer on top of the substrate, protecting it from further erosion. Steady state erosion of the substrate can only be achieved under conditions where for each incident ion one deposited atom is removed. In this case the surface concentration of the incident ion will increase with fluence until such conditions are established, and substrate erosion continues, being only partially reduced due to dilution in the implanted layer [29, 30]. Critical conditions for the transition from steady-state deposition to steady-state erosion were shown to depend on the self-sputtering yield of the incident ion material. At ion energies or angles of incidence, where the self-sputtering yield increases above unity, the transition occurs with only slight influence by the substrate material.

For the case of sputtering of W by C ions, Fig. 9.4a shows the weight change of the sample, as a function of fluence at normal incidence. After an initial weight loss a continuous weight increase is observed for normal incidence, while at angles of incidence larger than 35° a continuous erosion occurs [30]. This angle of 40° is just the angle of incidence where the self-sputtering of carbon increases above unity [31]. The curves corresponding to the data show kinetic Monte-Carlo code calculations, including effects of intermixing of implanted carbon atoms into the W substrate and subsequently the build-up of a carbon layer. The steady increase of the weight at large fluences proceeds according to $(1 - Y_{\mathrm{self}})$ of the carbon ions.

Thermal Effects

The conditions where net erosion turns into net deposition for carbon irradiation may further be complicated by effects of surface temperature, influencing the self-sputtering yield by radiation-enhanced sublimation (RES) as well as the diffusion and surface segregation of implanted impurities. An example is introduced in Fig. 9.4b, where the erosion of W due to C^+ bombardment

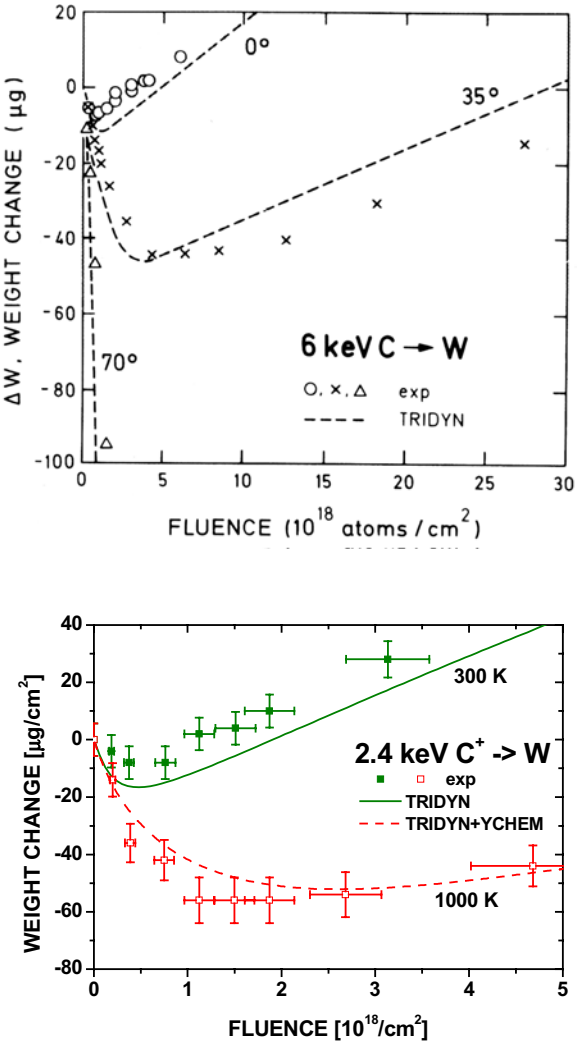

Fig. 9.4. (**a**) Fluence dependence of the sputtering yield of W with 6 keV C^+ ions in dependence of the angle of incidence. (**b**) Fluence dependence of the sputtering yield of W with 2.4 keV C^+ ions in dependence of the surface temperature

is shown also at 1030 K. A strong temperature dependence of the position of the transition point and of the slope of the weight gain in the deposition phase can be observed. Above 1000 K according to [32] noticeable C diffusion takes place in W and as seen from [28], the C self sputter yield increases due to RES. These two processes are, as simulations showed, responsible for the observed temperature dependence of the layer formation [33]. The diffusion thereby is responsible for the shift of the transition point to higher fluences because this C transport away from the surface yields a lower C concentra-

tion at the surface at a given fluence. This leads to higher C reflection and thus to a slower accumulation of C on the sample which shifts the transition point to higher fluences. The slow increase of the sample's weight in the deposition phase at temperatures above 300 K is due to RES. In this phase the W is shielded by the C-layer such that the dominant process that governs the weight change is C deposition and self-sputtering.

Sputtering by Simultaneous Impact of Multi-species Ions

The erosion properties of layers formed during bombardment with non-recycling ions are modified due to simultaneous bombardment with different ions such as DT fuel ions from the fusion plasma. Experimentally, these conditions were simulated, by the bombardment of W with 3.0 keV CH_3 at 300 K and 1000 K. The resulting particle energies are 2.4 keV for C and 200 eV for H. The erosion was evaluated from the experimental weight change of the sample [34].

To interpret the results the code package TRIDYN + DIFFUSEDC + YCHEM was developed [33]. In TRIDYN H ions were added as additional incident species with fraction $\xi_H = 75\%$ in the beam. In addition to the inclusion of chemical sputtering by YCHEM (see Sect. 9.3) a concentration dependent diffusion of carbon was added using a diffusion coefficient D(C) as determined from separate experiments [33]. The chemical sputter yield Y_{Chem} was taken from literature data and was 10%. In Fig. 9.5 the results of the calculation are compared to experimental data for irradiation of W with CH_3^+ at 1000 K [34] and with pure C at 1030 K. The simulations reproduce the experimental values well within the error bars. One can clearly see, that the

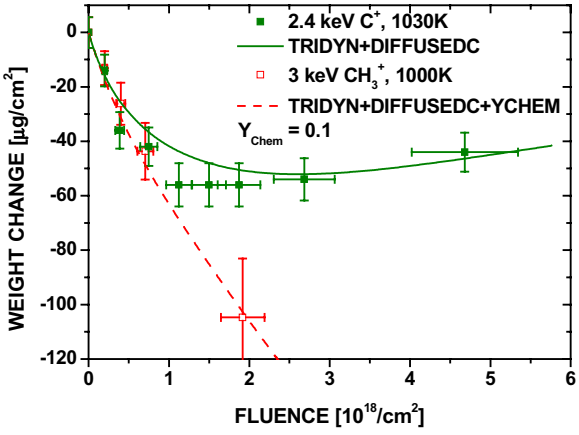

Fig. 9.5. Erosion of W as function of fluence for the bombardment with C^+ and CH_3^+ at 1030 K and 1000 K, respectively. The *solid curves* give the modeling results using the TRIDYN-DIFFUSEDC-YCHEM code package

additional chemical erosion due to the hydrogen ions inhibits layer growth and continuous W erosion takes place. The W is only eroded by the incident C. The H energy is below the sputtering threshold for W [5], while it is effective in chemically eroding carbon and keeping the W surface clean.

For the simulation at 300 K the diffusion of C can be neglected such that the DIFFUSEDC step could be omitted in the simulation and only TRIDYN+YCHEM were used. A chemical sputter yield of 4% was assumed. A similarly good agreement with the data is obtained as at 1000 K [32].

9.2.3 Extrapolation to Fusion Reactor Conditions

Using the code package validated for the case of CH_3 bombardment, the steady state erosion for different plasma temperatures and carbon concentrations can be obtained. By performing analogous modeling for the steady state erosion of W as function of plasma temperature and carbon concentration, the equilibrium weight change $dW/d\Phi$ at 300 K surface temperature was calculated. A negative $dW/d\Phi$ thereby indicates net erosion and a positive $dW/d\Phi$ net deposition. The result is depicted in Fig. 9.6. No W erosion occurs for zero C-content from the pure D-plasma in the plasma temperature range considered here. The erosion increases with C-concentration until at 4% a maximum of the erosion of W occurs. At higher C concentrations C accumulates in the surface layer resulting in less erosion. The thick black line indicates the erosion/deposition boundary.

For ITER the additional use of Be as main chamber wall material adds a further parameter to the mixed material composition, letting alone other

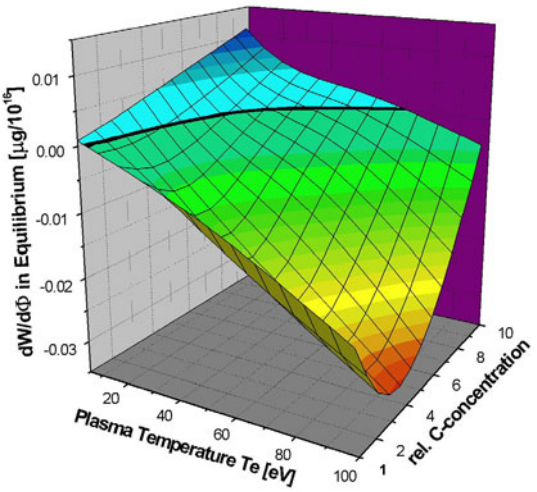

Fig. 9.6. Dependence of the erosion/deposition balance on plasma temperature T_e and the carbon concentration in the edge plasma in at %

intrinsic impurities such as oxygen. Predictions of erosion properties will depend on parameters such as inter-diffusion, compound formation, which cannot be predicted, but need to be investigated experimentally in controlled laboratory experiments.

9.3 Chemical Erosion

9.3.1 Present Understanding of Atomistic Processes

Since the reviews on chemical erosion of carbon in 1992 [35] considerable improvements have been reached in the fundamental understanding. The thorough investigations by Horn et al. [39] on the thermal chemical reactivity has been extended to the case of energetic ion bombardment by Roth and García-Rosales [41]. Simultaneously, new ion beam experiments at energies down to 10 eV [36–38] have improved the understanding of ion induced hydrocarbon emission.

Three processes determine the chemical erosion of carbon under low energy hydrogen bombardment [41]:

(a) The *reaction of thermalized ions* within the implanted surface proceeds via the hydrogenation of carbon atoms at the edges of sp^2 graphitic planes to CH_3C complexes (sp^3 configuration). At temperatures above 400 K CH_3 radicals can be released while at temperatures above 600 K recombinative hydrogen release (H_2) starts to reduce the chemical erosion yield (see Fig. 9.7). This thermal chemical erosion was elucidated in detail by Küppers et al. [39,40], clearing up all reaction cross-sections and activation energies, and the full temperature dependence was described analytically by Roth and García-Rosales [41]. For the thermal reaction no dependence on the hydrogen isotope was observed.
(b) The thermal reaction is *enhanced by radiation damage* introduced in the material which provides open bonds for hydrogen attachment. Damage is created by kinetic energy transfer from incident ions to lattice atoms and is, therefore, responsible for the dependence of the chemical erosion yield on hydrogen isotope mass. This yield enhancement is characterized by a threshold energy for damage production, E_{dam}. The basic thermal reaction below the threshold for damage production depends strongly on the crystalline perfection of the carbon material with maximum yields between 10^{-3} for well annealed pyrolytic graphite and 10^{-1} for amorphous a-C:D layers [42]. At energies where radiation damage amorphizes the graphite lattice, the strong dependence on the material structure disappears [43].
(c) At low surface temperatures all available carbon atoms are essentially hydrated but no thermal release of hydrocarbons occurs. However, hydrocarbon radicals are bound to the surface with much smaller binding

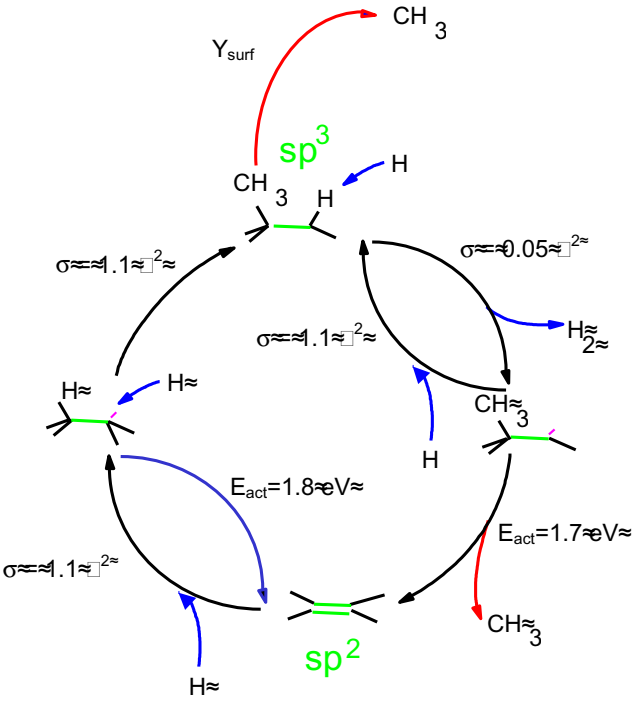

Fig. 9.7. The chemical erosion cycle after Küppers et al. [39, 40]

energy (≈ 1 eV) than carbon surface atoms in their regular lattice environment (7.4 eV). This leads to an *ion induced desorption of hydrocarbon radicals* which can be described in a manner analogous to damage production or bond breaking [47] using a threshold energy, E_{des}, in the low eV range. This process does not only produce saturated hydrocarbons, but also hydrocarbon radicals as has been demonstrated by collector experiments by Balden and Roth [38]. They showed that only 50% of the emitted species can be detected as saturated CH_4 molecules in residual gas analysis and about 50% of the eroded carbon atoms were retained on Al-collector strips in front of the target.

The cycle of chemical erosion, starting from open bonds at the edge of sp^2 graphitic lattice planes configuration through the fully hydrated state in the sp^3 configuration and via the splitting off of a hydrocarbon radical back to the sp^2 configuration is shown in Fig. 9.7 [41]. The clarification of the chemical reaction cycle including all cross-sections and reaction rates allows the formulation of a set of analytical equations describing the erosion yield as function of surface temperature, ion energy and ion flux [41, 44]. As an example of the degree of reproducibility of the data by the analytical equations the temperature dependence of the erosion yield is shown in Fig. 9.8

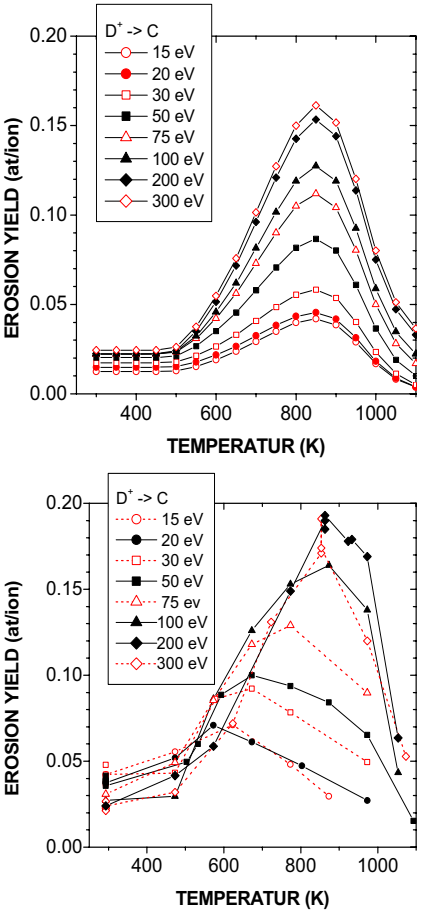

Fig. 9.8. Comparison of the temperature dependence of the experimental data of chemical erosion of carbon with modeling

for different ion energies. Clearly, the absolute yield and the position of the maximum, $T_{\max}$, is well reproduced, although a slight shift in $T_{\max}$ with energy is not included in the model.

Similar to the temperature dependence also the energy dependence of chemical sputtering can be reproduced adequately using the analytic description.

9.3.2 Eroded Species and Sticking Coefficient

For all three regimes of carbon erosion outlined above [44] the eroded species were investigated intensively. At room temperature and energies in the keV range, physical sputtering occurs with carbon atoms being eroded, predominantly. At elevated temperatures, chemical erosion increases the erosion yield

to a maximum around 500°C, where the spectrum of saturated hydrocarbons observable in residual gas analysis is dominated by methane, but with important contributions from heavier hydrocarbons increasing with decreasing ion energy [45]. Actually, for the chemical reaction with thermal hydrogen atoms at T_{max}, heavier hydrocarbons dominate the emission spectrum and the emission of CH_3 radicals replace the saturated methane. Another process occurs at low energies, i.e., below 100 eV, and room temperature [41, 46]. From the fully hydrogenated surface hydrocarbon radicals can be kinetically released in bond breaking processes close to the carbon surface [47]. In this case a complex mixture of saturated hydrocarbons and hydrocarbon radicals is expected to be released. In line-of-sight mass spectrometry again methane was identified as strong contribution [48], while the possibility of radical emission was not finally assessed. The sticking coefficient of the emitted species to surfaces is of high importance for the understanding of the deposition sequence in fusion devices. Most favorable would be the transformation of hydrocarbon radicals to saturated hydrocarbons with negligible sticking to walls, thereby preventing the accumulation of large amounts of tritium inside the fusion vessel and enabling effective pumping of hydrocarbons. Investigations in fusion devices [49, 50] have revealed a complicated deposition sequence involving the release of hydrocarbon radicals from the divertor plates which finally accumulate on cool remote surfaces.

It was attempted to distinguish the emission of unsaturated hydrocarbon radicals from their sticking behavior employing the *cavity technique* which has been previously described in detail [51–53]. Cavities have been exposed to the flux of hydrocarbon species emitted from carbon samples bombarded with deuterium ions at the high current ion source [54] The basic principle of this technique is that a flux of reactive particles deposits a film inside a defined geometry. The spatial variation of the film thickness is then determined by the *surface loss probability* β, i.e., the probability that the particle does not survive a wall collision; it either sticks to the wall (probability s) or reacts to a volatile, non-reactive species (probability γ). The surface loss probability β can be obtained from the fitting of the deposition pattern of hydrocarbons inside the cavity (see Fig. 9.9), while the surface sticking coefficient s can be is obtained from the simultaneous quantitative knowledge of the flux of hydrocarbons entering the cavity slit.

The evaluation of the cavity deposition for the three different regimes of chemical erosion has resulted in the finding, that apart from the emission of volatile hydrocarbons at elevated temperature and physical sputtering of carbon atoms at high energies, predominantly species with sticking coefficients around 0.02 are produced. A summary of results is given in Table 9.1.

Such species will be deposited in fusion devices in the vicinity of the location of erosion after few collisions and not travel deep into pump ducts and other remote areas. Similar conclusions are deduced from cavity collector probes introduced directly in fusion devices such as JET and ASDEX Upgrade [55, 56].

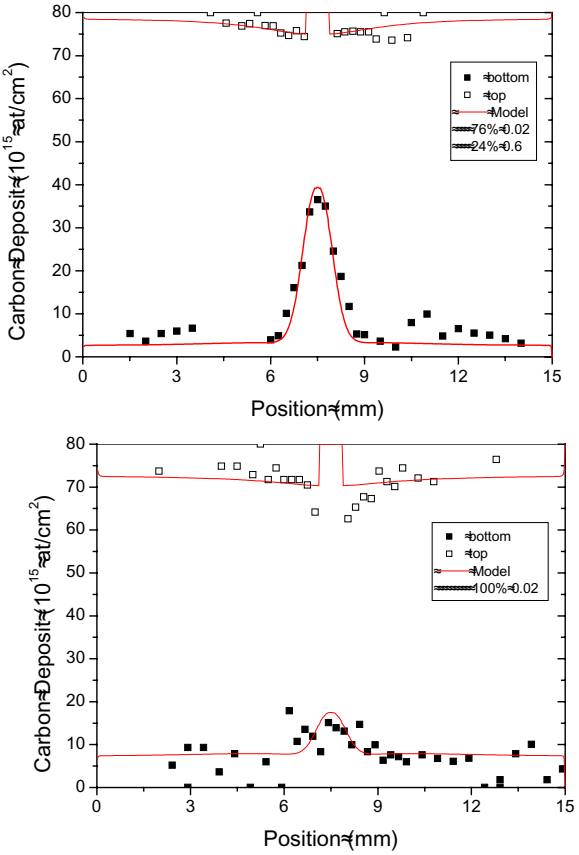

Fig. 9.9. (**a**) Distribution of deposited carbon in a cavity collecting the sputtered particle flux from a graphite sample bombarded with 1 keV D^+ at 475°C. The *solid curve* is a simulation of the deposition assuming a mixture of radical species with a sticking coefficient of 0.02 and 0.6. (**b**) Distribution of deposited carbon in a cavity collecting the sputtered particle flux from a graphite sample bombarded with 45 eV D^+ at room temperature. The *solid curve* is a simulation of the deposition assuming radical species with a sticking coefficient of 0.02

Table 9.1.

	Physical Sputtering	Thermal chemical erosion	Chemically enhanced sputtering
Sticking Coeff. 0.6	100%	24%	0
Sticking Coeff. 0.02	0	76%	100%
Sticking Coeff. close to 0	0	factor 1.5 from weight loss	0

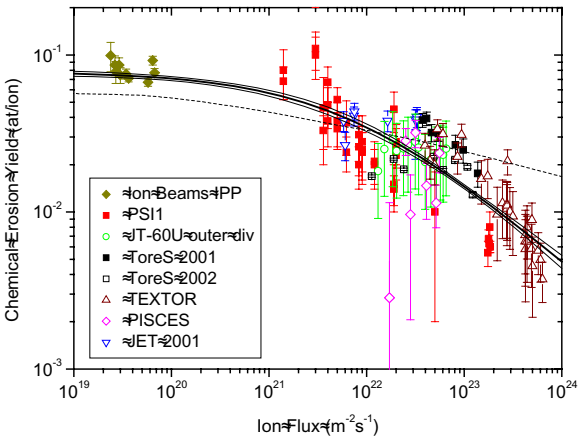

Fig. 9.10. Flux dependence of the chemical erosion yield for $T_{\max}$ and an ion energy of 30 eV determined from spectroscopic measurements in different fusion devices and plasma simulators. The *solid lines* are a fit using Bayesian probability theory and its confidence intervals [58, 59]. The *dashed line* is a prediction from an earlier analytic description [44]

9.3.3 Flux Dependence

The investigation and description of these processes has been performed for thermal hydrogen atom or ion fluxes of the order of 10^{16}–$10^{20}/\mathrm{m}^2\mathrm{s}$. The thermal reaction cycle predicts a pronounced shift of the temperature, $T_{\max}$, where the maximum yield occurs towards higher temperatures with increasing ion flux. This temperature shift with ion flux is well reproduced in the experimental data [27]. However, at fluxes above $10^{21}/\mathrm{m}^2\mathrm{s}$ as reached in plasma simulators or under tokamak conditions, the predicted temperature shift is clamped at 900°C. At these elevated temperatures, the thermodynamic equilibrium of H/C system shifts from CH_4-formation to H_2 release [57] and the erosion yield is expected to decrease with ion flux. Additionally, the onset of graphitization will lead to the annealing of radiation damage resulting in the suppression of the reactivity of the carbon material.

This has lead to the prediction that at such high fluxes the yield at $T_{\max}$ decreases. While in 1992 [35] a possible flux dependence of high fluxes could not be clarified within the scatter of the available data, the use of plasma simulators and edge plasmas in tokamaks has widely increased the data basis (Fig. 9.10). In-situ calibration of the spectroscopic signals for chemical erosion and normalization to a common ion energy of 30 eV yields now a data collection which clearly shows a decrease of the erosion yield with ion fluxes beyond $10^{22}/\mathrm{m}^2\mathrm{s}$, even stronger than predicted from the analytic description (dashed line) [58]. Data analysis using Bayesian probability theory [59] resulted in a decrease of the yield at high fluxes according to

$$Y(E,T,\Phi) = \frac{Y_{\mathrm{low}}(E,T)}{1+\left(\dfrac{\Phi}{6\times 10^{21}}\right)^{0.54}}\,. \tag{9.3}$$

9.3.4 Fluence Dependence and Surface Topography

Recently, in the fusion experiment DIII-D a steady decrease of the spectroscopic CD signal, representative for chemically eroded species, was observed over the course of several years [60]. After the use of the same tiles for 10 years in divertor application the CD band virtually disappeared. As possible reasons the frequent boronizations and the development of surface topography were discussed. As surface analysis of the tiles used in DIII-D did not show any significant traces of impurities, also the assumption of a reduction due to impurities was ruled out [61].

However, ion beam measurements on the same tiles after removal from DIII-D could not confirm the yield reduction in comparison with fresh tiles of the same material. Using mass spectroscopy the same hydrocarbon signals were measured on both samples [61]. On the other hand, simulation experiments in the plasma simulator PISCES-B could reproduce this effect [62]. It was tentatively attributed to the influence of a strong surface topography which developed during high fluence erosion. For physical sputtering the effect of enhanced surface roughness was shown to increase the erosion yield at normal incidence while at grazing angles of incidence yield did not increase as for polished surfaces [8, 9]. The effect of surface roughness on chemical erosion remains not clarified and should be investigated further.

9.3.5 Doping for Reduction of the Chemical Erosion Yield

In the last decades a number of investigations have been performed on the effect of dopants, i.e., of small additions (several at.%) of other elements to carbon, on the chemical erosion [63–69] and on the hydrogen retention [70–74]. Up to now the emphasis was put more on the choice of the dopant elements. However, recent investigations [75] suggest that microstructural effects, such as dopant distribution, dopant particle size and porosity, play also a very critical role. This means that the manufacturing procedure of doped carbon materials as well as the choice of the proper dopant elements or compounds and their grain sizes play an essential role in view of obtaining a carbon based material with optimized properties for application in high heat and particle flux regions of future fusion devices.

Up to now mostly commercially available materials have been investigated. In the majority of cases they had been optimized for other purposes, such as the space program. Regarding their optimization for plasma-facing application, there is little flexibility in the fabrication procedure. Moreover,

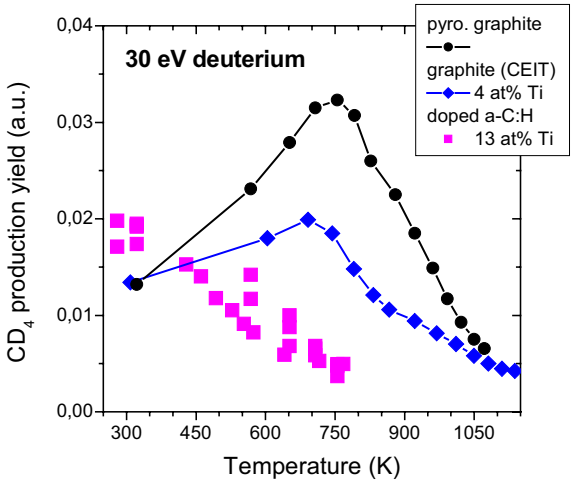

Fig. 9.11. Reduction of the thermal chemical erosion yield due to Ti doping of carbon materials

there is generally little open knowledge about details of the fabrication procedure, making the interpretation of their performance some times very difficult. Therefore in a project involving carbon manufacturers, metallurgical laboratories and ion beam erosion studies the optimization of carbon based plasma facing materials was undertaken [76] in view of a reduction of chemical erosion, while improving their thermal conductivity and mechanical properties [77]. This task requires a deeper understanding of the reduction mechanisms of chemical erosion of carbon materials by doping, together with a further development of the manufacturing procedure and a rigorous control of all steps involved.

Regarding the chemical erosion doping with B shows the most beneficial effects. However, if dopants are substitutionally soluble in graphite, as in the case of B [78], they induce a loss of thermal conductivity in the graphite lattice, resulting from increased phonon scattering [79].On the other hand, other dopants even have beneficial effects on the thermal conductivity and the thermal shock resistance of carbon based materials. It is known that some metals and carbides act as catalyst for the graphitization of amorphous carbon [80–82] resulting in a higher thermal conductivity. In Fig. 9.11 data for the chemical erosion of pyrolytic graphite are compared with data for fine grain graphite doped with 4% TiC with grain size below 1μm and for a deposited layer containing about 13% Ti in atomic distribution. The fine grain graphite was specially manufactured with regard to porosity, heat conductivity and homogeneity [69]. While fine grain doping can reduce the erosion yield only up to 30%, due to the limited influence of dopants at the surface of the carbidic precipitates, the introduction of Ti on an atomistic scale into the deposited layers virtually suppresses the chemical erosion at el-

evated temperatures [83]. Future developments must aim for the production of technologically usable doped CFC materials.

Recently, it could be demonstrated in the PISCES-B plasma simulator that Be impurity atoms in the eroding plasma can lead to a drastic suppression of chemical erosion already at concentrations as low as 0.15 at % [84].

9.3.6 Open Questions and Data Needs

The review of different erosion processes reveals considerable progress, both in experimental investigation and understanding, of physical sputtering and chemical erosion of plasma facing materials. The review leads to the identification of the following open questions and data needs:

Physical Sputtering

Main uncertainties remain in the treatment of compounds and intermixed materials. The main parameter governing sputtering is the surface binding energy which is insufficiently known for mixed materials.

In the material modification due to non-recycling ions in a hydrogen plasma the mobility of the constituents will modify the surface concentrations and influence the erosion of the substrate. These effects can only be investigated in a controlled way using dual ion beam experiments. Such a system is being commissioned at IPP and results for the interaction of different plasma facing materials are expected in the near future.

Temperature effects in physical sputtering are still under discussion. For the case of graphitic materials, it is known that displaced atoms throughout the collision cascade can diffuse to the surface and sublimate already at temperatures below 1000 K. It has been documented that similar effects exits for metals with low melting point. A model indicates a similar process as for graphite and a thorough investigation of this effects is necessary.

Chemical Erosion

In the field of chemical erosion the composition of hydrocarbons and radicals is not fully investigated, especially at the low ion energies expected in divertor application. The nature of the eroded species is coupled to their transport in the plasma and their sticking and re-erosion properties.

At high ion fluences the chemical erosion yield appears to decrease. This fluence dependence may originate from the development of a pronounced surface topography. Dedicated investigations are needed in plasma simulators where high fluences can be achieved.

The development of low erosion doped graphites has reached a point where chemical erosion at elevated temperatures can be suppressed. The important parameter appears to be the atomic distribution of metal carbide dopants. The future development must go in the direction of the production of doped bulk CFC materials.

References

1. G. Federici, C.H. Skinner, J.N. Brooks, J.P. Coad, Ch.Grisolia, A.A. Haasz, A. Hassanein, V. Philipps, C.S. Pitcher, J. Roth, W.R. Wampler, D.G. Whyte, Nucl. Fusion **41** (2001) 1967
2. P. Sigmund, Phys. Rev. **184** (1969) 383
3. W. Eckstein, García-Rosales, C., Roth, J., László, J., Nucl. Instr. Meth. **B83** (1993) 95
4. J. Roth, W. Eckstein, M. Guseva, Fus. Eng. Des. **37** (1997) 465
5. W. Eckstein, C. García-Rosales, J. Roth, W. Ottenberger, Sputtering data, Max-Planck-Institut für Plasmaphysik, Report IPP **9/82** (1993)
6. W. Eckstein, *Computer Simulation of Ion-Solid Interaction*, Springer Series in Material Science, Vol. 10, (Springer, Berlin 1991)
7. Y. Yamamura, J. Bohdansky, Vacuum **35** (1985) 561
8. M. Küstner, W. Eckstein, V. Dose, J. Roth, Nucl. Inst. Meth. B **145** (1998) 320
9. M. Küstner, W. Eckstein, E. Hechtl, J. Roth, J. Nucl. Mater. **265** (1999) 22
10. W. Eckstein, J.A. Stephens, R.E.H. Clark, J.W. Davis, A.A. Haasz, E. Vietzke, Y. Hirooka, Particle induced erosion of Be, C and W in fusion plasmas. Part B: Physical sputtering and radiation enhanced sublimation. In: *Atomic and Plasma-Material Interaction Data for Fusion*, Vol. 7B, (IAEA, Vienna, 1999) to appear
11. N. Matsunami, et al., Univ. Nagoya, Inst. of Physics, Report IPPJ-AM-32 (1983)
12. J. Roth, W.R. Wampler, W. Jacob, J. Nucl. Mater. **250** (1997) 23
13. W. Eckstein, J. Roth, W. Nagel, R. Dohmen, J. Nucl. Mater. **328** (2004) 55
14. E. Vietzke, A.A. Haasz, Chemical erosion. In: *Physical Processes of the Interaction of Fusion Plasmas with Solids*, W.O. Hofer, J. Roth (eds.) (Academic Press 1996) p. 135
15. J. Roth, J. Bohdansky, R.S. Blewer, W. Ottenberger, J. Borders, J. Nucl. Mater. **85-86** (1979) 1077
16. J. Roth, J. Nucl. Mater. **145-147** (1987) 87
17. W. Eckstein, J. Laszlo, J. Nucl. Mater. **183** (1991) 19
18. E. Hechtl, W. Eckstein, J. Roth, J. László, J. Nucl. Mater. **179-181** (1991) 290
19. J. Roth, J. Bohdansky, W. Ottenberger, Data on low energy light ion dputtering, Max-Planck-Institut für Plasmaphysik, Report IPP **9/26** (1979)
20. W. Eckstein, Max-Planck Institut für Plasmaphysik, private communication (1999)
21. J. Bohdansky, H. Lindner, E. Hechtl, A.P. Martinelli, J. Roth, Nucl. Instr. Meth. **B18** (1987) 509
22. M.I Guseva, A.Yu. Birukov, V.M. Gureev, L.S. Daneljan, S.N. Korshunov, Yu.V. Martynenko, P.S. Moskovin, Yu.A. Sokolov, V.G. Stolarova, V.S. Kulikauskas, J. Nucl. Mater **233-237** (1996) 68
23. R.P. Doerner, S.I. Krasheninnikov, K. Schmid, J. Appl. Phys. **95** (2004) 4471
24. R.P. Doerner, M.J. Baldwin, S. Krasheninnikov, D.G. Whyte, J. Nucl. Mater. **313-316** (2003) 383
25. R.W. Conn, R.P. Doerner, F.C. Sze et al., Nucl. Fusion **42** (2002) 1060

26. E.P. Vaulin, N.E. Georgieva, T.P. Martynenko, L.V. Feoktistov, Sov. J. Plasma Phys. **2** (1981) 437
27. J. Roth, J. Bohdansky, K.L. Wilson, J. Nucl. Mater. **111&112** (1982) 775
28. J. Roth, J. Bohdansky, W. Ottenberger, J. Nucl. Mater. **165** (1989) 193
29. W. Eckstein, J. Roth, E. Gauthier, J. László, Fus. Tech. **19** (1991) 2076
30. W. Eckstein, J. Roth, Nucl. Instr. Meth. **B53** (1991) 279
31. J. Roth, J. Bohdansky, W. Ottenberger, J. Nucl. Mater. **165** (1989) 193
32. K. Schmid, J. Roth, J. Nucl. Mater. **302** (2002) 96
33. K. Schmid, J. Roth, J. Nucl. Mater. **313-316** (2003) 302
34. K. Krieger, J. Roth, J. Nucl. Mat. **290-293** (2001) 107
35. J. Roth. In: *Atomic and Plasma-Material Interaction Processes in Controlled Thermonuclear Fusion*, R.K. Janev, H.W. Drawin (eds.) (Elsevier, Amsterdam 1993) p. 381
36. B.V. Mech, A.A. Haasz, J.W. Davis, J. Nucl. Mater. **255** (1998) 153
37. B.V. Mech, A.A. Haasz, J.W. Davis, J. Appl. Phys. **84** (1998) 1655
38. M. Balden, J. Roth, J. Nucl. Mater. **280** (2000) 39
39. A. Horn A. Schenk, J. Biener, B. Winter, C. Lutterloh, M. Wittmann, J. Küppers, Chem. Phys. Lett. **231** (1994) 193
40. M. Wittmann, J. Küppers J. Nucl. Mater. **227** (1996) 186
41. J. Roth, C. Garcia-Rosales, Nucl. Fusion **36** (1996) 1647 with corrigendum Nucl. Fusion **37** (1997) 897
42. E. Vietzke, K. Flaskamp, V. Philipps, G. Esser, P. Wienhold, J. Winter, J. Nucl. Mater. **145-147** (1987) 443
43. R. Yamada, K. Nakamura, K. Sone, M. Saidoh, J. Nucl. Mater. **95** (1980) 278
44. J. Roth, J.Nucl. Mater. **266-269** (1999) 51
45. J. Roth, E. Vietzke, A.A. Haasz, Atomic and Plasma–Wall Interaction Data for Fusion, Suppl. Nucl. Fusion **1** (1991) 63
46. J. Roth, J. Bohdansky, Nucl. Instr. Methods **B23** (1987) 549
47. E. Salonen, K. Nordlund, J. Keinonen and C. Wu, Phys. Rev. B **63** (2001) 195415
48. E. Vietzke, K. Flaskamp, V. Philipps, J. Nucl. Mater. **128/129** (1984) 545
49. J.P. Coad et al., J. Nucl. Mater. **290-293** (2001) 224
50. V. Rohde, M. Mayer, ASDEX Upgrade Team, J. Nucl. Mater. **313-316** (2003) 337
51. D.A. Doughty, J.R. Doyle, G.H. Lin, A. Gallagher, J. Appl. Phys. **67** (1990) 6220
52. Ch. Hopf, K. Letourneur, T. Schwarz-Selinger, A. von Keudell, Appl. Phys. Lett. **74** (1999) 3800
53. Ch. Hopf, T. Schwarz-Selinger, W. Jacob, A. von Keudell, J. Appl. Phys. **87** (2000) 2719
54. J. Roth, Ch. Hopf, J. Nucl. Mater. **334** (2004) 97
55. M. Mayer, A. von Keudell, V. Rohde, P. Coad, and JET-EFDA contributors, Mechanism of hydrocarbon layer formation in remote areas of fusion devices, 30th EPS Conference on Controlled Fusion and Plasma Physics, Europhysics Conference Abstracts (2003)
56. M. Mayer, Final Report for JET Task JWO-FT-3.4, Deposition and Erosion Studies, April 2003, unpublished
57. J. Roth. In: *Sputtering by Particle Bombardment, II*, R. Behrisch (ed.) (Springer Verlag Berlin, 1983) p. 91

58. J. Roth, R. Preuss, W. Bohmeyer, S. Brezinsek, A. Cambe, E. Casarotto, R. Doerner, E. Gauthier, G. Federici, S. Higashijima, J. Hogan, A. Kallenbach, A. Kirschner, H. Kubo, J.M. Layet, T. Nakano, V. Philipps, A. Pospieszczyk, R. Pugno, R. Ruggiéri, B. Schweer, G. Sergienko, M. Stamp, Nuclear Fusion **44** (2004) L21
59. V. Dose, J. Roth, R. Preuss, J. Nucl. Mater. **288** (2001) 153
60. D. Whyte, W.P. West, R. Doerner, N.H. Brooks et al., J. Nucl. Mater. **290-293** (2001) 356
61. P.B Wright, J.W. Davis, R.G. Macaulay-Mewcombe, C.G. Hamilton, A.A. Haasz, J. Nucl. Mater. **313-316** (2003) 158
62. R. Doerner, PISCES-B, private communication (2003)
63. J. Roth, J. Bohdansky and J.B. Roberto, J. Nucl. Mater. **128-129** (1984) 534
64. Y. Hirooka, R. Conn, R. Causey, D. Croessmann, R. Doerner, D. Holland, M. Khandagle, T. Matsuda, G. Smolik, T. Sogabe, J. Whitley, K. Wilson, J. Nucl. Mater. **176-177** (1990) 473
65. J.W. Davis and A.A. Haasz, J. Nucl. Mater. **195** (1992) 166
66. A. Pospieszczyk, V. Philipps, E. Casarotto, U. Kogler, B. Schweer, B. Unterberg, F. Weschenfelder, J. Nucl. Mater. **241-243** (1997) 833
67. J.P. Qian, J. Roth, J.R. Song, F. Zhang, L. Yang, G.T. Zhai, J. Nucl. Mater. **258-263** (1998) 706
68. M. Balden, J. Roth, C.H. Wu, J. Nucl. Mater. **258-263** (1998) 740
69. C. Garcia-Rosales, M. Balden, J. Nucl. Mater. **290-293** (2001) 173
70. V.Kh. Alimov, R. Schwörer, B.M.U. Scherzer and J. Roth, J. Nucl. Mater. **187** (1992) 191
71. A.A. Haasz and J. W. Davis, J. Nucl. Mater. **232** (1996) 219
72. M. Mayer, M. Balden, R. Behrisch, J. Nucl. Mater. **252** (1998) 55
73. M. Rubel, N. Almqvist, P. Wienhold, Ch. Wu, J. Nucl. Mater. **258-263** (1998) 787
74. M. Balden, E. Oyarzabal, E. de Juan Pardo, K. Durocher, J. Roth, C. García-Rosales, Physica Scripta **T103** (2003) 38
75. M. Balden, Physica Scripta **T81** (1999) 64
76. C. García-Rosales, M. Balden, J. Nucl. Mater. **290-293** (2001) 52
77. N. Ordás, C. García-Rosales, S. Lindig, M. Balden, H. Wang, Physica Scripta **T111** (2004) 190
78. C.E. Lowell, J. Am. Ceram. Soc. **50** (1967) 142
79. S. Marinkoviæ. In: *Chemistry and Physics of Carbon*, Vol. 19, P.A. Thrower (ed.) (Marcel Dekker, New York, 1984) p. 1
80. V.N. Parmon, Catalysis Today **51** (1999) 435
81. H. Marsch, A.P. Warburton, Carbon **14** (1976) 47
82. S.R. Dhakate, R.B. Mathur, O.P. Bahl, Carbon **35** (1997) 1753
83. E. de Juan Pardo, M. Balden, B. Cieciwa, C. García-Rosales, J. Roth, Physica Scripta **111** (2004) 62
84. K. Schmid, M. Baldwin, R. Doerner, J. Nucl. Mater. (2005) accepted for publication

10 Hydrogen Retention in and Release from Carbon Materials

A.A. Haasz and J.W. Davis

Results of hydrogen retention, as a function of incident ion energy, ion fluence, graphite structure and temperature, are presented, and their implication for ITER is discussed. During H^+ irradiation of graphite, once the near surface is saturated, essentially all of the incident H^+ is re-emitted from the surface – except for the small fraction that diffuses into the bulk – in the form of H_2 molecules, H° atoms, and hydrocarbons. The relative amounts of these species depend on temperature. During post-irradiation thermal desorption spectroscopy, again H_2, CH_4, and H° are released.

During D-T operational phases in TFTR and JET, a significant amount of T ($\sim 50\%$ in TFTR and $\sim 33\%$ in JET) was retained in co-deposits. Following the D-T campaigns, various attempts were made to remove tritium from the torus. In TFTR, tokamak pulses were found to be ineffective, while glow discharge cleaning (GDC) and air ventilation were found to be most effective. On the other hand, in JET, glow discharges were found to be ineffective, while tokamak pulses (assisted by ICRH) and bakeout of the vessel and ventilation of the torus were found to be most effective in removing tritium.

The removal of T from thick co-deposits (tens of μm) may require the removal of the co-deposits themselves by chemical and/or plasma-assisted oxidizing reactions in the presence of oxygen, or alternatively, via abrasive/mechanical techniques, such as pellet blast cleaning. From the extensive laboratory measurements of H/D/T removal rates from co-deposited films during exposure to air or oxygen, three key conclusions can be drawn: (i) D release occurs in conjunction with C erosion; (ii) D-removal and C-erosion rates depend strongly on film structure; and (iii) the D release rate during oxidation is a critical function of the specimen temperature.

10.1 Introduction

Next-step D-T burning fusion reactors, such as the International Thermonuclear Experimental Reactor (ITER), will require several kilograms of tritium [1, 2]. While most of the tritium will be contained in the fuel process loop, the interaction of the plasma with plasma-facing components (first-wall armour, limiters, and divertors) will lead to accumulation of tritium in the torus. Based on the amounts and distribution of D retention in TFTR and

JET, it appears that co-deposition could be an important mechanism for long-term fuel retention in next-generation tokamaks with carbon plasma-facing components.

Some of the tritium used for fuelling the discharge will be retained together with deuterium on the surfaces of plasma facing materials (PFMs) surrounding the core and divertor plasma. Although considerable effort has been expended on theoretical calculations to estimate the tritium inventory in ITER [3], large uncertainties exist in such calculations, mainly due to uncertainties in the edge plasma parameters, which strongly affect erosion, deposition and co-deposition rates and patterns. Moreover, mixed-materials effects arising from the simultaneous use of different PFMs to protect the in-vessel components introduce additional uncertainties for the operation of a tokamak like ITER.

Perhaps the two most important implications of tritium inventory buildup in the torus are the locking up of the fuel in the PFMs (reducing the available fuel in the machine), and the need to keep the in-vessel T inventory within a licensed limit due to safety considerations. Based on postulated accident scenarios for ITER, the administrative in-vessel limit of mobilizable tritium has been set to be 1,000 g [2]. When the accumulated T inventory in the torus reaches this level, operation will have to be discontinued and dedicated T-removal procedures must be applied.

Here we shall review the various mechanisms for hydrogen retention in carbon-based materials, and then we shall turn our focus to co-deposition, with particular attention paid to the removal of tritium from co-deposits obtained from current fusion devices.

10.2 Hydrogen Retention in Pure and Doped Carbon Materials

In the case of graphite or other carbon-based materials, essentially four mechanisms have been identified for the uptake and retention of hydrogen: (i) buildup of a saturated surface layer, (ii) chemisorption on inner porosity surfaces, (iii) intergranular diffusion and trapping, and (iv) co-deposition of hydrogen with carbon on plasma-exposed surfaces. Based on experimental data from TFTR e.g., [4,5] and JET [6,7] – the World's two largest tokamaks – and related modeling [3], we expect co-deposition to be the dominant mechanism for hydrogenic retention in ITER. Retention by other mechanisms such as implantation and surface adsorption, which may be significant for small short-pulse machines, is expected to rapidly reach saturation in ITER.

10.2.1 Implantation and Diffusion

The primary mechanisms involved in the retention of energetic hydrogen impacting on carbon materials are illustrated in Fig. 10.1. At low fluences and

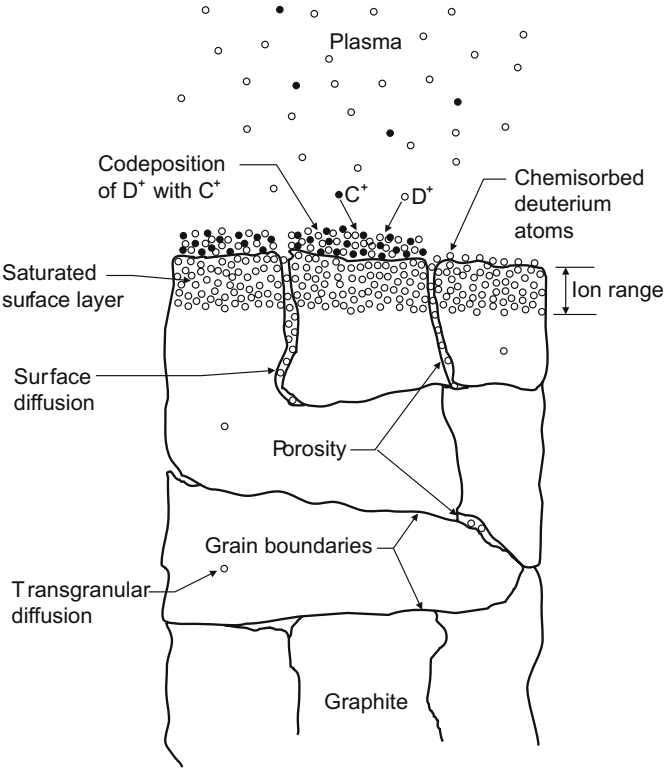

Fig. 10.1. Schematic of the primary mechanisms for hydrogen retention in graphite

low temperatures, essentially all non-reflected incident energetic hydrogen is retained in carbon materials [8,9]. However, once saturation of the implantation zone has been completed, nearly 100% re-emission occurs. The amount of hydrogen trapped in the implantation zone is approximately 0.4 H/C at 300 K [10], and concentrations at approximately this level extend from the surface to the maximum range of the incident ions. Lower energy ions will naturally have a shorter range, and thus a smaller trapped quantity, while the concentration remains approximately constant.

With increasing temperature, the amount of trapping in the implantation zone is reduced, leading to lower retention values [11–16], see Fig. 10.2. For temperatures greater than $\sim 1,000$ K, very little hydrogen remains trapped. As seen in the figure, this temperature dependence may be extended to lower temperatures as well [11], with greater retention in surfaces cooled below 300 K, implying trapped concentrations greater than 0.4 H/C.

Following saturation of the implantation zone, the amount of retained hydrogen continues to increase for most graphites, but at a much slower rate [9, 17, 18], see Fig. 10.3a). In order for more hydrogen to be trapped, it must be transported beyond the implantation zone by some form of diffu-

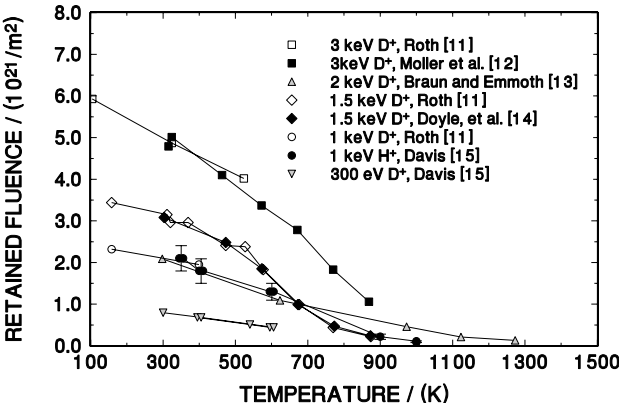

Fig. 10.2. Retained amounts of deuterium and hydrogen in graphite as a function of temperature during implantation, taken from various sources [16]

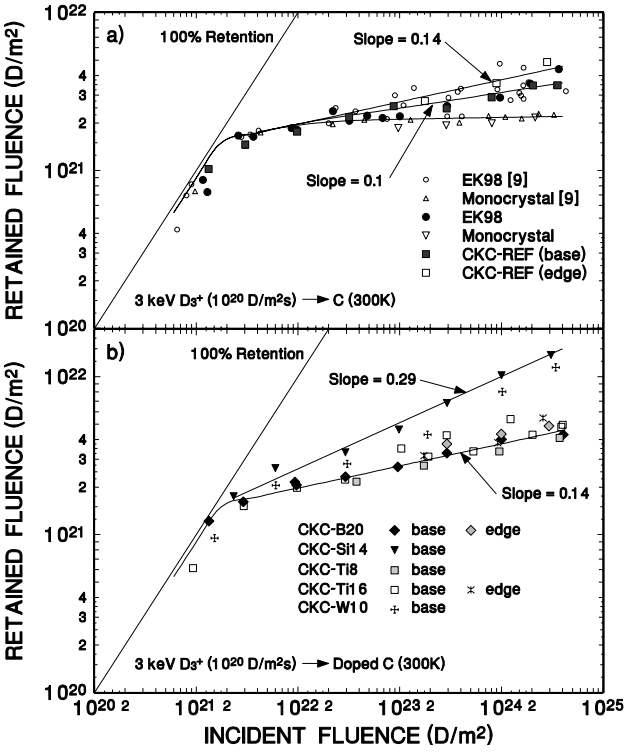

Fig. 10.3. TDS measurements of D retention in (**a**) pure graphites, and (**b**) doped graphites as a function of D^+ fluence [17]

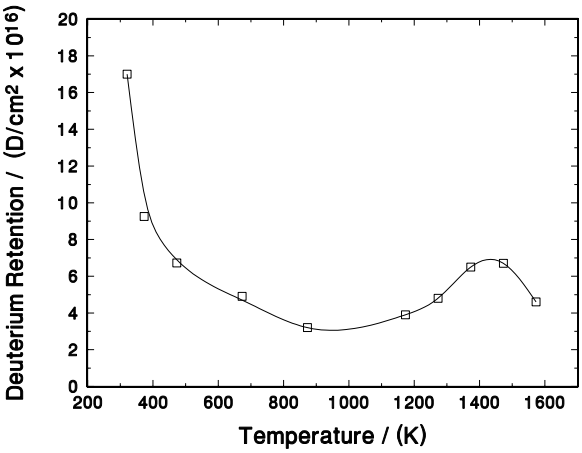

Fig. 10.4. Deuterium retention in POCO AXF-5Q graphite as measured by tritium dissolution counting. All specimens were exposed to a 100 eV ion flux of 5.6×10^{20} D/m^{2}s and a background deuterium pressure of 0.66 Pa for 1.5 h [19]

sion. At low temperatures, transport is thought to be primarily along internal porosity and grain boundaries, while at temperatures above $\sim 1,000$ K, transgranular diffusion becomes possible [19]. Low temperature transport of hydrogen several μm into graphite has been observed, for both molecular [20] and atomic hydrogen [21]. For some of the more porous types of graphite, particularly C/C composites, hydrogen has been measured several mm [22], or even ten's of mm into the material [23]. For graphite with very little internal porosity, such as single crystal graphite, diffusion beyond the implantation zone does not occur at low temperatures [9, 17, 24], see Fig. 10.3a).

The evidence for transgranular diffusion and trapping comes from an increase in hydrogen retention observed at $\sim 1,200$–$1,600$ K, see Fig. 10.4. The increase in retention is thought to be a result of hydrogen having access to trapping sites inside grains, which were inaccessible at lower temperature [19]. Such transport will be of greater importance in neutron-irradiated graphite, see below.

The trapping of hydrogen in the implantation zone of doped graphites tends to be similar to that in the undoped case, while beyond the implantation zone, the trapping tends to be similar to, or greater than, trapping in undoped materials [17, 20, 25]. Figure 10.3b shows the fluence dependence of doped graphite specimens prepared by Ceramics Kingston Ceramique (CKC). At this time, it is not clear whether the increase in retention is related to the existence of the dopants directly, or due to changes in structure induced by the dopants.

10.2.2 Co-deposition

Co-deposition entails the formation of hydrogenated carbon layers via the redeposition of eroded C atoms and C-containing molecules/radicals in combination with the fuel H, on both plasma facing and out of line-of-sight surfaces in the device. Such layers have been observed to exceed tens of μm (e.g., in TFTR [26, 27]), much thicker than the ion-implantation region, which only extends tens of nm. In addition, the co-deposited layer does not appear to have a limit to its thickness. The H/C ratio in the co-deposited layers is similar to that seen in the implantation zone, viz, ~ 0.4 at room temperature. Based on experience with current tokamaks [7, 28, 29] and predictions for ITER [3], most of the T in an ITER-type machine is expected to be trapped in co-deposits. Consequently, the removal of such layers has recently become a high priority issue. This will be addressed in Sect. 10.4.

10.2.3 Effect of Neutron Damage

Although direct experiments measuring hydrogen retention in neutron-irradiated graphite are very limited and cannot be done with a fusion neutron spectrum, they do give a clear indication of what may happen in a D-T burning reactor. Also, in addition to neutron exposures, a number of experiments have been performed where ion damage has been used to simulate neutron effects. Graphite specimens exposed to neutron fluences of up to 10 displacements per atom (dpa) in a fission reactor resulted in trapping levels being increased by up to two orders of magnitude [20, 30–34]. A direct comparison was also made with graphite specimens using ion damage to simulate neutrons [33]. The increase in retention appears to saturate at about 0.1–1 dpa [20, 30, 33, 34] at levels of approximately 1,000 appm, see Fig. 10.5. The factor of two difference between measurements from [33] and [20] for the same material (POCO graphite) is attributed to experimental differences. Typical trap concentrations in un-irradiated graphite are in the range 10–30 appm [33]. By comparison, D retention in the D^+-implanted zone of graphite at ~ 300 K is 0.4 H/C, however, neutrons will create trapping sites throughout the entire carbon tile. The conclusion is that neutron damage may result in a very large increase in hydrogen retention beyond the implantation zone, where hydrogen has access to damage sites. It was also found that the increase in trapping sites could be partly removed by heating to 1,773 K [30].

The effect of the neutron damage on H trapping was found to be strongly dependent on the structure of the irradiated material, with HOPG [33] and USB15 [20] being substantially less susceptible than some of the other graphites, see Fig. 10.5. This is possibly due to the lack of interconnected porosity in these materials which limits the accessibility of D to neutron damage sites [20]. Boron as a dopant may also affect the trapping process somehow [20].

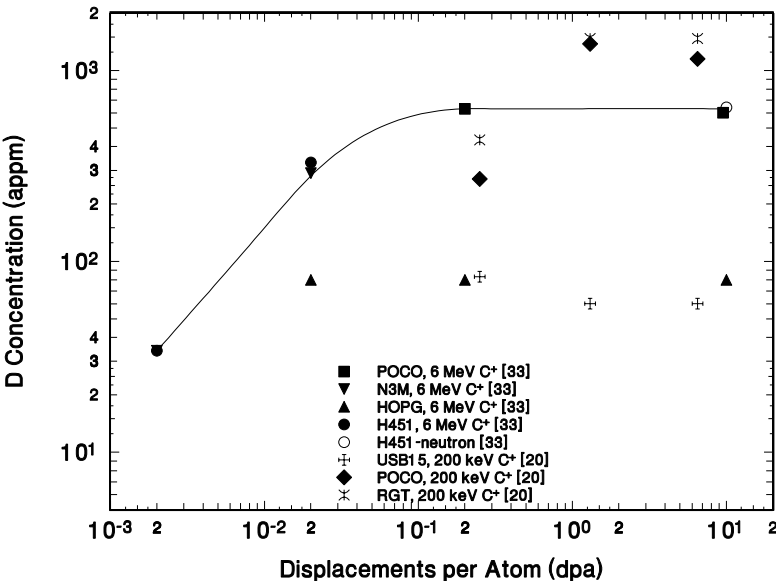

Fig. 10.5. D concentration vs damage in various types of graphite irradiated with 6 MeV C^+ [33], 200 keV C^+ [20] and neutrons [33]. Neutron and ion damage have similar effects on D retention. D retention increases with damage at low damage levels, but saturates at $\sim$ 0.1–1 dpa. The *line* represents a fit to the POCO and N3M data, see [33]

10.3 Hydrogen Release from Graphite

10.3.1 Re-emission

As indicated above, at low fluences and low temperatures, essentially all non-reflected hydrogen ions incident on a carbon surface are retained [8,9]. However, once the near-surface has been saturated, very nearly 100% of the incident hydrogen is re-emitted from the surface. At 1 keV and room temperature, saturation of the implantation zone will occur at $\sim 2 \times 10^{21} H^+/m^2 s$ [9,18]. At higher temperatures, saturation will occur at lower fluences, as trapping levels are reduced, see Sect. 10.2.1.

Re-emitted hydrogen can take three forms, the ratio of which is largely governed by the graphite temperature. At temperatures below $\sim 1,000$ K, the majority of hydrogen is generally released as molecular hydrogen, while some may also be released as hydrocarbons (chemical sputtering), see Fig. 10.6 [39]. In some circumstances (1 keV D^+ at $\sim$ 800 K), as much as 50% of the hydrogen may be released in the form of hydrocarbons (primarily methane). However, for conditions generally of interest for fusion ($\sim$ 10 eV energy), erosion yields are closer to 1–2% [69], implying $>$ 90% of the re-emitted hydrogen will be in the form of H_2, as long as temperatures remain below $\sim 1,000$ K.

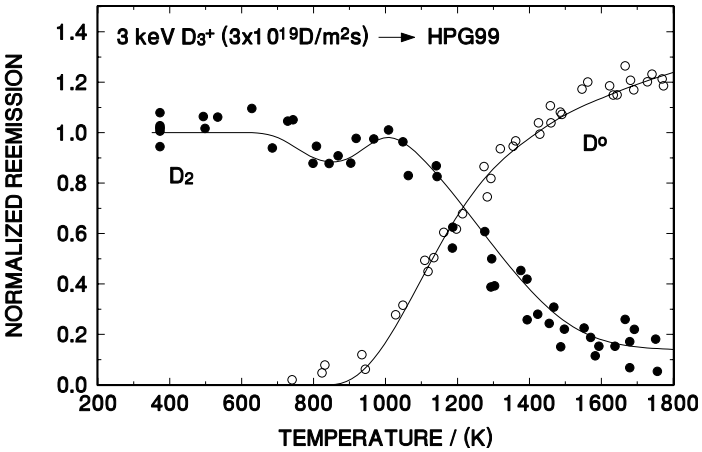

Fig. 10.6. Steady state re-emission of D° and D_2 as a function of specimen temperature. The line-of-sight QMS signals are normalized by the D_2 signals at 400 K. The *lines* are drawn as a guide to the eye [39]

Above ~ 800 K, for 1 keV D^+, an increasing fraction of the hydrogen is re-emitted as atoms from both pure and doped carbons [37–39], see Fig. 10.6. At temperatures between 1,200 and 1,300 K, we find about 50% of the H being released as atoms. As the temperature increases to $\sim 1,800$ K, the re-emitted hydrogen is dominated by atoms. It is noted that D atom re-emission at high temperatures is also observed for refractory metals, e.g., W, Mo, Ta, during D^+ irradiation [40].

Experiments employing a sudden change in incident flux density have indicated that the release of molecular hydrogen is a first order process [35, 36]. This possibly indicates the combination of a mobile surface hydrogen with an atom in a surface trap [36]. The order of the process will have implications on tokamak surfaces which will experience varying flux densities during a discharge.

10.3.2 Thermal Release During Thermal Desorption Spectroscopy (TDS)

The thermal release of D_2 from pure graphite is characterized by a broad peak centered at 1,000–1,300 K, depending on the ramping rate. Under some circumstances, a single desorption peak is measured [17, 39, 41–43], while sometimes a broad spectrum with multiple peaks is observed [44–46]. Measurements of implantation depth profiles, as a function of anneal temperature, indicate that hydrogen release is characterized by de-trapping followed by immediate release [47]. Thus, the broadness of the TDS peak indicates a distribution of trapping energies between 2 and 4 eV [36]. In addition to D_2, CD_4 and atomic D° are also observed [39], see Fig. 10.7. A constant fraction

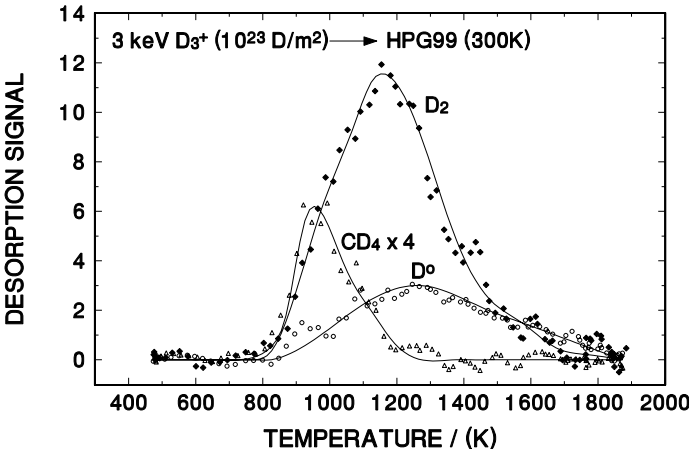

Fig. 10.7. Thermal desorption signals as a function of temperature. The temperature ramping rate was $\sim 20\,\mathrm{K/s}$. Temperature corrections regarding the speed of particles entering the line-of-sight QMS have not been applied, and thus relative magnitudes cannot be judged exactly from this figure [39]

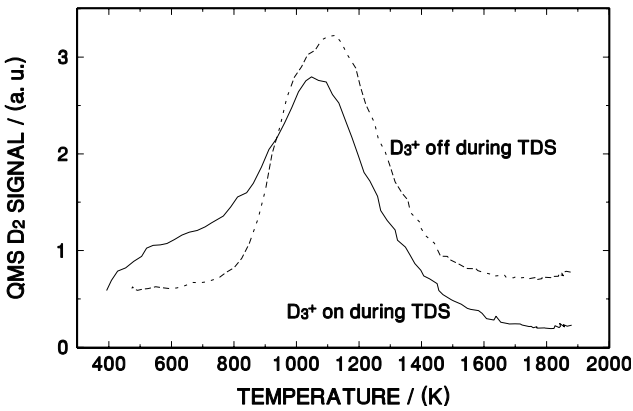

Fig. 10.8. Comparison of TDS profiles as a function of temperature for the beam-on and the beam-off cases. The total amounts of released D_2 for $T < 1,400\,\mathrm{K}$ are similar for the two cases [16]

of 15–20% of the released D is in the form of methane, provided the incident fluence was above a low fluence threshold [9, 41, 48]. It is also found that 15–20% of the hydrogen is released in the form of atoms [38, 39]. Methane tends to have a release temperature of $\sim$ 900–1,000 K, somewhat lower than that of molecular hydrogen, while the atoms are released at a somewhat higher temperature.

The heating of a specimen during ion bombardment results in an alteration of the TDS profiles [16], see Fig. 10.8. The release of molecular hydrogen

begins immediately upon the start of heating the specimen. In a tokamak this has the consequence that any heating of saturated graphite tiles during a discharge can result in a greater than 100% re-emission of hydrogen.

The TDS spectra for the CKC doped graphites are generally similar to pure graphite [17]. The primary exception is the Ti-doped graphite, where a lower temperature peak is also observed [17]. Mayer et al. [25], however, did observe more substantial differences between the TDS spectra of pure and doped graphites in their study, while Ashida et al. [49] found a sharper desorption peak for Fe-doped papyex than for undoped papyex. The details of the TDS profiles appear to be very dependent on the nature of the graphite, and possibly on the amount of damage done during ion implantation.

10.4 H-Isotope Removal from C-Based Co-deposits

The topic of H/D/T-carbon co-deposition in tokamaks is extensively reported on in a recently published major review of plasma-materials interactions [29]. During the three high power operational phases in TFTR, 1993–97, approximately 2.6 g of the 5.2 g tritium supplied to the vessel was retained ($\sim 50\%$), primarily in T-C co-deposits on the walls – with the carbon originating from TFTR's carbon limiter [28]. The plasma properties of the JET (divertor) edge plasma are quite different – colder, denser – than the TFTR (limiter) edge, and for some unknown, but presumably related reason, the carbon walls in JET are net sources of carbon, rather than sinks. Of the 35 g of tritium supplied to JET during D-T operation about 11.5 g was retained ($\sim 33\%$) in carbon co-deposits, found on cooled structures near the inside divertor, structures that were not in actual contact, and some not even in line-of-sight with the plasma. These retention levels in TFTR and JET correspond to levels after the D-T campaigns, prior to various attempts aimed at removing tritium from the torus. Similar carbon erosion and re-deposition – as well as D retention patterns – have been seen in JET, DIII-D and ASDEX Upgrade [50], thus indicating that this is evidently a common feature of divertor tokamaks. The present view is that future tokamaks, e.g., ITER, will employ divertors, rather than limiters and so the JET (divertor) results are likely to be more relevant than the TFTR (limiter) ones.

It is evident that the removal of tritium from the torus of ITER-like machines requires the removal of tritium from the co-deposited layers, or perhaps – depending on the technique used – the removal of the co-deposits themselves. Notwithstanding the observation that tritium retention in short-pulse machines will be affected by mechanisms other than co-deposition, the experience gained from TFTR and JET – the only tritium-burning tokamaks in the world – is of paramount importance for gaining some understanding of the T-removal processes. Here we present a brief review of the T-removal experience with TFTR and JET, and then review controlled laboratory and

Table 10.1. Most effective T removal techniques used in one or both machines: TFTR and JET

Machine operation:	Comments	
	TFTR	JET
D tokamak pulses	Ineffective	Tokamak pulses in D (few thousand) reduced the in-vessel inventory at end of DTE1 by a factor of 2.
D-GDC	Initial removal rate high ($>$ 18 mg/h), falling to 1 mg/h. Accesses only T on surfaces seen by the discharge.	Ineffective. Rarely used in DTE1 because of the heavy gas load on the exhaust gas processing system. The amount of T released was negligible ($\leq$ 40 mg).
He/O-GDC	Rate $\approx$ 5 mg/h – constant with time.	not applied
ICRF	not applied	Pulses with RF heating helped to remove significantly more T than ohmic pulses. Wall inventory was reduced from 4.4 to $\sim$ 2.9 g with $\sim$ 120 pulses.
Vessel venting	718 Torr air removed 220 mg T in $<$ 1 h, but it took about 24 h to process the air.	2 g T was released in 4 months of air ventilation of the torus at the end of the DTE1 campaign.
Remote tile exchange (RTE)	not applied	Divertor tiles, carriers and flakes have been physically removed in the RTE $\sim$ 0.6 g T.

tokamak experiments aimed at developing techniques for removing tritium from co-deposits in ITER-type machines.

10.4.1 Tritium Removal Experience in TFTR and JET

An excellent discussion of the various techniques used – and their effectiveness – to remove tritium from TFTR and JET during and subsequent to the D-T operation phases is available in [29]. Here we shall provide a brief summary. The techniques that were found to be effective in removing tritium from either one or both machines are listed in Table 10.1.

TFTR

The Tokamak Fusion Test Reactor was the first fusion facility with extensive experience with tritium fuelling and removal. During the 3.5 years of D-T operation, 3.1 g T was supplied to the plasma by neutral beam injection and 2.1 g by direct gas puffs, for a total of 5.2 g T. There were three periods of

plasma operations interspersed with cleanup campaigns to remove tritium [51]. The tritium input and exhaust were carefully tracked. During the three run periods (excluding periods of active T removal), 2.6 g T ($\sim$ 50% of the T supplied to the plasma) was retained in the vacuum vessel, a fraction similar to that found in earlier D measurements [27]. The fraction of tritium retained in the vessel was found to vary with discharge type, clean-up history and the period studied ([52] and references therein). The modeling of tritium retention in TFTR is reported in [53].

Active tritium removal by glow discharge cleaning (GDC) and air ventilation and other techniques resulted in the removal of substantial amounts of tritium ($\sim$ 2 g T) from the TFTR torus in periods between plasma operations [4]. *Deuterium tokamak pulses were found to be ineffective* in removing T from the torus. Deuterium glow discharges **(D-GDC) had an initially high removal rate**, but the *rate decreased* over several hours. The removal rate in *He/O glow discharges* (He + 10%O) was constant, but *low*, about 20 times less than found in laboratory experiments [5, 54]. Although, in the long run, He/O-GDC was found to be more effective than D-GDC, it was not pursued due to concerns about the effect of oxygen on subsequent plasma operation. **Air ventilation was found to be a simple and effective method of T removal.** Generally, relatively more T was released as the vessel temperature and/or air pressure was increased. The tritium inventory in TFTR after the final clean-up (including air vents and GDC) was 0.6 g (May 2000), corresponding to $\sim$ 12% long-term retention rate.

JET

An extended phase of D-T operations was carried out in the Joint European Torus from June to November 1997 as part of the MkII pumped-divertor campaign [55, 56]. During the D-T phase of the 1997 campaign (referred to as DTE1), 35 g of tritium entered the torus, of which 34.4 g was as gas fuelling and 0.6 g as neutral beams [7]. The T was introduced in a mixture with D, with the T content varying from 1% to 100%. Immediately after the last T-fuelled discharge, the amount of T remaining in the vessel was $\sim$ 11.5 g, i.e., about 33% of the T supplied to the torus.

The T-removal techniques used at JET can be grouped into two categories: techniques employing deuterium or hydrogen, which do not 'decondition' the vessel, and techniques involving venting of the torus. Of the deuterium techniques, only **tokamak pulses were found to be effective**. A series of discharges performed with D or H fuelling resulted in a reduction of the T inventory in the torus by a factor of about 2. It was found that additional heating of the plasma with **ICRH accelerated the tritium release**. *Glow discharges, D_2 gas soaks, N_2 vents, and ECRH discharges were found to be ineffective in removing significant amounts of tritium.* By the end of the MkIIa divertor campaign, about 6 g of T remained in the torus, and was being reduced by only $\sim$ 10 mg/day. This corresponds to $\sim$ 17% long-term

retention rate, very similar to that experienced in TFTR [4]. This persistent inventory appears to be largely in the form of co-deposited films that were not significantly affected by deuterium discharges. Following the DTE1 campaign, **bakeout** of the vessel and **ventilation of the torus** resulted in the release of a further 3.25 g of tritium. The estimated tritium inventory in the torus, as of December 1999, was ~ 2.1 g, corresponding to $\sim 6\%$ of the total tritium injected into the torus.

10.4.2 R&D of Co-deposit Removal Techniques

Techniques of tritium removal from co-deposited layers in next-generation tokamaks, such as ITER, have an important impact on machine operation. Attempts are being made to develop in-situ co-deposit removal techniques that would not overly constrain machine operation, both in terms of T removal and plasma performance recovery after cleanup. In addition to machine operation considerations, the tritium in the co-deposited layers will also have safety implications. During a severe accident, the vacuum vessel of an operating tokamak can be breached. If a significant inventory of tritium in the form of a saturated layer is present, much of this tritium can be released as tritium oxide as the film reacts with oxygen.

In principle, tritium could be removed from materials via thermal desorption and ion-induced desorption. However, the temperature requirement for thermal desorption from C-based materials is much higher, typically > 900 K [36], than the design temperatures for plasma-facing components, typically 500 K [2]. Ion-induced desorption at room temperature, or for that matter ion isotope exchange in the case of H, D, and T, is limited to depths corresponding to the ion range, typically a few nm for plasma discharges, and therefore will not reach the trapped T in the tens of μm thick co-deposits. Thus, the removal of T from thick co-deposits may require the removal of the co-deposits themselves by chemical and/or plasma-assisted oxidizing reactions in the presence of oxygen, or alternatively, via abrasive/mechanical techniques, such as pellet blast cleaning [57]. While the depth of T removal via ion-induced desorption is limited to the ion range, laser-induced heating – a technique extensively used in laser-induced thermal desorption spectroscopy, e.g., [58] – has the potential of reaching much deeper to release the tritium without the use of oxidation and the associated de-conditioning of the vessel walls. Such a laser-heating method has recently been tested by Skinner et al. [59], with promising results. The merits and shortcomings of the laser-heating, thermo-oxidation, and plasma discharge techniques are summarized in Table 10.2. In the remainder of this section we shall review results obtained for co-deposit removal using thermo-oxidation.

Table 10.2. Laser-heating, thermo-oxidation, and plasma discharge techniques for co-deposit removal [* These techniques require the introduction of oxygen into the torus and thus will require conditioning to remove the residual oxygen and water to recover plasma operation. Further work is needed to determine the effects of collateral damage]

Technique	Merits	Shortcomings
Laser heating	• Can be used without oxygen.	• Needs electro-mechanical and optical control to access location of co-deposits.
Air/O_2 with hot walls*	• Good removal efficiency at $T > 520\,K$; • Accessibility of shadowed regions, gaps, etc.	• Requires partial venting.
ECR + oxygen*	• Does not require vent or opening of the vacuum vessel; • Can be applied in the presence of strong magnetic fields; • Some experience exists in ASDEX and JFT-2.	• Erosion is line of sight (shadowed areas are eroded by neutrals at much lower rates); • Low erosion rates expected; • ECR was ineffective in JET.
ICR + oxygen*	• Does not require vent or opening of the vacuum vessel; • Can be applied in the presence of strong magnetic fields; • Some experience exists in TEXTOR and Tore Supra.	• Erosion is line of sight.
GDC + oxygen*	• Well-established tokamak practice; • Does not require vent or opening of the vacuum vessel.	• TF needs to be off; • Low film removal efficiency; • Limited access to shadowed areas.

Laboratory Studies of Co-deposit Removal via Thermo-Oxidation

From the extensive laboratory measurements of H/D/T removal rates from co-deposited films and D-implanted graphite during exposure to air or oxygen, three key conclusions can be drawn. First, we note that the release of D occurs in conjunction with C erosion [58, 60–64]. Second, the D-removal

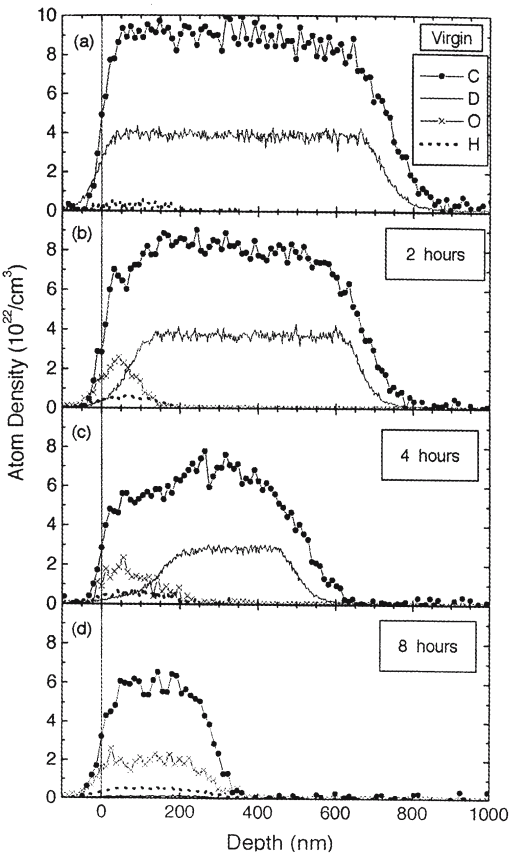

Fig. 10.9. Depth profile changes in carbon, deuterium, oxygen and hydrogen in a-C:D films due to air exposure at 650 K: (**a**) before annealing, (**b**) after annealing for 2 h, (**c**) after annealing for 4 h, and (**d**) after annealing for 8 h. The original film thickness was 730 nm. For each temperature step a fresh sample was used [62]

and C-erosion rates depend strongly on film structure. Third, D release rate during oxidation is a critical function of the specimen temperature.

The D-release rate during oxidation can be significant even at temperatures below 1,000 K. Wang et al. [62] measured the erosion of an a-C:D film at 650 K as a function of the annealing time in air. As seen in Fig. 10.9, initially D was released, and the thickness of the D-depleted and O-saturated layer increased with annealing time until it finally extended throughout the whole remaining co-deposit layer. Further annealing led to a thickness decrease until the complete layer was removed. Causey et al. also examined the release of tritium during air exposure at 623 K of thick co-deposit from TFTR (50 μm

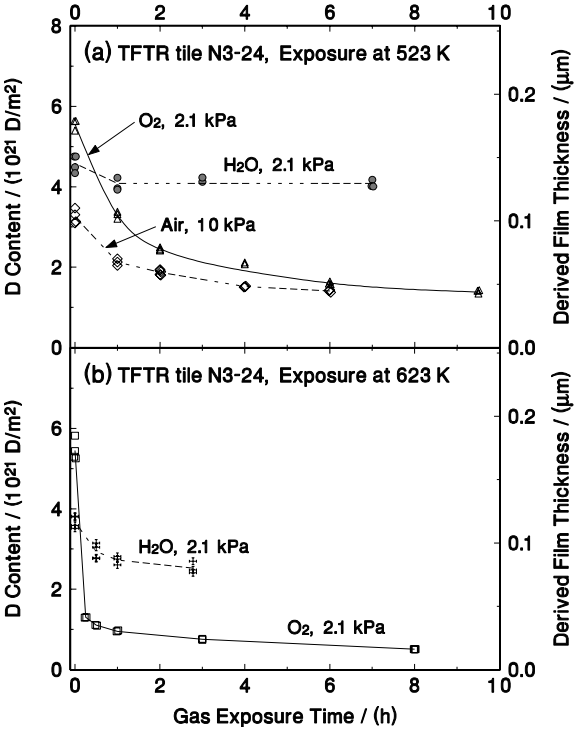

Fig. 10.10. D content of TFTR co-deposit as a function of gas (O_2, H_2O, air) exposure time at (**a**) 523 K and (**b**) 623 K [61]

with H/C $\sim$ 0.4) and observed that essentially all of the tritium was released in less than one hour [65]. By inference, if indeed the co-deposited layer was also eroded in this case, then the erosion rate would have been $> 50\,\mu$m/h.

From an analysis of the reaction products formed by exposing a laboratory-produced a-C:D film to $^{18}O_2$ at 470 K, Haasz et al. [60] concluded that essentially all of the D is removed via D_2O formation, and C is removed by the formation of $C^{18}O$ and $C^{18}O_2$. No D_2 and no methane were observed. Reaction product analysis performed by Alberici et al. [64] of a laboratory-produced a-C:D film exposed to oxygen also showed CO_2 to dominate the C release, and water, not D_2, to be the dominant D-containing reaction product. However, they needed temperatures > 700 K to activate the reactions.

D removal from hydrogenated films was also studied under exposure to other atmospheric gases. Nitrogen exposure and heating in vacuum at or below 570 K was found to have no effect on the release of deuterium from D-implanted layers [63]. On the other hand, exposure of D-implanted layers [63], as well as TFTR co-deposits [61], to water vapor did result in D removal, but with no evidence of C erosion. It is suggested that D is removed via isotope

Table 10.3. Derived C-erosion and measured D-removal rates for tokamak co-deposits during oxygen exposure at 16 Torr pressure

Temp. [K]	TFTR limiter [58,61] $\sim 0.15/5\,\mu m$ thick		JET divertor [61] $\sim 2\,\mu m$ thick		DIII-D divertor [61] $\sim 2\,\mu m$ thick	
	erosion [μm/h]	D-removal [10^{22}D/m^{2}h]	erosion [μm/h]	D-removal [10^{22}D/m^{2}h]	erosion [μm/h]	D-removal [10^{22}D/m^{2}h]
523	0.07/0.8	0.2/2	0.5	1	0.23	0.27
573	–/3.5	–/10	–	–	–	–
623	> 0.5/10	> 1.5/25	3.3	7	3.5	4.1

exchange between the impacting H_2O and the trapped D in the film [63]. Comparing the effectiveness of oxygen and water, oxygen was seen to be considerably more effective in removing the trapped D [61,63]. While isotopic exchange and reaction of the water with the carbon may occur, the reaction of oxygen directly with the hydrogen and carbon has the greater effect on the release of hydrogen. In the case of the TFTR co-deposit, initial D removal rates in water vapor were down by factors of 4–8, compared with oxygen under similar conditions (16 Torr and 520–620 K). As seen in Fig. 10.10, after about 1 h, no further D removal was observed with water, and a considerable amount of D was still left in the specimen [61].

Based on available results, it is evident that the D-removal and C-erosion rates depend on film structure, and differ greatly for laboratory-produced films and co-deposits produced in tokamaks. C-erosion rates from lab films and D-implanted layers are very similar and are of the order of a few to tens of nm/h at temperatures < 700 K. In contrast, measured C-erosion rates for tokamak co-deposits are 2-3 orders of magnitude higher under similar conditions. We note that C-erosion rates in oxygen or air (16 Torr) range from ~ 0.1–$1\,\mu m/h$ at 523 K to $\sim 10\,\mu m/h$ at 623 K. In Table 10.3, we show derived C-erosion rates and measured D-removal rates during oxygen exposure for several co-deposits obtained from major tokamak devices: TFTR, JET and DIIID. Recent oxidation results for TEXTOR co-deposits, using ozonized air or ozonized oxygen (few vol.% ozone), show that initial erosion rates of 1–$2\,\mu m/h$ could be achieved already at ~ 460 K [66].

It is evident that tritium can be removed from thick co-deposits of carbon and tritium by heating them in air or oxygen. According to the data in Table 10.3, if a reactor could be heated to approximately 620 K during baking, T-containing co-deposits of $\sim 10\,\mu m$ thickness could be eroded within hours. On the basis of these rates, thermo-oxidative removal of co-deposits via oxygen or air exposure is an option for ITER. Also, the limited experience gained from the controlled oxidation experiments in TEXTOR (see below) and the accidental loss of vacuum in JET [67] shows promising results for post oxidation plasma performance recovery.

Oxidation Experiments in TEXTOR

In order to gain confidence in projecting laboratory results for T removal from tokamak co-deposits to ITER-type reactors, it is absolutely essential that the T-removal techniques be first tested in current fusion devices. First experiments in a tokamak using oxygen with hot walls (620 K) to remove co-deposits have been performed in TEXTOR [68]. In the initial tests, the external pumps were closed and the vessel was filled with $^{16}O_2$ or with $^{18}O_2$ isotopes to pressures ranging from 0.005 to $\sim$ 0.2 Torr. At a filling pressure of $<$ 0.01 Torr, most of the oxygen was absorbed on the wall and the remaining 10-20% oxidized the deposits to form CO and CO_2 which were then released. At higher filling pressures ($\sim$ 0.2 Torr), the fraction of oxygen adsorbed decreased by 20-30%, whereas the fraction of CO formation was about constant and the formation of CO_2 increased. This behavior of the CO_2/CO ratio is in agreement with laboratory observations [60]. It has been found that the adsorption of oxygen ^{18}O on the walls leads to the release of $C^{16}O$ and $C^{16}O_2$, $C^{16}O^{18}O$ molecules by isotopic exchange processes. A significant increase of water partial pressures has been observed by the differentially pumped quadrupole mass spectrometers, but the available experimental diagnostics are not sufficient to separate the contributions from the co-deposits and other wall surfaces.

Encouragingly, TEXTOR did not experience any long-term adverse consequences after the use of oxygen to remove deuterium, and high performance plasma operation could be recovered after 15–30 min of GDC in helium and deuterium. The oxygen impurity content was initially 2–3 times higher than prior to oxidation, but was seen to decrease shot after shot, indicating a self cleaning process during plasma operation [68].

10.5 Conclusion

Hydrogen Retention

H retention in carbon-based materials during plasma or ion beam exposure occurs via four mechanisms: (i) buildup of a saturated surface layer, (ii) chemisorption on inner porosity surfaces, (iii) intergranular diffusion and trapping, and (iv) co-deposition of hydrogen with carbon on plasma-exposed surfaces. The hydrogen retained in the saturated layer, extending to the end of ion range ($\sim$ tens of nm), is a function of temperature, being $\sim$ 0.4 H/C at 300 K, and decreasing with increasing temperature. Following saturation of the implantation zone, mobile hydrogen from this zone will diffuse deeper into the material where it could be trapped. At low temperatures, the diffusion is along internal porosity and grain boundaries, while at T $>$ 1,000 K, transgranular diffusion becomes possible. The amount of H/D/T trapped beyond the implantation zone depends strongly on the structure of the graphite, e.g.,

for single-crystal graphite, diffusion beyond the implantation zone does not occur at low temperatures, while for porous graphites H has been measured at depths of several mm. Co-deposition results from the combined deposition of C and H from the plasma on surfaces. Co-deposited layers are typically tens of μm, with H content being similar to that seen in the implantation zone; there appears to be no limit to their thickness. In a reactor with neutrons present, H retention in the bulk will be dominated by trapping at neutron-induced damage sites.

Hydrogen Release

During irradiation, at low H^+ fluences and low graphite temperatures, essentially all non-reflected incident H^+ is retained in graphite. Once the near surface is saturated, nearly the entire incident H^+ is re-emitted from the surface – except for the small fraction that diffuses into the bulk – in the form of H_2 molecules, H° atoms, and hydrocarbons. The relative amounts of these species depend on temperature: nearly all H_2 at 300 K, H_2 plus hydrocarbons at ~ 800 K, and nearly all H° at $\sim 1,800$ K. During post-irradiation thermal desorption spectroscopy, again H_2, CH_4, and H° are released; the appearance of the desorption peaks occurs at different temperatures, methane at ~ 900 K, H_2 at $\sim 1,200$ K, and H° at $\sim 1,300$ K.

Tritium Removal Experience in TFTR and JET

During the three high power operational phases in TFTR, 1993–97, ~ 2.6 g of the 5.2 g tritium supplied to the vessel was retained ($\sim 50\%$), primarily in T-C co-deposits on the walls – with the carbon originating from TFTR's carbon limiter. Although the plasma properties of the JET (divertor) edge plasma are quite different – colder, denser – than the TFTR (limiter) edge, the carbon walls in JET are net sources of carbon, rather than sinks. Of the 35 g of tritium supplied to JET during D-T operation about 11.5 g was retained ($\sim 33\%$) in carbon co-deposits, found on cooled structures near the inside divertor, structures that were not in actual contact – and some not even in line-of-sight with the plasma. Following the D-T campaigns, various attempts were made to remove tritium from the torus. In TFTR, tokamak pulses were found to be ineffective, while glow discharge cleaning (GDC) and air ventilation during periods between plasma operations were found to be most effective in reducing the T inventory in the vessel. On the other hand, in JET, glow discharges were found to be ineffective, while tokamak pulses (assisted by ICRH) and bakeout of the vessel and ventilation of the torus were found to be most effective in removing tritium.

R&D of Co-deposit Removal

While in principle, tritium could be removed from materials via thermal desorption, heating to $> 900\,\mathrm{K}$ is required, which is much higher than the $\sim 500\,\mathrm{K}$ wall temperature in ITER. Also, ion-induced desorption can only reach depths corresponding to the ion range, typically a few nm for plasma discharges. Therefore, the removal of T from thick co-deposits (tens of μm) may require the removal of the co-deposits themselves by chemical and/or plasma-assisted oxidizing reactions in the presence of oxygen, or alternatively, via abrasive/mechanical techniques, such as pellet blast cleaning. From the extensive laboratory measurements of H/D/T removal rates from co-deposited films during exposure to air or oxygen, three key conclusions can be drawn: (i) D release occurs in conjunction with C erosion; (ii) D-removal and C-erosion rates depend strongly on film structure; and (iii) the D release rate during oxidation is a critical function of the specimen temperature. The D and C-containing reaction products during oxidation are D_2O, and CO/CO_2, respectively. C-erosion rates from lab-produced films and D-implanted layers are very similar and are of the order of a few to tens of nm/h at temperatures $< 700\,\mathrm{K}$. In contrast, measured C-erosion rates for tokamak co-deposits are 2–3 orders of magnitude higher under similar conditions. C-erosion rates in oxygen or air (16 Torr) range from ~ 0.1–$1\,\mu\mathrm{m/h}$ at 523 K to $\sim 10\,\mu\mathrm{m/h}$ at 623 K. In ozonized oxygen or air, erosion rates of 1–$2\,\mu\mathrm{m/h}$ could be achieved already at $\sim 460\,\mathrm{K}$. Thermal oxidation experiments performed in TEXTOR have produced reaction products in agreement with lab results. Encouragingly, TEXTOR did not experience any long-term adverse consequences after the use of oxygen to remove deuterium, and high performance plasma operation could be recovered after 15–30 min of GDC in helium and deuterium.

References

1. G. Federici, R.A. Anderl, P. Andrew et al., In-vessel tritium retention and removal in ITER, J. Nucl. Mater. **266-269** (1999) 14
2. G. Federici, R.A. Anderl, J.N. Brooks et al., Tritium inventory in the ITER PFCs: predictions, uncertainties, R&D status and priority needs, Fusion Eng. Design **39-40** (1998) 445–464
3. J.N. Brooks, G. Federici, D. Ruzic et al., Erosion/redeposition analysis: status of modeling and code validation for semi-detached tokamak edge plasmas, J. Nucl. Mater. **266-269** (1999) 58
4. C.H. Skinner, W. Blanchard, J.N. Brooks et al., Tritium experience in the Tokamak Fusion Test Reactor, Proc. 20th Symp. on Fusion Technology, Marseille, Sept. 1-11, 1998, Vol. 1, p. 153
5. D. Mueller et al., Tritium removal from TFTR, J. Nucl. Mater. **241-243** (1997) 897–901
6. P. Andrew, J.P. Coad, J. Ehrenberg et al., Experiments on the release of tritium from the first wall of JET, Nucl. Fusion **33** (1993) 1389–1404

7. P. Andrew, D. Brennan, J.P. Coad et al., Tritium retention and cleanup in JET, Fusion Eng. Design **47** (1999) 233
8. R. Seigele, J. Roth, B.M.U. Scherzer, S.J. Pennycook, Damage and deuterium trapping in highly-oriented pyrolytic graphite, J. Appl. Phys. **73** (1993) 2225
9. A.A. Haasz, J.W. Davis, Fluence dependence of deuterium trapping in graphite, J. Nucl. Mater. **209** (1994) 155
10. W.R. Wampler, C.W. Magee, Depth resolved measurements of hydrogen isotope exchange in carbon, J. Nucl. Mater. **103-104** (1981) 509
11. J. Roth, unpublished data. In: W. Moller, B.M.U. Scherzer, Modeling of hydrogen implantation in graphite, J. Appl. Phys. **64** (1988) 4860
12. W. Moller, P. Borgensen, B.M.U. Scherzer, Thermal and ion-induced release of hydrogen atoms implanted into graphite, Nucl. Instr. Meth. B **19/20** (1987) 826
13. M. Braun, B. Emmoth, Deuterium implantation in carbon at elevated temperatures, J. Nucl. Mater. **128-129** (1984) 657
14. B.L. Doyle, W.R. Wampler, D.K. Brice, Temperature dependence of H saturation and isotope exchange, J. Nucl. Mater. **103-104** (1981) 513
15. J.W. Davis, unpublished data, University of Toronto 1991
16. J.W. Davis, A.A. Haasz, Thermal desorption of graphite during deuterium ion bombardment, J. Nucl. Mater. **217** (1994) 206
17. A.A. Haasz, J.W. Davis, Deuterium retention in doped graphites, J. Nucl. Mater. **232** (1996) 219
18. G. Staudenmaier, J. Roth, R. Behrisch, J. Bohdansky, W. Eckstein, P. Staib, S.K. Erents, Trapping of deuterium implanted in carbon and silicon: a calibration for particle-energy measurements in the plasma boundary of tokamaks, J. Nucl. Mater. **84** (1979) 149
19. R.A. Causey, M.I. Baskes, K.L. Wilson, The retention of deuterium and tritium in POCO AXF-5Q graphite, J. Vac. Sci. Technol. A **4** (1986) 1189
20. V.N. Chernikov, A.E. Gorodetsky, S.L. Kanashenko, A.P, Zakharov, W.R. Wampler, B.L. Doyle, Trapping of deuterium in boron and titanium modified graphites before and after carbon ion irradiation, J. Nucl. Mater. **217** (1994) 250
21. P.C. Stangeby, O. Auciello, A.A. Haasz, B.L. Doyle, Trapping of sub-eV hydrogen and deuterium atoms in graphite, J. Nucl. Mater. **122-123** (1984) 1592
22. B. Emmoth, M. Rubel, E. Franconi, Deep penetration of deuterium in carbon based substrates exposed to the PISCES-A plasma, Nucl. Fusion **30** (1990) 1140
23. R.D. Penzhorn, N. Bekris, U. Berndt, J.P. Coad, H. Ziegler, W. Nagele, Tritium depth profiles in graphite and carbon fibre composite materials exposed to tokamak plasmas, J. Nucl. Mater. **288** (2001) 170
24. J.W. Davis, A.A. Haasz, D.S. Walsh, Flux and fluence dependence of H^+ trapping in graphite, J. Nucl. Mater. **176-177** (1990) 992
25. M. Mayer, M. Balden, R. Behrisch, Deuterium retention in carbides and doped graphites, J. Nucl. Mater. **252** (1998) 55
26. B.E. Mills, D.A. Buchenauer, A.E. Pontau, M. Ulrickson, Characterization of deposition and erosion of the TFTR bumper limiter and wall, J. Nucl. Mater. **162-164** (1989) 343
27. W.R. Wampler, B.L. Doyle, S.R. Lee et al., Deposition of carbon, deuterium and metals on the wall and limiters of the Tokamak Fusion Test Reactor, J. Vac. Sci. Technol. A **6** (1988) 2111-2115

28. C.H. Skinner et al., Plasma–wall interactions and tritium retention in TFTR, J. Nucl. Mater. **241-243** (1997) 214
29. G. Federici, C.H. Skinner, J.N. Brooks, J.P. Coad, C. Grisolia, A.A. Haasz, A. Hassanein, V. Philipps, C.S. Pitcher, J. Roth, W.R. Wampler, D.G. Whyte, Plasma-material interactions in current tokamaks and their implications for next-step fusion reactors, Nucl. Fusion **41** (2001) 1967
30. R.A. Causey, K.L. Wilson, W.R. Wampler, B.L. Doyle, The effects of neutron irradiation on the trapping of tritium in graphite, Fusion Technology **19** (1991) 1585
31. H. Atsumi, M. Iseki, T. Shikama, Trapping and detrapping of hydrogen in carbon-based materials exposed to hydrogen gas, J. Nucl. Mater. **212-215** (1994) 1478
32. H. Atsumi, M. Iseki, T. Shikama, Hydrogen behaviour in carbon-based materials and its neutron irradiation effect, J. Nucl. Mater. **233-237** (1996) 1128
33. W.R. Wampler, B.L. Doyle, R.A. Causey, K.L. Wilson, Trapping of deuterium at damage in graphite, J. Nucl. Mater. **176-177** (1990) 983
34. H. Atsumi, M. Iseki, T. Shikama, Hydrogen solubility and diffusivity in neutron-irradiated graphite, J. Nucl. Mater. **191-194** (1992) 368
35. J. W. Davis, C.S. Pitcher, A.A. Haasz, Re-emission of deuterium from graphite as a function of D^+ flux density, J. Appl. Phys. **76** (1994) 4511
36. A.A. Haasz, P. Franzen, J.W. Davis, S. Chiu, C.S. Pitcher, Two-region model for hydrogen trapping in and release from graphite, J. Appl. Phys. **77** (1995) 66
37. P. Franzen, E. Vietzke, A.A. Haasz, J.W. Davis, V. Philipps, Atomic re-emission of hydrogen from pure and boronized graphites at temperatures above 1000 K, J. Nucl. Mater. **196-198** (1992) 967
38. P. Franzen, E. Vietzke, Atomic release of hydrogen from pure and boronized graphites, J. Vac. Sci. Technol. A **12** (1994) 820
39. J.W. Davis, A.A. Haasz, Reemission and thermal desorption of D°, D_2 and CD_4 from graphite, J. Nucl. Mater. **220-222** (1995) 832
40. J.W. Davis, A.A. Haasz, Reemission of deuterium atoms from Mo, Ta and W during D^+ irradiation, J. Nucl. Mater. **223** (1995) 312
41. V. Philipps, E. Vietzke, M. Erdweg, K. Flaskamp, Thermal desorption of hydrogen and various hydrocarbons from graphite bombarded with thermal and energetic hydrogen, J. Nucl. Mater. **145-147** (1987) 292
42. Y. Gotoh, T. Yamaki, K. Tokiguchi, H. Shimizu, Thermal desorption spectroscopy of pyrolytic graphite cleavage faces after keV deuterium irradiation at 330–1000 K, J. Nucl. Mater. **191-194** (1992) 360
43. G. Hansali, J.B. Biberian, M. Bienfait, Ion beam implantation and thermal desorption of deuterium ion in graphite, J. Nucl. Mater. **171** (1990) 395
44. K. Ashida, K. Ichimura, M. Matsuyama, K. Watanabe, Thermal desorption of hydrogen, deuterium and tritium from pyrolytic graphite, J. Nucl. Mater. **128-129** (1984) 792
45. H. Atsumi, S. Yamanaka, P. Son, M. Miyake, Thermal desorption of deuterium and helium from ion irradiated graphite, J. Nucl. Mater. **133-134** (1985) 268
46. K. Nakayama, S. Fukuda, T. Hino, T. Yamashina, Thermal desorption process and surface roughness of POCO graphite irradiated by hydrogen ion beam, J. Nucl. Mater. **145-147** (1987) 301

47. J.A. Sawicki, J. Roth, L.M. Howe, Thermal release of tritium implanted in graphite studied by T(d,α)n nuclear reaction depth profiling analysis, J. Nucl. Mater. **162-164** (1989) 1019
48. S. Chiu, A.A. Haasz, Thermal release of simultaneously implanted H^+ and D^+ from graphite, J. Nucl. Mater. **210** (1994) 34
49. K. Ashida, K. Ichimura, M. Matsuyama, K. Watanabe, Thermal desorption of deuterium from graphite doped with iron, J. Nucl. Mater. **148** (1987) 217
50. D.G. Whyte, J.P. Coad, P. Franzen et al., Similarities in divertor erosion/redeposition and deuterium retention patterns between the tokamaks ASDEX Upgrade, DIII-D and JET, Nucl. Fusion **39** (1999) 1025
51. C.H. Skinner, W. Blanchard, J. Kamperschroer et al., Measurements of tritium retention and removal on the Tokamak Fusion Test Reactor, J. Vac. Sci. Technol. A **14** (1996) 3267-3274
52. D. Mueller, W. Blanchard, B.L. Doyle et al., Tritium retention and removal on TFTR, Proc. 17th IEEE/NPSS Symp. on Fusion Engineering, San Diego, CA, October 6-10, 1997
53. C.H. Skinner, J.T. Hogan, J.N. Brooks et al., Modeling of tritium retention in TFTR, J. Nucl. Mater. **266-269** (1999) 940
54. W.L. Hsu, Glow-discharge removal of codeposited carbon films in graphite-lined tokamak reactors, J. Vac. Sci. Technol. **A7** (1989) 1047
55. M. Keilhacker, D-T experiments in the JET tokamak, J. Nucl. Mater. **266-269** (1999) 1
56. P. Andrew, D. Brennau, J.P. Coad et al., Tritium recycling and retention in JET, J. Nucl. Mater. **266-269** (1999) 153
57. R. Nygren, Sandia National Laboratories, Albuquerque, personal communication
58. A.A. Haasz, J.W. Davis, The removal of codeposited layers from TFTR tiles by O_2 gas exposure, J. Nucl. Mater. **256** (1998) 65-68
59. C.H. Skinner, C.A. Gentile, A. Carpe et al., Tritium removal from codeposits on carbon tiles by a scanning laser, J. Nucl. Mater. **301** (2002) 98
60. A.A. Haasz, S. Chiu, J.E. Pierre, Y.I. Gudimenko, Thermo-oxidative erosion of amorphous hydrogenated carbon films, J. Vac. Sci. Technol. A **14** (1996) 184-191
61. J.W. Davis, A.A. Haasz, Oxygen removal of codeposited a-C:D layers from tokamak tiles, J. Nucl. Mater. **266-269** (1999) 478
62. W. Wang, W. Jacob, J. Roth, Oxidation and hydrogen isotope exchange in amorphous deuterated carbon films, J. Nucl. Mater. **245** (1997) 66
63. S. Chiu, A.A. Haasz, Chemical release of implanted deuterium in graphite, J. Vac. Sci. Technol. A **9** (1991) 747
64. S. Alberici, H.K. Hinssen, R. Moormann, C.H. Wu, Deuterium release rates in a-C:D layers during oxygen attack, J. Nucl. Mater. **266-269** (1999) 754
65. R.A. Causey, W.R. Wampler, D. Walsh, Comparison of the thermal stability of the codeposited carbon/hydrogen layer to that of the saturated implant layer, J. Nucl. Mater. **176-177** (1990) 987
66. R. Moormann, H.K. Hinssen, C.H. Wu, Oxidation of carbon based first wall materials of ITER, Proc. 18th IAEA Fusion Energy Conference, Sorrento, Italy, October 4-10, 2000, paper FTP1/29
67. C.J. Orchard, A.T. Peacock, G. Saibene, JET experience in recovery from large air leak incidents, J. Nucl. Mater. **200** (1993) 395

68. V. Philipps, H.G. Esser, J. von Seggern et al., Removal of redeposited layers and hydrogen release by oxygen ventilation of TEXTOR, J. Nucl. Mater. **266-269** (1999) 386
69. B.V. Mech, A.A. Haasz, J.W. Davis, Isotopic effects in hydrocarbon formation due to low-energy H^+/D^+ impact on graphite, J. Nucl. Mater. **255** (1998) 153

11 Interaction of Low-Energy Ions and Hydrocarbon Radicals with Carbon Surfaces

W. Jacob, C. Hopf, M. Meier, and T. Schwarz-Selinger

A review is given on the physical and chemical reactions that occur if atomic hydrogen, hydrocarbon radicals, and low-energy ions interact with carbonaceous surfaces. In a first set of experiments the surface loss probabilities of different hydrocarbon radicals are determined in low-temperature plasmas using the cavity technique. The following values were determined: $\beta(C_2H) = 0.90 \pm 0.05$, $\beta(C_2H_3) = 0.35 \pm 0.15$, and $\beta(CH_3, C_2H_5) \leq 10^{-2}$.

Another set of experiments was carried out in an UHV-based system working with well-defined, quantified particle beams. This system was employed to measure the sticking coefficient of methyl radicals (CH_3), the simultaneous interaction of CH_3 radicals and atomic hydrogen or low energy ions leading to chemical sputtering and ion-induced deposition, respectively, and the simultaneous interaction of all tree species (CH_3, H, and ions).

The sticking coefficient of methyl radicals on a hydrocarbon surface at 340 K is of the order of 10^{-5} to 10^{-4}. The temperature dependence of this process was determined in the range from 340 to 800 K. Simultaneous exposure of the surface to atomic hydrogen and CH_3 leads to an increase of the sticking coefficient up to 10^{-2} depending on the H flux. Simultaneous interaction of CH_3 and low-energy ions ($E < 1$ keV) also causes an enhancement of CH_3 sticking to about 10^{-2}.

Simultaneous interaction of atomic hydrogen and low-energy ions leads to chemical sputtering. Chemical sputtering occurs also at energies well below the threshold for physical sputtering. In addition, the rate of chemical sputtering is significantly higher than the sum of chemical erosion due to atomic hydrogen alone and physical sputtering due to ions. A microscopic model for the chemical sputtering mechanism is suggested which allows a quantitative description of the flux and energy dependence of the process.

11.1 Introduction

For the time being, one of the most crucial issues for a next-step device such as ITER is tritium retention. The actual ITER design uses beryllium for the main chamber wall and carbon as well as tungsten in the divertor [1, 2]. For this choice of materials, tritium co-deposition with eroded carbon is expected to be the dominant tritium retention mechanism. This holds also

for the planned scenario that only a small fraction of the total wall area, more precisely the divertor strike zones, are made of carbon [2]. General plasma-material interaction issues as well as the tritium retention problem for a nuclear fusion device are comprehensively reviewed in [1].

Present-day fusion experiments as well as ITER rely on the use of a divertor which efficiently pumps the impurities generated by erosion of the first wall due to charge exchange neutrals. This keeps the core plasma clean and minimizes radiative losses. In most existing fusion experiments the divertor surface consists of graphite tiles or carbon fibre composites which are exposed to a substantial incoming flux of ions and neutrals from the main plasma. This impinging species flux leads to erosion of the divertor tiles emitting carbon and hydrocarbon compounds into the gas phase. Most of all carbon and hydrocarbon species released in the divertor will re-deposit in relatively close proximity to their place of erosion. This balance between deposition and erosion is crucial for the performance of a divertor in a next-step device, since the total lifetime before replacement strongly depends on the ability to control this re-deposition.

However, the small fraction of carbon and hydrocarbon species that is not re-deposited in the divertor may escape from the divertor and also from the boundary plasma and cause deposition of hydrocarbon layers – often called *re-deposited* or *co-deposited* layers – on surfaces not in direct contact with the plasma. Indeed, thick re-deposited layers were observed on remote surfaces of JET [3, 4]. More recent investigations resulted in the detection of much thinner, but measurable, re-deposited layers in other tokamaks (e.g., TEXTOR [5] and ASDEX Upgrade [6–8, 42]). On many of these surfaces only neutral growth precursors can contribute to film deposition, because only they can traverse the magnetic field lines. A major concern is the large amount of hydrogen which is trapped in these re-deposited films [1, 10]. In a future fusion reactor this trapped hydrogen will partly be tritium, which will be lost for the fusion reactions. One aim of a future design is, therefore, to reduce this tritium retention for economy and safety reasons. Besides tritium retention, deposition of hydrocarbon layers on remote surfaces will adversely affect the optical reflectivity of diagnostic mirrors [11]. Both problems call for an improved understanding of the underlying basic processes which hopefully will help to mitigate the consequences. An improved understanding will also support the development of in-situ cleaning methods required to remove co-deposited layers.

The main objective of this article is to summarize the work performed at the Max-Planck-Institute for Plasma Physics in Garching over the past few years relevant to plasma–surface interaction processes in the system hydrogen and carbon. This includes a short review of the properties of amorphous, hydrogenated carbon layers, further on abbreviated as a–C:H, determination of reaction probabilities of reactive species such as atomic hydrogen and methyl radicals, and investigation of the simultaneous interaction of these species and low-energy ions with hydrocarbon surfaces. The reviewed ma-

terial represents two totally different experimental approaches: Deposition and erosion of a–C:H layers is studied applying low-temperature laboratory plasmas. As dominant diagnostic, in-situ real-time ellipsometry was used. Plasma-deposited layers were subsequently characterized by a variety of ex-situ analysis techniques, namely ion-beam analysis to determine the layer stoichiometry, profilometry for thickness measurement, infrared absorption spectroscopy, and thermal effusion spectroscopy. The surface loss probability of hydrocarbon radicals was also determined in low-temperature plasmas applying the cavity technique. The second class of experiments was carried out in an UHV-based system working with well-defined, quantified particle beams.

This article is organized as follows. In the next section, the properties of a–C:H layers are shortly summarized. The following section presents the experimental methods and set-ups applied in our experiments. Section 11.4.1 summarizes the knowledge about surface loss probabilities of different hydrocarbon radicals. The remainder of the article is dedicated to a review of the results from our particle-beam experiment MAJESTIX.

11.2 Properties of Hydrocarbon Layers

Due to its outstanding physical properties amorphous hydrogenated carbon (a–C:H) is a technologically very interesting material with a number of well-established and many potential applications. Since more than 30 years deposition and properties of a–C:H is thoroughly investigated. The state of the art of a–C:H preparation and its application was recently reviewed by Grill [12]. Further comprehensive reviews of properties and applications of various forms of amorphous carbon were compiled by Robertson [13] and Silva [14]. Besides these technical applications, a–C:H layers are a model system for the interaction of hydrogen plasmas with carbon surfaces because the actual state of the surface, in particular the hydrogen content, depend more on the actually impinging particle fluxes than on the bulk material [15, 16]. Consequently, it can be anticipated that a–C:H layers are a reasonable model system to study the plasma–surface interaction processes relevant to the interaction of fusion plasmas with carbonaceous materials.

Amorphous hydrocarbon films are usually prepared in low-temperature plasmas from a hydrocarbon precursor gas, which is dissociated and ionized in a discharge. Ions and radicals formed in the gas phase impinge on the substrates and lead to film growth. The surface reactions during growth and erosion of a–C:H were reviewed by Jacob [15]. The properties of a–C:H depend on a variety of deposition parameters, such as source gas [17], working pressure, and substrate bias voltage (ion energy) [15, 16, 18–20]. The physical properties such as hydrogen content, density, refractive index, hardness, and others are strongly correlated with each other [17].

Table 11.1. Physical properties of hydrocarbon films deposited with a remote electron cyclotron resonance plasma from three different C_2H_x source gases at three different dc self-bias voltages V_b. n_p represents the parallel component of the real part of the refractive index as measured by in situ ellipsometry. The film composition is obtained from ion-beam analysis. The total particle number densities n_C and n_H are calculated from the stoichiometry and the film thickness. Deposition parameters: pressure $p = 0.2\,\mathrm{Pa}$ adjusted with gas flow at constant pumping speed, absorbed microwave power density $P = 10\,\mathrm{kW\,m^{-3}}$ [17]

source gas	V_b (Volts)	n_p	n_C ($\times 10^{28}\,\mathrm{m^{-3}}$)	n_H ($\times 10^{28}\,\mathrm{m^{-3}}$)	H/(H + C) (at. %)	H/C (at. %)	ρ ($\mathrm{g\,cm^{-3}}$)
C_2H_6	floating	1.62	5.2	3.9	0.43	0.75	1.1
C_2H_4	floating	1.72	5.3	4.2	0.44	0.79	1.1
C_2H_2	floating	1.80	6.5	4.6	0.41	0.69	1.4
C_2H_6	−30	1.85	7.5	5.2	0.41	0.69	1.6
C_2H_4	−30	1.95	8.4	5.3	0.39	0.64	1.7
C_2H_2	−30	2.09	9.1	4.9	0.35	0.54	1.8
C_2H_6	−200	2.22	9.0	4.2	0.32	0.43	1.9
C_2H_4	−200	2.34	10.8	4.0	0.27	0.37	2.2
C_2H_2	−200	2.46	11.5	3.1	0.21	0.27	2.4

Hydrocarbon films have a typical hydrogen atom concentration ranging from 30 to above 50%. The hydrogen content depends strongly on the kinetic energy of the impinging ions during plasma-deposition. Films with a hydrogen atom concentration of about 50% are formed at low ion energies with almost all carbon atoms being sp^3 hybridized. These films are named polymer-like amorphous carbon films. At higher ion energies ($> 50\,\mathrm{eV}$) the hydrogen atom concentration decreases to 30% and about 60% of the carbon atoms in these films are sp^2 hybridized [21–24]. These layers are mostly called hard a–C:H or diamond-like carbon. Ions penetrating into the hydrocarbon layer displace predominantly bonded hydrogen due to the smaller threshold energy for displacement of hydrogen compared to that of carbon [15]. Penetration depth and displacement yield increase with increasing ion energy [15]. The displaced hydrogen atoms can be trapped again or form H_2 molecules either by recombination with another H atom or via abstraction of bonded hydrogen in the C:H network. The formed H_2 molecules are either trapped in internal voids or diffuse to the surface and desorb [25]. Consequently, the hydrogen content decreases with increasing ion energy. Simultaneously, the sp^2/sp^3 ratio increases according to the RCN (RCN = random covalent network) model [26,27]. These ion-induced effects, however, are of minor importance for the growth of polymer-like amorphous carbon films, since the kinetic energy of the incident ions is low ($< 30\,\mathrm{eV}$) and the film growth rate and the film properties are dominated by the surface reactions of radicals emanat-

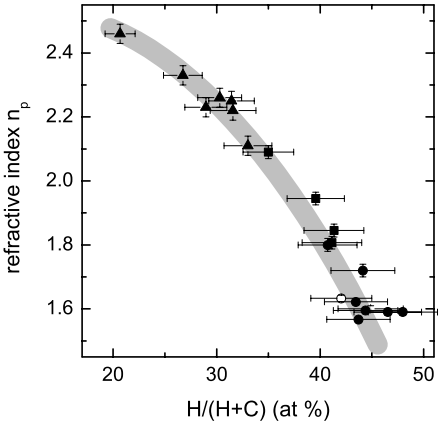

Fig. 11.1. Parallel component of the real part of the refractive index n_p as a function of the resulting hydrogen content H/(H+C) of the deposited films. Seven different hydrocarbon feed gases and three different dc self-bias voltages (V_b) were used. Solid circles correspond to deposition at floating potential, solid squares to $V_b = -30\,V$, and solid triangles to $V_b = -200\,V$. In addition, one data point for a 1 : 2 mixture of acetylene with hydrogen deposition at floating potential is included (*blank circle*). The *thick gray line* is only a guide to the eye

ing from the hydrocarbon plasma. The growth mechanisms for polymer-like amorphous carbon films were recently reviewed by von Keudell [28].

Typical properties of plasma-deposited a–C:H layers are summarized in Table 11.1.

As an example for the correlation of physical properties, Fig. 11.1 displays the parallel component of the real part of the refractive index n_p of a–C:H layers as a function of the hydrogen content [17]. The correlation seen in Fig. 11.1 holds not only for the variation of one experimental parameter with otherwise fixed deposition parameters, but also for a wide variation of deposition parameters such as dc self-bias voltage, precursor gas, and hydrogen admixture. It appears that this high correlation is an intrinsic property of the a–C:H system. Simplifying, we can say that the deposition process determines the hydrogen content, and that all other film properties are then to first order determined only by this resulting hydrogen content.

C:H layers have a limited thermal stability in the sense that they decompose at elevated temperature even in vacuum. The released product spectrum and the onset temperature for decomposition depend sensitively on the layer structure, in particular, the initial hydrogen content [29, 30]. Hard a–C:H layers with a typical H content of about 30% (see Table 11.1) start to decompose around 700 K with two distinct effusion maxima at about 800 and 1100 K [29, 30]. The product spectrum is dominated by H_2 with minor contributions of CH_4 and some higher hydrocarbons (C_xH_y). These results are in good agreement with published data on ion-beam deposited C:H layers [31,32], ion-bombarded pyrolytic graphite [33], and other plasma-

deposited layers [18,19,34]. With increasing initial hydrogen content the onset of thermal decomposition shifts to lower temperature and the contribution of hydrocarbon species increases. Soft C:H layers with typically more than 50% hydrogen start to decompose at around 400 K with CH_4 and C_2H_4 being the dominant release products [29,35]. Hydrocarbon fragments with up to 7 carbon atoms were detected in thermal effusion studies [35]. Interestingly, even for very soft (= hydrogen rich) layers temperatures of more than 1000 K are required to release all hydrogen [29,35].

11.3 Experimental

11.3.1 The Cavity Technique

The possible reactions of a radical species impinging upon a surface can be classified in the following way: The particle can either become reflected without reacting with a probability r, it can react with the surface to form a volatile, non-reactive species that desorbs with a probability γ, or it can effectively stick to the surface with a probability s. In principle, one might also consider reactions in which a different reactive species is formed, however it is assumed that this reaction channel is negligible.

With respect to deposition processes the most important of the mentioned quantities is the sticking coefficient s. However, its determination requires a rather high experimental effort. An experiment to measure s of selected species will be described in the next section. To get easier access to a figure of merit for the overall reactivity of a radical with surfaces often the *surface loss probability*

$$\beta = s + \gamma = 1 - r \tag{11.1}$$

is measured instead. It is the total probability that the particle is lost upon wall collision, i.e., it does not come back as the original species. It is an upper limit to the sticking coefficient.

An elegant yet technically simple method to determine surface loss probabilities is the cavity technique [30,36–38]: A cavity with a small entrance slit (see Fig. 11.2) or a different well-defined geometry – [39–41] is exposed to a flux of reactive species. The transport of the particles is studied via the cross-sectional film thickness profiles. The dimensions of the geometry are chosen much smaller than the mean free path of the neutral radical species so that gas phase collisions are negligible. Then the normalized profiles depend on the surface loss probability β only. If the total fluence of particles into the slit is not known no conclusions can be drawn concerning the sticking coefficient except $s \leq \beta$.

The cavities we use are completely disassembled after deposition. Measurement of the film thickness profiles can then be done by very different techniques. For sufficient film thickness a very convenient and fast measurement

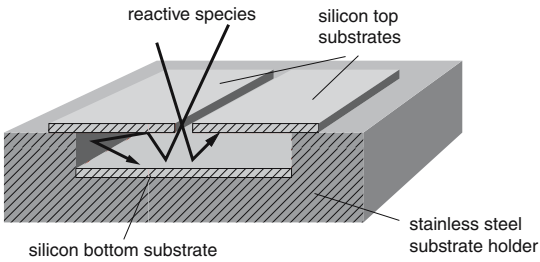

Fig. 11.2. Principle of a cavity probe: Reactive particles enter the cavity through the slit and deposit films on the inner surfaces. Their transport and thus the resulting film thickness profiles are determined by the surface loss probability

is obtained by profilometry. A more accurate measurement can be achieved by ellipsometry [37,38]. For very thin deposited layers ion-beam analysis is a highly sensitive technique [42]. It provides the further advantage that it directly measures the carbon areal density instead of measuring the thickness in units of length as the previously mentioned methods. Other authors used scanning electron microscopy of a cross-sectional cut through the probe [43], which is especially useful if the lateral dimensions of the probe geometry are small and access to the inner surfaces is difficult.

The value of β is derived via comparison with model calculations. Model calculations can be carried out with Monte Carlo methods: The particles start at random positions outside the cavity with a randomly chosen direction. The angular distribution of the particle directions does, however, not necessarily have to be uniform. Each particle is followed if it enters the slit and as long as it is inside the cavity. Upon each wall collision a fraction s of the particle sticks to the wall and a fraction $r = 1 - \beta$ is re-emitted with a cosine distribution with respect to the surface normal. When only a negligible part of the particle is left, e. g. 10^{-3}, the next particle is started outside the cavity. In general, the trajectories of more than 10^6 particles have to be calculated to reach good statistics. For convenience, $s = \beta$ is chosen in the calculation (this is equivalent to $\gamma = 0$). As said before, the normalized profiles depend on the surface loss probability β only, so that this choice has no influence on the profile.

A tremendous reduction of calculation time was achieved by a semi-analytical calculation. We consider the two-dimensional transport of reactive particles in a cross-section of the cavity like that shown in Fig. 11.3. The calculation is carried out in steps that correspond to 'particle generations': the nth generation is the set of particles that have undergone n wall collisions. In the first step of the calculation, the flux of the incoming particles (generation 0) onto all points on all inner walls of the cavity is calculated. In the second step, the flux of desorbing particles from all inner walls to all walls is calculated (first generation) and so on.

Consider the contribution $j_n(P_2)$ of the incident flux in P_2 of the n^{th} generation that comes from particles that desorb at point P_1 (see Fig. 11.3).

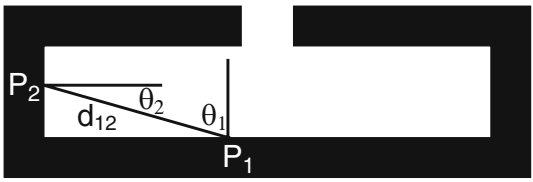

Fig. 11.3. Definitions for the semi-analytical simulation

It is proportional to the flux $j_{n-1}(P_1)$ of generation $n-1$ incident at P_1 times the reflection probability $r = 1-\beta$. Furthermore, because we assume a cosine angular distribution of reflected particles, it is proportional to $\cos\theta_1$. As the flux is defined as the number of particles per unit time and unit area *normal* to the surface also $\cos\theta_2$ enters. Finally, in the two dimensional case the distance d_{12} between P_1 and P_2 enters with the power (-1). We obtain

$$j_n(P_2) \propto (1-\beta)\cos\theta_1 \cos\theta_2 \, d_{12}^{-1} j_{n-1}(P_1). \tag{11.2}$$

The calculation is stopped after the mth generation if $r^m < 10^{-3}$, i.e., when only 10^{-3} of the initial flux is left. The film thickness profile, i.e., the local deposited film thickness $h(x)$, is proportional to the sum over all generations of incoming fluxes,

$$h(x) \propto \sum_{n=0}^{m} j_n(x). \tag{11.3}$$

Figure 11.4 shows three examples of calculation results. In the case of a large $\beta = 0.8$ strong deposition on the bottom substrate opposite to the slit is expected the shape of which reflects the incident angular distribution; examples are shown for initial angular distributions $j \propto \cos^n\theta_0$ with $n = 2$ and $n = 5$, where θ_0 is the angle with the surface normal. Some deposition is still expected on the inner side of the top substrates next to the slit that mainly comes from particles which were reflected once from the main deposition zone at the bottom. Only very little deposition should occur far away from the slit as particles on the average need more wall collisions to get there. It can also be seen that a more peaked angular distribution of the incident species leads to a more peaked deposition profile on the bottom substrate (compare upper and middle panel of Fig. 11.4). The situation is clearly different for $\beta = 0.01$. In that case the particles survive an average of 100 wall collisions and can, therefore, reach all inner wall areas with an almost constant probability. Significant deposition is also expected far away from the slit and film thickness is nearly uniform.

While the described semi-analytical calculation is much faster than the Monte Carlo method the latter has the advantage of being applicable to any geometry and is therefore more general. The semi-analytical calculation requires a relatively simple cavity geometry to be efficient. We checked for our geometry that the Monte Carlo method and the semi-analytical calculation yield identical results.

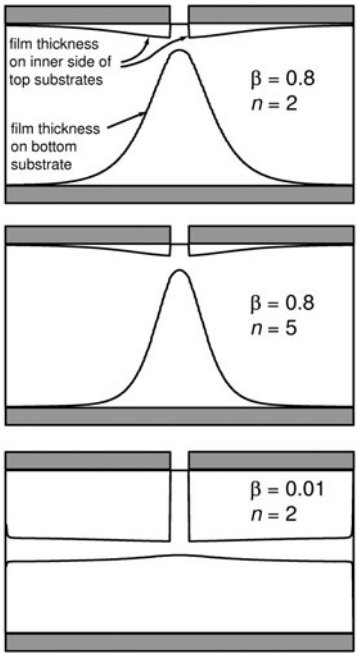

Fig. 11.4. Three simulated example profiles. As initial angular distribution of the particles $j \propto \cos^n \theta_0$ was assumed, where θ_0 is the angle between the surface normal of the cavity and the particle direction in the cross-section in Fig. 11.3. n and β are given for each simulation

11.3.2 Particle-Beam Experiments

Particle-beam experiments were carried out in the MAJESTIX device at IPP Garching. Different aspects of and modifications to the MAJESTIX set-up were described in several publications from our group [44–48]. A thorough and detailed description of the experimental set-up and applied techniques will soon be published [49].

In short: MAJESTIX is an UHV-based particle-beam experiment to study heterogeneous surface reactions relevant to plasma–surface interaction processes. The experiment comprises two radical beam sources and a source for low energy ions. A schematic sketch of the MAJESTIX experimental setup is shown in Fig. 11.5. As diagnostic tools real-time in-situ ellipsometry and infrared spectroscopy are implemented. The infrared sensitivity for thin films is enhanced through application of an optical cavity substrate. The fluxes of the radical beam sources are absolutely quantified for production of hydrogen atoms and methyl radicals. The ion source is also quantified for a wide variety of ionic species, e.g., He^+, Ar^+, H^+, H_2^+, H_3^+, and CH_3^+. Ion energies from above 1 keV down to 1 eV are achievable. The set-up allows to investigate heterogeneous surface processes of one single species or the simul-

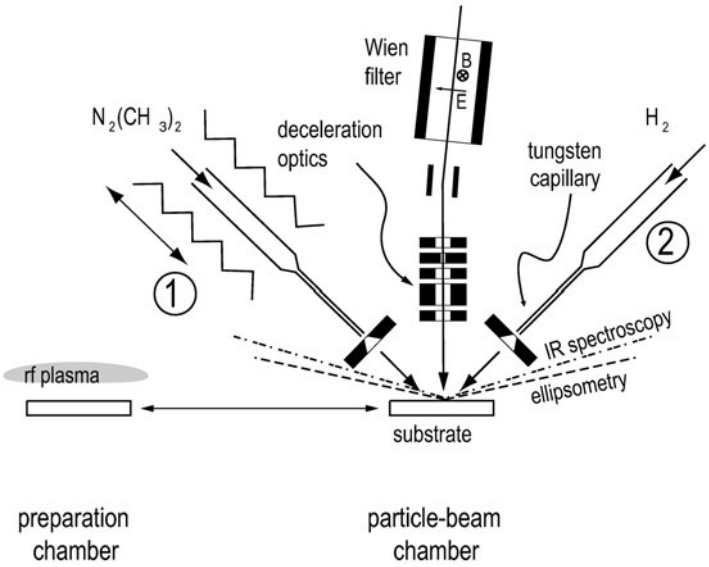

Fig. 11.5. Sketch of the MAJESTIX setup. The vacuum system is divided into a preparation chamber and a particle-beam chamber, separated by a gate valve. The preparation chamber is also used as load lock. The main components in the particle-beam chamber are the ion gun system, comprising a Wien filter and deceleration optics, two radical beam sources, and two lines of sight for the in-situ diagnostics ellipsometry and infrared spectroscopy. Radical source 1 is mounted on a movable flange thus allowing to change the distance from the tip to the sample surface and consequently the flux density at the sample surface. Radical source 2 is mounted in a fixed distance of 46 mm. Each source can either be run with Azomethane for production of CH_3, or H_2 or D_2 to produce atomic H and D, respectively

taneous interaction of up to three different, individually controllable species with a surface of interest. Running the radical sources to produce hydrogen and methyl radicals and the ion source with the mentioned ions, microscopic surface processes relevant for deposition and erosion of hydrocarbon layers in low-pressure gas discharges can be studied in great detail.

11.4 Results

11.4.1 Surface Loss Probabilities

The surface loss probability of a species of interest can be determined using the cavity technique as described in Sect. 11.3.1. So far, cavity probes have been applied in low-temperature plasma experiments in the laboratory and in the fusion experiments JET and ASDEX Upgrade.

Laboratory Experiments

Cavities were placed in electron cyclotron resonance discharges with hydrocarbon gases as precursors [30, 37, 38]. Three cavities were exposed simultaneously at three different remote positions: Cavity A close to the discharge with the slit pointing to the plasma, cavity B in A's direct vicinity, but with the slit pointing away from the plasma, and cavity C most distant with its slit towards the plasma. In all of these positions the ion flux is negligible due to confinement of the ions by the magnetic field of the ECR set-up. Experiments were performed with different hydrocarbon gases, namely CH_4, C_2H_2, C_2H_4, C_2H_6, C_3H_8, and C_4H_{10}.

Figure 11.6 shows the film thickness profiles of the exposed cavities. The data points denote the measured profiles and the solid lines the modeling results. When attempting to model the profiles it turns out that a single β is not sufficient to achieve reasonable agreement between data and simulation. On the other hand, it is even expected that not only one but a variety of radical species is present in a hydrocarbon discharge. Thus, if there is no mutual influence between the different species, the observed profile should be a superposition of single-β profiles.

This consideration is supported by a comparison of the profiles deposited from the same discharge but in different positions. The profiles differ significantly. An obvious difference is that the profiles in cavities B and C have more material deposited far away from the slit as compared to the center of the bottom substrate. As can be seen from Fig. 11.4, this would mean that – in terms of one single β – the surface loss probability changes with location and orientation of the probes. On the other hand, the total radical flux is most likely to consist of more than one species and it is reasonable to assume that they have different βs. Then the composition of the radical flux should depend on the location in the vacuum vessel due to different wall losses of the species given by their respective β: The more wall collision the particles experience on the average before they enter the slit of a cavity the more the flux of high β species will be suppressed compared to species with low β. This qualitatively explains the experimental results. The profiles are independent superpositions of the same set of single-β profiles. The different width of the central peak on the bottom substrate is caused by different angular distributions of the incoming radicals in the different positions. In our model calculation the angular distribution is assumed to be $\propto \cos^n \theta$, where n is used as fit parameter.

Another consideration concerns the profiles obtained for the different precursor gases. We expect the same radicals to be present in the plasmas of different gases. For example, C_2H_5 will certainly be produced in an ethane plasma by simple dissociation, but it will also be produced in a methane discharge due to various gas phase reactions. Therefore, it seems reasonable to model the profiles from all cavity positions and for all precursor gases with superpositions of one common set of single-β profiles. The question that arises

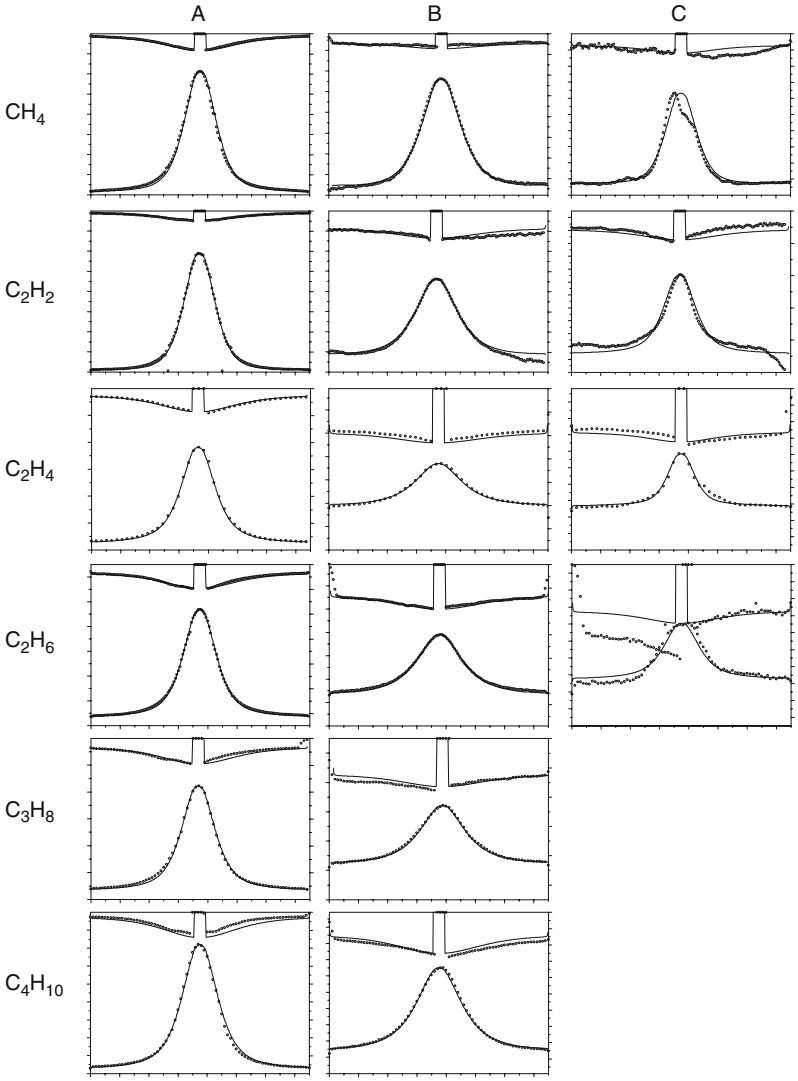

Fig. 11.6. Film thickness profiles of cavities exposed to plasmas of different precursor gases in three different positions in the vacuum vessel. The *dots* represent the measured profiles, the *solid lines* the calculated three-component fits. The profiles in each column are from the same position, the ones in a row are from the same precursor gas

is how many single-β profiles are needed. This question can be answered with singular value decomposition of the measured profiles, by asking how many independent measurements are hidden in the body of the measured profiles. The result is that three singular values are significantly different from zero,

i.e., superpositions of three single-β profiles are sufficient to model all experimental data [38].

The set of values of β leading to the best overall agreement is: $\beta_1 = 0.8$, $\beta_2 = 0.35$, and $\beta_3 < 10^{-2}$. For the calculation $\beta_3 < 10^{-3}$ was chosen, nevertheless the normalized profiles for all $\beta < 10^{-2}$ cannot be distinguished. Furthermore, one exception was made for the C_2H_2 profiles: $\beta_1' = 0.9$ was chosen because it improves the fit considerably in contrast to all other profiles, where $\beta_1 = 0.8$ leads to a better fit [38].

In order to relate the values to specific radicals additional information is required. Shiratani et al. [50] determined the surface loss probability of methyl radicals by measuring the time decay of the CH_3 signal of time-resolved ionization threshold mass spectrometry during the afterglow of a rf methane discharge. The value they found was $\beta(CH_3) \approx 10^{-3}$. Thus, we attribute β_3 to the CH_3 radical. Further information comes from mass spectra of the stable neutral species from discharges in our ECR set-up under conditions similar to those during the cavity experiments. In acetylene discharges C_2H_2 is clearly the most abundant stable species and hence C_2H is expected to be the most abundant radical. In the cavity experiments using acetylene, the component with $\beta_1' = 0.9$ dominates in cavity A and is still well visible in the more remote cavities B and C. It appears therefore plausible to assign C_2H to the highly reactive contribution with $\beta_1 = 0.8$ or $\beta_1' = 0.9$, respectively. A detailed discussion of the mass spectra and the corresponding cavity film thickness profiles can be found in [38]. An explanation of the different values for β_1 is also found in [38]. The additional assignment suggestions are that C_2H_3 contributes to $\beta_2 = 0.35$ and C_2H_5 to $\beta_3 \leq 10^{-2}$.

The question arises why there are only three discrete values of β although there are much more than just three radical species anticipated in the plasmas. The answer is twofold:

(i) Whereas $\beta_3 = 0.8$ or 0.9 is well determined by the experimental profiles and the uncertainty is only ± 0.05 the value $\beta_2 = 0.35 \pm 0.15$ is much less certain. It can, therefore, also be interpreted as a mean value for all species with medium surface loss probability. The value $\beta_3 \leq 10^{-2}$ is only an upper limit anyway, so some individual small values may contribute.

(ii) Still the important result so far is that the surface loss probabilities cover a range of at least two orders of magnitude and that there is a plausible assignment of the C_1H_x and C_2H_x radicals to the high, medium, and small β values. The physical cause of the large differences of the surface loss probability may be the different state of hybridization of the carbon in the radicals. The C_2H radical with its triple bond has more possible reaction pathways with the surface than radicals with double bonds or even radicals with single C–C bonds. Then the generalized assignment reads $\beta(sp^1) = 0.90 \pm 0.05$, $\beta(sp^2) = 0.35 \pm 0.15$, and $\beta(sp^3) \leq 10^{-2}$.

Cavity Probes in Fusion Devices

Two cavity probes were installed in the divertor of JET in the period from August 1999 till November 2001. One was installed below the septum and the other in the inner module of the divertor. The analysis of these cavities was published by M. Mayer in 2003 [51]. Thick deposits of up to 14 and 45 µm were found on the outside of the inner module and septum cavity, respectively. The corresponding maximum thicknesses inside the cavity at the position opposite to the entrance slit are 15 and 10 µm. Ion-beam analysis of the layers showed that they consist mainly of D and C with a D/C ratio of about 1. Interestingly, the morphology and density of the two samples is very different. While the layer from the inner module is smooth with a density typical of a–C:H layers, the one from the septum is very porous and has about half the density only. The reason for this obvious difference remains unclear. A fit of the deposition profiles in the cavities leads to the conclusion that the layers are mainly deposited from species with a high surface loss probability ($\beta \geq 0.9$) and a minor contribution of species with a low surface loss probability ($\beta < 10^{-2}$). New cavity probes were installed inside the JET divertor in November 2001. They are planed to be removed in 2004.

Cavity probes were also installed in ASDEX Upgrade, but yielded so far no evaluable results. In the first attempt in 2000, overheating caused a melting of the silicon wafer. For the second attempt, cavities were placed in a pump duct of ASDEX Upgrade from March to August 2001. The analysis of long term samples (plain silicon samples) exposed for the same period showed that the deposition in this region during this period was negligible [42]. However, in this case the pump duct itself can be considered as a cavity and the deposition pattern can be evaluated. Mayer et al. [8, 42] explained the observed deposition pattern by two radical species with surface loss probabilities $\beta \leq 10^{-3}$ and $0.1 \leq \beta \leq 0.9$. In the actual campaign four cavities are installed below the divertor of ASDEX Upgrade. They will be removed and evaluated in summer 2003.

11.4.2 Sticking Coefficient of CH_3 Radicals

It was emphasized in the previous sections that the cavity probe technique is sensitive to the surface loss probability of radicals rather than their sticking probability. The sticking probability is only accessible by experiments which allow to directly compare the rate of sticking to the flux of incoming species. The ability of the MAJESTIX experiment to perform such a task was described in Sect. 11.3.2. As a first example, we shall review our results on the sticking coefficient of methyl radicals on a–C:H surfaces.

A methyl radical flux of $j \sim 2 \times 10^{15}\,\mathrm{cm^{-2}s^{-1}}$ is directed to the surface of a pre-deposited a–C:D film. For film deposition, CD_4 was used as the plasma source gas instead of CH_4. Isotopic labelling of the substrate film is very advantageous for in-situ infrared spectroscopic measurements since it

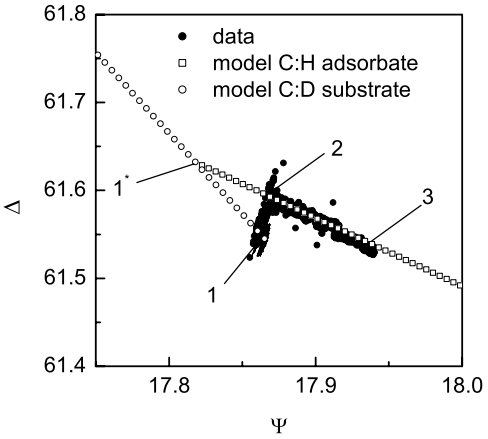

Fig. 11.7. Ellipsometric measurement during the interaction of CH_3 with an a–C:H surface at a temperature of 340 K. The CH_3 flux density is $j \sim 2 \times 10^{15}\,\mathrm{cm^{-2}s^{-1}}$

allows to distinguish between the substrate film and the layer that results from CH_3 adsorption [46]. High sensitivity is required in order to resolve monolayer changes within reasonable acquisition times (a few minutes). The a–C:D film was, therefore, deposited on a resonantly enhancing optical multilayer structure, a so-called optical cavity (for details, see [52]).

At a substrate temperature of 340 K, the adsorption of CH_3 is observed with ellipsometry. The change of the ellipsometric signal is depicted in Fig. 11.7. The points 1, 2, and 3 label consecutive stages in the evolution of the ellipsometry data points in the Ψ, Δ plane: point 1 represents the C:D layer at the beginning of the experiment. With the onset of the CH_3 flux, the ellipsometric angles shift at first to larger values of Ψ and Δ (point 1 to 2), followed by a shift to larger values of Ψ but smaller values of Δ (point 2 to 3).

This variation of the ellipsometric angles is compared with a two-layer optical model: the open squares correspond to a hard a–C:H film with refractive index $\hat{n} = 2.1 - i0.13$ and variable film thickness d. At point 1^*, the film thickness is $d = 31.62\,\mathrm{nm}$ while $d = 31.71\,\mathrm{nm}$ at point 1. A polymer-like film with refractive index $\hat{n} = 1.62 - i0$ on top of a 31.62 nm thick hard film is represented by open circles. In both model curves, film thickness increases by $\delta d = 0.01\,\mathrm{nm}$ between consecutive model points in the direction of decreasing values for Δ.

The measured shift of Ψ, Δ from point 1 to 2 in Fig. 11.7 can be understood by assuming that a surface layer of the hard C:D film (point 1^* to 1) is transformed into a polymer-like C:H:D film (point 1^* to 2) due to adsorption of CH_3 radicals at sp^2-coordinated carbon groups at the initial film surface: it is assumed, that this reaction is similar to the hydrogenation of sp^2 carbon groups by atomic hydrogen, which changes the hybridization of the sp^2 CC bond to sp^3 [53]. The extinction coefficient at 632.8 nm is related to the

concentration of sp^2-hybridized carbon atoms in the film [54]. A loss of these sp^2 groups via transformation into sp^3 groups becomes visible as a decrease of the extinction coefficient in the top-layer ($\kappa = 0.13$ changes to $\kappa = 0$). CH_3 adsorption at sp^2 CC groups at the surface also leads to a hydrogen rich surface layer with a lower density compared to that of the hard C:D substrate. This results in a decrease of the real part of the refractive index ($n = 2.1$ changes to $n = 1.62$) in the top layer. According to the optical models shown in Fig. 11.7, CH_3 adsorption at sp^2 CC groups occurs within a surface layer of 0.12 nm (point 1^* to 2 in Fig. 11.7). Consecutively, film growth proceeds in this case by formation of a polymer-like C:H film (point 2 to point 3 in Fig. 11.7). During steady state growth, CH_3 radicals chemisorb at dangling bonds. These dangling bonds in turn can be created by abstraction of surface-bonded hydrogen from the network (such that CH_3 impinges and a stable CH_4 molecule leaves the surface). Thus the sequence of chemisorption and hydrogen abstraction represents the steady state growth cycle.

The trajectory in the Ψ, Δ plane yields important structural information (via the optical constants). However, we need to evaluate the temporal information contained in the data in order to derive a sticking coefficient. Although not visible from the representation of Fig. 11.7, it shall suffice at this point to remark that along the way from point 2 to point 3, the evolution of data points reaches a steady-state growth rate. This growth rate can be converted into a number of carbon atoms incorporated from the gas phase, assuming the typical carbon atom density of polymer-like a–C:H films (see Sect. 11.2). As a result, this measurement yields a sticking coefficient in the range of 10^{-5}. It turns out that the angle of incidence has some impact on the numerical value: for CH_3 radicals impinging at 45°, a sticking coefficient of 10^{-4} was determined (see [44] and the remark in [9]). Nevertheless, the extremely low value of the sticking coefficient proves that CH_3 is by no means a reactive radical. (As we will show later, this statement needs not to be valid if additional species interact with the film surface at the same time.) This finding can be explained easily: if CH_3 is ineffective in abstracting surface-bonded hydrogen, then the creation of dangling bonds is the rate-limiting step. The cross-section for chemisorption of CH_3 at a dangling bond can be large (thus CH_3 being indeed 'reactive'), but still a small effective sticking coefficient results.

The experiment described above was performed at different temperatures. The resulting growth rates are summarized in Fig. 11.8. On the right vertical axis, the effective sticking coefficient is given. The surprising feature of this result is that in a certain temperature window (marked as region II) the observed growth rate is negative (expressed formally by a negative sticking coefficient). This means that CH_3, although usually considered as growth precursor, etches the film!

This finding can be explained by referring to the case of chemical erosion of hydrocarbon films by atomic hydrogen: the pioneering work of Küppers and co-workers [53] revealed that the elementary erosion reaction is not a direct

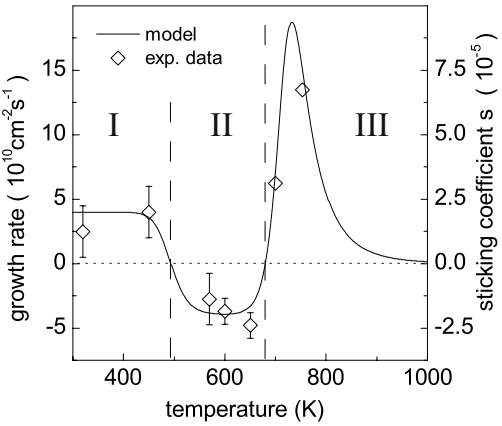

Fig. 11.8. Temperature-dependent sticking coefficient of CH_3 radicals at an a–C:H surface. The CH_3 flux density is $j \sim 2 \times 10^{15}\,\mathrm{cm}^{-2}\mathrm{s}^{-1}$. The absolute growth rate is given on the left vertical axis

abstraction of hydrocarbon groups by impinging atomic hydrogen. Rather, atomic hydrogen abstracts surface-bonded hydrogen, resulting in a surface dangling bond. At elevated temperatures, this dangling bond recombines via breaking of a neighboring CC bond and emission of a hydrocarbon radical. The latter process is visible as etching. Erosion of hydrocarbon films is, therefore, promoted by the existence of dangling bonds. Since dangling bonds can be created not only by atomic hydrogen, but also by methyl radicals, a chemical erosion process is superimposed on the process of film growth in our experiment. As the temperature is increased above $\sim 550\,\mathrm{K}$, erosion starts to dominate the net effect.

At even higher temperatures, the net growth rate (respectively, the effective sticking coefficient) becomes positive again. This effect is a consequence of spontaneous graphitization of the film: at sufficiently high temperatures, sp^3-hybridized carbon groups can spontaneously decompose to form sp^2-hybridized groups. For typical hard hydrocarbon films, this decomposition is accompanied by a loss of hydrogen from the film. The emission of hydrocarbon species during this process can be neglected. As a result of graphitization, sp^2 centers are formed at the surface. These are possible CH_3 chemisorption sites, as has already been discussed (Fig. 11.7). Summarizing, the interaction of the CH_3 beam with the surface leads to the formation of a graphitic adsorbate in this high temperature regime. The graphitic properties manifest themselves in two ways: first, a modeling of the ellipsometric measurements requires optical constants that are typical of a graphitic material. Second, the large number of sp^2 CH groups is visible by infrared spectroscopy: employing a beam of atomic deuterium, we were able to observe in real time the transformation of sp^2 CH groups into sp^3 CD groups as a result of a complete HD exchange.

The solid line in Fig. 11.8 results from a simple rate equation model which combines the above mentioned processes [46]. The model contains a number of microscopic parameters, most of which are known from other sources: the cross-section for chemisorption of CH_3 at a dangling bond can be estimated from our studies on synergistic growth with H and CH_3 (see next section!). The same value is assigned to the cross-section for chemisorption at a sp^2 site. The cross-section for hydrogen abstraction by CH_3 determines the CH_3 sticking rate at low temperatures (regime I). We find that it is of the order of 10^{-4} Å^2. The activation energy for the graphitization process is 2.4 eV, as is known from the literature. From chemical erosion with atomic hydrogen, the activation energy for the elementary erosion step (CH_3 emission) has been determined as $\sim$ 1.6 eV by Küppers. In our case, the location of the crossover between regime I and II requires a lower value of 1.25 eV (see [46] and the correction in [9]). This is attributed to the emission of hydrocarbon species larger than CH_3 and the fact that the formation enthalpy for such species is smaller. Indeed, Zecho et al. observed that during chemical erosion of C:H films by atomic hydrogen larger $C_{x>1}H_y$ species are formed at lower substrate temperatures compared to C_1H_y species [55]. The average length x of erosion products C_xH_y appears as a free fitting parameter in our model and determines the steady state erosion rate in the temperature regime II. A value of $x \sim 3.5$ describes our data best.

From the above findings and the proposed model, two important conclusions can be drawn. One concerns the temperature dependence of the deposition of C:H films from a methane plasma. Several models have been proposed to explain why deposition changes to erosion at elevated temperatures. Finally, von Keudell and Jacob gave a very simple explanation: they showed that the temperature-dependent deposition rate can be obtained by superimposing the temperature-dependent rate of chemical erosion by hydrogen and a temperature-independent gross deposition rate due to hydrocarbon particles [16]. Our results on the temperature-dependent sticking coefficient of CH_3 shed some new light on this discussion: it seems quite unnatural to treat the deposition of hydrocarbons as temperature independent and attribute the temperature dependence to the atomic hydrogen and hydrogen ions, respectively. We showed that it is really the stability of dangling bonds at the surface that decides whether the net effect is dominated by chemical erosion or by hydrocarbon chemisorption. In terms of elementary reactions, we explain our results by treating CH_3 equivalent to atomic hydrogen.

Another conclusion concerns the problem of re-deposition in remote areas of a fusion experiment. The important message of our findings is twofold: first, CH_3 is a fairly unreactive species at all temperatures. This is due to the fact that CH_3 has a very small cross-section for hydrogen abstraction, but dangling bonds are precursor states for deposition as well as erosion. There is no surface temperature (in the experimentally investigated range) which would allow for effective trapping of CH_3 radicals. On the other hand, deposi-

tion of CH_3 can be completely avoided at surface temperatures corresponding to regime II.

However, it has to be kept in mind that the rates for hydrogen abstraction as well as CH_3 chemisorption scale directly with the flux density of CH_3 radicals. In contrast, the rates for the elementary step of erosion as well as graphitization do not. As a result, the location of the temperature regimes described above will change with the CH_3 flux density. We can employ our model to extrapolate our laboratory findings to higher flux densities that are relevant for fusion devices. For example, for a CH_3 flux of $10^{18}\,\mathrm{cm^{-2}s^{-1}}$ the crossover between polymer-like film growth and erosion will occur at $\sim 600\,\mathrm{K}$ instead of $\sim 500\,\mathrm{K}$ [9].

11.4.3 Synergistic Interaction of CH_3 and Atomic Hydrogen

We let a beam of atomic hydrogen and a beam of methyl radicals interact with the film surface simultaneously. This can be considered the simplest of all multi-species experiments: first, H and CH_3 are the simplest radicalic hydrocarbon species. Second, by restricting ourselves to radicals, the interaction of the beams with the film is purely chemical and expected to be limited to the very surface. Third, the effect of each species separately is already known: the previous section described the temperature dependent interaction of CH_3 radicals with the a–C:H surface. The interaction of atomic hydrogen with carbonaceous materials has been studied extensively in the past by various groups [53, 56, 57]. A rate equation model describing chemical erosion by atomic hydrogen is well-established [53, 58].

Our experiment is performed near room temperature (340 K): as already described, at this low temperature the effective sticking coefficient of CH_3 is of the order of 10^{-5} to 10^{-4}, depending on the angle of incidence. Atomic hydrogen leads to chemical erosion of the film, although the erosion rate at this low temperature is quite small. Figure 11.9 shows what happens if both species impinge on the surface simultaneously. For a fixed CH_3 flux density of $5.5 \times 10^{14}\,\mathrm{cm^{-2}s^{-1}}$, the atomic hydrogen flux is varied in a broad range and the growth rate is measured after a steady state is reached. We express the steady state growth rate in terms of an effective CH_3 sticking coefficient, simply by dividing by the CH_3 flux density. In this experiment, the atomic hydrogen beam is directed parallel to the surface normal, CH_3 radicals impinge upon the surface at an angle of 45°.

The data show clearly that the effective sticking coefficient of CH_3 depends strongly on the presence of atomic hydrogen. It can be increased by about two orders of magnitude if the atomic hydrogen flux is sufficiently high. Given the knowledge about the effect of each particle beam separately, this finding proves that the simultaneous interaction of both species with the surface does not result in a sum effect. Rather, a true synergistic effect is established.

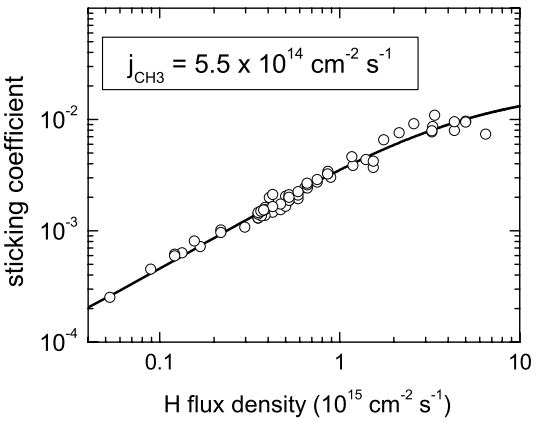

Fig. 11.9. Synergistic growth rate during interaction of an a–C:H film surface with a beam of CH_3 radicals (constant flux density) and a varying flux density of atomic hydrogen. The *open circles* represent the data points, the *solid line* is the result of the extended model (see text)

The main idea explaining this synergistic effect has been formulated already in our first article on this topic [59, 60]: the measured growth rate is a sum of the quite small chemical erosion rate and the CH_3 chemisorption rate. Both processes are proportional to the coverage of the surface with dangling bonds ($0 < \Theta_{\mathrm{db}} < 1$). In addition, the chemical erosion rate is also proportional to a temperature-dependent rate constant (which is small at this low surface temperature), whereas the CH_3 chemisorption rate is proportional to the product of the methyl flux density and the cross-section for CH_3 chemisorption. The decisive quantity is the number of dangling bonds at the surface. This number results from a balance of hydrogen abstraction and chemisorption events. If only CH_3 radicals are present, this balance is determined by the cross-sections for chemisorption of CH_3 and hydrogen abstraction by CH_3. Adding an abundant flux of atomic hydrogen, it is the corresponding cross-sections of hydrogen that determines the steady state dangling bond coverage. The synergistic growth effect is, therefore, explained by the abstraction cross-section of atomic hydrogen (about $0.05\,\text{Å}^2$ [53]) being much larger than that of CH_3 ($10^{-4}\,\text{Å}^2$, see Sect. 11.4.2).

This simple model grasps the main aspect causing the synergistic interaction between CH_3 and H. However, it fails in describing our experimental data in two ways: first, the flux dependence can be reproduced only poorly and is underestimated [45]. Second, the above model is not able to explain transient effects that can be observed upon switching on or off one of the two particle fluxes. Figure 11.10 shows the time-resolved growth rate in an experiment, where at time $t = 0$ a methyl flux of $j_{\mathrm{C}} = 2.0 \times 10^{15}\,\mathrm{cm^{-2}s^{-1}}$ is switched on in addition to an atomic hydrogen flux of $j_{\mathrm{H}} = 9 \times 10^{14}\,\mathrm{cm^{-2}s^{-1}}$ which is present all the time.

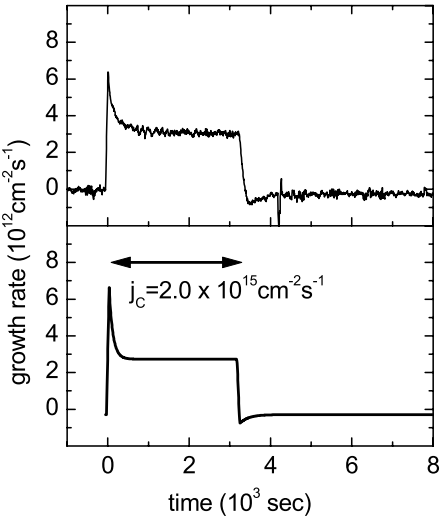

Fig. 11.10. Time-resolved growth rate in an experiment where at $t = 0$ a flux $j_C = 2.0 \times 10^{15}\,\mathrm{cm}^{-2}\mathrm{s}^{-1}$ of CH_3 is added to a permanent flux $j_H = 9 \times 10^{14}\,\mathrm{cm}^{-2}\mathrm{s}^{-1}$ of atomic hydrogen. At $t \sim 3200\,\mathrm{s}$, the CH_3 beam is switched off again. The upper panel shows the measurement. The lower panel shows the result of a model simulation (referred to as the extended model in the text)

The growth rate almost instantaneously rises to a value of above $6 \times 10^{12}\,\mathrm{cm}^{-2}\mathrm{s}^{-1}$ and then decreases to a lower steady state value of roughly $3 \times 10^{12}\,\mathrm{cm}^{-2}\mathrm{s}^{-1}$. Qualitatively, such a behavior can be expected in the framework of the simple model: the high number of dangling bonds as determined by the atomic hydrogen flux leads to a large CH_3 chemisorption rate at the instant the CH_3 flux is switched on. The number of dangling bonds is lower in steady state, consequently the measured growth rate. However, according to this simple model, the steady state should be reached within a time scale given by the CH_3 flux density and the CH_3 chemisorption cross-section. It turns out that this time scale is seconds, i.e., below the time resolution of the measurement. The time scale of the observed transient is much larger; it is of the order of 10^2 seconds. The simple model, therefore, fails in explaining the observed dynamical behavior. It further fails in explaining the existence of a negative spike which is observed after the CH_3 beam is switched off at $t = 3.2 \times 10^2\,\mathrm{s}$: the growth rate passes a minimum (the erosion rate passes a maximum), before a small steady state erosion rate is established due to the presence of the atomic hydrogen beam.

We are led to the conclusion that it is not sufficient to consider only dangling bonds (i.e., chemisorption sites) and hydrogen-terminated surface sites. An extended model is proposed which is described in detail in [28, 45]. We merely summarize the main aspects here: the incorporation of the impinging

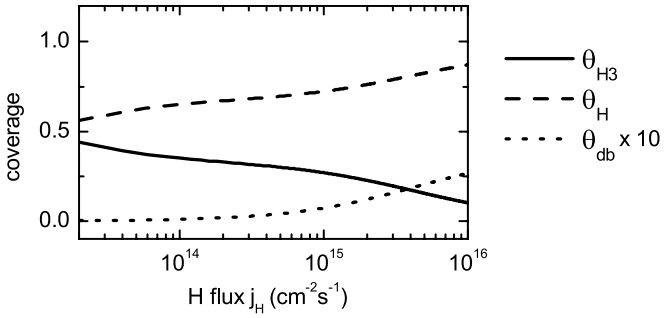

Fig. 11.11. Surface coverage with dangling bonds (Θ_{db}), hydrogen-terminated (cross linked) sites (Θ_{H}) and methyl-terminated sites (Θ_{H3}) as a function of the atomic hydrogen flux density

CH_3 radicals into the film network is described as a two-step process. First, CH_3 chemisorbs at a dangling bond. In a second step, dangling bonds created at neighboring methyl groups recombine with each other, i.e., cross linking occurs. One consequence of this cross-linking step is that it results in a lower hydrogen content in the film than the simple reaction scheme would predict: the sequence of hydrogen abstraction and CH_3 chemisorption would lead to a film stoichiometry of H:C=2:1. Such a high hydrogen content is, however, very untypical of a–C:H films. In contrast, the postulated process of cross-linking leads to the loss of one hydrogen atom per carbon atom. The other consequence of the extended model is that it allows to reproduce the growth rate data presented above.

Mathematically, the number of dangling bonds at the surface (coverage Θ_{db}), the number of hydrogen-terminated sites (coverage Θ_{H}), and the number of CH_3-terminated sites (coverage Θ_{H3}) are each described by a rate equation. This rate equation system can be solved either for steady state conditions or it can be integrated to yield time-dependent surface coverages. These coverages then determine the reactivity of the surface towards chemisorption or erosion. The solid line in Fig. 11.9 results from this extended model for steady state conditions. Apparently, the hydrogen flux dependence of the synergistic growth effect can be described very well, provided suitable values are assigned to the elementary reaction cross-sections. The saturation value for the CH_3 sticking coefficient resulting from the extended model for very high hydrogen fluxes is about 4×10^{-2}.

In Fig. 11.11, model results of the surface coverages Θ_{db}, Θ_{H} and Θ_{H3} are shown as a function of the atomic hydrogen flux density. The important point here is that a substantial fraction of the surface is dynamically covered with methyl groups (Θ_{H3}). In the framework of our model, these need to be cross linked with each other before they can be activated for further chemisorption events. Not visible from the logarithmic scaling is the fact that at zero hydrogen flux, Θ_{H3} is equal to one. It is this dynamical surface cov-

erage with methyl groups which causes the transient behavior of the growth rate shown in Fig. 11.10. The model calculation shown in the lower panel demonstrates that the model does indeed reproduce the ellipsometric measurement in the upper panel. The mechanism is as follows: at the instant the CH_3 flux is switched on the atomic hydrogen flux maintains a large number of dangling bonds at the surface (in this example, $\Theta_{\mathrm{db}} \approx 5\%$). Corresponding to this large dangling bond coverage, the initial CH_3 chemisorption rate is very large. Within a few seconds, Θ_{db} drops substantially (to $\Theta_{\mathrm{db}} \approx 0.5\%$) because the flux of CH_3 radicals saturates most dangling bonds and a new chemisorption/hydrogen-abstraction balance is established. Als already mentioned, this effect is too fast to be observed and this first initial spike is also not visible in the model calculation, because we applied some smoothing corresponding to the experimental time resolution. However, as CH_3 chemisorption proceeds, a surface coverage of CH_3 groups develops at the surface until a steady state value of $\Theta_{\mathrm{db}} \approx 50\%$ is reached. The model requires these methyl groups to get cross linked first. Consequently, the effective area that can be activated for further CH_3 chemisorption decreases correspondingly. This causes the slow decrease of the growth rate following the onset of the CH_3 beam.

The negative spike following the switching off of the CH_3 beam is explained by the model in the following way: the elementary process of chemical erosion is the recombination of a dangling bond via emission of a neighboring CH_3 end group. The formation of the end group is not explicitly described. Instead, this precursor formation rate is subsumed by the rate for the erosion process itself. However, chemisorption of CH_3 means that such precursors are formed directly. The model, therefore, describes erosion of bulk material separately from emission of previously chemisorbed methyl groups. The latter process is responsible for the initial etching spike following the switching off of the CH_3 beam: an increased etching rate is observed until the surface is emptied from methyl groups. We only mention at this point that the surface is depleted from methyl groups not only by erosion, but also by cross linking. Meier and von Keudell [45] report on the direct observation of the cross linking process by infrared spectroscopy.

The main conclusions that can be drawn from our studies on CH_3/H interaction with the film surface are the following: first, film growth is a two-step process in the sense that CH_3 radicals need to chemisorb and subsequently the methyl groups need to be cross linked with each other. Second, by virtue of its comparatively pronounced ability to create dangling bonds by hydrogen abstraction, both steps are very effectively triggered by the presence of atomic hydrogen. Third, although the true microscopic processes might be very complicated, it is remarkable that all experimental observations can be sufficiently described by a simple model. This model considers only three different types of surface coverages and relates them to a linear(!) rate equation system containing a rather limited number of (only seven) elementary reactions.

Apart from revealing the important microscopic processes, this model has another benefit: it allows to determine the corresponding cross-sections given

the fact that our particle beams are absolutely quantified and also the ellipsometric measurements yield an absolute growth rate. A parameter estimation procedure employing Bayesian probability theory was performed [61]. An important outcome of this analysis is that the probability for chemisorption of CH_3 at a dangling bond is of the order of one. It decreases to some extent with an increasing methyl surface coverage. This can be interpreted as a shielding effect of CH_3 groups on surface dangling bonds. Both findings correspond very well with results from molecular dynamics calculations performed by Träskelin et al. [62].

11.4.4 Chemical Sputtering

Thermally-activated chemical erosion of carbon due to atomic hydrogen is a well understood process [53, 58]. It leads to significant erosion rates above $\sim 400\,\mathrm{K}$ with a maximum at around 650 K. However, it has been observed that erosion by energetic hydrogen ions instead of thermal hydrogen atoms yields much higher erosion rates [63, 64]. At energies exceeding $\sim 200\,\mathrm{eV}$ the observed rates can be explained by physical sputtering. From an analytical description of the sputtering yield – the revised Bohdansky formula [65] – a maximum of the yield around 500 eV energy and a threshold energy of $\sim 40\,\mathrm{eV}$ are expected [66]. In contrast, experiments performed at room temperature show a constant erosion yield down to H^+ energies of 15 eV [64, 66]; i.e., significant erosion is observed in a temperature and energy regime where neither thermal chemical erosion nor physical sputtering provides an explanation. Due to the fact that obviously the energy of the ions as well as their chemical reactivity plays a role the phenomenon is frequently referred to as 'chemical sputtering'. The microscopic mechanism, however, remained unclear.

Roth and García-Rosales [66] suggested an analytical description of the erosion of graphite by hydrogen ions. They explain the low-temperature low-energy erosion by what they term 'kinetic hydrocarbon emission': The slowed down hydrogen ions react with the carbon to form weakly bound hydrocarbon groups at the surface. These hydrocarbons are subsequently sputtered by the incoming ions, and this process is possible at energies below the expected threshold energy of physical sputtering, since the surface binding energy of these surface groups is only $\sim 1\,\mathrm{eV}$.

Experiments solely using hydrogen ions have the disadvantage that the only incident species reacts both chemically and physically. Thus not only the yields of kinematic interactions such as displacement and physical sputtering change with energy, but also the depth distribution of the chemically reactive species. This leads to energy dependences which are difficult to interpret, such as the almost constant yield at low energies mentioned above. Experiments in which hydrogen ions and atomic hydrogen interact simultaneously with the sample partly circumvent the problem [67, 68]. In those experiments, performed at temperatures $> 500\,\mathrm{K}$, a substantial increase of the erosion yield was found compared to erosion by thermal H alone, even though the

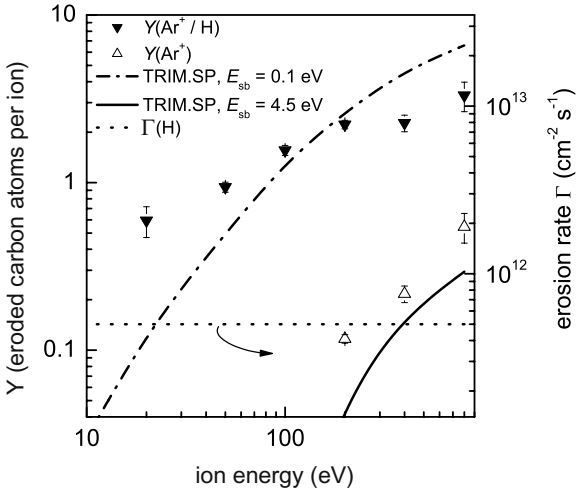

Fig. 11.12. Energy dependence of the erosion yield $Y(Ar^+)$ of physical sputtering of a C:H film by Ar^+ ions (*open symbols*) and the yield $Y(Ar^+|H)$ for chemical sputtering by a simultaneous flux of Ar^+ ions and H atoms (*full symbols*). The *dash-dotted* and *solid lines* are carbon erosion yields from TRIM.SP calculations for the sputtering of carbon by argon ions using a carbon-surface-binding energy of $E_{sb} = 0.1\,eV$ and of $E_{sb} = 4.5\,eV$, respectively. The *dotted line* gives the absolute erosion rate by the applied flux of H atoms only

ion flux was by roughly an order of magnitude smaller than that of thermal H. Unreactive Ar^+ ions were used by Vietzke et al. [69] in combination with H at ion energies of 500 eV and 5 keV. At room temperature they found an increase by about a factor of 10 of the desorbing flux of species with masses 15, 16, and 26 in the case of ion bombardment. Whereas experiments using hydrogen ions are found in the literature down to energies of 10 eV [70], data from experiments with non-reactive ions plus thermal H have until lately only been available at energies above 500 eV [69, 71, 72].

Recently Hopf et al. [48, 73] investigated erosion of amorphous hydrogenated carbon (a–C:H) films due to combined noble gas ion (Ar^+) and thermal atomic hydrogen atom impact in the low-temperature low-energy regime. A hard a–C:H film was exposed to either one of the beams alone or to the combined Ar^+ ion and H atom beams. The resulting erosion rates were measured in situ by real-time ellipsometry. The corresponding erosion yields were calculated by normalizing the measured rates to the ion flux density which was between 3×10^{12} and $4 \times 10^{12}\,cm^{-2}\,s^{-1}$. The hydrogen atom flux was $\sim 1.4 \times 10^{15}\,cm^{-2}\,s^{-1}$.

Figure 11.12 shows the erosion yield as a function of ion energy. As all experiments involving ions were performed at approximately constant ion flux density the yields on the left-hand scale correspond roughly to the rates given on the right-hand scale. The open symbols show erosion by ions only. Physical

sputtering is observed at energies of 200 eV and above. Below these energies the resulting rates are too low to be reliably detected in the experiment. For comparison Monte Carlo calculations were performed with the computer code TRIM.SP [74] for a C:H film with an H/(H+C) ratio of 0.3. As surface binding energy $E_{\mathrm{sb}} = 4.5\,\mathrm{eV}$ [75–77] was chosen. The result is shown as solid line; it agrees with the measured yields within a factor of two and reproduces well the energy dependence.

The erosion rate (right-hand scale) caused by the atomic hydrogen beam alone is shown as dotted line in Fig. 11.12. It is small at the substrate temperature of $T = 340\,\mathrm{K}$.

If, however, both beams simultaneously interact with the film the resulting erosion rate exceeds largely the sum of physical sputtering and thermal chemical erosion; clearly a new synergistic mechanism is active. This general result resembles the findings in the erosion experiments mentioned above. The new aspect of the experiment is that due to the separation between reactive ions and a larger flux of thermal H in the low-energy low-T regime a clear decrease of the yield with decreasing ion energy is observed.

If kinetic hydrocarbon emission as described above is the correct microscopic picture of this synergistic erosion, then the energy dependent yield should also be reproduced by TRIM.SP calculations. According to the model, only the carbon surface binding energy should have to be reduced. The dash-dotted line in Fig. 11.12 shows the result of such a calculation. In order to model a yield of the order of that in the experiment around 100 eV an extremely low value of $E_{\mathrm{sb}} = 0.1\,\mathrm{eV}$ has to be chosen. It is unreasonable to assume such a low surface binding energy because the species would thermally desorb from the surface at 340 K even without any ion bombardment. Furthermore, the energy dependence in the calculation is much stronger than in the experiment. Consequently, kinetic hydrocarbon emission has to be rejected as explanation.

A different system in which a synergistic ion–neutral erosion is known is the etching of silicon by fluorine and energetic species [78]. It is known [79] that without ion bombardment a SiF_x layer with a thickness of a few monolayers is formed at the surface; the erosion rate, however, remains small. Tu et al. [80] suggested that ion bombardment causes chemical reactions in the SiF_x layer which leads to the creation of volatile species. Based on a large number of experimental investigations Winters and Coburn [81] concluded, that this mechanism is the most likely explanation for the synergistic erosion. They define *chemical sputtering* as "a process whereby ion bombardment causes or allows a chemical reaction to occur which produces a particle that is weakly bound to the surface and hence easily desorbed into the gas phase". The major difference between this mechanism and kinetic hydrocarbon emission is that here the main effect of ion bombardment is to promote the chemical reaction, not to cause desorption. The latter will mostly occur thermally driven.

Based on this definition by Winters and Coburn [81] we propose the following mechanism for the chemical sputtering of a–C:H: (i) The incident ions

break C–C bonds within their penetration range leaving behind dangling bonds. (ii) The atomic hydrogen, which is known to penetrate roughly 2 nm into a–C:H [16,82], passivates the dangling bonds before they recombine otherwise. (iii) By repeating steps (i) and (ii) finally volatile hydrocarbons are formed below the surface which diffuse to the surface and desorb. The latter process is thermally driven.

The proposed mechanism is able to explain a couple of findings in the literature. It predicts that mainly passivated hydrocarbons, not radicals, should be found as erosion products. Vietzke et al. [71] indeed found that for erosion of graphite by 5 keV Ar^+ and thermal hydrogen the desorbing CH_4 flux is below 300 K higher than the CH_3 flux as opposed to higher temperatures where the CH_3 flux is higher. Furthermore, Vietzke [72] found that the energy distribution of the erosion products in the case of graphite erosion by 3 keV Ne^+ and thermal H at room temperature can be explained by a superposition of two Maxwellian distributions corresponding to 285 K and 1150 K. In case of a process, where the final desorption process is a physical sputtering process the mean energy of the sputtered particles is expected to be approximately equal to the surface binding energy. Thus, a surface binding energy of ~ 0.1 eV would be expected; this is, as already discussed, a completely unreasonable assumption. In contrast, the proposed chemical sputtering scheme predicts an energy distribution according to the specimen temperature, as diffusion and desorption proceed thermally activated. The 1150 K part of the energy distribution could be caused by some local heating of the film through ion impact which facilitates out-diffusion. Finally, in experiments with pulsed ion beams and continuous H flux [72] a time delay was detected between the ion impact and the desorption of the erosion products. In the frame of the proposed mechanism this time delay is simply the time needed for diffusion out of the film.

Based on this chemical sputtering mechanism we can calculate the expected energy dependence of the Ar^+/H experiment in Fig. 11.12 (open symbols). We assume that the yield of chemical sputtering is the integral over two depth dependent factors: (i) the yield $y_{\mathrm{bb}}(x)\mathrm{d}x$ at which ions break C–C bonds in an interval $\mathrm{d}x$ at a depth x below the surface and (ii) the probability $p_{\mathrm{pass}}(x)$ of the passivation of dangling bonds by atomic hydrogen. The latter reflects mainly the range distribution of hydrogen. We assume $p_{\mathrm{pass}}(x) = \exp(-x/\lambda)$ with $\lambda = 0.4$ nm which yields a maximum range of ~ 2 nm like experimentally found [16, 82]. To gain $y_{\mathrm{bb}}\mathrm{d}x$ we assume that bond breaking events are mainly caused by displacement of carbon atoms in the film. The corresponding yield $y_{\mathrm{dp}}^{\mathrm{C}}$ is calculated by TRIM.SP with a carbon displacement energy $E_{\mathrm{dp}}^{\mathrm{C}} = 5$ eV, which is a typical value of a carbon binding energy in hydrocarbons. Altogether we obtain

$$Y = a \int y_{\mathrm{dp}}^{\mathrm{C}}(x) \exp(-x/\lambda)\mathrm{d}x, \tag{11.4}$$

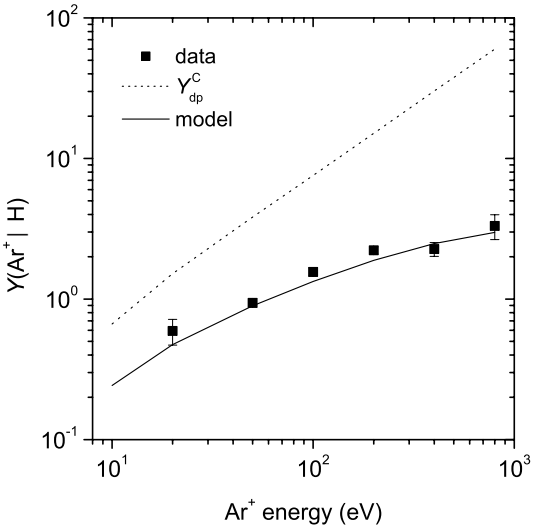

Fig. 11.13. Erosion yield $Y(Ar^+ |H)$ due to simultaneous exposure to Ar^+ ions and atomic hydrogen (*solid squares*) as a function of ion energy. The data are compared with a model according to (11.4) (*solid line*). For comparison, the *dotted line* denotes the total number of displaced carbon atoms per incident ion

where a is a scaling factor. Figure 11.13 shows a comparison between the yield calculated with $a = 0.4$ and the experimental data already shown as open symbols in Fig. 11.12. Obviously the agreement is very satisfying.

As the ion mass enters the calculated yield via the TRIM.SP calculation of $y^C_{dp}(x)$ (11.4) also allows to make predictions for other than Ar^+ ions. Figure 11.14 shows calculations for H_2^+, He^+, Ne^+, N_2^+, and Ar^+ ions together with the measured data for Ar^+ and H_2^+. For the case of molecular ions (H_2^+ and N_2^+) the calculations were done for twice the flux of atomic ions at half the energy (assuming disintegration upon impact). Due to the similar masses of nitrogen and carbon atoms a high fraction of the kinetic energy can be transferred in a collision between the two (≤ 0.994). Therefore, among the ion species in Fig. 11.14, the displacement yield and thus the chemical sputtering yield is expected to be highest for nitrogen ions. For higher or lower masses it becomes smaller again. The calculations also show a high chemical sputtering yield for Ne^+ ions. In Fig. 11.15 the model results for the species most relevant for a fusion device, namely H^+, D^+, T^+, and He^+ are shown. With increasing mass of the projectile, the chemical sputtering yield increases. The significant increase of the yield between T and He is due to the dependence of the nuclear scattering cross-section on the nuclear charge Z. The much higher calculated chemical sputtering yield of Ne compared with D (compare Figs. 11.14 and 11.15) is in accord with the observation by Wampler et al. [83] that detachment by injection of neon in DIII-D leads to a much stronger carbon erosion in the divertor as compared with deuterium.

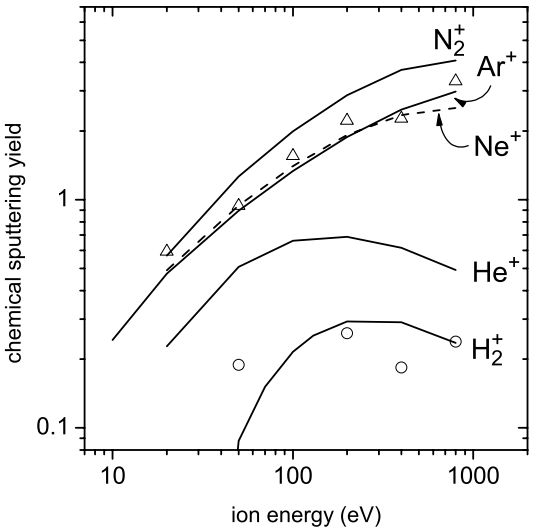

Fig. 11.14. Calculated chemical sputtering yields according to (11.4) assuming $a = 0.4$ (*solid lines*) for a variety of ion species. The measured yields for H_2^+ (*circles*) and Ar^+ (*triangles*) are also shown

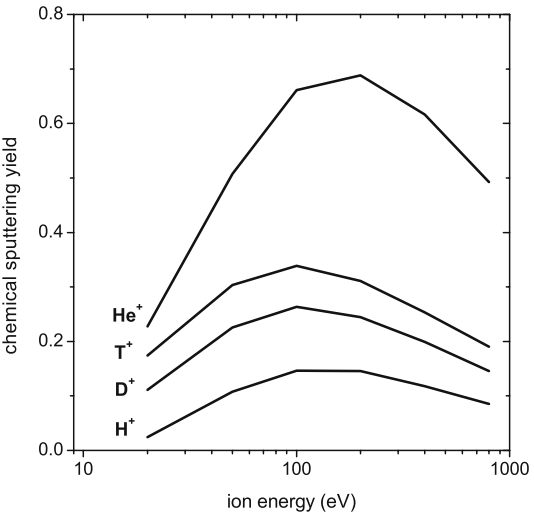

Fig. 11.15. Calculated chemical sputtering yields according to (11.4) ($a = 0.4$) for H^+, D^+, T^+, and He^+. The significant increase of the yield between T and He is due to the dependence of the nuclear scattering cross-section on the nuclear charge Z

Nitrogen injection into the divertor plasma of fusion machines has recently attracted some interest. First experiments in methane/hydrogen plasmas suggest that re-deposition of carbon might be completely suppressed [84]. The effect of this so-called 'scavenger technique' was attributed to gas phase reactions between nitrogen and hydrocarbon radicals which lead to a substantial reduction of the concentration of reactive hydrocarbons. However, another plausible explanation is that the higher chemical sputtering yield of nitrogen ions turns former deposition-dominated into erosion-dominated wall areas. Experiments to clarify this question are under way.

The proposed mechanistic model of chemical sputtering implies that there also exists a threshold energy. In the picture that (11.4) was based upon the threshold energy is given by the minimum energy required to transfer more than the displacement energy to the target carbon atoms. For $E_{\mathrm{dp}}^{\mathrm{C}} = 5\,\mathrm{eV}$ the threshold energy for Ar^+ ions would be expected to be $E_{\mathrm{th}}^{\mathrm{Ar}} = 7.0\,\mathrm{eV}$ and for H^+ $E_{\mathrm{th}}^{\mathrm{H}} = 17.6\,\mathrm{eV}$. However, it is to be expected that the displacement depends on the local binding structure; there will be a distribution of displacement energies rather than a fixed value. Therefore, the effective threshold energy should be somewhat lower than the values given above. Furthermore, molecular dynamics simulations [85] by Salonen et al. of the interaction of low-energy hydrogen ions showed that bond breaking does not necessarily require displacement. Bonds can also be broken if a hydrogen atom moves through the space between the two carbon atoms. Such events were found down to hydrogen energies of $\sim 1\,\mathrm{eV}$.

11.4.5 Ion-Induced Deposition

As was discussed in Sect. 11.4.3, the sticking coefficient of low-reactive radicals – in our example that of CH_3 – depends strongly on the surface condition. It can be increased by an additional flux of atomic hydrogen to the surface as H establishes a higher concentration of surface dangling bonds. Existing dangling bonds are the necessary prerequisite for chemisorption of CH_3. It was postulated [15, 86] that ion bombardment has the same effect because sputtering and displacement events leave behind dangling bonds. Indirectly the expected increase of the growth rate was observed in rf triode discharges for film deposition from tetramethylsilane [87] as well as for film deposition from fluorocarbon precursors [88].

To explicitly demonstrate ion-enhanced growth we simultaneously directed beams of methyl radicals and ions onto the sample a–C:H film [47, 89, 90]. Figure 11.16 shows the growth rate in the experiment with He^+ and H_2^+ ions, respectively, as a function of the ion energy. The He^+ flux density was $\sim 2 \times 10^{13}\,\mathrm{cm^{-2}\,s^{-1}}$, that of the H_2^+ ions was between $5 \times 10^{12}\,\mathrm{cm^{-2}\,s^{-1}}$ and $1.2 \times 10^{13}\,\mathrm{cm^{-2}\,s^{-1}}$. The methyl flux was constant at $2.2 \times 10^{14}\,\mathrm{cm^{-2}\,s^{-1}}$; therefore, we can convert the growth rate to the sticking coefficient which is given on the right-hand side. Additionally shown in Fig. 11.16 are the sticking coefficient of CH_3 alone (dotted line) and that of CH_3 combined with

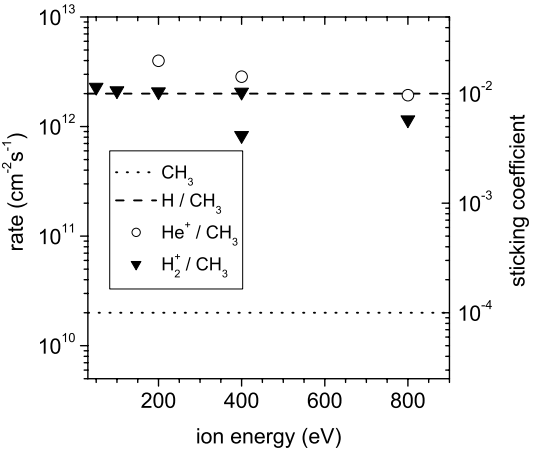

Fig. 11.16. Growth rate and sticking coefficient of CH_3 measured in experiments with different combinations of particle beams

$1.4 \times 10^{15}\,\mathrm{cm}^{-2}\,\mathrm{s}^{-1}$ of atomic hydrogen. Obviously the enhancement of the sticking coefficient due to ion bombardment and due to atomic hydrogen is of the same order of magnitude under our experimental conditions. The general trend of the growth rate to decrease with increasing energy (best visible in the He^+ experiments because all data points were recorded at the same ion flux) is a consequence of the decreasing energy deposition within the first mono-layers of the film as the ion penetration range increases. The effect can be quantitatively understood on the basis of TRIM.SP computer simulations [47]. The important action of the ion bombardment is the displacement of bonded hydrogen thus creating dangling bonds to which incoming CH_3 radicals can chemisorb. Consequently, we can anticipate a strong dependence on the mass ratio between the target atom (in this case hydrogen) and the impinging projectile. Light projectiles are best suited to displace hydrogen. Heavier projectiles displace increasingly more carbon atoms thus contributing to physical and chemical erosion which may counterbalance the growth due to chemisorption of CH_3.

Regarding the practical relevance of this process additional considerations are of importance: (i) As we have discussed in Sect. 11.4.1 the reactivity of hydrocarbon radicals – expressed in terms of their surface loss probability β – covers a wide range from $\sim 10^{-4}$ to close to unity. Although a high β does not necessarily mean a high sticking coefficient, we can assume that both quantities will be of the same order. Consequently, there are radicals which don't need activated surfaces to chemisorb. Ion bombardment is, however, only of major relevance for radical species with a low sticking coefficient. (ii) In typical technical deposition plasmas and fusion plasmas alike there are never only ions and carbon carrying radicals incident on the surface, but also atomic hydrogen. Thus, as a counteracting process also chemical sputtering

occurs. Depending on the flux ratios of the participating species and the ion energy the net effect may either be growth or erosion. Experiments applying three particle beams simultaneously to investigate the flux dependence of the growth/erosion rates are currently under way and will be published soon [90].

11.5 Conclusions

Two different experimental approaches to study surface reactions relevant to plasma–surface interaction processes in the system hydrogen and carbon were described. The first approach comprises investigations towards deposition and erosion of a–C:H layers in low-temperature laboratory plasmas. For this case, the surface loss probability of hydrocarbon radicals was determined applying the cavity technique. The second class of experiments was carried out in an UHV-based system working with well-defined, quantified particle beams. The MAJESTIX experiment at IPP Garching is capable of delivering three independently controllable, quantified particle beams. The available species are neutral atomic hydrogen, neutral methyl radicals, and one species of low energy ions (here we used Ar^+, He^+, and H_2^+).

The results regarding the determination of surface loss probabilities of various hydrocarbon radicals can be summarized as follows: The surface loss probabilities cover a range of at least two orders of magnitude. It is suggested that the reason for the large differences of the surface loss probabilities is the different state of hybridization of the carbon in the radicals. The C_2H radical with its triple bond has more possible reaction pathways with the surface than radicals with double bonds or even radicals with single C–C bonds. Consequently, the generalized assignment reads $\beta(\mathrm{sp}^1) = 0.90 \pm 0.05$ (C_2H), $\beta(\mathrm{sp}^2) = 0.35 \pm 0.15$ (C_2H_3), and $\beta(\mathrm{sp}^3) \leq 10^{-2}$ (CH_3, C_2H_5).

Microscopic surface reactions of atomic H, CH_3, and low energy ions were investigated quantitatively. The sticking coefficient of CH_3 alone on a C:H surface is of the order of 10^{-5} to 10^{-4} ($T = 340\,\mathrm{K}$). It is temperature and impact angle dependent. If atomic hydrogen and CH_3 interact simultaneously with a C:H surface, the sticking coefficient increases up to 10^{-2} depending on the H flux. Similarly to this enhancement of the sticking coefficient due to atomic H, the sticking of CH_3 can also be increased to about 10^{-2} by simultaneous bombardment of the surface with low energy ions (ion-induced deposition). Of significant importance for the erosion of plasma-facing components of fusion devices is the process of *chemical sputtering*. The simultaneous interaction of low-energy ions and atomic hydrogen causes erosion of C:H surfaces which is significantly higher than the sum of chemical erosion due to atomic hydrogen alone and physical sputtering due to ions. And above that, this process occurs also at energies below the threshold for physical sputtering. A microscopic model for the chemical sputtering mechanism was suggested which allows a quantitative description.

References

1. G. Federici, C.H. Skinner, J.N. Brooks, J.P. Coad, C. Grisolia, A.A. Haasz, A. Hassanein, V. Philipps, C.S. Pitcher, J. Roth, W.R. Wampler, D.G. Whyte: Plasma-material interactions in current tokamaks and their implications for next step fusion reactors. Nucl. Fusion **41**, 1967 (2001)
2. G. Federici, C.H. Skinner: this volume
3. P. Andrew, D. Brennan, J.P. Coad, J. Ehrenberg, M. Gadeberg, A. Gibson, M. Groth, J. How, O.N. Jarvis, H. Jensen, R. Lässer, F. Marcus, R. Monk, P. Morgan, J. Orchard, A. Peacock, R. Pearce, M. Pick, A. Rossi, B. Schunke, M. Stamp, M. von Hellermann, D.L. Hillis, J. Horgan: Tritium recycling and retention in JET. J. Nucl. Mater. **266-269**, 153 (1999)
4. J.P. Coad, N. Bekris, J.D. Elder, S.K. Erents, D.E. Hole, K.D. Lawson, G.F. Matthews, R.D. Penzhorn, P.C. Stangeby: Erosion/deposition issues at JET. J. Nucl. Mater. **290-293**, 224 (2001)
5. M. Mayer, V. Phillips, P. Wienhold, H.G. Esser, J. von Seggern, M. Rubel: Hydrogen inventories in nuclear fusion devices. J. Nucl. Mater. **290-293**, 381 (2001)
6. V. Rohde, H. Maier, K. Krieger, R. Neu, J. Perchermaier, and ASDEX Upgrade Team. Carbon layers in the divertor of ASDEX Upgrade. J. Nucl. Mater **290-293**, 317 (2001)
7. V. Rohde, M. Mayer, and the ASDEX Upgrade Team: On the formation of a–C:D layers and parasitic plasmas underneath the roof baffle of the ASDEX Upgrade divertor. J. Nucl. Mater **313-316**, 337 (2003)
8. V. Rohde, M. Mayer, and the ASDEX Upgrade Team: Characterisation and formation of a–C:D layers below the divertor of ASDEX Upgrade. Physica Scripta **T103**, 25 (2003)
9. M. Meier, A. von Keudell, W. Jacob: Consequences of the temperature- and flux-dependent sticking coefficient of methyl radicals for nuclear fusion experiments. Nuclear Fusion **43**, 25 (2003)
10. G. Federici, R. Anderl, J.N. Brooks, R. Causey, J.P. Coad, D. Cowgill, R. Doerner, A. Haasz, G. Longhurst, S. Luckhardt, D. Mueller, A. Peacock, M. Pick, C.H. Skinner, W. Wampler, K. Wilson, C. Wong, C. Wu, D. Youchison: Tritium inventory in the ITER PFC's: Predictions, uncertainties, R&D status and priority needs. Fusion Engineering and Design **39-40**, 445 (1998)
11. V.S. Voitsenya, A.F. Bardamid, V.N. Bondarenko, W. Jacob, V.G. Konovalov, S. Masuzaki, O. Motojima, D.V. Orlinskij, V.L. Poperenko, I.V. Ryzhkov, A. Sagara, A.F. Shtan, S.I. Solodovchenko, M.V. Vinnichenko: Some problems arising due to plasma-surface-interaction for operation of the in-vessel mirrors in a fusion reactor. J. Nucl. Mater. **290-293**, 336 (2001)
12. A. Grill: Diamond-like carbon: State of the art. Diamond Relat. Mater. **8**, 428 (1999)
13. J. Robertson: Diamond-like amorphous carbon. Review of Deposition methods, properties, and applications. Mat. Sci. Eng. Reports **37**, 129 (2002)
14. S.R.P. Silva: Properties of Amorphous Carbon. EMIS Datareviews Series No. 29, 2003
15. W. Jacob: Surface reactions during growth and erosion of hydrocarbon films. Thin Solid Films **326**, 1 (1998)

16. A. von Keudell, W. Jacob: Growth and erosion of hydrocarbon films, investigated by in situ ellipsometry. J. Appl. Phys. **79**, 1092 (1996)
17. T. Schwarz-Selinger, A. von Keudell, W. Jacob: Plasma chemical vapor deposition of hydrocarbon films: The influence of hydrocarbon source gas on the film properties. J. Appl. Phys. **86**, 3988 (1999)
18. P. Koidl, P. Oelhafen: Amorphous hydrogenated carbon films. In E-MRS Symp. Proc. Vol. XVII Les Editions des Physique, Les Ulis 1987
19. P. Koidl, C. Wild, B. Dischler, J. Wagner, M. Ramsteiner: Materials Science Forum **52-53**, 41 (1989)
20. A. von Keudell, W. Jacob, W. Fukarek: Role of hydrogen ions in PECVD of hydrocarbon films. Appl. Phys. Lett. **66**, 1322 (1995)
21. S. Kaplan, F. Jansen, M. Machonkin: Characterization of amorphous carbon-hydrogen films by solid-state nuclear magnetic resonance. Appl. Phys. Lett. **47**, 750 (1985)
22. M.A. Tamor, W.C. Vassell, K.R. Carduner: Appl. Phys. Lett. **58**, 592 (1991)
23. A. Grill, B.S. Meyerson, V. Patel, J.A. Reimer, M.A. Petrich: Inhomogeneous carbon bonding in hydrogenated amorphous carbon films. J. Appl. Phys. **61**, 2874 (1987)
24. C. Jäger, J. Gottwald, H.W. Spiess, R.J. Newport: Structural properties of amorphous hydrogenated carbon. III. NMR investigations. Phys. Rev. B **50**, 846 (1994)
25. W. Möller, B.M.U. Scherzer: Subsurface molecule formation in hydrogen-implanted graphite. Appl. Phys. Lett. **50**, 1870 (1987)
26. J.C. Angus, F. Jansen: Dense "diamondlike" hydrocarbons as random covalent networks. J. Vac. Sci. Technol. A, **6**, 1778 (1988)
27. W. Jacob, W. Möller: On the structure of thin hydrocarbon films. Appl. Phys. Lett. **63**, 1771 (1993)
28. A. von Keudell: Formation of polymer-like hydrocarbon films from beams of methyl radicals and atomic hydrogen. Thin Solid Films **402**, 1 (2002)
29. W. Jacob, C. Hopf, A. von Keudell, T. Schwarz-Selinger: Surface loss probabilities of hydrocarbon radicals on amorphous hydrogenated carbon film surfaces: Consequences for the formation of re-deposited layers in fusion experiment. In: *Hydrogen Recycling at Plasma Facing Materials*, Chung-Hsiung Wu (ed.) (Kluwer Academic Publishers 2000) pp. 331–337
30. A. von Keudell, C. Hopf, T. Schwarz-Selinger, W. Jacob: Surface loss probabilities of hydrocarbon radicals on amorphous hydrogenated carbon film surfaces: Consequences for the formation of re-deposited layers in fusion experiments. Nuclear Fusion **39**, 1451 (1999)
31. A. Schenk, J. Biener, B. Winter, C. Lutterloh, U.A. Schubert, J. Küppers: Mechanism of chemical erosion of sputter-deposited C:H films. Appl. Phys. Lett. **61**, 2414 (1992)
32. A. Schenk, B. Winter, J. Biener, C. Lutterloh, U. Schubert, J. Küppers: Growth and thermal decomposition of ultrathin ion-beam deposited C:H films. J. Appl. Phys. **77**, 2462 (1995)
33. V. Philipps, E. Vietzke, M. Erdweg, A. Flaskamp: Thermal desorption of hydrogen and various hydrocarbons from graphite bombarded with thermal and energetic hydrogen. J. Nucl. Mater. **145-147**, 292 (1987)
34. J. Ristein, R.T. Stief, L. Ley, W. Beyer: A comparative analysis of a–C:H by infrared spectroscopy and mass selected thermal effusion. J. Appl. Phys. **84**, 3836 (1998)

35. K. Maruyama, W. Jacob, J. Roth: Erosion behavior of soft, amorphous deuterated carbon films by heat treatment in air and under vacuum. J. Nucl. Mater. **264**, 56 (1999)
36. D.A. Doughty, J.R. Doyle, G.H. Lin, A. Gallagher: Surface reaction probability of film-producing radicals in silane glow discharge. J. Appl. Phys. **67**, 6220 (1990)
37. C. Hopf, K. Letourneur, W. Jacob, T. Schwarz-Selinger, A. von Keudell: Surface loss probabilities of the dominant neutral precursors for film growth in methane and acetylene discharges. Appl. Phys. Lett. **74**, 3800 (1999)
38. C. Hopf, T. Schwarz-Selinger, W. Jacob, A. von Keudell: Surface loss probabilities of hydrocarbon radicals on amorphous hydrogenated carbon film surfaces. J. Appl. Phys **87**, 2719 (2000)
39. A. Yuuki, Y. Matsui, K. Tachibana: A study on radical fluxes in silane plasma CVD from trench coverage analysis. Jpn. J. Appl. Phys. **28**, 212 (1989)
40. A. Matsuda, K. Nomoto, Y. Takeuchi, A. Suzuki, Y. Yuuki, J. Perrin: Temperature dependence of the sticking and loss probabilities of silyl radicals on hydrogenated amorphus silicon. Surf. Sci. **227**, 50 (1990)
41. A. Nuruddin, J.R. Doyle, J.R. Abelson: Surface reaction probability in hydrogenated amorphous silicon growth. J. Appl. Phys. **76**, 3123 (1994)
42. M. Mayer, V. Rohde, A. von Keudell, ASDEX Upgrade Team: Characterisation of deposited hydrocarbon layers below the divertor and in the pumping ducts of ASDEX Upgrade. J. Nucl. Mater. **313-316**, 429 (2003)
43. C.C. Tsai, J.C. Knights, G. Chang, B. Wacker: Film formation mechanisms in the plasma deposition of hydrogenated amorphous silicon. J. Appl. Phys. **59**, 2998 (1986)
44. A. von Keudell, T. Schwarz-Selinger, W. Jacob: Simultaneous interaction of methyl radicals and atomic hydrogen with amorphous hydrogenated carbon films. J. Appl. Phys. **89**, 2979 (2001)
45. M. Meier, A. von Keudell: Hydrogen elimination as a key step for the formation of a–C:H films. J. Appl. Phys. **90**, 3585 (2001)
46. M. Meier A. von Keudell: Temperature dependence of the methyl sticking coefficient on hydrocarbon film surfaces. J. Chem. Phys. **116**, 5125 (2002)
47. C. Hopf, A. von Keudell, W. Jacob: Direct verification of the ion-neutral synergism during hydrocarbon film growth. J. Appl. Phys. **93**, 3352 (2003)
48. C. Hopf, A. von Keudell, W. Jacob: Chemical sputtering of hydrocarbon films. J. Appl. Phys. **94**, 2373 (2003)
49. W. Jacob, C. Hopf, A. von Keudell, M. Meier, and T. Schwarz-Selinger: Particle-beam experiment to study heterogeneous surface reactions relevant to plasma-assisted thin film growth and etching. Rev. Sci. Instrum. **74**, 5123 (2003)
50. M. Shiratani, J. Jolly, H. Videlot, J. Perrin: Surface reaction kinetics of CH_3 in CH_4 rf discharge studied by time-resolved threshold ionization mass spectrometry. Jpn. J. Appl. Phys. **36**, 4752 (1997)
51. M. Mayer: Deposition and erosion studies, Final report for task JW0-FT-3.4, Fusion Technology Task Force at JET. Technical report (2003)
52. M. Katyiar, J.R. Abelson: Methods to enhance absorption signals in infrared reflectance spectroscopy: A comparison using optical simulations. J. Vac. Sci. Technol. A **13**, 2005 (1995)
53. J. Küppers: The hydrogen surface chemistry of carbon as a plasma facing material. Surf. Sci. Rep. **22**, 249 (1995)

54. J. Robertson, E.P. O'Reilly: Electronic and atomic structure of amorphous carbon. Phys. Rev. B **35**, 2946 (1987)
55. T. Zecho, B.D. Brandner, J. Biener, J. Küppers: Hydrogen-induced chemical erosion of a-C:H thin films: Product distribution and temperature dependence. J. Phys. Chem. B **105**, 6194 (2001)
56. E. Vietzke, K. Flaskamp, V. Phillips, G. Esser, P. Wienhold, J. Winter: Chemical erosion of amorphous hydrogenated carbon films by atomic and energetic hydrogen. J. Nucl. Mater. **145-147**, 443 (1987)
57. E. Vietzke, A.A. Haasz: Chemical erosion. In: W.O. Hofer and J. Roth (eds.): *Physical Processes of the Interaction of Fusion Plasmas with Solids* (Academic Press 1996) p. 135
58. A. Horn, A. Schenk, J. Biener, B. Winter, C. Lutterloh, M. Wittmann, J. Küppers: H atom impact induced chemical erosion reaction at C:H film surfaces. Chem. Phys. Lett. **231**, 193 (1994)
59. A. von Keudell, T. Schwarz-Selinger, M. Meier, W. Jacob: Direct identification of the synergism between methyl radicals and atomic hydrogen during growth of amorphous hydrogenated carbon films. Appl. Phys. Lett. **76**, 676 (2000)
60. A. von Keudell, T. Schwarz-Selinger, M. Meier, W. Jacob: Erratum: Direct identification of the synergism between methyl radicals and atomic hydrogen during growth of amorphous hydrogenated carbon films. Appl. Phys. Lett. **77**, 459 (2000)
61. M. Meier, R. Preuss, V. Dose: Interaction of CH_3 and H with amorphous hydrocarbon surfaces: Estimation of reaction cross-sections using Bayesian probability theory. New J. Phys. **5**, 133 (2003)
62. P. Träskelin, E. Salonen, K. Nordlund, A.V. Krasheninnikov, J. Keinonen, C.H. Wu: Molecular dynamics simulation of CH_3 sticking on carbon surfaces. J. Appl. Phys. **93**, 1826 (2003)
63. J. Roth, J. Bohdansky: Sputtering of graphite with light ions at energies between 20 and 1000 eV. Nucl. Instrum. Meth. B **23**, 549 (1987)
64. M. Balden, J. Roth: New weight-loss measurements of the chemical erosion yields of carbon materials under hydrogen ion bombardment. J. Nucl. Mater. **280**, 39 (2000)
65. C. García-Rosales, W. Eckstein, J. Roth: Revised formulae for sputtering data. J. Nucl. Mater. **218**, 8 (1994)
66. J. Roth, C. García-Rosales: Analytic description of the chemical erosion of graphite by hydrogen ions. Nucl. Fusion **36**, 1647 (1996)
67. A.A. Haasz, O. Auciello, P.C. Stangeby, I.S. Youle: Ion-induced synergistic effects for CH_4 production from carbon under H^+, H^0 and H_2 impact. J. Nucl. Mater. **128-129**, 593 (1984)
68. J.W. Davis, A.A. Haasz, P.C. Stangeby: Title hydrocarbon formation due to combined H^+ ion and H^0 atom impact on pyrolytic graphite. J. Nucl. Mater. **155-157**, 234 (1988)
69. E. Vietzke, K. Flaskamp, V. Philipps: Hydrogen formation in the reaction of atomic hydrogen with pyrolytic graphite and the synergistic effect of argon ion bombardment. J. Nucl. Mater. **111-112**, 763 (1982)
70. B.V. Mech, A.A. Haasz, J.W. Davis: Model for the chemical erosion of graphite due to low-energy H^+ and D^+ impact. J. Appl. Phys. **84**, 1655 (1998)
71. E. Vietzke, K. Flaskamp, V. Philipps: Differences in the CH_3 and CH_4 formation from graphite under bombardment with hydrogen ions and hydrogen atoms/argon ions. J. Nucl. Mater. **128-129**, 545 (1984)

72. E. Vietzke: Energy distribution of CD_4 and CD_3 chemically released from graphite by D^+ and D^0/Ne^+ impact. J. Nucl. Mater. **290-293**, 158 (2001)
73. C. Hopf, A. von Keudell, W. Jacob: Chemical sputtering of hydrocarbon films by low-energy Ar^+ ion and H atom impact. Nucl. Fusion **42**, L27 (2002)
74. W. Eckstein: *Computer Simulation of Ion–Solid Interactions*. Springer Series in Materials Science, 1st edn. (Springer, Berlin and Heidelberg 1991)
75. W. Eckstein, A. Sagara, K. Kamada: Incident angle dependence of sputtering yields for hydrogen bombardment of light elements. J. Nucl. Mater. **150**, 266 (1987)
76. W. Möller: Modeling of the sp^3/sp^2 ratio in ion beam and plasma-deposited carbon films. Appl. Phys. Lett. **59**, 2391 (1991)
77. W. Möller: Modeling and computer simulation of ion-beam- and plasma-assisted film growth. Thin Solid Films **228**, 319 (1993)
78. J.W. Coburn, H.F. Winters: Ion- and electron-assisted gas-surface chemistry – an important effect in plasma etching. J. Appl. Phys. **50**, 3189 (1979)
79. T.J. Chuang: Electron spectroscopy study of silicon surface exposed to XeF_2 and the chemisorption of SiF_4 on silicon. J. Appl. Phys. **51**, 2614 (1980)
80. Y.Y. Tu, T.J. Chuang, H.F. Winters: Chemical sputtering of fluorinated silicon. Phys. Rev. B **23**, 823 (1981)
81. H.F. Winters, J.W. Coburn: Surface science aspects of etching reactions. Surf. Sci. Reports **14**, 161 (1992)
82. J. Pillath, J. Winter, F. Waelbroek. In: P. Koidl and P. Oelhafen (eds.): *Amorphous Hydrogenated Carbon Films E-MRS Symposia Proc.*, Vol. XVII (Les Editions de Physique, Les Ulis, France 1987) p. 449
83. W.R. Wampler, D.G. Whyte, C.P.C. Wong, W.P. West: Erosion in the DIII-D divertor by neon-detached plasmas. J. Nucl. Mater. **313**, 333 (2003)
84. F.L. Tabarés, D. Tafalla, I. Tanarro, V.J. Herrero, A. Islyaikin, C. Maffiotte: Suppresion of hydrogenated carbon film deposition by scavenger techniques and their application to the tritium inventory control in fusion devices. Plas. Phys. Contr. Fusion **44**, L37 (2002)
85. E. Salonen, K. Nordlund, J. Keinonen, C.H. Wu: Swift chemical sputtering of amorphous hydrogenated carbon. Phys. Rev. B **63**, 195415 (2001)
86. W. Möller, W. Fukarek, K. Lange, A. von Keudell, W. Jacob: Mechanisms of the deposition of hydrogenated carbon films. Jpn. J. Appl. Phys. **34**, 2163 (1995)
87. P. Favia, R. Lamendola, R. d'Agostino: The role of substrate temperature and bias in the plasma deposition from tetramethylsilane. Plasma Sources Sci. Technol. **1**, 59 (1992)
88. R. d'Agostino: *Plasma Deposition, Treatment, and Etching of Polymers*, Chapter: Plasma Polymerization of Fluorcarbons (Academic Press 1990)
89. C. Hopf, A. von Keudell, W. Jacob: The influence of hydrogen ion bombardment on plasma-assisted hydrocarbon film growth. Diamond Relat. Mater. **12**, 85 (2003)
90. C. Hopf, W. Jacob, A. von Keudell: Ion-induced surface activation, chemical sputtering, and hydrogen release during plasma-assisted hydrocarbon film growth. J. Appl. Phys. (2005) in print

12 Tritium Inventory in the Materials of the ITER Plasma-Facing Components

G. Federici and C.H. Skinner

Managing the interface between a thermonuclear plasma and the solid material environment is arguably one of the highest technical challenges in the operation of a next-step deuterium-tritium (D-T) tokamak and in the successful development of future fusion power reactors. The most crucial issues (e.g., erosion/redeposition, tritium retention) came in to sharp focus during D-T operation of TFTR and JET and, in particular, in the process of designing ITER. Carbon-based materials have superior thermo-mechanical properties and do not melt (they sublime), however they retain high levels of tritium by co-deposition with eroded carbon that could severely constrain plasma operations in a next-step device with carbon plasma-facing components. Metallic materials avoid the tritium retention issue, but melt layer losses due to transient high energy deposition (e.g., type I ELMs and disruptions) may lead to severe damage and unacceptably short lifetimes and, in addition, maintaining plasma purity with high-Z materials is a concern.

A mix of several different plasma facing materials is likely to be used in ITER to meet the requirements of areas with different power and particle flux characteristics. Erosion, and the subsequent transport of impurities, will inevitably lead to a certain amount of material mixing between these materials, whose behavior in a tokamak is uncertain.

Despite remarkable advances in the knowledge base from experiments and theory, significant uncertainties associated with tritium retention and erosion lifetime remain in ITER. This area remains one of the grand challenges that must be met for magnetic fusion to achieve its promise as an attractive, environmentally acceptable energy source.

This paper surveys factors relevant to material choices in ITER, and reviews some of the most recent experimental findings, which shed some light on the complexity of the problem of predicting in-vessel tritium inventory. Current modeling predictions and the attendant uncertainties are discussed, together with the outstanding issues still remaining, leading to recommendations for dedicated research and development work required to address these topics.

12.1 Introduction

The technical basis for designing a next-step deuterium-tritium (D-T) burning plasma experiment has greatly expanded during the past two decades thanks mainly to remarkable improvements in plasma performance and control in today's machines and advances in various areas of physics and engineering. Integrating and extending these advances toward long pulsed or steady state burning plasmas is now the focus of international tokamak research, which is ready to proceed to the construction of ITER as a physics and technology integration step.

Despite great strides, the problems arising from plasma-material interactions (PMIs), together with the selection of plasma facing materials, still represent major challenges for the reliable and safe operation of a D-T next-step tokamak [1]. They also remain potential obstacles for the successful development of future fusion power reactors. These issues came into sharp focus during D-T operation of the Tokamak Fusion Test Reactor (TFTR) and the Joint European Torus (JET) and, in particular, in the process of designing ITER.

A key decision for ITER is the choice of plasma facing materials [2]. Their selection is complicated by the variety of requirements, which vary according to location in the device. These stem from the need to maintain plasma purity, and, particularly, for the divertor to handle high heat loads, while minimizing erosion, tritium retention, and dust production. For ITER, the use of beryllium on the first wall, and tungsten and carbon-fibre composites (CFCs) in the divertor, is currently seen as the optimal use of the presently explored materials. Vigorous research and development (R&D) efforts are underway to address the remaining issues associated with the use of these materials and to corroborate the physics basis for the evaluation of the plasma-facing component (PFC) erosion lifetime and the control of the in-vessel co-deposited tritium inventory.

This paper surveys factors relevant to material choices in ITER, briefly describing advantages and disadvantages of the various material options considered, with emphasis on the implications of the current choice on the problem of in-vessel tritium retention. Other PMI and technological issues associated with the development of robust PFCs for ITER and future fusion power reactors are dealt with elsewhere [3–6].

The organization of this paper is as follows: Section 12.2 reviews briefly the history of plasma facing materials used in tokamaks. Section 12.3 describes the primary candidate plasma facing materials for ITER and the criteria for their selection. It highlights some of the tritium-related constraints on a burning plasma experiment (BPX) operation schedule and provides a brief summary of some of the most recent and relevant experimental findings for the materials of interest. Section 12.4 discusses the current ITER tritium retention estimates and attendant uncertainties. Section 12.5 suggests directions and priorities for further R&D. Finally, a summary is provided in Sect. 12.6.

12.2 Historical Perspective

In the early stages of fusion research, the structural material of the vacuum vessel chamber was typically used as the plasma-facing material. These materials were generally stainless steels or Inconel [7]. They were readily available, easy to fabricate, join and clean, and had good thermal and vacuum properties. Without auxiliary heating, plasma temperatures were too low to fully ionize low-Z impurities, so they radiated energy from the plasma. To control low-Z impurities such as oxygen and carbon that might be desorbed from the surface of these metals, various surface conditioning techniques were developed, including baking, discharge cleaning, and gettering. Limiters were introduced to protect the vessel walls from unstable discharges and increased auxiliary power. By the late 1970's, various tokamaks were starting to employ auxiliary heating systems, primarily neutral beam injection (NBI). Experiments with NBI on the Princeton Large Torus (PLT) resulted in the first thermonuclear class temperatures to be achieved in experiments [8–10]. Refractory metals like tungsten and molybdenum were used as limiter materials to withstand the high heat fluxes without cracking and melting. PLT at the time used tungsten limiters, and at high powers and relatively low plasma densities, very high edge plasma temperatures and power fluxes were achieved, resulting in tungsten sputtering and subsequent core radiation from partially stripped tungsten ions. For this reason, PLT switched limiter material to nuclear grade graphite. Graphite has the advantage that eroded carbon atoms are fully stripped in the plasma core, thus reducing core radiation. In addition, the surface does not melt if overheated - it simply sublimes. This move to carbon by PLT turned out to be very successful, alleviating the central radiation problem. For these reasons, carbon has tended to be the favored limiter/divertor material in magnetic fusion research ever since.

By the mid-1980's, many tokamaks were operating with graphite limiters and/or divertor plates. In addition, extensive laboratory tests/simulations on graphite had begun, primarily aimed at understanding the chemical reactivity of graphite with hydrogenic plasmas, i.e., chemical erosion. Early laboratory results suggested that carbon would be eroded by hydrogenic ions with a maximum chemical erosion yield of Y $\sim$ 0.1 C/D+, a yield several times higher than the maximum physical sputtering yield [11, 12]. Another process, radiation-enhanced sublimation (RES), was discovered at elevated temperatures, which further suggested high erosion rates for carbon [13, 14]. The ability of carbon to trap high concentrations of hydrogenic species in co-deposited layers became clear in the early deuterium experience of TFTR [15] and JET [16] and became a significant operational concern during D-T operations in these machines [17, 18]. Carbon's problems, along with its poor mechanical properties in a neutron environment (which had been known for many years from fission reactor experience [19]), led to the consideration of beryllium as a plasma-facing material [20]. Beryllium has the advantage of being a low-Z material, has a low affinity for hydrogenic isotopes and a good

thermal conductivity. However, Be has several negative features, including a low melting temperature (1560 K), potential toxicity in manufacturing, and relatively high physical sputtering rates. Nevertheless, two small tokamaks tested beryllium (ISX-B [21], UNITOR [22]), and this led to extensive operation at JET with beryllium limiters, divertor plates and evaporative gettering [20]. One immediate and clearly beneficial effect of beryllium operation was the observation of strong oxygen gettering by the evaporated beryllium.

At present, carbon is the dominant material in the main-chamber of major tokamaks worldwide, with the exceptions of Alcator C-Mod [23], which uses molybdenum, ASDEX Upgrade [24–27], which uses tungsten on parts of the machine, and FT-U [28], which has used a variety of moderate to high-Z materials. In particular, the results of ASDEX Upgrade [26, 27] are very encouraging for the future, as they show that plasma performance can be maintained with high-Z materials. Many machines have also expanded graphite coverage to include virtually the entire vacuum vessel wall, in addition to the limiter/divertor plates, and used more heat-resistant CFCs (e.g., DIII-D [29]).

In general, the success with carbon in limiter machines led to the use of carbon for divertor plates, although there are a number of cases where metals have been used. The argument for carbon in the case of divertor plates is not as strong as in the case of limiter machines. Carbon or other low-Z materials are most suited to high edge plasma temperatures, typically at low plasma density, as one finds at the edge of a high-powered limiter device. Again, this is related to the fact that carbon is fully-stripped in the core of tokamak discharges and thus does not cool the plasma by line radiation. When the plasma temperature adjacent to material surfaces is low, on the other hand, as in most divertor plasmas, the incident particle energies can very often be below the physical sputtering threshold of higher-Z materials. In contrast, carbon has a weak energy threshold for chemical erosion. This, along with the fact that ion fluxes are very high in the divertor (high plasma density), means that relatively high erosion rates are expected and found in most cases for carbon divertor plates [30–32]. However, recent investigations show that, in existing machines, the inboard divertor is typically an area of net deposition, whereas the outboard divertor could be subject to net erosion or deposition, depending on the local plasma conditions [33]. As a consequence, large hydrogenic retention has been found in films forming primarily on cold surfaces. The last decade of divertor research has seen a return of interest to metals, which had been largely put aside in favor of carbon. Sputtered high-Z metal atoms, such as tungsten, have a lower ionization potential and lower velocity than sputtered carbon. They are quickly ionized close to the surface and are promptly redeposited onto the target near their point of origin. Divertor machines that have tried high-Z metal divertor plates in the low temperature/high recycling mode (e.g., molybdenum in Alcator C-Mod [23, 34, 35] and tungsten in ASDEX Upgrade [24]) have indeed found very low levels of net erosion at the divertor plate. High heat flux

components clad by tungsten, that meet the severe normal operation thermal load requirements of the divertor, have also been developed and successfully tested up to more than $20\,\mathrm{MW/m^2}$ (see, for example, [36, 37]), though the response to transient events, such as ELMs and disruptions, remains an issue and is being vigorously investigated [38–41].

12.3 Highlights of the ITER Design and Suitable Plasma-Facing Material Options

12.3.1 ITER Design

ITER will be the first fusion device with significant Q (the ratio of fusion power to additional heating power) and extended burn [42, 43]. The completion of the ITER Engineering Design Activities, in July 2001, has brought a mature design, cost estimate and safety analysis, that are supported by a body of validating physics and technology R&D [44]. A thorough discussion of the operation parameters and physics performance issues can be found elsewhere [38, 45–47]. A cutaway showing the main in-vessel components of the ITER design is illustrated in Fig. 12.1 and a brief description is provided below.

Vacuum Vessel, Blanket and First Wall

The vacuum boundary is formed by a double-walled vacuum vessel made of stainless-steel, which contains the blanket and divertor systems. The basic functions of the vacuum vessel are to provide a suitable vacuum in the plasma chamber, to support the in-vessel components, to assist in the nuclear shielding of the coils and to constitute the first confinement boundary. To this end, the vessel cooling system provides decay heat removal by natural convection even when the vacuum vessel and the blanket cooling loops are not functioning (no pumping action). The shielding in particular from neutron radiation has to be sufficient to reduce nuclear heating in the coils to manageable levels and to allow limited access for magnet repair inside the cryostat.

The shielding blanket is composed of water-cooled steel modules, which are directly supported by the vacuum vessel and are effective in moderating the 14 MeV neutrons, with a water-cooled copper mat bonded to the surface of the modules on the plasma side, and protected from interaction with the plasma by beryllium. Manufacturing considerations can be found elsewhere [48]. The first wall incorporates two start-up limiters located in two equatorial ports. With the aim to reduce cost and nuclear waste, the design includes a modular and separable first wall. This allows damaged or eroded blanket modules to be repaired inside the hot cell either by replacement of panels or by plasma spraying or other methods.

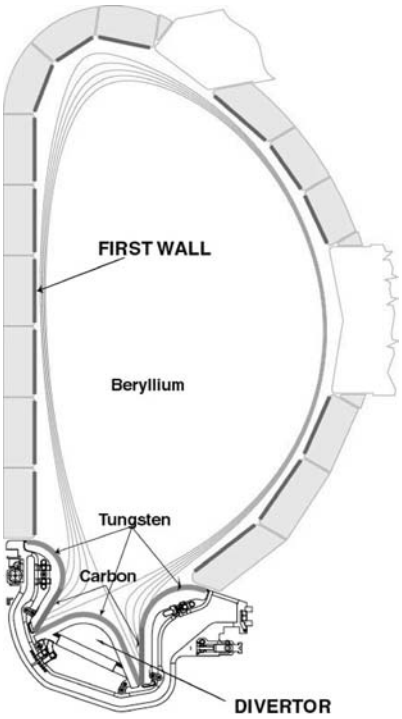

Fig. 12.1. Cutaway showing the layout of PFCs in ITER with different armour materials

Divertor

The divertor is designed to be very versatile, with components mounted on removable and reusable cassettes, supported on a pair of concentric toroidal rails that form part of the vacuum vessel. The divertor in ITER utilizes a so called "vertical target" geometry where a large fraction of the power in the Scrape-Off-Layer (SOL) is already removed upstream of material boundaries by a combination of radiation and charge exchange processes, thus maintaining the heat flux at the strike-points to a level of about 5–10 $\mathrm{MW/m^2}$. The target consists of the inboard and outboard vertical targets, which in their lower part interact directly with the SOL plasma and in their upper part act as "baffles" for the neutrals avoiding their backstreaming into the SOL and main plasma. The private flux region PFC consists of the dome located below the separatrix X-point, which sees mainly radiation charge exchange neutrals and helps baffle the neutrals. Finally, a semi-transparent liner protects the cassette body from direct line-of-sight of the plasma, while allowing gas pressures to be balanced between inboard and outboard target areas and allowing He and other impurities to be pumped away.

The ITER divertor is a crucial component for the performance of ITER. Its design is continually being updated and optimized, based on new information and understanding mainly from the Fusion Physics R&D Programme. Several design variants of the baseline are currently being investigated with the aim of minimizing the formation of hydrocarbon films in areas remote from the plasma [49] and/or ameliorating the problem of tritium control in the carbon co-deposits (e.g., by ensuring that regions of probable deposition are kept "hot" during operation [50], or by enhancing deposition in specially designed 'cold traps' for the hydrocarbons ($\sim 70\,\mathrm{K}$) [51, 52], which could be periodically heated to recover the tritium in the form of stable gas molecules). Detailed evaluations of these designs are on-going, but the complexity of including such a system is to be avoided if at all possible.

12.3.2 Plasma Facing Materials

The factors that affect the selection of plasma facing materials for ITER come primarily from the requirements of plasma performance (e.g., need to minimize impurity contamination and the resulting radiation losses in the confined plasma), engineering integrity, component lifetime (e.g., need to withstand thermal stresses, acceptable erosion), and safety (e.g., need to minimize tritium and radioactive dust inventories and avoid explosion hazards).

Currently, the ITER design uses beryllium for the first wall, and CFC as well as tungsten in the divertor. Each of these three candidate materials has some inherent advantages and disadvantages [1] (see Table 12.1), and their application depends on the specific operational requirements [53, 54] (see Table 12.2). The plasma-material interaction (PMI) issues are comprehensively reviewed in [1].

The longer pulse duration and cumulative run-time, together with the higher heat loads and more intense disruptions, represent the largest changes in operation conditions compared to today's experiments. Erosion of PFCs over many pulses, and distribution of eroded material, are critical issues that will affect the performance and the operating schedule of the ITER tokamak. Primary effects ensuing from erosion/re-deposition include plasma contamination, tritium co-deposition with carbon (if used in some parts of the divertor), component lifetime, dust, and formation of mixed-materials, whose behavior is still uncertain.

Beryllium is selected because it has the advantages of being a low-Z material with a good thermal conductivity and the ability to getter oxygen from the plasma. However, it has the disadvantage of high sputtering and low melting point (which limits its power handling capabilities). Tungsten is a high-Z material that will be used in the ITER divertor and possibly as a first wall material in later devices. The divertor is the preferred location for tungsten because net erosion is very low there due to low sputtering and high re-deposition (Sect. 12.2). Finally, CFC is chosen for a limited region near the strike points in ITER, due to its higher thermal shock resistance and higher

Table 12.1. Main advantages and shortcomings of candidate armour materials that are considered for the ITER design

Advantages	Shortcomings
CARBON-FIBRE-COMPOSITES (CFCs)	
• good power handling, good thermal shock and thermal fatigue resistance (low crack propagation); • does not melt (but sublimes) and preserves its shape even under extreme temperature excursions; • low radiation losses with influx to plasma due to low Z; • well-established joining technology; • broad tokamak operation experience; • in existing tokamaks, C erosion plays a beneficial role because of the reduction of the target power by radiation cooling of the divertor plasma. C radiates efficiently for temperatures down to $\sim 5\,\mathrm{eV}$.	• requires conditioning; • chemical erosion leads to reduction of lifetime and co-deposition of tritium with eroded carbon; • possible high erosion under disruption loads due to brittle destruction; • generates dust; • change of thermal conductivity due to n-irradiation; • mixed-material effects with Be can be beneficial or detrimental depending on the circumstances. They require R&D (Sect. 12.5).
BERYLLIUM	
• good oxygen gettering ability; • some tokamak practice exists (mainly JET); • because of low Z, low radiative power losses; • reparability by plasma-spraying; • well-established joining technology; • lower tritium inventory than C.	• reduced power-handling capability and resistance to disruptions because of the low melting temperature and high vapour pressure; • high physical sputtering yield; • toxic - requires controlled handling procedures; • co-deposition of tritium with Be could be significant if the level of O impurities is large or in the presence of C-mixing effects; • properties of thick BeO layers are not known; • n-induced brittleness; • mixed-material effects with carbon can be beneficial of detrimental depending on the circumstances. They require R&D (Sect. 12.5).
TUNGSTEN	
• low physical sputtering yield and high sputtering threshold energy; • no chemical sputtering in H-plasma; • promising (but limited) divertor tokamak experience; • the tritium inventory of tungsten is expected to be small. W does not co-deposit with H-isotopes; reparability by plasma-spraying; • well-established joining technology.	• low limit for plasma contamination due to high radiative losses; • melts under anticipated thermal quench disruption loads and Type-I ELMs at divertor plate; • unknown behavior of melt layer under disruptions; • re-crystallises (embrittles) at temperatures >1500 K; • low edge temperatures required for low sputtering; • safety concerns resulting from volatile oxides; • high activation and generates radioactive waste. • potential adverse effects arising from mixing of Be and W (e.g., formation of low melting point compounds).

Table 12.2. Operating conditions assumed for the design of the ITER PFCs during D-T operation. Considerations about design specifications of thermal loads during the H, D phases are discussed in the text. Further details can be found in [1]

	Divertor Target	Divertor Baffle/Dome	First wall (Start-up Limiter)
Material	CFC[(a)]/W	W	Be
No. of replacements	≤ 3	≤ 3	0 (> 3)
Baking temperature (°C)	520	520	520
Normal operation			
Lifetime (No. of cycles)	3000–10000	3000–10000	30000 (uncertain)
Peak surface heat flux (MW/m^2)	~ 10[(b)]	3	0.5 (~ 8 for ~ 100 s)
Peak particle flux ($10^{23}/m^2s$)	~ 10	< 0.1	0.01 (< 0.1)
ELM energy density (MJ/m^2)	< 1	uncertain	uncertain
ELM duration (ms)/ {Frequency}	0.2–1/ {~ 1 Hz}	–	–
Max. radiation damage[(c)] (dpa)	~ 0.7	~ 0.6	~ 1.7
Operating temperature design window during normal operation (K)	500–1500	500–900	500 (1200)
Disruptions (VDEs)			
Peak surface heat load[(d)] (MJ/m^2)	~ 10	uncertain	uncertain (< 60)
Duration (ms)/ {Frequency (%)}	1–10 {< 10} disruptions		(< 300 {1} VDEs)
Run-away electrons			
Peak surface heat load (MJ/m^2)		uncertain	~ 15
Duration (s)/ {Frequency (%)}		–	~ 0.1/ {< 10}

[(a)] Near vertical target strike-points. Tungsten elsewhere. [(b)] Slow transients $20\,MW/m^2$ lasting 10 s (10% frequency). [(c)] End-of-life. [(d)] This value is calculated assuming that the full thermal stored energy in ITER during D-T operation (~ 350 MJ) is all deposited in the divertor near the strike point with small broadening. Recent findings in existing tokamaks point to a small fraction of the energy reaching the divertor and spreading on the whole divertor surface (see text)

tolerance to ELMs and disruptions, because the operational lifetime of alternative materials such as tungsten in this region has significant uncertainties due to melt layer formation and losses.

The use of carbon in ITER will lead to tritium co-deposition, and operational availability of the machine will depend on the actual tritium co-deposition rate and the availability of reliable tritium co-deposition mitigation and/or removal techniques, which still need to be developed. An important uncertainty, which is being addressed by R&D, is the consequence of mixing of eroded materials, which will unavoidably occur and, in particular, whether the deposition of eroded Be from the wall at the target plate could reduce substantially the chemical erosion of carbon near the strike points and, thus, tritium co-deposition.

To address the tritium-co-deposition concern, primarily associated with the use of carbon, ITER will maintain the option to switch from CFC to W armour on the divertor targets prior to D-T operation. This change will depend on both the frequency and severity of ELMs and disruptions in the initial H/D plasmas, and the success of mitigating by design the occurrence of tritium co-deposition and/or on the availability of effective in-situ tritium removal techniques.

It is important to recognize that the plan to use carbon in ITER follows directly from the projected levels of thermal loads expected during plasma thermal transient events (e.g., type I ELMs and disruptions). Thus, efforts to better characterize power deposition during disruptions and ELMs, as well as to reduce ELM heat loads and to mitigate disruptions (see, for example, [55]) are very important due to the influence on these design choices.

12.3.3 Tritium-Related Constraints on a BPX Operation Schedule

Tritium is a very sensitive subject for public acceptance of fusion and will play a central role in the operation of a next-step experimental fusion facility, which will routinely use large amounts of tritium as fuel (e.g., 100 times more in ITER than in present experiments) in a mixture with deuterium. Tritium retention is a regulatory issue since the amount that can potentially be released in an accident sets the limits on plasma operation without removal. Fuel economy has never been an issue in deuterium-fuelled experiments and only recently have the limitations associated with the use of tritium, and its incomplete recovery in experiments in TFTR and in JET, brought the issue of fuel retention under closer scrutiny [56, 57]. Table 12.3 provides a list of key quantities related to tritium in existing tokamaks and a next-step device [18, 57–59].

With careful planning, both TFTR and JET have demonstrated safe tritium handling in a fusion machine. Special controls imposed on the handling of tritium [60–62] have required that the quantity of tritium retained in the torus be accounted for and the inventory limited [63, 64] in order to permit

Table 12.3. Tritium in current facilities and future devices [1]

Parameters	**TFTR**			**JET**		**Next-Step**
Year	**1993-95**	**1996**	**1997**	**1991**	**1997**	
Peak fusion power, MW	10.7	8.5	7.8	1.8	~ 16	500–1500
Total discharge duration, (s)	8	4.2	6.5	10–30	20–30	300–1000
Total number of discharges	14724	5324	3619	2	~ 593	$> 10^4$
Discharges with NBI	6134	2167	1609	2	$> 50\%$	–
Discharges with tritium NBI	500	124	107	2	~ 134	–
Typical # of tritium pulses per day	0–5	0–5	0–5	–	10	10–20
T processed by facility (g)	73	17	15	0.1	100	–
T introduced in the torus (g)	3.3	0.84	1.1	0.005	$35^{(a)}$	–
T introduced (g/pulse)	< 0.048	< 0.01	< 0.014	–	< 0.25	50–100
T retained in the torus and NBs (g)	1.7	1.6	1.8	0.004	$11.5^{(b)}$	< 20 g/pulse
Avg. retention (excluding cleanup)	$51\%^{(c)}$	$51\%^{(c)}$	$51\%^{(c)}$	–	40%	$< 10\%$
Increment of tritium inventory (g)	1.7	0.81	0.76	0.004	$11.5^{(d)}$	–
T removed at end of clean-up run (g)	0.96	0.49	0.84	0.0045	$5.5^{(d)}$	$90\%^{(e)}$
T remaining at end of clean-up run (g)	0.74	1.06	0.98	–	$\sim 6^{(d)}$	
T permitted in the vessel (g)	2			20 (first wall) 11 (cryopumps)		~ 350–$1000^{(f)}$
T permitted on site (g)	5			90		$\sim 4000^{(f)}$
Fuel cycle	closed			closed		closed
Exhaust processing	batch			batch		semicontinuous
Breeding blanket	N/A			N/A		Test modules$^{(g)}$

$^{(a)}$ 0.6 g by NBI and the rest by gas puffing. $^{(b)}$ This was the tritium inventory in all systems outside the active gas handling system (AGHS) (i.e., NBIs, torus), but individual analysis of batches of gas from the different subsystems indicate that the torus contributes $> 90\%$ of the inventory. $^{(c)}$ This is an average value over the period 93–97, excluding dedicated tritium removal campaigns. $^{(d)}$ Some clean-up was also done in the middle of DTE1, in order to repair a small water leak in the fast shutter of the neutral beam. At that time ~ 11.5 g of T_2 had been introduced into the torus (0.05 g from beams, the rest as gas puff) and about 4.4 g was retained on the walls. The wall load was reduced to ~ 2.9 g in a four-day period with $\sim$120 pulses with RF heating (ICRF). $^{(e)}$ Design target. $^{(f)}$ Significant uncertainties still exist. $^{(g)}$ It is expected that installation of a tritium breeding blanket capable of replenishing at least in part the tritium that is consumed will not be essential in a next-step experimental fusion facility, at least at the outset. Required breeding blanket technology development will be carried out in a next-step device mainly through installation of breeding blanket test modules, introduced through vessel ports specifically allocated and instrumented for this purpose. These modules may later be supplemented by a partial tritium breeding blanket

continued operation within the licensed site inventory limit. When the tritium in-vessel inventory approached the administrative safety limit, it was removed by extensive campaigns involving several weeks of glow discharge cleaning and deuterium operation. An extensive discussion of the tritium experience from both JET and TFTR is described elsewhere [1]. In summary, while tritium retention was not a significant limit to plasma operations in these machines, the high rate of tritium retention and slow rate of tritium removal would be unacceptable in ITER and in a fusion reactor.

Tritium is one of the main source terms in accident scenarios for ITER and to meet some of the key requirements for limitation of worker and public dose in accidents, limits need to be placed on the tritium inventory. Due to the ease of mobilization of tritium retained in co-deposited layers (co-deposited films in tokamaks start to decompose, releasing tritium, when exposed to air at temperatures $> 520\,\mathrm{K}$, [65–69]), a limit of $\sim 350\,\mathrm{g}$ is currently set for the in-vessel co-deposition inventory (and $120\,\mathrm{g}$ in the cryo-pumps). These limits are set to allow the full release of this inventory, under hypothetical accident conditions, without the need for public evacuation under the worst weather conditions.

Upon approaching this limit, operation in ITER will need to be discontinued and the subsequent availability of the machine for plasma operations will depend on the availability of efficient and fast tritium removal techniques that have yet to be fully demonstrated in a tokamak (Sect. 12.5). For comparison, in TFTR and JET several weeks were needed for tritium removal by glow discharge cleaning and air ventilation after several minutes only of cumulative D-T plasma operation. These methods are much too slow to cope with the higher duty cycle of a next step device. While the predictions are uncertain, it seems clear that in a relatively short period, ITER D-T plasma operations will stop and will not be allowed to restart until substantial amounts of tritium are removed from the vessel. The delay this will entail is highly uncertain since no relevant method to remove tritium has been established on a working tokamak. This is a major unsolved development task for next step devices with carbon PFCs. Techniques involving exposure to oxygen (e.g., thermo-oxidative erosion at temperatures above $570\,\mathrm{K}$, or oxygen plasma discharges) have been found to be most effective in laboratory experiments to remove T from a carbon surface (by removing the T-containing films) (see [1] and Refs. therein). However, their use in a tokamak remain highly speculative and a demonstration experiment in a tokamak is urgently needed (Sect. 12.5). Major drawbacks of techniques using oxygen, especially at elevated temperatures, include collateral damage to other in-vessel components, the recovery time for normal plasma operation, and the expense of processing the resulting tritium oxide. No practical method of localizing the oxidation to the area required (and avoiding oxygen exposure elsewhere) has been demonstrated, although various ideas are being explored.

Recently novel methods for tritium release relying on a laser [70, 71] or flash lamp [72] have been proposed and applied to remove co-deposited layers

on laboratory samples or tiles retrieved from machines. These techniques appear to be promising in-situ methods for tritium removal in a next step D-T device as they do not rely on oxidation, and avoid the associated deconditioning of the plasma-facing surfaces and the expense of processing large quantities of tritium oxide. There is an urgent need to apply candidate tritium removal techniques to existing tokamaks. Demonstration experiments inside the JET vessel have been conducted for the 2004 maintenance period. R&D is still needed, however, to address tritium co-deposited in relatively inaccessible areas (e.g., in narrow gaps between PFCs and pumping ducts) and, in the case of methods that remove the co-deposited film, to demonstrate the efficient collection of any resulting tritiated particles.

12.3.4 Summary of Recent Experimental Findings

General Remarks

Tritium retention and the control of the tritium inventory in ITER and future reactors strongly depend on the choice of plasma facing materials and their operational conditions (e.g., temperature of PFCs, flux density of impinging particles, plasma-edge conditions), and geometry effects (e.g., gaps, shaded regions, etc.). Retention can occur by (*i*) direct implantation of ions or neutrals in a shallow surface region and possibly also diffusion into the bulk (depending on the material used and temperature), (*ii*) co-deposition of tritium with eroded materials, primarily carbon or beryllium (the latter only if abundant O and/or C is also present) leading to a continuous accumulation of tritium, and (*iii*) production of tritium by transmutation nuclear reactions in beryllium which results in tritium inventory within the bulk material, principally in microscopic defect sites and helium bubbles.

Tritium retention mechanisms are reviewed in various papers (e.g., [1, 73] for C-based materials, [1, 74, 75] for beryllium and [1, 76] for tungsten). A qualitative summary of the retention and removal characteristics of the plasma facing materials considered for ITER is shown in Table 12.4 [76].

Co-deposition of tritium with carbon is potentially the major T repository for ITER even if the use of carbon is minimized to the divertor strike plates. Retention by other mechanisms is expected to be low and to contribute only marginally to the in-vessel tritium-uptake (Sect. 12.4). For this reason the focus here is on some recent experimental findings associated with (*i*) carbon erosion and deposition patterns in existing tokamaks, (*ii*) hydrocarbon film formation in areas of the divertor hidden from the plasma, and (*iii*) mixed-material effects.

Identification of Carbon Sources and Sinks in Existing Tokamaks

Most of the carbon-clad divertor tokamaks consistently show a robust flow of carbon to the inboard divertor leg, which is always subject to deposition,

Table 12.4. Summary of the retention and removal characteristics for leading plasma-facing material options for a next-step [76]

Material	**Tritium Retention Level**	**Release Temperature***
Beryllium (Bulk)	High after long-term neutron exposure	800–1200 K
Beryllium (Co-deposit)	Low to moderate, depending on oxygen in vessel	500–800 K
Tungsten	Low	1000–1400 K
Carbon (Saturated Layer)	Low	600–1000 K
Carbon (Pore Absorption)	Low	500–900 K
Carbon (Co-deposit)	Extremely high	600–1000 K (Vac), 400–600 K (Air)
Carbon (Bulk)	Potentially high, depending on temperature and neutrons	1200–1700 K

* Release temperatures are for vacuum unless otherwise stated

whereas the outboard divertor could be subject to net erosion or deposition, depending on the local plasma conditions [77]. The factor that influences this *net* carbon transport, and its resulting tritium retention (largely independent of operating regime) are (*i*) the main chamber wall, which is believed to be the largest source of carbon, (*ii*) the large SOL flow transports of carbon to the inboard target, whose origin is not well understood, (*iii*) local divertor processes, which ultimately determine where co-deposition occurs. The role of plasma edge conditions and of type-I ELMs on this phenomena is poorly understood.

Be-evaporation at JET and boronization in other devices act as metallic markers and allow studies of material transport. Surface analysis of JET and TEXTOR tiles show very clearly that long-range transport is only observed for carbon. In addition to markers, ^{13}C marked methane has been recently injected in various machines. As an example, Secondary Ion Mass Spectroscopy (SIMS) analysis of JET tiles show a strong enrichment of ^{13}C on top of the surface of the inboard divertor tiles whereas no corresponding ^{13}C was found in the outboard divertor. This proves that impurities are dragged towards the inboard divertor. However, the near top surface shows much more C and D than measured in deeper layers and on tiles from previous MKIIGB operation and no ^{13}C could be identified on the shadowed regions of the divertor tiles.

The installation of large areas of tungsten on the inner central column of ASDEX Upgrade [26] provides additional useful information on the migra-

tion of carbon and accentuates the importance of primary carbon sources. Interestingly enough, a strong carbon influx is found at the heat shield on the high-field side [78], even though 85% of the heat shield area is covered by tungsten coatings. Deposited carbon was found to be abundant on the surface of these tiles [26]. This carbon is subject to erosion and moves into the plasma. An equilibrium of erosion and deposition, which connects all surfaces in ASDEX Upgrade, is obtained during operation. Clearly, the carbon, which is seen to be eroded from the heat shield, originates from a net carbon source, possibly the guard limiters. The limiter carbon source is in most cases smaller than the heat shield source, but still it is of the same magnitude and could be responsible for supplying the deposited carbon. This carbon is recycling at the inner heat shield either on a discharge-to-discharge time scale, or even within a single discharge comparable to hydrogen recycling. The ongoing tungsten experiment at ASDEX Upgrade will give answers to this question, as more and more net carbon sources are replaced by tungsten surfaces.

Sources of carbon and beryllium in the main chamber of JET are being compared with the amount of material deposited in the divertor as measured by surface analysis [79]. Suitably weighted spectroscopic data have been integrated over the relevant periods of operation corresponding to the time between machine interventions in which divertor tiles were removed for analysis. The amount of carbon present on the plasma-facing sides of the divertor is measured by thickness monitoring and SIMS depth profiling. However, a significant part is transported to remote areas by transport processes induced by chemical erosion, and this has not been determined so far in detail. Ion beam analysis of the layers from MKIIA and previous MKIIGB operation show large amounts of Be (which is evaporated in JET only in the main chamber) in the inboard but little in the outboard divertor. This confirms that the main chamber is the main source of material which is deposited on the inboard divertor, and that SOL flows drive the Be and C impurities exclusively to the inboard divertor [1, 38]. Another important finding is that the layers are Be-rich on the plasma-facing sides with a typical Be/C ratio of 2 or larger, although Be is a minority in the down streaming impurity flux, as estimated from spectroscopic data (≈ 0.1 Be/C). Obviously, the carbon co-deposited together with the Be has been re-eroded, most probably by chemical erosion (physical sputtering is of similar strength for Be) and transported towards the cold areas of the louvers. These layers on the cold louvers are essentially free of Be demonstrating that the long range material transport is a speciality of carbon and not expected for any PFC metal material, such as Be or W. The analysis of the divertor carbon fluxes, based on the calibrated CIII spectroscopy [80], shows that that the total carbon flux from the divertor surfaces is about ten times the carbon flux entering the main plasma from the wall. Since the divertor is a net deposition zone, this implies that each carbon atom that arrives in the divertor from the main chamber makes at least ten steps before it is lost to remote areas. The average sputtering yields in the inboard divertor, outboard divertor, and main

chamber derived from combining the particle fluxes deduced from D_α with the carbon fluxes derived from CIII spectroscopy are all close to 4%.

Hydrocarbon Film Formation in Divertor Areas Remote from the Plasma

Deposition in the remote areas of the ITER divertor (see Fig. 12.2) is expected to occur because of the sticking of hydrocarbon radicals produced directly in areas of net erosion near the strike points and transported across the low-temperature plasma (few eV) at the divertor leg or from the interaction and transformation of species with the plasma.

Hydrocarbon radicals with high sticking probability (e.g., with sticking near unity, like C, CH, C_2H_x) would lead to film formation in areas of 'first bounce', i.e., near the divertor leg, underneath the divertor dome (Fig. 12.2). The large amount of hydrocarbon film deposits found in shaded regions of the inboard JET divertor (e.g., the cold louvres in front of the pumping duct) were explained by re-deposition of C_2H_x species [81]. Less reactive species, with much lower sticking probability, like CH_2, CH_3 and C_2H_5 would instead survive many wall collisions (of the order of 10^2–10^3) and migrate long distances, and can be deposited at regions very remote from the source [82] (e.g., the surfaces of the divertor cassettes and pumping ducts in Fig. 12.2). The competition between erosion and deposition will depend on local plasma parameters, atomic hydrogen concentration, surface temperature, and geometry effects.

Vigorous R&D is in progress in various tokamaks and in laboratory studies to investigate hydrocarbon film formation. The main results can be summarized as follows:

Surveys in Tokamaks

Recent measurements with an installed quartz microbalance in front of the inboard-louvre at JET [83], point to a different deposition pattern and to a lower deposition rate than during DTE1 [84]. A thorough investigation is underway to explain these differences and to model the observed dependence of the measured average growth rate from the position of the strike point (which is seen to have a major role), the frequency of ELMs and the temperature of the main chamber wall. Similarly, measurements with deposition monitors in ASDEX Upgrade [85, 86] and TEXTOR [87] showed that layers observed in areas remote from the plasma (i.e., underneath the baffle structure in ASDEX Upgrade and in the pumping duct in TEXTOR [87]) are formed primarily by species with high sticking probability. Only a very small amount of deposition was found in the pump ducts, revealing a low population of low sticking species. This is in contrast with early results in TEXTOR 94 where growth of polymer-like hydrocarbon layers with a deposition rate of 0.02 nm/s was observed on long term samples at a distance of 1 m away from the neutralizer

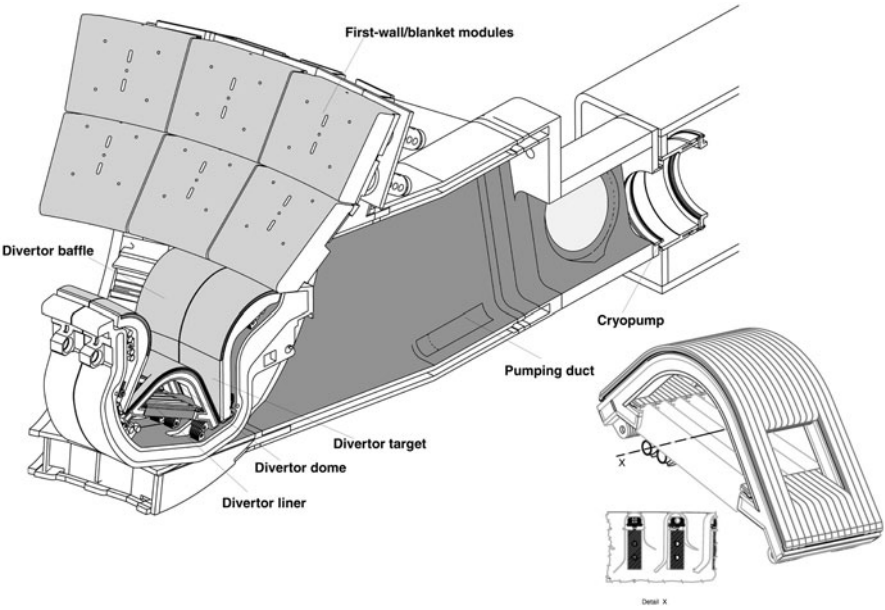

Fig. 12.2. Isometric view of the ITER divertor and pumping duct regions. One can see in *dark grey* the area hidden from the plasma near the plasma source and farther away where deposition of hydrocarbon radicals can potentially occur

plate of a pumped limiter [88]. Although the extrapolation of these results to ITER is uncertain, these results would suggest that under ITER conditions high sticking probability species will dominate.

Recent results from the National Spherical Torus Experiment [89] revealed hydrocarbon deposition averaging 0.1–0.2 nm per 0.5 s discharge on a plasma-facing quartz microbalance installed 0.8 m from the last closed flux surface. An identical microbalance in the same location but facing away from the plasma recorded deposition of low sticking probability radicals at a rate about 10% of the deposition on the plasma-facing surface. A hydrocarbon layer of 10–20 nm is sufficient to substantially affect optical reflectivity [90] and these results illustrate the potential for rapid degradation of important diagnostic mirrors in long pulse machines and the need for the development of in-situ cleaning methods.

Laboratory Studies

They include investigations in linear plasma devices (i.e., PSI-2 at IPP Berlin and PISCES-B at UCSD), where plasma conditions are very similar to those expected in the ITER divertor, and simpler plasma devices or particle beam experiments. Here individual processes can be investigated and understood in isolation and, generally, conditions are better controlled and diagnosed

than in tokamaks. Nevertheless, intrinsic complexities and problems remain, particularly with linear plasma devices, and often it is difficult to characterize quantities/parameters of interests and discriminate between synergistic causes/effects.

- The dependence of the surface temperature on the CH_3 sticking coefficient was investigated by Meier et al. [91, 92]. At low surface temperatures (<470 K), steady state film growth is observed corresponding to an effective sticking coefficient of $s(CH_3) \sim 10^{-5}$. The steady-state growth mechanism is described by the sequence of formation of dangling bonds by abstraction of surface-bonded hydrogen by CH_3 followed by chemisorption of CH_3 radicals on dangling bonds. At elevated temperature ($500 < T_s < 700\,K$), net growth changes into net erosion. At even higher surface temperatures ($> 700\,K$), the sticking coefficient of CH_3 becomes positive again and net deposition is observed.
- In preliminary experiments conducted in the PSI-2 facility [93], the temperature of the collecting surface where erosion of carbon is seen to overcome deposition was inferred to be lower (e.g., about 370 K) than that mentioned above. Further work is in underway to determine the dependence of the erosion and deposition mechanisms from the experimental parameters (Sect. 12.5).
- A pronounced effect of atomic hydrogen on the deposition rate was found in experiments using quantified radical-beam sources [94]. The sticking coefficient of methyl radicals can be enhanced by about two orders of magnitude if the surface is activated by a sufficiently high flux of atomic hydrogen (of the order of $10^{19}\,H/m^2\,s$).

Mixed-Material Effects

Mixed-materials effects, arising in particular from the simultaneous use of Be on the first wall components, introduce significant uncertainties for the operation of a tokamak like ITER. In particular, due to its low surface binding energy ($\sim 3\,eV$), Be will be subject to strong physical erosion and thus a beryllium plasma concentration in the range from 1% to 10% should be expected in the ITER divertor region. This could lead to the formation of a Be-rich film that could substantially reduce or eliminate the chemical erosion of carbon and reduce the consequent tritium co-deposition. Experiments to elucidate these effects are ongoing in the linear plasma simulator PISCES-B [75]. However, the beryllium-rich surface layer, if any, would tend to be removed periodically by ELMs and disruptions.

In order to investigate the influence of beryllium as a plasma impurity on the chemical erosion of carbon tiles at the divertor strike point, various types of carbons were exposed to a beryllium-seeded, steady state D-plasma in the PISCES-B facility (typical exposure parameters are: $n_e \sim 1$–$5 \times 10^{18}\,m^{-3}$, $\Gamma_D \sim 1$–$5 \times 10^{22}\,m^2 \times s^{-1}$, $T_{Sample} \sim 330$–$970\,K$ and a total exposure time

of up to 10^4 s). Chemical erosion was monitored by CD-band spectroscopy. A general feature observed in these experiments is the reduction of chemical erosion even at small (0.15%) beryllium impurity concentration. Post exposure Scanning Electron Microscopy (SEM) imaging revealed strong changes of the surface morphology (e.g., tall grass-like structures were observed on the samples exposed without Be seeding, whereas columnar structures appeared on the samples exposed with Be seeding).

12.4 ITER Tritium Retention Estimates and Uncertainties

Erosion and deposition constitute one of the key topics in preparation of ITER operation, as they influence the in-vessel tritium inventory and the lifetime of divertor tiles and other PFCs. Assessment of erosion is discussed elsewhere [39, 41].

Accurate estimates of the accumulation of tritium on the surface and in the bulk of the materials of the various PFCs of ITER and the degree of tritium permeation to the coolant are very important for determining the tritium supply requirements, for assessing the radiological hazards from routine operation and from potential accidents, and for decisions regarding the de-tritiation system.

Tritium co-deposition with eroded carbon, during the D-T phase, is anticipated to be the dominant tritium retention mechanism in ITER even if the use of carbon is limited to the divertor strike plates. Retention by implantation and bulk diffusion at the Be-clad surfaces of the first wall and W-clad surfaces of the divertor are expected to rapidly reach saturation, or to marginally contribute to the in-vessel tritium-uptake [95, 96]. In addition, adsorption of tritium at the inner surfaces of the porous CFC of the vertical target is expected to be very small (few g-T) and adsorbed tritium is not expected to significantly diffuse into the carbon matrix because the temperature of the majority of the bulk CFC will be significantly below 1200 K (Table 12.4).

The quantification of the co-deposition rate in ITER is still subject to large uncertainties and analysis carried out to date provide only general trends rather than accurate predictions. This subject is thoroughly discussed in several publications (see for example [97]). The main uncertainties arise primarily from the plasma edge physics parameters, which are anticipated to strongly affect the erosion, deposition and co-deposition patterns and rates, from uncertainties of the chemical erosion yields at high fluxes [33] and from the effect of temperature and H-atomic flux on deposition patterns and rates in areas hidden from the plasma.

Divertor erosion/co-deposition estimates in ITER are based on the REDEP/WBC code package [98–100]. Power fluxes as well as plasma particle fluxes (i.e., D-T ions and atoms, and impurities such as helium and carbon)

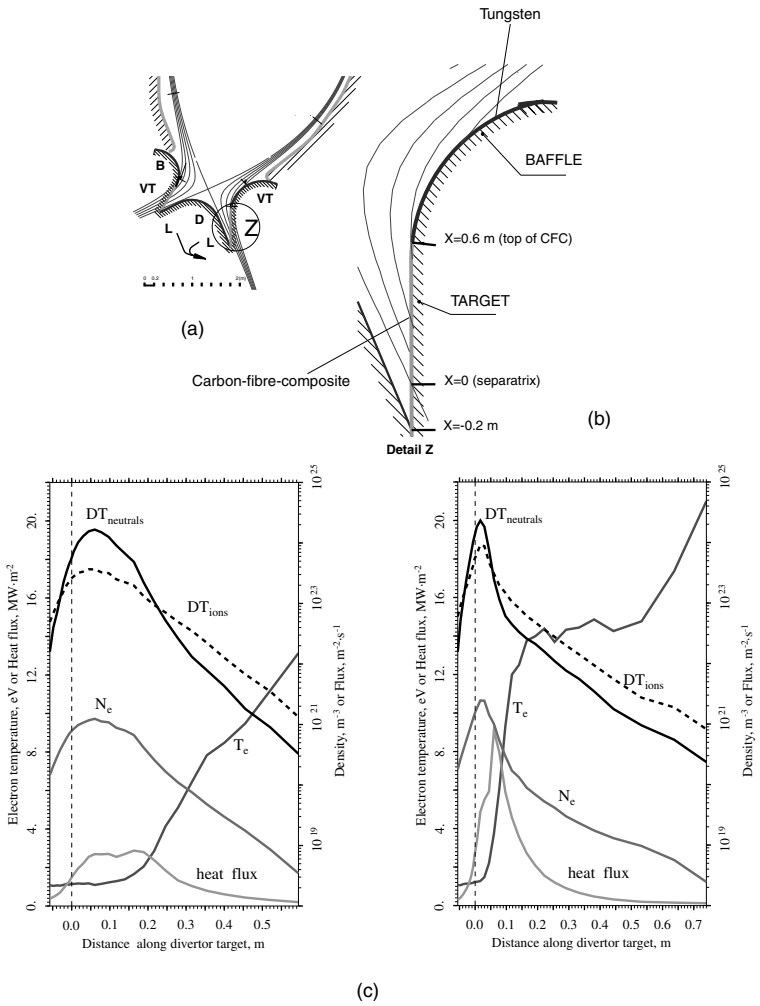

Fig. 12.3. (**a**) ITER poloidal cross-section showing the divertor vertical target (VT), divertor baffle (B), and divertor private region consisting of dome (D), and liner (L). (**b**) Detail of the divertor target. (**c**) Plasma temperature, density, particle and heat fluxes along the ITER outer divertor target for a reference semi-detached edge plasma. **Left**: inboard divertor target; **right**: outboard divertor target

are computed with the code B2–EIRENE [101, 102] (see Fig. 12.3). Chemical sputtering of carbon by D-T ions, atoms, and molecules, more important here than physical sputtering, is calculated using the yields of [103]. These yields at high fluxes remain uncertain [1], because their determination in plasma experiments is extremely difficult due to uncertainties in plasma parameters, redeposition fractions, and diagnostics interpretation. Co-deposition result-

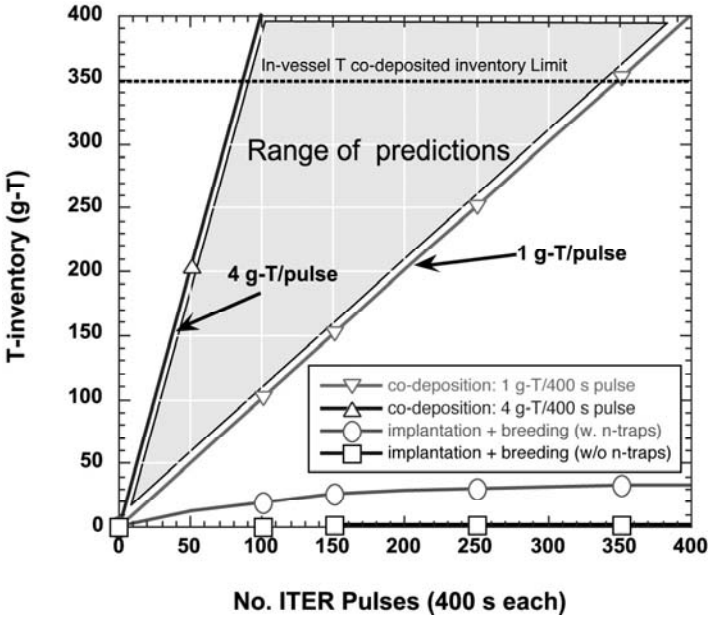

Fig. 12.4. Comparison of predicted rates of tritium accumulation due to co-deposition and implantation in the beryllium first wall including breeding. Each pulse is assumed to be 400 s

ing from carbon eroded from ELMs is not included, although recently ELMs were observed to affect deposition in JET (Sect. 12.3.4).

The maximum computed tritium co-deposition rate is expected to be $< 10\,\mathrm{gT}/1000\,\mathrm{s}$ (i.e., 4 gT/ITER pulse) (see Fig. 12.4). The peak net erosion rate is $\sim 20\,\mathrm{nm/s}$ (gross erosion rate 105 nm/s), occurring near the strike point. In addition, it is found that (*i*) carbon chemical sputtering in the detached region along each plate is the main source of net carbon erosion and tritium co-deposition, and chemical sputtering in the attached regions has essentially no contribution to net erosion (due to $\sim 100\%$ redeposition), (*ii*) physical sputtering of the entire plate contributes about 20% to the co-deposition, (*iii*) $\sim 75\%$ of growth/co-deposition occurs on the bottom of the divertor and/or dump plates, and $\sim 25\%$ occurs in the private-flux region. This latter point was established only for the ITER 98 design, but similar results are expected for the final ITER design. In addition to the divertor analysis, the tritium co-deposition in wall-sputtered redeposited beryllium has been computed and is estimated to be in the range of 0.1–0.4 g-T/400 s pulse. In ITER a first wall made of carbon would lead to an unacceptably high level of tritium co-deposition (i.e., $> 1\,\mathrm{gT}$/pulse [39]) (see Table 12.5).

Table 12.5. First wall erosion and resulting tritium co-deposition rates in the divertor[(a)] [39]

	Peak (average) erosion rate δ_M(μm/400 s)	Mass eroded δ_M (g/400 s)	T-codep. rate δ_T (g/400 s)
Be	0.027 (1.3×10^{-2})	17	0.1 (T/Be $\sim$ 0.05)
BeO[(b)]	0.016 (4.1×10^{-3})	5.3	0.1 (T/BeO $\sim$ 0.1)
W[(b)]	2×10^{-3} (1.2×10^{-3})	16	0
C[(b)]	0.016 (1.7×10^{-2})	24	~ 1

[(a)] it is assumed that this material will be transported to the divertor. [(b)] Shown only for comparison.

Retention by implantation and bulk diffusion on metallic surfaces of the first wall and divertor are expected to marginally contribute to the in-vessel tritium-uptake [96] (see Fig. 12.4).

12.5 Further Research and Development (R&D) Needs

Research in the area of tritium retention and release has increased substantially in just the last few years. However, there are still several issues that require further urgent work and whose resolution requires a coordinated R&D effort, involving extensive participation by all parts of the fusion community. A concise discussion on some of the areas of highest priority is provided below.

(a) Identification of Carbon Sources and Sinks in Existing Tokamaks

There has been increased effort in recent years to pin down carbon sources in existing machines i.e., to understand and (possibly) influence material transport toward the divertor and, most important, to elucidate the transport mechanisms of carbon inside the divertor and from the divertor volume towards remote areas or gaps. However, there are still large uncertainties, and further work is needed. Material data uncertainties with carbon include the possible flux dependence, if any, of carbon chemical sputtering, very low energy but non-thermal ($\sim$ 1–3 eV) hydrocarbon reflection coefficients, and overall properties of redeposited materials [33]. The tools to compare results between different devices are not clearly established and the underlying physics of the transport of the eroded carbon in the SOL by flows and drifts

is largely unclear. Finally, the present modeling tools for the local transport of carbon along the divertor plates toward shadowed areas or gaps can only marginally reproduce the experimental observations. Further development and use of in-situ time-resolved diagnostics (see (h)) can help improve understanding on the physics of erosion mechanisms in tokamak and the transport and re-deposition of eroded material and their dependence of plasma edge and operation parameters.

(b) Hydrocarbon Film Formation in Divertor Areas Remote from the Plasma

Investigations are in progress in several laboratories to better understand the chemistry and the patterns of hydrocarbon deposition, and the controlling parameters [104]. These experiments, aided by modeling, are expected to generate important data that will be used to optimize the divertor design to mitigate or off-set formation of T-rich films in plasma-hidden areas [105]. Unfortunately, a direct comparison of the modeling with available experimental results is not yet possible. Furthermore, the contribution of hydrogen atoms to the erosion process can be significant. This depends to a large degree on their density and temperature of the collecting surface, two parameters which could be measured to date only with a large uncertainty.

(c) Mixed-Materials

Material erosion, and the subsequent transport of impurities, will inevitably lead to a certain amount of material mixing between the in-vessel components that in ITER will be clad with different armour materials. For example, CFC surfaces will become doped with W or Be impurities and the metal surfaces will become contaminated with carbon or other metals. Erosion of beryllium in ITER will lead to the formation of beryllium-rich films (from Be eroded at the main wall) near the strike points on the carbon target plate, that could substantially reduce the chemical erosion of carbon and the consequent tritium co-deposition. Experiments to elucidate these effects are underway in the linear plasma simulator PISCES-B [75]. However, this mitigating effect could be inhibited by the local high temperature of the plate near the strike points and the occurrence of ELMs and disruptions, which would tend to remove periodically these films. In addition, there is some concern from potential adverse effects arising from mixing of Be and W, e.g., formation of low melting point compounds, which require further urgent investigations.

(d) Role of ELMs on Tritium Co-deposition in ITER

A further important point that requires further investigations in existing tokamaks is the contribution that type I ELMs could have in ITER on tritium co-deposition in areas of the divertor remote from the plasma. The

contribution of the ELM period to the total net erosion was found negligible in DIII-D, and it is the quiescent period that determines the net erosion rate [106]. However, unlike DIII-D, ELMs in ITER will cause erosion primarily by thermal ablation in addition to erosion by sputtering, and this could change the picture drastically. During the DTE1 phase at JET, hot ion ELMy H modes with large ELMs with the strike point at the base plate were mainly used. This configuration is expected to be especially effective to transport carbon towards the louver gap where most of the tritium was found to be trapped. Currently, more work is underway at JET to identify the underlying reasons for the large variations in the carbon deposition at the lower strike point position [84]. Although this analysis is not completed, the present results show that the largest deposition is for discharges with the strike point near the detector and with type I low frequency ELMs.

(e) Mitigation of Hydrocarbon Film Formation in Remote Areas of ITER

The possibility of inhibiting the formation of T-containing co-deposited films in carbon machines by the injection of suitable scavengers has been recently proposed [107]. In particular, the injection of nitrogen in H_2/CH_4 deposition plasmas has been found in laboratory studies to be able to completely suppress the formation of hydrogenated carbon films at N_2/CH_4 ratios ~ 1 Studies oriented to the understanding of the physical and chemical processes responsible for such effect are presently in progress in laboratory experiments. These include the characterization of the plasma species as well that of the by-products of the reaction, together with the relative role of the wall and gas phase processes. Simultaneously, the characterization of carbon migration in tokamak divertors by in-situ techniques such as QMB opens the possibility of testing the concept in various plasma scenarios. Ongoing experiments at ASDEX Upgrade and JET in this direction must be continued.

(f) In-situ Tritium Removal Techniques

No relevant method to remove tritium has been established on a working tokamak. Clearly, there is a need for engineering-scale demonstration experiments of tritium removal. First experiments in a tokamak using oxygen with hot walls (620 K) to remove co-deposits have been performed in TEXTOR [108]. However, the analysis carried out to date do not enable any reliable conclusion on the efficiency of oxygen injection of the total amount of D depleted from the machine. Encouragingly, TEXTOR did not experience any long term adverse consequences after the use of oxygen to remove deuterium, and high performance plasma operation could be recovered after 15–30 min of GDC in helium and deuterium.

A demonstration of a promising flash-lamp detritiation method has been carried out for the JET 2004 shutdown. Without established fast and efficient tritium removal method a satisfactory schedule of burning plasma operations in a machine with carbon PFCs appears impractical.

(g) Modeling and Improvement of Predictive Capabilities

Numerous efforts have been made recently to validate state-of-the-art erosion/redepostion codes (such as ERO and REDEP) against available experimental results. Typically, qualitative features can be modeled but, with a few exception quantitative agreement is not obtained. Unlike the situation for physical sputtering and/or higher edge plasma temperature regimes, where good code/data validation exists, the erosion/redeposition codes are not well validated for detached conditions. As an example, there is a large discrepancy between code/data results for JET, with the codes under-predicting co-deposition by factors of roughly 10–40 [97, 109]. More work is clearly needed in this area.

(h) Improvement of Wall and Plasma Edge Diagnostics

Most of the progress described above has been achieved mainly thanks to the installation of time-resolved diagnostics (e.g., QMB at JET, TEXTOR and ASDEX Upgrade – Sect. 12.3). So-called "*archeological studies*", primarily based on analysis of long term samples, removed during maintenance procedures or upgrades, have long provided the mainstay of PMI studies. Unfortunately, although they allow levels of erosion and surface modification to be accurately determined, relating the data obtained to specific conditions in the plasma–wall interaction region is difficult as the samples typically represent an integration over many shots and many different experimental campaigns. There is a strong case for the development of new, more advanced wall diagnostic techniques and time-resolved measurements (e.g., QMBs, sensitive Langmuir probes, charge exchange neutral measurements, IR camera, erosion/deposition collector probes, microbalances, laser desorption to measure D/C ratio of hydrocarbon films, sticking probes, molecular spectroscopy,) and substantially increased operational time allocated to PMI studies in existing devices to quantify the erosion and deposition effects and to better understand the underlying causes. Instrumentation and careful time resolved measurements will be also needed in ITER to control the inventory during operation. A range of diagnostics for tritium retention studies is being developed and will be installed at JET. The proposed diagnostics include additional QMBs to study effects of temperature and to monitor beryllium evaporation, rotating collectors, deposition monitors, and long term collectors in various parts of the divertor and main chamber. A poloidal set of especially designed tiles will be installed in the divertor, together with tiles at selected points on the inboard and outboard limiters.

(i) Material Experiments in Existing Tokamaks

Experiments in laboratory simulation facilities, while useful to probe fundamental processes, and to study phenomena in isolation, are not sufficient to address all aspects and uncertainties associated with co-deposition in

ITER. This will remain a major difficulty unless experimentally validated in tokamaks with impurities and relevant wall materials to provide a realistic test-bed which would closely mirror options proposed for the next-step device (e.g., beryllium walls and carbon and/or tungsten divertor proposed for ITER). Such experiments would indeed help answer questions including the magnitudes of erosion and tritium co-deposition, dust formation in the vessel, the ease of tritium removal from mixed-materials, as well as operational aspects (e.g., of using beryllium on the first wall).

(j) Selection of Plasma Facing Materials

Dedicated experiments in tokamaks are needed and partially underway focussing on the characterization of power deposition during type I ELMs, disruptions and development of disruption mitigation techniques. Generally, only a fraction of the plasma thermal energy lost during disruptions appears in the divertor [110, 111]. In addition, the power deposition profile in the divertor is found to be very wide, spreading over the whole divertor surface. If these results extrapolate to ITER, then a disruption would not damage a W-clad target. However, if the is the missing thermal and magnetic energy reached the main chamber, and if this energy is not sufficiently uniform, then additional damage to main chamber components may be expected. In particular, there is some concern that a Be first wall in ITER could be subjected to damage even during mitigated disruptions and Type I ELMs. Further work on this area is needed before drawing firm conclusions for ITER. This, together with a favorable operating experience with tungsten in the main chamber of ASDEX Upgrade, could lead to reconsideration of the use of Be on the first wall of ITER.

12.6 Conclusions

Safe management and accounting of tritium will be crucial for the acceptance of fusion as an environmentally benign power source. ITER will be routinely fuelled with mixtures of D and T, and tritium retention in plasma facing materials with CFC PFCs has emerged as a primary concern with strong implications for in-vessel component design, material selection, operational schedule and safety.

A key decision for ITER is the choice of plasma facing materials. Despite the prevalence and strong historic trend of operating tokamaks to rely on carbon-based PFCs in combination with oxygen gettering techniques such as boronization or siliconization (mainly to optimize plasma performance and to enable access to a large plasma operational space), its application to a D-T next-step must be restricted due to its strong chemical affinity to hydrogen-isotopes, which affects erosion lifetime and tritium inventory.

Currently, the ITER design contemplates the use of carbon only to clad the ITER divertor target, near the strike points, essentially because of its

greater resistance to excessive heat loads during ELMs and plasma disruptions. The first wall is clad with beryllium, and tungsten is used elsewhere in the divertor.

In this configuration, tritium co-deposition with eroded carbon is expected to be the dominant tritium retention mechanism in ITER. Retention by implantation and bulk diffusion on metallic surfaces of the first wall and divertor are expected to marginally contribute to the in-vessel tritium-uptake. The quantification of the co-deposition rate in ITER (currently estimated to be of the order of few g-T/pulse) is still subject to large uncertainties, which primarily arise from lack of understanding of underlying mechanisms and their dependence on plasma parameters and local geometrical conditions. Extrapolation from available tokamak experience (mainly JET) is very difficult because of the presence of carbon on the main chamber, which is believed to have contributed to large uptake observed during DTE1, and the lower temperature at the divertor surfaces hidden from the plasma, where co-deposited films form. Nevertheless, as long as carbon is used in ITER, efficient tritium recovery techniques (still to be developed and demonstrated in tokamaks) will be essential to control in-vessel tritium retention and to enable ITER to fulfill its mission.

The R&D program in current tokamaks and other fusion devices must continue to address the physics of the erosion mechanisms and the transport and re-deposition of eroded material and resulting mixing effects under conditions (e.g., plasma edge, materials, temperatures) as close as possible to those expected in ITER. These well-diagnosed experiments provide the database against which predictive models must be validated, and reliability of current projections to ITER tested. Dedicated experiments are underway to narrow the remaining uncertainties, in particular in the areas of mixed-materials and hydrocarbon transport and sticking probabilities.

However, ITER will operate with different main chamber materials than today's machines, and large uncertainties will remain until the proposed material-mix is validated in an existing tokamak. Nevertheless, some of the uncertainties are likely to persist – such that only ITER operation can precisely establish the co-deposition rate and the resulting implications on plasma performance and operation. The ITER design will have the flexibility to change the divertor and probably the entire first wall, albeit with consequences on machine availability, and the need to develop operating scenarios compatible with new materials. Replacement of first wall modules in ITER is much more complex than replacement of the divertor target cassettes and will lead to longer down times with implications for machine availability. In particular, the initial phase of operation with H- and D- plasmas will permit the exploration of these problem areas, to better quantify the resulting effects and the attendant uncertainties. Plasma edge and wall diagnostics in ITER, and adequate models sufficiently benchmarked against experiments, will be an essential element to implement this strategy.

Acknowledgements

The authors would like to acknowledge many fruitful discussions with scientists who are especially working on this field in the frame of the International Tokamak Program Activities (ITPA). Particular thanks to A. Loarte, V. Philipps, J. Roth, M. Shimada, M. Sugihara, G. Saibene, F. Tabares, and A.R. Polevoi for their direct contribution to this paper. This report was prepared as an account of work undertaken within the framework of ITER Transitional Arrangements (ITA). These are now conducted by the Participants, i.e., the European Atomic Energy Community, Japan, the Russian Federation, the USA, the People's Republic of China and the Republic of Korea under the auspices of the International Atomic Energy Agency. The views and opinions expressed herein do not necessarily reflect those of the Participants to the ITA, the IAEA or any agency thereof. Dissemination of the information in this paper is governed by the applicable terms of the former ITER-EDA Agreement. One of the authors (CS) acknowledges support from U.S. DOE Contract Nos. DE-AC02-76CH0307.

References

1. G. Federici, C.H. Skinner et al., Nucl. Fusion **41** (2001) 1967
2. U. Samm. In: this volume
3. V. Barabash, G. Federici, R. Matera, A.R. Raffray, and the ITER Home Teams, Phys. Scripta **T81** (1999) 74
4. M. Merola, M. Akiba, V. Barabash, I. Mazul, J. Nucl. Mater. **307-311** (2002) 1524
5. M. Merola et al., Fus. Eng. Des. **56-57** (2001) 173
6. H. Bolt et al., J. Nucl. Mater. **307-311** (2002) 43
7. G. McCracken, P.E. Stott, Nucl. Fusion **19** (1979) 889
8. J.P. Gunn et al., Plasma Phys. Contr. Fus. **41** (1999) B243
9. E.B. Meservey et al., J. Nucl. Mater. **93-94** (1980) 267
10. H. Eubank et al., PLT neutral beam heating results. In: Proc. 7th Conf. on Plasma Phys. Contr. Nucl. Fus. Res. held by the IAEA in Innsbruck (Austria) 1978, IAEA, Vienna Vol. 1 (1979) 167
11. E. Vietzke, A.A. Haasz. In: *Physical Processes of the Interaction of Fusion Plasmas with Solids*, Hofer, W.O., Roth, J. (eds.) (Academic Press, San Diego 1996). Section 4: Chemical erosion, p. 135
12. J. Roth, C. García-Rosales, Nucl. Fusion **36** (1996) 1647, with Corrigendum, Nucl. Fusion **37** (1997) 897
13. J. Roth et al., J. Nucl. Mater. **111-112** (1982) 775
14. V. Philipps et al., J. Nucl. Mater. **111-112** (1982) 781
15. W.R. Wampler et al., J. Vac. Sci. Technol **A6** (1988) 2111
16. J. P. Coad J. Nucl. Mater., **226** (1995) 156
17. C. H. Skinner et al., J. Vac. Sci. Technol., **A14** (1996) 3267
18. P.L. Andrew et al., Fus. Eng. Des. **47** (1999) 233
19. T.D. Burchell, Carbon **34** (1996) 297

20. P.R. Thomas et al., J. Nucl. Mater. **176-177** (1990) 3
21. P.K. Mioduszewski, Nucl. Fusion **26** (1986) 1171
22. J. Hackmann, J. Uhlenbusch, J. Nucl. Mater. **128-129** (1984) 418
23. I.H. Hutchinson et al., Phys. Plasmas **1** (1994) 1511
24. K. Krieger, H., Maier, R. Neu, and the ASDEX Upgrade Team, J. Nucl. Mater. **266-269** (1999) 207
25. R. Neu et al. J. Nucl. Mater. **290-293** (2001) 206
26. R. Neu et al. J. Nucl. Mater. **313-316** (2003) 116
27. R. Neu et al., Fus. Eng. Des. **65** (2003) 367
28. M.L. Apicella, Nucl. Fusion **37** (1997) 381
29. G.L. Jackson et al., J. Nucl. Mater. **220** (1995) 173
30. D.G. Whyte et al., J. Nucl. Mater. **241-243** (1997) 660
31. H.Y. Guo et al., J. Nucl. Mater. **241-243** (1997) 385
32. K. Shimizu et al., J. Nucl. Mater. **241-243** (1997) 167
33. J. Roth. In: this volume
34. W.R. Wampler et al., J. Nucl. Mater. **266-269** (1999) 217
35. D. Pappas et al., J. Nucl. Mater. **266-269** (1999) 635
36. G. Vieider et al., Fus. Eng. Des. **46** (1999) 221
37. M. Merola et al., J. Nucl. Mater. **283-287** (2000) 1068
38. A. Loarte. In: this volume
39. G. Federici et al., J. Nucl. Mater. **313-316** (2003) 11
40. A. Loarte et al., J. Nucl. Mater. **313-316** (2003) 962
41. G. Federici, A. Loarte, G. Strohmayer, Plasma Phys. Control. Fusion **45** (2003) 1523
42. R. Aymar et al., Plasma Phys. Control. Fusion **44** (2002) 519
43. ITER EDA Agreement and Protocol 2, ITER EDA Documentation Series No. 5, IAEA, Vienna, 1994
44. ITER Technical Basis, ITER EDA Documentation Series No 24, IAEA, Vienna, 2002
45. V. Mukhovatov et al., Comparison of ITER performance predicted by empirical, semi-empirical and theory-based transport models, 19th IAEA Fusion Energy Conference, 14-19 Oct. 2002, Lyon, France
46. M. Shimada et al., Nucl. Fusion **44** (2004) 350
47. H.D. Pacher, A. S. Kukushkin, G. W. Pacher and G. Janeschitz J. Nucl. Mater. **313-316** (2003) 657
48. K. Ioki et al., J. Nucl. Mater. **329-333** (2004) 31
49. W. Jacob. In: this volume
50. A. Makhankov et al., Fus. Eng. Des. **49-50** (2000) 275
51. I.I. Arkhipov et al., J. Nucl. Mater. **313-316** (2003) 342
52. C. Ibbott et al. Fus. Eng. Des. **56-57** (2001) 243
53. R. Parker et al., J. Nucl. Mater. **241-243** (1997) 1
54. G. Janeschitz et al., Nucl. Fusion **40** (2000) 1197
55. D.G. Whyte et al., Disruption mitigation using high-pressure noble gas injection in DIII-D, 19th IAEA Fusion Energy Conference, Lyon, France, 14-19 Oct. 2002 (paper EX/S2-4)
56. C. Skinner, G. Federici,Tritium issues in next step devices, International Conference on Advanced Diagnostics for Magnetic and Interial Fusion, Varenna, Italy, Sept 3-7, 2001
57. C.H. Skinner et al., J. Nucl. Mater. **266-269** (1999) 940

58. D. Mueller et al., Tritium retention and removal on TFTR. In: Proc. 17th IEEE/NPSS Symp. Fus. Eng., (San Diego, USA, 1997) Ed. IEEE, Piscataway New Jersey, IEEE 97CH36131, Vol. 1 (1998) 279
59. P.L. Andrew et al., J. Nucl. Mater. **266-269** (1999) 153
60. P.H. La Marche et al., Fus. Technol. **26** (1994) 427
61. C. Saville et al., Fus. Technol. **28** (1995) 1078
62. A. Nagy et al., TFTR tritium accounting system for DT operation. In: Proc. 16th IEEE/NPSS Symp. Fus. Eng., (Champaign, USA, 1995) Ed. IEEE, Piscataway New Jersey, IEEE 95CH35852, Vol. 2 (1996) 573
63. A.C. Bell, M. Wykes, B.J. Green, Fus. Eng. Des. **19** (1992) 169
64. J. DeLooper, Fus. Technol. **26** (1994) 1051
65. R.A. Causey, W.L. Chrisman, W.L., Hsu, R.A. Anderl, B. Wishard, J. Vac. Sci. Technol. **A7** (1989) 1078
66. R. Causey, W.R. Wampler, D. Walsh, D., J. Nucl. Mater. **176-177** (1990) 987
67. S. Chiu, A.A. Haasz, J. Vac. Sci. Technol. **A9** (1991) 747
68. A.A. Haasz, , J.W. Davis, J. Nucl. Mater. **256** (1998) 65
69. J.W. Davis, A.A. Haasz, J. Nucl. Mater. **266-269** (1999) 478
70. C.H. Skinner, C.A. Gentile, A. Carpe, G. Guttadora, S. Langish, K.M. Young, W.M. Shu, and H. Nakamura, J. Nucl. Mater. **301** (2002) 98
71. C.H. Skinner, et al., J. Nucl. Mater. **313-316** (2003) 496
72. K. Gibson, The removal of co-deposited hydrocarbon films from plasma facing components using high-powr pulsed flash lamp irradiation, J. Nucl. Mater. in press
73. A.A. Haasz. In: this volume
74. R.A. Anderl et al., J. Nucl. Mater. **273** (1999) 1
75. R.A. Doerner et al. In: this volume
76. R.A. Causey, J.N. Brooks, G. Federici, D. Petti, Fus. Eng. Des. **61-62** (2002) 525
77. D. Reiter. In: this volume
78. T. Putterich et al., Plasma Phys. Control. Fusion **45** (2003) 1873
79. G. Matthews et al., Material migration in JET, J. Nucl. Mater., in press
80. J.D. Strachan et al., submitted for publication in Nucl. Fusion (2002)
81. A. von Keudell, C. Hopf, T. Schwarz-Selinger, W. Jacob, Nucl. Fusion **39** (1999) 1451
82. M. Mayer et al., **313-316** (2003) 377
83. H.G. Esser et al., Fus. Eng. Des. **66-68** (2003) 855
84. V. Philipps et al., Recent results on long term fuel retention in JET and TEXTOR and predictions for ITER, 19th IAEA Fusion Energy Conference, Lyon, France, 14-19 Oct. 2002 (paper EX/P5-08)
85. V. Rohde et al., J. Nucl. Mater. **313-316** (2003) 429
86. V. Rohde, M. Mayer et al., J. Nucl. Mater. **313-316** (2003) 337
87. P. Wienhold et al., J. Nucl. Mater. **313-316** (2003) 311
88. M. Mayer, V. Philipps P. Wienhold, H.G. Esser, J. von Seggern and M. Rubel, J. Nucl. Mater. **290-293** (2001) 381
89. E.J. Synakowski, M.G. Bell, R.E. Bell, et al., The National Spherical Torus Experiment (NSTX) research program and progress towards high beta, long pulse operating scenarios, IAEA 2002 Lyon to be published in special issue of Nucl. Fusion 2003

90. V. Voitsenya et al., Rev. Sci. Instrum **72** (2001) 475
91. M. Meier, A. von Keudell, J. Chem. Phys. **116** (2002) 5125
92. M. Meier, A. von Keudell, W. Jacob, Nucl. Fusion **43** (2003) 25
93. G. Fussmann et al., Plasma Diagnostics, Max-Planck-Institut für Plasmaphysik, Annual Report 2002, p. 81
94. A. von Keudell et al., J. Applied. Physics **89** (2001) 2979
95. G. Federici et al., J. Nucl. Mater. **290-293** (2001) 260
96. G. Federici et al., Phys. Scripta, **T91** (2001) 76
97. J.N. Brooks et al., J. Nucl. Mater. **313-316** (2003) 424
98. J.N. Brooks, Nucl. Tech. Fusion **4** (1983) 33
99. J.N. Brooks, Phys. Fluids **8** (1990) 1858
100. J.N. Brooks, Fus. Eng. Des. **60** (2002) 515
101. D. Reiter et al., Plasma Phys. Contr. Fusion **33** (1991) 1579
102. R. Schneider et al., J. Nucl. Mater. **196-198** (1992) 810
103. G. Federici et al., J. Nucl. Mater. **266-269** (1999) 14
104. I. Arkhipov et al., J. Nucl. Mater. **290-293** (2001) 394
105. G. Federici et al., Modelling of deposition of hydrocarbon films underneath the divertor and in the pumping ducts of ITER, J. Nucl. Mater., in press
106. J.N. Brooks, D.G. Whyte, Nucl. Fusion **39** (1999) 525
107. F.L. Tabares et al., Plasma Phys. Control. Fusion **44** (2002) L37
108. V. Philipps et al., J. Nucl. Mater. **266-269** (1999) 386
109. A. Kirschner et al., Plasma Phys. Control. Fusion **45** (2003) 309
110. G.F. Matthews et al., Nucl. Fusion **43** (2003) 999
111. G. Pautasso et al., Analysis of the power deposition in ASDEX Upgrade disruptions, to be presented at the European Physical Society Conference in St. Petersburg, July 2003

13 Mixed and High-Z Plasma-Facing Materials in TEXTOR

E. Vietzke, A. Pospieszczyk, S. Brezinsek, A. Kirschner, A. Huber, T. Hirai, Ph. Mertens, V. Philipps, and G. Sergienko

The main concerns with graphite in a fusion device are associated with its large chemical erosion by hydrogen isotopes and oxygen and by the formation of hydrogen-rich carbon layers, which in the case of tritium, results in a high tritium inventory. Laboratory experiments show a reduced erosion yield of doped carbon materials. Therefore, test limiter experiments have been performed in TEXTOR to investigate alternative materials under plasma exposure. The erosion and redeposition results of some mixed materials, such as amorphous Si/C-films ("siliconization"), Si-doped CFC (NS31), B_4C-coated copper, are reviewed in comparison to carbon from test limiter investigations in TEXTOR discharges. In the first two cases, the C and O flux on the toroidal limiter was reduced and no SiD_x formation at a limiter temperature of 550 K was observed. The surface temperature of the B_4C coated copper limiter reached 1200 K for a power load of 4 MW/m^2. No severe delamination of the B_4C coating occurred after 80 exposures. For a direct comparison twin limiter experiments on C/W and W/Ta were performed. The D_γ line of the re-emitted D flux was about 25% larger on C than on W. The re-deposition of C on initially pure W limiter was modeled by the ERO-TEXTOR code. The build-up of a net-deposition zone and a net-erosion zone on the W limiter was in agreement with the experimental observations.

13.1 Introduction

During the last two decades of fusion research all fusion devices, with few exceptions, have implemented low-Z carbon based materials as plasma-facing materials. This has improved the performance of these devices, significantly contributing to the steady increase of the fusion triple product of density, temperature and energy confinement. Optimization of the core plasma performance was the main driver for the use of graphite. A large operational database exists for these materials, which allows a reasonable prediction of the global plasma performance for future devices. Graphite materials are currently used, in general in combination with special wall conditioning procedures like boronization, siliconization, lithium injection or beryllium evaporation [1–4], which reduce the oxygen impurities and improve the density control. These plasma-facing components have to withstand the α-particles

and external heating power [5], including off-normal events such as high heat loads from disruptions or runaway electrons. Furthermore, the α-particles have to be exhausted efficiently.

Plasma conditions and wall materials must also enable a sufficient lifetime of the first wall components for economic reasons. Chemical erosion of graphite leads to significant erosion yields even under low-temperature, cold plasma conditions and can seriously limit the lifetime. Since the tokamak is a fairly closed system, most of the eroded material will be re-deposited somewhere inside the machine. The question of tritium retention and overall inventory in the device is closely connected to the chemical erosion and to possible co-deposition as well [6, 7]. In order to minimize the net-erosion and optimize the lifetime of wall components, the re-deposition should be concentrated in areas of major erosion. Another way to minimize chemical erosion is the use of mixed materials, which – in laboratory experiments – display a reduced erosion yield in comparison to pure graphite.

The most promising alternative category of plasma-facing materials are the high-Z materials. These materials have acceptable thermo-mechanical properties, the possible advantage of very low or negligible erosion at low plasma temperatures and a moderate uptake of tritium. These advantages compete with their strong poisoning effect of the plasma and allow, therefore, only a narrow operational regime compared to operation with graphite walls. Although interesting new experiences have recently been obtained with high-Z wall materials in several devices [8–15], the present database is not such that their use on a large scale in future devices such as ITER is confirmed, which urgently calls for more experiments in present devices.

Therefore, major activities on TEXTOR were to analyze the erosion and deposition processes including local particle transport, on studying the hydrogen recycling and on investigating the behavior of several test limiters made of different materials or of different samples of doped carbons during TEXTOR discharges. The materials investigated in comparison to pure carbon were thin boron or silicon films on all walls (so-called boronization and siliconization), silicon-doped CFC material (NS31), tungsten and tungsten-coated graphite, tantalum and thick B_4C-coated copper as the limiter material. NS31 is a reference material for the lower divertor target foreseen for ITER, and B_4C-coated copper is foreseen for the first wall of the stellarator W7-X in Greifswald.

13.2 Silicon–Carbon Material

13.2.1 Siliconization

The siliconization results in a reduction of the oxygen impurity and also initially in a suppression of the carbon content in the plasma [16] as seen in Fig. 13.1. Silicon is released mainly by physical sputtering. An experimental

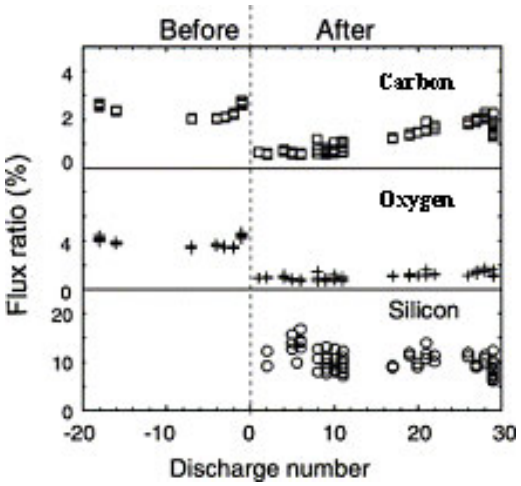

Fig. 13.1. Evolution of the relative flux ratios before and after siliconization of carbon, oxygen and silicon measured on the ALT toroidal limiter as a function of shot number. The data are for a density of $3 \times 10^{13}/\mathrm{cm}^3$ with 1.3 MW nuclear beam heating (co-injection)

confirmation was given in front of a test limiter by laser- induced fluorescence in situ, albeit for the case of doped material, in [17]. But no significant SiD_4 release was observed at a wall temperature of 570 K and also the Si deposition on C surfaces does not significantly affect the hydrocarbon formation (Fig. 13.2).

However, the silicon deposited at the wall has a large influence on the plasma performance. It gave access to high density ($1.7 \times n_{Greenwald}$) due to postponed MARFEs and improved the energy confinement ("Radiative-Improved-Mode, (RI-mode)" with radiation from intrinsically sputtered Si) [18].

13.2.2 Silicon-Doped CFC Material

Silicon-doped CFC material (NS31) was exposed as a test limiter to the TEXTOR plasma [19]. In Fig. 13.3 some results are shown in comparison to pure graphite. It was found that the methane formation is slightly reduced compared to that on a pure graphite target. The yield is between 2–3% over the whole range of plasma densities, while on graphite the yield increases with plasma density. At the highest densities ($\sim 5 \times 10^{19}\,\mathrm{m}^{-3}$) the reduction factor reaches about 2. The overall carbon ion flux from the silicon-doped graphite limiter is only slightly reduced compared to that for graphite limiters. Although the material contains only about 1.0–1.5% of Si, a remarkable Si/D flux between 0.12% and 0.4% was observed spectroscopically. More about spectroscopic observation of SiI and SiII can be found in [20]. A significant chemical erosion in the form of SiD_x has not been detected.

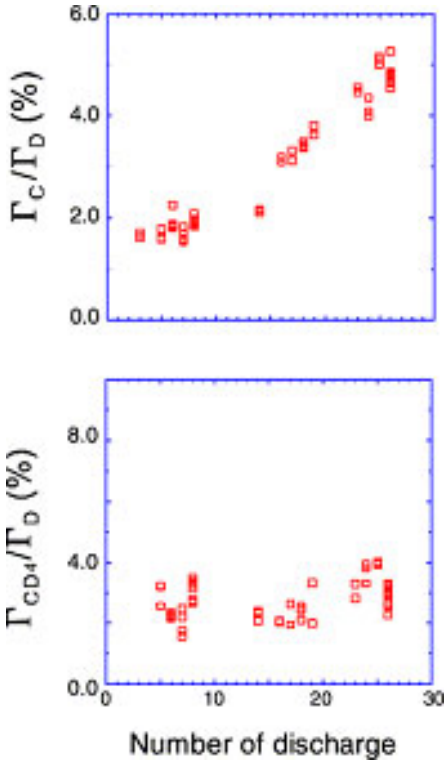

Fig. 13.2. Development of the C^+ and CD flux ratio as function of the discharge number for a graphite test limiter inserted in a freshly siliconized TEXTOR environment

At surface temperatures exceeding about 1800 K (see Fig. 13.4) the silicon evaporation begins to overcome the sputtered Si-flux leading to an increase of the Si concentration in the plasma and of the total radiation losses. Surface analysis revealed the formation of microcracks and holes. A depletion of silicon was observed in areas of the highest power load with values of 0.03% in and 0.02% between the fibres. Part of the released silicon was found on the limiter surface in the vicinity of the tangency point.

13.3 Twin Limiter Experiments

Twin limiter experiments allow us to directly compare two different material properties influenced by the tokamak edge plasma. First, carbon and tungsten have been investigated and compared as plasma-facing materials [21–25]. With the same D-flux impinging on the carbon and tungsten surfaces, the intensity of the D_γ-line is about 20–30% larger on carbon (Fig. 13.5). This can

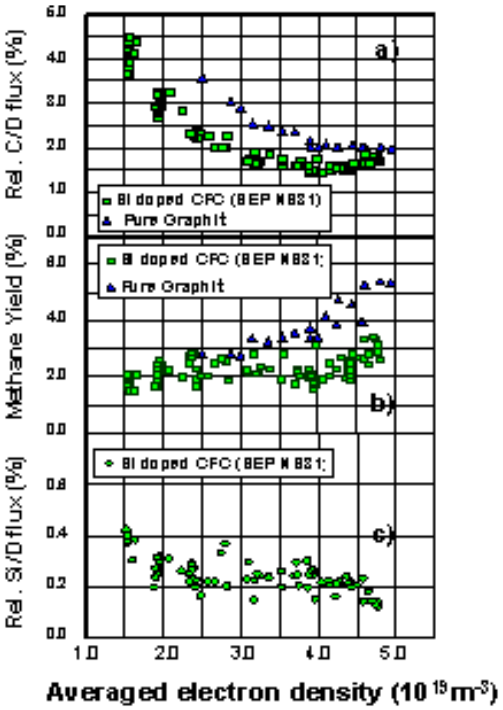

Fig. 13.3. Evolution of the relative flux ratios of carbon (**a**), methane (**b**) and silicon (**c**) measured from pure graphite and Si-doped CFC limiters as a function of the average electron density

be explained by the different hydrogen reflection properties and a different branching ratio of hydrogen release as atoms or molecules. A post-mortem analysis showed no carbon layer ($<10^{19}$C/m^2) in the erosion region of the tungsten limiter. However, during the plasma exposure a carbon flux is spectroscopically observed on both sides, where the maximum intensity of the CII flux from the carbon surface is only ≈20% larger than that from the tungsten surface. This demonstrates that the majority of the carbon release from both surfaces is due to recycling of carbon impurities in the plasma edge and that only a small part of the detected carbon is due to bulk erosion of the graphite limiter. The amount of carbon, which is released in the form of hydrocarbons from the tungsten surface, is negligible compared to the graphite surface. The heat depositions on both sides under the same plasma conditions is about 30% larger on the carbon surface compared with the tungsten surface (Fig. 13.6). This can be explained by the different energy reflection coefficients.

The disadvantage of using tungsten apart from a possible melt layer loss is its difficult machining. Another high-Z material, tantalum, has a high ductility with the great advantage of easy machining, but it forms hydrides at a

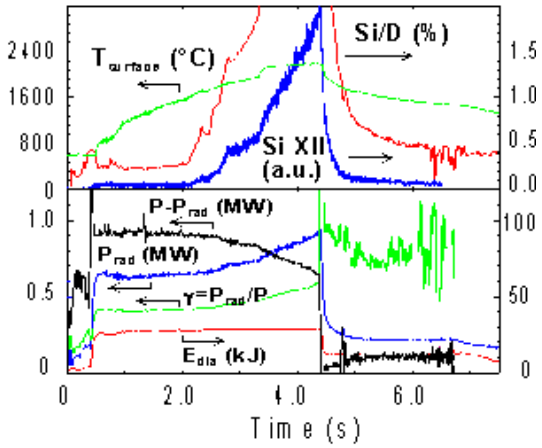

Fig. 13.4. Example of a discharge with silicon evaporation from a test limiter made of Si-doped CFC (SEP NS31). The figure shows the time traces of the local silicon fluxes from the limiter (Si/D), the line-integrated radiation of Si XII emission, the local surface temperature of the limiter measured at the location of maximal power loading, the energy loss due to plasma radiation (P_{rad}), the radiation level $\gamma = P_{\mathrm{rad}}/P$, the diamagnetic energy E_{dia} and the convective power on the test limiter $P - P_{\mathrm{rad}}$, respectively

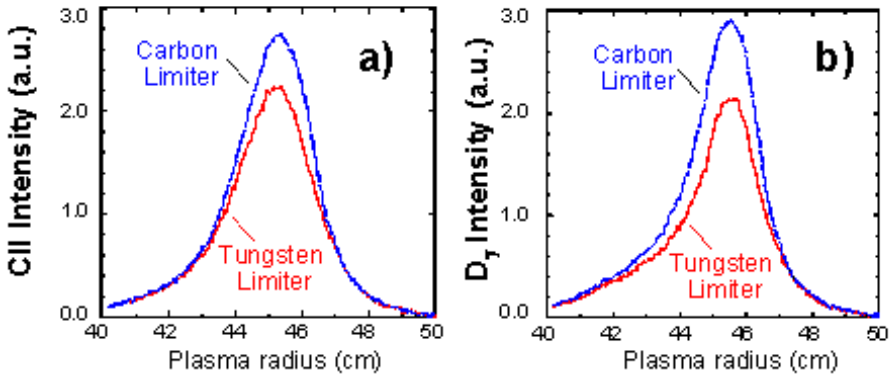

Fig. 13.5. Radial distribution of CII (**a**) and D_γ (**b**) from tungsten and carbon limiters

relatively low temperature. Thus, Ta–W twin limiter experiments have been started in order to compare the hydrogen recycling on these high-Z materials and their behavior under high-power exposure [26].

Both materials have similar masses and therefore similar reflection coefficients for hydrogen. But, Ta is an exothermic hydrogen occluder and W an endothermic one. Thus, different hydrogen release properties are expected. Figure 13.7 shows the temperature-dependent D_β light intensity in front of Ta

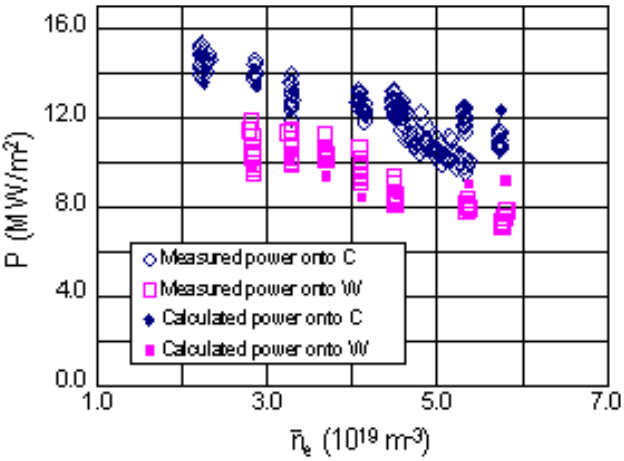

Fig. 13.6. Density dependence of the absorbed heat flux onto C- and W-limiters

and W surfaces. In the case of Ta, the D_β intensity increases with temperature above 1300 K. The decay length of the emitted D_γ light from the Ta surface along the minor radius became shorter above 1300 K. These results can be explained by a continuous change from molecular hydrogen releases at low temperature over a mixture of molecular and atomic hydrogen to pure atomic release at high temperatures, as is observed in the hydrogen/deuterium release process from carbon surfaces in ion beam experiments [27] and limiter experiments in tokamaks [28–30]. A slight difference of the threshold temperature for the increase of the atomic contribution has been observed for C (1100 K) and Ta (1300 K).

Another result in this comparison is a surface temperature excursion. Under comparable power fluxes, the surface temperature evolution during plasma exposure is different for Ta and W: the Ta surfaces reached up to 2100 K and W up to 1600 K. This difference is due to the difference in thermal conductivities (Ta: 58 $Wm^{-1}K^{-1}$, W: 177 $Wm^{-1}K^{-1}$). The surface temperatures of the Ta limiter increased shot by shot under the same comparable D-flux, which is due to a degradation of the thermal conductivity. It is associated with significant surface modification such as grain growth, cracking, re-crystallization and plastic deformation due to heat load. On the other hand, the thermal properties of W did not show a degradation over a number of discharges. As one can expect from the result, W did not have any serious modification on it and had still a shiny surface, which is the same as in previous experiments [22, 31].

Post-mortem analysis has also been carried out. Microstructural observation at the cross-section showed that significant grain growth, re-crystallization and plastic deformation due to thermal stress occurred. Surface analysis indicated that the deuterium concentration was less than 0.1%

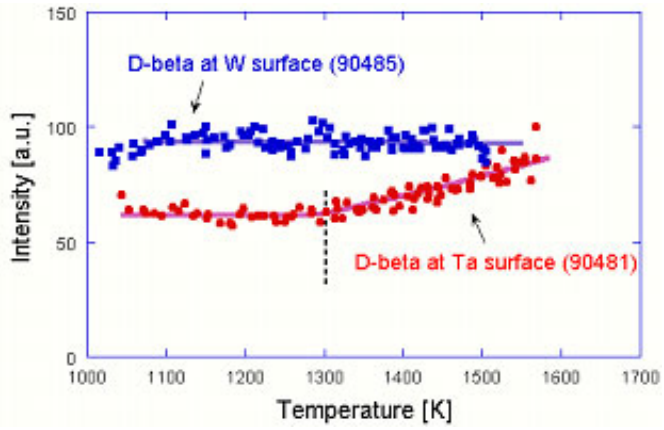

Fig. 13.7. D_β emission from Ta and W as a function of surface temperature measured by a pyrometer. Above 1300 K, D_β emission from the Ta surface increases linearly with the surface temperature

in the subsurface region. Accordingly, even though Ta has exothermic properties, the impact of deuterium in Ta would not be significant, as long as the temperature was kept at high values (above 700 K in these experiments).

Experiments performed with a poloidal tungsten limiter system on TEXTOR confirmed the previous results with tungsten test limiters [32]. For certain conditions – e.g., a strong carbon coating which is favored by the wall conditioning procedures, the all-carbon surrounding and the limiter rest-position – the discharges were practically unaffected by the use of the poloidal limiter system as main limiters. In particular, there has been no restriction for operation at any density with auxiliary heating. For ohmic conditions, the same density with test limiters – and even higher – could be reached. At high levels of radiated power no severe accumulation of tungsten in the plasma center could be detected. The blocks could in general withstand surface temperatures below 1700 K and most of them survived even temperatures above 3000 K without exfoliation.

13.4 B_4C-Coated Copper Limiter

For the W7-X stellarator experiment, a first-wall concept with actively cooled stainless-steel panels as plasma-facing components with low atomic number coatings, in particular boron carbide (B_4C) layers, is being developed [33]. The aim of the B_4C coating is to avoid accumulation of high-Z impurities in the plasma during steady-state operation. It allows continuous boronization of the walls with its advantages of low chemical erosion and oxygen gettering.

Similar limiter blocks have been inserted through vacuum lock systems, exposed to higher heat loads and diagnosed in detail in- and ex-situ as well.

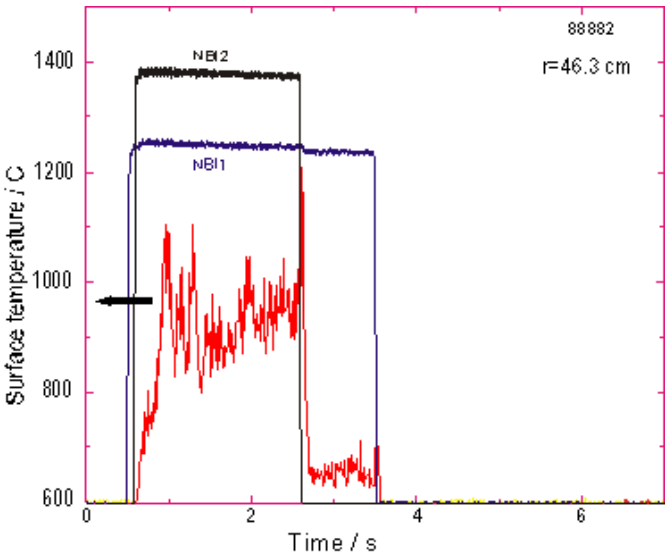

Fig. 13.8. The surface temperature excursion of a test limiter (made of copper coated with 170 µm thick B_4C) during exposure in TEXTOR near the last-close flux surface. The plasma was heated auxiliary by two neutral beams of 1.5 and 1.3 MW/m^2. The resulting load on the test limiter amounted to 4 MW/m^2

The surface temperature excursion during an plasma exposure is shown in Fig. 13.8. The plasma was heated auxiliary by two neutral beams of 1.5 and 1.3 MW/m^2. The resulting load on the test limiter amounted to 4 MW/m^2. The 170 µm thick B_4C layer was rapidly heated up to 1300 K and cooled down, as the pyrometer signals show. The surface layer withstood such an exposure and did not detach from the copper. Increasing the deposited heating power above 8 MW/m^2 led to melting of the B_4C coating (see Fig. 9 in [33]).

In order to test this wall concept in a comparable plasma surrounding, the five top and bottom poloidal carbon limiter blocks in TEXTOR have been replaced by copper tiles coated with a 170 µm vacuum-plasma-sprayed B_4C layer and exposed permanently at a position 1 cm behind the last closed flux surface for several months under various plasma conditions. No disturbance of plasma performance due to surface charging of the B_4C coatings with low electrical conductivity was found [33, 34]. Concerning erosion and hydrogen inventory the limiters behave in general as any low-Z object in a carbon surrounding and show similar properties to that of a pure graphite surface. The hydrogen inventory may be higher. During the discharges, video observation showed the emission of glowing particles from the limiter surfaces, presumably due to arcing [33].

Distinct craters developed on the coating on both limiter types down to the copper bulk and are assumed to be caused by electrical arcs. This has not

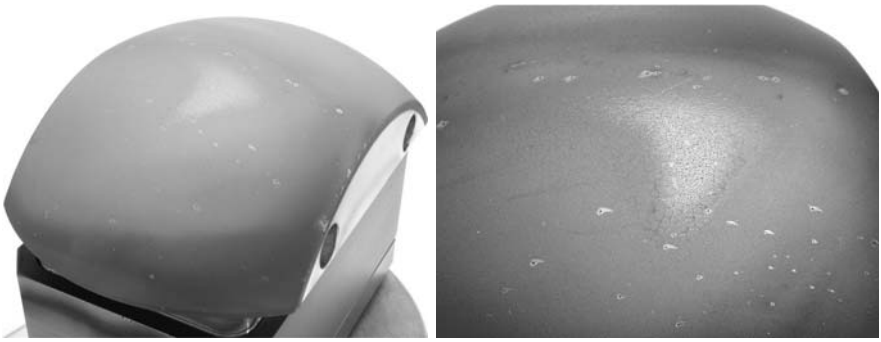

Fig. 13.9. The surface of a test limiter (made of copper coated with 170 µm thick B_4C) after 80 exposures in TEXTOR near the last-close flux surface. The melting zone is clearly seen, especially in the magnification at the **right**-hand side, where also a number of craters are visible, possibly caused by electrical arcs

been clarified yet and is the subject of further investigations as to whether the arcs are triggered by surface or surface roughness or whether the electrically insulating B_4C layer triggered the enhanced arc formation. The arc probability measured across the surface of the top poloidal limiter seems to be affected by adjacent obstacles rising into the SOL which trigger predominantly bipolar arcs. They are observed during the whole discharge and not only at the start or the end. It seems that the changes of resistivity by, for example, melting suppresses further arcing. In the course of the experiments the craters are covered by carbon deposition from the graphite surrounding. No negative influence of the arcing on the properties of the coating and on the plasma behavior has been detected so far; however, further experiments with Si-doped B_4C layers, which are slightly better conducting, will be carried out in the future. This might help to suppress the formation of holes right from the beginning after the insertion into the boundary plasma. The temperature of the coating during a plasma discharge rises and decays extremely fast, indicating that the heat contact from the coating to the substrate determines the thermal response of the coating rather than the heating of the copper bulk. However, despite reaching the melting temperature of the B_4C coating and cracking, no severe delamination of the coating occurred (see Fig. 13.9). The plastic deformation of the copper and the high adhesion strength of the coating seem to compensate the thermo-mechanical stresses resulting from the mismatch in thermal expansion.

13.5 Modeling of Erosion, Deposition and Impurity Transport with the ERO-TEXTOR Code

Simulating erosion and re-deposition processes in fusion devices lead to a better understanding of the processes involved. The 3-dimensional Monte-Carlo code ERO-TEXTOR [35,36] has been developed to model the plasma-wall interaction and the transport of eroded particles in the vicinity of test limiters exposed to the edge plasma of TEXTOR. Important problems concerning the lifetime of various wall materials (high Z vs. low Z) under different plasma conditions and the transport of eroded impurities into the main plasma can be treated with the ERO-TEXTOR code. Recently, the divertor geometries have been implemented to carry out simulations for JET, ASDEX and ITER [37]. In addition, first attempts have been made to simulate erosion and re-deposition processes in the linear plasma device PISCES to analyze the effect of beryllium.

An important effort is the development of an adequate surface model for mixed materials and erosion. The following Fig. 13.10 shows as one example the simulated surface composition of an initially pure tungsten limiter (spherically shaped) which was exposed to the edge plasma of TEXTOR. Carbon as the main impurity of the background plasma can be deposited at the limiter surface. The spatial distribution of the carbon and tungsten concentration after having reached equilibrium inside the interaction layer is a result of the local erosion and deposition fluxes. At the locations where the carbon concentration is less than 100%, the incoming carbon flux (sum of background flux and re-deposition) is in balance with the outgoing carbon flux. Only the tungsten in these regions suffers from a continuous erosion. The build-up of net-deposition zones at the toroidal edges (100% carbon) and a net-erosion zone in the middle part of the limiter is in agreement with experimental observations [32].

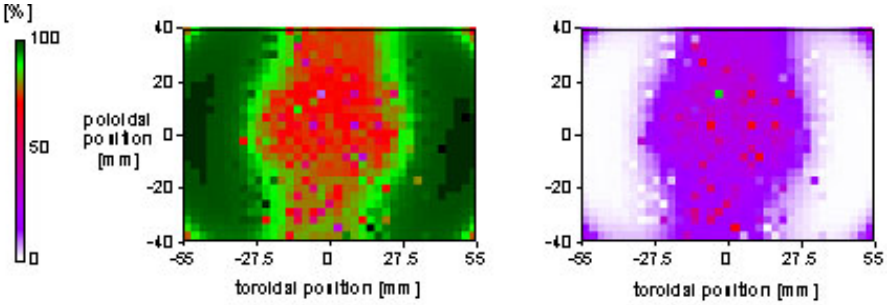

Fig. 13.10. Distribution of carbon (**left**) and tungsten (**right**) inside the interaction layer of an initially pure tungsten limiter after having reached stationarity. The pictures show a top view of the limiter. The plasma parameters of a typical ohmic shot of TEXTOR were used as described in [36]

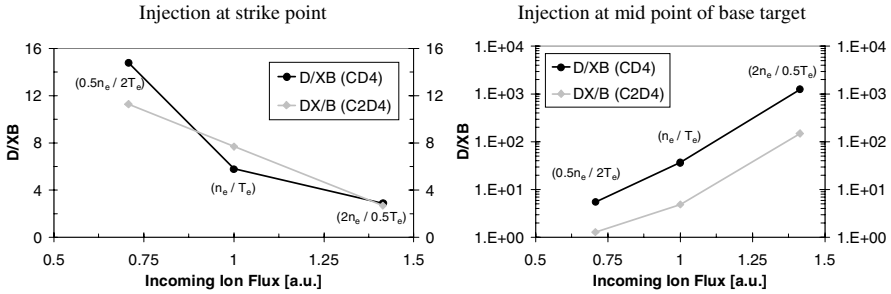

Fig. 13.11. Modelled D/XB for CD from externally injected CD_4 and C_2D_4 into the JET MkIIa divertor

The transport and re-deposition of externally injected $^{13}CH_4$ through a test limiter exposed to the edge plasma of TEXTOR has been analyzed in detail. The result was that the measured low ^{13}C deposition efficiency (less than 0.5%) at the test limiter cannot be modelled, if standard assumptions (significant sticking of hydrocarbons, chemical erosion yield of 1.5%) are used. Assuming zero sticking for hydrocarbons returning to the limiter and using the Ehrhardt-Langer database for the dissociation rate coefficients of hydrocarbons lead to a modelled deposition efficiency of about 2.5% [38]. If instead of the Ehrhardt-Langer data the newest rate coefficients from Janev and Reiter [39, 40] are used, the modelled ^{13}C deposition further increases to about 14%, whereas the deposition pattern is very similar to the experimental one, again assuming zero sticking for hydrocarbons. However, the spatial distribution of CH and CII emission can be reproduced quite well in both cases (Ehrhardt-Langer and Janev-Reiter). The low deposition, therefore, seems to be a plasma-wall interaction effect. Indeed, if an enhanced re-erosion of re-deposited carbon (chemical erosion yield of about 8%) together with zero sticking is assumed, the low deposition efficiency can be simulated [41, 42]. A more detailed discussion of the influence of different databases for hydrocarbon dissociation rate coefficients can be found in [43]. In addition, the influence of sticking assumptions and geometry effects on calculated D/XB values is discussed. A parameter study for MkIIa clearly demonstrates the dependence on the puffing location and on plasma parameter for D/XB values coming from externally injected CH_4, see Fig. 13.11.

Simulations of the hydrocarbon transport in the divertor MkIIa of JET show that the experimentally observed high amount of carbon deposition at the shadowed regions of the inner louvres can only be explained, if a high re-erosion of deposited carbon is assumed [44]. This is in agreement with the above described ^{13}C deposition in TEXTOR. The transport of physically sputtered beryllium can be well described by the simulations: compared to carbon high amounts of beryllium are deposited at plasma-facing regions and not further re-eroded due to the lack of chemical erosion and the low electron temperatures leading to ion energies below the sputtering threshold [42].

First calculations of beryllium transport in PISCES have also been carried out. The axial profile of BeII emission can be well reproduced. The simulated amount of re-deposition of sputtered beryllium is relatively small (about 2%). The main reason for this is the radial transport (caused by diffusion, radial electrical field and friction) leading to a loss of beryllium, which cannot contribute to a re-deposition. However, additional calculations and a detailed comparison with experimental findings is necessary. The influence of the beryllium deposition at the graphite samples on the chemical erosion is one of the open questions still to be addressed and is a matter of particular interest for ITER.

13.6 Conclusions and Outlook

The positive effect on the plasma performance of boron or silicon as wall coatings is well established. The question arises whether or not the necessary boron or silicon concentration at the walls can be provided by using boron- or silicon-doped wall material. Unfortunately, this question cannot yet be answered from the test limiter experiments performed in TEXTOR, due to the relatively small active area of the test limiters as compared to the total area of the main limiters and the wall. But in all investigated cases, a depletion of the doping material in the surface by extensive plasma exposure has been observed. Therefore, it is questionable, whether doped carbon material can serve as a sufficient source for B and Si. In the worst case, only carbon is left at the surface, with the drawback of high chemical erosion and a small thermal conductivity of the doped material. In the near future, no further experiments addressing this aspect are planned in TEXTOR . TEXTOR presently is and will be routinely operated with carbon limiter and wall conditioning by boronization and only in special cases by siliconization.

The main goals of these experiments were to test the materials themselves under plasma exposure and to see the influence on the plasma performance. Especially, it could be shown under which conditions and under which maximum power load the used materials survive (B_4C coating on copper, W, 0.5 mm W on graphite, Ta). Most of these materials are very promising. B_4C-coated copper is now build in Wendelstein 7-X and tungsten is a very suitable material for target plates for medium power load. Such experiments will soon be continued with a tungsten brush test limiter. This structure should reduce the surface stress under plasma power load.

As mentioned in the introduction, one goal of some experiments was to examine, to which extent the chemical erosion of doped materials is reduced. For example, the methane formation by plasma exposure of NS31 (Si-doped CFC with 1.0–1.5% Si) was reduced by a factor of two in comparison to graphite. The interpretation of this result (as of others, e.g., C flux from W) is very complex. We have to be aware that the measurements were done in a carbon machine and we have to take into account the carbon fluxes onto

the limiters, i.e., we have to model both the erosion and deposition processes. A very successful tool is the ERO-TEXTOR code which has been and will be applied to diverse experiments and also be extended to Be/W systems. Using the results of the mixed materials test limiter experiments, the ERO-TEXTOR code might then be able to predict the behaviour of the Be/W/C system foreseen for ITER.

Acknowledgements

The authors would like to thank the following colleagues for their support: T. Ohgo, K. Ohya, M. Rubel, B. Schweer, T. Tanabe, M. Wada, and P. Wienhold.

References

1. J. Winter, H.G. Esser, L. Könen et al., J. Nucl. Mater. **162-164** (1989) 713
2. J. Winter, H.G. Esser, G.L. Jackson et al., Phys. Rev. Lett. **71** (1993) 1549
3. U. Samm, P. Bogen, H.G. Esser et al., J. Nucl. Mater. **220-222** (1995) 25
4. D.J. Campbell and the JET Team, J. Nucl. Mater. **241-243** (1997) 379
5. Iter Physics Basis, Nucl. Fusion **39/11Y**, special issue (1999)
6. C.H. Skinner, E. Amarescu, G. Ascione et al., J. Nucl. Mater. **241-243** (1997) 214
7. P. Andrew, D. Brennan, J.P. Coad et al., J. Nucl. Mater. **266-269** (1999) 153
8. V. Philipps, T. Tanabe, Y. Ueda et al., Nucl. Fusion **34** (1994) 1417
9. R. Neu, K. Asmussen, K. Krieger et al. Plasma Phys. Control. Fusion **38** (1996) A165
10. N. Noda, R. Neu, V. Philipps et al., J. Nucl. Mater. **241-243** (1997) 227
11. R. Neu, V. Rohde, A. Geier et al., J. Nucl. Mater. **290-293** (2001) 206
12. F. Alladio, M.L. Apicella G. Apruzzese et al., Plasma Phys. Control. Fusion **36** (1994) B253
13. M.L. Apicella, G. Apruzzese, M. Borra et al. Nucl. Fusion **37** (1997) 381
14. B. Lipschultz, J. Goetz, B. LaBombard et al., J. Nucl. Mater. **220-222** (1995) 50
15. M. Mayer, R. Behrisch, K. Plamann et al., J. Nucl. Mater. **266-269** (1999) 604
16. V. Philipps, A. Huber, H.G. Esser et al., J. Nucl. Mater. **290-293** (2001) 1190–1194
17. Ph. Mertens et al., Proc. 7th Int. Symp. Laser-Aided Plasma Diag., K. Muraoka (ed.), Fukuoka, LAPD-7 (1995) 150
18. J. Rapp, W. Biel, H. Gerhauser et al., J. Nucl. Mater., **290-293** (2001) 1148–1154
19. A. Huber, V. Philipps, T. Hirai et al., Physica Scripta **T91** (2001) 61–64
20. A. Huber, I. Beigman, D. Borodin et al., Plasma Phys. Control. Fusion **45** (2003) 89
21. A. Huber, V. Philipps, A. Pospieszczyk et al., J. Nucl. Mater. **290-293** (2001) 276–280

22. K. Ohya, R. Kawakami, T. Tanabe et al., J. Nucl. Mater. **290-293** (2001) 303–307
23. M. Rubel, V. Philipps, A. Pospieszczyk, H. Renner, Europhysics Conference Abstracts **25A** (2001) (Proc. 28th EPS Conf.) P5.092
24. T. Tanabe, T. Ohgo, M. Wada et al., Fusion Engineering and Design **49-50** (2000) 355–362
25. M. Rubel, T. Tanabe, V. Philipps et al., J. Nucl. Mater. **283-287** (2000) 1089–1093
26. T. Hirai, V. Philipps, A. Huber et al., J. Nucl. Mater. **313-316** (2003) 67
27. P. Franzen, E. Vietzke, J. Vac. Sci. Technol. **A12** (1994) 820
28. A. Pospieszczyk, Ph. Mertens, G. Sergienko et al., J. Nucl. Mater. **266-269** (1999) 138–145
29. S. Brezinsek, P.T. Greenland, J.D. Hey et al., 28th EPS Conference on Contr. Fusion and Plasma Phys. Funchal, ECA **25A** (2001) 2077
30. S. Brezinsek, Ph. Mertens, A. Pospieszczyk et al., Contrib. Plasma Phys. **42** (2002) 668
31. V. Philipps, A. Pospieszczyk, A. Huber et al., J. Nucl. Mater. **258-263** (1998) 858–864
32. A. Pospieszczyk, T. Tanabe, V. Philipps et al., J. Nucl. Mater. **290-293** (2001) 947
33. S. Kötterl, H. Bolt, H. Greuer, Physica Scripta **T91** (2001) 117–123
34. A. Pospieszczyk, B. Schweer, V. Philipps, J. Nucl. Mater. **313-316** (2003) 223
35. U. Kögler, J. Winter, Jül-Report 3361, Forschungszentrum Jülich GmbH, Jülich 1997
36. A. Kirschner, V. Philipps, J. Winter, U. Kögler, Nucl. Fusion **40**, No. 5 (2000) 989
37. A. Kirschner, A. Huber, V. Philipps et al., J. Nucl. Mater. **290-293** (2001) 238
38. P. Wienhold, H.G. Esser, D. Hildebrandt et al., J. Nucl. Mater. **290-293** (2001) 362
39. R. Janev, D. Reiter Jül-Report 3966, Forschungszentrum Jülich, ISSN 0944-2952 2002
40. R. Janev, D. Reiter Jül-Report 4005, Forschungszentrum Jülich, ISSN 0944-2952 2002
41. P. Wienhold, V. Philipps, A. Kirschner et al., J. Nucl. Mater. **313-316** (2003) 311
42. A. Kirschner, S. Brezinsek, H.G. Esser et al., Contributions to the 30th EPS Conference on Contr. Fusion and Plasma Phys. St. Petersburg, Russia (2003)
43. A. Kirschner, J.N. Brooks, V. Philipps et al., J. Nucl. Mater. **313-316** (2003) 444
44. A. Kirschner, J.N. Brooks, V. Philipps et al., Plasma Phys. Control. Fusion **45** (2003) 309

14 Beryllium and Liquid Metals as Plasma Facing Materials

R.P. Doerner

14.1 Introduction

There are two important aspects of plasma facing materials (PFM). The first is the effect that the PFM has on the plasma and the second involves the effect of the plasma on the PFM. The primary issue for the first case is the impurity concentration in the plasma due to the release of material from the plasma-facing surfaces. Impurities can result in an increase of radiated power losses from high-temperature plasmas, a dilution of the fuel species in fusion plasmas, and the possible deposition of impurities in locations where they are not desirable in all plasmas. In addition to impurity release from the PFM, the amount of hydrogen recycling will also affect the conditions of the edge plasma. In the second case, the physical and chemical properties of the surface can change due to material erosion of the surface or accommodation of the plasma ion species within the wall material. Changes to the properties of the wall material can, of course, then feedback to further impact the first issue.

As plasma confinement devices become larger, more powerful, use tritium as fuel and possess the ability to operate for longer duration pulses, both of these PFM issues force a shift away from carbon as the first wall material. Compared to carbon, beryllium has a lower mass and will, therefore, radiate less power as an impurity in high-temperature plasma. Beryllium also does not suffer from the problem of erosion due to the formation of volatile molecules, as carbon does. And finally, as designers face the safety issues associated with building and licensing a facility capable of operating for long pulses with a tritium containing fuel supply, the low solubility limit of hydrogen in beryllium becomes a major advantage. The safety issues associated with the toxicity of beryllium are not a particular disadvantage because those safeguards do not exceed the requirements already necessary in a tritium-containing device [1]. For these reasons, beryllium has evolved into the material of choice for the majority of the plasma-facing components in proposed burning plasma experiments, such as ITER [2] and FIRE [3]. This chapter will first summarize the current state of knowledge on plasma interaction with beryllium containing surfaces.

Any static plasma-facing component surface, subject to erosion, will have obvious disadvantages with regards to a limited lifetime. The concept of flow-

ing liquid metal plasma-facing components [4] has been proposed to address this and other concerns, however proving the compatibility of such a system with high temperature plasma remains to be shown. Plasma liquid-surface interaction issues are currently under investigation and the properties of plasma interacting with lithium and gallium surfaces will also be summarized here.

The objectives of this chapter are to first review and summarize the present status of knowledge relating to the erosion behavior of beryllium and the liquid metals. The important role of impurities in the erosion behavior will be highlighted. Hydrogen fuel retention in all three materials will then be discussed from both a safety viewpoint and from the viewpoint of controlling fuel recycling from the wall. While this chapter focuses on only a small subset of the issues associated with plasma-surface interactions, readers interested in understanding the breath of interrelated issues experienced by plasma facing materials are directed toward a recent review article [5].

14.2 Erosion

Erosion can be divided into three categories: physical sputtering (which is independent of surface temperature), chemical erosion (which peaks in the temperature range where volatile species are formed and then decreases with increasing temperature) and sublimation/evaporation (which increases exponentially at elevated temperature). This chapter will examine the information available concerning the first and third processes, as none of the three materials discussed here (beryllium, lithium and gallium) appear to form volatile molecules in combination with typical plasma ion species. That is not to imply, however, that surface chemistry in unimportant to the erosion process of these materials. Many metals will form stable molecules with either the plasma fuel ions, forming hydrides, or with typical plasma impurity ions, forming oxides, nitrides and carbides. In the temperature range of interest here, the stable surface molecules that form on beryllium, lithium and gallium surfaces tend to reduce the erosion of metal atoms from the plasma-exposed surface.

14.2.1 Physical Sputtering of Beryllium

Physical sputtering results from elastic transfer of energy from the incoming plasma ions to target atoms within the plasma-facing surface. A target atom can be sputtered if it receives sufficient energy during the collisional cascade resulting from the stopping of the incident ion to overcome the surface binding energy of the material. The larger the surface binding energy, the lower the physical sputtering rate. Because physical sputtering is a classical process, it is relatively easy to calculate the expected loss rate of atoms from a surface when it is subjected to a known flux of energetic particles. Monte-Carlo type codes (for example, TRIM [6]) are typically used to calculate physical

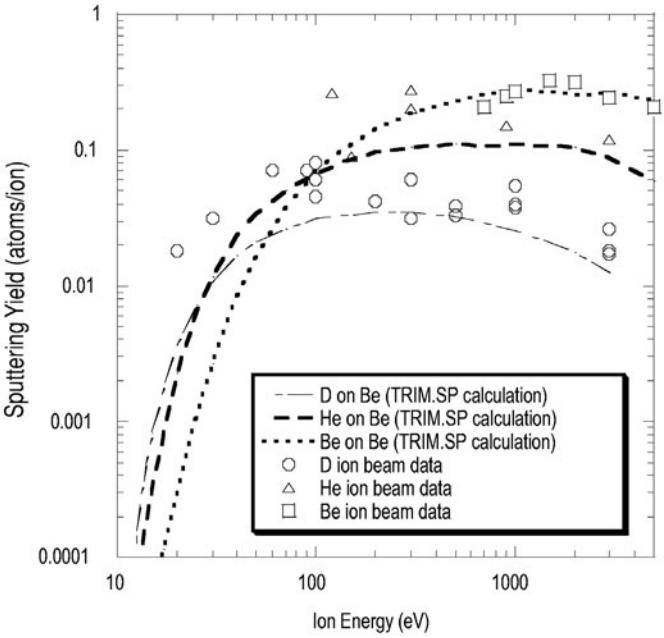

Fig. 14.1. Comparison of calculated and measured sputtering yields of beryllium as a function of the incident ion energy for a variety of projectiles at normal incidence. Calculated values are taken from [7], measured values from [9]

sputtering, resulting in the creation of extensive databases of sputtering rates based on ion mass, energy and angle of incidence for a wide variety of target materials [7]. For clean beryllium surfaces, at temperatures below about one half the melting temperature, these calculations show good agreement with the measured physical sputtering yield.

Figure 14.1 shows a typical graph of the normal incidence sputtering yield of beryllium as a function of the incident ion energy for several different ion species. Also shown in the figure is a prediction of the sputtering yield obtained with TRIMSP [8]. As can be seen in the figure, as long as the surface is clean, one can fairly accurately predict the expected erosion rate of a beryllium surface exposed to plasma bombardment.

Another factor that will impact the sputtering rate of beryllium exposed to plasma bombardment is the angle of incidence of the incoming particles with respect to the surface normal. While the effect of incident angle certainly alters the sputtering rate of a surface, in reality rough surfaces tend to obscure the magnitude of the effect [9]. Of paramount concern in the estimation of the physical sputtering rate of any material is under what conditions runaway self-sputtering can occur. For the case of a low temperature beryllium surface, self-sputtering exceeds unity only at incident energies exceeding 1 keV, while at the same time the incident angle of the incoming ions must exceed 60°

with respect to the surface normal [10]. Unfortunately, as we will see later in this chapter, once the temperature of the surface increases the erosion rate of a surface will be a combination of terms and may exceed the incident ion flux under much less stringent conditions.

14.2.2 Mixed-Material Erosion

Of course, it is important to have an accurate knowledge of the surface composition in a given situation to predict an accurate physical sputtering rate. Oxygen impurities in the incident plasma, or in the residual background gas will readily oxidize the surface of a beryllium sample and depending on the ratio of the arrival rate of oxygen atoms at the surface to the sputtering rate of the surface oxide, one can measure the sputtering rate from either a beryllium, or a beryllium-oxide, sample. Careful control of the residual gas pressure during ion beam measurements [9] has shown this effect. In addition to oxygen atoms being removed from the surface due to sputtering, it is also possible to deplete oxygen atoms from the surface of a beryllium sample by diffusion of the surface oxygen into the bulk of the beryllium sample. At temperatures exceeding 600°C, beryllium will diffuse through beryllium oxide [11] resulting in an increase in the measured sputtering rate due to the decrease of oxide coverage on the surface. The difference in sputtering rate expected between a beryllium oxide surface and a pure beryllium surface is only about a factor of 2–3. While this difference is significant, we will see later that other temperature dependent effects can induce much larger increases in the erosion rates of surfaces exposed to particle bombardment at elevated temperature.

Carbon impurity deposition from the incident plasma can also influence the sputtering rate of a beryllium plasma-facing surface. Two effects can influence the erosion of beryllium atoms in this case. The first is the relatively straightforward geometrical effect of the change in surface area coverage of beryllium as carbon atoms begin to deposit on, and cover, parts of the surface. The second effect is the more complicated issue of surface chemistry impacting the erosion rate by the formation of a beryllium carbide surface.

The first effect lends itself to a modeling solution. By careful accounting of the deposition rate compared to subsequent erosion rates of both the substrate material as well as the depositing material, the change in the surface composition can be accounted for in a standard TRIM-type model. An interesting transition can occur from a state of initial erosion to subsequent deposition, and vise versa, during a simulated exposure (with constant incident parameters) due to deposition of impurities initially some distance within the bulk material [12]. In a process similar to implanting, or doping a marker at a known depth in a material, an impurity rich layer will develop. The surface erosion, on the other hand, will not be affected by this marker layer and will continue to erode until the marker layer eventually becomes the new surface. At such time the erosion of the surface will change (either

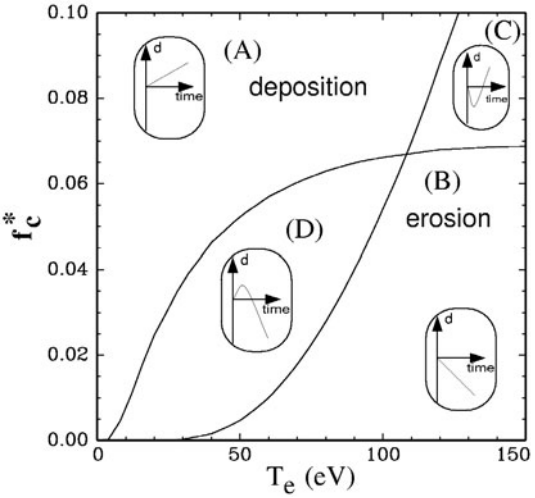

Fig. 14.2. Time dependent erosion behavior may remain constant (as in regimes A and B) or may change from erosion to deposition (as in C), or from deposition to erosion (as in D). Figure used with permission from [12]

increase or decrease depending on the situation) and one may transition from and erosion-dominated regime to a deposition dominated one. This behavior is shown schematically in Fig. 14.2. This transitional behavior from one regime to another underscores the importance of performing tests of plasma facing materials under conditions as close as possible to those expected in their final application.

The results from these modeling runs compare favorably to carefully controlled plasma exposure measurements. Figures 14.3 and 14.4 show the predicted and experimentally observed deposition and erosion dominated regimes for a carbon containing deuterium plasma incident on beryllium samples under several different bombardment conditions. The results in Fig. 14.4 at low surface temperature can be compared to those shown in Fig. 14.3, where the sample temperature was kept low enough in the modeling to avoid any impurity diffusion and minimize any chemical effects. Subsequent modeling efforts are now attempting to include surface temperature effects, but knowledge of the fundamental parameters, such as diffusion rates of carbon in beryllium are not yet well documented.

As mentioned above, beryllium carbide may also form in the surface layer, changing the surface binding energy and thereby the sputtering rate. In equilibrium, beryllium and carbon have been shown to chemically react to form a carbide at temperatures above 500°C [11]. However, during energetic particle bombardment of a surface the carbide will form even during room temperature bombardment [13, 14]. Unlike oxygen that usually produces a thin passivating oxide surface on a metal, carbon layers can continue to grow until

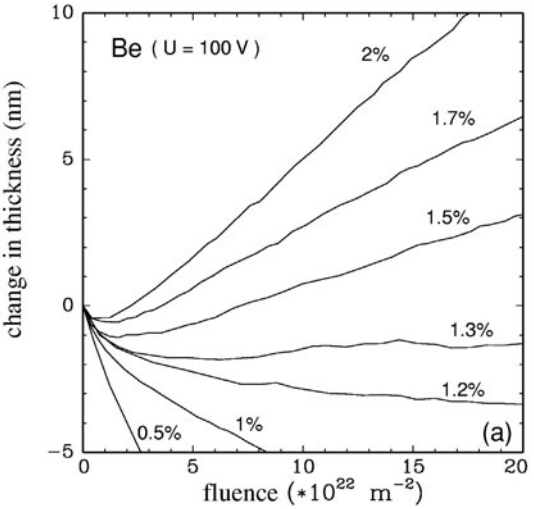

Fig. 14.3. Calculated deposition thickness of a carbon layer on a beryllium substrate exposed to a 100 eV deuterium plasma containing a varying concentration of carbon impurities. From [12]

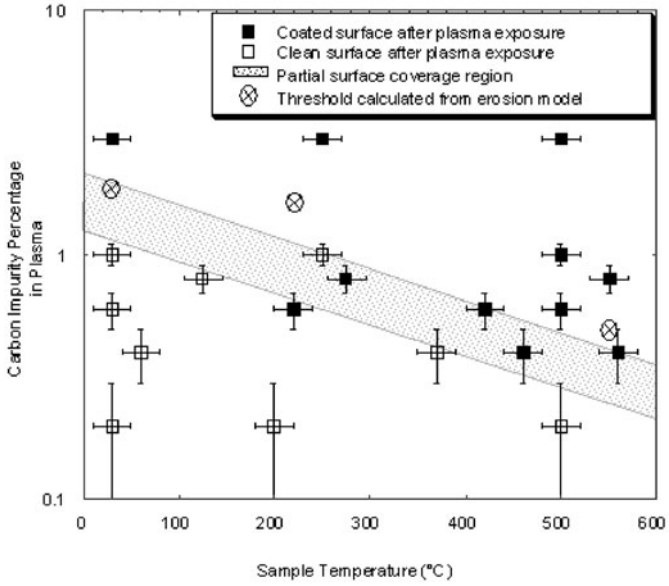

Fig. 14.4. Measured carbon impurity layer after exposure to deuterium plasma at 100 eV (from [15]). At low temperature the experimental data compares favorably with the calculated values in Fig. 14.3

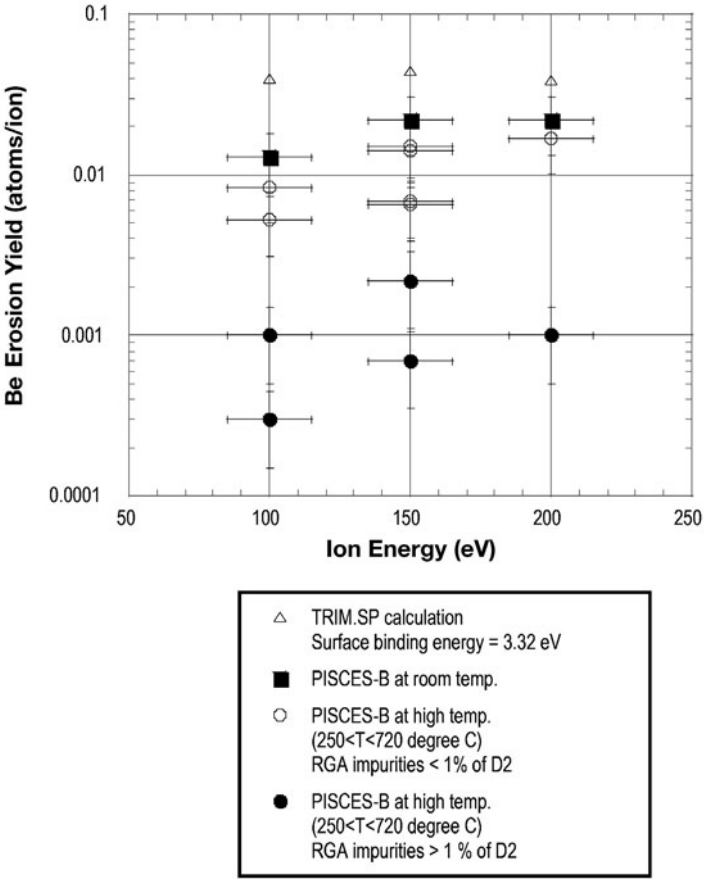

Fig. 14.5. Beryllium erosion rate depends both on impurity concentration in the incident plasma, as well as the sample temperature during the exposure. From [16]

the behavior of the carbon surface dominates and the underlying substrate is no longer important in the plasma-material interaction [13, 15]. This occurs when the implantation depth equals the thickness of the impurity film that has formed on the surface of the material being exposed to the plasma. In the case of carbon on a beryllium surface, the removal rate is dependent on the surface temperature not only because of the diffusion of carbon into the beryllium substrate and the chemical interactions between beryllium and carbon, but also because of the temperature dependence of the chemical erosion of carbon.

The measured erosion of a beryllium surface will therefore be dependent not only on the impurity concentration in the incident plasma, but also on the temperature of the sample surface during the plasma exposure. An example of this effect is shown in Fig. 14.5, where the deposition of a carbon impurity

layer during deuterium plasma bombardment is seen to almost eliminate the material loss rate from the underlying beryllium substrate [16]. In addition to affecting the erosion of the substrate material, we will see later in this chapter that the formation of impurity layers can drastically impact the hydrogen isotope retention of a plasma-facing component.

Erosion during mixed impurity species bombardment of beryllium has also shown unexpected chemical effects that play a dominant role in determining the erosion rate of the substrate material. Bombardment of a beryllium sample with a CO^+ ion beam produces an equilibrium surface state consisting of beryllium oxide, elemental carbon and C–O compounds [13]. The chemical erosion of CO limits the carbon accumulation on the surface and therefore beryllium continues to be eroded. The complicated and interrelated nature of plasma-surface interactions requires measurements to be made in a situation that includes as many of the conditions of the final application as possible.

14.2.3 Physical Sputtering of Liquid Metal Surfaces

The process of physical sputtering is not expected to differ dramatically between a solid and a liquid surface. The primary difference is the change in the surface binding energy as a function of the temperature of the surface [17]. The temperature dependent surface binding energy has two components. The first is the change due to the change of state of the surface. The surface binding energy is reduced by the heat of fusion when the material changes from a solid to a liquid state. This change is, however, quite small with the heat of fusion of most materials being only a few percent of the surface binding energy. The second component is due to the empirical scaling of the binding energy with temperature [18], such that at the critical point of the material the surface binding energy goes to zero. This effect is effectively by definition, since at the critical point there is no longer a difference between the liquid and gaseous states of a material.

Gallium is an interesting liquid in that its melting temperature is only 30°C. In effect this means that in almost any experimental configuration one will be investigating an interaction with a liquid surface. During such low temperature exposure of gallium surfaces, calculations using the TRIM code [19] have been verified to accurately predict the physical sputtering yield [20], see Fig. 14.6. Gallium is of interest as a plasma-facing material because of its relatively low vapor pressure [21], but as we will see later in this chapter its erosion behavior at elevated temperature means one must use care in determining its maximum acceptable operating temperature.

Lithium is the other primary liquid metal being considered as a plasma-facing material. Lithium has the intriguing property that its melting temperature is 181°C, which means that it can be studied in either its solid or liquid state. Measurements of the physical sputtering yield of lithium across the phase transition (Fig. 14.7 [22]) have verified that no modifications to sputtering theory are needed to predict sputtering from liquid surfaces. One

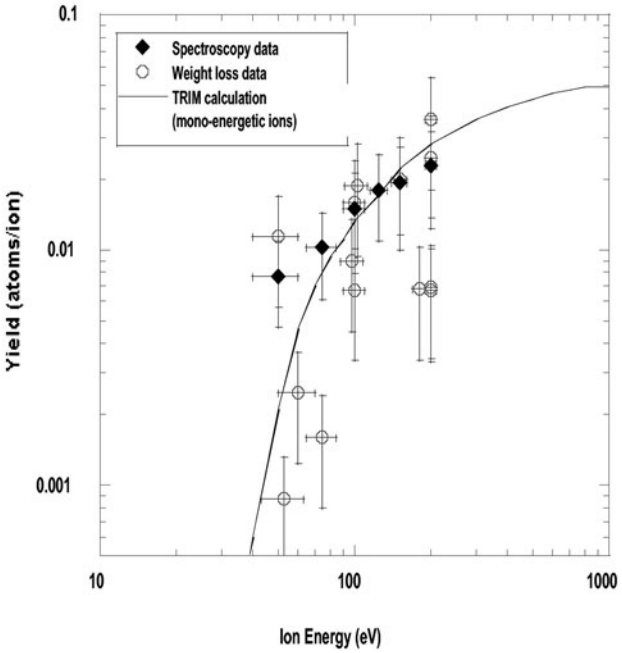

Fig. 14.6. Energy dependence of the sputtering yield for liquid gallium exposed to deuterium plasma bombardment (from [20]). Weight loss and spectroscopic data agree well with the theoretical predictions of the sputtering yield

advantage for using lithium as a plasma-facing material is the fact that it is an alkaline metal. Typically, alkaline metals exhibit a large secondary ion sputtering yield [23] and lithium is no exception. The secondary ion yield for lithium has been measured to be approximately constant, about 65%, over a range of ion energies [24]. This means that about 2/3 of all sputtered material is lost as ions from the surface of lithium. In a plasma environment, where a sheath exists at the surface of a plasma-facing component [25], these sputtered ions will not enter the plasma, but rather will be immediately returned to the lithium surface effectively reducing the neutral particle sputtering yield by a factor of three.

One serious constraint involved with the use of lithium as a plasma-facing material is its relatively high vapor pressure [21]. This restricted maximum permissible operating temperature coupled to its transition to a solid state below 181°C, means that lithium has a narrow temperature window in operational space. As will be discussed in the next section, enhanced erosion at elevated temperature will further restrict the size of this window.

In summary, the sputtering properties of liquid surfaces are fairly well understood and do not preclude their use as plasma facing materials. There are, however, other mechanisms that can remove material from a liquid surface

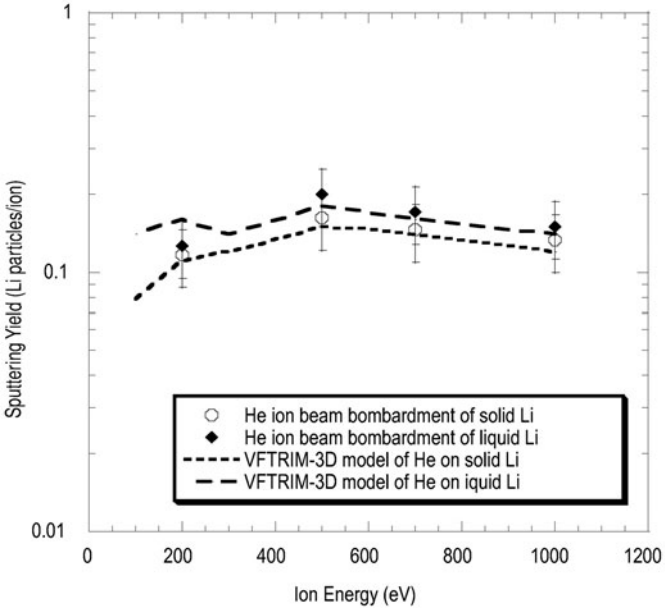

Fig. 14.7. Comparison between solid and liquid lithium sputtering by a helium ion beam at 45° incidence angle (from [22]). The sputtered particle flux is comprised af about 2/3 sputtered ions and 1/3 sputtered neutral atoms

in a magnetically confined plasma environment. The incident flux of plasma gas ions, either helium or hydrogen isotopes, may coalesce within the liquid surface to form bubbles. Bubbles that continue to grow will eventually intersect the surface of the liquid plasma-facing material and then rupture. This process would lead to the macroscopic ejection of material from the liquid, which could in principle find its way into the confined plasma volume.

Another mechanism that could result in macroscopic material ejection arises from magnetohydrodynamic (MHD) forces acting on a liquid metal. A conducting liquid moving through a spatially, or temporally, varying magnetic field will experience forces that will vary in magnitude and direction as the liquid crosses the field. These forces must be carefully considered during the design of any flowing liquid system to avoid droplet formation or splashing of the liquid. In addition, current flow within the liquid surface can result in bulk $J \times B$ forces that can cause the ejection of droplets from the liquid surface [26], or even the removal of the entire volume of the liquid. It may be possible, by careful control of current paths, to limit the impact of $J \times B$ forces on the liquid surface or even to use these forces to help stabilize the liquid surface. However, it is not yet clear how well understood the current paths in the edge of a magnetically confined plasma really are. In any case, the issues associated with deployment of a liquid plasma-facing material in

a magnetically confined plasma environment appear to be related to bulk forces on the liquid, rather than with sputtering phenomena.

One innovative technique that has been developed to limit the mobility of a liquid plasma-facing surface is the capillary pore system [27]. This system has been successfully deployed in a tokamak environment [28]. Although this system addresses many of the mobility and erosion issues of a liquid plasma-facing surface, as will be discussed later in this chapter in order to achieve the full benefits from a low-recycling boundary a larger scaled-up version of this system will need to be developed.

14.2.4 Erosion of Surfaces at Elevated Temperature

The standard picture of erosion from a chemically inert surface exposed to energetic particles can be divided into two categories. The first, physical sputtering, is independent of surface temperature and proportional to the incident particle flux such that the physical sputtering rate, $R_{ps} = Y_{ps}{}^{*}J_{in}$ (where Y_{ps} is the temperature independent physical sputtering yield and J_{in} is the incident particle flux). The second is the sublimation/evaporation rate, J_o, which does not depend on the flux of incident particles and strongly increases with increasing surface temperature.

The erosion rate is, therefore, expected to remain constant, with increasing temperature, until the sublimation/evaporation rate becomes comparable to the physical sputtering rate. As the surface temperature increases further, the increase expected from sublimation should dominate the erosion. This conventional picture, however, is contradicted by experimental data where the erosion yield is found to be temperature dependent and a strong increase in the erosion rate is observed at temperatures less than those expected from thermodynamic sublimation (see Fig. 14.8).

Nelson [29] first observed this dramatic increase in the loss rate of material from metal surfaces at elevated temperature while subjected to ion beam bombardment. The increase in the loss rate began at a lower temperature than could be explained by the vapor pressure of the material, yet the enhanced loss term had the same characteristic dependence on temperature as that exhibited by surface evaporation. Subsequent measurements on a variety of materials, including W [30] and C [31, 32] exhibited similar behavior.

Several theories have been proposed to explain the increase in loss rate from a surface with increasing temperature [29, 31], but each has limitations and drawbacks. A recent theory has been proposed [33] which involves the creation of a population of less strongly bound surface adatoms during energetic particle bombardment. Adatoms are less tightly bound to the surface because their coordination number of nearest neighbor atoms is reduced compared to a 'standard' surface, or lattice, atom. This decreased surface binding energy will allow an adatom to thermally leave the surface at a lower temperature than expected from the thermodynamic vapor pressure of the material. Whether this new theory proves to be correct will have to be investigated

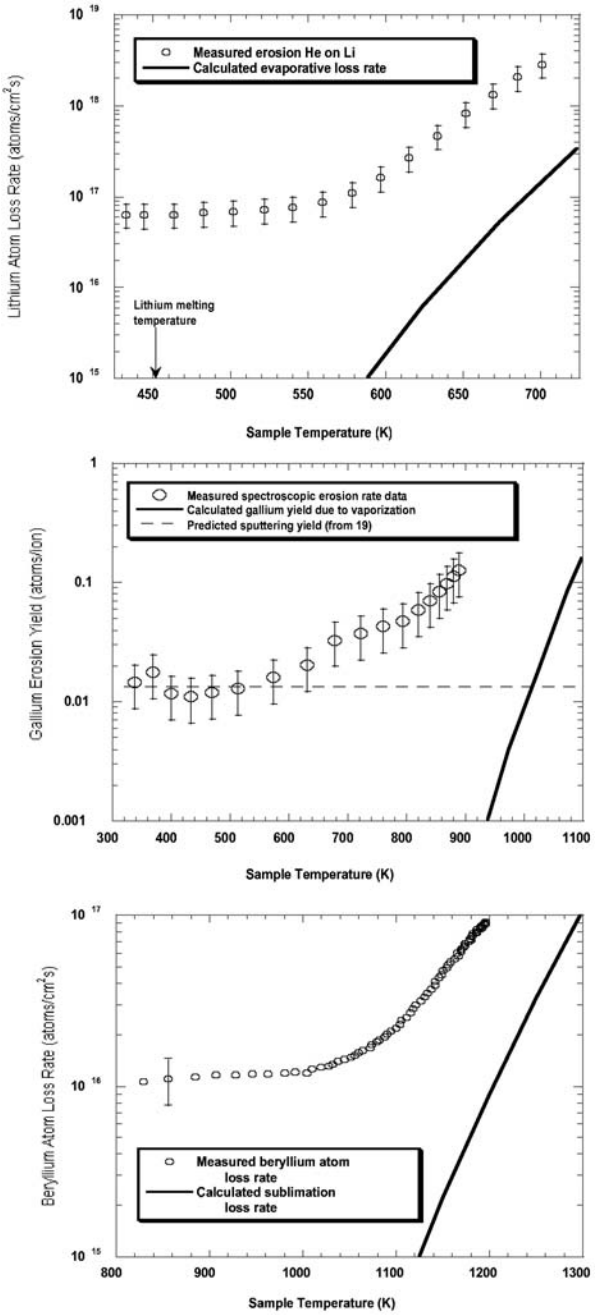

Fig. 14.8. Erosion rates at elevated surface temperature exceeds the combination of physical sputtering and evaporation/sublimation for both liquid and solid samples, lithium (**top**), gallium (**middle**) and beryllium (**bottom**)

by specifically designed experiments, but the experimental evidence of the premature evaporation effect is undeniable. Figure 14.8 shows the temperature dependent loss rate of atoms, along with the expected loss rate due to the vapor pressure, of all three of the materials relevant to this chapter: beryllium, lithium and gallium.

The implication of this enhanced particle loss rate from elevated temperature surfaces is a reduction in the maximum allowable operating temperature of any plasma-facing component, either solid or liquid. In the case of a solid surface, such as beryllium, this means that the maximum allowable heat flux to the surface will be reduced. In the case of a liquid plasma-facing component, such as lithium or gallium, it will mean that the liquid will have to have a higher velocity as it travels through any high-heat flux region near the confined plasma volume to limit the temperature rise of the liquid surface.

14.3 Hydrogen Isotope Retention

A critical concern in any burning plasma experiment is accumulation of fuel species (i.e., tritium) within the plasma confinement chamber. The level of in-vessel tritium retention will ultimately determine the operational down time of a device (due to the safety necessity of removing the accumulated tritium inventory) and may, in a worst case scenario, even prevent licensing of burning plasma reactors. The materials that comprise the plasma-facing components are the primary culprits for retaining tritium in one of two ways. First, the tritium can be directly implanted and trapped within the plasma-facing material and second, material that is eroded from the plasma-facing component can redeposit with tritium elsewhere in the device.

Another reason that hydrogen retention within a plasma-facing material is important is connected with the recycling of neutral molecules from the material in the region of the edge plasma. By controlling the recycling in the boundary of plasma confinement devices it is possible to access improved plasma confinement regimes [34]. During short duration discharges it is possible to reduce recycling using clever wall conditioning techniques [35]. Achieving low-recycling walls in a steady state, or long pulse, environment will require an innovative approach to the concept of plasma facing materials.

14.3.1 Retention in Beryllium

The hydrogen isotope retention properties of beryllium surfaces are fairly well understood. Two excellent review articles [36,37] have been written that deal extensively with this issue. This section will briefly summarize the understanding presented in those articles. Readers desiring more details are advised to find it within those papers.

Beryllium exhibits an interesting fluence dependent hydrogen retention behavior. During low fluence exposures of beryllium to deuterium ion beams,

the retained amount of deuterium increases linearly with increasing fluence [38]. Eventually, however, a saturation value is reached where the retained amount of deuterium levels off and reaches a constant value with increasing fluence [39]. The explanation for this saturation effect has been attributed to the formation of small deuterium bubbles within the beryllium [40]. Deuterium bubbles continue to form during implantation until eventually they begin to intersect one another and a complicated interconnected porosity develops [41]. This porosity can intersect the surface of the material providing a path out of the bulk for the deuterium present within the bubbles/porosity.

The saturated deuterium retention value varies with both the energy of the incident ions and the surface temperature of the beryllium sample [36]. For low energy ions (on order of 100 eV) the retention saturates at about 10^{21} D atoms/m^2. This value increases up to about 10^{22} D atoms/m^2 for ion energies in the keV range, indicating that the saturations value scales roughly with the mean range of the incident particles. The temperature of the sample plays a critical role in the saturation value of deuterium in beryllium regardless of the energy of the incident particles. The retained amount of deuterium saturates at a value about an order of magnitude lower during high-temperature exposures ($\sim 600^\circ$C) as compared to those exposures conducted at lower surface temperature ($\sim 100^\circ$C).

Even though the retention scales with the mean range of the incident particles, the resulting porosity extends well beyond the implantation depth of particles. While the implantation depth of a 300 eV deuterium ion is only on the order of 10 nm, surface voids extending well below a micron deep into the surface have been observed after such exposures [42]. It is believed that the depth of the voids result from the saturation of the implantation zone with incident deuterium particles, this saturation forces some of the deuterium within the implantation zone deeper into the near surface region of the beryllium where it can become trapped at sites within the beryllium. Additional deuterium atoms encounter the filled trapping sites and start the process of coalescence into bubbles at those locations. As the fluence increases mobile vacancies cause the voids to grow and interconnect with other such voids, eventually creating a path for the trapped deuterium molecules back to the surface of the material. Untrapped deuterium atoms within the beryllium can then reach the surface of the interconnected porosity and recombine with other deuterium atoms to leave the beryllium.

This global picture of the change in the surface morphology of a beryllium surface used as a plasma-facing component can explain the gas fill behavior observed in tokamaks using beryllium components. Initially beryllium surfaces act as a strong pump for deuterium; this is due to the incident deuterium recombining on the surfaces of the porosity within the beryllium. The formed deuterium molecules can then flow through the porous channels, either deeper into the beryllium or back toward the surface. However, the flow back toward the surface is a tortuous path through the labyrinth of channels

and, therefore, it takes some time before the molecules are released back to the edge plasma. Throughout the discharge this process of a saturated layer formation forcing deuterium into the beryllium continues, which could account for the continual, but decreasing with time, pumping observed during discharges using a beryllium plasma-facing material [43]. After the discharge is terminated the beryllium walls will act as a gas source as the remaining deuterium within the beryllium finds it way to the surface of the porosity and then slowly finds its way back out of the channels making up the beryllium plasma–facing surface [44]. This slow release of deuterium removes any remaining untrapped deuterium atoms from the beryllium bulk and prepares the surface to be able to again act as a pump during the subsequent discharge.

It is postulated that the remaining, small retention in beryllium is due to trapped deuterium within the beryllium (at trapping sites and in small voids unconnected to the surface) as well as due to the bonding of deuterium with beryllium oxide that can exist on the walls of these interconnected labyrinths [45]. Even though beryllium can be thought of as being a pump throughout a limited duration plasma discharge its rate of pumping compared to the incident particle flux is small (i.e., it still exhibits high recycling).

14.3.2 Retention in BeO and Mixed Be Materials

Ultimately, the hydrogen isotope retention in existing plasma confinement devices is not governed by hydrogen uptake in the pure materials that make up the plasma-facing components, but rather by co-deposition/coimplantation of eroded material with the abundant hydrogen species present in the edge region of the device. This is particularly true of carbon co-deposition (see chapter by Haasz and Davis), but is also true for beryllium containing layers. Beryllium will readily form an oxide and this oxide, like most metal oxides, will react with hydrogen isotopes to form hydroxides.

A series of measurements were made that illustrate this effect. In the first experiment [46], a hydrogen ion beam was used to sputter deposit beryllium onto a silicon sample. Because of the low deposition rate, the resultant material had reacted with the small amount of residual oxygen within the vacuum chamber to form beryllium oxide. The hydrogen retention in this material was quite large at low temperature, as shown in Fig. 14.9. In the subsequent experiments [47], a high-flux plasma simulator was used to deposit a beryllium layer in a short amount of time to reduce the interaction of the sputtered beryllium with residual oxygen molecules and thereby reduce the concentration of beryllium oxide in the sample. As can be seen in the figure the amount of deuterium retained in the film dropped dramatically. The results indicate that hydrogenic species will not be retained within beryllium layers that form due to eroded material transporting and depositing in regions away from plasma bombardment. However, depending on the amount of oxygen present in a device the deposited layers may be depositions rich

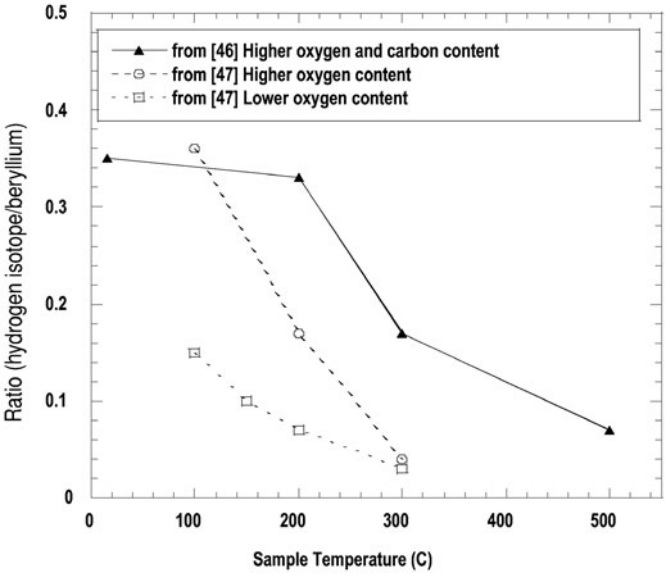

Fig. 14.9. The amount of hydrogen re-deposition with beryllium depends on the impurity content present in the redeposited layers

in BeO, in which case the amount of hydrogenic species incorporated in the layers can rival that of co-deposition of carbon and hydrogen.

Of course, oxygen is not the only impurity that will react with beryllium. Another material that is important in forming mixed-material layers with beryllium is carbon. The saturated value of retention that has been found in beryllium surfaces exposed to a large deuterium ion fluence could easily be overshadowed if a carbon rich layer forms on the beryllium surface due to impurity carbon ions in the incident plasma flux. The hydrogen retention properties of plasma deposited carbon films has been shown to dominate the total retention in beryllium samples exposed to the plasma at lower temperature. Once the sample temperature during exposure approaches 500°C there is little difference between the retention in Be/C mixed-material layers compared to clean beryllium samples [48]. The temperature dependence of the retention of carbon containing mixed material layers, as well as that of clean beryllium surfaces is shown in Fig. 14.10. There are two possible explanations for the reduced retention in the mixed-material layers formed at elevated temperature. The first is that beryllium carbide forms more readily at elevated temperature and less retention is expected in beryllium carbide [11]. The second is that carbon films deposited at elevated temperature also tend to retain less hydrogen isotopes [49].

In the JET tokamak experience, it is more difficult to separate the retention effects due to different species. In general, regions of high deuterium and

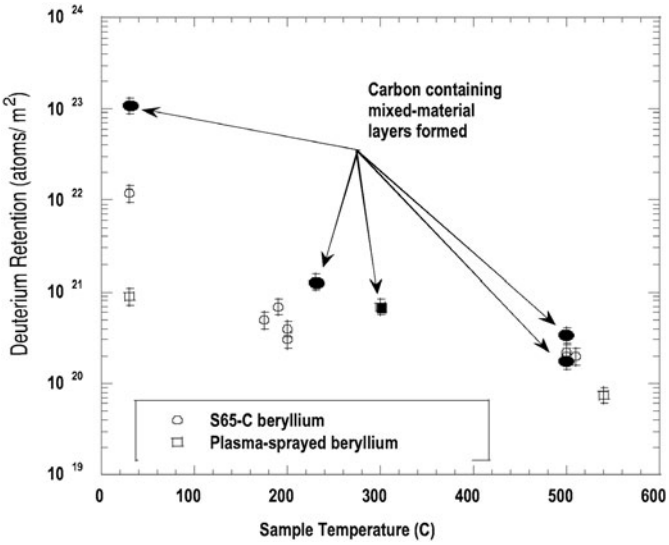

Fig. 14.10. Deuterium retention in beryllium samples can increase when mixed-material layers form. The temperature dependence of the retention in the mixed-material layers is similar to that expected from a pure carbon sample

tritium retention correspond to regions of net deposition of a combination of beryllium and carbon on either wall or divertor tiles [50]. However, the global tritium accumulation in JET is dominated by co-deposits that form in areas without a direct line-of-sight of plasma-facing surfaces [51]. Because of the high sticking coefficient of beryllium atoms on surfaces, it can be concluded that this retention can be attributed to hydrocarbon deposition in these remote areas.

The role that impurities play with regards to hydrogen retention in beryllium surfaces cannot be understated. Clearly a carbon-coated surface can exhibit the retention properties expected of a graphite surface, regardless of the substrate material, so careful consideration must be given to the choice of other plasma facing materials. However, even in an all metal machine tritium accumulation may still be a significant problem. The measured retention in beryllium surfaces is thought to be associated with unavoidable formation of beryllium oxide on the surface and throughout the surfaces that comprise the interconnected porosity that develops during plasma exposure. A self-consistent approach must be adopted when integrating the erosion of the first wall (i.e., how much beryllium oxide is expected) and the retention expected in both the first wall material as well as any redeposited beryllium.

14.3.3 Retention in Li and Ga

One of the primary advantages for using a liquid metal as a plasma-facing material is the potential to achieve a continuously low-recycling boundary condition at the wall. In essence, a low recycling wall will reduce the power loss term associated with disassociation, ionization and radiation from neutral particles in the boundary plasma. Lower power loss terms in the edge plasma will lead to a higher temperature boundary condition for the confined plasma. In turn the higher edge plasma temperature will lead to a reduction in the temperature gradient within the core plasma and thereby, improved confinement throughout the device [52]. This scenario is predicated on the trapping of a significant fraction of the incident ions (predominantly hydrogen isotopes) in the plasma-facing material. For a long-pulse, high-power machine, a static wall is incapable of performing this task.

A liquid surface provides two benefits toward being able to provide a low-recycling boundary. The first is the natural ability of a liquid to flow through the plasma–wall interaction zone and thus constantly present a new surface to the plasma. The second advantage of utilizing a liquid surface, rather than say a moving solid surface, is the high diffusion rate in liquids compared to solids. Typically, the hydrogen diffusion rate is several orders of magnitude larger in a liquid than in a solid. This permits the use of the entire volume of the liquid to retain the incident particle flux, rather than the much smaller implantation, or diffusion, zone in a solid plasma-facing component.

In the case of lithium, low recycling is expected because the chemical reaction of lithium with hydrogen is exothermic, resulting in the formation of hydrides that are trapped in solution [53]. Initial measurements of the retention of hydrogen ions, from a low-flux ion beam, in liquid lithium suggested that the recycling from lithium should be low [54]. However, due to the low total exposure fluence [55] during these measurements, the solubility limit of hydrogen in lithium was never reached. The issue of how the recycling properties of lithium respond once the solubility limit was exceeded has been investigated by Baldwin [56]. These measurements showed that once the solubility limit was reached, the lithium-hydride would precipitate out of solution within the liquid, but that the remaining liquid lithium would continue to trap incident hydrogen ions until the entire volume of lithium was stoichiometrically converted into lithium-hydride. Once the sample was fully converted to lithium-hydride, high recycling of the incident particle flux was reestablished. Figure 14.11 shows the retained amount of hydrogen within a lithium sample as a function of the incident particle flux from these experiments. No temperature dependence on the ability of the liquid lithium to trap hydrogen was observed.

In conjunction with these measurements of hydrogen retention in liquid lithium the release rate of the trapped hydrogen back out of the solution was measured [57]. The recombination rate from the liquid surface was determined to agree well with models that had been developed for solid surfaces [58]. The

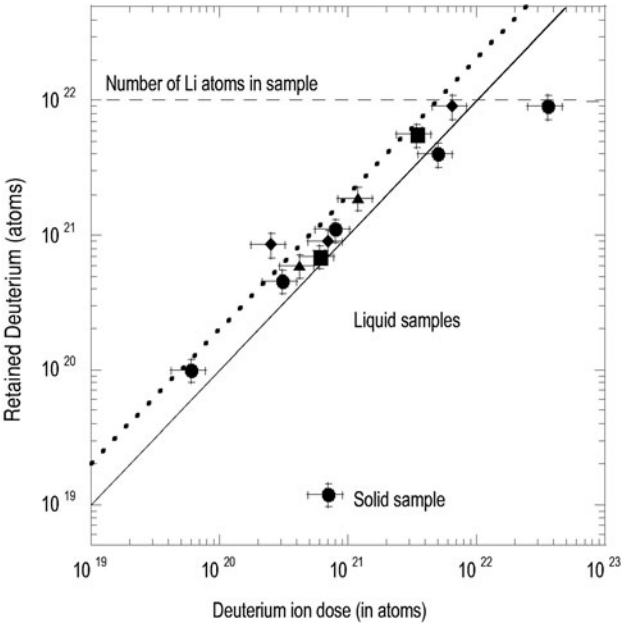

Fig. 14.11. Plot of deuterium retention in lithium samples exposed over a wide range of ion fluence (from [56]). The different symbols reflect the sample temperature during the plasma exposure. The *solid line* is a plot of the ion fluence. An estimate of the total energetic atom fluence arising from charge exchange, dissociation and ion bombardment is given by the *dotted line*

conclusion of this set of experiments was that a low-recycling plasma-facing component, using lithium was feasible from the point of view of the hydrogen interactions with the molten surface. Similar measurements using incident helium ions detected no retention of the helium in the liquid lithium [56].

A low-recycling boundary for a magnetically confined plasma may offer benefits from the point of view of confinement, however it presents other problems, for example with respect to fuelling of the confined plasma. While a solid wall in a long pulse device offers effectively 100% recycling from the surface, lithium effectively offers zero. Other flowing liquids may offer the possibility of a recycling coefficient somewhere in between these two extremes.

Circumstantial evidence was observed in the post-bombardment surface morphology of gallium samples that were exposed to deuterium plasma and then rapidly cooled [20]. Small voids were observed in the sample surface that may have resulted from the coalescence of bubbles during the sample cool down period. Consistent with this view was the fact that the amount of deuterium retained in the samples was independent of the sample exposure conditions. Follow-up experiments are being performed to determine whether gallium samples exposed to deuterium plasma at elevated temperature (around

400°C) may retain deuterium while hot and release the deuterium as they cool. The results of these measurements will determine whether gallium could provide an opportunity to obtain a midrange recycling condition by simply adjusting the flow speed of a liquid gallium surface exposed to the confined plasma.

Again, as in the case of lithium, no retention was observed in gallium samples exposed to helium plasma bombardment. There is conjecture that, in a flowing system, helium atoms may coalesce to form bubbles and that these bubbles could be retained in the flowing liquid, thereby providing some amount of helium pumping. Whether this technique proves practical remains to be seen, but the issue of helium pumping for a flowing liquid surface exposed to a burning plasma environment is still a concern.

It should also be mentioned that in a boundary condition employing a low recycling liquid divertor (not necessarily the entire wall surface), the issue of tritium accumulation within the vacuum vessel may decrease significantly. First, because tritium incident on the liquid surface is retained in the flowing liquid and removed from the system, but also because by definition in a low recycling boundary condition the amount of neutral gas in the plasma edge is reduced, which in turn limits the quantity available for redeposition with eroded material. Another beneficial, natural consequence of a low recycling boundary arising from the low edge neutral density is a reduction of the charge exchange particle flux to the plasma-facing surfaces. This reduction of the energetic particle flux to the first wall will reduce its erosion and should result in a decrease of wall impurities in the core plasma.

14.4 Conclusion

Beryllium is currently the first wall material of choice for next step magnetically confined plasma devices. In part this arises from its successful deployment in the JET tokamak. While there are certainly benefits that can be argued for its use, there are also still unknowns and even drawbacks to its use. One can argue that its low atomic number and ability to getter oxygen from the vacuum are aspects that make it desirable in a plasma confinement environment. One can also argue that its relatively low melting temperature and the affinity of beryllium oxide to co-deposit with hydrogen make its applicability to future long pulse, high power devices questionable.

A recognized benefit from using a large area beryllium first wall is the ability of the wall to act, at least transiently, as a pump to improve startup and edge plasma properties. This transient pumping ability should be more correctly thought of as a hydrogen reservoir, collecting hydrogen during a discharge and then releasing the accumulated hydrogen before a subsequent discharge. While this ability has proven beneficial in existing machines, during longer pulse, or steady state, facilities the startup benefits may continue to be realized, but the limits of this reservoir will eventually be reached.

An unresolved issue related to the use of a beryllium, or any solid material, as a first wall is the issue of mixed-materials. Although the properties of beryllium may lend themselves to its use in a particular environment, those properties can change dramatically as material from other locations in the machine is eroded, transported and then deposited on the beryllium plasma facing surfaces. Such mixed-material surfaces can dominate the rate of long-term tritium accumulation within a device and may severely restrict its operational lifetime.

While still in its infancy the prospect of liquid plasma facing surfaces may offer a potential solution to many of these concerns. Of course, many unanswered questions remain regarding the use of liquids in a magnetic confinement environment. The capability to continuously renew a plasma facing surface is attractive from both an erosion and a tritium accumulation viewpoint. It is also this ability of the material to flow that removes any rigidity from the equation and restricts the ability of the material to withstand applied forces. The main challenge faced in the deployment of liquids as plasma facing surfaces is to control their motion in an environment where all the parameters encountered by the surface may not be well known and will most certainly vary in both space and time.

The entire field of plasma-facing component development is a series of trade-offs and compromises. The knowledge basis for using a beryllium plasma facing material is quite well developed. In part because of its maturity additional questions regarding its use have arisen. On the other hand, the experience level associated with liquid plasma facing surfaces is almost nonexistent. Additional work in this area will be needed to realistically evaluate their merits.

References

1. A.D Haigh, M.A. Pick, Fusion Engr. and Design **37** (1997) 531
2. G. Janeschitz, ITER JCT and HTs, J. Nucl. Mater. **290-293** (2001) 1
3. D.M. Meade, Fusion Engr. and Design **63-64** (2002) 531
4. M.A. Abdou, The APEX Team, A. Ying et al., Fusion Engr. and Design **54** (2001) 181
5. G. Federici, C.H. Skinner, J.N. Brooks et al., Nucl. Fusion **41** (2001) 1967
6. R. Aratari, W. Eckstein, Nucl. Instrum. Meth. B **42** (1989) 11
7. W. Eckstein, Max-Plank-Institut für Plasmaphysik, IPP Report, IPP **9/132** (2002)
8. J. Biersack, W. Eckstein, Appl. Phys. A **34** (1984) 73
9. J. Roth, W. Eckstein, M. Guseva, Fusion Engr. and Design **37** (1997) 465
10. E. Hechtl, J. Nucl. Mater. **220-222** (1995) 883
11. J. Roth, W.R. Wampler, W. Jacob, J. Nucl. Mater. **250** (1997) 23
12. D. Naujoks, W. Eckstein, J. Nucl. Mater. **230** (1996) 93
13. P. Goldstrass, Ch. Linsmeier, J. Nucl. Mater. **290-293** (2001) 71
14. R.P. Doerner, S.C. Luckhardt, R. Seraydarian et al., Physica Scripta **T81** (1999) 35

15. R.P. Doerner, A.A. Grossman, S. Luckhardt et al., J. Nucl. Mater. **266-269** (1999) 392
16. J. Won, F.E. Spada, R. Boivin et al., J. Nucl. Mater. **241-243** (1996) 1110
17. A. Grossman, R.P. Doerner, S. Luckhardt, J. Nucl. Mater. **290-293** (2001) 80
18. J.M. Howe, *Interfaces in Materials: Atomic Structure, Thermodynamics and Kinetics of Solid-Vapor, Solid-Liquid and Solid-Solid Interfaces* (Wiley, New York 1997)
19. J.Laszlo, W. Eckstein, J. Nucl. Mater. **184** (1991) 22
20. R.W. Conn, R.P. Doerner, F.C. Sze et al., Nucl. Fusion **42** (2002) 1060
21. D.R. Lide (ed.), *Handbook of Chemistry and Physics*, 74th edn, (CRC Press, Boca Raton, Ann Arbor, London, Tokyo 1993)
22. J.P. Allain, D.N. Ruzic, M.R. Hendricks, J. Nucl. Mater. **290-293** (2001) 180
23. A.R. Krauss, D.M. Gruen, J. Nucl. Mater. **85-86** (1979) 1179
24. J.P. Allain, D.N. Ruzic, Nucl. Fusion **42** (2002) 202
25. P.C. Stangeby. In: *Physics of Plasma–Wall Interactions in Controlled Fusion*, D.E. Post and R. Behrisch (ed.) (Plenum Press, New York 1986)
26. G. Antar, R.P. Doerner, R. Kaita et al., Fusion Engr. and Design **60** (2002) 157
27. B.I. Khripunov, V.B. Petrov, V.V. Shapkin et al., J. Nucl. Mater. **290-293** (2001) 201
28. V.A. Evtikhin, I.E. Lyublinski, A.V. Vertlov et al., Fusion Engr. and Design **56-57** (2001) 363
29. R.S. Nelson, Philos. Mag. **11** (1965) 291
30. E.P. Vaulin, N.E. Georgieva, T.P. Martynenko et al., Sov. J. Plasma Phys. **2** (1981) 437
31. J. Roth, W. Moller, Nucl. Instr. Meth. Phys. Res. B **7/8** (1985) 788
32. V. Philipps, E. Vietzke, H. Trinkaus, J. Nucl. Mater. **179-181** (1991) 25
33. R.P. Doerner, S.I. Krasheninnikov, K. Schmid, submitted to Phys. Rev. Lett. (2003)
34. J.A. Snipes, E.S. Marmar, J.L. Terry et al., J. Nucl. Mater. **196-198** (1992) 686
35. J. Winter, J. Nucl. Mater. **176-177** (1990) 14
36. R.A. Anderl, R.A. Causey, J. W. Davis et al., J. Nucl. Mater. **273** (1999) 1
37. R.A. Causey, J. Nucl. Mater. **300** (2002) 91
38. R.A. Langley, J. Nucl. Mater. **85-86** (1979) 1123
39. A.A. Haasz, J.W. Davis, J. Nucl. Mater. **241-243** (1997) 1076
40. V.N. Chernikov, V.Kh. Alimov, A.V. Markin et al., J. Nucl. Mater. **233-237** (1996) 860
41. V.Kh. Alimov, V.N. Chernikov, A.P. Zakharov, J. Nucl. Mater. **241-243** (1997) 1047
42. R.A. Anderl, M.R. Hankins, G.R. Longhurst et al., J. Nucl. Mater. **196-198** (1992) 986
43. J.Ehrenberg, P. Andrew, L. Horton et al., J. Nucl. Mater. **196-198** (1992) 992
44. J. Ehrenherg, V. Philipps, L. De Kock et al., J. Nucl. Mater. **176-177** (1990) 226
45. V.Kh. Alimov, V.N. Chernikov, A.P. Zakharov et al., J. Nucl. Mater. **241-243** (1997) 1047
46. M. Mayer, J. Nucl. Mater. **240** (1997) 164
47. R.A. Causey, D.S. Walsh, J. Nucl. Mater. **254** (1998) 84

48. R.P. Doerner, A.A. Grossman, S. Luckhardt et al., J. Nucl. Mater. **266-269** (1999) 392
49. B.L. Doyle et al., J. Nucl. Mater. **103-104** (1982) 513
50. M. Rubel, J.P. Coad, N. Berkis et al., J. Nucl. Mater. **313-316** (2003) 321
51. J.P.Coad, N. Bekris, J.D. Elder et al., J. Nucl. Mater. **290-293** (2001) 224
52. S.I. Krasheninnikov , L.E. Zakharov, G.V. Pereverzev, Phys. Plasmas **10** (2003) 1678
53. E. Veleckis, J. Nucl. Mater. **79** (1979) 20
54. A.K. Fischer, D.V. Steidl, C.E. Briant et al., Nucl. Sci. Eng. **63** (1977) 191
55. S.K. Erents, G.M. McCracken, P. Goldsmith, J. Phys. D, Appl. Phys. **4** (1971) 672
56. M.J. Baldwin, R.P. Doerner, S.C. Luckhardt et al., Nucl. Fusion **42** (2002) 1318
57. M.J. Baldwin, R.P. Doerner, R. Causey et al., J. Nucl. Mater. **306** (2002) 15
58. M.A. Pick, K. Sonnenberg, J. Nucl. Mater. **131** (1985) 208

Part IV

Databases

15 IAEA Databases and Database Establishment Programs

R.E.H. Clark and D. Humbert

15.1 Introduction

In this chapter the activities and capabilities of several data centers are summarized. In the first section the work of the Atomic and Molecular (A+M) Data Unit of the International Atomic Energy Agency (IAEA) is described, including the advisory groups to the Unit, the research projects coordinated by the Unit and the various products resulting from these projects. This is followed by a section on the extensive database established at the National Institute for Fusion Science (NIFS) in Japan, detailing the capabilities of the Internet interface to the databases, the research projects contributing to the databases, and the connection of NIFS, as well as other databases, in the Data Center Network of the IAEA. The following section gives an overview of the databases maintained at the National Institutes of Standards and Technology (NIST) in the United States. The accessibility of the data through the Internet, scope of the databases, related databases, and quality of the data are described as well as examples of the interactive interface to the data. The extensive Atomic Data and Analysis Structure (ADAS) Project is discussed in detail in the next section. The general principles of ADAS, summaries of the relevant codes and data organization, the off-line ADAS system, errors and uncertainties of the data and current projects are described. The next section gives a thorough review of the current status of the database on collision processes of hydrogen. An overview of the important processes is given, along with an assessment of the available data as well as a summary of the additions needed by the fusion community. The data needs are closely connected to the processes for which these data are needed and the areas for which gaps exist are clearly described. The final section of this chapter describes the important work on electron impact ionization cross-sections of hydrocarbon molecules. Partial and total cross-sections, as well as the ion kinetic energy distribution for several hydrocarbons have been measured over a wide range of impact electron energy. The details of the experimental method are explained followed by a careful presentation of the results. These contributions to databases represent a large and continuing effort that is of high importance to the further development of fusion devices.

15.2 Overview

In this section we summarize the work undertaken by the Atomic and Molecular (A+M) Data Unit of the International Atomic Energy Agency. The A+M Unit has as its goal the establishment of databases of atomic, molecular, and plasma-material interaction data for support of fusion energy research. The Unit carries out a number of programs to fulfil this goal. These programs result in the establishment of databases which are put in electronic form and made accessible to the fusion community on a database server with connection to the Internet.

In the next subsection we will discuss the two external advisory groups for Unit activities. The next subsection will then describe Coordinated Research Projects, the primary method used to fulfil the goals of the Unit. We then give a description of the products available to the fusion research community through the A+M Unit. These include the electronic databases, publications, as well as some computational capabilities.

15.3 Advisory Groups

There are two separate external entities which offer recommendations to the A+M Unit: the Atomic and Molecular Data Subcommittee of the International Fusion Research Council (IFRC) and the Atomic and Molecular Data Center Network.

IFRC Subcommittee

The IFRC Subcommittee meets bi-annually. It provides the Unit with a strong link to the fusion community. The Subcommittee provides suggestions for areas in need of increased research activities for generation of data in specific areas in fusion research. The recommendations of the Subcommittee form the basis for the Unit planning in the IAEA budget cycle. At the meetings the Subcommittee also reviews the activities of the Unit in the previous two year cycle. In addition the Subcommittee recommends additional activities that may be of benefit to the Unit. The subcommittee also offers advice between meetings on a variety of issues through informal exchanges. There are currently ten members of the Subcommittee. These are listed in Table 15.1. Members are appointed by the full IFRC as needed to keep the Subcommittee at full strength.

Data Center Network

The second entity that gives regular input to the Unit is the Data Center Network. This Network also meets biannually. It is made up of representative from 13 institutions from around the world, all having well-established capabilities in the area of data generation in support of fusion energy. The

Table 15.1. A+M Subcommittee members

Name	Country
N.J. Peacock	United Kingdom
M. Crisp	United States
R. Guirlet	France
R.K. Janev	Macedonia
Yu.V. Martynenko	Russian Federation
E. Menapace	Italy
J. Roth	Germany
T. Kato	Japan
W.P. West	United States

representatives review data priorities at the bi-annual meeting and revise the list of priorities as needed. During the interval between the meetings the data centers provide specific data as needs arise. Recently work has been undertaken to begin electronic links among the data centers, allowing a user to access specific data from a number of data centers from one search engine. Work on the prototype search engine is continuing. Bibliographic data from the data centers are collected periodically and used in the publication of the *International Bulletin on Atomic and Molecular Data for Fusion* (the *Bulletin*). Current members of the Data Center Network are listed in Table 15.2.

Table 15.2. Members of Data Center Network

Name	Institution	Country
V.R. Barabash	D.V. Efremov Sci. Res. Inst.	Russian Federation
J. Bretagne	Laboratoire de Physique de Plasmas	France
W. Eckstein	Max-Planck-Institut fur Plasmaphysik	Germany
A. Godunov	Troitsk Inst. of Innov. and Fus. Res.	Russian Federation
T. Kato	NIFS	Japan
Yu.V. Martynenko	Kurchatov Institute	Russian Federation
E. Menapace	ENEA	Italy
Yu.V. Ralchenko	Weizmann Institute	Israel
Y. Rhee	Korea At. En. Res. Inst.	Republic of Korea
D.R. Schultz	Oak Ridge Nat. Lab.	United States
TBA	Japan At. En. Agency	Japan
W.L. Wiese	NIST	United States
Yongshen Sun	CRAAMD	China

Table 15.3. Molecular Data for Edge Plasmas

Participant	Research areas
K. Becker	Cross-section measurements
M. Capitelli	Collisional–radiative models
M. Chibisov	Charge exchange calculations
P. Defrance	Cross-section measurements
U. Fantz	Collisional–radiative models
Y. Hatano	Photoabsorption measurements
Z. Herman	Charge transfer, chem reaction measurements
M. Larsson	Dissociative recombination measurements
T. Maerk	Cross-section measurements
S. Matejcik	Cross-section measurements
I. Schneider	Reactive collisions between electrons and molecules

Table 15.4. Atomic and Molecular Data for Plasma Diagnostics

Participant	Research areas
T. Evans	Beam diagnostics
G. Fussman	Measurements in EBIT
B. Gilbody	Charge transfer measurements
R. Hoekstra	Charge transfer measurements
R. Janev	Cross-section calculations
P. Krstic	Vibrationally resolved transitions
L. Mendez	Charge transfer calculations
Z. Luo	Ionization cross-section measurements
M. Panov	Electron capture and excitation calculations
A. Pospieszczyk	Measurements of rate coefficients
H. Summers	Database system for fusion
H.P. Winters	Beam experiments

15.4 Co-ordinated Research Projects

The primary means of generating new data is through Coordinated Research Projects (CRP). A typical CRP is a three to five year project with a specific focus. The CRPs are established in response to a specific need. The topic is frequently suggested through the IFRC Subcommittee meeting.

Once a topic has been identified, a meeting of experts in the area will be convened for a one-time planning meeting. At that meeting the potential scope of a CRP will be outlined and potential participants identified. A specific proposal for the CRP will be formulated. This proposal will be

Table 15.5. Tritium Inventory in Fusion Reactors

Participant	Research areas
V.Kh. Alimov	Deuterium retention
S. Artemov	Measurement of tritium retention
N. Bekris	Detritiation of tiles
R. Causey	Tritium uptake in co-deposited layers
J.P. Coad	Tritium retention and detritiation
R. Doerner	Properties of mixed material layers
A. Haasz	Hydrogen retention in tugsten
A. Pisarev	Modeling of release of ion implanted hydrogen
J. Roth	Deuterium retention in tungsten
C. Skinner	Laser removal of tritium
T. Tanabe	Tritium retention in PFM

submitted to an approval process within the Agency with thorough review by an internal panel.

Upon approval the CRP is formally established. The participants are invited to enter into a formal contract to participate in the CRP. A small number of participants with financial needs may be offered limited financial support; the bulk of the researchers are supported by their home institution, with the exception of travel support for meetings at Agency Headquarters.

The CRP commences with a Research Co-ordination Meeting (RCM) held at Agency Headquarters. At the first RCM the researchers will be asked to summarize their current research areas. Specific tasks relevant to the CRP and within the expertise of the group will be identified. A detailed work plan can then be formulated outlining the tasks to be performed by each participant. Contact among the members is maintained electronically and by planned informal gatherings at other meetings. A final RCM is held to review the final results of the CRP. Each participant is invited to submit an article on the results produced for publication in the journal *Atomic and Plasma-Material Interaction Data for Fusion* (APID). Finally, as the data undergo evaluation, they are added to the electronic databases maintained by the Unit.

Normally the Unit has two to four CRPs active at any time. A normal CRP spans a three year interval, but it is possible to extend this in some circumstances to an additional one or two years. Topics of current CRPs include tritium inventory in fusion reactors, atomic and molecular data for fusion plasma diagnostics, and data for molecular processes in edge plasmas. Tables 15.3–15.5 identify the participants of the current CRPs. Recently completed CRPs include the topics of charge exchange cross-section data for fusion plasma studies, radiated power, and plasma-interaction data for mixed materials, with results now available in the APID series [1–3].

15.5 A+M Unit Products

15.5.1 Electronic Databases

Numerical Data

With the advances in computing and Internet capability, the most useful method of making data available is in electronic form. The A+M Unit maintains a server with access to the large amounts of data stored in electronic form. The data are accessed through a database management tool which allows users to search for and select specific types of data from the large numbers of types available. The home page for the Unit has the URL: http://www-amdis.iaea.org/, which contains links to the database server, as well to a number of other useful tools. The A+M Unit data are accessed through the Aladdin software. The general categories of data are collisional database, H neutral beam database, particle–surface interactions, and elementary processes in H–He plasmas. Each general category has a number of subcategories. For example, the collisional database includes charge exchange, excitation by electron and heavy particles, ionization processes and more, with a total of 36 processes. Table 15.6 summarizes the collisional processes available, while Table 15.7 shows the particle-surface interactions. The users can select the process of interest to view the various entries for that process. At this point the user has options on selection criteria such as the element or accuracy range. Upon selecting various options, the user is presented with a list of data entries fitting the selection criteria. Any number of entries may next be selected for display. Energy ranges for all selections are set by default to the range of validity of the data, with the option of the user changing the range. After submitting the request, the user is presented with tables of numeric data and, optionally, a graph of all the selected data. Also available on request are fitting coefficients to the data to be used in evaluation functions. These evaluation functions are also available. This gives the user a very comprehensive method of accessing any particular piece of numerical data in the extensive numerical databases maintained by the A+M Unit.

Bibliographic Data

In addition to the numeric data, the Unit maintains a separate database of bibliographic information relevant to fusion research. This database has been built up from contributions from the Data Center Network. Those submissions are also used, as noted above, in the publication of the *Bulletin*. The complete bibliographic database is now also available through a search engine. A link to that search engine is also found on the home page of the Unit. The search engine allows a user to search by a number of criteria such as authors, year of publication, type of transition, initial reactant, final reactant, etc. Upon finding the relevant bibliographic entries, the search engine also compiles a complete list of every author appearing on any entry found,

Table 15.6. Collisional Processes

Descriptor	Name of Process
ASDET	Associative Detachment
ASION	Associative Ionization
BEM	Spectral Band Emission
CHEMION	Chemical Ionization = Penning + Associative + Other Ionization
CX	Charge Exchange (Single), Total
CX2	Double Charge Exchange Total
CXSS	State Selective Electron Capture, Single
DEST	Destruction of Projectile or Target
DEXC	Collisional Deexcitation (of target)
DEXC+STRIP	Projectile Deexcitation by Stripping
DIS	Direct (Impact) Dissociation
DISCX	Dissociative Charge Exchange
DISCX2	Double Dissociative Charge Exchange
DISEXC	Dissociative Excitation of Molecules
DISION	Dissociative Ionization of Molecules, Single
DISION+STRIP	Dissociative Ionization of Molecules with Projectile Stripping
DISION2	Double Dissociative Ionization of Molecules
DISION2+STRIP	Double Dissociative Ionization of Molecules with Projectile Stripping
DISTI12	Dissociative Transfer Ionization
ELDET	Electron Detachment
ELDET+CX	Electron Detachment + Electron Capture
ELDET2	Double Electron Detachment
ELP	Electron Production
ELREM	Electron Removal (from target)
EXC	Electronic and Heavy Particle Excitation (of target)
ION	Electronic and Heavy Particle Ionization (of target), Single
ION2	Heavy Particle Double Ionization (of target)
IP	Ion Production
IPP	Ion-Pair Production
LEM	Spectral Line Emission
MNREC	Mutual Ion–Ion Neutralization
PENION	Penning Ionization
PX Heavy	Particle Exchange
PXION	Particle Exchange with Ionization
STRIP	Stripping (of projectile)
STRIP2	Double Stripping

Table 15.7. Particle-Surface Interactions

Descriptor	Name of Process
RAENER	Reflection of Atoms (energy distribution)
RE	Energy Reflection
RES	Radiation-Enhanced Sublimation
SAANGLE	Sputtering by Atoms (angle distribution)
SAENER	Sputtering by Atoms (energy distribution)
SATM	Sputtering by Atoms Leading to Molecule Emission (chemical erosion)
SSATM	Synergistic Sputtering by Atoms Leading to Molecule Emission (chemical erosion)

so that a comprehensive author list for that particular topic is viewable at the same time. Additional information, such as energy range for transitions, experiment or theoretical results, etc. is available for each entry.

Plasma Properties

The CRP on radiated power loss generated a large volume of data on plasmas with a range of temperatures and electron densities. This information has now been published in the APID [2]. Some of the data are now also available from the Unit home page.

Because of the different nature of these data, they are not accessed in the same manner as other numerical data. In this case, the user can specify a desired electron temperature and density. The interface will then interpolate on the data to obtain plasma properties such as ionization balance, average charge, and radiated power at the required plasma parameters. The data are displayed in tabular and graphical form. These data are available for the elements neon, silicon, argon, titanium, and iron over a range of electron temperatures and densities of interest for fusion plasmas.

The underlying atomic physics data, consisting of cross-sections for electron collision processes, radiative processes, and autoionization/di-electronic recombination will also soon be available. These complete sets of data are large and could not be accommodated by the existing database server. However, a new server is coming on-line and will be able to hold this extensive new database. In the future the entire sets of data for all five elements will be available through ftp retrieval.

Cross-Section Calculations

At times there is a need for cross-section data that is not available on the Unit databases, or on any other accessible database. It is often useful to have a reasonable estimate to a cross-section rather than no information at all. A rapid calculational technique to calculate electron impact excitation cross-sections, called the average approximation has been well-known for some time

[4]. This technique was originally formulated using only hydrogenic target states and Coulomb functions for the free electrons. This method has now been extended by J. Peek to use Hartree–Fock target states, calculated by the method of R. Cowan [5]. This capability allows a user to generate the energy levels of an arbitrary ion of any atom relevant to fusion and to use the atomic structure in the calculation of cross-sections for excitation. These calculations are quite rapid, taking only a matter of seconds to carry out.

The interface which runs these codes carries out extensive checks on input so that a user cannot attempt to carry out calculations for non-existent orbitals, or energies below the threshold for a transition. It is hoped that similar methods of allowing users to access codes at other institutions will be developed. Preliminary work is now being carried out at the Los Alamos National Laboratory to determine the feasibility of making some of the atomic physics codes from that institution available to outside users. If this effort is successful it is hoped that similar efforts can be initiated at other institutions so that in the future it will be possible to generate data for a wide range of processes of interest to fusion energy research.

Search Engines

With the advent of the Internet, a number of databases containing data useful to fusion energy research have become available to the world-wide-web. However, in order to find data in these databases a user must first become familiar with the interface to each database to be searched. This is often a time-consuming activity.

Y. Ralchenko and D. Humbert have developed prototype search engine to carry out the search of a number of remote databases. With this search engine, a user enters a request once only. The request is reformulated by the search engine for each of a number of different database interfaces at different institutions. The requests are sent to databases selected by the user. The search engine gathers the responses from each database and displays the results to the user. Information on each database is available as are links to the databases.

An extension of this search capability to databases of bibliographic databases has been undertaken by D. Humbert. A prototype search engine has been developed. A difficulty in this search is in the classification of types of processes used by different databases. This has lead to a preliminary effort to introduce a standardized set of classifications for processes among a number of databases.

References

1. *Atomic and Plasma-Material Interaction Data for Fusion*, Vol. 10, ed. by R.E.H. Clark (International Atomic Energy Agency, Vienna 2002)
2. *Atomic and Plasma-Material Interaction Data for Fusion*, Vol. 11, ed. by R.E.H. Clark (International Atomic Energy Agency, Vienna 2003)
3. *Atomic and Plasma-Material Interaction Data for Fusion*, Vol. 12, ed. by R.E.H. Clark (International Atomic Energy Agency, Vienna 2003)
4. J.M. Peek and J.B. Mann: Phys. Rev. A **16**, 2315 (1977)
5. R.D.Cowan: *Theory of Atomic Structure and Spectra* (University of California Press, Berkeley, CA 1981)

16 NIFS DATABASE and Cooperation with IAEA DCN

T. Kato and I. Murakami

We are working on atomic and molecular data and their application with the collaboration of Japanese scientists as well as foreign scientists in the Data and Planning Center (DPC) of the National Institute for Fusion Science (NIFS). We organize working groups to compile atomic data and to apply atomic data in plasmas. The atomic numerical databases in NIFS can be used through the World Wide Web. They are explained in this paper. The domestic and international collaboration in our center are described.

16.1 Introduction

In the Data and Planning Center (DPC) of the National Institute for Fusion Science (NIFS) we are working on atomic and molecular data and their application with the collaboration of Japanese scientists as well as foreign scientists. We organize working groups to compile atomic data and to apply atomic data in plasmas.

We work as one of the world atomic data centers. We send our results to the scientists throughout the world and play a role as an international data center by gathering international information and promoting personal exchanges.

We perform data activities on the basis of working groups organized with Japanese scientists for data compilation, evaluation and dissemination. We are also interested in atomic data code development as well as the application of atomic processes to real plasmas through the codes of collisional–radiative models. The combination of collisional–radiative model and energy–particle transport codes can produce general codes for diagnostics and modeling. When some problems are found during applications, these problems can inspire the improvement of atomic data as a feedback from plasma to atomic physics.

As a future plan, we would like to explore a new field where atomic and nuclear physics are related in plasmas and systemize them. Extensions of our research to non-equilibrium, non-thermal and non-isotropic plasma, especially polarization spectroscopy are considered. We would like to develop quantum molecular dynamics for plasma–wall interactions, plasma radiation science, high-density plasma states, and atomic processes in high fields. These

are related to the expansion of the plasma parameters of atomic and molecular data activities.

International collaboration is very important and indispensable in order for data activities to include a very wide range of atomic data.

16.2 NIFS DATABASE

We work on atomic and molecular (AM) numerical databases for fusion science and related fields. The numerical data have been collected and evaluated by the working groups on basic data for atomic and molecular data as well as plasma-material interaction (PWI) data. These data are indispensable for plasma modeling, diagnostics, or data analysis in fusion or plasma experiments. Four kinds of numerical data, which are listed below, can be retrieved through the World Wide Web. Users can retrieve the data by elements or other attributes and display them in a tabular and in a graphical form. The data produced by different authors for a certain transition can be compared on one graph. This is an advantage of our database. Bibliographic databases are also available as described below. They are used independently or in connection with the numerical databases. The databases are available through the Web at URL = `http://dbshino.nifs.ac.jp/` and free of charge for research purpose for registered users. It is possible to register at the same URL address. Another Web page which gives an introduction to AM databases is available at `http://dpc.nifs.ac.jp/amdata/`.

We have four kinds of numerical databases, AMDIS, CHART, SPUTY and BACKS, as shown in Table 16.1. We are now going to open a new database for molecular collisions: AMOL for data by electron impact and CMOL for data by ion impact. AMOL includes cross-sections and/or rate coefficients on total scattering, elastic scattering and momentum transfer, excitation, ionization, dissociation, attachment and recombination. CMOL includes cross-sections, rate coefficients and branching ratios on excitation, ionization, charge transfer, dissociation, association, elastic scattering and momentum transfer, and rearrangement. At the moment we are compiling the data mainly for H_2 (D_2, HD), CO, CO_2, H_2O, Hydrocarbon (CH_4, C_2H_6 etc.), SF_6, etc.

The number of registered database users is 750 from 46 countries (April 2003). The distribution of the users by country is shown in Fig. 16.1.

We have other numerical databases which you can use without registration (`http://dpc.nifs.ac.jp/amdata/`) as follows:

(a) ALADDIN contains the rate coefficients for ionization and recombination and the photo-ionization cross-sections of impurity ions in Aladdin format.
(b) Data on sputtering yield, reflection coefficients and mean range calculated by Dr. W. Eckstein using the Monte Carlo program code (TRIM.SP) [1,2].
(c) Data tables of rate coefficients for electron dissociative attachment to molecular hydrogen calculated by J. Horacek et al. [3].

Table 16.1. Numerical databases in NIFS (The number of the data sets are indicated in parenthesis. April, 2003)

AMDIS	
AMDIS-ION	Cross-sections for electron impact ionization. Dissociations of molecules by electron impact are also compiled. (1 456 sets).
AMDIS-EXC	Cross-sections for electron impact excitations (21 455 sets).
AMDIS-REC (New)	Cross-sections and rate coefficients for electron impact recombination (25 785 sets).
CHART	Cross-sections for charge transfer and ionization of atoms, ions, and molecules by ion/atom collisions (4 390 sets).
SPUTY	Sputtering yields for monatomic solids by ions (1 244 sets).
BACKS	Particle- and energy-backscattering coefficients of light ions from solids. Distributions of energy and angle of scattered particles also are included (282 sets).
AMOL (new)	Cross-sections and rate coefficients for molecules by electron impact (1002 sets).
CMOL (new)	Cross-sections, rate coefficients and branching ratios for molecules by heavy particle impact (758 sets).

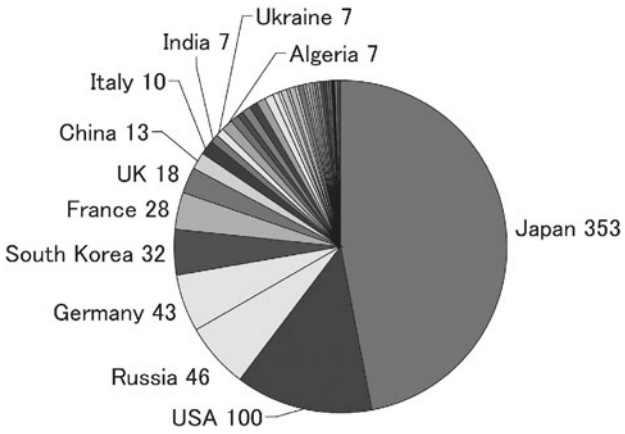

Fig. 16.1. Number of registered database users by country (as of Apr 2, 2003)

(d) Ion fractions of various element in plasmas [4–6].
(e) A numerical database for satellite lines has been made recently as a collaboration with KAERI under the Korea–Japan CUP collaboration program and it is available at URL=`http://dprose.nifs.ac.jp/DB/Auto/`, which will be explained in Sect. 16.3.2.

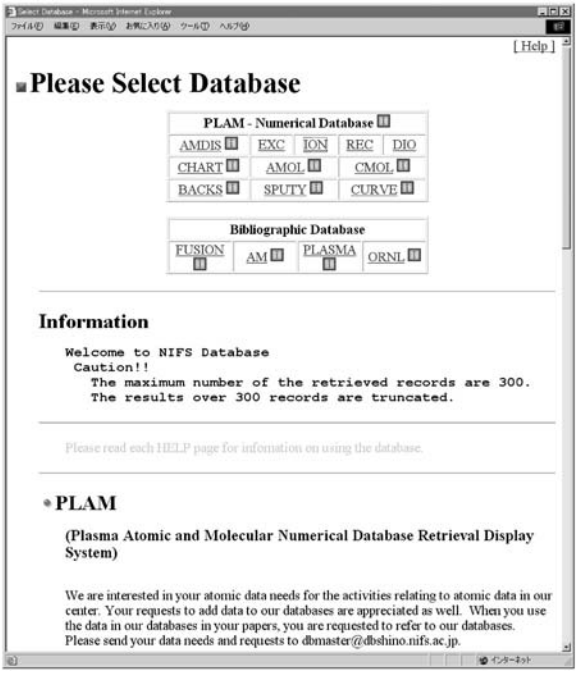

Fig. 16.2.

(f) A fusion device database (`http://dpc.nifs.ac.jp/fudev/`) gives the parameters of fusion machines in the world.
(g) Information on nuclear reaction data (`http://dpc.nifs.ac.jp/Ndata/index.html`) gives review papers which contain the analytical form of reaction rates and cross-sections. Internet Sites for available reactions are also listed.

16.3 IFS DPC Collaboration Program

16.3.1 Domestic Collaboration

In order to advance the data activities and application of the data to plasma physics mentioned above we organize working groups with the physicists of universities in Japan. We had the following working groups in 2002. The name of the key person is indicated with the title of the collaboration program. These working groups are supported for travel expenses to visit our Institute to organize the meetings.

(a) AM data compilation and update for NIFS databases, M. Kimura (Yamaguchi Univ.)

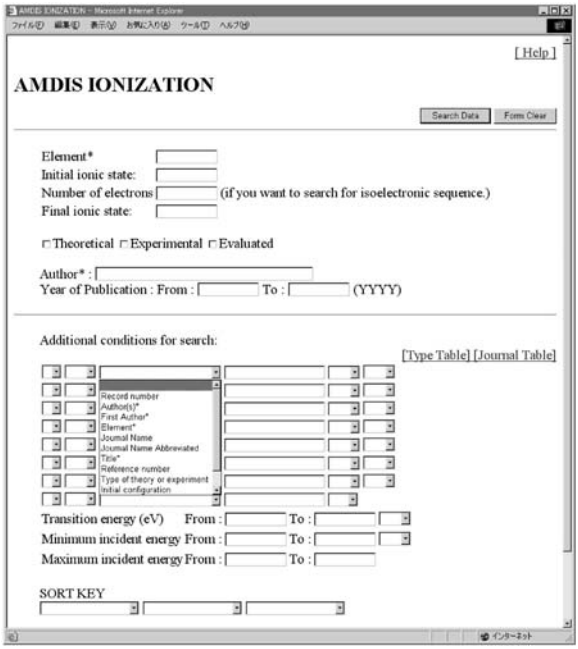

Fig. 16.3. Retrieval page for electron impact ionization database (AMDIS-ION)

(b) Development of atomic data and atomic kinetics codes of multiple charged ions, A. Sasaki (JAERI)
(c) Atomic data evaluation and data fitting, H. Sato (Ochanomizu Univ.)
(d) Atomic and molecular processes in divertor plasmas, T. Fujimoto (Kyoto Univ.)
(e) Impurity ion spectrum radiation power in the fusion plasmas, M. Yoshikawa (Tsukuba Univ.)
(f) Isotope effect on electron transfer cross-section of $p + H_2/D_2$, M. Kimura (Yamaguchi Univ.)
(g) Ionization and charge transfer for the collisions between low-energy protons and molecules in fusion reactor plasmas, M. Kimura (Yamaguchi Univ.)
(h) Survey of the most recent information about nuclear fusion reaction data, M. Sasao (Tohoku Univ.)
(i) Plasma–wall interaction in steady-state magnetic fusion devices and new plasma-facing component concept development, M. Nishikawa (Osaka Univ.)
(j) Plasma–wall interaction databases and related simulation code library, K. Morita (Nagoya Univ.)

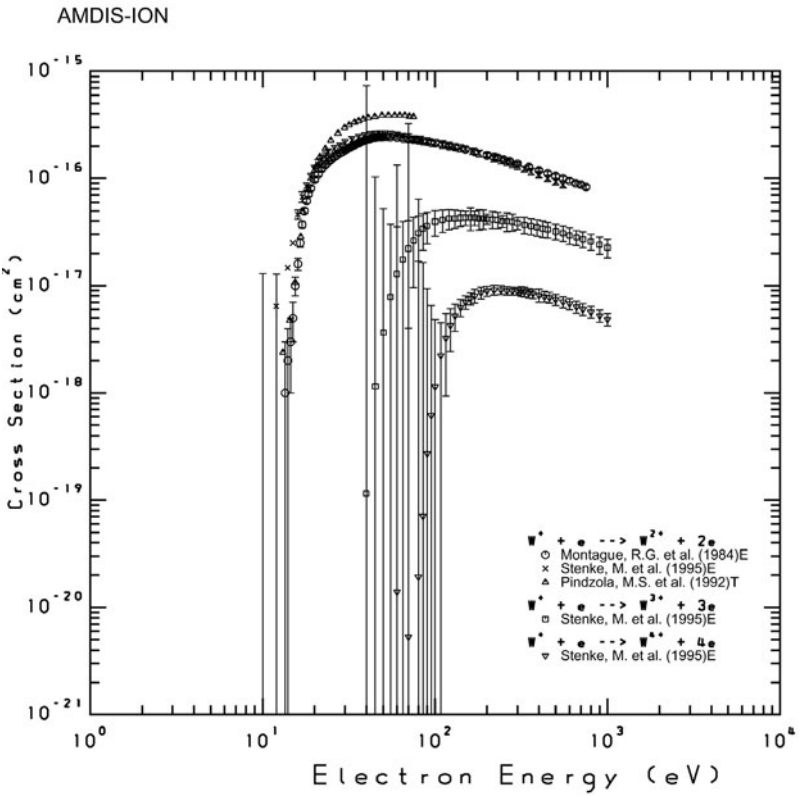

Fig. 16.4. Graphic output example for the electron impact ionization of W^+ (AMDIS ION)

16.3.2 International Collaboration

In carrying out the programs introduced above, collaborations with foreign institutes as well as domestic institutes are important. Long-term visitors for collaborations in 2002 were Dr. O. Tolstikhin (Kurchatov Inst.), Prof. A. Starostin (Kurchatov Inst.), Prof. Xinwen Ma (Inst. Modern Physics, CAS), Dr. A. Whiteford (Univ. Strathclyde - JET), Prof. H. Schuch (Stockholm Univ.), Prof. E. Lindroth (Stockholm Univ.), Prof. C.Z. Dong (Northwest Normal Univ., Lanzhou) etc. We continue a Japan–Korea collaboration program. We initiated a Japan–China collaboration program on "Atomic processes in plasmas" under the Core University Program from 2002. As a Japan–US collaboration, we worked with Livermore scientists on atomic processes in fusion plasmas.

(a) The Japan–Korea collaboration program was initiated in 1998 under the Core University Program with Kyoto University and Seoul National University. The key persons on atomic processes are Takako Kato (NIFS,

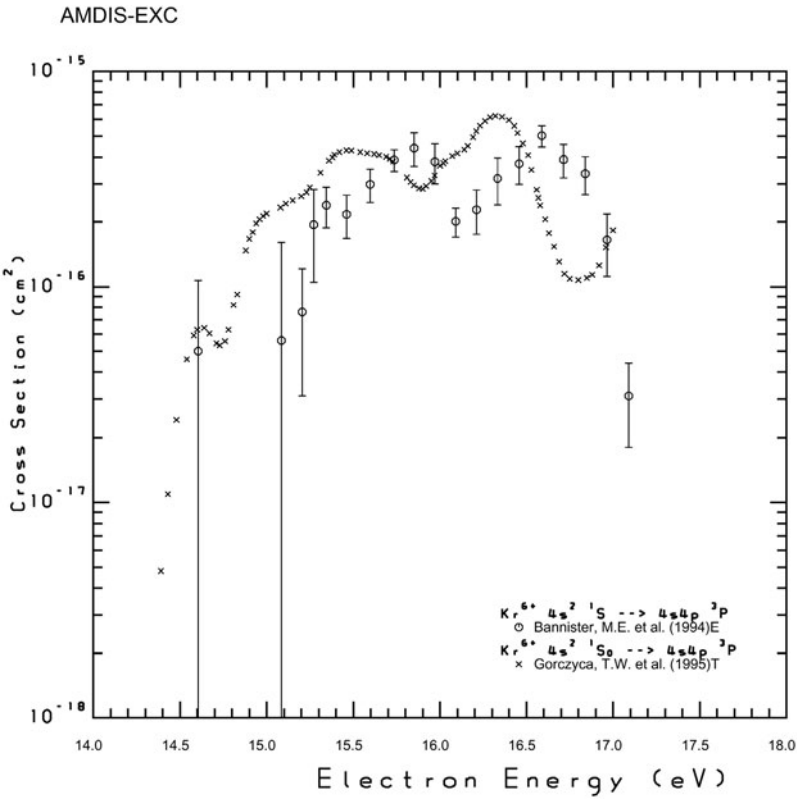

Fig. 16.5. Graphic output example for the electron impact excitation cross-section of Kr^+ (AMDIS EXC)

Japan) and Dong Eon Kim (Pohang Institute of Science and Technology, Korea). We started with mutual visits and personal exchanges at the beginning. Starting in the last 5 years, several collaborations are now active. The program on "Radiation Processes in High-Density Plasmas" began in 2001 as a five-year project. Topics are polarization spectroscopy, databases for autoionization, X-ray lasing plasmas, electron molecule collisions, molecular data for planetary and cometary, harmonic generation in laser irradiation, etc. A new database for autoionizing states has been opened at URL = `http://dprose.nifs.ac.jp/DB/Auto`. Wavelengths and line intensity factors for dielectronic satellite lines are compiled. Numerical data are stored as tables in text files and graphic output is available for dielectronic satellite line spectra. NIFS has compiled numerical data and KAERI (Korean Atomic Energy Research Institute) has developed graphic tools. Currently datasets for He-like, Li-like, Be-like, and B-like ions for small-Z elements are stored. We welcome your contribution for data submission.

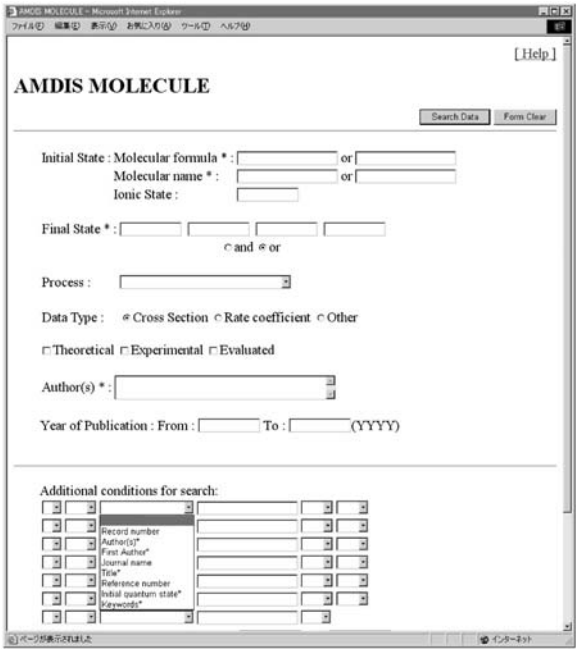

Fig. 16.6. Retrieval page for molecular collision database (AMOL)

(b) The Japan–China Collaboration on "Atomic and Molecular Processes in Plasma" is now going on as a six year project from April 2001 to March 2007 under the Core University Program with NIFS and Institute of Plasma Physics (IPP), China. The key persons on atomic processes are T. Kato (NIFS, Japan) and Wan Boanian (IPP, China). Several scientists visit each other to understand their work. Atomic collision experiment has been done as collaboration work on electron momentum spectrometer for molecules.

16.4 Data Center Network (DCN)

The collaboration programs with the members in DCN and our center are described in this section as follows.

(a) *IAEA.* As a member of DCN organized by Dr. R. Clark in IAEA, NIFS DPC organize the DCN meeting which is held every two years. We enable our database AMDIS to be accessible through Genie (Search Engine for Atomic Data, `http://www-amdis.iaea.org/GENIE/`) of IAEA without registration. The number of users of our database through IAEA is increasing.

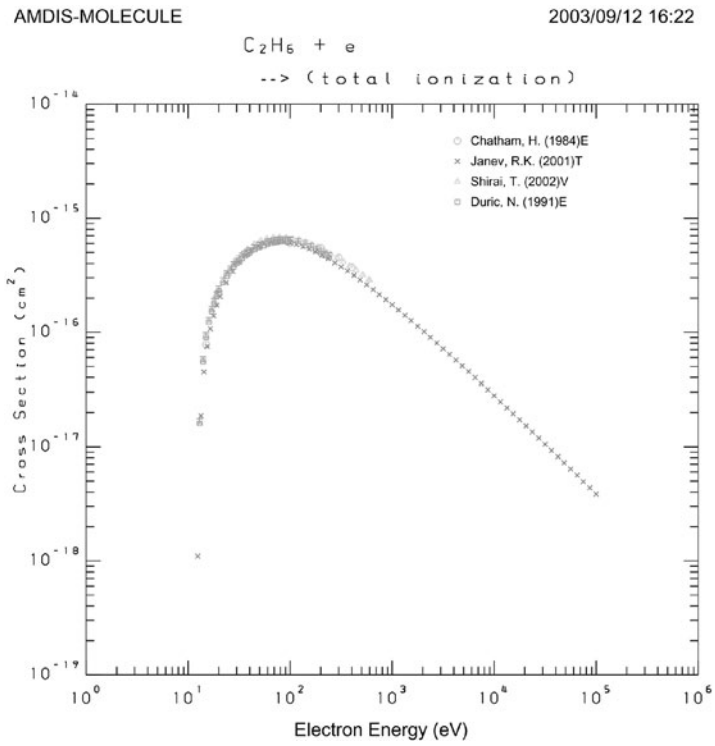

Fig. 16.7. Graphic output example for total ionization cross-section of C_2H_6 (AMOL)

(b) *KAERI (Korean Atomic Energy Research Institute, Korea).* Dr. Yongjoo Rhee at KAERI in Korea is a representative from Korea as a member of DCN in IAEA. The ASRG (Atomic Spectroscopy Research Group) is a subgroup embedded in the Laboratory for Quantum Optics of KAERI, specialized in the study of atomic spectroscopy. It is devoted to the development of precision measurement techniques of atomic spectroscopic parameters such as energy levels, autoionization levels, isotope shifts, hyperfine structures, multi-photon ionization schemes, etc., using the resonance ionization spectroscopy methods. It is responsible for the AMO database systems AMODS (Atomic Molecular and Optical Database Systems, (`http://amods.kaeri.re.kr/`). Information on the atomic and molecular structures, transition lines and probabilities, laser propagation characteristics, collisional cross-sections, and fundamental constants are being compiled in this site. Spectral lines of almost all the elements are available, originally derived from the archives of CDS (*C*entre de *D*onnes astronomiques de *S*trasbourg). It contains a downloadable PC version

Table 16.2. Bibliographic Databases in NIFS

FUSION	Bibliography for fusion sciences and plasma physics, extracted from INSPEC.
AM	Bibliography for atomic and molecular physics, extracted from INSPEC.
ORNL	Bibliography for atomic collisions, compiled by Oak Ridge National Laboratory.

of MCDF2002(new) as well as lecture notes. They have a mirror DB of NIST ASD.

(c) *APCM (Institute for applied physics and computational mathematics).* Dr. Jun Yan is the representative from China and they are making their own database in IAPCM in China. The AM database CANDB has been created and the English version is now available. Data can be retrieved through the Web (`http:// www.camdb.ac.cn/`) on spectra, ionization potentials (2 300 records), energy levels (75 000 records), electron-impact excitation (30 000 records), electron-impact ionization (1 100 records), dielectronic recombination, autoionization (18 000 records), opacity, bibliography (6 000 records) and photon ionization (1 200 records). They have a plan to create a molecular database.

(d) *ORNL (Oak Ridge National laboratory).* At the controlled fusion atomic data center at ORNL, whose director is Dr. D. Schultz, they are creating a bibliographic database for atomic collisional processes. They send us their database every few months and we install it into our own database system Oracle as the database "ORNL". The bibliographic database "ORNL" can be retrieved as a database in NIFS as shown in Table 16.2.

(e) We are updating our database for sputtering yield SPUTY, adding the data calculated by W. Eckstein in Max-Plank-Institut fur Plasmaphysik in Germany using TRIM code [2].

(f) We are using ADAS code by H. Summers in U.K. for plasma diagnostics for the "Large Helical Device (LHD)" at NIFS.

(g) We are going to set up a joint project with Russian scientists (Dr. A. Faenov et al.) for a database (Atomic-database SPECTR-W3, `http://spectr-w3.snz.ru`).

16.5 Recent Research Activities

We have performed data evaluation for hydrocarbons with the help of Prof. R. Janev. As a guest professor at NIFS, he worked on the data evaluation of charge exchange by proton impact and ionization by electron impact. They are published as NIFS DATA series [7, 8]. Dr. Y. Ralchenko and

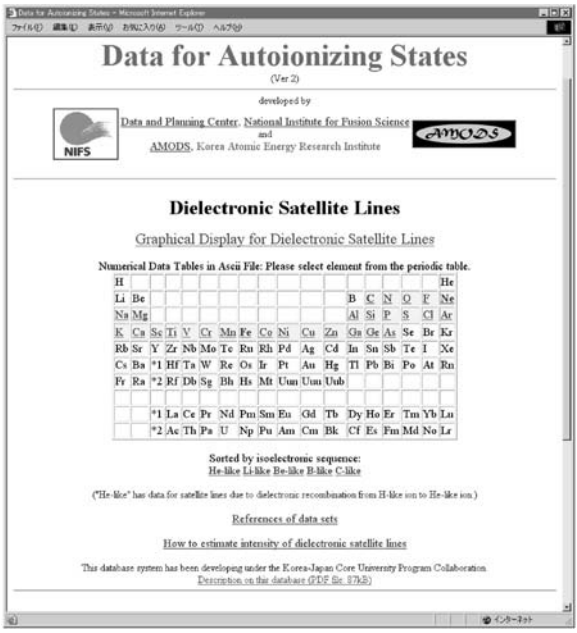

Fig. 16.8. Homepage of autoionization data made by KALRI and NIFS

Fig. 16.9. Homepage of China atomic databases

Prof. R. Janev, as guest professors, worked to provide a recommended data set for electron impact ionization and excitation cross-sections for He atoms [9].

State selective dielectronic recombination rate coefficients from Li-like ions to Be-like ions (C, O, Ne, Fe ions) and for carbon L-shell ions have been calculated [10–13]. These data are used to develop collisional–radiative models including dielectronic recombination to excited states [14–17]. The population kinetics of L-shell ions and atoms have been developed and their results have been applied to plasma diagnostics.

Collisional–radiative models of He-like ions including doubly excited states with collisional processes between doubly excited states have been developed and applied to analyze the X-ray spectra from laser-produced plasmas. This code is also used to derive the effective excitation, ionization and recombination rate coefficients in high-density plasmas [18]. H-like Li spectra produced by charge exchange recombination with neutral hydrogen in magnetic field have been studied with collisional–radiative models [19]. Total, partial and differential ionization cross-sections in proton–hydrogen collisions at low energy have been studied [20].

We perform numerical modeling of atomic processes in various real plasmas including LHD fuel-pellet ablation and short-pulse laser interaction plasmas [21]. We are developing a mixed quantum-classical code to study excited hydrogen atom formation in neutrals of back scattered protons at wall surfaces.

16.6 Conclusion

NIFS databases are widely used directly and through IAEA Genie (only for excitation and ionization cross-sections). New molecular databases will be open soon. A new database for dielectronic satellite lines has been created. In order to store your data in our databases, we are grateful if you send us your numerical data which have been published in a Journal. Organized international collaboration for database would be more efficient for data evaluation and data compilation.

References

1. W. Eckstein, *Computer Simulation of Ion-Solid Interactions* (Springer-Verlag, Berlin, Heidelberg 1991)
2. W. Eckstein, IPP-Report 9/132 (2002)
3. J. Horacek, K. Houfek, M. Cizek, I. Murakami, T. Kato, NIFS-DATA-73 (2003)
4. M. Arnaud, R. Rohtenflug, Astron. Astrophys. Suppl. Ser. **60**, 425–457 (1985)
5. M. Arnaud, J. Raymond, Astrophys. J. **398**, 394–406 (1992)
6. P. Mazzotta, G. Mazzitelli, S. Colafrancesco, N. Vittorio, Astron. Astrophys. Suppl. Ser **133**, 403–409 (1998)

7. R.K. Janev, J.G. Wang, T.Kato, NIFS-DATA-64 (2001)
8. R.K. Janev, J.G. Wang, I. Murakami, T. Kato, NIFS-DATA-68 (2001)
9. Yu.V. Ralchenko, R.K. Janev, T. Kato, D.V. Fursa, I. Bray, F.J. de Heer, NIFS-DATA-59 (2000)
10. U. Safronova, T. Kato, J. Phys. B **31**, 2501 (1998)
11. T. Kato, U. Safronova, M. Ohira, Physca Scripta **55**, 185 (1997)
12. U. Safronova, T. Kato, M. Ohira, J. Quant. Spectrosc. Radiat. Transfer **58**, 193 (1997)
13. I. Murakami, U. I. Safronova, T. Kato, NIFS-DATA-66 (2001)
14. I. Murakami, T. Kato, U. Safronova, NIFS-DATA-50 (1999); I. Murakami, U.I. Safronova, T. Kato, J. Phys. B **32**, 5331 (1999)
15. I. Murakami, K. Moribayashi, T. Kato, NIFS-DATA-47 (1998)
16. I. Murakami, U.I. Safronova, T. Kato, Can. J. Phys. **80**, 1525 (2002)
17. T. Kato, M. Kato, R. More, S-Y Zou, M. Goto, S. Morita. In: *Current Developments in Atomic, Molecular and Chemical Physics with Applications*, ed. by Man Mohan (Kluwer Academic/Plenum Publishers 2002) pp. 265–272
18. N. Yamamoto, T. Kato, R. More, T. Fujimoto, Rapid Communications, J. Plasma and Fusion Res. **78**, 193–195 (2002); T. Kato, N. Yamamoto, R. More, H. Nishimura, F. Rosmej, Proc. Inertial Fusion Science and Applications (2003)
19. S. Zou, T. Kato, I. Murakami, J. Phys. Soc. Jpn. **72**, 287–293 (2003)
20. S. Zou, L. Pichl, M. Kimura, T. Kato, Phys. Rev. A **66**, 042707 (2002)
21. H. Yoneda, H. Morikami, K. Ueda, R. More, Phys. Rev. Letters **91**, 075004 (2003)

17 The NIST Atomic Structure Databases

W.L. Wiese

The NIST atomic structure databases are reviewed, with special emphasis on the comprehensive Atomic Spectra Database (ASD). Most of the data critically compiled at NIST over the last 35 years are included in this large database. The main features of the World Wide Web based database are discussed in some detail, and an outlook on future expansions and updates is provided.

17.1 Introduction

Spectroscopists at the National Institute of Standards and Technology (NIST) and its predecessor, the National Bureau of Standards (NBS), have been producing, evaluating and compiling atomic structure data for more than 80 years, starting with the formation of an atomic spectroscopy group under the leadership of W.M. Meggers in 1920. The early work focused on the production of accurate spectroscopic data, but beginning in 1945, the NBS group also performed full-time spectroscopic data evaluation and compilation. By this time, a fairly large amount of atomic structure data had accumulated in the international scientific literature, and Charlotte E. Moore, who had joined the group then, started to critically compile a general table of atomic energy levels that would cover at least some stages of ionization of the great majority of chemical elements. Thirteen years later, in 1958, she completed a three-volume set of "Atomic Energy Levels" [1] that became the standard data set on atomic structure for a long time to come. Nevertheless, these tabulations were still rather incomplete. They did not contain any data for the higher stages of ionization of heavier elements and only rudimentary data for many moderately charged ions.

In the following four decades, from 1960 to 2000, a dozen other major tabulations on atomic structure data were published at NIST, covering again energy levels [2, 3], but also wavelengths of spectral lines [4–8] and their transition probabilities [9–13] (the latter are a measure of the intensities of the lines and an equivalent quantity, the oscillator strength, is also often used). The cost to produce these data volumes, i.e., books that were several hundred pages strong, remained low as long as the U.S. Government Printing Office agreed to publish them at materials cost, which was until about 1980.

After that date, recourse had to be taken to commercial publishers, such as the American Chemical Society and the American Institute of Physics. The costs of the publications then increased to a point at which many college and university libraries – not to mention individual scientists – could no longer afford to purchase them. Thus, the market to support new large data volumes dried up, – it appears that the period of printed reference data books has essentially passed.

17.2 Data Dissemination on the Internet

The "Internet" publishing medium came along at the right time, and it permits NIST to disseminate its reference data as a free service over the World Wide Web to a very large number of scientists, engineers and students, a larger number than ever before. This electronic medium also has the great advantage that all the NBS/NIST spectroscopic reference data could now be integrated into one single large database. We have called this the NIST "Atomic Spectra Database" (ASD) and it has the URL address `http://physics.nist.gov/asd`.

Figure 17.1 shows the first part of the home page of the database on the World Wide Web. This comprehensive database contains practically all the

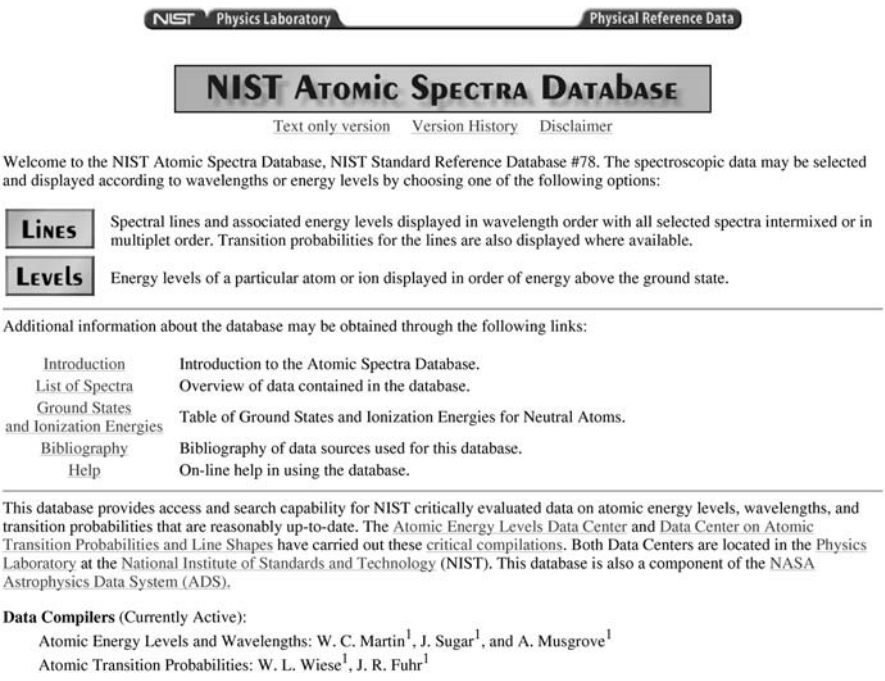
NIST Physics Laboratory — Physical Reference Data

NIST Atomic Spectra Database

Text only version Version History Disclaimer

Welcome to the NIST Atomic Spectra Database, NIST Standard Reference Database #78. The spectroscopic data may be selected and displayed according to wavelengths or energy levels by choosing one of the following options:

LINES — Spectral lines and associated energy levels displayed in wavelength order with all selected spectra intermixed or in multiplet order. Transition probabilities for the lines are also displayed where available.

LEVELS — Energy levels of a particular atom or ion displayed in order of energy above the ground state.

Additional information about the database may be obtained through the following links:

Introduction	Introduction to the Atomic Spectra Database.
List of Spectra	Overview of data contained in the database.
Ground States and Ionization Energies	Table of Ground States and Ionization Energies for Neutral Atoms.
Bibliography	Bibliography of data sources used for this database.
Help	On-line help in using the database.

This database provides access and search capability for NIST critically evaluated data on atomic energy levels, wavelengths, and transition probabilities that are reasonably up-to-date. The Atomic Energy Levels Data Center and Data Center on Atomic Transition Probabilities and Line Shapes have carried out these critical compilations. Both Data Centers are located in the Physics Laboratory at the National Institute of Standards and Technology (NIST). This database is also a component of the NASA Astrophysics Data System (ADS).

Data Compilers (Currently Active):

Atomic Energy Levels and Wavelengths: W. C. Martin[1], J. Sugar[1], and A. Musgrove[1]

Atomic Transition Probabilities: W. L. Wiese[1], J. R. Fuhr[1]

Fig. 17.1. Partial home page of the NIST Atomic Spectra Database

atomic spectroscopic data critically compiled by NIST scientists during the period 1966 through 1998, but for each transition only the most accurate result compiled by us is presented. The database thus contains the equivalent of several thousand pages of earlier NBS/NIST data books, and the very successful format of the data books is retained. For the preparation of this large database, especially for the creation of the search engine and web interface, the NIST data compilers obtained the assistance of a number of expert colleagues who made it user-friendly and fully interactive. Their names are shown on the home page.

17.3 The Scope of the NIST ASD Database

(a) *Spectral line data:* The ASD database covers at least one or two spectra of all chemical elements, up to einsteinium (atomic number Z = 99). For light and medium heavy elements, with atomic numbers $Z = 1$ (hydrogen) through Z = 28 (nickel), significant amounts of line data are available for practically all stages of ionization. For the heavier elements, starting with copper (Z = 29), data are only available for the neutral atoms and the first three or four stages of ionization and sometimes for even fewer. Figure 17.2 shows the spectra for which line data are included in the database.
In total, the database contains the wavelengths of 91,000 lines of about 900 spectra in the range from 0.1 nm to 2,000 µm. Also, for about one-half of the lines, atomic transition probabilities are available with estimated uncertainties, which are listed by code letters (A $\leq \pm 3\%$, B $\leq \pm 10\%$, C $\leq \pm 25\%$, D $\leq \pm 50\%$).

(b) *Atomic energy level data:* The database contains about 70,000 energy levels. The coverage is quite substantial for the light and medium heavy elements, from hydrogen (Z = 1) through krypton (Z = 36). For these, data on almost all stages of ionization are included. For heavier elements, significant amounts of data have been only compiled for the neutral atoms and the first three to five ions of the lanthanides or "rare earth" elements ($57 \geq Z \geq 71$) and for numerous ions of Mo (Z = 42), because of their importance for magnetic fusion energy research.

(c) *General arrangement of the tables:* The atomic structure data are tabulated in two separate parts: (a) Tables for atomic energy levels, and (b) tables for spectral lines. The latter include atomic transition probabilities when they are available.

The data pages with the most extensive information are those of spectral lines for which transition probabilities are available and for which the energy levels are displayed. As will be seen later in one of the examples, these pages contain for each spectral line the wavelength (if desired, both in air and vacuum), the lower and upper energy levels of the transition, the spectroscopic

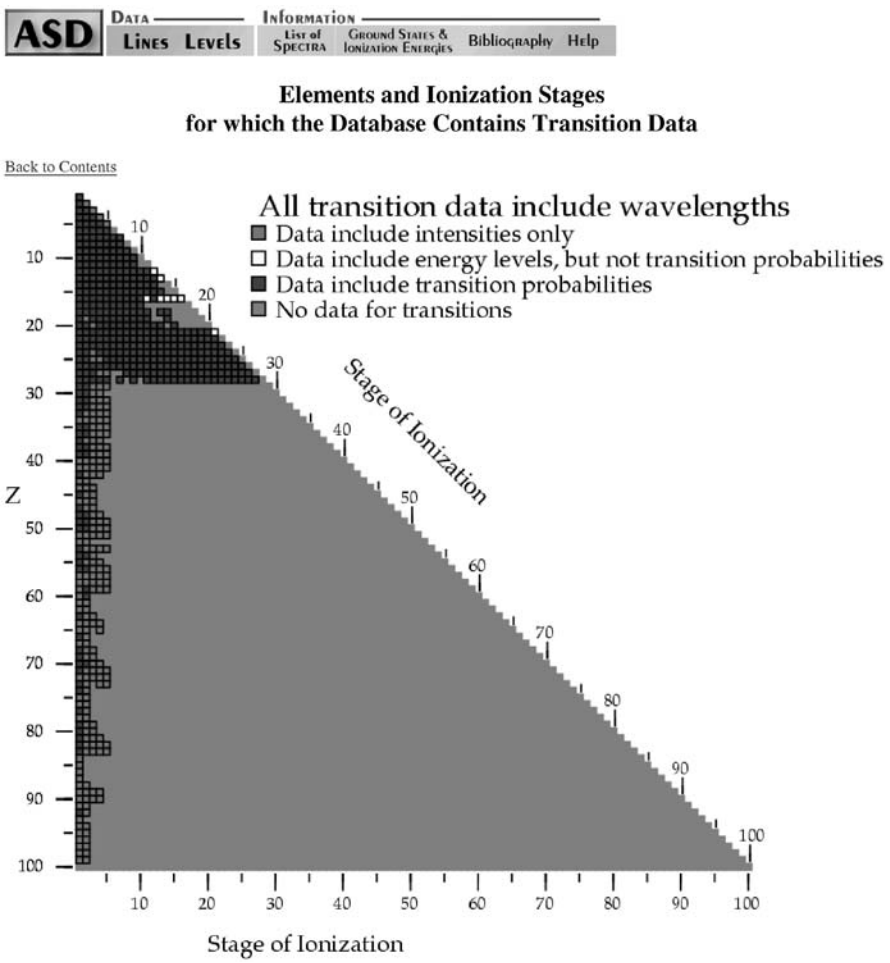

Fig. 17.2. Overview of the spectra for which the ASD contains transition data, i.e., wavelengths and transition probabilities

notation of lower and upper state including the total angular momentum quantum numbers and the statistical weights, the atomic transition probability with its estimated uncertainty, and running numbers for pertinent literature references. If a spectral line is of a type different from the usual electric dipole (E1 or allowed) transition, this is noted in a column "Type" (otherwise the column is left blank). The symbols most often appearing there are "M1" for magnetic dipole, and "E2" for electric quadrupole lines, both normally referred to as forbidden lines.

17.4 Interactive Features

The NIST ASD database has been designed to handle various user needs, and thus it provides many different display and output options. Users may precisely specify their queries to focus on the specific data they are interested in, possibly in several successive steps.

The various options and search criteria are clearly listed in several introductory front pages and they are discussed in a general information section, where also other special features of the database are reviewed. In addition, this section includes a short compendium on atomic spectroscopy, which contains the basic physics, formulas and conversion factors in atomic spectroscopy, as well as a discussion of spectroscopic notations.

17.5 Related NIST Databases

In support of the comprehensive ASD database, the NIST team has also assembled several related databases and put these on the World Wide Web:

(a) A bibliographic database on atomic transition probabilities containing about 7 500 entries.
(b) A bibliographic database on spectral line shapes and shifts containing about 1 300 entries for the time period 1992 to the present.
(c) A data table on the ground levels and ionization energies for neutral atoms.
(d) A special table on wavelengths, energy levels and transition probabilities for lines in the soft X-ray range, from 20 Å to 170 Å, for highly charged ions of neon (Ne V to Ne VIII), magnesium (Mg V to Mg X), silicon (Si VI to Si XII) and sulfur (S VII to S XIV). This is principally in response to needs for the Chandra X-ray Observatory, but some of these spectra should also be of interest to the fusion energy research community.
(e) A database on electron impact ionization cross-sections containing mostly molecular data (72 species), but including ionization cross-sections for the H and He atoms.
(f) An atlas of the spectrum of the platinum/neon hollow cathode lamp, containing about 5 000 lines in the spectral range 1130–4330 Å, very useful for spectrometer calibrations.
(g) A Handbook of Basic Atomic Spectroscopic Data.

Furthermore, a bibliographic database on wavelengths and atomic energy levels is in preparation.

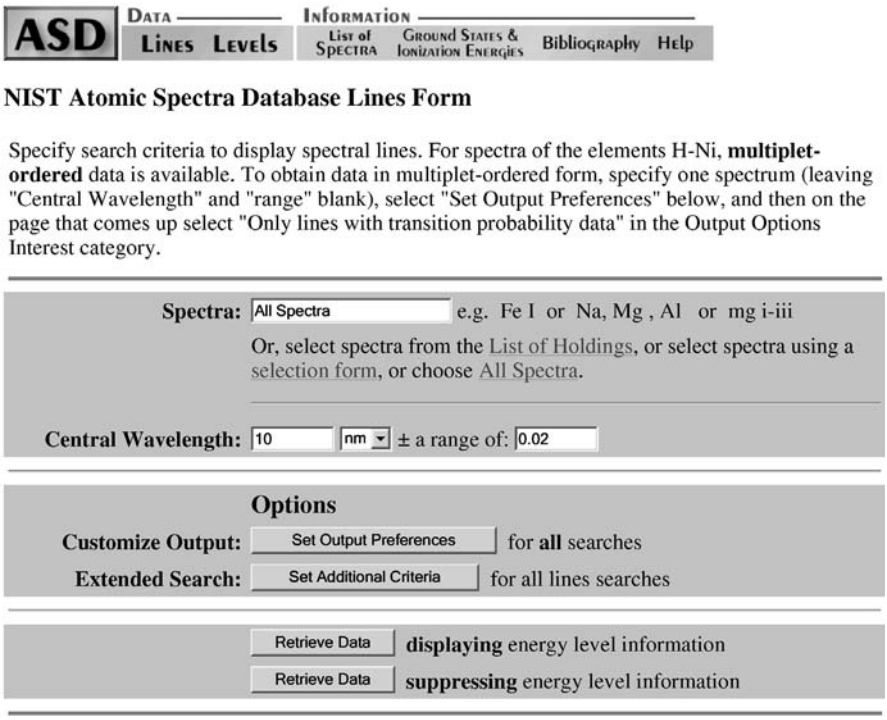

Fig. 17.3. Sample of the ASD Lines Form, illustrating a search for a "mystery" line near 10 nm

17.6 Some Sample Searches

To illustrate the use of the database, we provide some sample searches for frequently recurring queries:

(a) *A search for a mystery line:* Let us assume, that a spectral line is observed very close to 10 nm (100 Å), within a wavelength interval of 0.01 nm. Figure 17.3 shows the filled-out ASD lines form for a search on *all* spectra. Furthermore, let us assume that the user's preference is to retrieve the data with the display of energy level information. Figure 17.4 shows the answer, i.e., the total number of lines found in this interval. (For this example, the interval has been purposely set small (but larger than ±0.01 nm) to get all listed lines on one page).

(b) *Verification of the mystery line:* Let us say that the Fe X line at 10.0026 nm appears to be the most likely line the user was searching for, since he experimented with a hot plasma that contained an iron impurity. He would thus want to confirm his suspicion with observations of other nearby Fe X lines. Using the same "lines" form as before (Fig. 17.3), but

ASD | Data: Lines Levels | Information: List of Spectra, Ground States & Ionization Energies, Bibliography, Help

NIST Atomic Spectra Database Lines Data (Wavelength Ordered)
Wavelength=10 nm, ± 0.02
10 Lines of Data Found

Spec.	Wavelength Vac. (nm)	Rel. Int.	A_{ki} (10^8 s^{-1})	Acc.	E_i (cm^{-1})	E_k (cm^{-1})	Configurations	Terms	J_i-J_k	$g_i g_k$	Type	TP Refs.	Line Refs.
Ni XXIII	9.9812		2.3e+01	E	1 078 500	2 080 600	$2s(^2S)2p^3(^2P) - 2p^4$	$^3P^o - {}^1D$	1-2	3-5		1	
Co XX	9.9890		6.70e+02	C	107 420	1 108 520	$2s^2 2p^4 - 2s2p^5$	$^3P - {}^3P^o$	1-0	3-1		1	
Co IX	9.9921		5.30e+02	D-	2 451	1 003 240	$3p^6 3d - 3p^5 3d(^3F^o)4s$	$^2D - {}^2F^o$	$^5/_2$-$^7/_2$	6-8		ls	
Ti XII	9.9934		6.9e-02	C	217 042	1 217 700	$2p^6(^1S)3p - 2p^6(^1S)4p$	$^2P^o - {}^2P^o$	$^3/_2$-$^3/_2$	4-4	E2	1,ls	
V XIII	9.998		6.0e+01	D	1 392 780	2 393 000	$2p^6(^1S)4p - 2p^6(^1S)8s$	$^2P^o - {}^2S$	$^3/_2$-$^1/_2$	4-2		ls	
Mn XVII	10.000		8.31e+02	C+	0	1 000 000	$2s^2 2p^5 - 2s2p^6$	$^2P^o - {}^2S$	$^3/_2$-$^1/_2$	4-2		1	
V XVII	10.0016		6.3e+00	E	0	999 840	$2s^2 2p^3 - 2s(^2S)2p^4(^1S)$	$^4S^o - {}^2S$	$^3/_2$-$^1/_2$	4-2		1	
Fe X	10.0026		2.600e+3	D	388 709	1 388 450	$3s^2 3p^4(^3P)3d - 3s^2 3p^4(^3P)4f$	$^4D - {}^4F^o$	$^7/_2$-$^9/_2$	8-10		3	
Ni XXII	10.011		1.02e+02	C	400 100	1 399 000	$2s^2 2p^3 - 2s(^2S)2p^4(^3P)$	$^2P^o - {}^2P$	$^3/_2$-$^3/_2$	4-4		1	
Co XXII	10.0135		4.39e+01	C	0	998 650	$2s^2 2p^2 - 2s(^2S)2p^3(^2P^o)$	$^3P - {}^3P^o$	0-1	1-3		1	

Fig. 17.4. Response of the database to the query of Fig. 17.3, i.e., the output of transition data in ASD for all spectra of all elements for a central wavelength of 10 nm, with a range of ±0.02 nm

ASD | Data: Lines Levels | Information: List of Spectra, Ground States & Ionization Energies, Bibliography, Help

NIST Atomic Spectra Database Lines Data (Wavelength Ordered)
Wavelength=10 nm, ± 0.4 Fe X
12 Lines of Data Found

Wavelength Vac. (nm)	Rel. Int.	A_{ki} (10^8 s^{-1})	Acc.	E_i (cm^{-1})	E_k (cm^{-1})	Configurations	Terms	J_i-J_k	$g_i g_k$	Type	TP Refs.	Line Refs.
9.6121		8.70e+02	D	0.0	1 040 350	$3s^2 3p^5 - 3s^2 3p^4(^3P)4s$	$^2P^o - {}^2P$	$^3/_2$-$^3/_2$	4-4		3	
9.6786		7.80e+02	D	15 683.1	1 048 890	$3s^2 3p^5 - 3s^2 3p^4(^3P)4s$	$^2P^o - {}^2P$	$^1/_2$-$^1/_2$	2-2		3	
9.7122		3.50e+02	D	0.0	1 029 630	$3s^2 3p^5 - 3s^2 3p^4(^3P)4s$	$^2P^o - {}^4P$	$^3/_2$-$^3/_2$	4-4		3	
9.7593		7.0e+01	E	15 683.1	1 040 350	$3s^2 3p^5 - 3s^2 3p^4(^3P)4s$	$^2P^o - {}^2P$	$^1/_2$-$^3/_2$	2-4		3	
10.0026		2.600e+3	D	388 709	1 388 450	$3s^2 3p^4(^3P)3d - 3s^2 3p^4(^3P)4f$	$^4D - {}^4F^o$	$^7/_2$-$^9/_2$	8-10		3	
10.1733		1.800e+3	D	426 763	1 409 730	$3s^2 3p^4(^3P)3d - 3s^2 3p^4(^3P)4f$	$^4F - {}^4G^o$	$^5/_2$-$^7/_2$	6-8		3	
(10.1846)		1.700e+3	E	428 298	1 410 200	$3s^2 3p^4(^3P)3d - 3p^4(^3P)4f$	$^4F - {}^4G^o$	$^3/_2$-$^5/_2$	4-6		3	
10.2095		2.900e+3	D	417 653	1 397 130	$3s^2 3p^4(^3P)3d - 3s^2 3p^4(^3P)4f$	$^4F - {}^4G^o$	$^9/_2$-$^{11}/_2$	10-12		3	
10.2192		2.900e+3	D	450 751	1 429 300	$3s^2 3p^4(^1D)3d - 3s^2 3p^4(^1D)4f$	$^2G - {}^2H^o$	$^9/_2$-$^{11}/_2$	10-12		3	
10.2829		2.100e+3	D	511 800	1 484 290	$3s^2 3p^4(^1S)3d - 3s^2 3p^4(^1S)4f$	$^2D - {}^2F^o$	$^3/_2$-$^5/_2$	4-6		3	
(10.3319)		2.600e+3	D	(481 700)	1 449 600)	$3p^4(^1S)3d - 3p^4(^1S)4f$	$^2D - {}^2F^o$	$^5/_2$-$^7/_2$	6-8		3	
(10.3724)?		1.700e+3	E	452 730?	1 416 800)	$3s^2 3p^4(^3P)3d - 3p^4(^3P)4f$	$^2F - {}^2G^o$	$^5/_2$-$^7/_2$	6-8		3	

Fig. 17.5. Sample search for Fe X transitions near 10 nm, in a range of ±0.4 nm, wavelength ordered, with energy level data and spectral classifications

ASD | Data — Lines Levels | Information — List of Spectra, Ground States & Ionization Energies, Bibliography, Help

NIST Atomic Spectra Database Lines Data (Wavelength Ordered)
Wavelength=10 nm, ± 4 Fe X
29 Lines of Data Found

Wavelength Vac. (nm)	Rel. Int.	g_k	A_{ki} (10^8 s^{-1})	Acc.
7.5685		6	7.80e+02	D
7.6006		4	1.300e+3	D
7.6495		4	1.400e+3	D
7.6822		2	1.800e+3	D
7.7627		6	4.80e+02	D
7.7728		6	2.80e+02	D
7.7810		4	8.00e+02	E
7.7865		6	1.600e+3	D
7.8151		4	4.40e+02	D
7.8771		4	4.00e+02	E
9.4012		6	4.70e+02	D
9.5339		2	5.90e+02	D
9.5374		4	5.50e+02	D
9.6121		4	8.70e+02	D
9.6786		2	7.80e+02	D
9.7122		4	3.50e+02	D
9.7593		4	7.0e+01	E
10.0026		10	2.600e+3	D
10.1733		8	1.800e+3	D
(10.1846)		6	1.700e+3	E
10.2095		12	2.900e+3	D
10.2192		12	2.900e+3	D
10.2829		6	2.100e+3	D
(10.3319)		8	2.600e+3	D
(10.3724)?		8	1.700e+3	E
(10.4248)		8	1.400e+3	D
10.4638		10	2.100e+3	D
13.7027?		6	1.50e+02	D
13.9868		8	2.20e+02	D

Fig. 17.6. A search for the extended Fe X spectrum from 6 to 14 nm, with energy level data omitted

specifying now Fe X as the spectrum and covering a wider wavelength range, for example ±0.4 nm, he will obtain the table shown in Fig. 17.5. The table shows several other Fe X lines close by, that are about as strong as the 10.0026 nm line, for example, the 10.2095 nm line. This may be derived from the very similar products of g_k and A_{ki} as well as the fact that the upper energy levels are almost the same. Thus, if these other lines show up in his spectrum, too, he has verified that he observes Fe X.

ASD | Data: Lines Levels | Information: List of Spectra, Ground States & Ionization Energies, Bibliography, Help

NIST Atomic Spectra Database Levels Data
Fe X 16 Lines of Data Found
Bound on E_k=450000

Configuration	Term	J	Level (cm^{-1})	Leading percentages		
$3s^2\,3p^5$	$^2P^o$	$^3/_2$	*0 .0*			
		$^1/_2$	*15 683 .1*			
$3s3p^6$	^2S	$^1/_2$	289 249	77	23	$3s^2\,3p^4\,(^1D)3d\ ^2S$
$3s^2\,3p^4\,(^3P)3d$	^4D	$^7/_2$	388 709	97		
		$^5/_2$	388 709	95		
		$^3/_2$	390 050	94		
		$^1/_2$	391 555	96		
$3s^2\,3p^4\,(^3P)3d$	^4F	$^9/_2$	417 653	94		
		$^7/_2$	422 795	89		
		$^5/_2$	426 763	94		
		$^3/_2$	428 298	90		
$3s^2\,3p^4\,(^1D)3d$	^2P	$^3/_2$	431 928	45	33	$3s^2\,3p^4\,(^3P)3d\ ^2P$
$3s^2\,3p^4\,(^1D)3d$	^2D	$^3/_2$	434 614	43	27	$3s^2\,3p^4\,(^3P)3d\ ^2D$
$3s^2\,3p^4\,(^3P)3d$	^4P	$^1/_2$	434 800	96		
		$^5/_2$	441 853	45	23	$3s^2\,3p^4\,(^1D)3d\ ^2D$
$3s^2\,3p^4\,(^3P)3d$	^2F	$^7/_2$	440 840	55	28	$3s^2\,3p^4\,(^1D)3d\ ^2G$

Fig. 17.7. ASD output of energy levels for the Fe X spectrum, with an upper bound of 450 000 cm^{-1}

(c) *Spectrum overview:* An overview of a specific spectrum, i.e., an extended line list, is conveniently obtained by suppressing the energy level information. Figure 17.6 shows such a listing for the Fe X spectrum from 6 nm to 14 nm, again utilizing the ASD lines form, Fig. 17.3.

(d) *Atomic Energy levels listing*: Figure 17.7 shows the related atomic energy levels for the spectrum of Fe X, with a cut-off (because of space limitations) at 450 000 cm^{-1}.

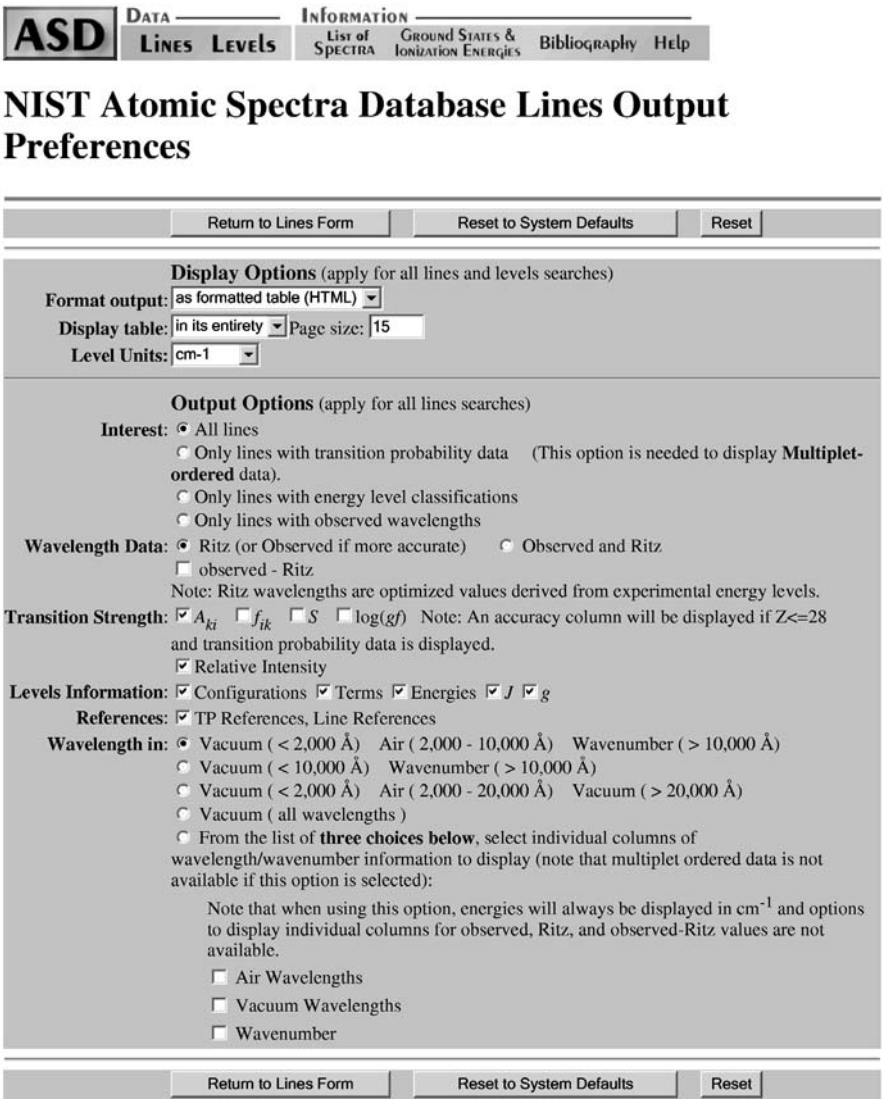

Fig. 17.8. ASD Lines Output Preferences Form, showing the large variety of user options

We want to emphasize here that the database is quite flexible and allows many other options. For example, in the lines form, if one clicks in the "Options" field on "Set Output Preferences," the "Output Preferences" form (Fig. 17.8) comes up, and one may select oscillator strengths f rather than transition probabilities, one may select vacuum or air wavelengths, etc. If one clicks on "Set Additional Criteria," one may, for example, limit the search to lines of at least a certain minimum transition strength.

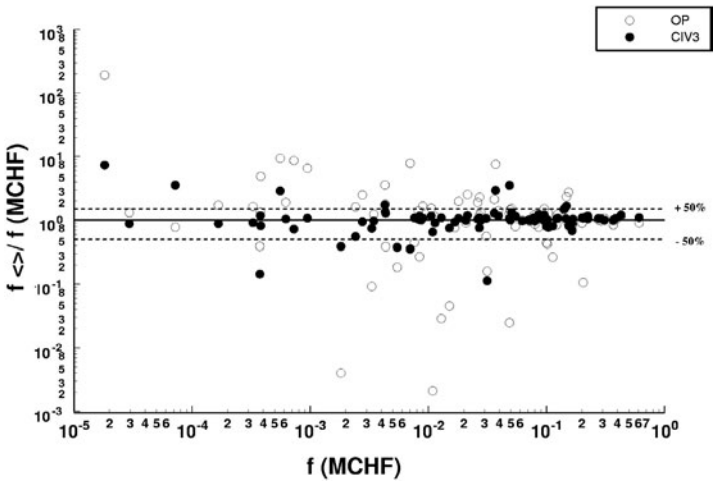

Fig. 17.9. Comparisons of the results of three recent advanced atomic structure calculations [15–17]. The ratios of the oscillator strengths (f-values) of [15] and [16], as well as [17] and [16] are plotted on a logarithmic scale against the MCHF [16] oscillator strengths

17.7 Data Quality

It is important to note that a great difference in quality exists between the best available data for wavelengths and energy levels on one hand and those for transition probabilities on the other hand. The data compiled for wavelengths and energy levels have been almost all obtained experimentally and have been determined with great precision to at least five, and often six or seven significant figures, and the uncertainties are estimated to affect only the last one or two digits. Thus, for many practical purposes, the uncertainties are negligible. For the transition probabilities, however, the situation is quite different. For the majority of the spectral lines, we estimate the uncertainties to be still as large as 25% to 50%. Furthermore, these estimates are often not very firm, because the great majority of the compiled data are from calculations for which normally no uncertainty estimates are provided. Our estimates are thus usually obtained from data comparisons when they are available for that spectrum, from general assessments of the theoretical methods and from extrapolations to similar spectra where comparisons with experimental data could be made, and where firm error assessments were provided for these. A typical example of the still unsatisfactory data situation is provided in Fig. 17.9 for the spectrum of S VIII [14].

This spectrum presents an instructive case for the large uncertainties in atomic transition probabilities, obtained even with sophisticated multiconfiguration calculations. For this ion, three extensive and detailed atomic structure calculations have been undertaken in the last ten years [15–17].

These are R-matrix calculations, which are part of the international Opacity Project (OP) [15], theoretical results from the MCHF database collection by Tachiev and Froese Fischer [16], and calculations by Blackford and Hibbert with the CIV 3 code [17]. In Fig. 17.9 the ratios of the OP and CIV oscillator strengths to the MCHF results are plotted on a logarithmic scale versus the MCHF oscillator strength (f-value) data.

The dashed lines indicate an error band of ±50% around a perfect ratio of one. The largest disagreements are observed between the OP and MCHF data, while the agreement between the MCHF and CIV 3 results is clearly better, and it is especially good for the strong lines, from $f = 1$ down to about $f = 0.05$. But for many weaker transitions, the agreement between the MCHF and CIV data is also not good. We followed up on these cases in more detail, and noticed that the disagreements between the MCHF and CIV 3 results become especially large for those transitions for which either their upper or lower level or both are of a mixed nature. Mixed means here that the main contribution to the wave function composition of the level is less than 80%. This is in contrast to "pure" situations where the leading wave function term is larger than 90%.

17.8 Outlook

As Fig. 17.2 shows, the coverage of wavelength and transition probability data in the NIST ASD database becomes very incomplete for elements with atomic numbers $Z \geq 29$. The only spectra covered for these heavy elements are those of the neutral atom and those of up to four-times charged ions. For atomic energy levels the present coverage for heavy elements is even less. But among the heavier elements are several that are of considerable interest to fusion energy research, specifically Kr, Xe, Mo, Ta and W. We have compiled data

Table 17.1. Planned Additions and Updates for the NIST Atomic Spectra Database

Within Two Years	Within Five Years
Highly ionized atoms of Ti, V, Cr, Mn, Fe, Co, Ni, Cu, Kr, and Mo	H, D, He, Li, Be, B, Na, Mg, Al, Si, Ar, Ca, Sr, Ba
Ba I and II	Ne, Ar, Kr, Xe
Fe I and II	W (All available spectra)
Ne V-Ne VIII, Mg V-Mg X, Si VI – Si XII, S VIII-S XIV (soft X-ray lines from 20 Å −170 Å)	
Strong transitions of all neutral and singly ionized atoms	

on numerous spectra of Kr and Mo, which are now available in book form [8] and will be included in the next version of ASD. Work is also underway at NIST to compile spectroscopic data for Xe and W, but completion of these large projects is still some time away. Other recent or current NIST compilation work on atomic structure data that we plan to add to the ASD database concerns the transition probabilities of Ba I and Ba II [18]; and of Fe I and Fe II; also, we plan to include updated spectral data for the most important and frequently used transitions of all neutral and singly ionized atoms, with pertinent energy levels; and the earlier noted collection of soft X-ray transitions of Ne, Mg, Si and S [14].

On a longer time frame, i.e., within five years, we plan to update and add spectral data for H, D, He, Li, Be, B, Ne, Na, Mg, Al, Si, Ar, Ca, Kr, Sr, Xe and Ba. These compilations will include all stages of ionization for which data are available. Table 17.1 above summarizes the planned extensions and updates of the NIST ASD database.

Acknowledgement

This work was partially supported by the Office of Fusion Energy Science of the U.S. Department of Energy.

References

1. C.E. Moore: *Atomic Energy Levels*, Nat. Bur. Stand. (U.S.) Circular 467 Vol. I (1949)(H through V); Vol. II (1952) (Cr through Nb); and Vol. III (1958) (Mo through La, Hf through Ac) (U.S. Gov. Print. Off., Washington, D.C)
2. W.C. Martin, R.Zalubas, L. Hagan: *Atomic Energy Levels – The Rare Earth Elements*, Nat. Stand. Ref. Data Ser., Nat. Bur. Stand. (U.S.) 60 (U.S. Gov. Print. Off., Washington, D.C. 1978)
3. J. Sugar, C. Corliss: Atomic energy levels of the iron-period elements: Potassium through Nickel, Phys. Chem. Ref. Data **14**, Suppl. 2 (1985)
4. C. E. Moore: *An Ultraviolet Multiplet Table*, Nat. Bur. Stand. (U.S.) Circular 488, Sec.1 (1950) (H through V); Sec. 2 (1952) (Cr through Nb); Sec. 3 (1962) (Mo through La, Hf through Ra), Sec. 4. (1962) (finding list-H through Nb) and Sec. 5 (1962) (finding list Mo through La, Hf through Ra). (U.S. Gov. Print. Off., Washington, D.C.)
5. W.F. Meggers, C.H. Corliss, B.F. Scribner: *Tables of Spectral Line Intensities*, Part 1. Arranged by Elements, Nat. Bur. Stand. (U.S.), Monograph 145 (1975)
6. J. Reader, C.H. Corliss, W.L. Wiese, G.A. Martin: *Tables of Line Spectra of the Elements*, Part 1. Wavelengths and Intensities, Nat. Stand. Ref. Data Sys., Nat. Bur. Stand. (U.S.), No. 68 (1980)
7. C.E. Moore: *Tables of Spectra of Hydrogen, Carbon, Nitrogen and Oxygen Atoms and Ions*, ed. by J.W. Gallagher (CRC Press, Boca Raton 1993)
8. T. Shirai, J. Sugar, A. Musgrove, W.L. Wiese: Spectral data for highly ionized atoms: Ti, V, Cr, Mn, Fe, Co, Ni, Cu, Kr and Mo, J. Phys. Chem. Ref. Data, Monograph 8 (2000)

9. W.L. Wiese, M.W. Smith, B.M. Glennon: *Atomic Transition Probabilities, Vol. I, Hydrogen through Neon*, Nat. Stand. Ref. Data Ser., Nat. Bur. Stand. (U.S.) 4 (Gov. Print. Off., Washington, D.C. 1966)
10. W.L. Wiese, M.W. Smith, B.M. Miles: *Atomic Transition Probabilities, Vol. II, Sodium through Calcium*, Nat. Stand. Ref. Data Ser., Nat. Bur. Stand. (U.S.) 22 (U.S. Gov. Print. Off., Washington, D.C. 1969)
11. G.A. Martin, J.R. Fuhr, W.L Wiese: Atomic transition probabilities: Scandium through Manganese, J. Phys. Chem. Ref. Data **17** Suppl. 3 (1988)
12. J.R. Fuhr, G.A. Martin, W.L. Wiese: Atomic transition probabilities: Iron through Nickel, J. Phys. Chem. Ref. Data **17** Suppl. 4 (1988)
13. W.L. Wiese, J.R. Fuhr, T.M. Deters: Atomic transition probabilities of Carbon, Nitrogen and Oxygen, J. Phys. Chem. Ref. Data, Monograph 7 (1996)
14. L.I. Podobedova, A. Musgrove, D.E. Kelleher, J. Reader, J. Fuhr, W.L. Wiese: Atomic spectral data for the Chandra X-ray observatory, Parts I-IV, J. Phys. Chem. Ref. Data (in press) and http://physics.nist.gov/chandra
15. *The Opacity Project*, Vol. I, compiled by the Opacity Project Team, (Instit. of Phys. Publ., Bristol 1995) and http://www.legacy.gsfc.nasa.gov/topbase/
16. G. Tachiev, C. Froese Fischer: http://www.vuse.Vanderbilt.edu/∼cff/mchf_collection/
17. H.M.S. Blackford, A. Hibbert: At. Data Nucl. Data Tables **58**, 101 (1994)
18. J.Z. Klose, J.R. Fuhr, W.L. Wiese: Critically evaluated atomic transition probabilities for Ba I and Ba II, J. Phys. Chem. Ref. Data **31**, 217 (2002)

18 The Atomic Data and Analysis Structure

H.P. Summers and M.G. O'Mullane

18.1 Introduction

The Atomic Data and Analysis Structure (ADAS) Project is a shared activity of a consortium of fusion and astrophysical laboratories directed at developing and maintaining a common approach to analyzing and modeling the radiating properties of plasmas.

ADAS had its origins at the JET Joint Undertaking experiment of the European fusion programme in 1984. It was decided to implement atomic modeling sufficient for the long term future of the fusion programme including central maintenance of fundamental and derived atomic data, precise and optimized interfacing to experimental diagnostic analysis and quality control of theoretical plasma modeling data – all from the testing environment of a large experimental spectroscopy division. Under these guide lines, the Atomic Data and Analysis Structure began and evolved into a professionally coded interactive computational support system linked to virtually all spectroscopic diagnostic and plasma modeling activities at JET [1].

In the early nineties, Permission was given for the conversion of ADAS into a UNIX based system with IDL as its graphical interface to increase its availability outside JET. In 1994, the ADAS Project was set up to implement the conversion, self-funded by subscription of the sponsoring laboratories, under the management of the University of Strathclyde and the guidance of a Steering Committee. Subsequent to the conversion, ADAS changed into an on-going development and maintenance project. Membership of the ADAS Project has now increased from the original five to more than twenty laboratories worldwide including most of the main fusion laboratories and the scope of ADAS codes and data has increased many fold.

The Steering Committee appraises the progress of the project annually, approves new members and makes adjustments to the scientific objectives of the project. Programmers maintain ADAS software on participant laboratory workstations over the Internet. New releases, updates and corrections are distributed and installed approximately every six months at the participant laboratories. The ADAS Project holds a workshop annually for sharing of experience in the use of ADAS and for co-ordinating scientific development of ADAS amongst the participants. By this method, a unique facility for the

ADAS consortium has been created, tightly linked to experiment, beyond the scope of the individual member laboratories.

The primary information and documentation on ADAS is on the world-wide-web at `http://adas.phys.strath.ac.uk`. The ADAS manual is currently at version 2.7 [2] and the most recent bulletin is that dated 18 August 2003. The complete set of ADAS codes and data is restricted to member laboratories, but extensive key derived data are made available to third parties and fundamental data in ADAS formats, which are the product of ADAS shared initiatives, enter the public domain.

18.2 General Principles of ADAS

ADAS seeks to provide integrating modeling. This is based on a number of strategic objectives which have become points of principle. These are to separate local atomic tasks from non-local issues, to provide derived atomic data close-linked to experimental spectroscopic data reduction, to provide consistent source function inputs to theoretical plasma modeling and to provide central management of atomic data.

ADAS is centred on generalized collisional–radiative (GCR) theory. The theory recognizes relaxation time-scales of atomic processes and how these relate to plasma relaxation times, metastable states, secondary collisions etc. Attention to these aspects – rigorously specified in generalized collisional–radiative theory – allow an atomic description suitable for modeling and analyzing spectral emission from most static and dynamic plasmas in the fusion and astrophysical domains [3, 4].

From these time-scales, it may be assumed in most circumstances that the free electrons have a Maxwellian distribution and that the dominant populations of impurities in the plasma are those of the ground and metastable states of the various ions. The dominant populations evolve on time-scales of the order of plasma diffusion time-scales and so should be modeled dynamically, that is in the particle number continuity equations, along with the momentum and energy equations of plasma transport theory. The excited populations of impurities on the other hand may be assumed relaxed with respect to the instantaneous dominant populations, that is they are in a *quasi-equilibrium*. The quasi-equilibrium is determined by local conditions of electron temperature and electron density. So, the atomic modeling may be partially de-coupled from the impurity transport problem into local calculations which provide quasi-equilibrium excited ion populations and effective emission coefficients (PEC coefficients) and then effective source coefficients (GCR coefficients) for dominant populations which must be entered into the transport equations. The solution of the transport equations establishes the spatial and temporal behaviour of the dominant populations which may then be re-associated with the local emissivity calculations, for matching to and analysis of observations.

It is helpful to consider the relationship of calculated spectral features to observed features. The starting point is the emission associated with a particular impurity excited level. It is called a *feature primitive* and is the set of transition energies and transition probabilities originating from the level. These purely atomic quantities determine positions and relative emissivities of spectrum lines driven by the level population. The level and its population may be a bundled one. All the component lines associated with the bundle constitute the feature primitive in this case, statistical weights alone determining their relative emissivities. No knowledge of the excited state population structure is required to prepare feature primitives. A local quasi-equilibrium population calculation, which may include both *resolved* and *bundled* levels, establishes the dependence of the populations of excited levels on each metastable state. In turn this allows combination of feature primitives to form a *feature*. A feature is the set of line positions and local emissivities associated with a metastable and is determined by a local excited population calculation. A *superfeature* is a set of line of sight integrals of spectral emission. It is obtained by combining features with the line of sight distribution of metastable populations derived from an impurity transport calculation. A superfeature includes line broadening and distortions due to the dynamics of the plasma along the line of sight. It is at the superfeature level that the confrontation of experiment and theory takes place. ADAS may be viewed as providing the tools for *feature primitive* $\rightarrow$ *feature* $\rightarrow$ *superfeature* spectral synthesis.

18.3 ADAS Code and Data Organization

ADAS software comprises an interconnected package of computer codes and data collections comprising four main components, namely, an interactive system, a library of key subroutines, a large database of fundamental and derived atomic data and integrated off-line packages for large-scale calculations. The interactive part provides immediate display of important fundamental and derived quantities used in analysis together with a substantial capability for preparation of derived data – generally by collisional–radiative calculations. It also allows exploration of parameter dependencies and diagnostic prediction of atomic population and plasma models. The second part is non-interactive but provides a set of subroutines which can be accessed from the user's own codes – typically, to draw in necessary data from the derived ADAS database. The off-line packages reflect a move in the ADAS Project to 'in-house' fundamental collision rate production.

18.3.1 IDL-ADAS

IDL-ADAS, the on-line interactive part of ADAS, currently includes $\sim$ 70 codes, organized into eight code series, as show in Table 18.1.

Table 18.1. ADAS series

Series	Content
ADAS1	Entry and validation of fundamental atomic data
ADAS2	Excited state populations of ions in a plasma
ADAS3	Charge exchange related emission
ADAS4	Recombination, ionization and radiated power
ADAS5	General interrogation programs
ADAS6	Data analysis programs
ADAS7	Creating and Using Dielectronic Data
ADAS8	Structure and Excitation Calculations

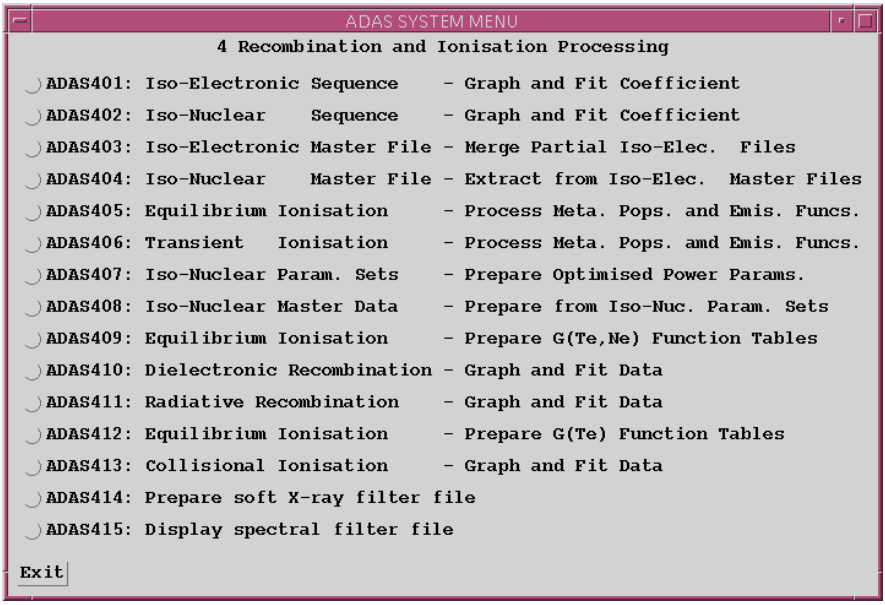

Fig. 18.1. Series 4 concerns the ground and metastable populations of ions in a plasma and their preparation and calculation for dynamical plasma models. It operates with *GCR* recombination and ionization coefficients, associated power loss coefficients and metastable fractions. The scope of series 4 is quite large extending into short wavelength filters modifying observed radiative power, astrophysical contribution function generation and parametrization of ionization and recombination

Figure 18.1 shows the selection menu for series 4. A typical interactive code operates through a sequence of three successive screens, namely *input*, *processing* and *output*. The input screen is for input file selection and directs the user to the appropriate data class (called *ADAS data formats* or *adf*'s for short) libraries in the central ADAS database or to a user's personalized database – in ADAS organization. Such input is commonly a collection of

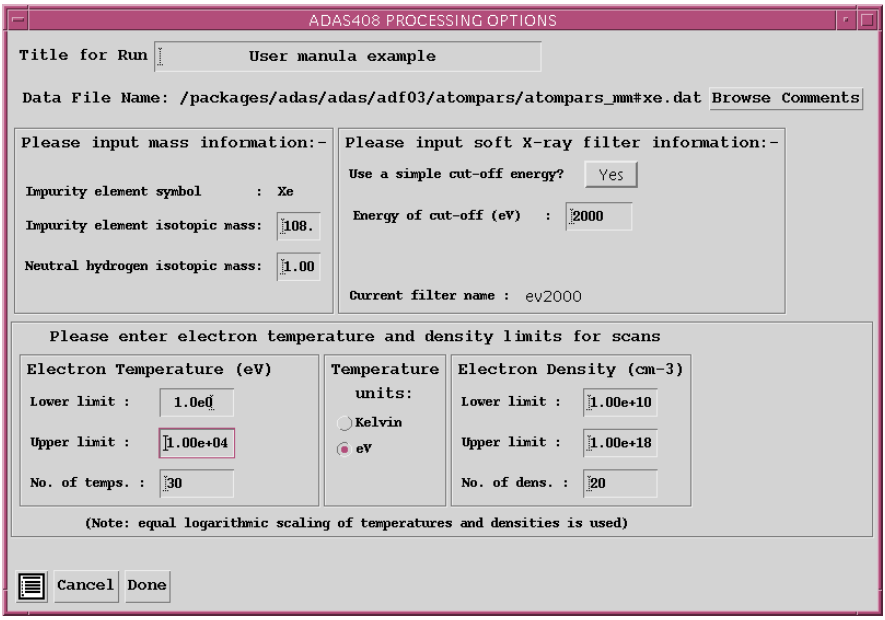

Fig. 18.2. ADAS408 generates recombination, ionization and radiated power data from parametric representations of the various coefficients. Electron temperature and density ranges are specified on the processing screen along with atomic masses. This code can accept special filter files which describe the soft X-ray pass band of arbitrary window/detector combinations and modify the calculated radiated power. ADAS408 delivers output data in the ADAS data format *adf11* - a principal data class accessed by plasma modeling codes

fundamental cross-section data. The processing screen allows user entry of parameters such as electron temperature and density defining the model cases to be executed. The output screen controls graphical display of results and output data files. These output files are often of derived data such as *PEC* coefficients, organized according to other ADAS data formats for entry into the databases. Figure 18.2 shows the processing screen of the code ADAS408.

The hierarchical code organization is illustrated in Fig. 18.3. This is by code series and then individual codes. ADAS provides extensive Fortran and IDL subroutine libraries which are available for use in a user's own codes and analysis programs. The IDL subroutines support the user's interface to interactive ADAS and graphical presentation of results. Modular basic atomic calculation routines, utilities and access routines to the ADAS data classes are mostly provided in Fortran but generally with IDL versions which use the Fortran through C wrappers. In particular *read_adf<nn>.pro* and *run_adas<nmm>.pro* IDL procedures give access to ADAS data or run ADAS codes at the IDL command line – independent of interactive ADAS. The libraries now include ~ 700 subroutines.

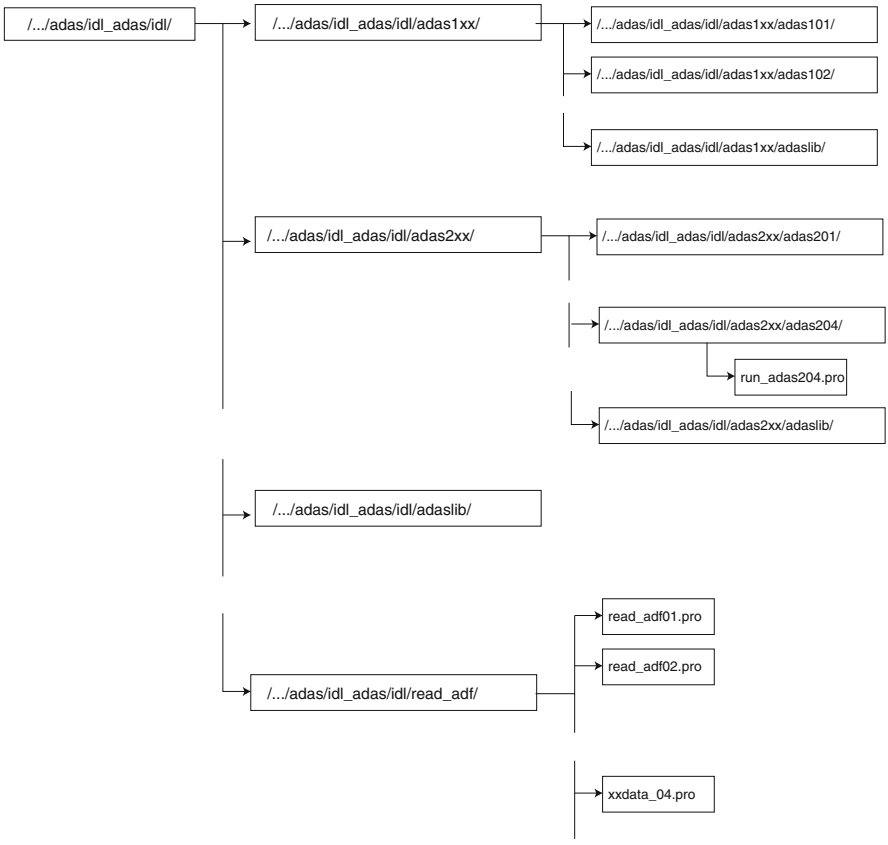

Fig. 18.3. The organization of the IDL code directories by series (e.g., */adas1xx*) and then by code (e.g., */adas101*). The general procedure library is at */idl/adaslib* and there are series specific libraries (e.g., */adas1xx/adaslib*). Stand-alone procedures, such as *run_adas204.pro*, are associated with the applicable IDL-ADAS code. Note the stand-alone data access procedures such as *read_adf02.pro* and *xxdata_04.pro* for use at the IDL command line. They return important selected content and the whole content of the named ADAS data format respectively

18.3.2 Data and Data Formats

There are 44 distinct data formats in the ADAS databases and the total size is currently $\sim$ 1.5 Gbyte. Each format has its layout and content precisely described and these prescriptions are rigidly adhered to in preparation of both central ADAS data and personal data for use by the ADAS package. A full description of all the ADAS data formats is given in appendix A of the ADAS manual. Some of the most important fundamental data and derived data formats are given in Table 18.2 and Table 18.3 respectively.

Table 18.2.

Series	Content
adf01	bundle-n and bundle-nl charge exchange xsects. from H, He and Li donors
adf02	ion impact cross-sections with named participant
adf04	specific ion data including, energies, A-values and collisional rate coeffts.
adf08	state selective radiative recom. coeffts. resolved by metastable parent
adf09	state selective dielectronic recom. coeffts. resolved by metastable parent
adf23	state selective ionis. coeffts. resolved by initial and final metastable states

Table 18.3.

Series	Content
adf11	collisional–radiative recom., ionis, and rad. power coeffts. by element
adf12	charge exchange effective emission coefficients for hydrogen-like ions
adf13	ionization per photon coefficients resolved by metastable driver
adf15	photon emissivity coefficients resolved by metastable driver
adf20	G(Te) (contribution) functions for differential emission measure studies
adf21	effective stopping coefficients for H and He beams
adf22	effective emission coefficients for H and He beams
adf40	envelope feature emissivity coefficients for heavy element ions
adf44	envelope feature emissivity functions for heavy element ion partitions

Data is archived under SCCS version control and all data sets contain a tail section giving attribution and update history. A number of ADAS data sub-directories have a year number, such as *'89'* associated with the name. The year number is often used in ADAS to give the year of introduction of a new approximation and is not necessarily the year of production. Thus *89* in the *adf11* data format denotes the baseline parametric form of stage to stage recombination and ionization data widely used in fusion laboratories. *96* denotes the much higher precision generalized collisional–radiative data which is valid at all densities and is metastable resolved.

Figure 18.4 shows a typical photon emissivity coefficient from the *adf15* subdirectory for carbon. The coefficient, which is for a specific spectrum line of an ion is a function of electron temperature and electron density. Separate entries are present in the database for the parts of the emissivity driven by different metastables of the ion itself and of its parent ion – that is via excitation and recombination.

18.3.3 Offline-ADAS

The ADAS Project has over the years placed great emphasis on the atomic modeling of the light elements hydrogen to neon, paralleling the light element strategy for plasma facing wall materials in the fusion programme. Compre-

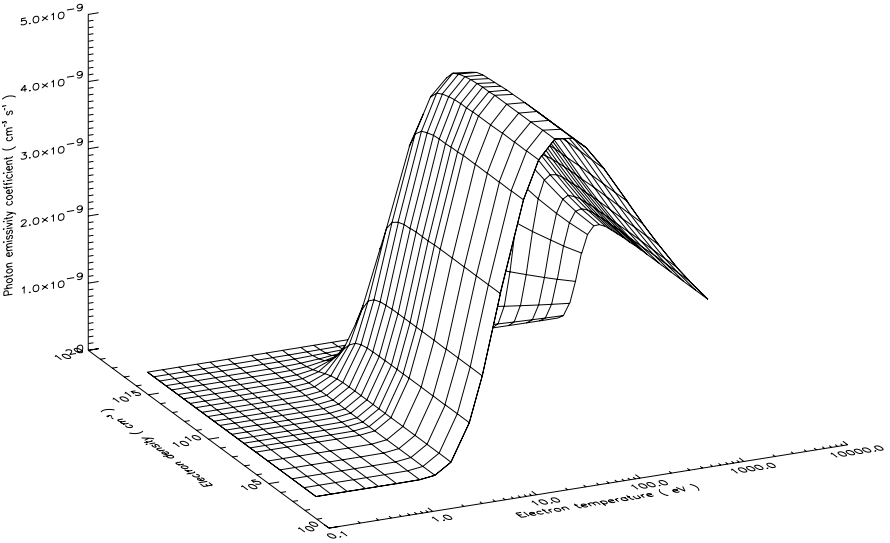

Fig. 18.4. The excitation photon emissivity coefficient for C II ($2s^2 3s^2 S$–$2s^2 2p^2 P$) at 858 Å, driven from the ground term $2s^2 2p^2 P$. The emissivities are calculated in the *GCR* picture and so there are equivalent entries in the database for emissivities driven by excitation from the metastable $2s2p^2\ ^4P$ and by recombination (free electron capture) from $2s^2\ ^1S$ and $2s2p^3 P$ and by charge transfer – also from the latter two parent terms

hensive derived atomic data is available within the ADAS databases for such elements to high precision within the full *GCR* picture. Progress towards a fusion reactor and the plans for the ITER international tokamak has now focussed attention on medium weight to heavy elements, such as tungsten, which are likely to be essential materials in power loaded first wall surfaces. Within the ADAS project, it is recognized that for very heavy species, the atomic data and modeling should be approached in a layered manner. That is large scale coverage can only be achieved in lower precision approximations. Calculations at the highest level of precision need to be strongly targeted. The manipulation of large scale data and its merging with precise data must be handled carefully for it to remain usable in an effective manner, close to experiment, by the spectral analyst. Thus the ADAS Project broadly operates on three layers of precision, called *baseline*, *level 1* and *level 2*. *adf11 89* data is at baseline level, while *adf09* LS-coupled dielectronic data is at level 1. *adf04* files in intermediate coupling, built from R-matrix cross-section calculations and *adf09* intermediate-coupled dielectronic data are at level 2.

For heavy elements and long iso-electronic sequences, in-house ADAS data provision is being moved progressively from on-line interactive calculations to off-line computation – working upwards from the baseline. In this off-line scenario, interactive ADAS is used to define regions of interest and to

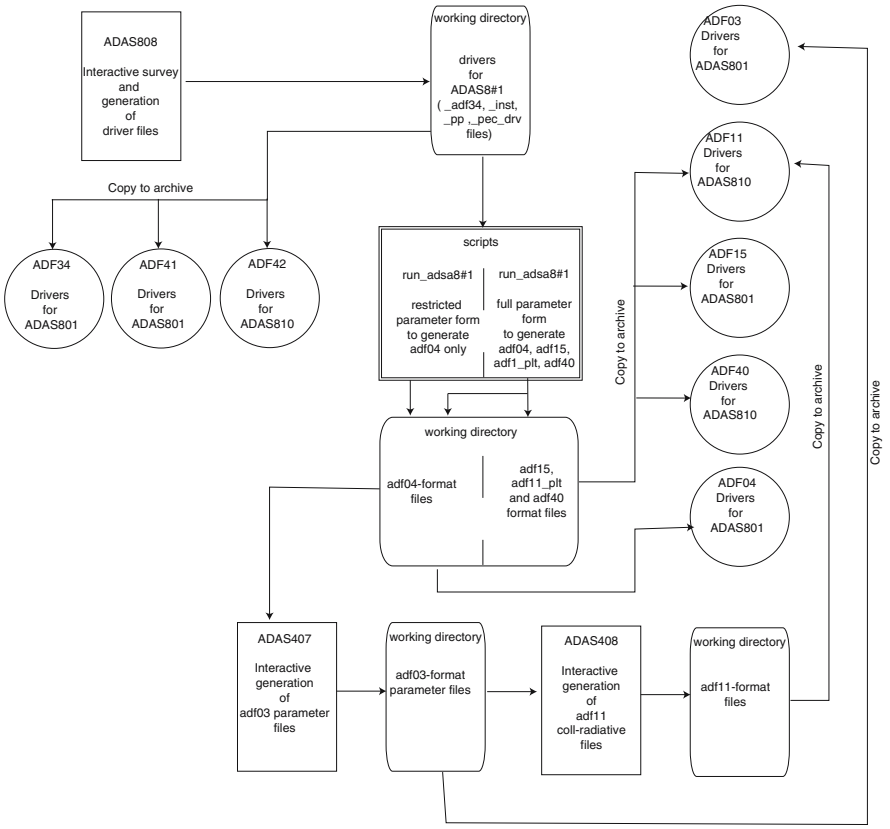

Fig. 18.5. Schematic of the off-line package ADAS8#1 for production of *adf11*, *adf15* and *adf40* baseline data. Circles denote datasets and rectangles denote codes. ADAS808 is executed on-line to prepare driver datasets for ADAS8#1. ADAS808 includes an approximate whole spectrum synthesis to allow focus on regions of interest or spectrometer ranges and to allow regulation of the scale of the subsequent off-line computations

create complete collections of drivers for these off-line computations. The off-line calculations are controlled by scripts which typically initiate a number of large codes sequentially. The scripts are designed for execution on large parallel machines but must be tuned to available resources. The separate off-line code parts parallel on-line interactive ADAS, maintaining consistency but with enhanced dimensions. Baseline data is now prepared automatically in such off-line computations – the package is called ADAS8#1 and its flowchart is shown in Fig. 18.5.

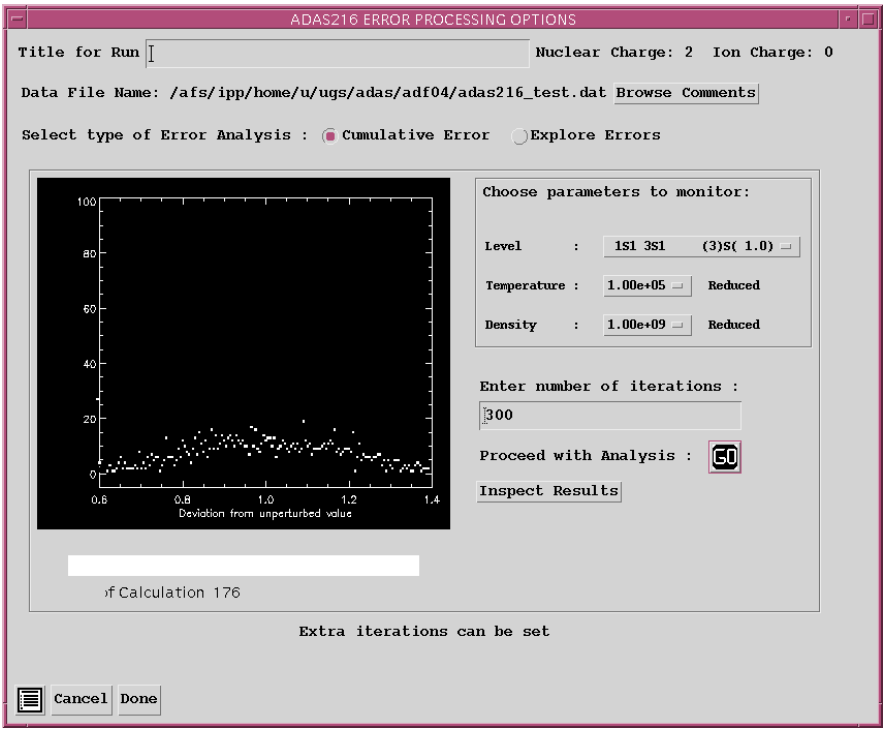

Fig. 18.6. Example for ADAS error analysis. Shown here is the cumulative statistical error (see text) being built up for an excited level of He I by the interactive code ADAS216

18.4 Current Directions

There are three main developments underway at this time – error analysis, non-Maxwellians and spectral visualization for heavy species [5].

18.4.1 Errors and Uncertainties

In very large part, the underlying fundamental reaction cross-sections and Maxwell averaged rate coefficients come from theory. Assignment of an error to theory is uncommon, although there are usually broad opinions as to the likely uncertainty of a particular approximation. Although assignment of uncertainties to theoretical cross-section data is difficult, it does matter since otherwise inferences drawn from the confrontation with experiment may be misleading. Derived effective coefficients, such as *adf15* data depend on many individual reactions, some well known and others less well known, and the balance of importance of the individual contributors depends on the electron temperature and density. Starting from the premise that there are errors

assigned to each individual fundamental reaction rates which are Gaussian distributed and independent, two pieces of information are valuable. Firstly, it is helpful to know the individual reaction which is the dominant source of error in the derived coefficient as a motivation for refinement of theoretical calculations. Secondly, for the spectral analyst, the cumulative statistical error on the derived coefficient is what matters. Both errors can be estimated, for example, the first by varying each fundamental reaction rate by its error in turn and recalculating the derived coefficient and the latter by Monte Carlo sampling from all the individual errors and then repeating the calculation of the derived coefficient and the process many times until statistics are built up. Figure 18.6 shows the cumulative statistical error being built up for an excited level of He I by the interactive code ADAS216. It works on an input *adf04* file which includes an *error block*. In the ADAS development, we distinguish 'locked' parameters as distinct from 'search' parameters in optimized fitting of models to experiment. Search parameters return a fit uncertainty or confidence level, the locked parameters must carry an error with them. An effective rate coefficient is such a locked parameter. In an organized framework, the database (of *.dat* files) has an error database (*.err* files) exactly paralleling it in archive library structure and in file organization. The issue then is realistic uncertainties in the fundamental reactions which is being pursued within the collaborations of the ADAS Project.

18.4.2 Non-Maxwellian Electron Distributions

The development is motivated by situations when the inputs and outputs to the free-electron energy are sufficiently large and rapid that energy redistribution is incomplete. Such a situation is well known in weakly ionized laboratory discharge plasmas when electron energy gain in the accelerating electric fields is lost in neutral atom or molecule excitation or by the electrons diffusing to the walls. Steady state distribution functions with the high energy tail depleted relative to a Maxwellian result, tending to the Druyvesteyn form in the pure elastic and diffusion limit. A contrasting situation of enhancement of the high energy tail of Maxwellians occurs in magnetically confined fusion experiments with neutral beam and lower hybrid heating. It also occurs in astrophysics. Topical at this time is the role of the modified two-stream instability in planetary atmospheres, comets and supernovas remnants. Consequential energized electron distribution functions are believed to lead to X-ray line and continuum emission as observed by the CHANDRA and XMM spacecraft [6].

The objective is to enable use of non-Maxwellian distributions in both predictive modeling and in deductive spectral analysis. In the former, ADAS should allow exploration of the effect of different degrees of non-Maxwellian character on predicted emission, ionization state etc. In the latter, the typical progress of analysis is that one should deduce, from spectral line ratios, some sort of non-Maxwellian parameter, analogous to electron tem-

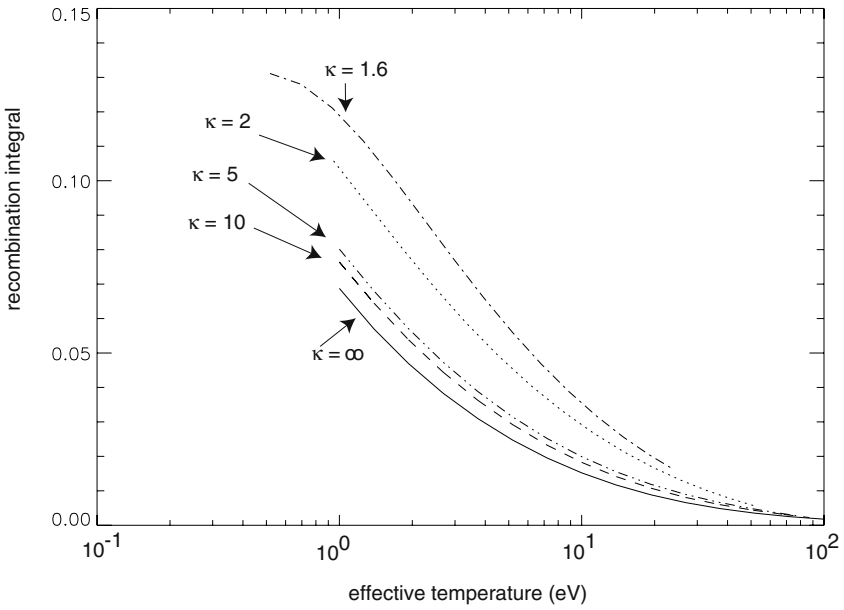

Fig. 18.7. The integral over the bound-free Gaunt factor which enters the expression for the radiative recombination coefficient. Results are for the κ distribution family for capture into the ground n = 1 shell of hydrogen. The *curves* are generated by numerical quadrature over the distribution function. The limiting Maxwellian curve is the analytic expression $e^{\mathrm{I_H/kT}} E_1(I_\mathrm{H}/\mathrm{kT})/T_\mathrm{e}^{3/2}$ and corresponds to $\kappa \to \infty$. The x-axis coordinate is $T_\mathrm{eff} \equiv 2\bar{E}/3$

perature itself. For both these purposes and for consistency with ADAS data structures and population models, we have introduced 'families of non-Maxwellians', $f_{\mathrm{p},T_\mathrm{eff}}(E)$, characterized by a T_eff related to mean energy and a non-Maxwellian parameter p. The families may be either analytic or numerical and are archived in the data format *adf37*. The individual reaction rates coefficients and the collisional–radiative modeling of excited populations and emission driven by electron collisions must be re-worked. Figure 18.7 illustrates the sort of modified rate coefficients which enter the key ADAS data structures (especially *adf04*).

18.4.3 Spectral Visualization for Heavy Species

For heavy species, the many ionization states coupled with their many open shells in intermediate coupling can lead to a grass-like spectrum. For this *quasi-continuum* it is not practicable or informative to separate or distinguish individual lines. In ADAS, the composite emission as a function of wavelength, in a spectral interval is described by an *envelope feature emissivity coefficient* or *FPEC* for short. As for a *PEC*, it is associated with a

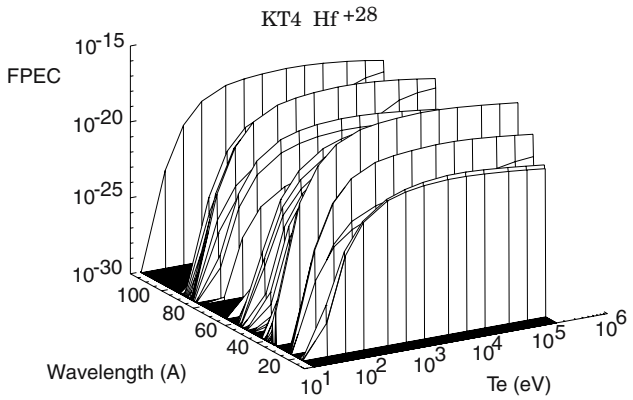

Fig. 18.8. Excitation FPEC for Hf^{+28} driven by the ground term. The electron density is $3 \times 10^{13}\,cm^{-3}$. The spectral range matches the KT4 spectrometer on the JET tokamak

particular driving metastable of an ion and is a function of electron temperature and density. Such an *FPEC* is illustrated in Fig. 18.8. *FPEC*s are archived in format *adf40* and can combine with grouping of ionization stages, partial ionization balances, filters etc. to provide a comprehensive handling of very complex systems, equivalent to that used for light elements. This development is closely connected with heavy element baseline.

18.5 ADAS Special Projects

The ADAS Project initiates and/or participates in a number of international collaborative projects to procure key fundamental data on atomic processes required for modeling and spectral analysis of plasmas. Generally the product of these projects is specified according to ADAS data formats. The results enter the ADAS databases but are also made available through descriptive publications and by locating the primary data in publicly available databases. Current projects include the "DR project", the "Ionization Project" and the light element GCR project, which provide extensive data in the *adf09*, *adf23* and *adf04* formats respectively. The DR project is summarized briefly here.

18.5.1 The DR Project

A programme is underway to calculate multi-configuration intermediate coupling dielectronic recombination rate coefficients from the (ground plus) metastable levels of an ion to all possible final states, resolved by level, and/or bundling, appropriate for the *GCR* modeling. It will cover elements applicable to astrophysics and magnetic fusion viz. He, Li, Be, B, C, N, O, F, Ne, Na, Mg, Al, Si, P, S, Cl, Ar, Ca, Ti, Cr, Fe, Ni, Zn, Kr, Mo and Xe. The first

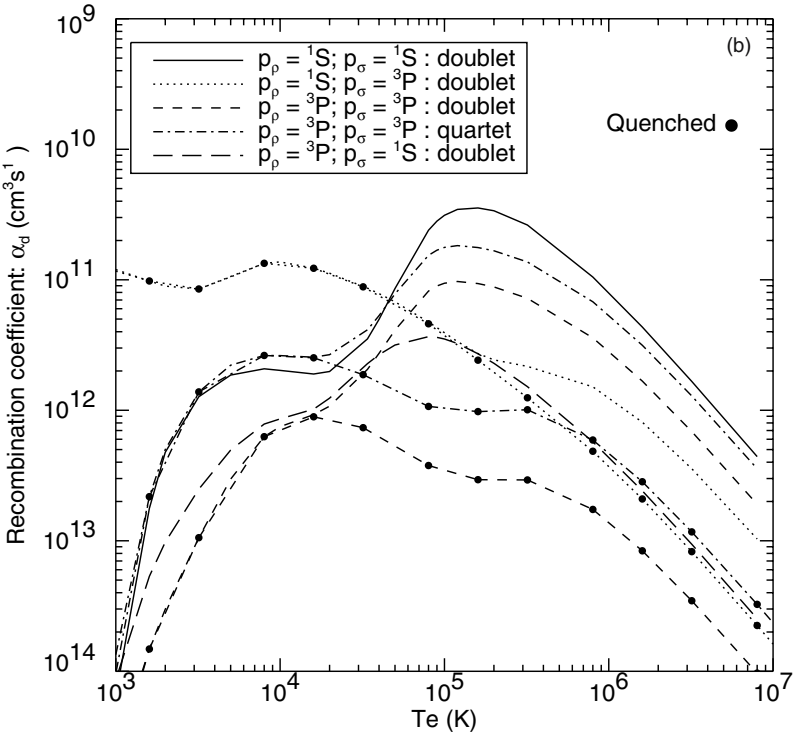

Fig. 18.9. The graph contrasts $\alpha_d^{(\mathrm{tot})}(p_\rho \to p_i \to p_\sigma)$ vs T_e for the dielectronic recombination of O^{4+} ions in various approximations at zero density. p_ρ= $O^{4+}(2s^2\ ^1S)$ and $O^{4+}(2s2p\ ^3P)$, p_σ=$O^{3+}(2s^22p\ ^2P)$ and $O^{3+}(2s2p^2\ ^4P)$: *Level 1* results separated by spin system and final parent. Excited states built on the $2s2p\ ^3P$ parent have a spin change autoionization pathway. The *level 1* metastable resolved totals do not include this loss. Within an LS-coupled GCR picture using *level 1* data, spin-breakdown Auger data is included explicitly in the GCR calculations for the correct linking of systems built on the $2s^2\ ^1S$ and $2s2p\ ^3P$ parents. The relevant final parent changing Auger data is included in the *adf09* data file specification. For comparison with simpler treatments, the totals including quenching of n-shells > 4 built on the $2s2p\ ^3P$ parent are also shown

phase of the work is the H- through Ne-like sequences. *Level 1* LS-coupling data for many elements of these sequences was calculated by Badnell (1991–92, unpublished) for incorporated into the ADAS database under data format *adf09*. This has provided the pathway for complete utilization of the detailed *level 2* data that is now being produced. The first phase is nearing completion and is being published as a series of articles in Astronomy and Astrophysics (see [7]). The second phase of the work is now commencing for Na-like through Ar-like sequences.

It is noted that the *level 2* approach encompasses the LS- forbidden autoionization rates which can occur in low-Z ions, the LS-forbidden radiative rates which occur in higher Z ions and finally, dielectronic recombination via fine-structure transitions which is completely absent in LS-coupling. The latter gives rise to a large underestimate of the low-temperature dielectronic recombination rate coefficient in some iso-electronic sequences. Some results are illustrated in Fig. 18.9.

Acknowledgement

The ADAS Project depends on and acknowledges the contribution of all its participants.

References

1. H.P. Summers: *Atomic Data and Analysis Structure*, JET Joint Undertaking Report JET-IR(94)06 (1994)
2. H.P. Summers: *The IDL-ADAS Users Manual*. `http://adas.phys.strath.ac.uk`
3. H.P. Summers, M.B.Hooper: Plasma Physics **25**, 1311 (1983)
4. R.W.P. McWhirter, H.P. Summers: Atomic radiation from low density plasma. In: *Applied Atomic Collision Physics*, Vol. 2, Plasmas, ed. by C.F. Barnett, M.F.A. (Acadademic Press, London)
5. H.P. Summers, N.R. Badnell, M.G. O'Mullane, A.D. Whiteford et al.: Plasma Phys. Control. Fusion **44**, 323 (2002)
6. R. Bingham, B.J. Kellett, J.M. Dawson, V.D. Shapiro, V.D.A. Mendis: Astrophys. J. Supple. **127**, 233 (2000)
7. N.R. Badnell, M.G. O'Mullane, H.P. Summers, Z. Altun, M.A. Bautista, J. Colgan, T.W. Gorczyca, D.M. Mitnik, M.S. Pindzola, O. Zatsarinny: Astron. & Astrophys. **406**, 1151 (2003)

19 Collision Processes of Atomic and Molecular Hydrogen in Fusion Plasmas: The Cross-Section Data Status

R.K. Janev

Collision processes of atomic and molecular hydrogen in fusion plasmas and their cross-section data status are discussed in the context of neutral hydrogen beam plasma heating, divertor plasma cooling, and power and particle exhaust, as well as core and edge plasma diagnostics. Special attention is devoted to the processes involving excited (electronically and vibrationally) states of hydrogenic species. A complete kinetic scheme for a coupled H/H_2 collisional–radiative model of fusion edge/divertor plasma is presented. The status of corresponding collision database is discussed in detail, and its major gaps identified. The directions of further developments of this database are outlined.

19.1 Introduction

Collision processes of atomic and molecular hydrogen with plasma electrons, protons and impurity ions play a critical role in several fusion research areas. Injection of energetic neutral (atomic) hydrogen beams in fusion plasmas is one of the major methods of plasma heating, the efficiency (e.g., extent of beam penetration) and characteristics (e.g., energy deposition profile) of which strongly depend on the collision processes of beam atoms (excitation, ionization, charge exchange) with plasma electrons, protons and impurity ions [1]. Less energetic neutral hydrogen atomic beams are also routinely used as standard core plasma diagnostic tools (charge exchange recombination spectroscopy, CXRS, and H-beam emission spectroscopy) [2]. In the low temperature edge plasma regions, and particularly in the cold divertor regions, where plasma temperature can be as low as $\sim 1\,\mathrm{eV}$, molecular hydrogen (introduced here either externally, for plasma cooling purposes, or as a result of plasma–wall hydrogen recycling process) can be present in concentrations comparable to (or higher than) plasma density. Collision processes of hydrogen molecules (which can be also vibrationally and rationally excited) with other edge/divertor plasma constituents (electrons, protons, neutral H-atoms, low-charged impurity ions) strongly effect the ionization and dissociation balance in these regions, the edge/divertor plasma cooling, power and particle exhaust, plasma momentum dissipation, etc. [3]. Atomic line or molecular band emissions, resulting from the products of these processes,

usually serve as a basis for edge/divertor plasma diagnostics (H_α [4] and Fulcher band [5] emission spectroscopies). Establishment of comprehensive cross-section databases for collision processes involving H and H_2 to meet the needs in the above fusion research areas has been a continuous effort since the beginning of seventies. The most prominent early critically assessed cross-section data collections are those of Barnett and his associates [6, 7], Takayanagy and Suzuki [8] and three UKAEA Culham reports [9–11]. The database for the H-atom collisional–radiative (CR) model, albeit limited to electron-impact and radiative processes, was also established at the beginning of seventies (Johnson [12]), when a similarly complete cross-section database for electron-impact processes of H_2 was also published [13]. Most of these cross-section databases (exceptions are [12, 13]) were dealing with processes of un-excited H and H_2. The first comprehensive collision database for H and H_2 that has also included the collision process of excited H and H_2 (with the vibrational excitations of H_2 and H_2^+ treated in an effective way), and that has coupled the collision kinetics schemes of H and H_2, was published in [14].

This reference also provided information on the energetics (energy loss/gain by the reactants/products) for each reaction, required as input in kinetic Monte Carlo transport codes and for interpretation of Balmer series lineshape diagnostics results.

During the late 1980's and 1990's, motivated by the atomic and molecular data needs of conceptual and engineering design of International Thermonuclear Experimental Reactor (ITER) [15], the work on establishment of H and H_2 collision databases for fusion has shifted towards inclusion of collisions of these species with plasma impurity ions and processes involving vibrationally excited H_2 molecules. The calculation of attenuation kinetics of 650 KeV/amu neutral D-beam for ITER required to include excitation, ionization and charge exchange processes (of ground and excited H-atoms) with protons and plasma impurity ions, that resulted to establishment of an extended CR model for H [16, 17]. Increased demands of CXRS diagnostics for state-selective electron capture cross-sections of H on fully stripped impurity ions has stimulated the work on establishment of such databases [18–20]. The newly developed divertor concept for ITER, based on the active role of high-density, cold molecular and atomic hydrogen gas to dissipate the plasma power and momentum in divertor region and achieve plasma detachment conditions, has motivated significant efforts on cross-section generation for electron- and proton-impact processes involving vibrationally excited molecular hydrogen [21–26], as well as for elastic (momentum transfer) collisions of H^+, H_2^+ and H on plasma edge neutrals (H and H_2) [27–29]. A significant part of these efforts has been coordinated by the Atomic and Molecular Data Unit of International Atomic Energy Agency [30] and other international collaborations [31, 32].

In the present review we shall discuss the current status of cross-section database for collision process of H and H_2 in fusion plasmas, with particular attention to processes involving electronically and vibrationally excited states

of these species. Emphasis will be placed on the completeness of the kinetic scheme for a coupled H/H_2 CR model and on the gaps in the corresponding collision database. The possible directions of further development of coupled H/H_2 models will also be briefly discussed.

19.2 Hydrogen Atom Collision Processes

The traditional kinetic scheme of a CR model for atomic hydrogen (see, e.g., [12]) includes only the electron impact and radiative processes of $H(n)$, $n \geq 1$,

$$e + H(n) \leftrightarrow e + H(n'), \quad n' > n = 1, 2, ... \tag{19.1}$$

$$e + H(n) \leftrightarrow e + H^+ + e, \quad n \geq 1 \tag{19.2}$$

$$e + H^+ \rightarrow e + H(n) + h\nu, \quad n \geq 1 \tag{19.3}$$

$$H(n') \rightarrow H(n) + h\nu, \quad n' > n = 1, 2, ... \tag{19.4}$$

where n is the principal quantum number of the hydrogen atom state. Analytic expression for the cross-sections of these processes are given in [12,14,17], with those in [17] being based on the most recent experimental and theoretical data. When solving the coupled equations for the level populations, the practical choice of the uppermost level $n'_{\max}$ is dictated by the competition of radiative and collisional mixing processes (the Seaton collisional limit, see, e.g., [33]), or convergence considerations. In the context of energetic neutral hydrogen beam penetration in fusion plasmas, when the beam atom velocity is such that proton-atom collision times are comparable with the radiative life-times of excited H-atom states, the proton impact processes, such as

$$H^+ + H(n) \leftrightarrow H^+ + H(n'), \quad n' > n = 1, 2, ... \tag{19.5}$$

$$H^+ + H(n) \rightarrow H^+ + H^+ + e, \quad n \geq 1, 2, ... \tag{19.6}$$

$$H^+ + H(n) \leftrightarrow H(n') + H^+, \quad n, n' = 1, 2, ... \tag{19.7}$$

dominate over processes (19.1–19.3). The most accurate presently available cross-sections for these processes are given in [17]. However, in plasmas with temperatures below $\sim 1000\,\mathrm{eV}$, proton-impact excitation and ionization processes (19.5), (19.6) have negligible rate coefficients with respect to electron-impact processes (19.1), (19.2). In the low-temperature ($\lesssim$ 2–3 eV) and high neutral density ($n_H \sim 10^{(14-15)}\mathrm{cm}^{-3}$) divertor plasmas, the following processes involving excited hydrogen atoms may become important:

$$H(m) + H(n) \leftrightarrow H(n) + H(m), \quad m, n = 1, 2, 3...(m \neq n) \tag{19.8}$$

$$H(m) + H(n) \rightarrow H^+ + H(n') + e, \quad m, n \geq 2, 3, ..., n' < n \tag{19.9}$$

$$H(m) + H(n) \leftrightarrow H(m) + H(n'), \quad m = 1, 2, ..., n' > n \gg m \tag{19.10}$$

$$\mathrm{H}(m) + \mathrm{H}(n) \rightarrow \mathrm{H}^+ + \mathrm{H}(m) + e, \quad m = 1, 2, ..., n \gg m \tag{19.11}$$

$$\mathrm{H}(m) + \mathrm{H}(n) \rightarrow (\mathrm{H}_2^{**}) \rightarrow \mathrm{H}_2^+(v) + e, \quad m = 1, 2, ..., n \geq 2 \tag{19.12a}$$

$$\rightarrow \mathrm{H}(m') + \mathrm{H}^+ + e, \quad m' > m \tag{19.12b}$$

These processes have been much less studied than (19.1)–(19.7), and the corresponding cross-section database is rather sparse even for the $m = 1$ case. However, the cross-sections for some of these processes might be sufficiently large to compensate for the relatively low concentrations of excited atoms in the plasma. In general, their cross-sections should scale as $n^4\sigma_0$, where σ_0 is the corresponding cross-section for ground state ($m = n = 1$) atoms. The cross-sections for excitation transfer reaction (19.8) and Penning ionization reaction (19.9) are proportional to the oscillator strengths for the $m \rightarrow n$ and $n \rightarrow n'$ transitions, respectively. The resonant excitation and ionization processes (19.10) and (19.11) involving Rydberg atoms proceed with conservation of total electron energy (internal energy conversion) and have, therefore, large cross-sections, as demonstrated in [34]. The associative ionization process (19.12a) has been experimentally investigated for $m = 1$ and $n = 2, 3, 4\,(l = 0$ states) [35] and shows large cross-sections. The non-associative ionization channel (19.12b), however, has not been investigated as yet.

In divertor regions with temperatures below a few eV, H^- ions may be formed by radiative electron attachment

$$e + \mathrm{H}(n) \rightarrow \mathrm{H}^- + h\nu, \quad n = 1, 2, ... \tag{19.13}$$

and by dissociative electron attachment on $\mathrm{H}_2(v)$ molecules (see next section). The process (19.13) with $n = 1$ is by far more important than those with $n \geq 2$, and its cross-section is well known [8]. H^- are subject to the fast processes

$$e + \mathrm{H}^- \rightarrow e + \mathrm{H} + e \tag{19.14}$$

$$\mathrm{H}^+ + \mathrm{H}^- \rightarrow \mathrm{H}(n) + \mathrm{H}, \quad n = 2, 3 \tag{19.15}$$

$$\mathrm{H}^- + \mathrm{H}(n) \rightarrow \mathrm{H}(n) + \mathrm{H}^-, \quad n = 1, 2, 3 \tag{19.16}$$

$$\mathrm{H}^- + \mathrm{H}(n) \rightarrow \mathrm{H}_2(N^{1,3}\Lambda_\sigma; v) + e \tag{19.17a}$$

$$\rightarrow \mathrm{H} + \mathrm{H}(n') + e, \quad n' \leq n \tag{19.17b}$$

$$\mathrm{H}^- + \mathrm{H}^+ \rightarrow \mathrm{H}_2^+(X^2\Sigma_u^+; v) + e \tag{19.18}$$

which have been all experimentally or theoretically studied in the past. The cross-sections for processes (19.14)–(19.17) can be found in [14] (for reactions (19.16) and (19.17) only for $n = 1$), and for the process (19.18) in [35]. The available cross-section for reaction (19.18) is vibrationally unresolved. For

reaction (19.17a) with $n = 1$, however, vibrationally resolved cross-sections do exist [36].

The three-body association reactions

$$H^+ + H + H(n) \rightarrow H^+ + H_2(v), \quad n \geq 1 \tag{19.19a}$$

$$\rightarrow H + H_2^+(v) \tag{19.19b}$$

$$H + H + H(n) \rightarrow H + H_2(v), \quad n \geq 1 \tag{19.20}$$

have recently been studied theoretically for $n = 1$ (19.19) in [37] and (19.20) in [38]), but they appear to be too slow to play an appreciable role in fusion divertor plasmas (at least when the density n_H is not too high).

The above survey of collision processes involving hydrogen atoms in fusion edge/divertor plasmas indicates that there are still major gaps in the corresponding database, particularly for the processes involving excited hydrogen atoms. It should also be noted that some processes in the extended CR model for H, such as (19.12a), (19.17a), (19.18), (19.19) and (19.20), establish a coupling between the kinetic schemes of H and H_2 CR models. This coupling is further reinforced by direct electron and proton dissociative processes with molecular hydrogen and its ions (see next section).

In the context of hydrogen neutral beam attenuation kinetics in fusion plasmas, and charge exchange core plasma diagnostics, the important hydrogen atom processes are those with highly stripped impurity ions, A_Z^{q+} (where Z is the atomic number of impurity, and q is its charge)

$$A_Z^{q+} + H(n) \rightarrow A_Z^{q+} + H(n'), \quad n' > n \geq 1 \tag{19.21}$$

$$A_Z^{q+} + H(n) \rightarrow A_Z^{q+} + H^+ + e, \quad n \geq 1 \tag{19.22}$$

$$A_Z^{q+} + H(n) \rightarrow A_Z^{q-1}(n', l') + H^+, \quad n, n' \geq 1, \; l' = 0 - (n' - 1) \tag{19.23}$$

The total cross-sections for these processes for fully stripped ions ($q = Z$) are given in [17]. For the cross-sections of reactions with $n \geq 2$, appropriate, scaling relationships have been used. Cross-section scaling relationships can be used also for the reactions with incompletely stripped ions having $q \geq 2$ in the case of reactions (19.21) and (19.22), and $q \gtrsim 5$ in the case of charge exchange reaction (19.23), provided the collision energy is sufficiently high (e.g., above $\sim$ 15–20 keV/amu). Cross-sections for state-selective electron capture in the low-energy region ($\lesssim$ 25 keV/amu) are available only for a limited number of fully stripped low-Z impurities ($Z = 2 - 8$ [19, 20, 39]). At high energies ($\sim$ 25 keV/amu), such data are available for a broader range of fully stripped ions ([18,40,41]). For incompletely stripped A_Z^{q+} ions, with $Z \lesssim 10$, the available state-selective electron capture data are collected and reviewed in [42, 43]. It has to be noted that the complex collision dynamics of state-selective charge exchange process at intermediate and low energies does not allow establishing of reliable cross-section scaling relationships. Therefore,

sophisticated experimental measurements or theoretical calculations have to be performed for each particular incompletely stripped ion colliding with atomic hydrogen in order to determine the state selective charge exchange cross-section in a given collision energy range. With decreasing the collision energy both the experimental and theoretical determination of these cross-sections are becoming increasingly more involved.

19.3 Collision Processes of Molecular Hydrogen and Its Ions

The low temperatures of edge/divertor plasmas (from $\sim$ 20–30 eV down to $\sim$ 1 eV) support the existence of high-density molecular hydrogen in these regions. There is evidence that divertor hydrogen molecules are vibrationally and rotationally excited, and their radiation in the Fulcher band ($3d^3\Pi_u(v) \rightarrow 2a^3\Sigma_g^+(v')$ transitions) has even been used for edge/divertor plasma diagnostics in some tokamaks [5, 44]. Collision processes of vibrationally excited hydrogen molecules play an important role in the overall edge/divertor kinetics and, in particular, they can be a critical factor in volume plasma recombination [45,46] under certain conditions. Many important collision processes of hydrogen molecules and their ions have been recently reviewed in [47]. The present review, however, will give a comprehensive list of all processes, which need to be included in a vibrationally resolved H_2 CR model. The processes involving rotationally excited states, however will be excluded from the present survey.

19.3.1 Collision Processes of Hydrogen Molecules

The quantum state of H_2 molecule is characterized by the set of quantum numbers $(N^{1,3}\Lambda_\sigma^\pi, v_\lambda)$, where $N^{1,3}\Lambda_\sigma^\pi$ refers to the electronic molecular state (N is the state principal quantum number in the united limit, Λ is the projection of total electron angular momentum, 1,3 (singlet, triplet) is the spin multiplicity of the state, $\sigma = g, u$ is the state symmetry, π is its parity) and v_λ is the vibrational quantum number of $N^{1,3}\Lambda_\sigma^\pi$ state. For simplicity, the indices (1,3), σ, π and λ will, generally, be omitted in the reaction description. We note that many $(N\Lambda)$ states of H_2 have dissociative character.

We start with the basic processes involved in the vibrational population of a given $(N\Lambda)$ state. These processes include:

$$e + H_2(N\Lambda; v) \rightarrow e + H_2(N\Lambda; v') \tag{19.24}$$

$$e + H_2(N\Lambda; v) \overset{(H_2^-)^{**}}{\longrightarrow} e + H_2(N\Lambda; v') \tag{19.25}$$

$$e + H_2(N\Lambda; v) \overset{H_2^*(N'\Lambda';v'')}{\longrightarrow} e + H_2(N\Lambda; v') + h\nu, \ (N' > N) \tag{19.26}$$

$$\mathrm{H}^+ + \mathrm{H}_2(N\Lambda; v) \rightarrow \mathrm{H}^+ + \mathrm{H}_2(N\Lambda; v') \tag{19.27}$$

$$\mathrm{H}^0 + \mathrm{H}_2(N\Lambda; v) \rightarrow \mathrm{H}^0 + \mathrm{H}_2(N\Lambda; v') \tag{19.28}$$

$$\mathrm{H}_2(N\Lambda; v) + \mathrm{H}_2(N\Lambda; v') \rightarrow \mathrm{H}_2(N\Lambda; v') + \mathrm{H}_2(N\Lambda; v) \tag{19.29}$$

where H^0 designates the ground state hydrogen atom. The processes (19.24)–(19.29) have been studied only for the ground electronic state, $\mathrm{X}^1\Sigma_g^+$, of H_2. Direct e-impact vibrational excitation (19.24) is a relatively weak process and its cross-sections for some transitions are available in [14]. The indirect vibrational excitation mechanisms (19.25) and (19.26) are much stronger. Complete sets of cross-section data for $X^1\Sigma_g^+(v) \rightarrow X^1\Sigma_g^+(v')$ transitions via the lowest intermediary $(H_2^-)^{**}$ resonant states are provided in [48,49], while for transitions via the $\mathrm{H}_2^*(B^1\Sigma_u^+)$ and $\mathrm{H}_2^*(C^1\Pi_u)$ excited states (reaction (19.26)) such data sets are given in [21]. A complete set of proton-impact excitation cross-section for $v \rightarrow v'$ transitions in $X^1\Sigma_g^+$ state of H_2 is given in [50]. The cross-sections for $T - v$ and $v - v'$ transfer reactions [29] and [27,28], respectively, can be calculated by the Schwartz–Slawsky–Herzfeld (SSH) model [51] (with appropriate extensions for higher energies).

As mentioned above, the processes (19.24)–(19.29) have not been studied for electronically excited states of H_2. An estimate of the cross-sections for processes (19.24), (19.27)–(19.29) for $N \geq 2$ can be made by the SSH model. The available and relatively simple theoretical methods (such as the Born, Born–Rudge and impact-parameter method) can be used to calculate also the cross-section for reactions (19.26), but the difficulties of determining the higher resonant states of H_2^- prevent easy estimates of cross-sections for reactions (19.25) when $N \geq 2$.

Electron-impact electronic excitation, ionization and dissociation processes are among the most important collision processes that H_2 molecules undergo in a low-temperature plasma. These include

$$e + \mathrm{H}_2(N\Lambda; v) \rightarrow e + \mathrm{H}_2(N'\Lambda'; v'), \quad N' \geq N \tag{19.30}$$

$$e + \mathrm{H}_2(N\Lambda; v) \overset{\mathrm{H}_2^*(N'\Lambda';\epsilon_c)}{\longrightarrow} e + \mathrm{H}(m) + \mathrm{H}(n), \quad N' \geq N, m, n \geq 1 \tag{19.31}$$

$$e + \mathrm{H}_2(N\Lambda; v) \overset{\mathrm{H}_2(N'\Lambda')^{diss}}{\longrightarrow} e + \mathrm{H}(m) + \mathrm{H}(n), \quad N' \geq N, m, n \geq 1 \tag{19.32}$$

$$e + \mathrm{H}_2(N\Lambda; v) \overset{(\mathrm{H}_2^-)^{**}}{\longrightarrow} e + \mathrm{H}(m) + \mathrm{H}(n), \quad m, n \geq 1 \tag{19.33}$$

$$e + \mathrm{H}_2(N\Lambda; v) \overset{(\mathrm{H}_2^-)^{**}}{\longrightarrow} \mathrm{H}^- + \mathrm{H}(n), \quad n \geq 1 \tag{19.34}$$

$$e + \mathrm{H}_2(N\Lambda; v) \rightarrow e + \mathrm{H}_2^+(X^2\Sigma_g^+; v') + e \tag{19.35}$$

$$e + \mathrm{H}_2(N\Lambda; v) \overset{\mathrm{H}_2^+(X^2\Sigma_g^+;\epsilon_c)}{\longrightarrow} e + \mathrm{H}^+ + \mathrm{H}(n) + e, \quad n \geq 1 \tag{19.36a}$$

$$e + \mathrm{H}_2(N\Lambda; v) \overset{\mathrm{H}_2^+(2p\sigma^2\Sigma_u^+)}{\longrightarrow} e + \mathrm{H}^+ + \mathrm{H}(n) + e, \quad n \geq 1\ . \tag{19.36b}$$

Allowed excitation transitions are those between $N\Lambda$-states with different g, u-symmetries, and most intense among them are those preserving the total spin (singlet-singlet and triplet-triplet transitions). The intermediary state in reaction (19.31) is a bound electronic state, but the transition takes place to the vibrational continuum of this state. The intermediary state in reaction (19.32) is a dissociative state that lies completely in the vibrational continuum. The reaction (19.33) is similar to reaction (19.26), except that the decay of $(H_2^-)^{**}$ resonance (auto-detachment) takes place in the vibrational continuum.

The processes (19.30)–(19.36) have so far been studied (experimentally and theoretically) only for the ground electronic state of H_2, $N\Lambda = X^1\Sigma_g^+$, with a few exception for the excitation process (19.30). $v - v'$ resolved excitation (as well as v-resolved dissociative excitation reaction (19.31)) cross-sections are available for the transitions from $X^1\Sigma_g^+$ to $2E/F^1\Sigma_g^+$, $2B^1\Sigma_u^+$, $2C^1\Pi_u$, $3B'\Sigma_u^+$, $3D^1\Pi_u$, $4B''^1\Sigma_u^+$ and $4D'^1\Pi_u$ [21] (in this reference, however, only the cross-sections summed over v' are presented). v-resolved excitation cross-sections are available also for the $X^1\Sigma_g \to 2b^3\Sigma_u^+$ transition [21, 52], while for the transitions $X^1\Sigma_g^+ \to 2a^3\Sigma_g^+$, $2e^3\Pi_u$, $3h^3\Sigma_g$ and $3d^3\Pi_u$ $v - v'$ resolved cross-section calculations are presently in progress [53]. All these cross-sections have been calculated by the quantum impact-parameter (first order) method, (QIPM). Total cross-sections for $X \to a, b, c, e, d$ singlet-triplet transitions have been calculated also by using the Born–Ochkur and Born–Rudge method [54]. For transitions between excited states, $v - v'$ resolved cross-sections calculations exist only for $2B'\Sigma_u \to 3I^1\Pi_g$ [21] and $2a^3\Sigma_g \to 3d^3\Pi_u, 2c^3\Pi_u \to 3h^3\Sigma_g^+, 2c^3\Pi_u \to 3g^3\Sigma_g^+$ [55] transitions, performed by QIPM.

From the point of view of establishing a CR model for H_2, it is necessary to have $v - v'$ resolved cross-sections for all transitions between the electronic states with $N \leq 3$ and for the high-Λ states (P, R, S, V-singlets and p, r, s, m-triplets) from the group of $N = 4$ states. For the transitions to (and between) the states with higher N, the excitation cross-sections can be obtained by scaling those for $N \leq 3 (N \leq 4)$ (within the same series $^{1,3}\Lambda_\sigma$ of states) according to the N^{-3} rule.

For the dissociative excitation process (19.32), proceeding via purely dissociative $(N'\Lambda')^{\text{diss}}$ states, only the cross-sections for $X'\Sigma_g^+(v) \to b^3\Sigma_u^+$ transitions are available. The purely dissociative states of H_2 having $N \geq 4$ are not well known from molecular structure calculations, and they energetically lie far away from the ground $X^1\Sigma_g^+$ state. The transitions to them from $X^1\Sigma_g^+$ should be, therefore, much weaker. They can be nevertheless important in producing two excited atomic products at high collision energies. However, the process (19.32) may become important for $N \geq 2$ initial states, and it should be included in the kinetic scheme of H_2 CR models.

The processes (19.33) and (19.34) are dynamically mutually coupled (as well as with the process (19.25)), and the corresponding theoretical calcula-

tions describe these processes within the same computational framework. There have been many cross-section calculations for these process when $N\Lambda = X^1\Sigma_g^+$ and when $(H_s^-)^{**}$ represents the two lowest resonant states of H_2^-. The results of most recent v-resolved cross-section calculations can be found in [21,56]. There are, however, no cross-section data for these two types of processes for the excited, $N \geq 2$, states. It has been contemplated, however, that the cross-section for the dissociative attachment process (19.34) for $N \geq 2$ should be very large (with rate coefficients in the few-eV region of $\sim 10^{-5}$–$10^{-6}\,\mathrm{cm}^3/\mathrm{s}$). This has recently been supported by indirect experimental observations [57] and a crude theoretical model [58].

Reactions (19.35), (19.36) have been studied theoretically for $N\Lambda = X^1\Sigma_g^+$ on several occasions, and v-resolved cross-sections, obtained within the Grizinsky–Bauer–Bratky (GBB) model [59, 60], are presented in [21]. (Total experimental cross-sections for these reactions for the $X^1\Sigma_g^+(v = 0)$ initial state are given in [14].) The simplicity of GBB model permits to perform $v-v'$ resolved cross-section calculations also for transitions from excited ($N \geq 2$) states, but such calculations have not been published. It should be mentioned, however, that the accuracy of GBB method is (at best) within a factor of two, and more accurate quantal calculations of the cross-sections of processes (19.35), (19.36) are desirable. For transitions from the initial $N\Lambda$ states with $N \geq 3$, the cross-sections of reactions (19.35), (19.36) within a given ${}^{1,3}\Lambda_{g,u}$-series of states can be scaled (approximately as N^2).

The most important heavy-particle collision processes of hydrogen molecules in edge/divertor plasmas are

$$H^+ + H_2(N\Lambda; v) \;\rightarrow\; H(n) + H_2^+(X^2\Sigma_g^+; v'), \quad n \geq 1 \tag{19.37}$$

$$H^+ + H_2(N\Lambda; v) \;\rightarrow\; H(n) + H^+ + H, \quad n \geq 1 \tag{19.38}$$

$$H^+ + H_2(N\Lambda; v) + M \;\rightarrow\; H_3^+(v') + M \tag{19.39}$$

$$H(n) + H_2(N\Lambda; v) \xrightarrow{H_3^*} H_3^+(v') + e, \quad n \geq 1 \tag{19.40}$$

$$H(n) + H_2(N\Lambda; v) \xrightarrow{H_3^*} H_2^+(X^2\Sigma_g^+; v') + H(m) + e; \quad n, m \geq 1 \tag{19.41a}$$

$$\xrightarrow{H_3^*} H_2(N'\Lambda'; v') + H^+ + e \tag{19.41b}$$

$$\xrightarrow{H_3^*} 2H + H(n), \quad n \geq 1 \tag{19.41c}$$

$$H(n) + H_2(N\Lambda; v) \rightarrow H(m) + H_2(N'\Lambda'; v'), \quad m \neq n; N' \neq N \tag{19.42}$$

Since population densities of excited species in a plasma are always considerably smaller than those of corresponding ground states, at least one of the reactants in reactions (19.40)–(19.42) must be in its ground state to ensure

a significant role of the process in the collision kinetics. The charge exchange process (19.37) is particularly important since it converts the plasma H^+ ions into molecular H_2^+ ions, that at low temperatures ($T \lesssim 3\,\text{eV}$) rapidly recombine with plasma electrons. At such low temperatures, formation of H_2^+ ions by electron impact ionization (process (19.35)) is a much less effective process. The processes (19.37) and (19.38) for $N\Lambda = X^1\Sigma_g^+$ have been studied by both classical-trajectory surface-hoping (CTSH) method [22, 23] and by the quantal infinite-order sudden approximation (IOSA) method [24–26]. Consistent sets of $v - v'$ resolved cross-sections have been obtained for these reactions for collision energies up to $\sim 10\,\text{eV}$. Plausible extrapolations of these cross-section data for (19.37) to higher energies can be made by using the few v resolved data of [61]. For the $N \geq 2$ excited states of H_2, processes (19.37), (19.38) have not been studied. However, if N is sufficiently high ($N \geq 3-4$), the $H_2(N\Lambda, v)$ molecule can be considered in the "Rydberg-atom" approximation, and the total cross-section of reaction (19.37) can be estimated from scaling properties of electron capture reactions ($\sigma_{cx} \sim N^4$). The cross-section of dissociative charge transfer reaction (19.38) should also scale similarly as that for electron capture for the high-N-states.

The processes (19.39)–(19.42) have not been studied so far. The CTSH calculations for the $H^+ + H_2(X^1\Sigma_g^+; v)$ system [22,23] indicate that long-lived transient states of H_3^+ complex are formed during the slow collision, particularly for the high initial vibrational states of $H_2(X^1\Sigma_g^+; v)$. Stabilization of these states by a third particle M (enabling for total energy and angular momentum conservation) should take place with high probability. In the reaction (19.40) with $n \gg 1$ and $N = 1$, the required third body for the process (19.39) to take place can be the Rydberg electron in $H(n \gg 1)$. In a quantum-mechanical picture, reaction (19.40) is an associative ionization process which, as we have seen in Sect. 19.2, is very effective in the atomic $H(ns) + H(1s)$ ($n = 2, 3, 4$) case [35]. Reactions (19.41) are only the non-associative counterparts of the same H_3^* formation process (or different decay channels of the unstable H_3^* state). The excitation transfer reaction (19.42) is the molecular version of the corresponding atomic process, (19.8); it is important only at sufficiently high densities of reactants.

19.3.2 Decay Processes of Electronically Excited H_2 States

Bound electronically excited states of H_2 may radiatively decay to lower states subject to the selection rules: $g \leftrightarrow u$, singlet $\leftrightarrow$ singlet, triplet $\leftrightarrow$ triplet. The final state in these transitions may be either a bound or a dissociative state, i.e.,

$$H_2(N^{1,3}\Lambda_{g,u}; v) \rightarrow H_2(N'^{1,3}\Lambda'_{u,g}; v') + h\nu, \quad N' \geq N \tag{19.43}$$

$$H_2(N^{1,3}\Lambda_{g,u}; v) \rightarrow H_2(N'^{1,3}\Lambda'_{u,g})^{diss} + h\nu, \quad N' \geq N \tag{19.44}$$

While the emission from process (19.43) has a band character, that from the process (19.44) is continuous. Most of the calculations have been per-

formed for the $N'^1\Lambda_u(v') \rightarrow X^1\Sigma_g^+(v)$ transitions, the upper state being $2B^1\Sigma_u^+, 2C^1\Pi_u$ [62, 63] and some $N \geq 3$ states [64, 65]. Transitions from the lowest bound triplet states to the dissociative $2b^3\Sigma_u^+$ state have been calculated in [66, 67].

There are also a number of non-radiative processes by which the excited $(N\Lambda, v)$ states can decay. Auto-ionization and pre-dissociation are the most prominent ones,

$$\mathrm{H}_2(N\Lambda; v) \rightarrow \mathrm{H}_2^+(X^2\Sigma_g^+; v') + e, \quad N \geq 2 \tag{19.45}$$

$$\mathrm{H}_2(N\Lambda; v) \rightarrow \mathrm{H}_2(N'\Lambda'; \epsilon_c)^{\mathrm{diss}} \rightarrow \mathrm{H}(1s) + \mathrm{H}(n) \tag{19.46}$$

Auto-ionization takes place when the vibrational energy of the $N\Lambda$ electronic state ($N \geq 2$) is larger than its ionization energy. For the singlet states $\mathrm{H\overline{H}}$, D, J, O, B'', P, R, S, the first vibrational levels, starting from which these states auto-ionize, (i.e., for $v \geq v_0$) are $v_0 = 12, 7, 7, 4, 10, 5, 4, 4$, respectively. For the triplet states d, g, j, k, r, s the corresponding v_0-levels are: $v_0 = 7, 7, 7, 4, 4, 4$, respectively. For sufficiently high $N\Lambda$-states, only the first one or two vibrational levels are non-auto-ionizing.

The pre-dissociation results from a non-adiabatic coupling between electronic states $(N\Lambda; v)$ and $(N'\Lambda'; \epsilon_c)$ at internuclear distances (usually smaller than the equilibrium distance) that correspond to the vibrational continuum of $N'\Lambda'$ state, or when the $N'\Lambda'$ state is a purely dissociative one. Auto-ionization and pre-dissociation probabilities for $Np\sigma(v)$ and $Np\pi(v)(N \geq 4)$ states have been calculated in [68], while for the states with $N \leq 3$ they have been evaluated from experimental measurements [69,70]. Auto-ionization and pre-dissociation rates are very high ($\sim 10^8\,\mathrm{s}^{-1}$ for $N = 3, 4$), and rapidly increase with increasing v. More experimental or theoretical information is needed for these processes.

The potential energy curves for some electronic states (such as $3I^1\Pi_g$, $3i^3\Pi_g$ and $3h^3\Sigma_g^+$) exhibit maxima at finite internuclear distances ($\sim 4{-}6a_0$), so that the upper vibrational states of these electronic states are unstable against dissociation by quantum-mechanical tunnelling. The decay probabilities (or lifetimes) of such vibrational states are still unknown, except for the $3h^3\Sigma_g^+$ electronic state [55, 71].

19.3.3 Collision Processes of H_2^+ Ions

The vibrational distribution of $\mathrm{H}_2^+(X^2\Sigma_g^+; v)$ ions, created by various ionizing (or auto-ionizing) processes of $\mathrm{H}_2(N\Lambda; v)$ discussed in previous two sub-sections, is subject to further redistribution due to collision processes

$$e + \mathrm{H}_2^+ \rightarrow e + \mathrm{H}_2^+(v') \tag{19.47}$$

$$\mathrm{H}^+ + \mathrm{H}_2^+ \rightarrow \mathrm{H}^+ + \mathrm{H}_2^+(v') \tag{19.48}$$

$$\mathrm{H} + \mathrm{H}_2^+ \rightarrow \mathrm{H} + \mathrm{H}_2^+(v') \tag{19.49}$$

$$\mathrm{H}_2^+(v_1) + \mathrm{H}_2(X; v_2) \rightarrow \mathrm{H}_2^+(v_1') + \mathrm{H}_2(X; v_2'), \Delta v_{12} \approx \Delta v_{12}' \quad (19.50)$$

$$\mathrm{H}_2^+(v_1) + \mathrm{H}_2(X; v_2) \rightarrow \mathrm{H}_2(X; v_2') + \mathrm{H}_2^+(v_1') \quad (19.51)$$

The process (19.47) has been subject to many theoretical studies [72–74]. The cross-section for $v \rightarrow v'$ transition is dominant for $v' = v + 1$, and rapidly decreases when $\Delta v = |v - v'|$ increases. The Born–Oppenheimer method used in [72, 73] for cross-section calculations of process (19.47) can also be applied to calculate the cross-sections for the process (19.48). Cross-section calculations have recently been performed for the process (19.49) with the IOSA method in the energy region up to $\sim 9\,\mathrm{eV}$ [75]. The processes (19.50) and (19.51) have been studied in [76] and [77], respectively, where their cross-sections can be found.

The dominant electron-impact process at low collision energies is the dissociative recombination

$$e + \mathrm{H}_2^+(X, v) \rightarrow \mathrm{H}_2^{**}(2p\sigma_u^2) \rightarrow \mathrm{H}(1s) + \mathrm{H}(n \geq 2) \quad (19.52)$$

which has been subject to many experimental [78] and theoretical [79, 80] studies. The most detailed cross-section calculations of reactions (19.52) have been performed in [80] by using the multi-channel quantum defect theory (MQDT). The n-distribution of excited products from reaction (19.52) obtained in MQDT calculations support the earlier semi-empirical assessment [14], at least for the lower v-states.

The radiative and three-body recombination processes,

$$e + \mathrm{H}_2^+(X; v) \rightarrow e + \mathrm{H}_2(N\Lambda; v') + h\nu \quad (19.53)$$

$$e + e + \mathrm{H}_2^+(X; v) \rightarrow e + \mathrm{H}_2(N\Lambda; v') \quad (19.54)$$

play much lesser role than the dissociative recombination (19.52), and their cross-sections should be close to those in the atomic case [81].

At higher collision energies, the most important electron-impact processes of $\mathrm{H}_2^+(X; v)$ are

$$e + \mathrm{H}_2^+(X^2\Sigma_g^+; v) \rightarrow e + \mathrm{H}_2^+(N^2\Lambda)^{\mathrm{diss}} \rightarrow e + \mathrm{H}^+ + \mathrm{H}(n), \quad N \geq 2,\ n \geq 1 \quad (19.55)$$

$$e + \mathrm{H}_2^+(X; v) \rightarrow e + \mathrm{H}^+ + \mathrm{H} + e \quad (19.56)$$

where $(N^2\Lambda)^{\mathrm{diss}}$ indicates a dissociative state. We note that in the Franck–Condon region of $\mathrm{H}_2^+(^2\Sigma_g^+; v)$ states, all excited states of H_2^+ have a dissociative character. For $N = 2$ ($N^2\Lambda = 2p\sigma_u$, the first electronically excited state of H_2^+), accurate v-selective cross-section calculations were performed recently within the MQDT [80], which differ significantly from the earlier Born calculations [82]. The cross-sections of dissociative excitation process (19.55) for $N \geq 3$ can be estimated by using the MQDT cross-section [80] for $N = 2$ and the N^{-3} scaling.

The cross-section for dissociative ionization process (19.56) is experimentally known for $v = 0$ [83] (see also [14]). The cross-sections for $v \geq 1$ can be roughly estimated from the cross-section for $v = 0$ by using the I_v^{-1} scaling of ionization cross-section, where I_v is the transition energy from $H_2^+(X; v)$ energy level to the $(H^+ + H^+)$ interaction potential at the internuclear distance equal to the equilibrium distance of $H_2^+(X; v)$.

The most important heavy-particle collision processes of H_2^+ are

$$H(n) + H_2^+(X; v) \to H^+ + H_2(N\Lambda; v'), \quad n \geq 1 \tag{19.57}$$

$$H(n) + H_2^+(X; v) \to H(n) + H + H^+, \quad n \geq 1 \tag{19.58a}$$

$$\to H^+ + H(n) + H, \quad n \geq 1 \tag{19.58b}$$

$$H_2^+(X; v_1) + H_2(N\Lambda; v_2) \to H_3^+(v_3) + H(n), \quad n \geq 1 \tag{19.59}$$

$$H_2^+(X; v_1) + H_2(N\Lambda; v_2) \to H_2(N'\Lambda'; v_2') + H_2^+(X; v_1') \tag{19.60}$$

The charge exchange and dissociation processes (19.57) and (19.58) have recently been studied within the IOSA formalism for $n = 1$ and $N\Lambda = X^1\Sigma_g^+$ in [24–26], respectively, where the corresponding $v - v'$ and v-resolved cross-sections are given for collision energies up to $\sim 9\,\text{eV}$. For $n \geq 2$, these processes have not been studied as yet. As argued earlier, in connection with reactions (19.37) and (19.38), for sufficiently high n-states, the reaction (19.57) should attain a quasi-resonant character (with a cross-section scaling $\sigma_{cx} \sim n^4$), while the dissociation results mainly from the pre-dissociation of highly excited molecular states formed by electron capture (the channel (19.58b)). Reaction (19.59) is an important rearrangement process studied only for $N\Lambda = X^1\Sigma_g^+$. The cross-section for this reaction (in the case of $H_2(X; v_2)$) shows a strong sensitivity on the vibrational states v_1 and v_2 of reactants. Cross-section measurements for this reaction, with unknown v_1 and v_2 initial distributions, may vary by a factor 3–5 [84]. Accurate state selective (in terms of v_1, v_2, v_3, and n) cross-section determination for this reaction is a significant challenge for the theoretical and experimental atomic physics.

The charge exchange reaction (19.60) has resonant nature when $v_1' = v_1$ and $N'\Lambda' v_2' = N\Lambda v_2$. However, the plethora of Franck–Condon $v_2 \to v_1'$ and $v_1 \to v_2'$ transitions, accompanying the electron transition even in the $N'\Lambda' = N\Lambda$ case, immediately opens a large number of quasi-resonant, coupled charge transfer channels that destroy the resonance in the low (eV) energy region. The reaction (19.60) has been experimentally studied only for $N'\Lambda' = N\Lambda = X^1\Sigma_g^+$, and mainly with vibrationally unexcited reactants. (The corresponding cross-section is given in [14] and [85].) For the $N'\Lambda' = N\Lambda = X^1\Sigma_g^+$ case of reactions (19.60), quantum-mechanical coupled-state state-selective cross-section calculations have been performed for all v_1, v_2 initial states [77, 86]. For high-N states, an "atomic" model can be adopted to estimate the cross-section of reaction (19.60).

19.3.4 Processes Involving H^- and H_3^+ Ions

Collision processes of H^- ions with molecular hydrogen and its ions have not received much attention until recently, although their cross-sections may be large. The most important among these processes for divertor plasma conditions are

$$H^- + H_2(N\Lambda; v) \overset{(H_2^-)^{**}}{\longrightarrow} H + H + H(n) + e, \quad n \geq 1 \tag{19.61}$$

$$\overset{(H_2^-)^{**}}{\longrightarrow} H + H^- + H(n), \quad n \geq 1 \tag{19.62}$$

$$\overset{(H_2^-)^{**}}{\longrightarrow} H + H_2(N\Lambda; v') + e \tag{19.63}$$

$$H^- + H_2^+(X, v) \rightarrow H + H_2(N\Lambda; v'), \quad N \geq 2 \tag{19.64}$$

$$H^- + H_2^+(X, v) \rightarrow H_3^+(v') + e \tag{19.65}$$

$$H^- + H_3^+(v) \overset{H_3^*}{\longrightarrow} H + H_2(N\Lambda; v') + H(n), \quad n \geq 1 \tag{19.66a}$$

$$\overset{H_3^*}{\longrightarrow} H + 2H + H(n), \quad n \geq 1 \tag{19.66b}$$

Processes (19.61)–(19.63) are similar to electron-impact processes (19.33), (19.34) and (19.25), except that in the present case the intermediate $(H_2^-)^{**}$ resonant state is formed not by capture of a free electron but rather by capture of loosely bound electron from H^-. There may be also other mechanisms for electron detachment processes (19.61) and (19.63) and for the dissociation process (19.62).

The electron capture process (19.64) is the molecular version of $H^- + H^+$ mutual neutralization process. The collision dynamics in both cases is governed by the non- adiabatic coupling of initial ionic state with the covalent states of the exit reaction channels that takes place at large distances between colliding particles. In fact, for a given initial v-state of H_2^+, the availability of many vibrational states v' in the $(N\Lambda)$ electronic states of H_2 can provide a more favorable position of the non-adiabatic coupling region on the inter-particle (ion-ion) axis for maximizing the transition probability. Some initial qualitative studies of this process have appeared [87], but detailed $v - v'$ resolved cross-sections are still not available.

Associative reaction (19.65) has been studied experimentally for $v = 0$, and its total (unresolved in v_3) cross-section is known to very low ($\sim 0.05\,\text{eV}$) collision energies [35]. Associative detachment cross-section (as well as that for associative ionization of neutral particles) shows an E^{-1} energy dependence at collision energies below $\sim 1 - 2\,\text{eV}$. Collision processes (19.66a) and (19.66b) of H^- with H_3^+ have not been studied as yet. It is anticipated that

the cross-sections for these reactions should be large due to large charge exchange cross-section for formation of the unstable intermediary complex H_3^*. Using simple models for the mutual neutralization reactions [88], one can easily estimate the cross-section for H_3^* formation. The branching ratio for the H_3^* decay channels then can be taken to be close to the H_3^* branching ratio of the corresponding channels in dissociation $e + H_3^+$ recombination:

$$e + H_3^+(v_3) \xrightarrow{H_3^*} H_2(N\Lambda; v') + H(n), \quad n \geq 1 \tag{19.67a}$$

$$\xrightarrow{H_3^*} H + H + H(n), \quad n \geq 1 \tag{19.67b}$$

The total cross-section of reaction (19.67) has been measured by many authors (see reviews [78, 89]) with undefined v_3-vibrational distribution in $H_3^+(v_3)$. The results differ by a factor of ten. Recent storage-ring experiments have produced accurate cross-section for the $e + H_3^+(v = 0)$ case and an accurate branching ratio of H_3^* decay channels (19.67a) and (19.67b) [90]. This branching ratio is energy dependent: for energies below $\sim$ 2–3 eV dissociation channel (19.67b) is stronger, while for higher energies the opposite is true.

The H_3^+ ions produced in the processes (19.59), (19.63), (19.40) are certainly vibrationally excited, with a different vibrational-state distribution for each H_3^+-production process. There are also indications [91] that the $H_2(X'\Sigma_g^+; v')$ product of reaction (19.67a) is vibrationally highly excited ($v' \geq 5$). A detailed theoretical study of reactions (19.67), resolving the $N\Lambda-$, $(v_3 - v')-$, and n-channels would be extremely useful, but (at present) very difficult to perform.

While dissociative recombination process (19.67) is a dominant $e + H_3^+$ process at low ($\lesssim 15\,\text{eV}$) collision energies, the dissociative excitation

$$e + H_3^+(v_3) \to e + H_2^+(X; v') + H(n), \quad n \geq 1 \tag{19.68}$$

becomes dominant above $\sim$ 20 eV. Similarly as in H_2^+, the electronically excited states of H_3^+ are all repulsive (in the Franck–Condon region of $H_3^+(X; v_3)$), and their excitation leads to prompt dissociation. The total (vibrationally unresolved in v' and n) cross-section for reaction (19.68) with $H_3^+(v_3 = 0)$ ions has been measured [92] and has a threshold at $E_{th,0} \simeq 15\,\text{eV}$. The total cross-sections for $v_3 \geq 1$ of reaction (19.68) can roughly be estimated by using the known $\sigma(v_3 = 0)$ and the $E_{th,v}^{-1}$ scaling of excitation cross-sections (valid at energies sufficiently far from the threshold).

19.4 Major Gaps in the H/H_2 Collision Database

With the exception of reactions (19.21)–(19.23), all other processes considered in previous two sections have to be, in principle, included in a collisional scheme aiming at description of edge/divertor plasma kinetics in a broad plasma temperature range, e.g., $\sim$ 0.5–300 eV. In different parts of this range,

the role of considered processes, obviously, varies, and rates of some of them may be negligible with respect to those of other processes in certain divertor plasma regions. Nevertheless, modeling of plasma kinetics in the entire divertor volume requires a complete set of important collision processes. Since the rates of collision processes depend both on concentrations of reactants and corresponding rate coefficients, and the reactant concentrations themselves are determined by (time-dependent, in general) coupled rate equations, strict criteria for reduction of collisional kinetic scheme cannot be set forth *a priori* in the entire temperature range considered. Therefore, when constructing a complete H/H_2 CR model for divertor plasma studies, all processes discussed in previous two sections have to be included.

As we have seen in Sects. 19.2 and 19.3, the cross-section data for many considered processes are still not available, and for some processes, the existing data have large uncertainties. From a viewpoint of a self-consistent H/H_2 CR model that includes also the vibrational states of molecular species, the major gaps and uncertainties in the collision database are related to the following groups of processes:

(a) $v - v'$ resolved cross-sections for excitation and ionization processes involving excited $H_2(N\Lambda; v)$ states with $N = 2 - 4$ including the $v - v'$ excitation processes within a given $N\Lambda$-state. The existing, incomplete set of data for these processes is based mainly on first order (Born-type) impact-parameter method [21], the accuracy of which in the threshold region is not adequate;
(b) Auto-ionization and pre-dissociation of excited $H_2(N\Lambda; v)$ states with $N \geq 3$, (particularly the v-dependence of auto-ionization and pre-dissociation rates);
(c) Processes involved in vibrational kinetics of H_2^+ ion;
(d) Heavy-particle collision processes involving $H^-, H(n \geq 1)$ and $H_2(N\Lambda; v)$ $(N \geq 1)$ species (especially: electron transfer, heavy-particle rearrangement, associative/dissociative processes);
(e) $v - v'$ and n-resolved processes involved in the formation and destruction of H_3^+ ions;
(f) Radiative transition probabilities of $H_2^*(N\Lambda; v)$ states with $N \geq 3$.

Some of the gaps in the database can be filled by routine (but tedious and time-consuming) calculations using simplified theoretical models (e.g., BGG-model for electron-impact excitation and ionization of $H_2(N\Lambda; v)$ states, the more involved impact-parameter method for excitation, etc.) For some of above listed processes (such as those mentioned under (d) and (e)), however, it is necessary to develop appropriate theoretical models for description of their dynamics.

In the kinetic neutral particle transport codes (such as DEGAS, EIRENE, etc.), besides the cross-section (or rate coefficient) information on atomic collision processes, information on energy and angular distribution of reaction products is also required. We have omitted this aspect in our discussions of

plasma edge/divertor collision processes in Sects. 19.2 and 19.3. We mention here, however, that for the vast majority of processes discussed in Sects. 19.2 and 19.3, this information is not available. In the kinetic codes certain *ad hoc* assumptions (e.g., isotropic angular distribution of products, etc.) are usually adopted for these distributions.

19.5 Concluding Remarks

The presented analysis of the status of collisional database for atomic and molecular hydrogen in fusion plasmas shows that on the level of inclusion of vibrational degrees of freedom of molecular species, this database is presently far from its completeness and and self-consistency. Collision processes of vibrationally excited molecular species (H_2, H_2^+, H_3^+), however, do play an essential role in collisional plasma kinetics and they cannot be ignored. In the situation when the full, vibrationally resolved, collision database is incomplete, a reasonable approach in constructing a self-consistent H/H_2 kinetic scheme is to use reaction cross-sections (or rate coefficients) averaged over the distribution of vibrational states. In many occasions, the non-state-selective experimental data (e.g., performed with reactants extracted from a plasma source), already represent such averaged cross-sections (or rate coefficients) (albeit for a specific vibrational distribution defined by a given plasma source temperature). This approach (followed, e.g., in [14]) is sufficient for neutral particle transport modeling of edge/divertor plasmas, but does not meet the needs of molecular diagnostics of these plasmas. Therefore, the efforts on generation of vibrationally state-selective cross-section data for processes involving molecular hydrogenic species must continue.

It should be noted that majority of the available data for processes discussed in Sects. 19.2 and 19.3 are pertinent to the light H/H_2 isotopes of hydrogen. In a D-T fusion reactor plasma, the processes enumerated in Sects. 19.2 and 19.3 will take place for D, T atoms and D_2, DT and T_2 molecules and their ions. The vibrational energy levels in the molecular species of heavier hydrogen isotopes are different than those in H_2; this introduces differences in the corresponding cross-sections for the same types of processes (even after an appropriate mass scaling of vibrational energies). More importantly, there are certain types of molecular reactions that proceed via formation of an intermediary complex (such as $(H_2^-)^{**}$, $(H, H_2^+)_v^*$, H_3^*, and their isotopic variants), the decay lifetime of which for various decay channels strongly depends on its isotopic structure. For instance, the cross-sections of seemingly similar particle exchange processes such as $D^+ + H_2 \rightarrow HD^+ + H$ and $H^+ + D_2 \rightarrow HD^+ + D$ differ by a factor of 5 at 2–3 eV, while for $D^+ + H_2 \rightarrow HD + H^+$ and $D^+ + HD \rightarrow D_2 + H^+$ the difference amounts to a factor of 10 [84, 93]. Particularly strong isotope dependence exhibit the processes that proceed via formation of $(A_2^-)^{**} (A = H, D, T)$ resonant states: the mass dependence of the cross-section appears in an exponential factor (the

survival probability of the system in the resonant state) [21, 54]. The auto-ionization and pre-dissociation probabilities of electronically excited molecular states also exhibit a strong isotopic effect [68]. The cross-section information on the processes that show isotope effects for the heavier hydrogen isotopes is presently very limited.

In Sects. 19.2 and 19.3 we have emphasized the important role of processes involving vibrationally excited molecular species in the edge/divertor plasma kinetics. Evidence exists from several Tokamaks (TEXTOR, ASDEX Upgrade, etc) that hydrogen molecules in edge/divertor plasmas may be also rotationally highly excited. An important parameter in the dynamics of all inelastic electron-molecule collision processes is the transition energy between initial and final reaction states. High rotational excitations within a given initial vibrational state can significantly change (decrease) the value of transition energy and thereby affect the corresponding inelastic cross-section (decrease its threshold and increase its magnitude). Rotational excitation of excited molecular states may also significantly affect (in general, increase) their auto-ionization and pre-dissociation probabilities. The completion of major gaps in the present collisional H/H_2 database (Sect. 19.4), its extension to heavier hydrogen isotopes, and inclusion of the effects of rotational excitation of molecular species are the desirable lines of its future developments.

References

1. C.D. Boley, R.K. Janev, D.E. Post, Phys. Rev. Lett. **52**, 534 (1984)
2. R.C. Isler, Phys. Rev. Lett. **38**, 1359 (1977); V.V. Afrosimov et al., JETP Lett. **28**, 501 (1979); R.J. Fonck et al., Appl. Phys. Lett. **42**, 239 (1983)
3. R.K. Janev, M.F.A. Harrison, H. W. Drawin, Nucl. Fusion **29**, 109 (1989)
4. D.H. McNeill, J. Nucl. Mater. **162-164**, 476 (1989); D. Reiter et al., J. Nucl. Mater. **196-198**, 1059 (1992)
5. U. Fantz, B. Heger, Plasma Phys. Control. Fusion **40**, 2023 (1998); ibid **43**, 907 (2001)
6. C.F. Barnett et al., *Atomic and Molecular Collision Cross-Sections of Interest in Controlled Thermonuclear Research*, ORNL-3113 (1961); revised In: ORNL-3113 (1964). (Oak Ridge National Laboratory, Oak Ridge, Tenn., USA 1961, 1964)
7. C.F. Barnett et al., *Atomic Data for Controlled Fusion REsearch*, Vol. I ORNL-5206 (1977); Vol. II: ORNL-5207 (1980) (Oak Ridge National Laboratory, Oak Ridge, Tenn., USA)
8. K. Takayanagi, H. Suzuki, *Cross-Sections for Atomic Processes*, Vol. 1 (Institute of Plasma Physics, Nagoya University, Nagoya, Japan 1978)
9. E.L. Freeman, E.M. Jones, *Atomic Collision Processes in Plasma Physics Experiments: I*, UKAEA Rept. No. CLM-R137 (Culham Laboratory, Abingdon, England 1974)
10. E.M. Jones, *Atomic Collision Processes in Plasma Physics Experiments: II*, UKAEA Rept. No. CLM-R175 (Culham Laboratory, Abingdon, England 1977)

11. K.L. Bell, H.B. Gilbody, J.G. Hughes et al., *Atomic and Molecular Data for Fusion, Part 1*, UKAEA Rep. No. CLM-R216 (Culham Lab., Abingdon, England 1982)
12. L.C. Johnson, Astrophys. J. **174**, 227 (1972)
13. W.T. Miles, R. Thompson, A.E.S. Green, J. Appl. Phys. **43**, 678 (1972)
14. R.K. Janev, W.D. Langer, K. Evans, D.E. Post, *Elementary Processes in Hydrogen-Helium Plasmas* (Springer-Verlag, Berlin-Heidelberg 1987)
15. *Technical Basis for the ITER Final Design Report*, ITER EDA Documentation Series No 16 (IAEA, Vienna, Austria 1998)
16. R.K. Janev, C.D. Boley, and D.E.Post, Nucl. Fusion **29**, 2125 (1989)
17. R.K. Janev, J.J. Smith, At. Plasma-Mater. Interact. Data Fusion, **4**, 1 (1993)
18. Dz.S. Belkic, R. Gayet, A. Salin, At. Data Nucl. Data Tables **51**, 59 (1992)
19. R.K. Janev, R. Phaneuf, H. Tawara, T. Shirai, At. Data Nucl. Data Tables **55**, 201 (1993)
20. C. Harel, H. Jouin, B. Pons, At. Data Nucl. Data Tables **68**, 279 (1998)
21. R. Celiberto, R.K. Janev, A. Laricchiuta, M. Capitelli, J.M. Wadehra, D.E. Atems, At. Data Nucl. Data Tables **77**, 161 (2001)
22. A. Ichihara, O. Iwamoto, R.K. Janev, J. Phys. B 33, 4747 (2000)
23. A. Ichihara, O. Iwamoto, K. Yokoyama, Atom. Plasma-Mater. Interact. Data Fusion **9**, 193 (2001)
24. P.S. Krstic, D.R. Schultz, R.K. Janev, Phys. Scripta T**96**, 61 (2002)
25. P.S. Krstic, Phys. Rev. A **66**, 042717 (2002)
26. P.S. Krstic, R.K. Janev, Phys, Rev. A **67**, 022708 (2003)
27. A.V. Phelps, J. Phys. Chem. Ref. Data **19**, 653 (1990)
28. P. Bachmann, D. Reiter, Contrib. Plasma Phys. **35**, 45 (1995)
29. P.S. Krstic, D.R. Schultz, Atom. Plasma-Mater. Interact. Data Fusion. **8**, 1 (1998)
30. Atom. Plasma-Mater. Interact. Data Fusion **2** (1992), **3** (1992), **5** (1995), **9** (2001), **10** (2002); Physica Scripta **T28** (1989), **T37** (1991), **T62** (1996)
31. R.K. Janev (ed.), *Atomic and Molecular Processes in Fusion Edge Plasmas* (Plenum Press, New York 1995)
32. R.K. Janev, D.R. Schultz (eds.), Phys. Scripta **T96** (2002)
33. L.A. Vainshtein, I.I. Sobelman, E.A. Yukov, *Excitation of Atoms and Broadening of Spectral Lines*, 2nd edn (Springer-Verlag, Berlin 1998)
34. R.K. Janev, A.A. Mihajlov, Phys. Rev. A **20**, 1890 (1979); ibid **21**, 819 (1980)
35. F. Broullaird, X. Urbain, Phys. Scripta **T96**, 86 (2002)
36. R.J. Bieniek, J. Phys. B **13**, 4405 (1980)
37. P.S. Krstic, R.K. Janev, D.R. Schultz, J. Phys. B **36**, L249 (2003)
38. A.E. Orel, J. Chem. Phys. **87**, 314 (1987); T.A. Jacobs et al., ibid **47**, 54 (1967)
39. E.A. Solovev, J.A. Stephens, R.K. Janev, Atom. Plasma-Mater. Interact. Data Fusion, **9**, 179 (2001)
40. R.E. Olson, Phys. Rev. A**16**, 531 (1977); J. Phys. B**13**, 483 (1980)
41. ORNL Controlled Fusion Atomic Data Centre website: www-cfadc.phy.ornl.gov
42. R.K. Janev, H.P. Winter, W. Fritsch. In: [31], p. 341.
43. Atom. Plasma-Mater. Interact. Data Fusion **6** (1995), **9** (2001), **10** (2002)
44. S. Brezinsek, A. Pospieszczyk et al., J. Nucl. Mater. **313-316**, 967 (2003)
45. R.K. Janev, D.E. Post, W.D. Langer et al., J. Nucl. Mater. **131**, 10 (1984)
46. S.I. Krasheninnikov, A.Yu. Pigarov, D. Sigmar, Phys. Lett. A **214**, 285 (1996); ibid. **222**, 251 (1996)

47. A.Yu. Pigarov, Phys. Scripta **T96**, 16 (2002)
48. J.N. Bardsley, J.M. Wadehra, Phys. Rev. A **20**, 1398 (1979)
49. J.M. Wadehra, Appl. Phys. Lett. **35**, 917 (1979); Phys. Rev. A **29**, 106 (1984)
50. P.S. Krstic, D.R. Schultz, Phys. Rev. A **60**, 2118 (1999); J. Phys. B **32**, 2415, 3485 (1999)
51. R.N. Schwartz, I. Slawsky, K.F. Herzfeld, J. Chem. Phys. **20**, 1591 (1952)
52. D.T. Stibbe, J. Tennyson, Astrophys. J. Lett. **513**, L147 (1999); New J. Phys. **1**, 21 (1998); C.S. Trevisan, J. Tennyson, Plasma Phys. Contrl. Fusion **44**, 2217 (2002)
53. A. Laricchiuta, R. Celiberto, R.K. Janev (2004), in preparation
54. S. Chung, C.C. Lin, E.T.P. Lee, Phys. Rev. A **12**, 1340 (1975)
55. A. Laricchiuta, R. Celiberto, R.K. Janev, Phys. Rev. A **60**, 022707 (2004)
56. I.I. Fabrikant, J.M. Wadehra, Y. Xu, Phys. Scripta, T **96**, 45 (2002)
57. L.A. Pinnaduwage, W.X. Ding, D.L. McCorcle et al., J. Appl. Phys. **85**, 7064 (1999); P.G. Datskos, L.A. Pinnaduwage, J.F. Krelkopf, Phys. Rev. A **55**, 4131 (1997)
58. M. Capitelli, R. Celiberto, A. Eletskii, A. Laricchiuta, Atom. Plasma-Mater. Interact. Data Fusion **9**, 47 (2001)
59. M. Gryzinski, Phys. Rev. A **138**, 305, 322, 336 (1965)
60. E. Bauer, C.D. Bratky, J. Chem. Phys. **43**, 2466 (1965)
61. D. Elizaga, L.F. Errea, J.D. Gorfinkiel et al., Atom. Plasma-Mater. Interact. Data Fusion **9**, 167 (2001)
62. A.C. Allision, A. Dalgarno, At. Data **1**, 289 (1970); T.L. Stephens, A. Dalgarno, J. Quant. Spectrosc. Radiat. Tranfer **12**, 569 (1972)
63. M. Glass-Maujean, P. Quadrelli, K. Dressler, At. Data Nucl. Data Tables **30**, 273, 310 (1984)
64. M. Glass-Maujean, P. Quadrelli et al., Phys. Rev. A **28**, 2868 (1983)
65. H. Abgrall et al., Can. J. Phys. **72**, 856 (1994)
66. W.H. Smith, R. Chevalier, Astrophys. J. **177**, 835 (1972)
67. T.I. Kwok et al., Phys. Rev. A **34**, 1962 (1986); S.L. Guberman, A. Dalgarno, Phys. Rev. A **45**, 2784 (1992)
68. R.S. Berry, S.E. Nilsen, Phys. Rev. A **1**, 395 (1970)
69. J.M. Ajello, D. Shemansky, T.L. Kwok, Y.L. Yung, Phys. Rev. A **29**, 636 (1984)
70. P.M. Guyon, J. Breton, M. Glass-Maujean, Chem. Phys. Lett. **68**, 314 (1979); ibid. **63**, 591 (1979)
71. E.R. Wouters, B. Buijsee, J. Los et al., J. Chem. Phys. **106**, 3974 (1997)
72. R.F. Boikova and V.D. Ob'edkov, Sov. Phys. JETP **27**, 772 (1968)
73. W.D. Robb and L.A. Collins, Phys. Rev. A **22**, 2474 (1980)
74. N. Nakashima, H. Takagi, H. Nakamura, J. Chem. Phys. **86**, 726 (1987); B.K. Sapral, J. Tennyson, Mon. Nat. Roy. Astron. Soc. **236**, 909 (1993)
75. P.S. Krstic, D.R. Schultz, J. Phys. B **32**, 2451 (1999)
76. C.L. Liao, C.X. Liao, C.Y. Ng, J. Chem. Phys. **81**, 5672 (1984); P.M. Guyon et al., Chem Phys. **119**, 145 (1988)
77. T.F. Moran, M.R. Flannery, D.L. Albritton, J. Chem. Phys. **62**, 2869 (1975)
78. J.B.A. Mitchell. In: [31], p. 225, and references therein
79. I.F. Schneider, A. Suzor-Weiner, Contrib. Plasma Phys. **42**, 6 (2002), and references therein
80. H. Takagi, Phys. Scripta **T96**, 52 (2002)

81. V.P. Zhdanov, Optics and Spectroscopy **57**, 1098 (1984)
82. J. Peek, Phys. Rev. **140**, 11 (1965); ibid. **154**, 52 (1967)
83. B. Peart, K.T. Dolder, J. Phys. B **6**, 2409 (1973)
84. F. Linder, R.K. Janev, J. Botero. In: [31], p. 397
85. C.F. Barnett et al., *Atomic Data for Fusion*, Vol. 1, ORNL-6068 V.1 (1990)
86. T.F. Moran, J.R. Roberts, J. Chem. Phys. **49**, 3411 (1968)
87. M.J.J. Eerdem et al., Phys. Rev. A **51**, 3369 (1995)
88. B.M. Smirnov, *Asymptotic Methods in Theory of Atomic Collisions* (Atomizdat, Moscow, 1973). (In Russian)
89. J.B.A. Mitchell, At. Plasma-Mater. Interact. Data Fusion **9**, 97 (2001)
90. S. Datz, M. Larsson et al., Phys. Rev. Lett. **74**, 896 (1995); Phys. Rev. A **52**, 2901 (1995)
91. K.C. Kulander, M.F. Guest, J. Phys. B **12**, L501 (1979); H.H. Michels, R.H. Hobbs, Astrophys. J. **286**, 27 (1984)
92. B. Peart, K.T. Dolder, J. Phys. B **7**, 1567 (1974); ibid **8**, L143 (1975); F.B. Yousif et al., Phys. Rev. A **44**, 5653 (1991)
93. J.G. Wang, P.C. Stancil, Phys. Scripta **T96**, 86 (2002)

20 Partial and Differential Electron Impact Ionization Cross-Sections for Small Hydrocarbon Molecules

G. Gluch, S. Feil, P. Scheier, W. Schustereder, T. Tepnual, L. Feketeova, C. Mair, S. Matt-Leubner, A. Stamatovic, and T.D. Märk

Total and partial cross-sections for electron impact ionization of CH_4 (and other hydrocarbon molecules) were determined from threshold to 1000 eV. Ion kinetic energy distributions were measured applying a deflection and retarding field method. The extraction of ions from the ion source was simulated fully three dimensionally including the presence of a guiding magnetic field for the electrons. Thereby discrimination factors were determined as a function of the initial ion kinetic energy. Multiplication of these factors with the ion signal leads to accurate relative partial cross-sections. By normalizing the sum of these partial cross-sections to an absolute value for the total cross-section taken from the literature absolute partial cross-sections were obtained that agree well with previous measurements where a complete collection of the product ions has been demonstrated. In addition, with the present method it is possible to determine cross-sections that are differential with respect to the initial kinetic energy of the ion.

20.1 Introduction

Because of obvious advantages (low radiative capacity and high heat resistivity) carbon based materials are today widely used in current tokamaks. Moreover, these materials (e.g., in form of graphite or carbon-carbon composites) are also being considered as one of the plasma facing materials in the divertor design of the International Thermonuclear Experimental Reactor (ITER) [1]. The interaction of the hydrogenic tokamak plasma with these carbon based walls will however, lead to the production and release of a variety of hydrocarbon molecules and ions. In subsequent collisions in the plasma (with electrons and protons) including ionization, dissociation and recombination reactions, these compounds will be further modified. Under typical divertor plasma conditions (with temperatures in the range of about 1–20 eV) fragmentation processes leading to their atomic counterparts H and C and H^+ and C^+ may not be so effective, therefore leading to a situation where these heavier hydrocarbons will be transported into the adjacent plasma and thus must be considered in any diagnostics of these plasma regions.

It is interesting to note that in two recent workshops dedicated to the atomic and molecular data situation for tokamak fusion science [2] it tran-

spired in a very clear fashion that many more data (i.e., more accurate and in a wider range than previously considered) are urgently needed on these processes in particular at the eve of starting the most challenging period in fusion research with the imminent construction of ITER. For instance; chemical erosion of carbon based wall materials by formation of hydrogen and hydrocarbon molecules is a crucial issue in tokamaks with respect to target lifetime and tritium retention by co-deposition. Unfortunately, there exist still large uncertainties in the dependence of chemical erosion on the various plasma parameters. One way to determine these properties is to measure/simulate the photon-efficiency S/XR or D/XB involving modeling of the hydrocarbon transport and the CD emission. In the past the data compilation of the Ehrhardt and Langer report [3] were used for this purpose, but as shown recently [4] using newer data increases the D/XB values dramatically up to a factor of about 60 and concomitantly calculated re-deposition decreases by a factor of up to about 100. This results in much longer lifetimes of these hydrocarbons. This shows conclusively the necessity of improved data sets for hydrocarbons, important contributions to the released fluxes coming from systems as large as C_3H_8 (see [5]). In a similar fashion Janev and Reiter [6] argued recently, that there are several sub-components to this problem (i.e., the use of carbon because of its low atomic mass and its capability to withstand high heat fluxes despite the carbon re-deposition and tritium co-deposition problem) such as (i) large scale convection in the SOL, (ii) the source of carbon at the walls, and (iii) the plasma chemistry and neutral hydrogen transport. In order to separate the former two from the third, by means of numerical plasma edge simulation codes, a detailed and accurate knowledge of the cross-sections of the relevant plasma chemical processes is required including among others electron impact ionization and dissociation.

Dissociative ionization of molecules induced by electron impact is an important process not only in edge plasmas in fusion reactors, but also in many other areas such as low-temperature plasmas, radiation chemistry, mass spectrometry, and chemical analysis [7–12]. Ionic and neutral fragments produced via dissociative ionization often carry substantial amounts of kinetic energy, and the kinetic energy distribution of a particular fragment determines the energy deposition and the energy transfer pathways in the corresponding media. Thus, the modeling of environments where dissociative ionization processes are important requires knowledge not only of the production efficiency and the nature of fragment ions produced (in terms of partial ionization cross-sections) but also of their kinetic energy distribution (in terms of cross-sections differential in ion kinetic energy, i.e., energy differential cross-sections). Furthermore, different dissociation pathways leading to the formation of the same fragment ion may have different threshold energies and thus different exothermicities. Therefore the kinetic energy distribution for a given fragment ion can depend strongly on the electron energy.

Fragment ions that are formed with high kinetic energies often are collected in ion sources of experiments to investigate cross-sections with consid-

erably reduced efficiency and this fact has a strong influence on the cross-section values determined [13–16]. Nevertheless, recently specially dedicated instruments were constructed to assure complete collection efficiency thus allowing to measure accurate absolute partial and total cross-sections [17, 18]. With commercial instruments comparable results can only be obtained if the discrimination factor for high energetic fragment ions is determined. For a standard double focusing two sector field mass spectrometer equipped with a modified Nier-type ion source Poll et al. [13] demonstrated that ion trajectory calculations of the extraction region of this ion source allows the determination of the corresponding ion loss. After correction of the ion efficiency curves with these discrimination factors the agreement with the above mentioned data from the specially dedicated instruments is extremely good. In order to get information on the kinetic energy of the ions a deflection method was applied in the direction perpendicular to the plane of the mass spectrometer. The present work is an extension of this method and in contrast to Poll et al. [13] the kinetic energy distribution of the fragment ions is used to determine for the first time ion kinetic energy differential cross-sections for these fragment ions. Furthermore, highly energetic ions like H^+ and H_2^+ were measured here too which was not possible in the study of Poll et al. [13]. The determination of the kinetic energy distributions of the fragment ions as a function of the electron energy allows to distinguish between different ionization processes that lead to the production of a given fragment [19, 20]. Hydrocarbon molecules are known to form fragment ions with broad kinetic energy distributions ranging from thermal energies to many electronvolts [13, 19, 21–23]. This is especially true for light fragment ions such as H^+ and H_2^+ as a result of the momentum conservation. In some cases, such as, for instance, propane, many of the energetic ions are formed with higher probabilities than the thermal ions (see, e.g., Poll et al. [13] and references cited therein).

Hydrocarbon molecules are abundant constituents of planetary atmospheres and major compounds in combustible gas mixtures and in fusion edge plasmas [7–11]. Methane is the simplest of these hydrocarbon molecules. Acetylene, C_2H_2, is the simplest hydrocarbon molecule that contains 2 carbon atoms. Thus absolute total and partial photon [24–27] and electron [15, 28–34] ionization cross-sections and nascent fragment ion energy distributions [19, 20, 28, 36–40] have been studied extensively for these molecules. For the deuterated methane molecule electron impact ionization and dissociative ionization cross-sections were determined for the CD_x (x=1−4) molecule and radicals applying a fast neutral beam technique [41]. Electron impact total ionization cross-sections have been determined also theoretically applying the BEB (Binary-Encounter-Bethe) model [42], the DM (Deutsch-Märk) method [43] and the JK (Jain-Khare) method [44]. Partial electron impact ionization cross-sections were calculated for methane [45, 46] as well as total electron impact cross-sections for various CH_x radicals [47]. The dissocia-

tion pathways of partially and fully deuterated acetylene were investigated to obtain information of one of the smallest dications, i.e., $C_2H_2^{2+}$ [39, 40].

All previous studies [19, 20, 34, 37, 48–50] found that essentially all fragment ions of hydrocarbon molecules are formed with complex energy distributions with two major components, a low-energy component comprised of thermal and/or quasi-thermal ('slow') ions with maximum kinetic energies of ~ 0.3 eV and energetic ('fast') ions with a broad energy distribution from 0.5 eV to ~ 10 eV. It has been suggested that several dissociation pathways contribute to the formation of the various fragment ions, as demonstrated by the different appearance energies that were measured for the respective slow and fast component in the kinetic energy distribution of a given fragment ion [20, 50].

20.2 Experimental

The presently used apparatus is a double focusing Nier-Johnson two-sector-field mass spectrometer of reversed geometry with a Nier-type electron-impact ion source and has been described in detail in earlier publications [6, 16, 40, 51]. Figure 20.1 shows the experimental setup schematically. The lower part of the figure displays cuts through images of the ion source as it was used for the ion trajectory simulations, performed utilizing SIMION 7.0 [52] for Windows. The potential array includes more than 16 million points and the maximum deviation from the real ion source is less than 5%. In addition some contour lines of the electrostatic potential are displayed together with 500 ion trajectories. On the left side a weak penetrating field is used for the ion extraction whereas on the right side the pusher and the first two lenses generate a homogeneous electric field in the ion source housing that extracts the ions much more efficiently. The initial kinetic energy of the fragment ions simulated in this figure is 1 eV. The filament was set in the present simulations 100 V lower than the ion source housing (resulting in an electron energy of 100 eV) and the wehnelt (a box surrounding the filament that generates a narrow electron beam and reduces its energy spread) is set 100 V higher than the ion source potential. The small size of the opening where the electrons enter the ion source housing reduces the influence of the filament and wehnelt, thus the potential field on this side of the ion source is practically undisturbed. In contrast, the opening where the electrons leave the ion source and are collected in a faraday cup, is much larger and thus the faraday cup that is set 24 V higher than the ion source disturbs the potential field in the ion source housing substantially close to the opening. The effect of the faraday cup is especially strong in the case of a weak penetrating extraction field. Ions that are generated close to the opening of the faraday cup are pushed into the center of the ion source and towards the extraction slit. Thereby these ions gain an additional component to their initial velocity into the z-direction and generate an artifact peak in the z-profile. Fortunately this

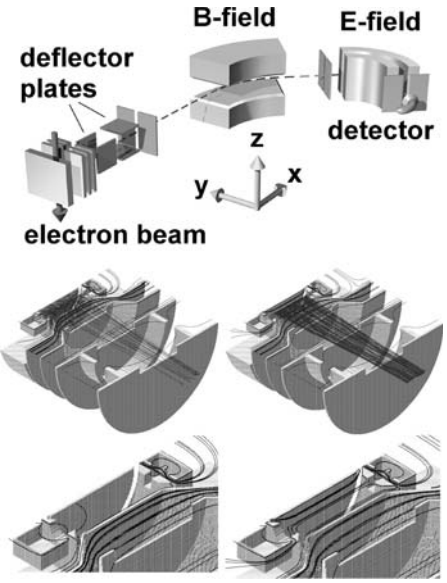

Fig. 20.1. Schematic view of the experimental setup. The two pairs of parallel plates for deflection of the ion beam perpendicularly to the beam direction are designated as deflector plates. **Below** sectional scans through the ion source, used for the ion trajectory simulations, are shown. On the **left** side a weak penetrating field, formed by the third lens from the front, is extracting a small fraction of ions having an initial kinetic energy of 1 eV. On the **right** side a homogeneous extraction field generated with the front and back side of the ion source housing extracts about 10 times more ions. The contour lines of the electrostatic potential are drawn as *thick lines* for both modes of operation. The simulation includes the potential fields formed by the filament (100 eV electron energy), wehnelt and faraday cup (+24 V higher than the ion source housing)

peak is only located at one side of the z-profile and well separated from the regular peak. This is the reason why usually only slightly more than one half of the complete z-profiles needs to be measured.

Stagnant target gas is crossed by a well-characterized magnetically collimated electron beam with a FWHM energy spread of ~ 0.5 eV. The purity of the methane used was 99.995% and of the acetylene 99.9%. Product ions are extracted from the ion source either by a weak penetrating electric field (typically 50 V/m) or by a strong homogeneous electric field (5 kV/m), generated with the lenses that build the front and back side of the interaction region of the electron beam with the neutral molecules, and accelerated to 3 kV. Before entering the analyzing part of the mass spectrometer through a narrow entrance slit the ions pass two pairs of perpendicular deflection plates that allow in principle a steering of the ion beam. For cross-section measurements these deflection plates are used to sweep the totally extracted ion beam across the

entrance slit [53] and integrating the detected ion signal. In all other modes of operation, the deflection plates are not used to sweep the ion beam across the mass spectrometer entrance slit but are kept at fixed voltages and are only used for minor corrections of the ion trajectories to maximize the ion flux into the mass spectrometer. After passing through a magnetic sector field followed by an electric sector field the ions are detected by a secondary electron multiplier operated in a counting mode. The combined action of the two sector fields in a double focusing mass spectrometer results in a focusing of the ions within the plane of the instrument that accounts for angular and spatial spreads of the starting points of the ions and for small variations in the kinetic energy. However, the only way to compensate a velocity component outside of the plane of the instrument (z-direction, see Fig. 20.1) are the so called z-deflector plates right after the ion source. The ion yield measured as a function of the z-deflection voltage allows, in addition, to integrating the ion current over the z-direction (see above) the determination of the kinetic energy distribution for a given fragment ion [13, 19]. However, the normally applied weak extraction field cannot extract fragment ions that have initial kinetic energies into the z-direction larger than 100 meV (see the ion trajectory simulations shown in Fig. 20.1). With the pusher (located in the back of the ion source and the first lenses that form the front of the interaction region of the electrons and the neutral molecules, it is possible to generate a strong homogeneous electric field that is able to extract even the ions with highest initial kinetic energy into the z-direction. This mode of operation has to be chosen to determine accurate kinetic energy distributions of swift fragment ions. A detailed description of the procedure needed to deduce the kinetic energy distribution from a z-profile (ion yield versus z-deflector voltage) will be published soon.

20.3 Results

Mass spectra of methane and acetylene, ionized by electrons of 100 eV kinetic energy, are shown in Fig. 20.2. The electron current was set to 10 μA and the hydrocarbon pressure in the ion source was 6×10^{-5} Pa. Ions originating from the residual gas in the background (9×10^{-7} Pa) were subtracted by mass spectra that were measured without hydrocarbon gas in the inlet system. The mass spectra were not corrected for discrimination effects due to initial kinetic energies of fragment ions and thus the peak heights do not correlate with the cross-section values for this electron energy. The electron impact ionization cross-sections and kinetic energy distributions for all ions that are labelled in the mass spectra are shown in this study. At a mass per charge ratio of 3 and 6 the H_3^+ and C^{2+} ions can be identified, however, the ion intensity for these ions is too low for further analysis. It is interesting to note that in case of methane the relative ion yield for H_3^+ and C^{2+} normalized to the CH_4^+ parent ion agrees well with the corresponding values published by

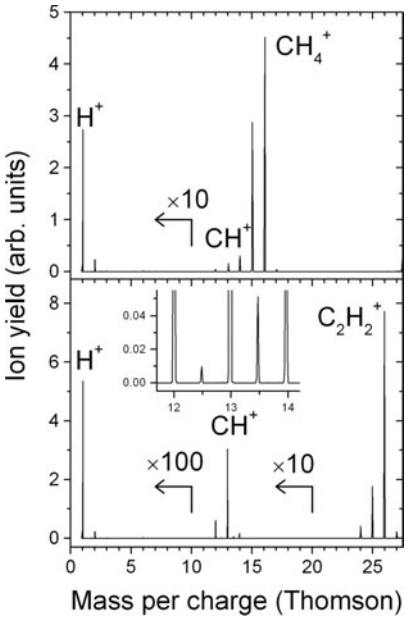

Fig. 20.2. The **upper** part shows the positive ion mass spectrum of CH_4 and the **lower** part the positively charged product ions of C_2H_2. The electron energy was set in both cases to 100 eV and an electron current of 10 µA was used. The pressure in the ion source was 6×10^{-5} Pa and the gas was thermalized at a temperature of 500 K. The *arrows* indicate that the ion signal was multiplied with a factor of 10 and 100, respectively, for mass per charge ratios lower than the position indicated by the vertical line at the beginning of the arrow. The insert in the lower part shows the doubly charged ions $^{12}C_2H^{2+}$ and $^{13}C^{12}CH_2^{2+}$ that hardly can be seen in the complete mass spectrum due to the low intensity. Both mass spectra were not corrected for reduced ion extraction and detection efficiency

Ben-Ithzak et al. [38] for proton impact ionization at a projectile energy of 4 MeV. The mass spectrum of C_2H_2 clearly reveals the presence of doubly charged ions at mass per charge ratios of 12.5 and 13.5 resulting from C_2H^{2+} and $^{13}C^{12}CH_2^{2+}$, respectively (see insert in Fig. 20.2). From the abundance of the latter one it is possible to determine the amount of the doubly charged ion $^{12}C_2H_2^{2+}$ that overlaps with $^{12}CH^+$ at a mass per charge ratio of 13. At electron energies higher than 50 eV it turns out that the ion yield of the doubly charged ion is the major contribution to the peak at 13 Thomson.

Figure 20.3 shows ion beam profiles in the z-direction of the parent ions CH_4^+ and $C_2H_2^+$ in comparison to Ar^+, taken at an electron energy of 100 eV. From these curves ion kinetic energy distributions were derived and are shown below the z-profile diagram. For this, in principle, the first derivative of the z-profile has to be plotted as a function of the square of the z-deflection voltage and multiplied by a factor that is determined by the geometry of the

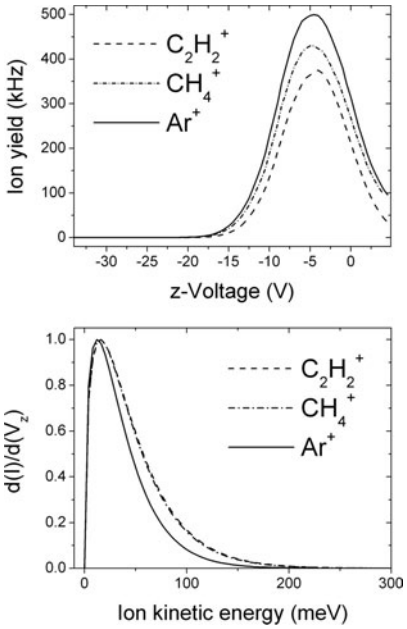

Fig. 20.3. The **upper** diagram shows the ion beam profiles of the CH_4^+ and $C_2H_2^+$ parent ions and Ar^+ in the z-direction. The ion signal was measured as a function of the voltage on the z-deflector pair. The electron energy was set to 100 eV. In the **lower** diagram the initial ion kinetic energy distributions were calculated from these z-profiles and compared to Ar that has been introduced as a cold gas jet

deflector plates and the acceleration voltage of the mass spectrometer (for details see [13,54]). The kinetic energy of these ions is only determined by the ion source temperature that was 500 K throughout the present investigations. The difference between the Ar^+ and the two hydrocarbon parent ions can be explained by two reasons: (i) Ar was introduced as a narrow collimated gas jet that could not get into thermal equilibrium with the ion source and thus the temperature of the neutral atoms was much colder than 500 K. (ii) both, the methane and acetylene, parent ions have the same mass per charge ratio as the first fragment ions that contain one ^{13}C isotope, i.e., $^{13}CH_3^+$ and $^{13}C^{12}CH^+$. These fragment ions will contribute with $\sim 1\%$ and 2% to the $^{12}CH_4^+$ and $^{12}C_2H_2^+$ ion signals, respectively. Those fragment ions have a higher average kinetic energy than parent ions and thus widen the z-profiles of the $^{12}CH_4^+$ and $^{12}C_2H_2^+$ ions. The $^{13}CH_4^+$ and $^{13}C_2H_2^+$ ions are parent ions that cannot be contaminated with fragment ions, however, the ion yield is about two and four orders of magnitude smaller than for the ^{12}C containing molecules, respectively. Figure 20.4 shows the z-profiles and kinetic energy distributions of $^{13}CH_4^+$ and $^{12}CH_4^+$ compared to argon that was introduced through a molecular beam source and the same stagnant gas inlet as the hydrocarbon

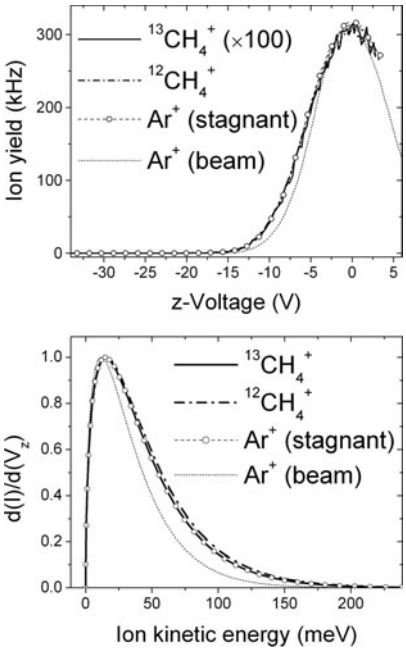

Fig. 20.4. The **upper** panel shows the ion beam profiles in the z-direction of $^{12}CH_4^+$ and $^{13}CH_4^+$ in comparison to Ar^+ introduced as a stagnant gas target and as a molecular beam. The ion signal was measured as a function of the voltage on the z-deflector pair. The electron energy was 100 eV for all four measurements. In the **lower** diagram the initial ion kinetic energy distributions were calculated from the z-profiles

molecules. The average kinetic energies of all ions presented in this paper are listed in Table 20.1. Both, the ion kinetic energy distributions and the average kinetic energy values indicate that the lower temperature of Ar, if introduced as a molecular beam, is responsible for the discrepancy shown in Fig. 20.3.

Figure 20.5 shows the z-profiles of the fragment ion CH^+ from both molecules, measured at two different electron energies, i.e., 30 eV and 80 eV. The lower part displays the ion kinetic energy distributions that were derived from these z-profiles. The CH^+ fragment ion produced by electron impact to CH_4 has a narrow Maxwell–Boltzmann type kinetic energy distribution that becomes wider with increasing electron energy. In contrast, the same ion originating from C_2H_2 reveals a more complex and much wider kinetic energy distribution. It consists of two distinct contributions, one Maxwell–Boltzmann part with an average energy of about 150 meV and a high energy part with an average kinetic energy of about 750 meV. Such a high initial kinetic energy is the typical result of an electronically excited state or a Coulomb repulsion of two fragment ions formed by dissociation of a multiply charged precursor ion. Furthermore, an additional low kinetic energy contri-

Table 20.1. Average ion kinetic energies derived as the first momentum of the ion kinetic energy distributions shown in Fig. 20.3, 20.4, 20.5 and 20.7

	ion	average ion kinetic energy (meV)
Figure 20.3	$C_2H_2^+$	47
	CH_4^+	46
	Ar^+ (beam)	38
Figure 20.4	$^{13}CH_4^+$	44
	$^{12}CH_4^+$	46
	Ar^+ (stagnant)	44
	Ar^+ (beam)	36
Figure 20.5	CH^+ / C_2H_2 (80 eV)	702
	high energy part	873
	low energy part	157
	$C_2H_2^{2+}$	42
	CH^+ / C_2H_2 (30 eV)	503
	high energy part	678
	low energy part	133
	CH^+ / CH_4 (80 eV)	127
	CH^+ / CH_4 (30 eV)	97
Figure 20.7	C^+ / C_2H_2	554
	high energy part	926
	low energy part	165
	C^+ / CH_4	146
	high energy part	165
	low energy part	54
	H^+ / C_2H_2	1093
	high energy part	1547
	low energy part	402
	H^+ / CH_4	867
	high energy part	1194
	low energy part	322

bution can be seen at 80 eV electron energy with an average energy value of about 40 meV. This indicates the presence of a parent ion, i.e., the doubly charged acetylene, $C_2H_2^{2+}$. Note that the kinetic energy distribution of the doubly charged acetylene shown in Fig. 20.5 was divided by a factor of 5 and it was omitted in the total kinetic energy distribution of the CH^+ determined at an electron energy of 80 eV.

The potential curves displayed in Fig. 20.6 schematically show the possibilities for the production of highly energetic fragment ions. Depending on the internuclear distance of the neutral molecule that defines the Franck–Condon region and the electronic state that will be reached by the electron impact

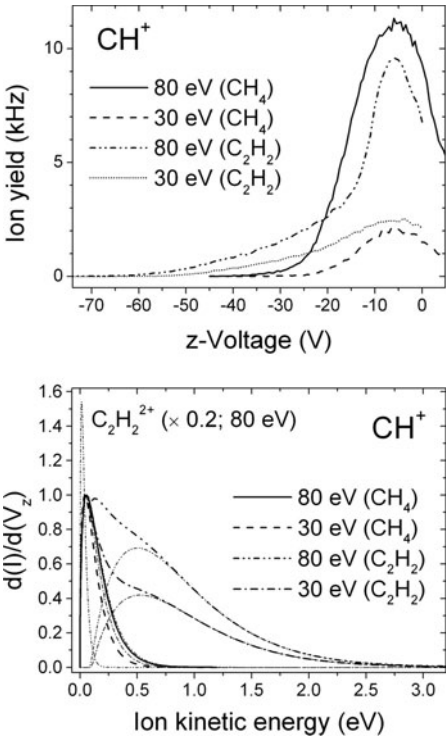

Fig. 20.5. The **upper** panel shows the ion beam profiles of the CH^+ fragment ion in the z-direction. The ion signal was measured as a function of the voltage on the z-deflector pair. Different line styles designate different electron energies and different neutral precursor molecules. In the **lower** diagram the initial kinetic energy distributions are displayed that were calculated from the z-profiles shown above. CH^+ originating from methane reveals a single Maxwell-Boltzmann type energy distribution whereas the initial kinetic energy distribution of the same fragment ion originating from acetylene can be into two parts (designated as *thin lines*). The sum of the two contributions is displayed as a *thick line* in the same line style

a fragment ion is formed with substantially different initial kinetic energies. Often fragmentation channels that need high electron energies to become possible lead to high kinetic energies of the fragment ion. This is especially true for the dissociation of multiply charged ions into two or more fragment ions. Furthermore, momentum conservation defines the distribution of the total energy that is released during a dissociation process among the fragments. Thus light fragment ions generally reveal wide kinetic energy distributions and wide z-profiles. Contrary to the expected widening of the kinetic energy distribution at higher electron energies a significant contribution with extremely low kinetic energy is observed for CH^+ from acetylene at an electron energy of 80 eV that was not present at 30 eV (see also above). The answer to

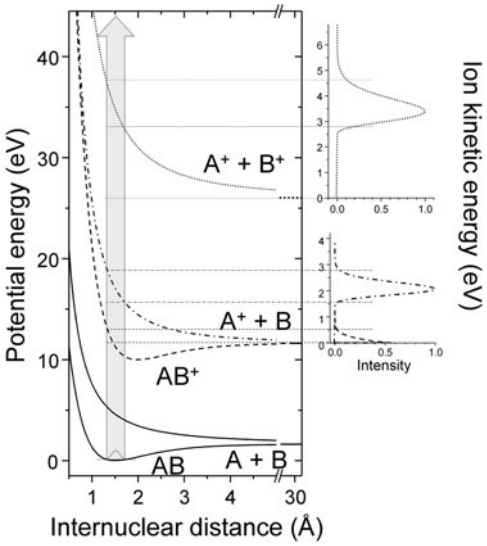

Fig. 20.6. Potential energy diagram displaying the potential energy curves of the neutral, singly and doubly charged molecule AB. The *shaded* region represents the Franck–Condon region. The internuclear distance of the molecule AB has a strong influence on the kinetic energy of the separating fragments

this surprising result can be found in the mass spectrum of C_2H_2. At an electron energy of 80 eV the doubly charged ion $C_2H_2^{2+}$ is responsible for more than 50% of the ion yield at a mass per charge ratio of 13 Thomson. This dication is a parent ion and free of any kinetic energy contributions due to dissociation processes. The appearance energy of the $C_2H_2^{2+}$ is 32.7 eV [54] and therefore, this narrow part of the z-profile is missing at 30 eV electron energy.

In the upper part of Fig. 20.7 we show the ion yields of C^+ and H^+ as a function of the z-deflection voltage, measured at an electron energy of 100 eV. In the lower part the ion kinetic energy distributions that were derived from these z-profiles are displayed. The kinetic energy distribution of both ions consists of two parts and the high energy component reaches up to several eV, thus indicating Coulomb repulsion of the ionic fragments of a multiply charged precursor ions.

According to ion trajectory calculations, ions with such high initial kinetic energies into the z-direction will be displaced roughly 4 mm from the beam axis when they reach the z-deflector. However, the distance between the two plates of the z-deflector is less than 5 mm. The present experimental setup starts to loose those ions being emitted into the z-direction at initial kinetic energies larger than 2 eV. Thus only ions starting into the direction of the mass spectrometer (x-direction) will be transmitted. Fiegele et al. [23] demonstrated recently the possibility of ion kinetic energy analysis with a sector field mass spectrometer applying a retarding field method. The same

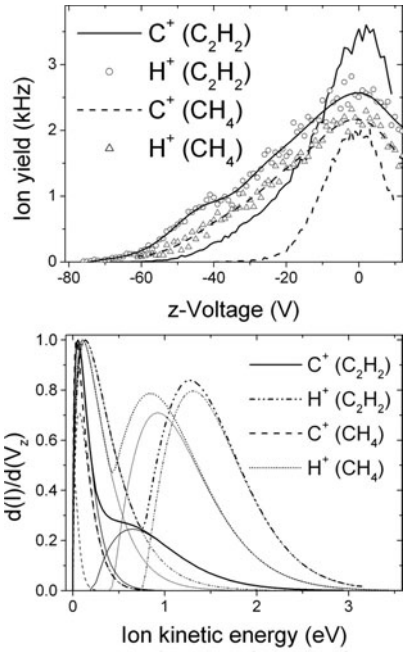

Fig. 20.7. The **upper** panel shows the ion beam profiles of the C^+ and H^+ fragment ions in the z-direction, produced by electron impact ionization of methane and acetylene at an electron energy of 100 eV. The ion signal was measured as a function of the voltage on the z-deflector pair. In the **lower** diagram the initial kinetic energy distributions are displayed that were calculated from the z-profiles shown above. The initial kinetic energy distribution of both fragment ions consist of two parts designated as *thin lines*. The sum of the two contributions represents the total initial kinetic energy distribution and is displayed as a *thick line* in the same line style

experimental setup that was used in [23] has been applied recently for the ion kinetic energy analysis of the fragment ions from methane [34]. For C^+ the agreement between the retarding field method and the z-profile analysis was very good, however, the high energy peak of the H^+, resulting from a dissociation of a doubly charged precursor ion could not be observed by the z-deflection method due to discrimination effects discussed above.

Latimer et al. [20] determined in their study concerning the synchrotron ionization of CH_4 the kinetic energy of the H^+ fragment as a function of the photon energy in the range between 12 eV and 60 eV. Their energy spectra of fragment protons and deuterons exhibit three different contributions. The low energy part starts below the $(2a_1)^{-1}$ threshold at 22.4 eV and indicates the existence of autoionizing Rydberg states which converge to the A state from below. These Rydberg states have been observed previously in the production of excited H atoms by electron impact [55]. At photon energies higher than

26.6 eV, all the $(2a_1)^{-1}$ states are accessible and the fragment protons and deuterons appear with a group of energies centered at 2.2 eV. In electron impact experiments a similar group with an energy around 2.35 eV has been observed [22]. Finally, at photon energies higher than 35 eV, the threshold for double photo-ionization [56], Latimer et al. [20] detected an additional group of protons having an average kinetic energy of 3.7 eV. This energy, however, turns out to be much smaller than the average kinetic energy of H^+ from ion pair formation obtained by proton impact [38] or another photo-dissociation study by Fournier et al. [57] yielding a value of about 6 eV. Except for the high energy part exceeding 3 eV the ion kinetic energy distribution of H^+ determined with the retarding potential method agrees well with the results published by Latimer et al. [20]. A possible reason for the differences at high kinetic energies could be a reduced ion detection efficiency of the experimental setup used in [20]. It is interesting to note that the third group consisting of these high energetic ions of the present study has an average kinetic energy of about 6 eV which agrees well with the proton impact results of Ben-Itzhak et al. [38] and the photo-ionization study of Fournier et al. [57].

In previous investigations it was pointed out that high kinetic energies of fragment ions have a strong influence on the ion collection efficiency and thus on resulting cross-sections derived from ion efficiency curves [2, 13–18]. Poll et al. [13] calculated discrimination factors for ions with different initial kinetic energies performing ion trajectory simulations of their ion source, a similar experimental set-up as the one in the present investigation. These previous calculations neglected the presence of a magnetic field for guiding the electrons. In [34] the effect of this magnetic field having a field strength of about 40 mT was included in a refined ion trajectory simulation that clearly revealed for H^+ and to a smaller degree also for H_2^+ a substantial deflection of the ions into the y-direction due to the magnetic field. Furthermore, the lack of computer memory at that time forced Poll et al. [13] to approximate the ion source with an planar and symmetric geometry. Applying a newer version of SIMION [52] and utilizing modern computers with 1 GB RAM the extraction of the ions out of the Nier-type ion source was simulated here with increased resolution of the potential array (see Fig. 20.1; geometric deviations to the real ion source are less than 5%). Furthermore, no approximations of planar or spherical geometry were made – the lenses were treated fully three-dimensional. In addition to the simulations that were performed recently in [34], the electrostatic fields generated from the filament, the wehnelt and the faraday cup that is used for measuring the electron current passing the ion source, are included in the present simulations. Thereby more reliable discrimination factors were derived.

Figure 20.8 shows the resulting correction factors for H^+ derived from the present simulations, including a magnetic field of 37 mT in the center part of the ion source, in comparison to the values published by Poll et al. [13] and Gluch et al. [34]. In contrast to [13] and based on the findings in [34] for each electron energy and each ion a characteristic discrimination

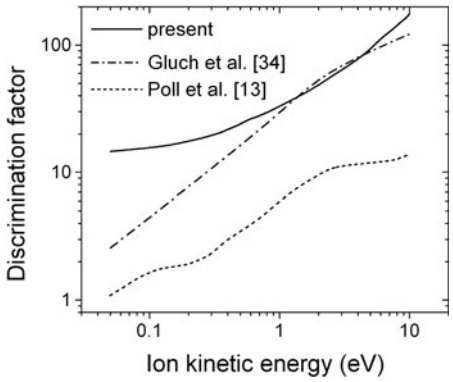

Fig. 20.8. Discrimination factor as a function of the initial kinetic energy of a fragment ion obtained by ion trajectory simulations. For the present simulations the ion source and the electrostatic lenses were treated fully three-dimensionally (see Fig. 20.1) and the maximum deviation from the real ion source was less than 5%. The *dashed line* represents the discrimination factors that were derived by Poll et al. [13] approximating the lenses infinitely long in the z-direction. The *dash-dotted line* are the discrimination factors that were derived in [34]. The potential array was more than a factor 10 smaller (less RAM of the computer) and thus the differences between simulation and reality were in the order of 15%

factor was derived from the corresponding z-profile. In addition the present discrimination factors were determined using the complete kinetic energy distributions and not only the first momentum of the curve. Thereby a more reliable cross-section value can be obtained since the correction factor is not a linear function of the kinetic energy (see Fig. 20.8).

Multiplying the mass selected ion signal at each electron energy with the corresponding discrimination factors the resulting ion signal becomes proportional to the relative partial cross-section. Adding up all ion signals the resulting sum is proportional (with the same factor) to the total electron impact ionization cross-section. At an electron energy of 100 eV we determined this calibration factor (summation method, see [8]) by normalizing our relative total cross-section to the absolute total cross-section of Rapp and Englander Golden [58]. Using this same normalization factor absolute partial cross-sections for CH^+, C^+ and H^+ from both precursor molecules were derived and are shown in Fig. 20.9. For comparison, the diagrams in Fig. 20.9 also include some of the previously published partial cross-sections for CH_4 and C_2H_2 product ions formed by electron impact. The agreement to the data determined with specially designed instruments for complete ion collection efficiency [14, 15] is for all ions reasonably good. In contrast the values published by Adamczyk et al. [16] and Chatham et al. [28] are for all fragment ions significantly smaller than the present data and the results reported by [14, 15]. In the case of H^+ the data differ by a factor of 5.

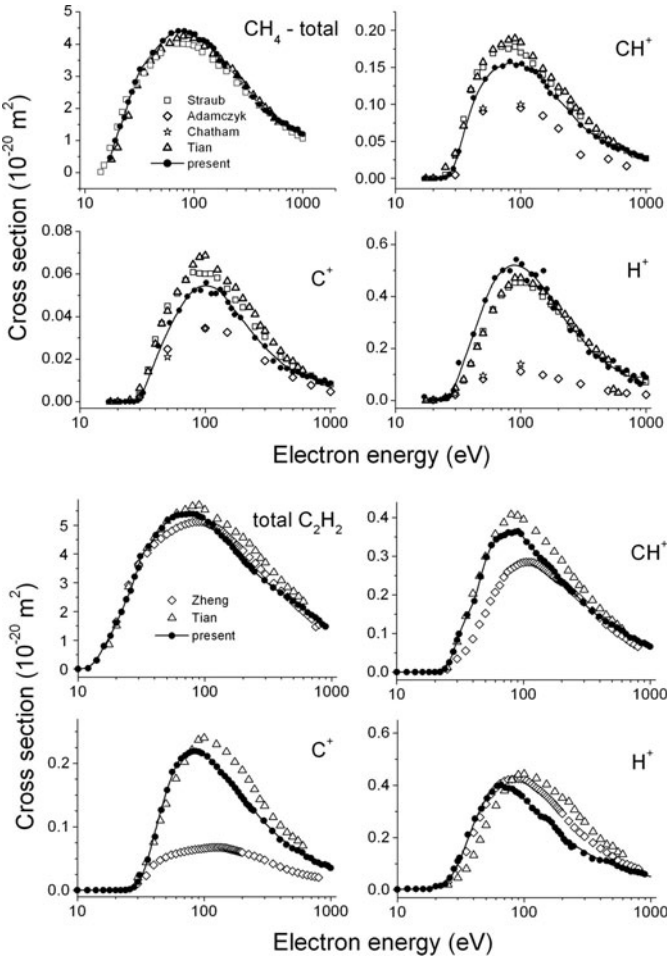

Fig. 20.9. Absolute partial cross-sections for the formation of product ions by electron impact ionization of CH_4 and C_2H_2. The present values (*filled symbols* and *lines*) are compared with data from the literature. There is good agreement with two experiments where complete ion detection was demonstrated (*open square*: Straub et al. [14], *open triangle*: Tian and Vidal [15], and *open diamonds*: Zheng and Srivastava [35])

The perfect agreement to the partial cross-sections that were performed with instruments that were specially designed for cross-section measurements for fragment ions that have initial kinetic energies larger than 5 eV clearly demonstrates the success of the present correction method. Furthermore, this work clearly demonstrates that commercial instruments can be applied for the determination of partial ionization cross-sections. As in the studies by Stebbings and co-workers [14] and Tian and Vidal [15] the present method

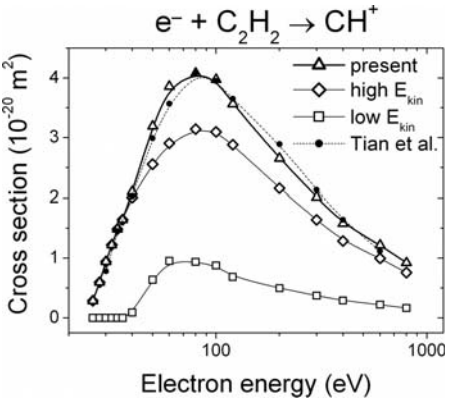

Fig. 20.10. Absolute partial electron impact ionization cross-section differential with respect to the initial ion kinetic energy of the ions having a mass per charge ratio of 13 Thomson, i.e., the CH^+ fragment ion and the doubly charged parent ion $C_2H_2^{2+}$, produced by electron impact ionization of acetylene at an electron energy of 100 eV. The threshold energy of the low kinetic energy contribution, designated with open squares is about 37 eV and represents the ions with an average initial kinetic energy of about 45 meV. The data designated high E_{kin} (*open diamonds*) represent the ions with an average initial kinetic energy of $\sim$ 40 meV and $\sim$ 700 meV. Also shown are the (total) partial cross-sections for CH^+ and $C_2H_2^{2+}$ production, the present values constituting the sum of the low E_{kin} and high E_{kin} data (designated as *open triangles*) and the data by Tian et al. designated by *full dots*

especially in combination with the retarding potential method gives in addition the ion kinetic energy distribution of the fragment ions.

In Fig. 20.10, as an example differential (with respect to the ion kinetic energy) partial cross-sections for the formation of mass 13 from acetylene is shown. The electron energy was set to 100 eV as for the mass spectra shown in Fig. 20.2. The ion yield at a mass per charge ratio of 13.5 Thomson clearly demonstrates the presence of doubly charged $^{13}C^{12}CH_2^{2+}$ and enables the determination of the ion yield of $^{12}C_2H_2^{2+}$ from the isotopic abundance of ^{13}C which is 1.1%. At an electron energy of 100 eV about 50% of the ion yield at 13 Thomson can be attributed to the doubly charged acetylene. However, the mass spectra were not corrected due to reduced ion extraction and detection efficiency. The doubly charged parent ion $C_2H_2^{2+}$ has an initial kinetic energy that is purely determined from the ion source temperature (about 45 meV). In contrast the initial kinetic energy distribution of CH^+ ranges to very high energies when the ion is formed by dissociation of a doubly charged precursor [39, 40] (see Fig. 20.5). Taking into account the discrimination factors shown in Fig. 20.8 the ion yield of the swift fragment ion CH^+ is amplified by about a factor of 3. Already in 1972 Ast et al. [59] observed that in the series of $C_nH_2^{2+}$ ions the dissociation into H^+ and C_nH^+ has a metastable component with microsecond lifetime for n odd, but not for n even. Thissen et

al. [39] determined from their photoelectron-photoion-photoion coincidence (PEPIPICO) studies of the dissociation pathways of $C_2H_2^{2+}$ that the lifetime for deprotonation of doubly charged acetylene is about 80 ns. This lifetime would be too short that such a deprotonation reaction could be observed via mass analyzed ion kinetic energy (MIKE) scans in the second field free region of the presently used instrument. Nevertheless we checked for this reaction and observed a clear MIKE peak for the reaction $C_2H_2^{2+} \rightarrow C_2H^+ + H^+$. From the width of the peak we determined the total kinetic energy that was released (KER) to be 3.8 eV. This value agrees well with the KER values obtained by Thissen et al. [39], especially for lower ionizing photon energies ($h\nu < 38$ eV).

The present study on CH_4 and C_2H_2 was intended as an exploratory study to test the reliability of the methods used and developed in our laboratory (For more details and data on CH_4 see [34]). The agreement with the recent investigations by Straub et al. [14] and Tian and Vidal [15] that were performed with instruments specially designed for partial cross-section measurements clearly demonstrates that it is possible to correct ion efficiency curves measured with a standard instrument for reduced ion collection efficiency. Furthermore, the initial kinetic energy distribution for all product ions can be measured with two different methods, i.e., z-deflection and retarding potential. Due to different processes (ion pair formation or fragmentation of a singly charged precursor ion) the ion kinetic energy distribution of some fragment ions consists of more than one distinct contribution. The ionization threshold for these contributions often differs substantially and gives a hint to the process that leads to the formation of the fragment ion. The present experimental setup enables us also to determine partial cross-sections that are differential with respect to the initial kinetic energy of the ion when it is formed.

Acknowledgement

This work was partially supported by the FWF, ÖNB and ÖAW, Wien, Austria and the European Commission, Brussels. This work has been carried out within the Association EURATOM-ÖAW. The content of the publication is the sole responsibility of the authors and does not necessarily represent the views of the EU Commission or its services.

References

1. Technical basis for the ITER Final Design Report, ITER EDA Documentation Series No. 16 (IAEA, Vienna, Austria 1998)
2. Annual ADAS workshop, Cadarache, 20-22 Oct.2002; and IAEA Technical Meeting on Atomic and Plasma-Material Interaction Data for Fusion Science and Technology, Jülich, 28-31 Oct. 2002
3. A.B.Ehrhardt, W.D.Langer: Report PPPL-2477 (Princeton Plasma Physics Laboratory, USA (1987)

4. A. Kirschner, J.N. Brooks, V. Philipps, P. Wienhold, A. Pospioszczyk, R.K. Janev, U. Samm: IAEA technical meeting on Atomic and Plasma-Material Interaction Data for Fusion Science and Technology, Jülich, 28-31 Oct.2002, P12
5. A.A.Haasz, J.A.Stephens, E.Vietzke, Atom. Plasma-Mater. Interact. Data Fusion **7**, part A, (1998) p. 5
6. R.K.Janev, D.Reiter, Jül-3966, Bericht FZ Jülich, 2002, pp. 1–46
7. L.G. Christophorou (ed.), *Electron Molecule Interactions and their Applications* (Academic Press, Orlando, FL 1984)
8. T.D. Märk, G.H. Dunn (eds.), *Electron Impact Ionization* (Springer, Wien 1985)
9. L.C. Pitchford, B.V. McKoy, A. Chutjian, S. Trajmar (eds.), *Swarm Studies and Inelastic Electron-Molecule Collisions* (Springer, New York 1987)
10. R.K. Janev (ed.), *Atomic and Molecular Processes in Fusion Edge Plasmas* (Plenum, New York 1995)
11. J.P. Mohr, W.L. Wiese (eds.), *Atomic and Molecular Data and their Applications*, AIP Conf. Proc. 434 (AIP, Woodbury, NY 1998)
12. K.Becker (ed.), *Novel Aspects of Electron-Molecule Collisions* (World Scientific, Singapore 1998)
13. H.U. Poll, V. Grill, S. Matt, N. Abramzon, K. Becker, P. Scheier, T.D. Märk: Int. J. Mass Spectrom. Ion Processes **177** (1998) 143
14. H.C. Straub, D. Lin, B.G. Lindsay, K.A. Smith, R.F. Stebbings: J. Chem. Phys. **106** (1997) 4430
15. C. Tian, C.R. Vidal, J. Phys. B: At. Mol. Opt. Phys. **31** (1998) 895
16. B. Adamczyk, A.J.H. Boerboom, B.L. Schram, J. Kistemaker, J. Chem. Phys. **44** (1966) 4640
17. H.C. Straub, P. Renault, B.G. Lindsay, K.A. Smith, R.F. Stebbings, Phys. Rev. A **52** (1995) 1115
18. C. Tian, C.R. Vidal, J. Chem. Phys. **108** (1998) 927
19. R. Fuchs, R. Taubert, Z. Naturforschg. **19a** (1964) 494
20. C.J. Latimer, R.A. Mackie, A.M. Sands, N. Kouchi, K.F. Dunn, J. Phys. B: At. Mol. Opt. Phys. **32** (1999) 2667
21. J. Apell, C. Kubach, Chem. Phys. Lett. **11** (1971) 486
22. R. Locht, J.L. Olivier, J. Momigny, Chem. Phys. **43** (1979) 425
23. T. Fiegele, C. Mair, P. Scheier, K. Becker, T.D. Märk, Int. J. Mass Spectrom. **207** (2001) 145
24. K. Kameta, N. Kouchi, M. Ukai, Y. Hatano, J. Electron Spectrosc. Relat. Phenom. **123** (2002) 225
25. J.A.R. Samson, G.N. Haddad, T. Masuoka, P.N. Pareek, D.A.L. Kilcoyne, J. Chem. Phys. **90** (1989) 6925
26. G. Dujardin, D. Winkoun, S. Leach, Phys. Rev. A **31** (1985) 3027
27. T. Hayaishi, S. Iwata, S. Sasanuma, E. Ishiguro, Y. Morioka, Y. Iida, M. Nakamura, J. Phys. B **15** (1982) 79
28. H. Chatham, D. Hills, R. Robertson, A. Gallagher, J. Chem. Phys. **81** (1984) 1770
29. O.J. Orient, S.K. Srivastava, J. Phys. B: At. Mol. Phys. **20** (1987) 3923
30. E. Krishnakumar, S.K. Srivastava, J. Phys. B: At. Mol. Opt. Phys. **23** (1990) 1893
31. C. Vallance, S.A. Harris, J.E. Hudson, P.W. Harland, J. Phys. B: At. Mol. Opt. Phys. **30** (1997) 2465

32. H.C. Straub, D. Lin, B.G. Lindsay, K.A. Smith, R.F. Stebbings, J. Chem. Phys. **106** (1997) 4430
33. N. Duric, I. Cadez, M. Kurepa, Int. J. Mass Spectrom. Ion Proc. **108** (1991) R1
34. K. Gluch, P. Scheier, W. Schustereder, T. Tepnual, L. Feketeova, C. Mair, S. Matt-Leubner, A. Stamatovic, T.D. Märk, Int. J. Mass Spectrom. **228** (2003) 307
35. S-H. Zheng, S.K. Srivastava, J. Phys. B: At. Mol. Phys. **29** (1996) 3235
36. R. Fuchs, R. Taubert, Z. Naturforschg. **19a** (1964) 1181
37. M.D. Burrow, S.R. Ryan, W.E. Lamb Jr., L.C. McIntyre Jr., J. Chem. Phys. **71** (1979) 4931
38. I. Ben-Itzhak, K.D. Carnes, D.T. Johnson, P.J. Norris, O.L. Weaver, Phys. Rev. A **49** (1994) 881
39. R. Thissen, J. Delwiche, J.M. Robbe, D. Duflot, J.P. Flament, J.D.H. Eland, J. Chem. Phys. **99** (1993) 6590
40. M. Davister, R. Locht, Chem. Phys. **191** (1995) 333
41. V. Tarnovsky, A. Levin, H. Deutsch, K. Becker, J. Phys. B: At. Mol. Opt. Phys. **29** (1996) 139
42. K.K. Irikura, Y.K. Kim, M.A. Ali, J. Res. Nat. Inst. Stand. Tech. **107** (2002) 63
43. H. Deutsch, K. Becker, S. Matt, T.D. Märk, Int. J. Mass Spectr. **197** (2000) 37
44. S.P. Khare, M.K. Sharma, S. Tomar, J. Phys. B: At. Mol. Opt. Phys. **32** (1999) 3147
45. V. Dose, P. Pecher, R. Preuss, J. Phys. Chem. Ref. Data **29** (2000) 1157
46. M.E. Galassi, R.D. Rivarola, M. Beuve, G.H. Olivera, P.D. Fainstein, Phys. Rev. A **62** (2000) 022701
47. K.N. Joshipura, M. Vinodkumar, U.M. Patel, J. Phys. B: At. Mol. Opt. Phys. **34** (2001) 509
48. R. Stockbauer, Int. J. Mass Spectrom. Ion Phys. **25** (1977) 401
49. R. Taubert, Adv. Mass Spectrom. **1** (1959) 489
50. H.E. Stanton, J.E. Monahan, J. Chem. Phys. **41** (1964) 3694
51. H.U. Poll, C. Winkler, D. Margreiter, V. Grill, T.D. Märk, Int. J. Mass Spectrom. Ion Proc. **112** (1992) 1
52. SIMION 7.0, David A. Dahl, Idaho National Engineering and Environmental Laboratory
53. V. Grill, G. Walder, P. Scheier, M. Kurdel, T.D. Märk, Int. J. Mass Spectrom. Ion Proc. **129** (1993) 31
54. J.R. Appling, B.E. Jones, L.E. Abbey, D.E. Bostwick, T.F. Moran, Org. Mass Spectrom. **18** (1983) 282
55. C.Y.R. Wu, D.L. Judge, J. Chem. Phys. **75** (1981) 172
56. P.A. Hatherly, M. Stankiewicz, L.J. Frasinski, K. Codling, Chem. Phys. Lett. **159** (1989) 355
57. P.G. Fournier, J. Fournier, F. Salama, P.J. Richardson, J.H.D. Eland, J. Chem. Phys. **83** (1985) 241
58. D. Rapp, P. Englander-Golden, J. Chem. Phys. **43** (1965) 1464
59. T. Ast, J.H. Beynon, R.G. Cooks, Org. Mass Spectrom. **6** (1972) 749

Index